Evaluating the Variability of Static Carbon Dioxide Storage Capacity Estimates through Integrated Analysis of Reservoir Structure, Aquifer Performance and Thermodynamic Behaviour: Case Studies from Three Depleted Triassic Gas Fields on the UK Continental Shelf

CLARKE, AMY,LOUISE

Evaluating the Variability of Static Carbon Dioxide Storage Capacity Estimates through Integrated Analysis of Reservoir Structure, Aquifer Performance and Thermodynamic Behaviour: Case Studies from Three Depleted Triassic Gas Fields on the UK Continental Shelf

Amy Louise Clarke

A thesis submitted in partial fulfilment of the requirements for the degree of

Doctor of Philosophy at Durham University

Department of Earth Sciences

Durham University

2014

Declaration

I declare that this thesis, which I submit for the degree of Doctor of Philosophy at Durham University, is my own work and not substantially the same as any which has previously been submitted at this or any other university.

Amy L. Clarke
Department of Earth Sciences
Durham University
May 2014

“There is no question that climate change is happening; the only arguable point is what part humans are playing in it.”

Sir David Attenborough

Abstract

Evaluation of the variability of theoretical and effective CO_2 storage capacity estimation within depleted gas reservoirs is dependent on the integrated analysis of reservoir structure, aquifer performance and thermodynamic behaviour.

Four published theoretical CO_2 storage capacity methods and one effective method have been used to estimate the capacity and variability of two Triassic depletion drive reservoirs and two Triassic water drive reservoirs located within the UK Southern North Sea and East Irish Sea Basin. Input parameters to the storage capacity equations have shown a degree of natural variability whereas others are more accurately constrained. As such, attempts have been made to more accurately constrain the most variable input parameters.

The geometric, petrophysical and production characteristics of the reservoirs are analysed. Material balance methods are used to assess the reservoir drive mechanism of the reservoirs. If reservoirs are found to experience a water drive, the aquifer strength is estimated. The gas compressibility factor, gas formation volume factor and CO_2 density is estimated under initial reservoir temperature conditions using six equations of state for comparison of results. These results are then input to storage capacity equations producing a range of estimates.

The most susceptible parameter to variability was the cumulative volume of water influx to a reservoir, W_e. Variability was also found to be the result of error in estimation of the original gas in place. As such, the water drive reservoirs made further use of aquifer modelling to achieve more precise estimates of OGIP and W_e.

The effective capacity coefficients for the various reservoirs have been estimated to assess the proportion of pore space available for CO_2 storage. The effective CO_2 storage capacity constitutes a fraction of the theoretical CO_2 storage capacity which ranges between 0 (no storage possible) and 1 (all theoretically accessible pore volume is occupied by CO_2). Overall, it was found that depletion drive reservoirs have the potential to store greater volumes of CO_2 than water drive reservoirs whose aquifer waters occupy the newly liberated pore space.

Acknowledgements

This project was funded by the National Environment Research Council. Additional funding was provided by Badley Geoscience Ltd and IHS Energy, allowing me to attend several conferences and receive training, data and technical support for which I am extremely grateful.

Firstly, I would like to thank my primary supervisor, Jonny Imber. Jonny, you have been a fantastic supervisor over the past four years. Thank you for always making time to talk to me and your constant enthusiasm for my project. You have been a true inspiration and it has been a genuine pleasure discussing the more challenging parts of the project. You have been an endless source of support, guidance and patience throughout my PhD. I have learnt a great deal from your approach to science and attention to detail and they will have a lasting effect on me in the future.

I would like to thank my other supervisors at Durham University; Richard Davies, Jeroen van Hunen and Susie Daniels. Thank you all for your support, motivation and discussion. Richard, I have greatly enjoyed our discussions and the way you always manage to motivate me and keep me inspired about my project. Jeroen, thank you for your help and guidance with some of the maths within my project – greatly appreciated! Susie, thank you for your thoughtful comments and discussion, particularly throughout the time I have been writing-up.

I would also like to thank my two supervisors from industry, Graham Yielding from Badley Geoscience Ltd. and Adrian Heafford from IHS Energy. Graham, I greatly appreciate the time you have taken over the years to help with my project, both in terms of teaching me how to use TrapTester more effectively and in the discussion of my interpretations. Adrian, thank you for your support and input into my project and your fast response to data requests.

Next, I would like to thank people who are not named supervisors on this project, but whom I am indebted to for their help, support and input over the past four years. I would like to thank Jon Gluyas and Simon Mathias from Durham University. Jon, thank you for sharing your vast knowledge and expertise of the petroleum industry. Simon, thank you for challenging my interpretations and providing interesting discussion throughout my project.

I would like to thank Dave Sendra (now at RSI), Mark Diaz and the rest of the subsurface team at IHS Energy. Dave, thank you for providing opportunities for me to visit the office, present my research regularly and collect data for my project. Mark, I greatly appreciate our discussions of the pressure data, which I have used extensively in my project. Thank you all for your help in data provision for my project.

I would also like to thank Alan Roberts, Michiel van Noorden, Dave Quinn and Peter Bretan from Badley Geoscience Ltd. for their interest in my project, and technical support over the years. Thank you for your regular invitations to visit the office and work alongside you.

Thanks also to Mark Stone from BG Group who has visited Durham University on numerous occasions and has spent time discussing my interpretations of production data used extensively within this project.

Thanks to Dave Stevenson, Gary Wilkinson and Matthew Hepburn for IT support and seismic and well data loading within the Department of Earth Sciences at Durham University. Thanks also to Badley Geoscience Ltd., Landmark, NIST and Oracle for provision of academic licences for TrapTester, Seisworks, RefProp and Crystal Ball software, respectively.

I would like to thank my family and friends for their support and encouragement over the years. A big thank you to all my friends within the department, and those who have now left, for all the fun times we have had together in Durham. Finally, a big thank you to my family, particularly my parents, who have encouraged and supported me all the way through my education and university career, have celebrated my successes with me and have never failed to reassure me during the more stressful periods!

Dedicated to

Lynne and John

Table of Contents

List of Figures

co-exist. Outside of the vapour-liquid saturation line the equilibrium state will be single phase. Liquid phases occur within the top section of the graph above the supercritical fluid region; vapour phases occur on the bottom left-hand-side of the graph, to the left of the supercritical region. The steps from low CO_2 density to high CO_2 density define the phase change between the gaseous and supercritical phases. As pressure increases, the CO_2 moves from the gaseous phase to the supercritical phase and this occurs over a shorter pressure differential and at lower pressures when the temperature is low.....11

Figure 1.6 Techno-Economic Resource Pyramid for CO_2 Geological Storage Capacity (after Bradshaw et al. (2007) and Bachu et al. (2007)). Theoretical storage capacity includes the entire pyramid, effective capacity the top three sections, practical capacity the top two sections and matched capacity only the top section. 13

Figure 1.7 Theoretical CO_2 Storage Capacity (Gigatons, Gt) within Gas Fields by Region. Note the degree of variability in estimates for the Hewett Gas Field. Also note the estimates of theoretical CO_2 storage capacity within the South and North Morecambe Gas Fields are similar to the theoretical CO_2 storage capacity estimates for the entire East Irish Sea Basin.....20

Figure 1.8 A simplified workflow for the evaluation of depleted gas reservoirs with respect to CO_2 storage.....26

Figure 2.1 Schematic diagram showing the depositional environments of sedimentary rocks. After Fichter et al. (1991). 31

Figure 2.2 (Overleaf). Examples of structural trapping mechanisms, after Gluyas and Swarbrick (2003). (a) Tilted fault blocks in an extensional regime. The seals are overlying mudstones and cross-fault juxtaposition against mudstones. (b) A rollover anticline on a thrust. Petroleum accumulations may occur on both the hanging wall and the footwall. The hanging wall accumulation is dependent upon sub-thrust fault seal, whereas at least part of the hanging wall trap is likely to be a simple four-way dip-closed structure. (c) The lateral seal of a trap against a salt diaper and a compactional drape trap over the diaper crest. (d) A trap associated with diapiric mudstone, with a lateral seal against the mud-wall. Traps associated with diapiric mud share many features in common with those associated with salt. In this diagram, the diapiric mud-wall developed at the core of a compressional fold. (e) A compactional drape over a basement block commonly creates enormous low relief traps. (f) Gravity-

List of Tables

Table of Units

ABBREVIATION	DEFINITION	UNITS
A	Reservoir/play area	m^2
B_g	Gas formation volume factor	Dimensionless
B_{gas}	Gas formation volume factor in the reservoir at the end of production	Dimensionless
B_{gi}	Gas formation volume factor at initial reservoir conditions	Dimensionless
B_{iCO2}	CO_2 formation volume factor at initial reservoir conditions	Dimensionless
B_{igas}	Gas formation volume factor at initial reservoir conditions	Dimensionless
B_w	Water formation volume factor	Dimensionless
C_a	Capacity coefficient for aquifer strength	Dimensionless
C_b	Capacity coefficient for buoyancy	Dimensionless
C_e	Effective capacity coefficient	Dimensionless
c_{fluid}	Bulk compressibility of reservoir fluid	Pa^{-1}
C_h	Capacity coefficient for heterogeneity	Dimensionless
C_m	Capacity coefficient for mobility	Dimensionless
c_{res}	Bulk compressibility of reservoir rock	Pa^{-1}
C_w	Capacity coefficient for water saturation	Dimensionless
Δt	Diffusion time	seconds
Δx	Diffusion distance	m
E	Gas expansion factor	Dimensionless
E_i	Gas expansion factor at initial reservoir conditions	Dimensionless
F_{IG}	Fraction of injected gas	Dimensionless
G	Original gas in place	m^3
g	Gravitational acceleration	m/s^2
G_{ihc}	Volume of initial hydrocarbons	m^3
G_{injCO2}	Cumulative volume of injected CO_2	m^3
G_p	Cumulative volume of produced gas	m^3
G_{phc}	Volume of produced hydrocarbons	m^3
h	Reservoir height/thickness	m
H_{res}	Hydraulic head	m
φ	Reservoir porosity	Dimensionless
k	Permeability	m^2
κ_ϕ	Hydraulic diffusivity	m^2/s
λ	Wavelength	m
L	Aquifer lengh	m
μ	Fluid viscosity	Pa s
M_{CO2e}	Effective mass storage capacity for CO_2	tonnes
M_{CO2t}	Theoretical mass storage capacity for CO_2	tonnes
mf_i	Mass fraction of an individual component	Dimensionless
m_i	Mass of an individual component	g/mol
M_{injCO2}	Effective mass storage capacity for injected CO_2	tonnes

ABBREVIATION	DEFINITION	UNITS
m_m	Mass of gas mixture	g/mol
ν	Velocity	m/s
N_i	Mole number of an individual component	mol
N_m	Sum of the mole numbers within a gas mixture	g/mol
OGIP	Original gas in place	m^3
P	Reservoir pressure	Pa
P_{cr}	Critical pressure	Pa
P_i	Reservoir pressure at initial reservoir conditions	Pa
P_{ihc}	Pressure at initial reservoir conditions	Pa
P_r	Reservoir pressure	Pa
P_R	Reduced pressure	Dimensionless
P_{res}	Reservoir pressure	Pa
$P_{reshc/CO2}$	Pressure of residual hydrocarbon/carbon dioxide mix	Pa
P_s	Surface pressure	Pa
P_{sc}	Pressure at standard conditions	Kelvin
ρ	Density	kg/m^3
R	Universal gas constant	$J\ K^{-1}\ mol^{-1}$
ρ_{CO2r}	Density of carbon dioxide at reservoir conditions	kg/m^3
r_e	External boundary radius	m
r_{eD}	Dimensionless radius	Dimensionless
R_f	Recovery factor	Dimensionless
r_o	Reservoir radius	m
ρ_w	Water density	kg/m^3
S_w	Water saturation	Dimensionless
T	Reservoir temperature	Kelvin
t	Time	seconds
T_{cr}	Critical temperature	Pa
t_D	Dimensionless time	Dimensionless
T_r	Reservoir temperature	Kelvin
T_R	Reduced temperature	Dimensionless
T_{res}	Reservoir temperature	Kelvin
T_s	Surface temperature	Kelvin
T_{sc}	Temperature at standard conditions	Kelvin
URR	Volume of ultimate recoverable reserves	m^3
V	Specific volume	m^3/kg
V_{GAS}	Volume of ultimate recoverable reserves	m^3
V_{iw}	Volume of injected water	m^3
V_m	Molar volume	m^3/mol
V_{pw}	Volume of produced water	m^3
w	Aquifer width	m
$W_D(t_D)$	Dimensionless cumulative water influx function	Dimensionless

ABBREVIATION	DEFINITION	UNITS
W_e	Cumulative water influx into a reservoir	m^3
W_p	Cumulative volume of produced water	m^3
y_i	Mole fraction of an individual component	Dimensionless
Z	Acoustic impedance	kg/m^2-s
z	Gas compressibility factor	Dimensionless
z_{gas}	Gas compressibility factor in the reservoir at the end of production	Dimensionless
z_i	Gas compressibility factor at initial reservoir conditions	Dimensionless
z_{iCO2}	CO_2 gas compressibility factor at initial reservoir conditions	Dimensionless
z_{ihc}	Gas compressibility factor at initial reservoir conditions	Dimensionless
z_r	Reservoir compressibility	Dimensionless
z_{res}	Reservoir gas compressibility factor	Dimensionless
$z_{reshc/CO2}$	Gas compressibility factor of residual hydrocarbon/carbon dioxide mix	Dimensionless
z_s	Surface compressibility	Dimensionless

1 Introduction

1.1. GLOBAL RESPONSES TO CLIMATE CHANGE

There is significant scientific evidence to suggest that anthropogenic carbon dioxide (CO_2) emissions are having an effect on climate (IPCC, 2005, 2013). It has long been recognised that the more adverse effects of climate change can threaten the availability of water and food supplies to the global population, as well as affecting individuals' health, general land use and the environment (Stern, 2006).

The United Nations Framework Convention on Climate Change (UNFCCC) was established in 1992 to mark the international response to climate change. This *encouraged* the 37 industrialised countries and the European community to work towards a stabilisation in CO_2 emissions (UNFCCC, 2013). For complete stabilisation emission levels are required to meet those of the Earth's natural capacity to remove greenhouse gases from the atmosphere (Stern, 2006). Following the Kyoto Protocol in 1997 (UNFCCC, 1998), the commitment towards emission reduction targets for the individual countries involved became *legally binding*. The Kyoto Protocol set a target of an overall 5% emissions reduction compared to 1990 levels to occur between 2008-2012, however each individual nation has its own personal target to meet. Currently, there are 195 Parties to the UNFCCC and 192 Parties to the Kyoto Protocol (UNFCCC, 2013).

1.2. UK EMISSION REDUCTION TARGETS AND THE ROLE OF CARBON STORAGE IN UK EMISSIONS REDUCTION

The UK Government is committed to meeting a reduction in greenhouse gas emissions by 12.5% below base year (1990) levels over the 2008-2012 period under the Kyoto Protocol, 1997 (DECC, 2013). This equates to average annual emissions

of 682.4 $MtCO_2$ equivalent over the time period. Additionally, the UK Government also has a domestic target it aims to meet as defined by the Climate Change Act, 2008. This requires a reduction in greenhouse gas emission by at least 34 % below base year levels by 2020, and 80 % by 2050 (DECC, 2013). In order to achieve this, five year carbon budgets have been used to set the trajectory to 2050.

Provisional results for 2012 indicate a reduction in CO_2 emissions of 26.7% below 1990 levels excluding emissions trading, and 24.9% below 1990 levels including emissions trading (DECC, 2013).

The UK is predicted to rely on fossil fuel combustion for energy generation for at least the next few decades (Holloway et al., 2006). As such, the UK Government plans to incorporate carbon capture and storage (CCS) into its policies for addressing climate change and working towards a low carbon economy (DECC, 2011). CCS has been recognised as a promising new technology to mitigate the effects of CO_2 on climate (Holloway, 2009). It involves the capture and transport of CO_2 from point sources, and long-term storage of supercritical CO_2 in geological media such as depleted oil and gas fields, deep saline aquifers and unmineable coal seams (IPCC, 2005, 2013), as illustrated in Figure 1.1.

The UK is optimally placed to benefit from carbon capture and storage, being an island surrounded by a now partially depleted, but a once major hydrocarbon province. Theoretical CO_2 storage capacity estimates (see section 1.5) for the UK continental shelf lie within the range of 1200×10^6 and 3500×10^6 tonnes CO_2 within depleted oil reservoirs and up to 6100×10^6 tonnes CO_2 within depleted gas reservoirs (Holloway, 2009). The majority of these depleted oil and gas fields lie within the Southern North Sea, Central and Northern North Sea, Inner and Outer Moray Firth, East Irish Sea Basin and the Wessex Basin.

CO_2 will be captured from point source emitters located within selected business clusters (industry located within a local geographic jurisdiction) and transported to an allocated storage site. It is more efficient and cost-effective to transport the CO_2 through one large pipeline rather than creating a point-to-point system which would need to be adopted by each individual point source emitter. The Department for Energy and Climate Change (DECC, 2009) have defined several potential CCS clusters within the UK including the Thames-Medway

Valley, Yorkshire-Humber, Teesside, East Scotland and Liverpool Bay. It is likely that when CCS becomes a fully established industry within the UK that other CCS clusters will be constructed from other point source emitters in an attempt to further reduce emissions.

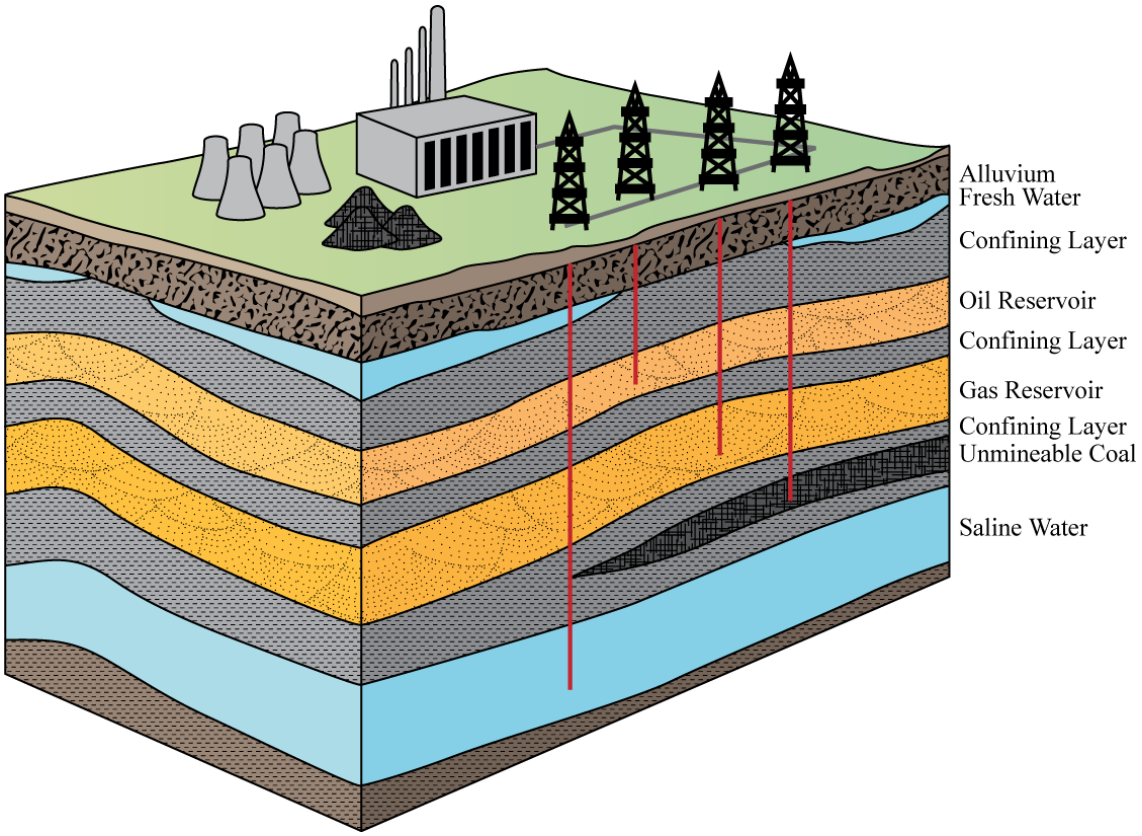

Figure 1.1 Schematic diagram for carbon capture and storage. Carbon dioxide is captured from point source emitters such as power stations fuelled by fossil fuels. The carbon dioxide is then transported, for example via pipeline, compressed to a supercritical state and injected into geological formations such as oil and gas reservoirs, unmineable coal seams and saline aquifers. Adapted from IPCC (2005).

1.3. RATIONALE FOR STORAGE WITHIN UK TRIASSIC DEPLETED GAS RESERVOIRS

This thesis focusses on CO_2 storage within depleted gas fields on the UK continental shelf. The UK offshore depleted gas fields are predicted to provide much larger theoretical CO_2 storage capacities than UK offshore oil fields - 6100 x

10^6 tonnes CO_2 within gas fields compared to between 1200 x 10^6 and 3500 x 10^6 tonnes CO_2 within oil fields (Holloway, 2009).

Compared to alternative CO_2 storage complexes such as unmineable coal seams and deep saline aquifers, a great amount is known about the dynamic behaviour of depleted gas fields throughout hydrocarbon production through detailed geological characterisation and extensive monitoring. Most importantly, this includes information about reservoir drive mechanism, i.e. how hydrocarbons have been produced from the reservoir. Depletion drive, or volumetric, reservoirs are isolated, closed systems and do not receive pressure support of fluid from outside sources such as water influx from neighbouring aquifers. Hydrocarbons are produced utilising the natural reservoir pressure as the driving force for the flow of gas to the surface (Hagoort, 1988). Conversely, water drive reservoirs are open systems that receive pressure support and fluid from neighbouring aquifers or shale layers. Key information on the degree of compartmentalisation (if any) within a reservoir, which may cause a barrier to flow both throughout production and during CO_2 injection, is usually well constrained throughout the productive lifetime of a gas reservoir.

A wealth of data exists for most depleted gas fields including, but not limited to, production data (e.g. annual and cumulative produced hydrocarbon volumes and production rates), pressure data, wireline data, borehole data and well core analyses. Through integrated analysis of those data sets, a thorough understanding of dynamic reservoir behaviour throughout the productive lifetime of the field can be established. Conceptual models for reservoir behaviour throughout their storage lifetimes can then be developed. As such, the use of depleted gas reservoirs can reduce some of the risk associated with CO_2 storage: depleted gas reservoirs and traps have successfully held and sealed hydrocarbons over geological timescales, therefore, it can be inferred they may be suitable for long-term CO_2 storage (IPCC, 2005, 2013).

CO_2 storage is considered within UK Triassic reservoirs in this thesis. The Triassic Sherwood Sandstone Group (also known offshore within the North and Southern North Sea as the Bunter Sandstone Formation) is a major sandstone unit with many of the basic characteristics necessary for CO_2 storage including

structural traps (such as anticlines), good porosity and permeability, large storage capacities and a good lateral and vertical seal provided by the overlying Haisborough Group and/or Mercia Mudstone Group (Bentham, 2006; Brook et al., 2003; Kirk, 2006). Furthermore, the Triassic sandstone sequence is host to many productive gas reservoirs, and the overlying Haisborough Group/Mercia Mudstone Group is a proven hydrocarbon seal – one of the fundamental characteristics of a prospective CO_2 storage site.

1.4. CASE STUDY TRIASSIC DEPLETED GAS RESERVOIRS

The Triassic reservoirs of the Hewett Gas Field of the Southern North Sea and the North and South Morecambe Gas Fields of the East Irish Sea Basin are considered within this thesis for CO_2 storage. The Hewett Gas Field was the second largest UK North Sea gas field and the third largest UK gas field (Figure 1.2), with 38.4 billion cubic metres of natural gas in place, as estimated by industry. The field is located 16 km NE of Bacton on the Norfolk Coastline and encompasses three major reservoirs: the Triassic Upper and Lower Bunter Sandstone reservoirs and the Permian Zechsteinkalk reservoir.

The South Morecambe Gas Field is the second largest UK gas field located 32 miles west of Blackpool (Figure 1.3) with 149.1 billion cubic metres of gas in place, as estimated by industry. The North Morecambe Gas Field is again of significant capacity (but smaller than South Morecambe) and is situated just to the north, separated from the South Morecambe Gas Field by a northeast-southwest graben. Both the North and South Morecambe contain Triassic gas producing reservoirs of the Sherwood Sandstone Group.

These fields are considered for CO_2 storage within this thesis due to their significant CO_2 storage capacities and their good reservoir quality (porosity and permeability). There is a substantial amount of data available for the four reservoirs, including production, pressure, porosity and permeability data making them useful reservoirs for the development of best practice workflows for their characterisation with respect to CO_2 storage. These data can be used to identify the

reservoir drive mechanism of the storage sites, as this can have a substantial impact on CO_2 storage capacity.

Another important characteristic is the ability to compress and store CO_2 within the prospective storage sites as a supercritical fluid as indicated by IPCC guidelines (IPCC, 2005, 2013).

A substance behaves as a supercritical fluid when at a temperature and pressure above its vapour-liquid critical point where specific liquid and gas phase boundaries do not exist. The critical temperature of CO_2 is 31 °C (304.15 K) and its critical pressure is 7.38 MPa. Its critical point occurs where these two points intersect on the phase diagram (Figure 1.4).

When CO_2 is held above its critical temperature and pressure it adopts properties between a gas and a liquid (Çengel and Boles, 2011). There is no liquid/gas phase boundary meaning the properties can be "tuned" to be more in line with a liquid or a gas by adjusting the temperature and pressure (Çengel and Boles, 2011). Critical pressure is not dependent on temperature and vice versa, critical temperature is not dependent on pressure (Çengel and Boles, 2011), (Figure 1.4).

Another key property of supercritical CO_2 is its effect on CO_2 density, and therefore volume. As pressure increases, CO_2 density increases (Figure 1.5) and CO_2 volume decreases. A marked increase in CO_2 density occurs where an increase in pressure results in the phase change from vapour to liquid across the vapour-liquid saturation line (Figure 1.5). Consequently, a greater volume of CO_2 can be stored if conditions within the prospective reservoir favour storage of supercritical CO_2. These conditions can be predicted using Figure 1.4 and Figure 1.5.

The Intergovernmental Panel on Climate Change, IPCC, recommend storage in depleted gas reservoirs at depths greater than 800 m, depending on the local geothermal gradient of the storage site (IPCC, 2005, 2013). Assuming the reservoir is at hydrostatic pressure, CO_2 will behave as a supercritical fluid. However, in practice, most depleted gas reservoirs, initially hydrostatically pressured, are left substantially under-pressured post-production (as is the case for the four reservoirs considered within this thesis – the Hewett Upper Bunter, Hewett Lower Bunter, South Morecambe Sherwood Sandstone and North Morecambe

Sherwood Sandstone reservoirs). Therefore, it is more appropriate to consider CO_2 density changes with pressure and temperature (see Figure 1.5).

The initial and final reservoir temperature and pressure conditions for the four reservoirs considered here for CO_2 storage have been plotted on Figure 1.4. At initial reservoir pressure and temperature conditions (prior to production) all four reservoirs would hold CO_2 in a supercritical state as their individual temperatures and pressures exceed the critical temperature and critical pressure of CO_2. However, post production, reservoir pressure has dropped in all four reservoirs meaning that CO_2 would be likely to be held now in the gaseous phase. As temperature data is unavailable for analysis, the extent to which temperature has dropped throughout production is not known. Therefore, in some instances (such as the South and North Morecambe fields), any injected CO_2 could be held as a vapour or even a liquid depending on the specific conditions. Once the reservoirs are re-pressurised with CO_2 it would be possible for the CO_2 to be held in a supercritical state. To achieve this, it will be necessary for the pressure to exceed the critical pressure (the maximum pressure may be limited by the CO_2 column height that can be supported by the cap rock and trap-closing faults). The temperature will also need to exceed the critical temperature. This may be possible within the Hewett Gas Field, however, within the South and North Morecambe Gas Fields it is more likely that CO_2 will be held as a compressible liquid post-injection as a result of the temperature drop throughout production (Van Der Meer, 2005).

It is clear that dynamic reservoir modelling of the changing phase behaviour throughout CO_2 injection is required to ensure that a volume of CO_2 can be injected into the reservoir and that it can be stored securely and can make efficient use of the utilisable pore space. Although these are important considerations, the dynamic modelling of reservoir phase behaviour is beyond the scope of this thesis. Here, static models of phase behaviour can be used to improve the accuracy of CO_2 storage capacity estimations. This will be described in more detail in section 1.6 and Chapter 3.

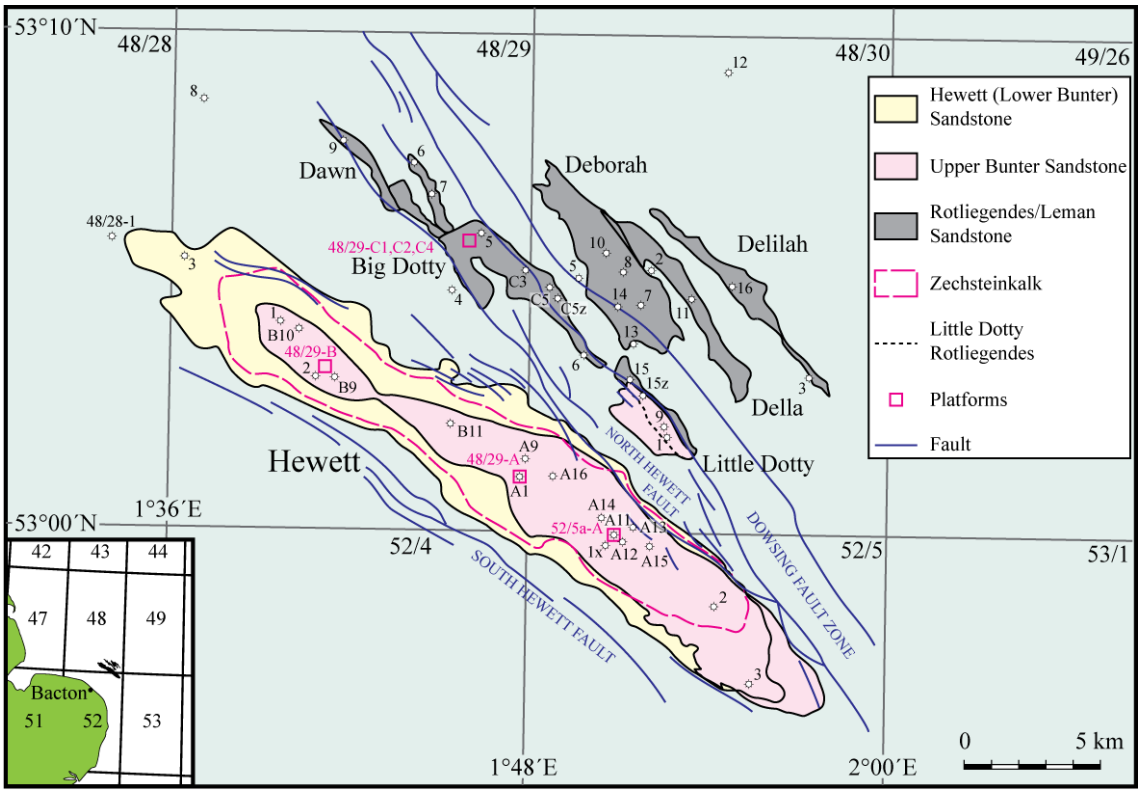

Figure 1.2 Location, Structure and Areal Extent of the Gas Fields of the Hewett Unit, Southern North Sea. The limit of the areal extent is defined by the original gas-water contact within each reservoir prior to production, or fault closure of the traps. After Cooke-Yarborough and Smith (2003).

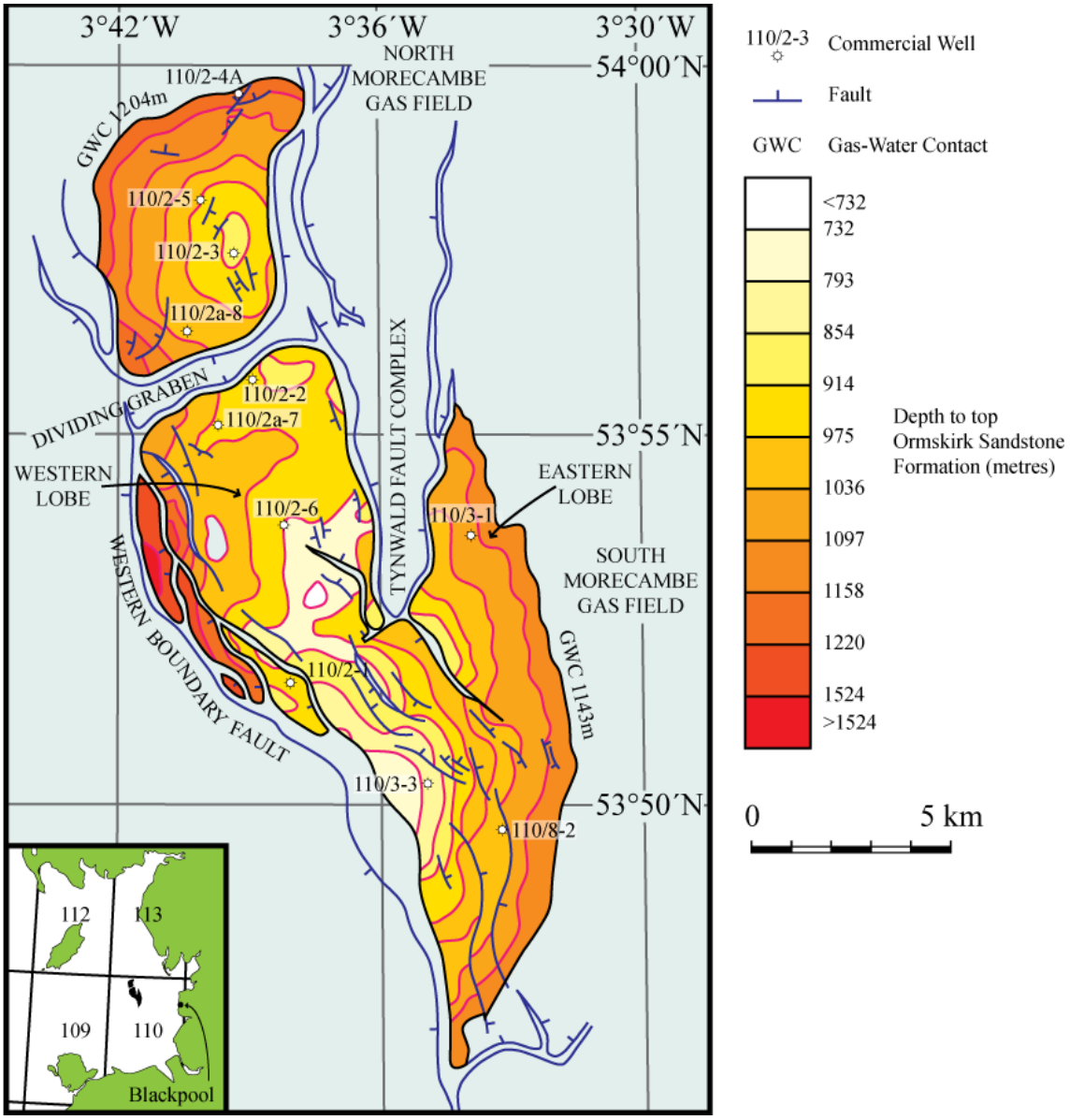

Figure 1.3 The Location, Structure and Areal Extent of the South and North Morecambe Gas Fields of the East Irish Sea Basin. The limit of the areal extent is defined by the original gas-water contact within each reservoir prior to production and fault closure. After Jackson et al. (1995).

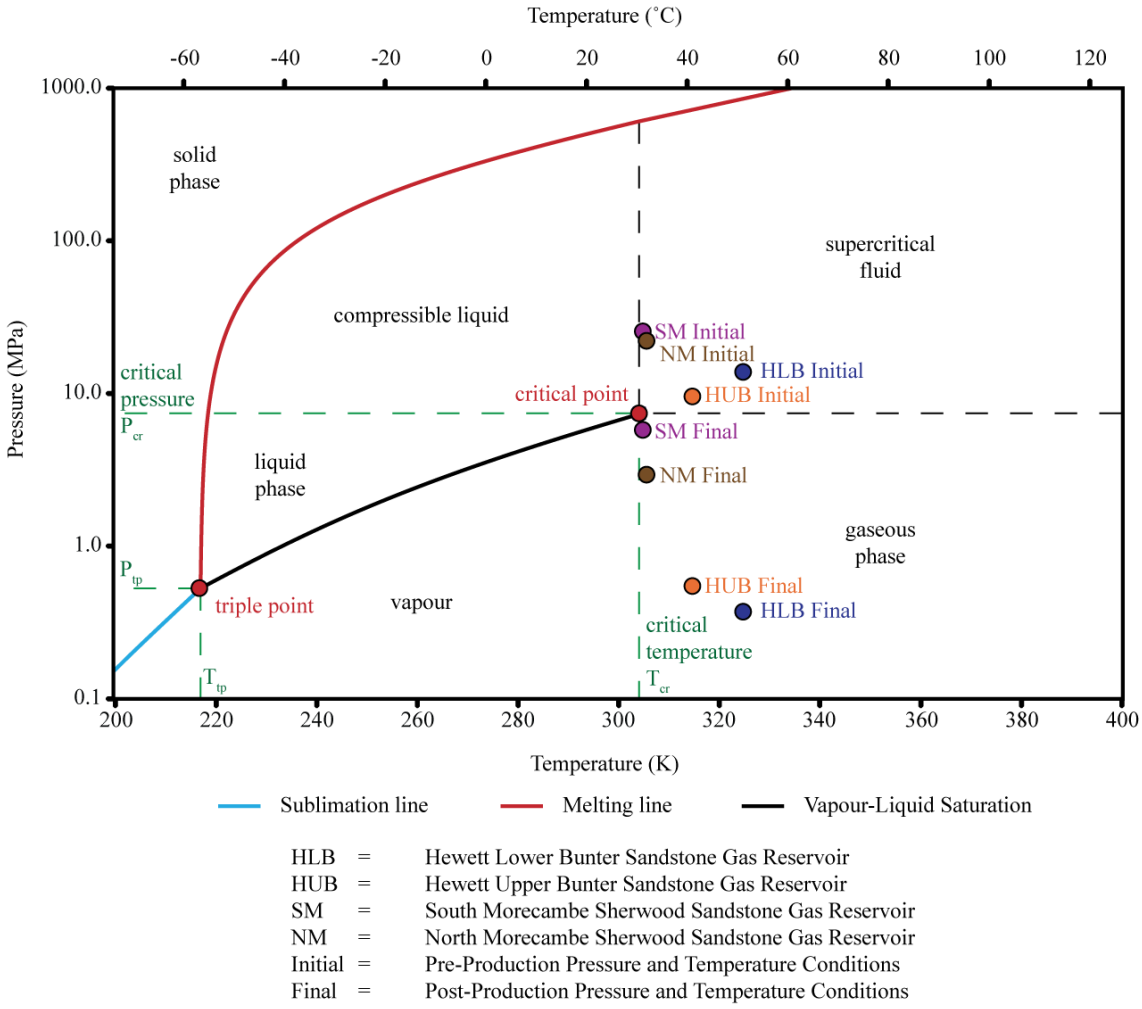

Figure 1.4 Phase diagram for the pure substance, CO_2. The sublimation line, melting line and vapour-liquid saturation line have been estimated using RefProp software (Lemmon et al., 2013) and the Peng-Robinson equation of state (Peng and Robinson, 1976). The phase diagram indicates the phases of CO_2 present at any given temperature and pressure. The critical point is defined by the critical temperature of CO_2 (31.1 °C or 304.25 K) and the critical pressure of CO_2 (7.38 MPa). The triple point occurs where all three phases are in equilibrium together, i.e. the solid-liquid equilibrium (melting line - red), liquid-vapour equilibrium (vapour-liquid saturation line - black) and the solid vapour equilibrium (sublimation line - blue).

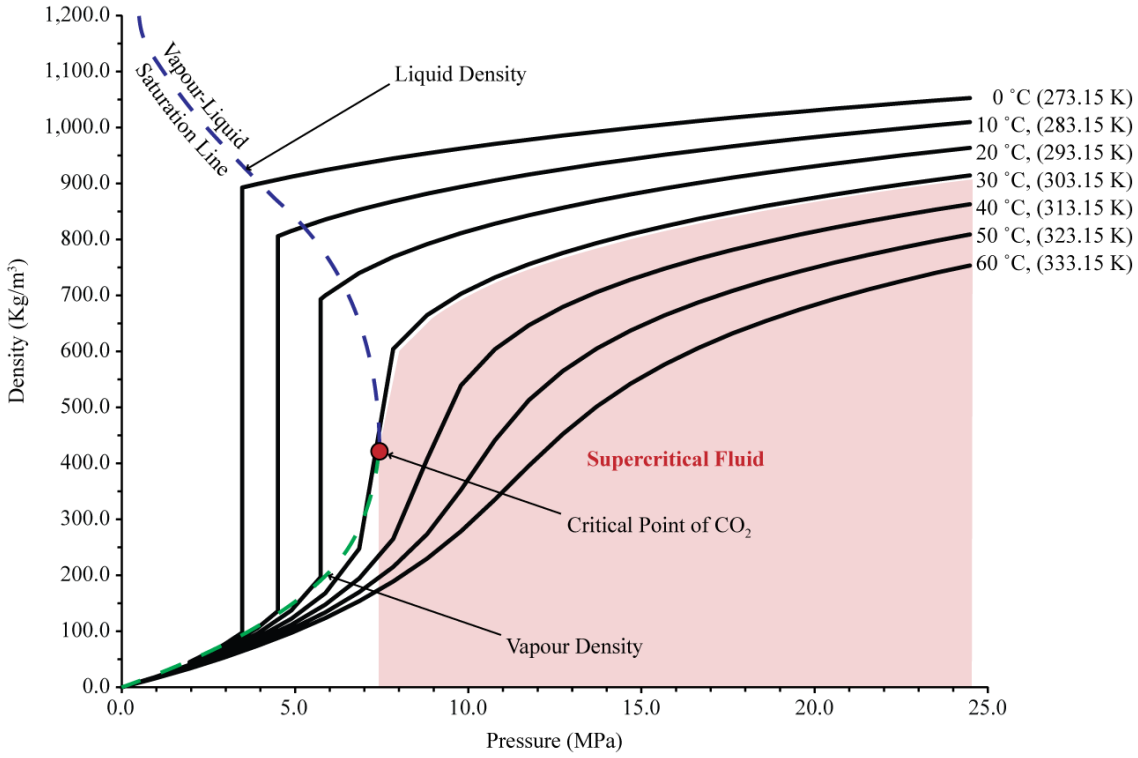

Figure 1.5 Isotherms of CO_2 density with increasing pressure. Fluid properties, including the vapour-liquid saturation line, have been estimated using RefProp software (Lemmon et al., 2013) and the Peng-Robinson equation of state (Peng and Robinson, 1976). The vapour-liquid saturation line consists of the liquid density line (blue dashed curve) and the vapour density line (green dashed curve). Within the vapour liquid saturation line (on the left hand side of the graph) liquid and vapour can co-exist. Outside of the vapour-liquid saturation line the equilibrium state will be single phase. Liquid phases occur within the top section of the graph above the supercritical fluid region; vapour phases occur on the bottom left-hand-side of the graph, to the left of the supercritical region. The steps from low CO_2 density to high CO_2 density define the phase change between the gaseous and supercritical phases. As pressure increases, the CO_2 moves from the gaseous phase to the supercritical phase and this occurs over a shorter pressure differential and at lower pressures when the temperature is low.

1.5. THE TECHNO-ECONOMIC RESOURCE PYRAMID

As previously stated, the depleted gas and oil fields on the UK continental shelf offer a large theoretical storage capacity in the order of billions of tonnes of CO_2. CO_2 storage capacity is a geological resource (a quantity of a commodity estimated to exist at a given time within a jurisdiction or geographic area) (Bachu et al., 2007). It can therefore be described in terms of resources and reserves (Bachu et al., 2007; Bradshaw et al., 2007; CSLF, 2005; Frailey et al., 2006a). Reserves are a subset of resources, being those quantities of a commodity that are known to exist and are commercially recoverable under present technological and economic conditions (Bachu et al., 2007).

A Techno-Economic Resource-Reserve Pyramid for CO_2 Storage Capacity has been developed (see Figure 1.6), expressed in mass (megatons, Mt or gigatons, Gt) CO_2 (Bradshaw et al., 2007; CSLF, 2005). The theoretical storage capacity encompasses the entire techno-economic resource pyramid and is the physical limit of what the geological system can accept, giving a maximum upper limit to storage capacity estimates (Bachu et al., 2007). It represents the entire pore space of the storage complex, or the pore space with known displaceable resident fluids (Bachu et al., 2007). It always gives an unrealistic estimate as further characterisation of the storage complex will reveal other physical, technical, regulatory or economic limitations on the utilisable storage capacity (Bachu et al., 2007).

The effective storage capacity is a subset of the theoretical storage capacity and occupies the top three sections of the techno-economic resource pyramid (see Figure 1.6). It has previously been known as the "Realistic Capacity" in Bradshaw et al. (2007) and the discussion paper of the Carbon Sequestration Leadership Forum (CSLF, 2005). The effective storage capacity applies technical (geological and engineering) limitations to the theoretical storage capacity estimate, including the physical accessibility of the storage complex (Bachu et al., 2007).

Practical storage capacity, previously called "Viable Capacity" in Bradshaw et al. (2007) occupies the top two sections of the techno-economic resource pyramid (see Figure 1.6). It imposes limitations to the effective storage capacity estimate in terms of technical, legal and regulatory, infrastructure and general

economic barriers to CO_2 geological storage. The estimate tends to be constantly redefined with new technologies, policies, regulations and economic changes.

Matched storage capacity occupies the top section only of the techno-economic resource pyramid (see Figure 1.6). The capacity is defined by matching large-scale, stationary CO_2 emitters with the geological storage site and determines the site's adequacy in terms of capacity, injectivity and supply rate.

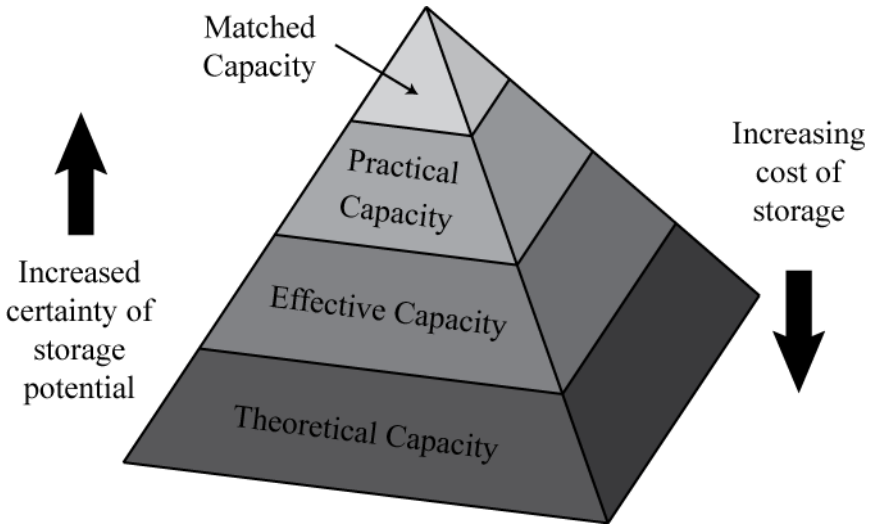

Figure 1.6 Techno-Economic Resource Pyramid for CO_2 Geological Storage Capacity (after Bradshaw et al. (2007) and Bachu et al. (2007)). Theoretical storage capacity includes the entire pyramid, effective capacity the top three sections, practical capacity the top two sections and matched capacity only the top section.

1.6. CO_2 STORAGE CAPACITY ESTIMATION

At the geological characterisation level, only the theoretical CO_2 storage capacity and the effective CO_2 storage capacity can be defined within this thesis in the absence of other information on technical, legal and regulatory, infrastructure and general economic barriers to CO2 geological storage, necessary for the estimation of practical and matched CO_2 storage capacity estimation.

It is necessary to be as accurate as possible in the estimation of any storage capacity estimate (theoretical, effective, practical or matched). Governments worldwide are dependent on accurate and reliable CO_2 storage capacity estimations for assessing the viability of CO_2 storage within their respective jurisdictions and to put policies in place (Bradshaw et al., 2007). Furthermore, industry needs accurate CO_2 storage capacity estimates for business decisions concerning site selection and development (Bradshaw et al., 2007). Often, the theoretical and effective CO_2 storage capacity estimates will be used as first-order results for this assessment.

Previously published estimates of theoretical CO_2 storage capacity have shown variability (see Figure 1.7). In addition, there are few studies at present that focus on effective CO_2 storage capacity estimation, especially in reference to individual reservoirs or gas fields.

Figure 1.7 and Table 1.1 show the variability of previously published estimates of theoretical CO_2 storage capacity in gas reservoirs both globally and within the UK. Out of the regions depicted within the UK, the greatest range of variability can be observed within the Hewett Gas Field which shows variability by a factor of 3.72. In comparison, the region with the lowest range of variability can be observed within the East Irish Sea Basin, showing a variability factor of 1.05, the majority of this storage capacity lies within the South and North Morecambe gas fields. It is important to note that the South Morecambe Gas field and the Hewett Gas Field are the second and third largest gas fields on the UK continental shelf. As such, any variability in their storage capacity estimate will affect final UK estimates.

There needs to be more transparency than the previously published literature in future articles, clarifying exactly how theoretical, effective, practical and matched CO_2 storage capacity estimates have been arrived at. In addition to stating which data has been used, estimates should also state limitations, such as data, time and knowledge, at the time of assessment and indicate the purpose and use to which the estimates should be applied (Bradshaw et al., 2007). This will assist both governments and industry in judging the viability of storage sites and when forming policy (Bradshaw et al., 2007).

Prior studies on public perception indicate that the public is not generally well informed about CCS (IPCC, 2005, 2013). This may be due to the public not necessarily regarding anthropogenic climate change as a relatively serious problem (IPCC, 2005, 2013). Hence, there is limited acceptance of the need for large reductions in CO_2 emissions to reduce the threat of global climate change (IPCC, 2005, 2013).

One study on public perceptions of CCS (Shackley et al., 2004) found a general interest from the public in the UK's potential CO_2 storage capacity. This occurred when the public was first presented with the idea of CCS, followed by the provision of more background information (Shackley et al., 2004). One of the main conclusions from the study suggested that the uncertainties concerning the risks of CCS has to be better addressed and reduced before CCS could gain greater public acceptance (Shackley et al., 2004).

As is demonstrated by Figure 1.7, there are difficulties in accurately estimating theoretical CO_2 storage capacity. The variability in theoretical CO_2 storage capacity estimation may be a result of (1) the method of theoretical CO_2 storage capacity estimation used, (2) the equation of state used to model parameters such as CO_2 density, ρ_{CO2r}, and the gas compressibility factor, Z, and (3) the variability of parameters input into the individual storage capacity methods. Currently, it is often unclear how previously published estimates have been arrived at, or which method of estimation has been used.

There are two main approaches to estimating the theoretical CO_2 storage capacity of depleted gas reservoirs. The first approach adapts the geometrically based STOOIP method used frequently in the oil and gas industry to estimate the volume of reserves, for example, the method of Bachu et al. (2007):

$$M_{CO_2 t} = \rho_{CO_2 r}\left[R_f A h \varphi (1 - S_w) - V_{iw} + V_{pw}\right] \tag{1.1}$$

where, $M_{CO_2 t}$ is the theoretical mass storage capacity for CO_2 in a reservoir at in situ conditions, ρ_{CO2r} is CO_2 density at reservoir conditions, R_f is the recovery factor, A is reservoir thickness, h is reservoir height, φ is reservoir porosity, S_w is

water saturation, V_{iw} is the volume of injected water and V_{pw} is the volume of produced water.

The second approach to estimating theoretical storage capacity is based on the principle that a variable proportion of the pore space occupied by the recoverable reserves will be available for CO_2 storage (e.g. the methods of Bachu et al. (2007) (equation 1.2), Holloway et al. (2006) (equation 1.3), and Tseng et al. (2012) (equation 1.4):

$$M_{CO_2t} = \rho_{CO_2r} R_f (1 - F_{IG}) OGIP \left[\frac{(P_s Z_r T_r)}{(P_r Z_s T_s)}\right] \tag{1.2}$$

$$M_{CO_2t} = \left(\frac{V_{GAS}[stp]}{B_{igas}} . \rho_{CO_2r}\right) \tag{1.3}$$

$$M_{CO_2t} = \frac{\rho_{CO_2r}(G_{phc} . B_{gas})}{B_{iCO_2}} = \frac{\rho_{CO_2r}(G_{phc} . z_{gas})}{z_{iCO_2}} \tag{1.4}$$

where, F_{IG} is the fraction of injected gas; OGIP is the original gas in place; P is pressure; Z is the gas compressibility factor; T is temperature, and subscripts "r" and "s" denote reservoir and surface conditions respectively; V_{GAS} [stp] is the volume of ultimately recoverable gas at standard conditions; B_{igas} is the gas formation volume factor at initial reservoir conditions (gas volume at reservoir conditions/ gas volume at standard conditions); G_{phc} is the cumulative volume of hydrocarbon gas produced at standard conditions; B_{gas} is the gas formation volume factor at reservoir conditions at the end of gas production; B_{iCO_2} is the CO_2 formation volume factor at initial reservoir conditions; z_{gas} is the gas compressibility factor at reservoir conditions at the end of gas production; Z_{iCO_2} is the CO_2 compressibility factor at initial reservoir conditions.

Effective storage capacity estimation within depleted gas reservoirs is much more difficult to constrain as it often relies upon knowledge of coefficients that reduce storage capacity from theoretical to effective e.g. methods of Bachu et al. (2007):

$$M_{CO_2e} = C_m C_b C_h C_w C_a M_{CO_2t} \equiv C_e M_{CO_2t} \quad (1.5)$$

where, M_{CO_2e} is the effective reservoir capacity for CO_2 storage, the subscripts m, b, h, w and a stand for mobility, buoyancy, heterogeneity, water saturation, and aquifer strength respectively, and the coefficient C_e is a single effective capacity coefficient that incorporates the cumulative effects of all the other.

Unfortunately, there are difficulties in estimating the values of the capacity coefficients and few published studies that calculate them (Bachu et al., 2007). Additionally, there are no data specifically relating to CO_2 storage in depleted gas reservoirs (Bachu et al., 2007). Mostly, capacity coefficient values are calculated through numerical simulations, for example, Bachu and Shaw (2005) for aquifer invasion and values of the coefficient, C_a (Bachu et al., 2007).

Generally, for depleted gas reservoirs there are approximate values expected for each capacity coefficient (Bachu and Shaw, 2003):

- The expected values for the capacity coefficient for mobility, C_m, are ≤ 1 as reservoir fingering effects will be small to negligible within a gas reservoir. Reservoir fingering occurs where two fluids (such as oil and water) bypass sections of reservoir as they permeate through creating an uneven, or fingered, profile. This results in an inefficient sweeping action and mainly occurs in oil reservoirs resulting in significant volumes of oil being unrecoverable (Bachu and Shaw, 2003).
- The expected value for the capacity coefficient for buoyancy, C_b, is also approximately equal to 1 as CO_2 density is greater than methane density at reservoir conditions, therefore any injected CO_2 is likely to fill the reservoir from the bottom upwards (Bachu and Shaw, 2003).
- The expected value for the capacity coefficient for water saturation, C_w, is 1 as the effect of initial water saturation has already been considered in estimations of theoretical CO_2 storage capacity (Bachu and Shaw, 2003).

- The expected value for the capacity coefficient for heterogeneity, C_h, is likely to be high, approaching 1, as the reduction in CO_2 storage capacity is much less by comparison with oil reservoirs (Bachu and Shaw, 2003).

Due to the complexity of capacity coefficient estimation, alternative methods, such as that of Tseng et al. (2012) can be used to estimate effective CO_2 storage capacity. This is an analytical method for estimation within a producing gas reservoir with, and without, a water drive:

$$M_{injCO2} = \rho_{CO2r} . G_{injCO2} \tag{1.6}$$

Where,

$$G_{injCO2} = G_{phc} - G_{ihc} + \frac{P_{reshc/CO2}}{z_{reshc/CO2}} \left(\frac{z_{ihc}}{P_{ihc}} G_{ihc} - W_e \frac{T_{sc}}{P_{sc} T} \right) \tag{1.7}$$

where, M_{injCO2} is the effective mass storage capacity for CO_2 in a reservoir at in situ conditions; G_{injCO2} is the cumulative volume of injected CO_2; G_{ihc} is the volume of initial hydrocarbon gas in pace at standard conditions; $P_{reshc/CO2}$ is the pressure of a gas reservoir with a mixture of gas and CO_2 during CO_2 injection; $z_{reshc/CO2}$ is the gas compressibility factor of the mixture of hydrocarbon gas and CO_2; z_{ihc} is the gas compressibility factor at initial reservoir conditions; P_{ihc} is the initial gas reservoir pressure; W_e is the cumulative water influx at reservoir volume; T_{sc} is the temperature at standard conditions; P_{sc} is the pressure at standard conditions; and T is the reservoir temperature.

The method of Tseng et al. (2012) is a more precise method for estimating effective CO_2 storage capacity within depleted gas reservoirs as it uses parameters for which the values are generally well constrained within most depleted gas reservoirs and are routinely gathered by the operators.

From the above examples of theoretical and effective CO_2 storage capacity methods it is possible to see that equations 1.2, 1.4 and 1.7 involve the estimation of the gas compressibility factor, Z. The gas compressibility factor, or Z-factor is a correction factor for the deviation of a real gas from ideal behaviour at given

pressures and temperatures, and can be estimated using various equations of state. The particular equation of state used determines the degree of correction for deviation from ideal behaviour. Different equations of state are suited to different substances and pressure and temperature conditions. Through application of various equations of state, a range of estimations of Z-factor can be input to both theoretical and effective CO_2 storage capacity equations resulting in a range of possible capacities.

More robust storage capacity estimations can also be achieved through accurate estimation of storage capacity input parameters, for example, reservoir geometry (area and height), CO_2 density and the gas compressibility factor. Some parameters are well-constrained, single values, for example, the initial reservoir pressure. Other parameters, such as reservoir porosity, vary substantially. In most cases an average value will be used in theoretical CO_2 storage capacity equations. However, greater accuracy in storage capacity estimation can be achieved by considering the entire range of variability.

As has been stated previously, CO_2 storage capacity estimation is variable. Many of the published storage capacity estimations are within the public domain, for example, studies by Bentham (2006) and Brook et al. (2003). In summary, the primary aim of this thesis is to investigate the sources of variability between published CO_2 storage capacity estimates, which will be a key step towards gaining public acceptance of CCS technology.

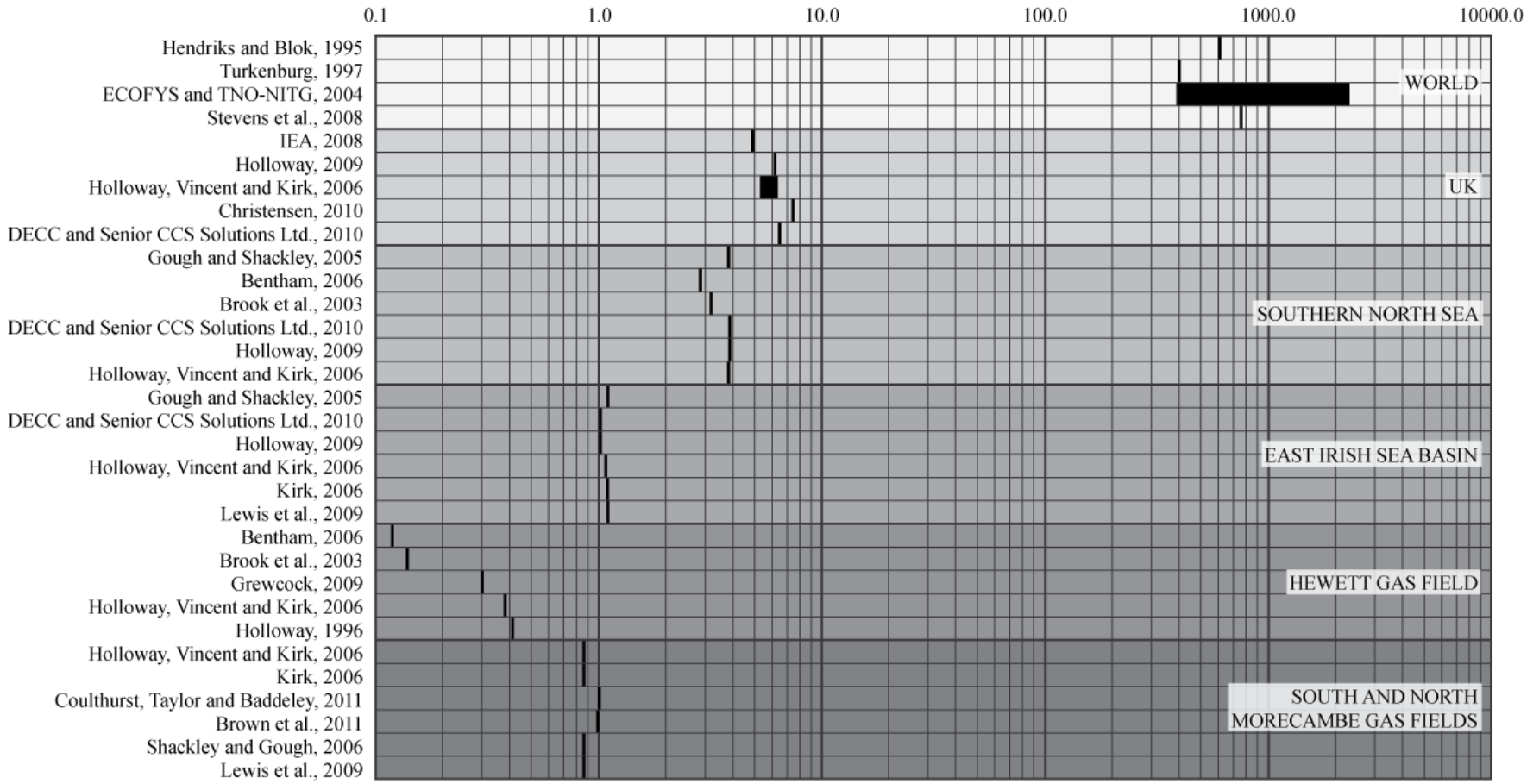

Figure 1.7 Theoretical CO_2 Storage Capacity (Gigatons, Gt) within Gas Fields by Region. Note the degree of variability in estimates for the Hewett Gas Field. Also note the estimates of theoretical CO_2 storage capacity within the South and North Morecambe Gas Fields are similar to the theoretical CO_2 storage capacity estimates for the entire East Irish Sea Basin

REGION	THEORETICAL CO_2 STORAGE CAPACITY RANGE (Gt CO_2)	VARIABILITY FACTOR
World	392.00 - 2126.00	5.42
UK	4.90 - 7.45	1.52
Southern North Sea (SNS)	2.81 - 3.90	1.39
East Irish Sea Basin (EISB)	1.00 - 1.05	1.05
Hewett Gas Field (SNS)	108.24 - 402.50	3.72
South and North Morecambe Gas Fields (EISB)	0.87 - 1.00	1.15

Table 1.1 Published Theoretical CO_2 Storage Capacity Estimates and their Variability

1.7. RESEARCH PROBLEM, AIMS AND OBJECTIVES

This thesis investigates the variability in theoretical and effective CO_2 storage capacity estimation within four depleted, or partially depleted, gas reservoirs: the Hewett Upper and Lower Bunter Sandstone reservoirs of the Southern North Sea, and the North and South Morecambe Sherwood Sandstone reservoirs of the East Irish Sea Basin.

Variability in CO_2 storage capacity estimates occurs for a number of reasons. Firstly, there are several published methods of theoretical CO_2 storage capacity estimation including Bachu et al. (2007), equations 1.1 and 1.2, Holloway et al. (2006), equation 1.3, and Tseng et al. (2012), equation 1.4. These methods are based on assessment of reservoir geometry, or material balance using historical gas production data. Studies including Bentham (2006), Brook et al. (2003), Holloway et al. (2006) and Kirk (2006) have used one of the above methods to estimate theoretical CO_2 storage capacity within a group of reservoirs. The use of these equations to estimate CO_2 storage capacity is appropriate as they can estimate the maximum reservoir pore volume and are based on approaches (such as the STOOIP equation and material balance) that are used regularly in the petroleum industry to estimate the volume of reserves in place. However, there has not previously been a comparison or evaluation of geometrical versus material balance approaches to CO_2 storage capacity estimation within a single reservoir. It is therefore unknown as to whether the particular method used will produce a conservative or significant over-estimate of available pore space for CO_2. As such, this thesis will apply both geometric and material balance approaches of theoretical CO_2 storage capacity estimation to the four case study reservoirs and compare and evaluate the results.

Published work generally assesses the theoretical CO_2 storage capacity of groups of reservoirs. There are few studies that have estimated the effective CO_2 storage capacity of these reservoirs, and only two published methods on how to estimate effective capacity including the method of Bachu et al. (2007), equation 1.5, and the method of Tseng et al. (2012), equations 1.6 and 1.7. The method of Bachu et al. (2007), relies on several capacity coefficients to be known including the coefficients for mobility, buoyancy, heterogeneity, water saturation and aquifer

strength. These are rarely measured within reservoirs and as such, this method of storage capacity estimation is seldom usable. In comparison, the effective CO_2 storage capacity method of Tseng et al. (2012), is based upon the material balance approach and utilises parameters that are readily measurable and are generally included in historical production and pressure data from depleting or depleted gas reservoirs. This study will use the effective method of Tseng et al. (2012) to reduce the theoretical CO_2 storage capacity results. The effective capacity coefficients will be estimated for the case study reservoirs to assess the proportion of pore space available for CO_2 storage. The effective CO_2 storage capacity constitutes a fraction of the theoretical CO_2 storage capacity which ranges between 0 (no storage possible) and 1 (all theoretically accessible pore volume is occupied by CO_2. The results for both the depletion drive and water drive case study reservoirs will be compared and evaluated.

Both theoretical and effective CO_2 storage capacity estimates derived from an individual method will display variability, depending on the variability and uncertainty of individual input parameters. One such parameter that shows variation is the gas compressibility factor (Z-factor). The Z-factor can be estimated in the laboratory, however, it is more commonly estimated analytically using equations of state. In the published literature it is often not obvious how the Z-factor has been estimated and/or which equations of state have been used in its estimation. In the absence of this information, it is unclear whether the use of the equation of state is appropriate to the pressure-temperature environment of the reservoir being analysed. It is important to know the equation of state used as CO_2 storage capacity equations estimate capacity based on the initial pre-production pressure measurement (i.e. highest reservoir pressure): gases are more compressible at higher pressure and equations of state demonstrate greater variability in their predictions of compressibility at higher pressure. This study will use several equations of state, all of which are suitable for use within the natural gas pressure-temperature environment, to estimate Z-factors. The results will be input into the CO_2 storage capacity equations to evaluate the variability in storage capacity estimates arising from the use of different Z-factors.

Another parameter that shows a high degree of variability is reservoir porosity. Mean values for reservoir porosity are often used in CO_2 storage capacity equations. This approach can be applied quickly to a large group of reservoirs, however, it does not honour all the available data for that reservoir. This thesis uses Monte Carlo simulation – repeated random sampling to minimise risk of an unknown probabilistic entity – to honour all available porosity data for each of the studied reservoirs. Reservoir porosity data is a necessary input parameter to the geometric theoretical CO_2 storage capacity method of Bachu et al. (2007), equation 1.1, and will produce a range of storage capacities for a reservoir as a result of Monte Carlo simulation. Again, these results will be compared and evaluated with the results produced from the material balance approach to theoretical CO_2 storage capacity estimation.

In some of the case study reservoirs within this thesis, the reservoir drive mechanism (i.e. depletion or water drive) has previously been erroneously identified based on material balance (P/z) plots. The difficulties of differentiating between water drive and depletion drive reservoirs through the use of P/z plots is well documented (Agarwal et al., 1965; Bruns et al., 1965; Chierici et al., 1967; Dake, 1978; Hagoort, 1988; Pletcher, 2002; Vega and Wattenbarger, 2000). In some cases, water drive reservoirs have been wrongly characterised as depletion drive reservoirs. Therefore, any estimate of the original gas in place (OGIP) will be an over-estimate, hence the CO_2 storage capacity estimate will be reduced as a greater proportion of the pore space will be occupied by water.

Published work has attempted to include the reservoir drive mechanism to limit the CO_2 storage capacity estimate. For example, the work of Bentham (2006) stated that 90% of the pore space could be occupied by CO_2 within depletion drive reservoirs, 65% within water drive reservoirs, and 77.5% within reservoirs experiencing both pressure depletion and water drive. This approach can be applied quickly to a group of reservoirs, however, it is too simplistic for site specific characterisation of individual storage sites within depleted gas reservoirs.

This thesis will determine the drive mechanism of the four case study reservoirs using both P/z plots and Cole plots. Cole plots can be used to easily distinguish between depletion and water drive gas reservoirs, and can also give an

indication of aquifer strength. The OGIP within depletion drive reservoirs can be estimated via linear extrapolation of the trend line on P/z plots. Water drive reservoirs are more complex and the use of aquifer models is necessary to quantify the volume of aquifer influx into a reservoir and the volume of reduction in OGIP, and hence storage capacity, in reservoirs where water production has not been metered throughout the productive lifetime. This study will then explore the difference in estimates of theoretical CO_2 storage capacity for depletion and water drive reservoirs.

Published work has not attempted to assess the dynamic behaviour of a reservoir in pressure communication with a neighbouring reservoir through a shared aquifer with respect to CO_2 storage. This thesis aims to establish a workflow which will be used to evaluate the suitability of such a reservoir for CO_2 storage. The historical production and pressure data of the four case study reservoirs is used to identify any possible pressure communication between neighbouring reservoirs. If identified, a three-dimensional structural model of the storage site and any reservoirs found to be in pressure communication will be constructed. Investigations into the fault seal capabilities of any fault critical for successful storage within the individual sites will be analysed and potential communication pathways examined. The implications for CO_2 storage will be evaluated and discussed.

The approaches outlined above should improve the accuracy of existing theoretical CO_2 storage capacity estimates as it considers the degree of variance of the input parameters, uses several different methods for capacity estimation, demonstrates the effect of using different equations of state and identifies geological limitations to CO_2 storage such as erroneously identified reservoir drive mechanisms and the dynamic behaviour of reservoirs in pressure communication. Figure 1.8 shows the workflow that will be used throughout this thesis to evaluate the reservoirs as to their suitability and capacity for CO_2 storage. Further details can be found in Chapter 3.

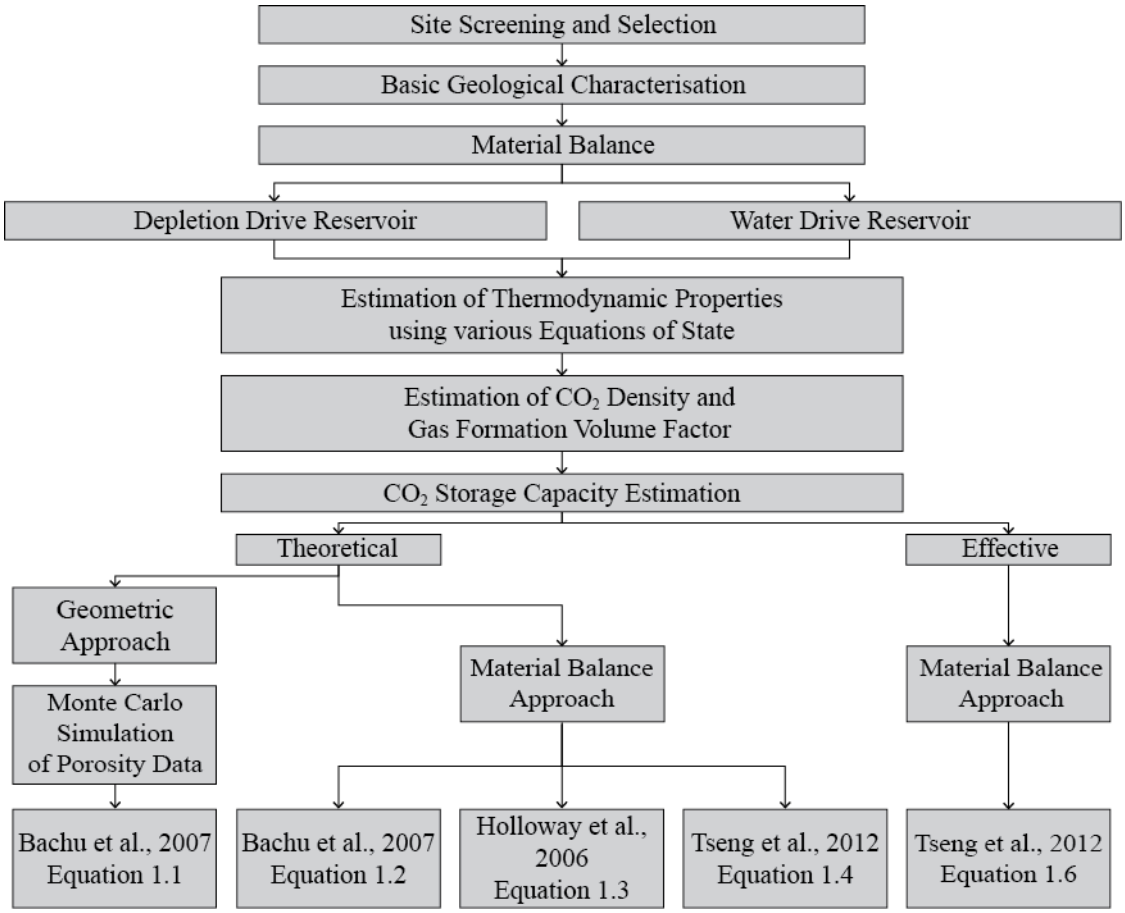

Figure 1.8 A simplified workflow for the evaluation of depleted gas reservoirs with respect to CO_2 storage

1.8. THESIS OUTLINE

Chapter 2 details the complexity of UK Triassic stratigraphy and structural evolution with details of post-depositional diagenetic effects that have affected the quality of individual gas reservoirs and outlines the consequences for CO_2 injection and storage.

Chapter 3 outlines the methodologies that have been adopted and developed for characterisation of depleted gas reservoirs both with and without a water drive. The chapter also introduces the data sets used for analysis.

Chapters 4, 5 and 6 encompass detailed geological characterisation of the reservoirs investigated within this thesis. They also simulate reservoir fluid phase behaviour post-production and throughout injection with a direct emphasis on the gas compressibility factor, Z. They discuss the suitability of each reservoir for CO_2 storage.

Chapter 4 looks at the Hewett Lower Bunter Sandstone reservoir and involves the characterisation process for a relatively "simple" gas reservoir which has not experienced associated water drive with production.

Chapter 5 applies the methods adopted in Chapter 4 to the Hewett Upper Bunter Sandstone reservoir. This reservoir is more complex both in terms of its productive behaviour, as a result of water drive and communication with a neighbouring reservoir. As such, further methods have been developed and applied to allow successful geological characterisation of this reservoir.

Chapter 6 applies and tests the developed methods in Chapters 4 and 5 to the South and North Morecambe Sherwood Sandstone reservoirs.

Chapter 7 evaluates the variability of theoretical CO_2 storage capacity estimation through comparison of methods and differences in reservoir drive mechanisms. Chapter 7 also evaluates the variability of effective CO_2 storage capacity estimation through substitution of theoretical CO_2 storage capacities to determine the effective capacity coefficient. These results will be used to consider global applications of the methods developed within this thesis. Finally the limitations of the study are considered and suggestions made as to further research.

Chapter 8 concludes the thesis. Appendices can be found at the end of the thesis.

2 Stratigraphy, Depositional History and Structure of the UK Triassic Sequence

2.1. INTRODUCTION

The following chapter introduces the Triassic successions within the UK Southern North Sea and the East Irish Sea Basin. The chapter provides an overview of the stratigraphy and depositional history of the Triassic successions and the tectonic, structural and diagenetic events that took place following deposition leading to their current status as productive reservoirs. This will provide the basis from which work on the viability of carbon storage within these reservoirs will stem.

Some of the key attributes for successful CO_2 storage within depleted gas reservoirs are similar to the attributes that enabled a gas accumulation in the first place. These include, but are not limited to, the reservoir characteristics, a physical trap and a sealing cap rock.

For a formation to be an economically viable petroleum reservoir, and therefore a good candidate for CO_2 storage, it must be porous, permeable, have a significant volume of reserves, and thus a significant CO_2 storage capacity (Gluyas and Swarbrick, 2003). Sandstone and limestone are the most common reservoir lithologies (Gluyas and Swarbrick, 2003). The best reservoirs globally are often "young": there has been less opportunity for tectonism and cementation post-deposition which can destroy intrinsic reservoir properties (Gluyas and Swarbrick, 2003).

The reservoirs assessed in this thesis are sandstone reservoirs. There are many environments under which sandstone deposition can occur, including: alluvial fans, aeolian dunes, lakes, fluvial systems, deltas, shallow marine systems and submarine fans (Gluyas and Swarbrick, 2003), see Figure 2.1. The reservoir

sandstones of the Upper and Lower Bunter Sandstone Formation within the Hewett Gas Field, Southern North Sea, were deposited as alluvial plain sandstones (Cooke-Yarborough and Smith, 2003). The reservoir sandstones of the Morecambe North and South Gas Fields, East Irish Sea Basin, are a mixture of fluvial and aeolian deposits (Meadows and Beach, 1993a). The depositional environments of the reservoir sandstones will be further explored in sections 2.4.2 and 2.5.2.

Allen and Allen (1990) defined three trap categories as structural, stratigraphic and hydrodynamic. The traps assessed in this thesis are structural traps. Structural traps may be generated through tectonic, diapiric, compactional and gravitational processes (see Figure 2.2) and are host to almost the entire world's discovered petroleum (Gluyas and Swarbrick, 2003).

Structural traps rely upon the physical trapping of CO_2 below low permeability cap rocks (IPCC, 2005), see Figure 2.3. As the time since the end of injection increases, structural trapping becomes less important, and residual, solubility and mineral trapping processes increase (Figure 2.3).

The cap rock, or seal, is a fundamental part of the trap and prevents petroleum from migrating upward through the rock (Gluyas and Swarbrick, 2003). Thus, rocks that have previously sealed hydrocarbons are expected to be able to seal carbon dioxide (IPCC, 2005). Seals can be subdivided into membrane seals (i.e. petroleum can leak when the pore pressure differential across the seal exceeds the threshold displacement pressure and fluids can pass through the capillary pore system of the seal; the leak is just enough to bring the pore pressure below the threshold displacement pressure) and hydraulic seals (i.e. petroleum preferentially leaks by fracturing where the threshold displacement pressure is so high that the pressure gradient for fracturing is less than the pressure gradient for membrane seal failure; after hydraulic failure the pore fluid pressure will be reduced and the fracture will close) (Gluyas and Swarbrick, 2003). Effective sealing lithologies are mudrocks (including shale) and less commonly, halite (Gluyas and Swarbrick, 2003).

Mudstones are extremely fine-grained sedimentary rocks, deposited in deep marine settings in a low energy environment. Shales are mudstones (or siltstones) with a high degree of fissility, formed as a result of compaction following

deposition. Halites are found in evaporite deposits, and have formed through crystallisation out of evaporating brine lakes and/or seas.

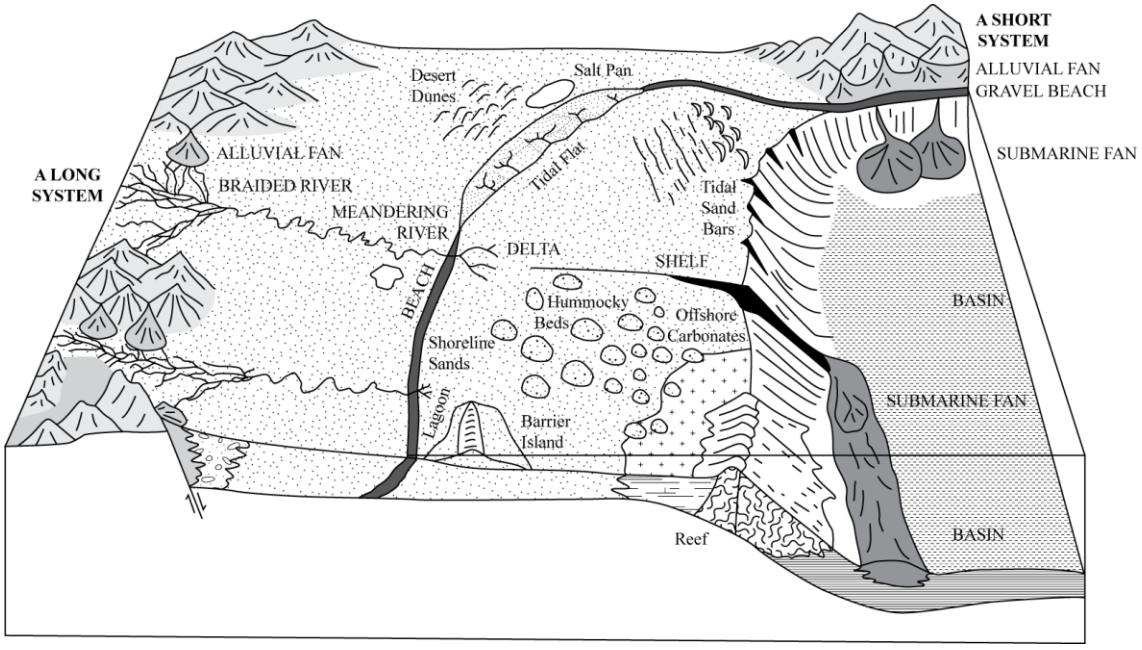

Figure 2.1 Schematic diagram showing the depositional environments of sedimentary rocks. After Fichter et al. (1991).

Figure 2.2 (Overleaf). Examples of structural trapping mechanisms, after Gluyas and Swarbrick (2003). (a) Tilted fault blocks in an extensional regime. The seals are overlying mudstones and cross-fault juxtaposition against mudstones. (b) A rollover anticline on a thrust. Petroleum accumulations may occur on both the hanging wall and the footwall. The hanging wall accumulation is dependent upon sub-thrust fault seal, whereas at least part of the hanging wall trap is likely to be a simple four-way dip-closed structure. (c) The lateral seal of a trap against a salt diaper and a compactional drape trap over the diaper crest. (d) A trap associated with diapiric mudstone, with a lateral seal against the mud-wall. Traps associated with diapiric mud share many features in common with those associated with salt. In this diagram, the diapiric mud-wall developed at the core of a compressional fold. (e) A compactional drape over a basement block commonly creates enormous low relief traps. (f) Gravity-generated trapping commonly occurs in deltaic sequences. Sediment loading causes gravity-driven failure and produces convex-down (listric) faults. The hanging wall of the fault rotates, creating space for sediment accumulation adjacent to the fault planes. The marker beds (grey) illustrate the form of the structure, which has many favourable sites for petroleum accumulation.

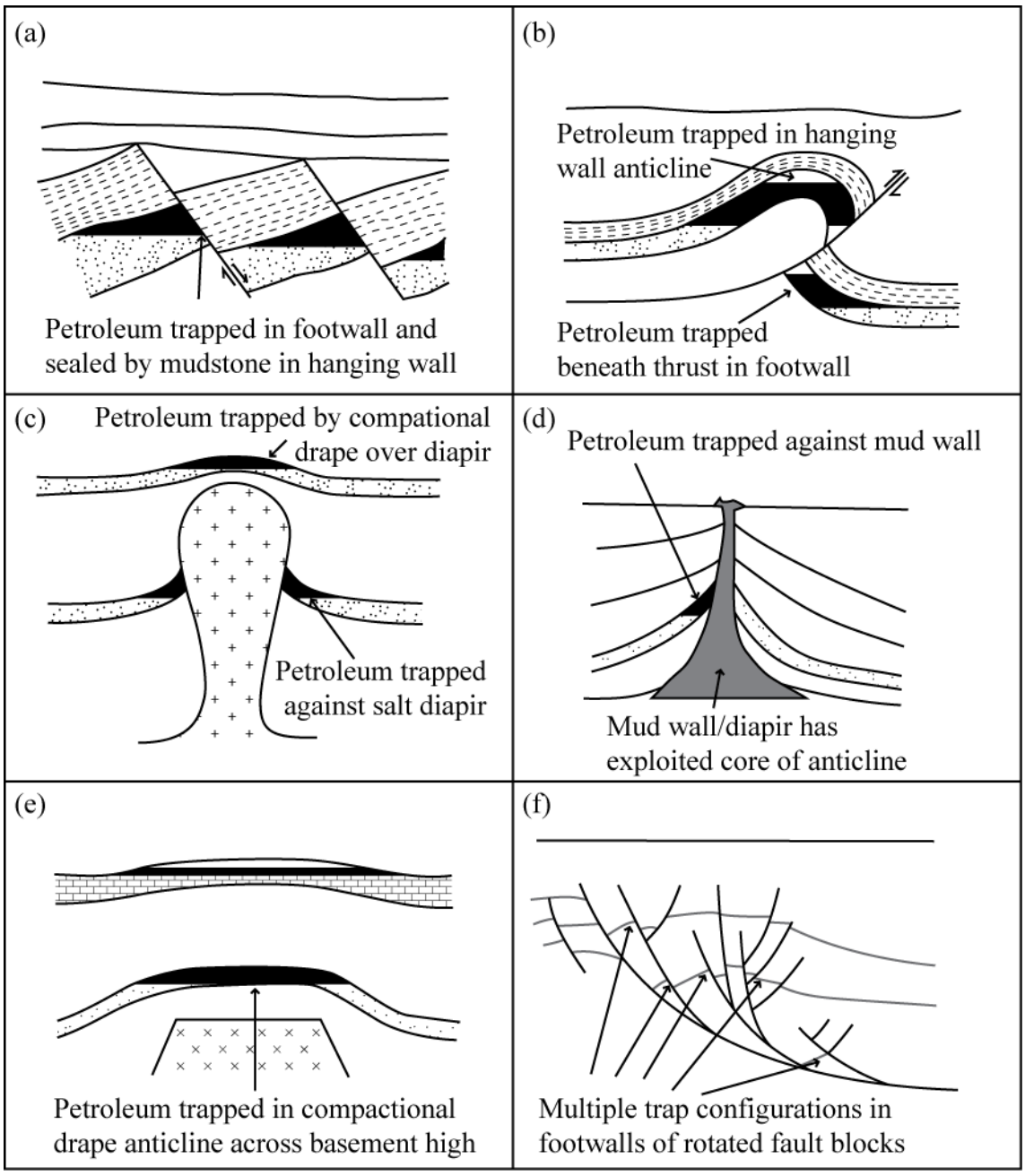
(a)
Petroleum trapped in footwall and sealed by mudstone in hanging wall
(b)
Petroleum trapped in hanging wall anticline
Petroleum trapped beneath thrust in footwall
(c)
Petroleum trapped by compational drape over diapir
Petroleum trapped against salt diapir
(d)
Petroleum trapped against mud wall
Mud wall/diapir has exploited core of anticline
(e)
Petroleum trapped in compactional drape anticline across basement high
(f)
Multiple trap configurations in footwalls of rotated fault blocks

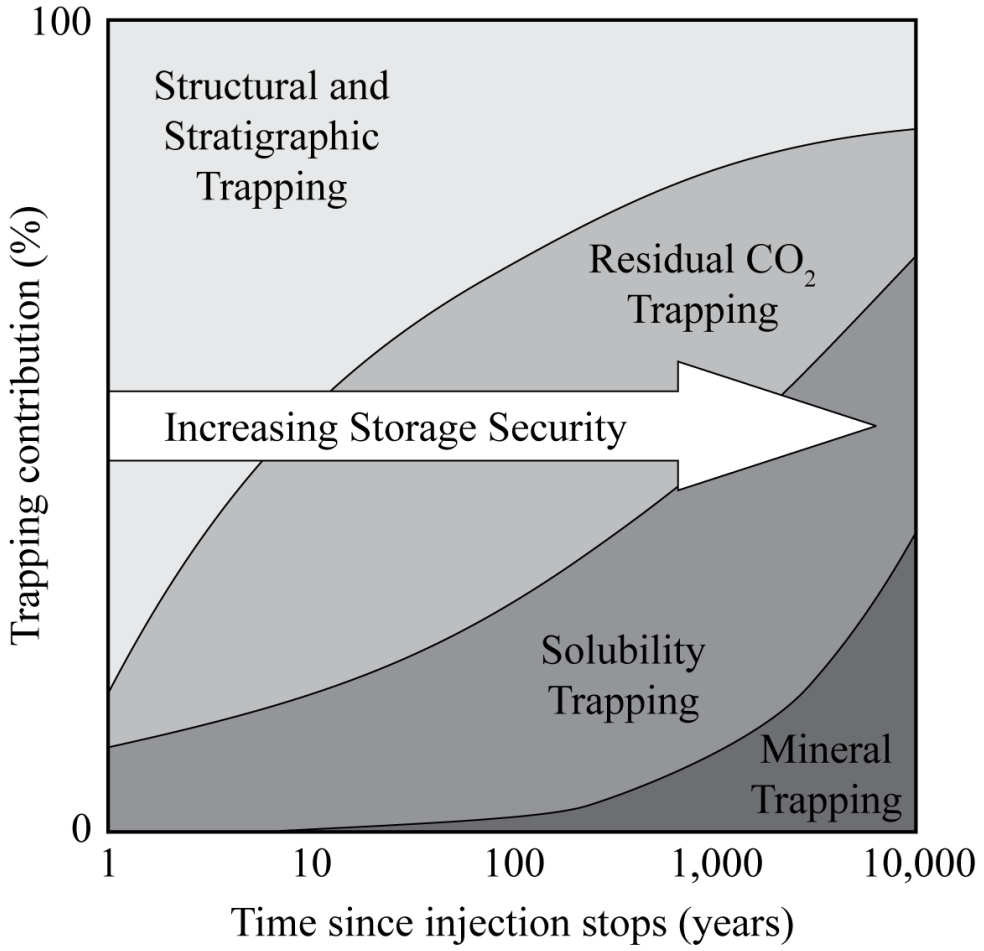

Figure 2.3 Storage security depends on a combination of physical and geochemical trapping. Over time, the physical process of residual CO_2 trapping decreases, and the geochemical processes of solubility trapping and mineral trapping increase. After IPCC (2005).

2.2. LATE PALAEOZOIC AND EARLY MESOZOIC GLOBAL TECTONICS AND CLIMATE

The Late Palaeozoic to Early Mesozoic was characterised by an extensive period of continental drift and collisions through the Appalachian-Variscan Orogeny, ultimately resulting in the creation of the supercontinent of Pangaea (Cameron et al., 1992; Glennie, 1990; Woodcock and Strachan, 2012) (see Figure 2.4). Continental drift and collisions marking the onset of the Appalachian-Variscan Orogeny commenced during the Devonian (dated 416 Ma ± 2.8 Ma – 359.2 Ma ± 2.5 Ma), were heavily active throughout the Carboniferous (dated 359.2 Ma ± 2.5 Ma – 299 Ma ± 0.8 Ma) and ceased during the early Permian (Cameron et al., 1992; Glennie, 1990; Woodcock and Strachan, 2012). This period encompasses the convergence of the southern continent of Gondwana with the northern continent of Laurussia, forming Pangaea. Pangaea remained intact throughout the Triassic until the Middle Jurassic when first continental break-up began (Cameron et al., 1992; Glennie, 1990; Woodcock and Strachan, 2012).

Figure 2.5 shows the palaeogeographical reconstruction of the Middle Triassic across the UK and north-west Europe (adapted from Tyrrell et al. (2012)). The locations of the Hewett Unit Gas Fields and Morecambe Gas Fields have been included. The figure shows the distribution of massifs and sedimentary basins including highs, continental deposits and marine deposits.

Figure 2.6 summarises the global and local climate and sea-level changes throughout the late Carboniferous to Early Jurassic. The formation of Pangaea resulted in a predominantly arid climate and the deposition of Permian red-beds as the super-continent drifted northwards (Woodcock and Strachan, 2012). There was a maritime influence in southern Europe from the Tethys Ocean, however, throughout the rest of Pangaea, a widespread, extreme continental monsoon climate prevailed (Woodcock and Strachan, 2012). In northern Europe the climate resulted in the formation of desert sands, followed by later marine limestones and evaporites.

Following uplift and rifting during the Early Triassic, siliciclastic detritus was deposited (Woodcock and Strachan, 2012). There is also a suggestion of a wetter climate being prevalent due to the abundance of fluvial deposition (Woodcock and Strachan, 2012) (see Figure 2.6). In the UK, this resulted in deposition of the Sherwood Sandstone Group, a siliceous sediment which would later form high quality sandstone reservoirs.

Throughout the Mid- to Late-Triassic there was a return to arid/semi-arid climates with the deposition of evaporites and calcrete soils preserved in the Mercia Mudstone Group (Woodcock and Strachan, 2012). The Mercia Mudstone Group would later form a good quality cap rock to the Sherwood Sandstone Group reservoirs.

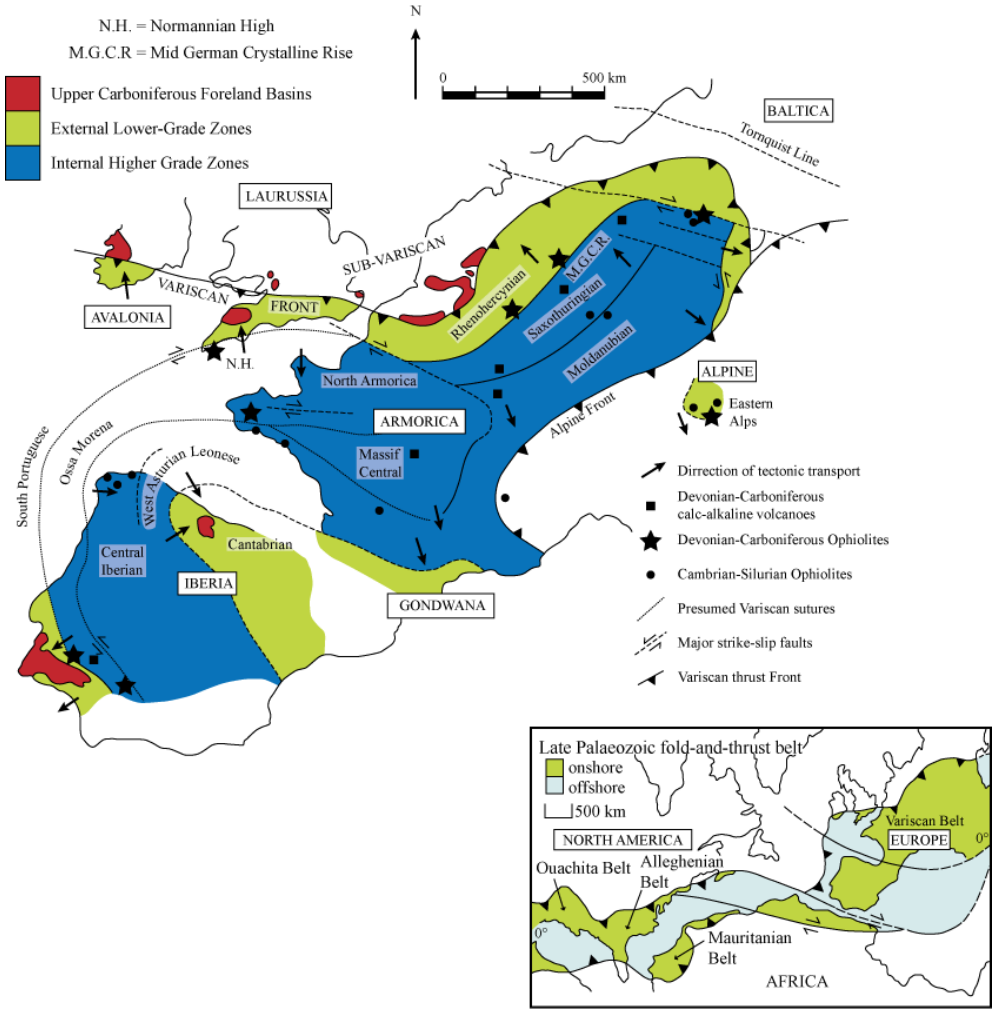

Figure 2.4 The Appalachian-Variscan Orogenic belt of Europe. Adapted from Woodcock and Strachan (2012).

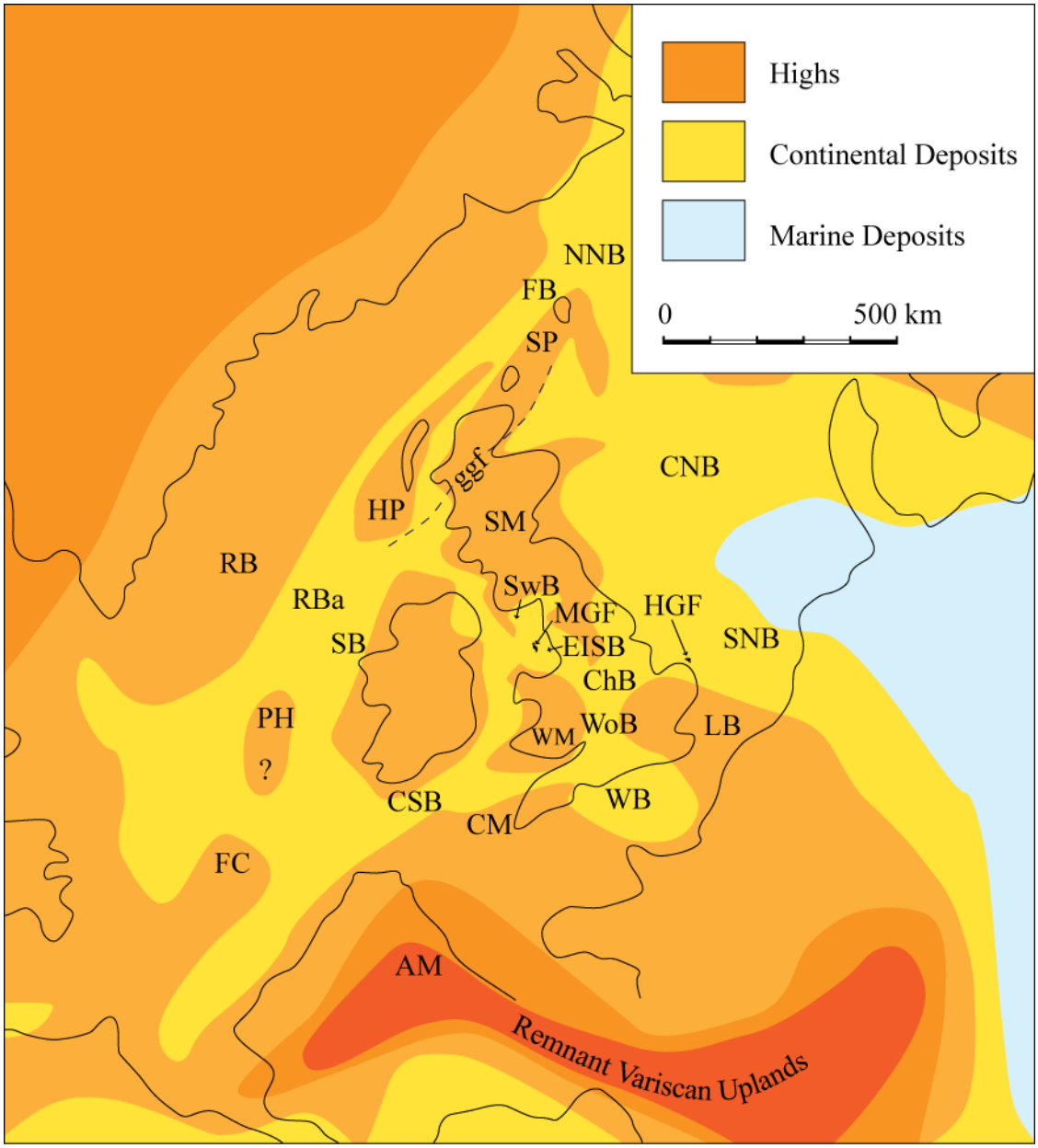

Figure 2.5 Schematic palaeogeographical reconstruction of the Middle Triassic showing the distribution of massifs and sedimentary basins. AM, Armorican Massif; CM, Cornubia Massif; FC, Flemish Cap; HP, Hebridean Platform; IM, Irish Massif; LB, London-Brabant High; PH, Porcupine High; RB, Rockall Bank; SM, Scottish Massif; SP, Shetland Platform; ChB, Cheshire Basin; CNB, Central North Sea Basin; CSB, Celtic Sea Basins; EISB, East Irish Sea Basin; FB, Faeroe-Shetland Basin; NNB, Northern North Sea Basin; RBa, Rockall Basin; SB, Slyne Basin; SNB, Southern North Sea Basin; SwB, Solway Basin; UB, Ulster Basin; WM, Welsh Massif; WB, Wessex Basin; WoB, Worcester Basin; ggf, Great Glen Fault (blue dashed line); MGF, Morecambe Gas Fields; HGF, Hewett Unit Gas Fields. Adapted from Tyrrell et al. (2012).

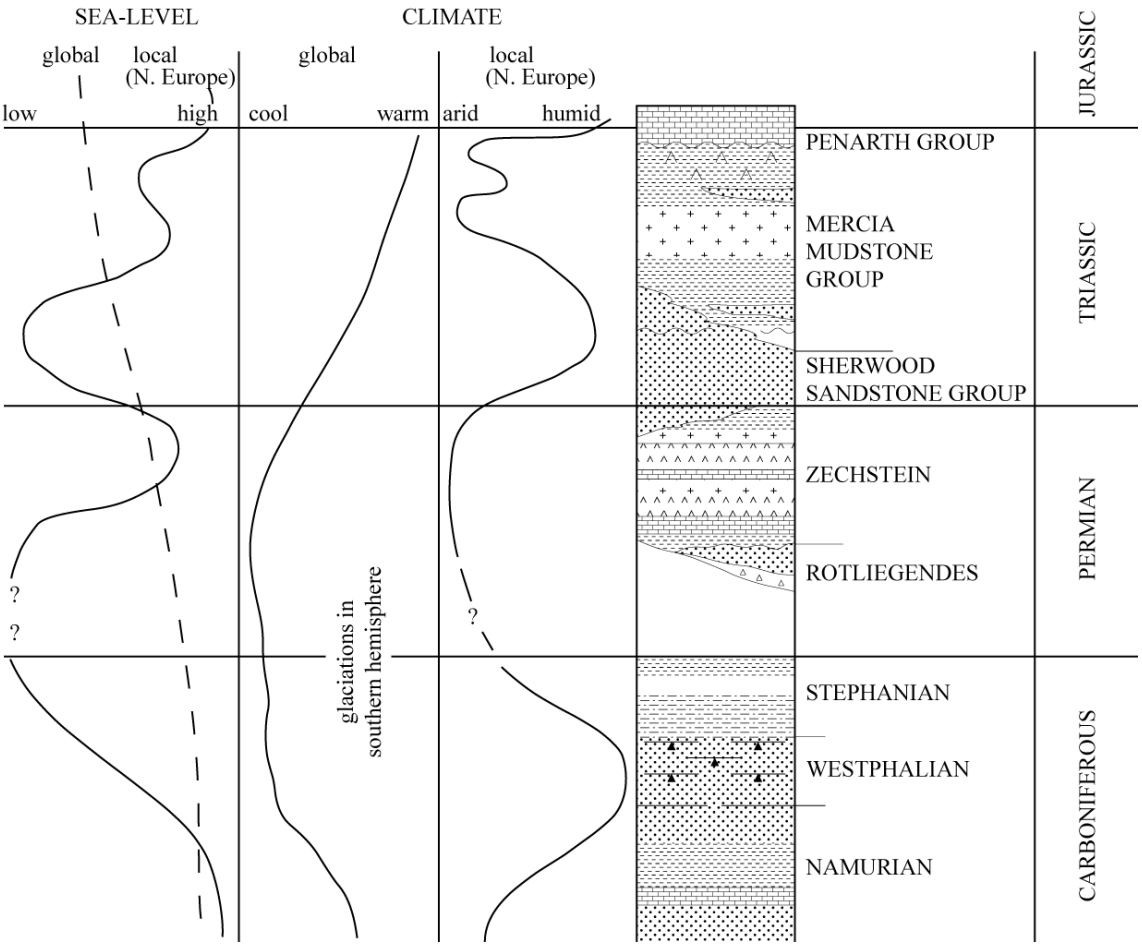

Figure 2.6 Changes in sea-level and climate through the Late Carboniferous to Early Jurassic. After Woodcock and Strachan (2012).

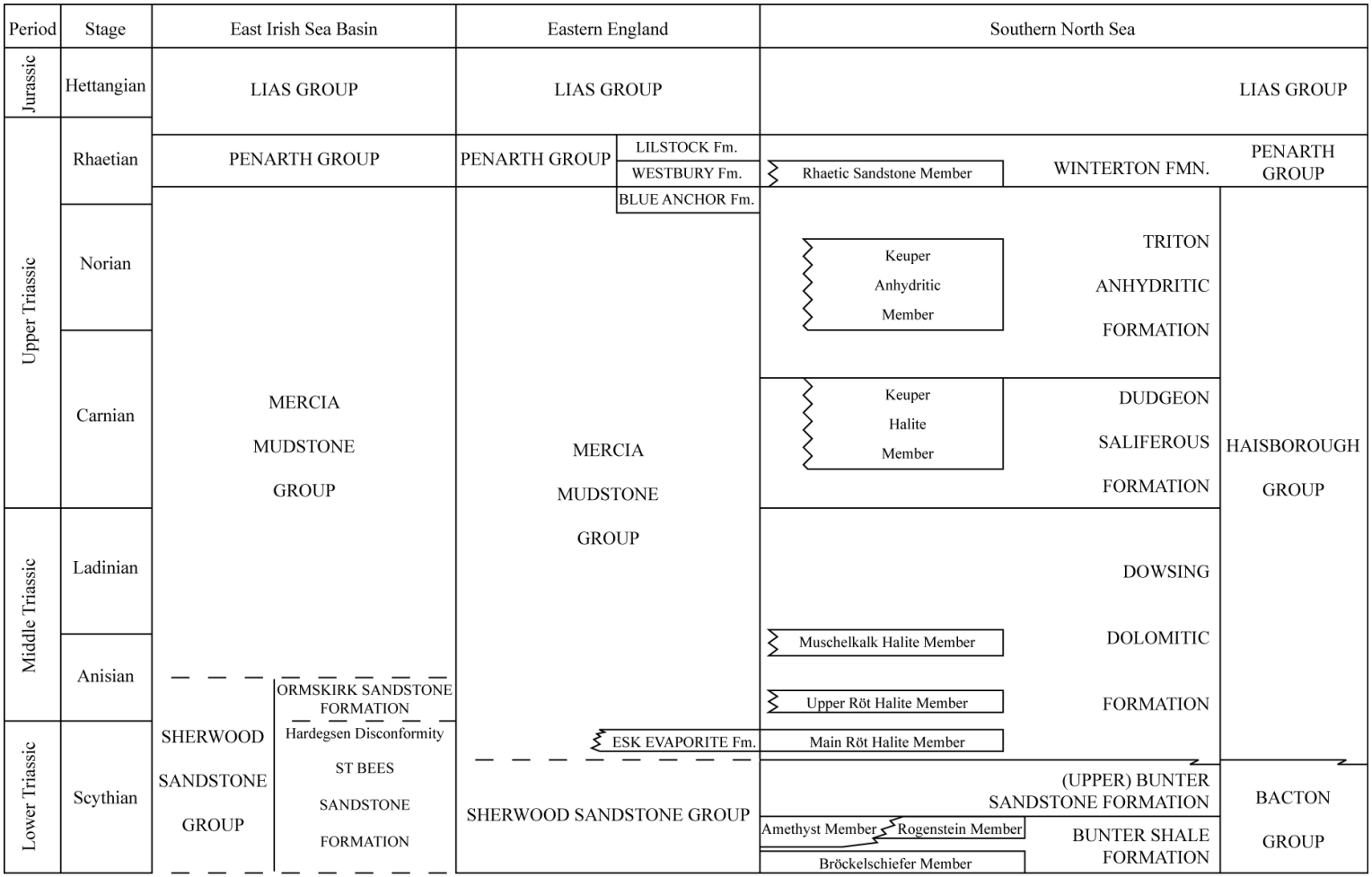

Figure 2.7 Correlation of UK onshore and offshore Triassic Strata. The Lower Bunter Sandstone occurs within the Bröckelschiefer Member of the Bunter Shale Formation. The base of the Mercia Mudstone Group is diachronous within the East Irish Sea Basin and Eastern England. Adapted from Jackson et al. (1995) and Cameron et al. (1992).

2.3. UK TRIASSIC STRATIGRAPHY

Figure 2.7 shows a correlation of the UK Triassic succession both onshore and offshore. UK Triassic stratigraphy is dominated by red bed deposits of predominantly aeolian origin and evaporite deposits. There is much difficulty in confidently establishing the age (Lower, Middle or Upper Triassic) of individual stratigraphic units of the UK Triassic succession (Warrington et al., 1980; Woodcock and Strachan, 2012). The base of the UK Triassic succession is diachronous and cannot be identified with confidence despite there being successions spanning the Permo-Triassic boundary (Warrington et al., 1980; Woodcock and Strachan, 2012). Previous attempts have seen Warrington et al. (1980) using the Bröckelschiefer (the base of the German Triassic succession) to mark the base of the UK Triassic succession.

However, the UK hosts many well developed sedimentary successions of Mid Triassic age. The Muschelkalk facies is missing in the UK, however, coeval deposits occur in red bed sequences (Cameron et al., 1992; Warrington et al., 1980). Warrington et al. (1980) also defined the upper limit of the Triassic succession, marked by the base of the planorbis subzone (Hettangian Stage).

Within the UK Triassic succession there are three major lithostratigraphical units: the Sherwood Sandstone Group, Mercia Mudstone Group and the Penarth Group (Warrington et al., 1980). The Sherwood Sandstone Group (Lower to Middle Triassic) is roughly comparable to units formerly known as the Bunter Sandstone Formation. The Bunter Sandstone Formation is old terminology that has now been abandoned following the publication by Warrington et al. (1980). However, for the purposes of this study, this old terminology will be retained for use in the Hewett study (see section 2.4), where the reservoirs have been named after the Bunter Sandstone.

2.3.1. THE SHERWOOD SANDSTONE GROUP

The Sherwood Sandstone Group (260-230 Ma) is a thick sequence of sandstones (Warrington et al., 1980). Some of the natural geological structures that

have formed in the Sherwood Sandstone Group, both onshore and offshore the UK, such as anticlines, have served as mostly high quality oil and gas reservoirs (Glennie, 1990). A select few of these reservoirs have been proposed to be suitable for carbon dioxide storage complexes (Bentham, 2006; Kirk, 2006).

The base of the Sherwood Sandstone Group is strongly diachronous and spans the Permo-Triassic boundary (Warrington et al., 1980). Despite this, there are great difficulties in identifying the base of the Triassic at outcrop. The top is also diachronous spanning much of the Scythian and into the Anisian and Ladinian in some areas (Warrington et al., 1980).

The sandstones encountered are red, yellow and brown in colour, and there is also a considerable amount of colour mottling (Warrington et al., 1980). Deposition occurred in a fluvial environment, more precisely, within streamflood and braided stream settings (Benton et al., 2002). The group comprises coarse-grained facies of well-sorted conglomerates and cross-bedded sandstones deposited within metre-scale fining-upward cycles (Benton et al., 2002). The conglomerates were deposited on upland margins as alluvial fan deposits (Benton et al., 2002). They grade upwards into aeolian red sandstone and siltstone units. Ripple marks and desiccation cracks are common within the siltstone units, and they are occasionally accompanied with evaporites including anhydrite and gypsum and calcareous palaeosols (Steel (1974b) in: Benton et al. (2002)). The siltstone units are indicative of overbank deposits of established fluvial systems or playa lake deposits (Steel (1974a) in: Benton et al. (2002)), and the presence of calcareous palaeosols and evaporites indicate arid conditions. The sandstones generally show good porosity and permeability (Kirk, 2006) – intrinsic properties that have previously made them high quality gas reservoirs, and properties necessary for a potential high quality CO_2 storage reservoir.

The Sherwood Sandstone Group mostly lacks fossils with some major units completely void, and those that are present only prevail on a local scale. However, there is generally an abundance of fossils within the uppermost units, particularly in the Midlands, providing evidence of a marine origin within the Anisian (Benton et al., 2002; Warrington et al., 1980). These prevail in argillaceous sediments (containing substantial amounts of clay): amphibians and reptiles have been

observed in lag deposits within cross-bedded channel fills, whereas plants, invertebrates and vertebrates tend to be distributed throughout (Benton et al., 2002). Unfortunately, these fossiliferous units cannot be used for biostratigraphic correlation.

2.3.2. THE MERCIA MUDSTONE GROUP

The Mercia Mudstone Group overlies the Sherwood Sandstone Group (Figure 2.7). The Mercia Mudstone Group is a proven hydrocarbon seal to oil and gas reservoirs of the Sherwood Sandstone Group, for example, the reservoirs within the East Irish Sea Basin (Kirk, 2006). It is hoped to serve as the direct cap rock to the reservoirs of the Sherwood Sandstone Group that are to be used for carbon dioxide storage (Bentham, 2006; Kirk, 2006).

The Mercia Mudstone Group consists of units formerly known as the Keuper Marl. The Mercia Mudstone Group comprises a sequence of argillaceous formations (Warrington et al., 1980). The lower boundary is generally sharp, but can also be easily identified in some gradational sequences where mudstone and siltstone beds dominate over sandstone beds. Like the Sherwood Sandstone Group, the base of the Mercia Mudstone Group is strongly diachronous (Warrington et al., 1980). The base can be dated as being Scythian in age in Eastern England; however, it is much younger within the East Irish Sea Basin where it is observed to be Anisian and in some cases Ladinian in age.

The thickest sequences of the Mercia Mudstone Group are found to accumulate in fault-bounded basins, however there was vast coverage over the Sherwood Sandstone Group, Permian strata and Carboniferous and older rocks (Howard et al., 2008). Thicknesses are variable, ranging from barely 200 m to over 1350 m in basinal areas (Warrington et al., 1980).

The mudstones are generally red in colour, with lesser amounts of green and grey mudstones, and siltstones. Thick halite bearing units are developed in basinal successions including those in Dorset, Somerset, Worcestershire, Staffordshire, Cheshire, west Lancashire, south Cumbria, and east and north Yorkshire (Howard et al., 2008). Thin gypsum and anhydrite deposits and sandstone beds are widely

developed at certain stratigraphic levels (Howard et al., 2008). The group was deposited in a subaqueous environment, most likely within playas or inland sabkha environments with intermittent connections to the sea. Wind-blown sedimentary deposits are also likely to contribute to the succession (Warrington et al., 1980).

Mercia Mudstone Group deposition ceased during the Rhaetian when rising sea levels flooded the mudflats and resulted in deposition of the marine muds of the Westbury Formation (Penarth Group) (Warrington (1992) in: Howard et al. (2008)).

2.3.3. THE PENARTH GROUP

The Penarth Group (formerly Rhaetic) is not a direct cap rock to the reservoirs considered for carbon storage within this thesis. However, it marks the final Triassic deposition, overlying the Mercia Mudstone Group, and as such forms overburden strata. The Penarth Group is widespread across the UK consisting of the Westbury Formation, overlain by the Lilstock Formation. The Penarth Group is composed of a series of lagoonal and/or shallow marine deposits of mudstone, siltstone and limestone (Gallois, 2008). Currently the Triassic-Jurassic boundary marking the top of the Penarth Group is unresolved (Gallois, 2008).

2.4. THE SOUTHERN NORTH SEA TRIASSIC SEQUENCE

Offshore the UK within the Southern North Sea, the Sherwood Sandstone Group is known as the Bunter Sandstone Formation, and the Mercia Mudstone Group is equivalent to the Haisborough Group (Warrington et al., 1980). The Triassic stratigraphy of the Southern North Sea is marked by the Bunter Shale Formation and Bunter Sandstone Formation of the Bacton Group (Lower Triassic – Scythian stage) overlain by the Haisborough Group comprising the Dowsing Dolomitic Formation (Lower to Middle Triassic), Dudgeon Saliferous Formation (Upper Triassic – Carnian stage) and Triton Anhydritic Formation (Upper Triassic – Carnian to Rhaetian stage) (Cameron et al., 1992). The Penarth Group (Upper Triassic – Rhaetian stage) and Lias Group (Upper Triassic to Jurassic – Rhaetian to Hettangian stage) lie conformably at the top of the sequence (Cameron et al., 1992).

Chapters 4 and 5 of this thesis focus on the potential for CO_2 storage within the Triassic Bunter depleted gas reservoirs of the Hewett Gas Field of the Southern North Sea. The following sections (2.4.1 to 2.4.4) describe the play elements that have previously made the Hewett Unit a good quality petroleum system.

2.4.1. SOURCE ROCKS

The underlying Carboniferous Westphalian coal measures are the primary source to the Hewett Unit Gas Fields (Cameron et al., 1992; Cooke-Yarborough, 1991; Cooke-Yarborough and Smith, 2003). The Late Jurassic saw gas generation with contemporaneous migration through faults that extend from the Jurassic units down through the Carboniferous stratigraphy (Cooke-Yarborough and Smith, 2003). Hydrogen sulphide, present in the Hewett Upper Bunter Sandstone reservoir gas was most likely sourced from the action of sulphate-reducing bacteria on anhydrite in the presence of hydrocarbons with carbon dioxide and nitrogen liberated as by-products (Cooke-Yarborough and Smith, 2003). Anhydrite is believed to have been sourced within the overlying Haisborough Group sediments (Cooke-Yarborough and Smith, 2003).

2.4.2. RESERVOIR ROCKS

The Hewett Gas Field of the Southern North Sea is host to three productive reservoirs, two of which are of the Triassic Bunter Sandstone Formation. Figure 2.8 shows the distribution and thickness map of the Upper Bunter Sandstone Formation within the Southern North Sea. The Lower Bunter Sandstone Formation (also known as the Hewett Sandstone Formation) occurs within the Bröckelschiefer Member (Cameron et al., 1992; Cumming and Wyndham, 1975). The distribution of the Lower Bunter Sandstone Formation is shown in Figure 2.9. A depositional model of the Upper and Lower Bunter Sandstone Formation of the Southern North Sea is illustrated in Figure 2.10. The third productive reservoir is of the Zechsteinkalk deposited during the Permian. This reservoir is not considered here for carbon storage due to the reservoir's complex compartmentalisation (Cooke-

Yarborough and Smith, 2003) which is poorly understood and would be too costly to develop for carbon storage as the drilling of more wells would be required (Bentham, 2006) .

2.4.2.1. THE HEWETT GAS FIELD LOWER BUNTER SANDSTONE FORMATION RESERVOIR

The Lower Bunter Sandstone formation is concentrated along a narrow belt on the northern flank of the London-Brabant Massif (Cameron et al., 1992). It is composed of alluvial sandstones (Cooke-Yarborough and Smith, 2003) and consists of well-sorted, medium to coarse grained, red-brown, quartzose sandstones (Cameron et al., 1992).

Reservoir properties (such as porosity and permeability) are very good with average porosities of 23% and average permeabilities of 1000 mD. The main control on reservoir quality within the Hewett Unit is governed by the Dowsing Fault Zone (see Chapter 1, Figure 1.2) (Cooke-Yarborough and Smith, 2003). Porosity and permeabilities tend to decrease in the reservoirs to the east of the Dowsing Fault Zone, where there are fault throws of approximately 200 m and, therefore, reservoir rocks have been subject to a higher degree of compaction (Cooke-Yarborough and Smith, 2003).

2.4.2.2. THE HEWETT GAS FIELD UPPER BUNTER SANDSTONE FORMATION RESERVOIR

The Hewett Upper Bunter Sandstone reservoir (also known as the Bunter Sandstone Formation) is shallower than the Hewett Lower Bunter Sandstone reservoir. Fine-grained clastic sedimentation of the Bunter Shale Formation ceased and fluvial channel and sheetflood sands of the Upper Bunter were deposited during a time of regional basin subsidence (Cooke-Yarborough and Smith, 2003). Rapid deposition of the Upper Bunter Sandstone Formation occurred as a result of uplift of the London-Brabant Massif (Cooke-Yarborough and Smith, 2003).

Local to the Hewett Upper Bunter Sandstone reservoir are alluvial plain sandstones (Cooke-Yarborough and Smith, 2003). They consist of fine-grained, upward-coarsening, red, orange and white sheet-sands (Cameron et al., 1992).

The Hewett Upper Bunter Sandstone reservoir enjoys good reservoir properties similar to those of the Hewett Lower Bunter Sandstone reservoir with average porosities of 21% and average permeabilities of 500 mD (Cooke-Yarborough and Smith, 2003).

2.4.3. CAP ROCKS

The Bunter Shale Formation of the Bacton Group is the direct cap rock to the Hewett Lower Bunter Sandstone reservoir (see Figure 2.12). The Bunter Shale is an anhydritic, red-brown mudstone with minor amounts of shale (Cooke-Yarborough and Smith, 2003). Deposition was within a floodplain environment (Cooke-Yarborough and Smith, 2003).

The Dowsing Dolomitic Formation of the Haisborough Group is the direct cap rock to the Hewett Upper Bunter Sandstone reservoir, comprising red, silty mudstones with intercalated halite members (see Figure 2.12). It was deposited in a floodplain environment under coastal sabkha or shallow marine conditions (Cooke-Yarborough and Smith, 2003). It is equivalent to the lower part of the Mercia Mudstone Group.

2.4.4. STRUCTURE

The structure of the Hewett Unit (previously illustrated in Chapter 1, Figure 1.2) is dominated by a NW-SE Variscan structural trend. The Dowsing Fault Zone and South Hewett Fault were originally part of an extensional Carboniferous fault system placed in transpression during the Variscan Orogeny as a result of the northward movement of the London-Brabant Massif (Cooke-Yarborough and Smith, 2003). They have later undergone reactivation and younger Permian and Mesozoic fault systems have developed from them (Cooke-Yarborough and Smith, 2003).

During the late Triassic and Jurassic, extensional/transtensional movement was prevalent along the South Hewett Fault, North Hewett Fault and Dowsing Fault Zone (Cooke-Yarborough and Smith, 2003).

The structural anticline characteristic of the Hewett Gas Field did not develop until the late Cretaceous and underwent tightening during the Oligocene due to inversion along the South Hewett Fault (Cooke-Yarborough and Smith, 2003).

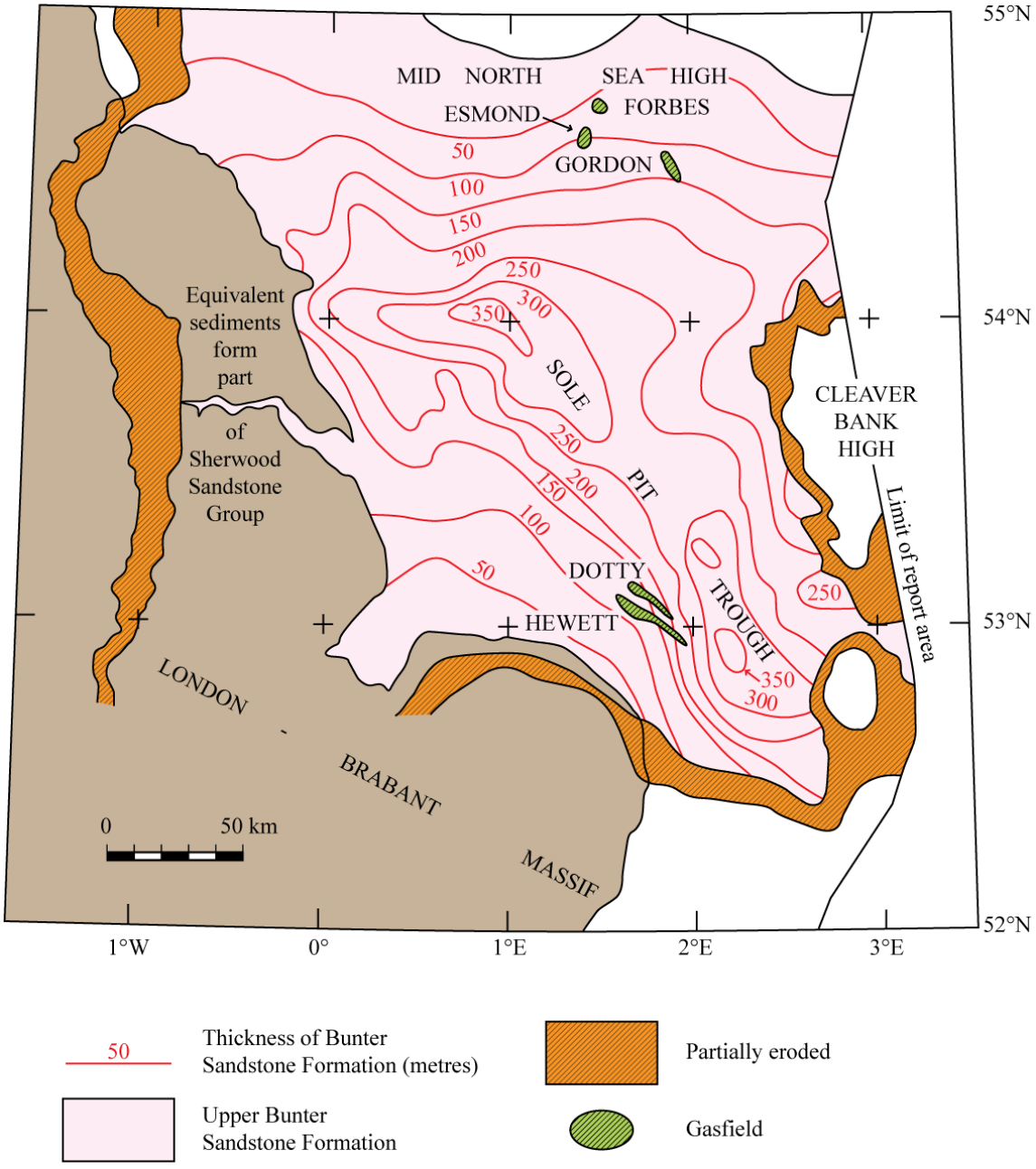

Figure 2.8 Distribution and Thickness of the Upper Bunter Sandstone Formation within the Southern North Sea. After Cameron et al. (1992).

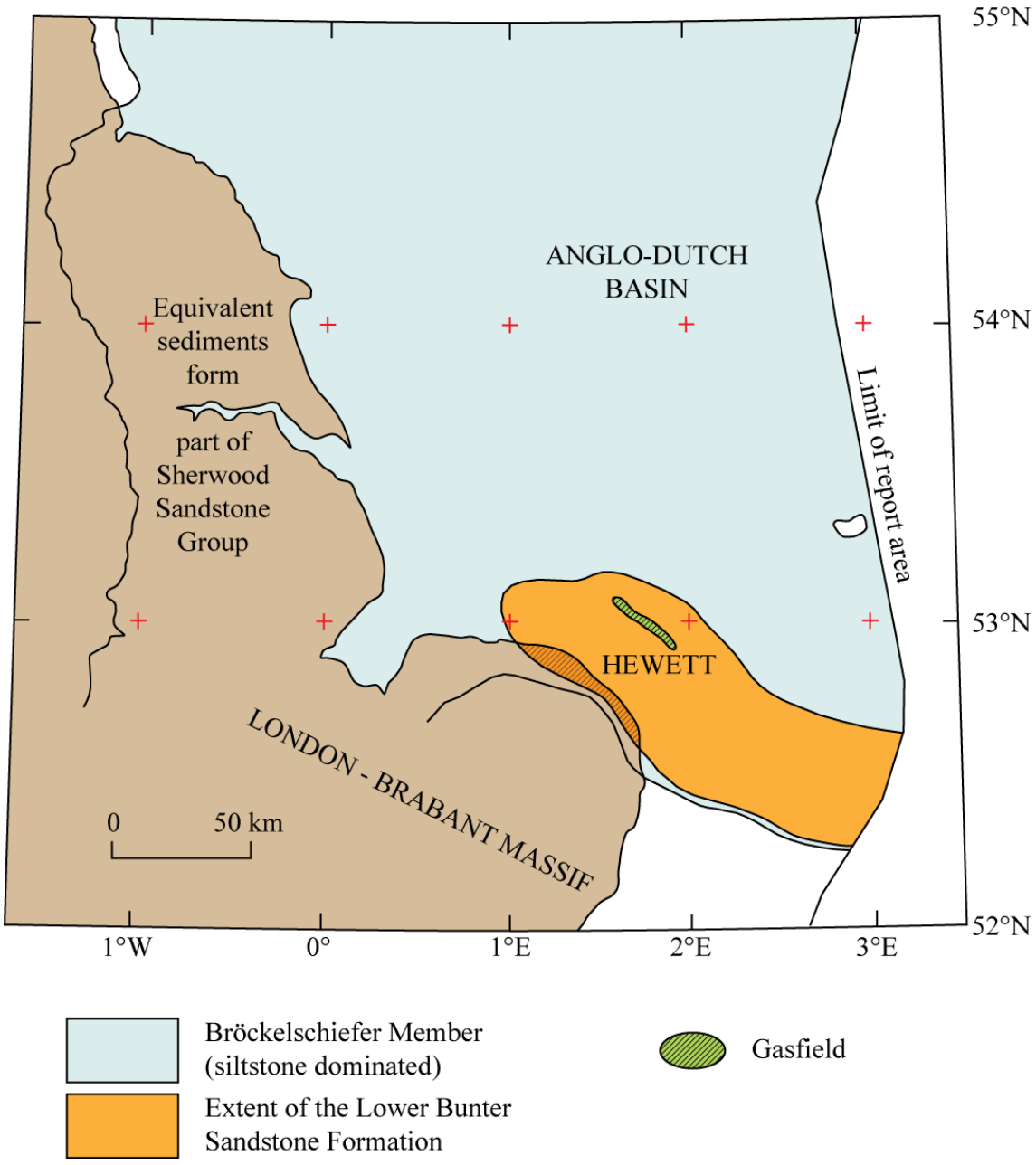

Figure 2.9 Distribution of the Lower Bunter Sandstone Formation within the Bröckelschiefer Member. After Cameron et al. (1992).

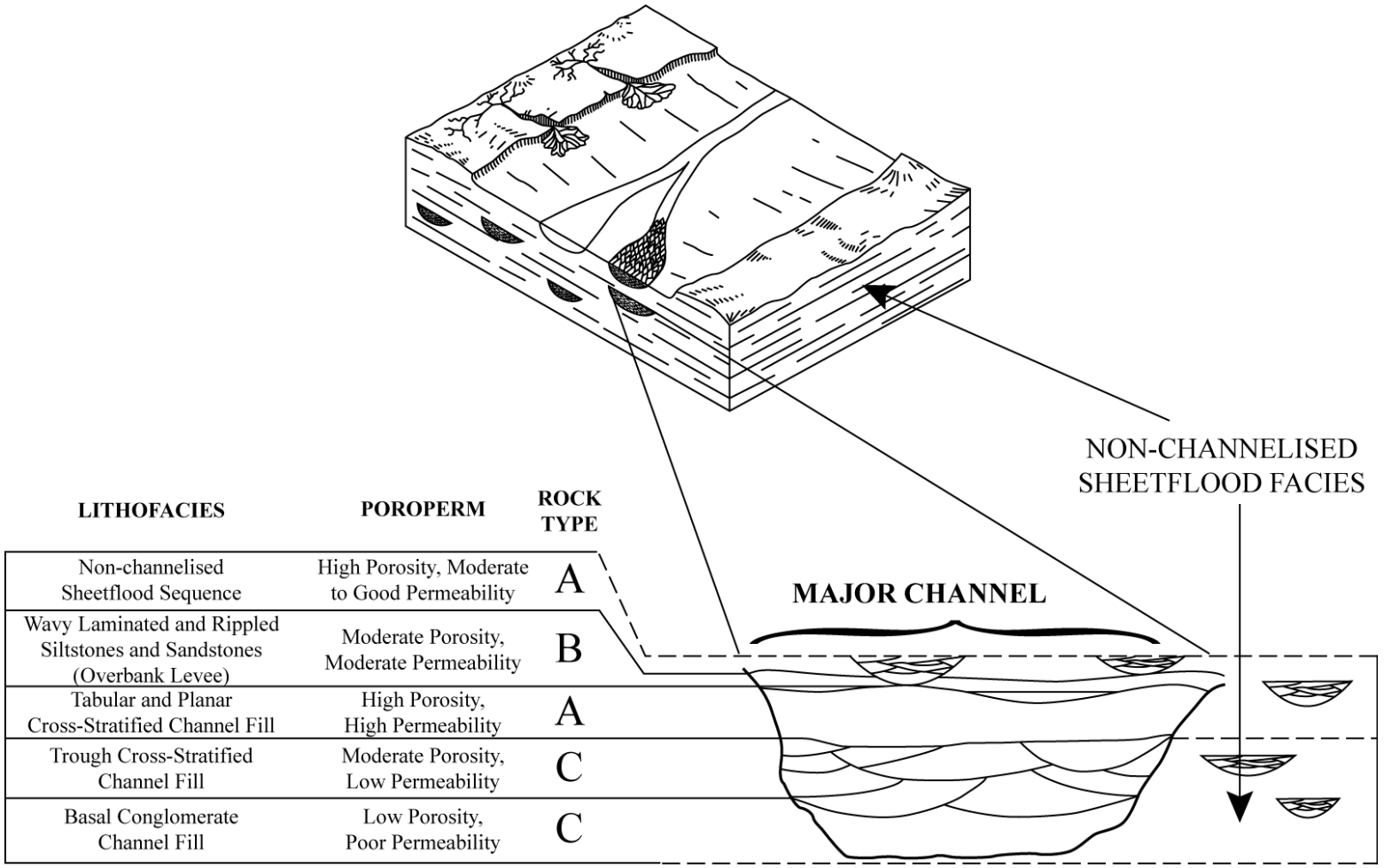

Figure 2.10 Depositional model of the Bunter Sandstone Formation, Southern North Sea. Adapted from Ketter (1991).

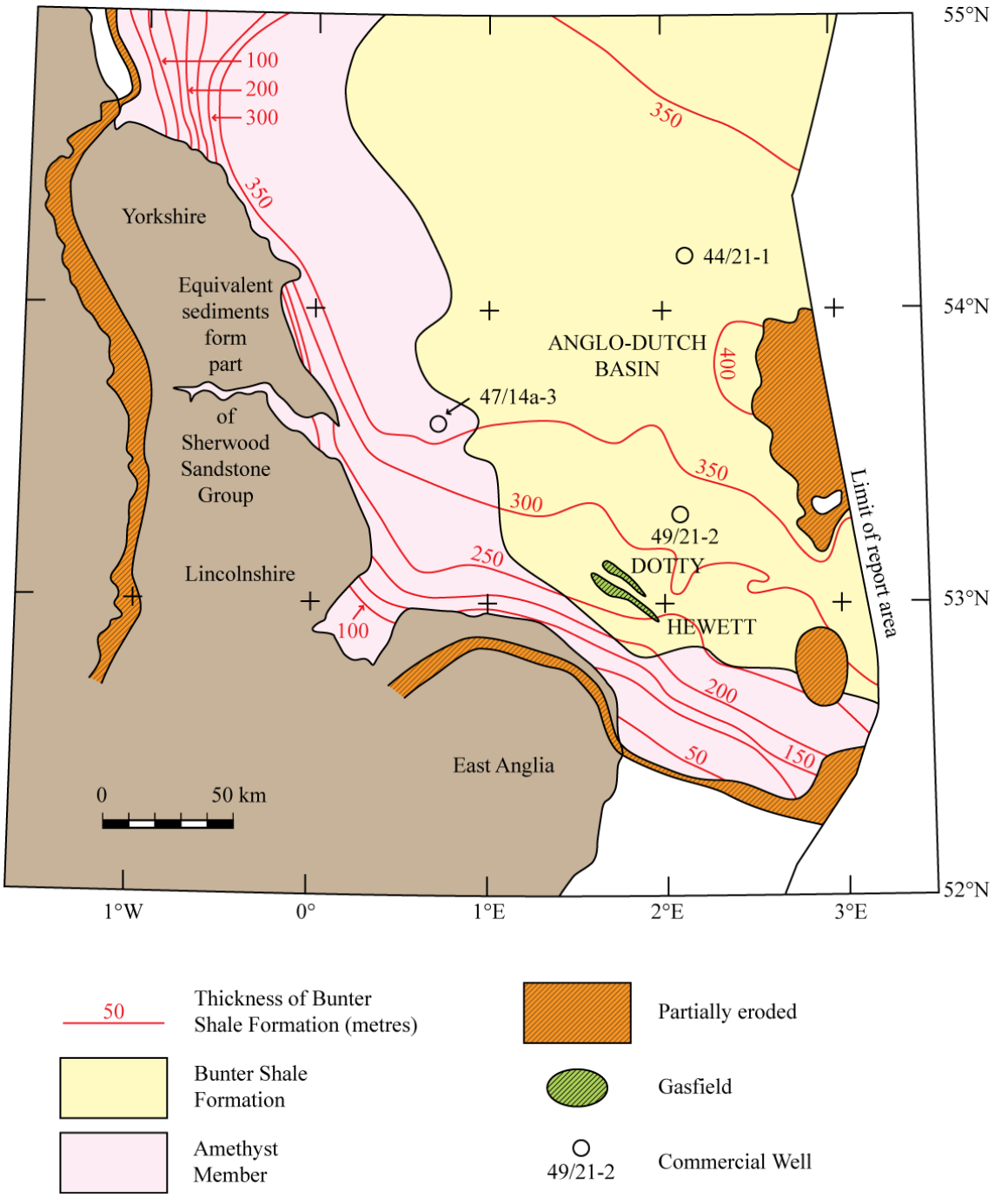

Figure 2.11 Distribution and thickness of the Bunter Shale Formation, Southern North Sea. After Cameron et al. (1992).

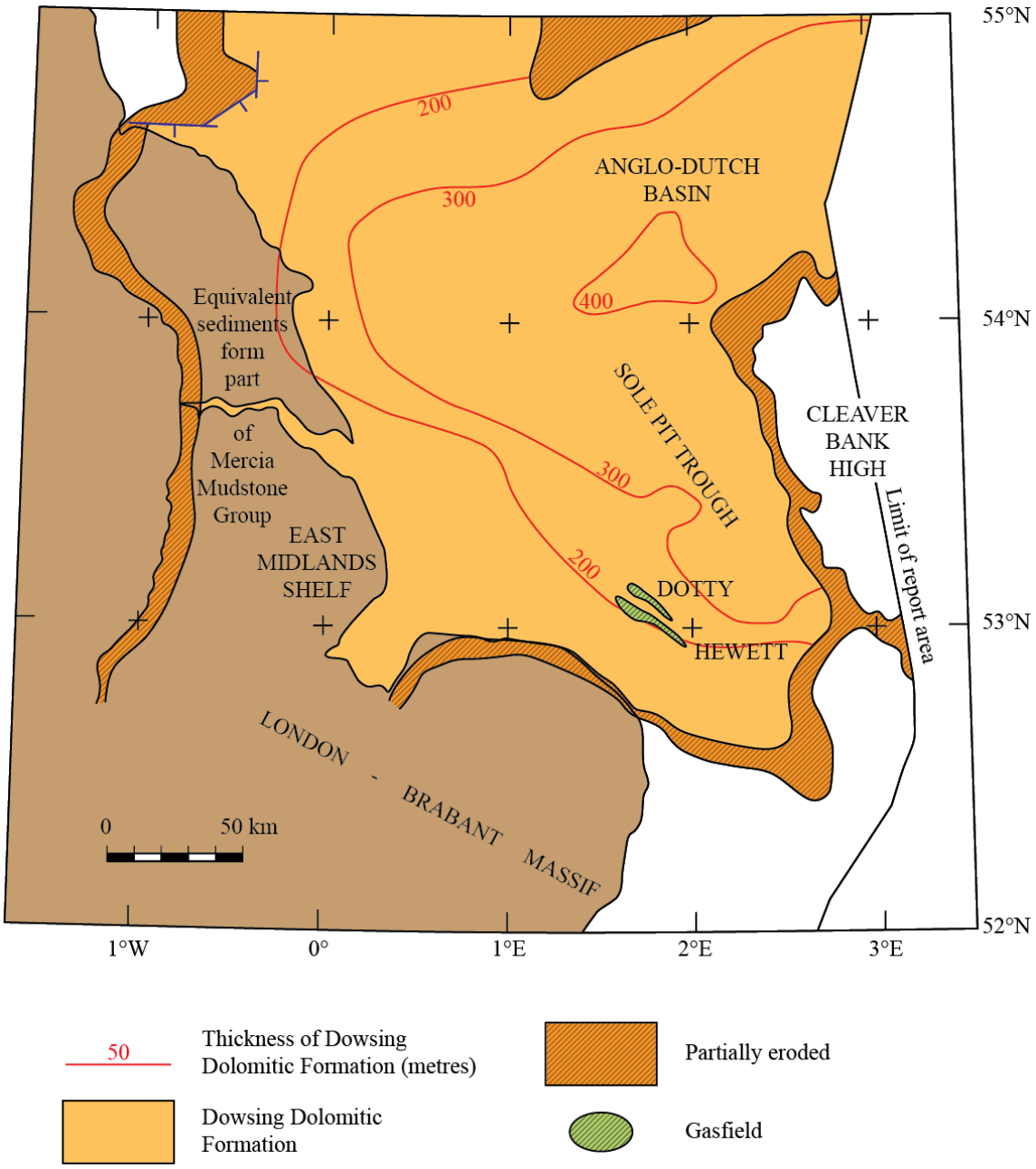

Figure 2.12 Distribution and thickness of the Dowsing Dolomitic Formation, Southern North Sea. After Cameron et al. (1992).

2.5. THE EAST IRISH SEA TRIASSIC SEQUENCE

Within the East Irish Sea the Triassic strata are subdivided into the Sherwood Sandstone Group, Mercia Mudstone Group and the Penarth Group in agreement with the correlations of Warrington et al. (1980), although the Penarth Group has not been proven offshore (Jackson et al., 1995). They lie conformably over the top of Late Permian rocks and are overlain by Lower Jurassic strata (Jackson et al., 1995). The Triassic strata within the East Irish Sea Basin represent thick sandstone sequences: up to 2000 m thickness within the Sherwood Sandstone Group and 3200 m within the Mercia Mudstone Group offshore the UK (Jackson et al., 1995).

The Sherwood Sandstone Group of the East Irish Sea can be further subdivided into the St. Bees Sandstone Formation (Scythian) which is overlain by the Ormskirk Sandstone Formation (Lower Anisian). The Mercia Mudstone Group directly overlies the Ormskirk Sandstone Formation of the Sherwood Sandstone Group. The Mercia Mudstone Group consists of a series of interbedded units of halites and mudstones spanning the Lower Anisian to the Lower Rhaetian. Within the Upper Norian and Lower Rhaetian it is likely that the sediments are actually representative of the Penarth Group, although this has not been proven offshore (Jackson et al., 1995).

Sedimentation patterns were influenced by Late Palaeozoic topography with highlands surrounding the East Irish Sea Basin, namely the Longford Down Massif, the Southern Uplands Massif, the Lake District Massif, the Isle of Man, the Ramsey-Whitehaven Ridge, and the Welsh Massif (see Figure 2.13). Studies by Meadows and Beach (Meadows and Beach, 1993a; Meadows and Beach, 1993b) have defined lateral seismic facies variations within the Ormskirk Sandstone Formation of the East Irish Sea. Figure 2.14 and Figure 2.15 show the distribution of seismic facies in the lower and upper Ormskirk Sandstone Formation respectively, as defined by Meadows and Beach (1993a) using seismic and wireline logs. Figure 2.16 and Figure 2.17 are schematic diagrams of palaeogeography for the lower and upper Ormskirk Sandstone Formation based on Figure 2.14 and Figure 2.15 respectively.

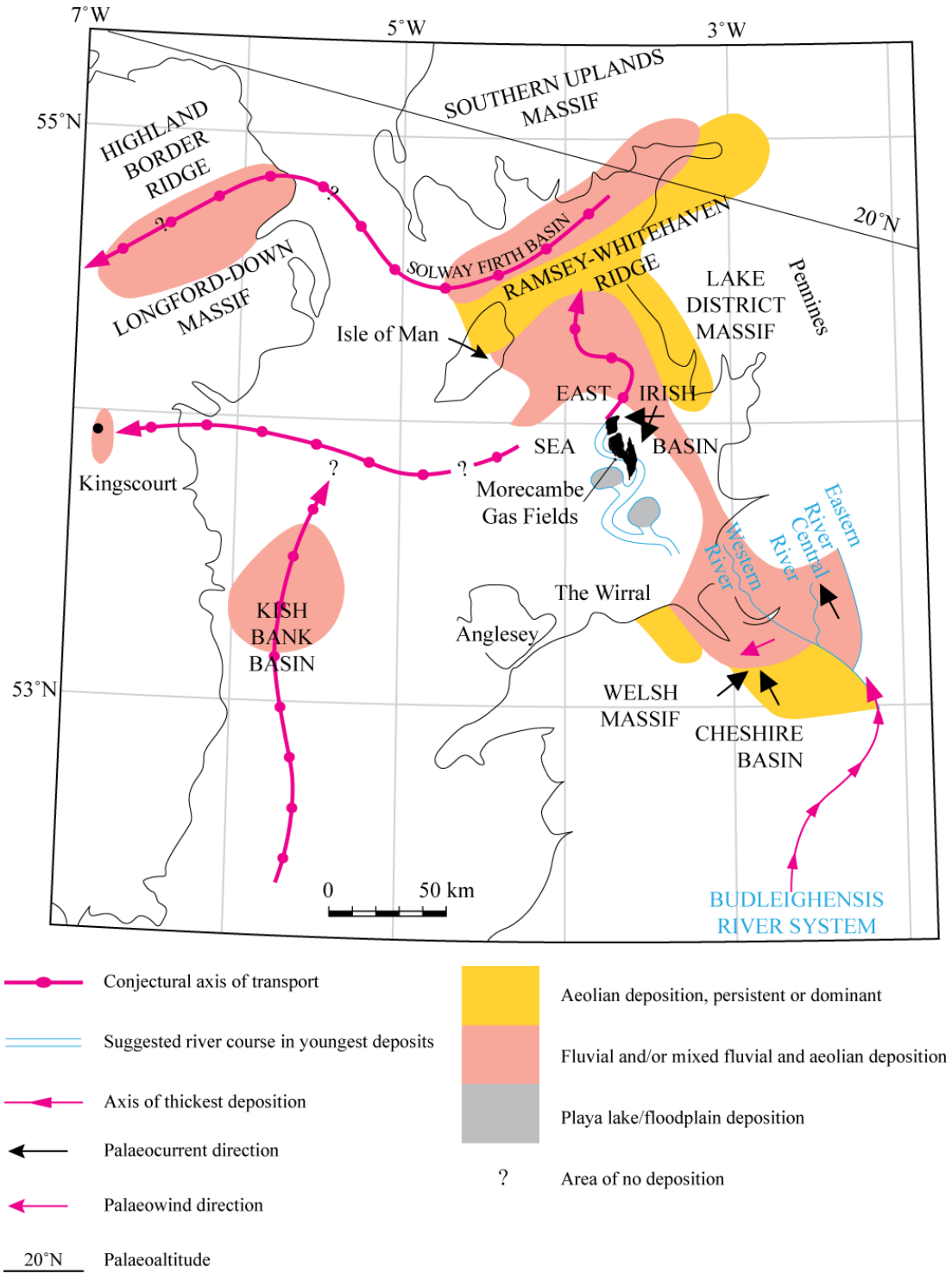

Figure 2.13 Possible palaeogeography during deposition of the East Irish Sea Basin Lower Triassic Sequence. After Jackson et al. (1995).

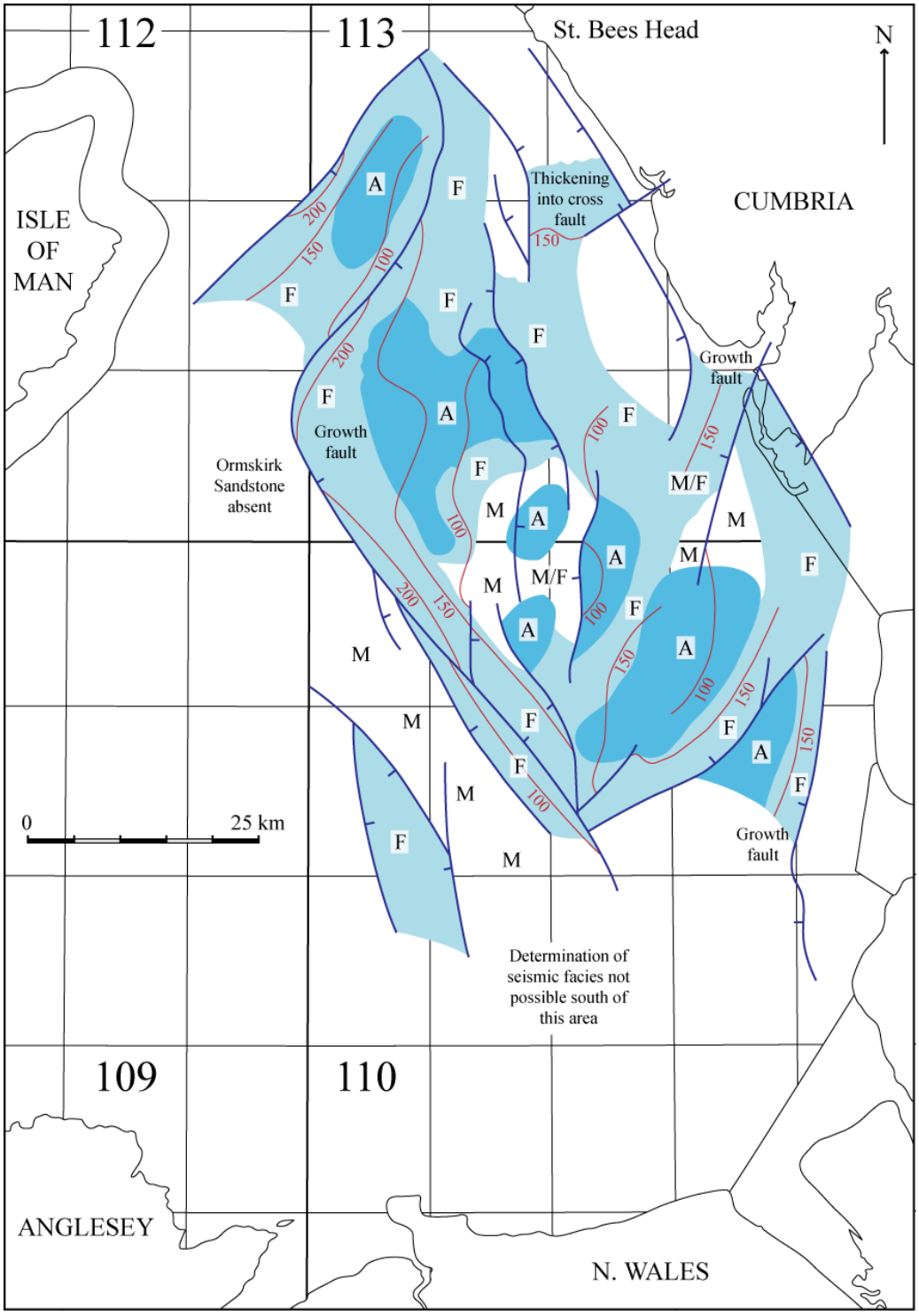

Figure 2.14 Distribution of seismic facies in the lower Ormskirk Sandstone Formation with isochores shown in red. F: seismic character interpreted as representing mainly fluvial channel deposits. A: seismic character interpreted as representing mainly sandflat deposits. M: areas of low frequency layered seismic character possibly representing mixed fluvial and sandflat deposits. Time isochores are for the whole Ormskirk Sandstone interval. After Meadows and Beach (1993a).

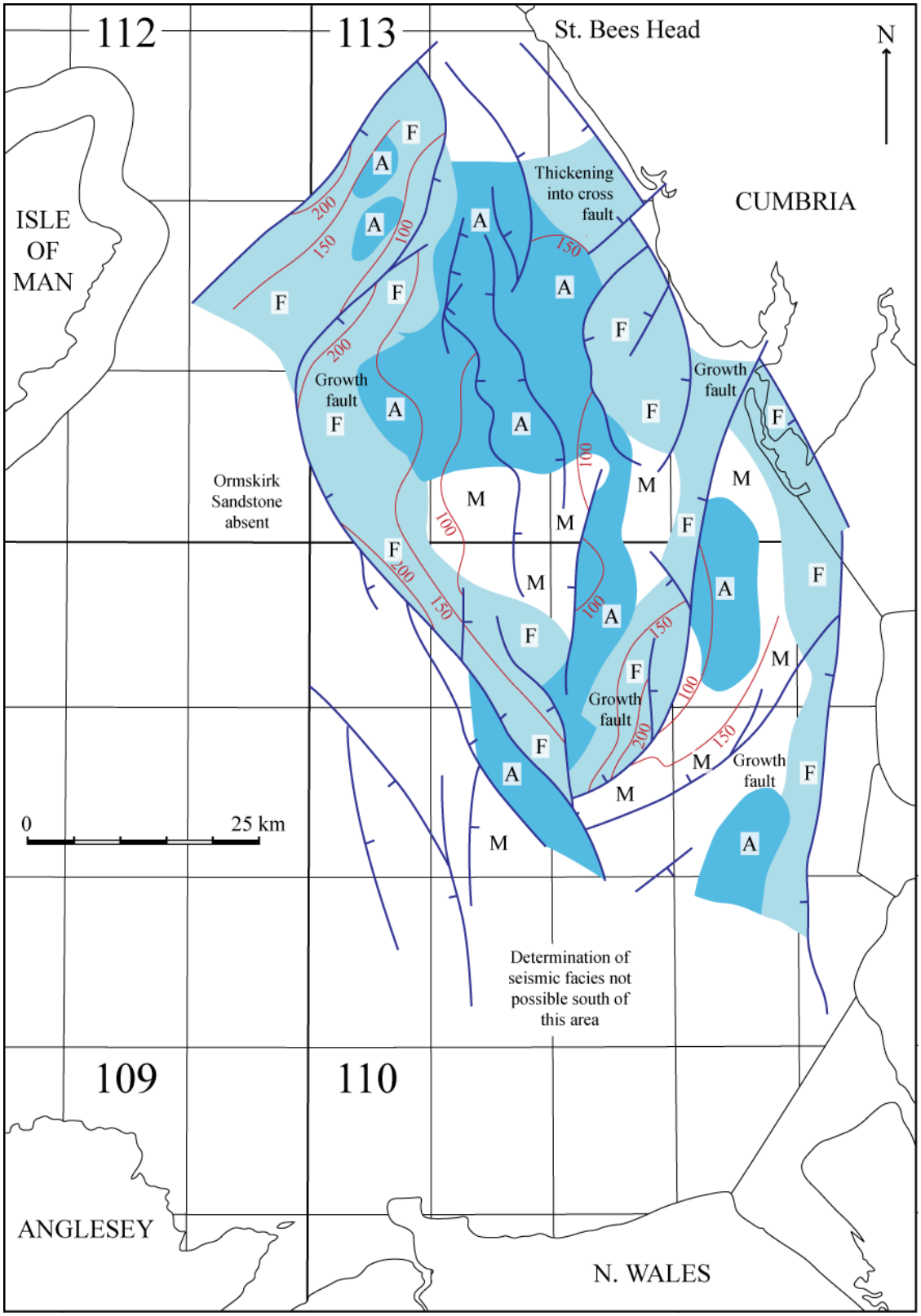

Figure 2.15 Distribution of seismic facies in the upper Ormskirk Sandstone Formation. Comments as Figure 2.14. After Meadows and Beach (1993a).

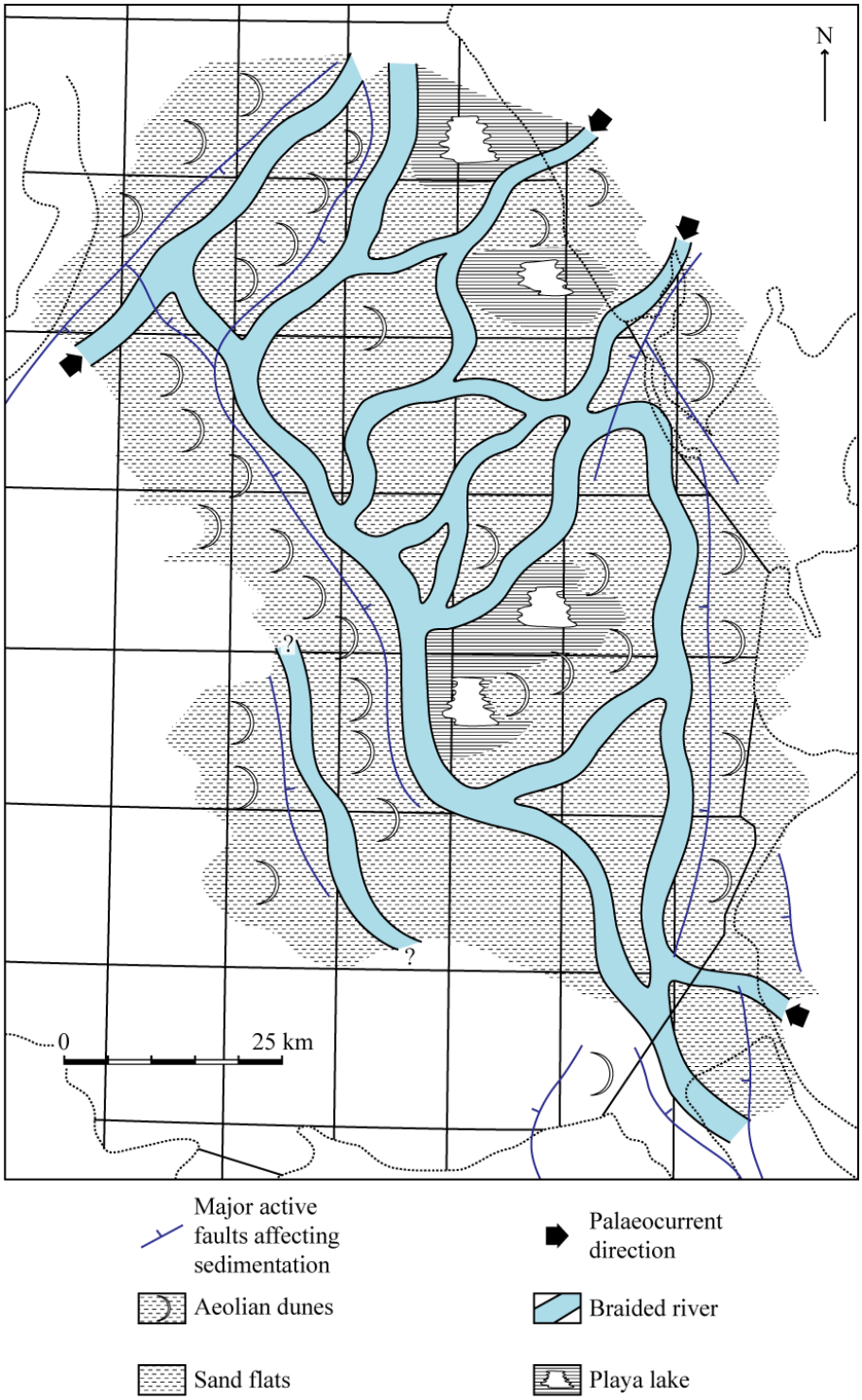

Figure 2.16 Schematic palaeogeography for the lower part of the Ormskirk Sandstone Formation based on facies identified in wells and seismic characteristics illustrated in Figure 2.14. Palaeoflow from the Cheshire Basin in the southeast is supported by onshore exposures, while that from Cumbria (Lake District Massif) and from the west is inferred due to the absence of exposure or well data at this stratigraphic level. After Meadows and Beach (1993a).

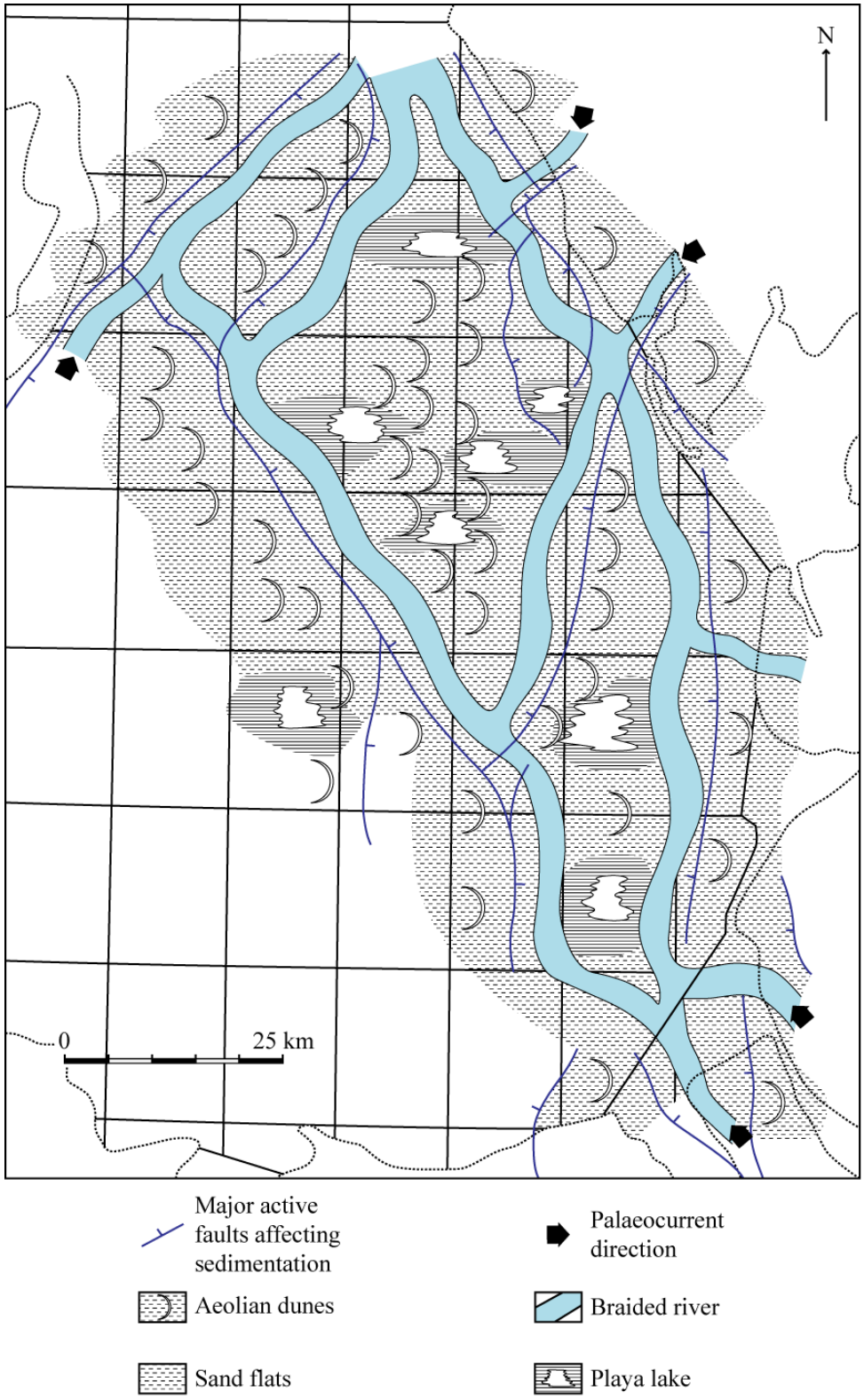

Figure 2.17 Schematic palaeogeography for the upper part of the Ormskirk Sandstone Formation based on facies identified in wells and seismic characteristics illustrated in Figure 2.15. Comments as Figure 2.16. After Meadows and Beach (1993a).

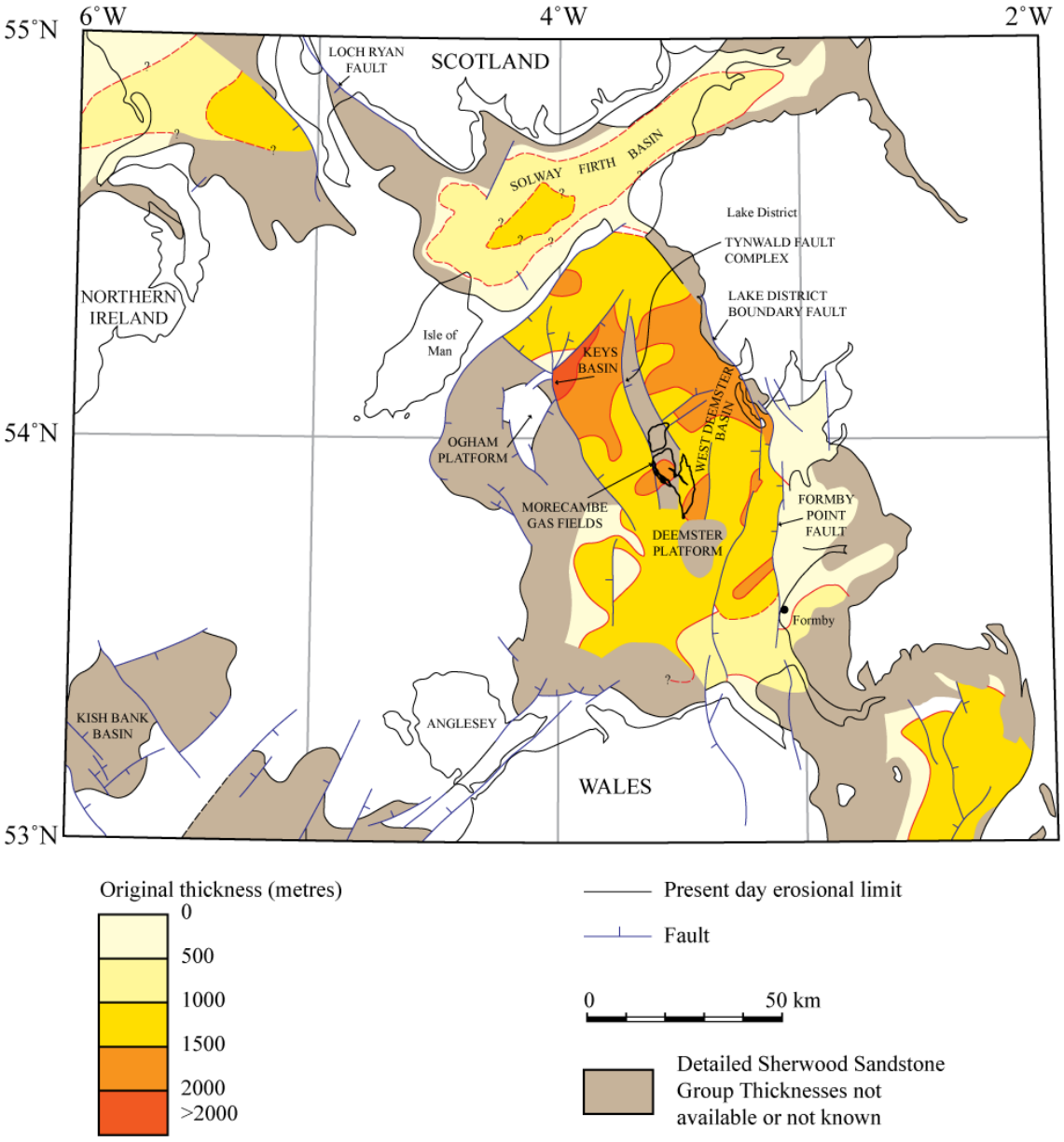

Figure 2.18 Distribution and thickness of the Sherwood Sandstone Group within the East Irish Sea Basin. After Jackson et al. (1995).

2.5.1. SOURCE ROCKS

The source rocks to both the South and North Morecambe Triassic reservoirs are the underlying Carboniferous Westphalian coals and shales (Stuart and Cowan, 1991). The gas present in North Morecambe prior to production consists of 6.88% CO_2 and South Morecambe has a maximum of 0.6% CO_2 (Stuart, 1993). Due to the CO_2 content of the North Morecambe gas field exceeding that of South Morecambe it is suggested that the North Morecambe structure is older as there has been less opportunity for thermal maturation within the source rock before migration to the trap (Stuart, 1993).

2.5.2. RESERVOIR ROCKS

The Triassic sequence of the East Irish Sea Basin exceeds 2400 m in the Morecambe area. It lacks any datable fossils, therefore, as will be described in sections 2.5.2.1. and 2.5.2.2. reservoir zonation is defined on the basis of lithostratigraphy, facies association and diagenetic stages. The distribution and thickness of the Sherwood Sandstone Group within the East Irish Sea Basin is shown in Figure 2.18. A depositional model of the Sherwood Sandstone Group of the Morecambe area of the East Irish Sea Basin is illustrated within Figure 2.19.

2.5.2.1. THE SOUTH MORECAMBE FIELD SHERWOOD SANDSTONE GROUP RESERVOIR

The Sherwood Sandstone Group of the South Morecambe Field is a thick sequence of fluvial (braided stream and sheetflood) sandstones (Stuart and Cowan, 1991) with main production from the Ormskirk Sandstone Formation and top St. Bees Sandstone Formation over a gross thickness of 1463 m (Bastin et al., 2003). There are two main ways to describe the reservoir. The first is to describe it in terms of facies deposition, due to the degree of heterogeneity observed within the units. The second is to describe in terms of platy illite distribution, a diagenetic characteristic that hampers reservoir performance. The latter description is more

important in terms of characterising reservoir quality and will therefore be more important in terms of carbon dioxide storage capabilities.

Five major facies associations can be recognised within the South Morecambe Gas Field reservoir sequence. These have previously been described in detail by Bushell (1986), Colter and Ebbern (1978) and Stuart and Cowan (1991). They include Facies A and A' (major channel sandstones), Facies B (secondary channel sandstones), Facies C (non-channelised sheetflood sandstones), Facies D/E (non-reservoir) and Facies F (Aeolian facies).

Previous studies have suggested a layered distribution of Facies A major channel sandstones and Facies C sheetflood sandstones indicating Sherwood Sandstone Group deposits were the result of widespread major braided channel sedimentation across the entire Morecambe area due to the advance and retreat of the fluvial system (Stuart and Cowan, 1991). Recent studies have placed greater emphasis on the areas of the reservoir affected by platy illite (Bastin et al., 2003; Bushell, 1986; Cowan and Boycott-Brown, 2003; Knipe et al., 1993; Stuart, 1993; Stuart and Cowan, 1991).

The reservoir has experienced diagenesis in the form of cementation and compaction. Platy illite precipitation is the predominant diagenetic phase, however quartz and dolomite cements form over 95% of total cements. Other diagenetic components include fibrous illite, anhydrite, gypsum, hematite, pyrite, anatase, late stage ankerite, calcite and kaolinite (Stuart and Cowan, 1991).

Several studies have focussed on describing the distribution of the platy illite affected zone (e.g. Stuart (1993) and Stuart and Cowan (1991)) which is diffuse and variable. Stuart and Cowan (1991) have mapped the top platy illite surface within the Morecambe South Gas Field (see Figure 2.20). The presence of platy illite is considered to be the controlling factor on reservoir performance, particularly impeding porosity and permeability. Within the South Morecambe Sherwood Sandstone reservoir, authigenic platy illite is widespread across the northern and western areas, forming beneath a palaeo-gas-water-contact during the Late Jurassic (Bastin et al., 2003; Bushell, 1986; Woodward and Curtis, 1987). Within the illite affected zone (below the palaeo-gas-water-contact), platy illite levels reach 11% before declining downwards into the underlying aquifer (Bastin et

al., 2003). The Eastern flank of the field is unaffected by platy illite (Bastin et al., 2003).

Differential compaction is considered to be the second most important control on reservoir performance (Stuart and Cowan, 1991). Compaction is prevalent in the northern limb of the South Morecambe Gas reservoir causing a localised reduction in reservoir quality (Stuart and Cowan, 1991).

There is evidence to suggest that cementation has helped to maintain reservoir quality in terms of secondary porosity via dissolution of cement during burial (Stuart and Cowan, 1991). This has restored intergranular porosity resembling the primary pore system (Stuart and Cowan, 1991).

2.5.2.2. THE NORTH MORECAMBE FIELD SHERWOOD SANDSTONE GROUP RESERVOIR

The North Morecambe Sherwood Sandstone Group reservoir is similar in terms of facies associations and deposition to that of the South Morecambe Gas Field. A study by Stuart (1993) suggests there are nine facies-defined reservoir units present within the North Morecambe reservoir, however, lateral correlation of these units beyond North Morecambe is somewhat subjective. The units are named NMI to NMIX.

Reservoir unit NMIX is the St Bees Sandstone Formation consisting of sandstones of facies B, C, D/E and minor amounts of A, all with low reservoir properties (porosity/permeability). Reservoir units NMVII, NMIV and NMII are units dominated by facies A (major channel sandstones) resulting in a fairly homogenous internal organisation and permeability distribution. In the illite free zone permeability is high, between 100-1000 mD. The units include minor amounts of facies C and D/E within thin intervals. Reservoir units NMVIII, NMVI, NMV, NMIII and NMI are non-channelised sandstone sequences of Facies C and associated Facies B.

Once again the North Morecambe reservoir has experienced several stages of diagenesis and burial similar to that of South Morecambe. During the Triassic, early diagenesis involved calcite and non-ferroan micro-nodule precipitation with

minor amounts of quartz and feldspars (Stuart, 1993). Later in the Triassic and Jurassic, intermediate diagenesis and deep burial resulted in quartz cementation coeval with platy illite precipitation (Stuart, 1993). Precipitation of dolomite/ankerite followed shortly after. Thermal decarboxylation at this time resulted in feldspar and calcite dissolution from the early diagenesis stage, leading to secondary porosity generation (Stuart, 1993). The Cretaceous and Tertiary saw a final late stage of diagenesis. A second phase of gas generation during the Cretaceous resulted in the lowering of the gas-water-contact into the illite affected zone, inhibiting cement precipitation (Stuart, 1993).

The major control on reservoir performance in the North Morecambe Sherwood Sandstone reservoir is again governed by platy illite distribution which can reduce permeability by up to two orders of magnitude in affected areas (Stuart, 1993). The top platy illite surface has been mapped by Stuart (1993) (see Figure 2.21).

2.5.3. CAP ROCKS

The South and North Morecambe reservoirs are overlain by the Mercia Mudstone Group (see Figure 2.22). Thick (tens to hundreds of metres) evaporite cycles consisting of alternating mudstones and halites were deposited throughout the mid to late Triassic as a result of recurring basin flooding and drying (Stuart, 1993). Four cycles exist over both South and North Morecambe, however, additional cyclic mudstone and halite deposits can be found above the fourth cycle over North Morecambe, which are not present above South Morecambe (Stuart, 1993).

2.5.4. STRUCTURE

The Permo-Triassic strata of the East Irish Sea Basin were deposited within an extensional tectonic regime (Bastin et al., 2003). The East Irish Sea Basin is cut by many NE-SW, NW-SE and N-S trending faults, and can be divided into two main structural domains (Knipe et al., 1993): major easterly dipping faults in the

north of the East Irish Sea Basin (including the Keys Fault, Lagman Fault and Tynwald Fault System), which induce tilting towards the southwest or west; and westerly to south-westerly dipping faults in the south (including the Crosh Vusta Fault and Formby Point Fault), which induce tilting towards the east. Together, these two domains control the structural evolution of the basin (Knipe et al., 1993).

The Morecambe Gas Fields are situated in the centre of the East Irish Sea Basin within a half graben (Stuart, 1993) at the junction of these two fundamental structural domains (Knipe et al., 1993). The fields have a complex tilting history as a direct result of their location and have formed along a complex transfer zone (Knipe et al., 1993).

The Morecambe Gas Fields (structure previously illustrated in Chapter 1, Figure 1.3) consist of two isolated structural traps separated from each other by an ENE-WSW trending graben (Knipe et al., 1993). The South Morecambe Gas Field is structurally complex and can be divided into two major areas separated by a N-S trending "central" graben. West of the graben lies the South Morecambe horst area, becoming narrow in the south approaching a region of complex faulting (Knipe et al., 1993). The eastern bounding fault is the southern tip of the Tynwald Fault. East of the graben the reservoir dips east towards the Crosh Vusta Fault (Knipe et al., 1993). In comparison, the North Morecambe Gas Field is an anticlinal structure, dip-closed to the north and bounded by faults to the west, east and south (Knipe et al., 1993).

Two main depocentres are present in the vicinity of the Morecambe fields. To the west the Permo-Triassic depocentre is associated with the Keys fault and to the southeast another Permo-Triassic depocentre is associated with the Crosh Vusta Fault (Knipe et al., 1993). The Crosh Vusta depocentre is older than that of the Keys fault and controlled early southward tilting patterns in the southern part of the Morecambe field and nearby strata (Knipe et al., 1993). However, there is evidence indicating later westerly flow downslope towards the Keys Fault (Knipe et al., 1993).

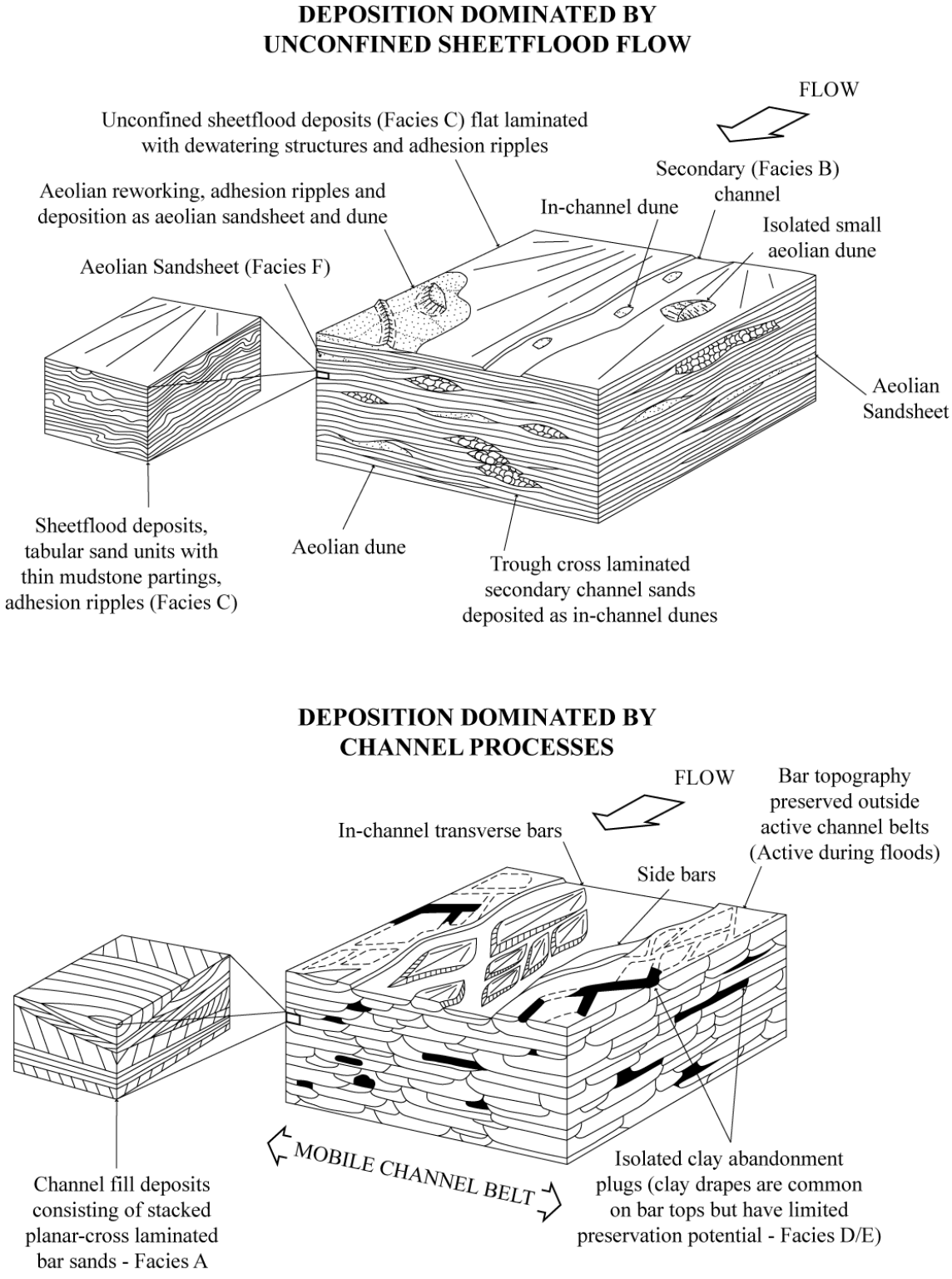

Figure 2.19 Sherwood Sandstone Group Depositional Model within the Morecambe Area of the East Irish Sea Basin. After Stuart and Cowan (1991).

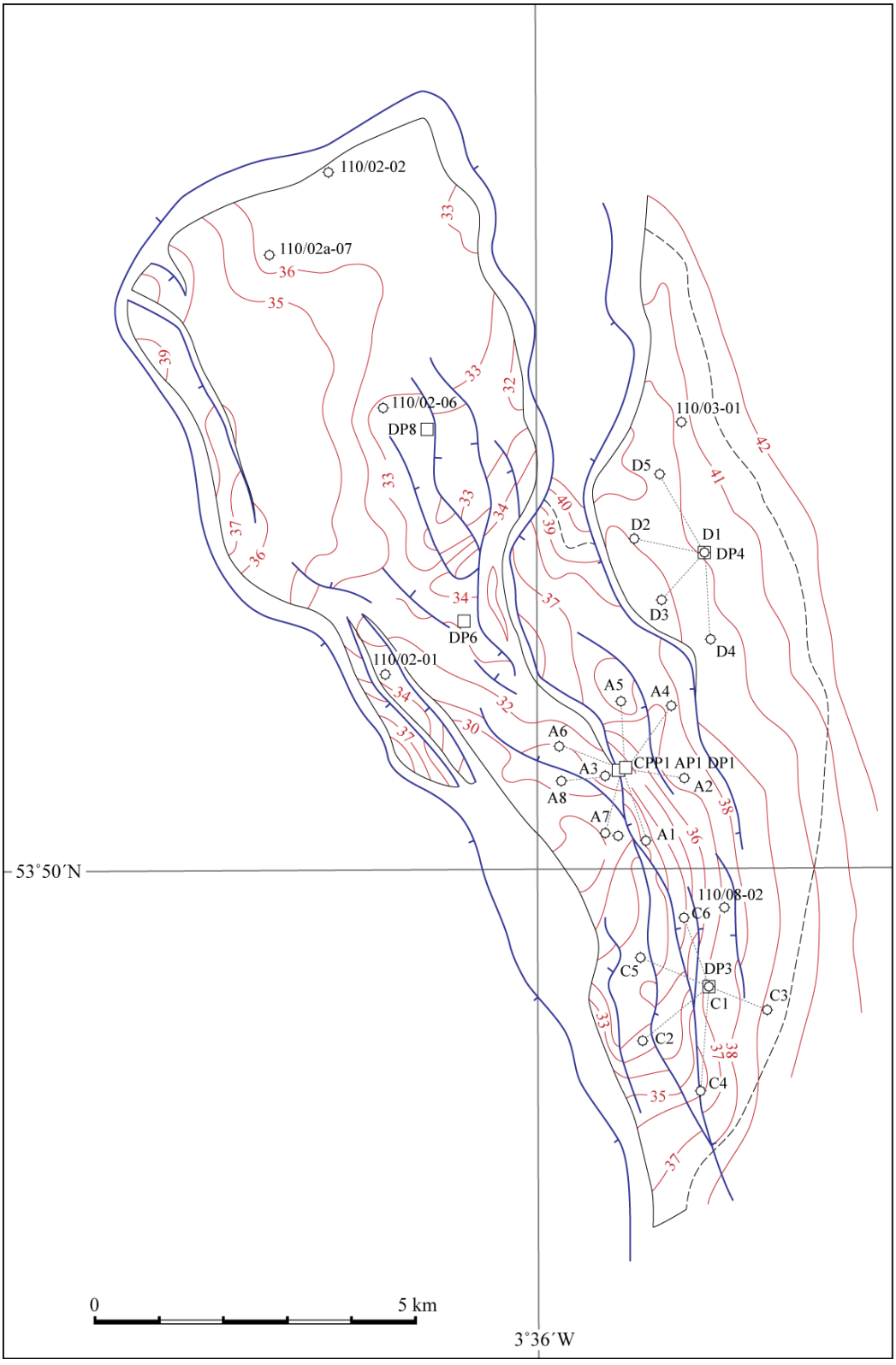

Figure 2.20 The top platy illite surface within the Morecambe South Gas Field, East Irish Sea Basin. Faults are shown at their mapped positions at Top Sherwood Sandstone. Only major faults are shown. The contour interval is 100 ft (30.5 m). After Stuart and Cowan (1991).

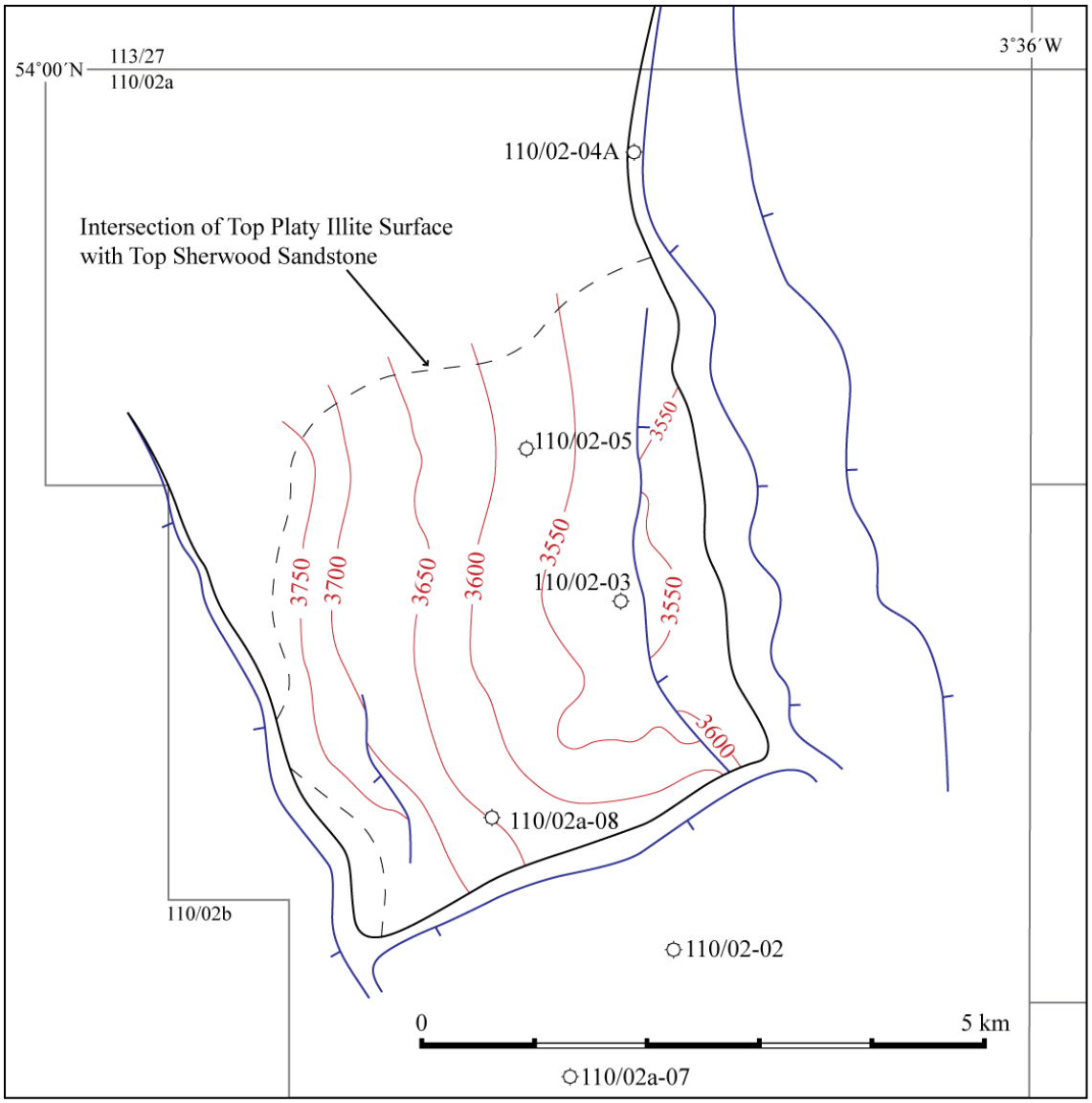

Figure 2.21 The Morecambe North Gas Field top platy illite depth structure map. After Stuart (1993).

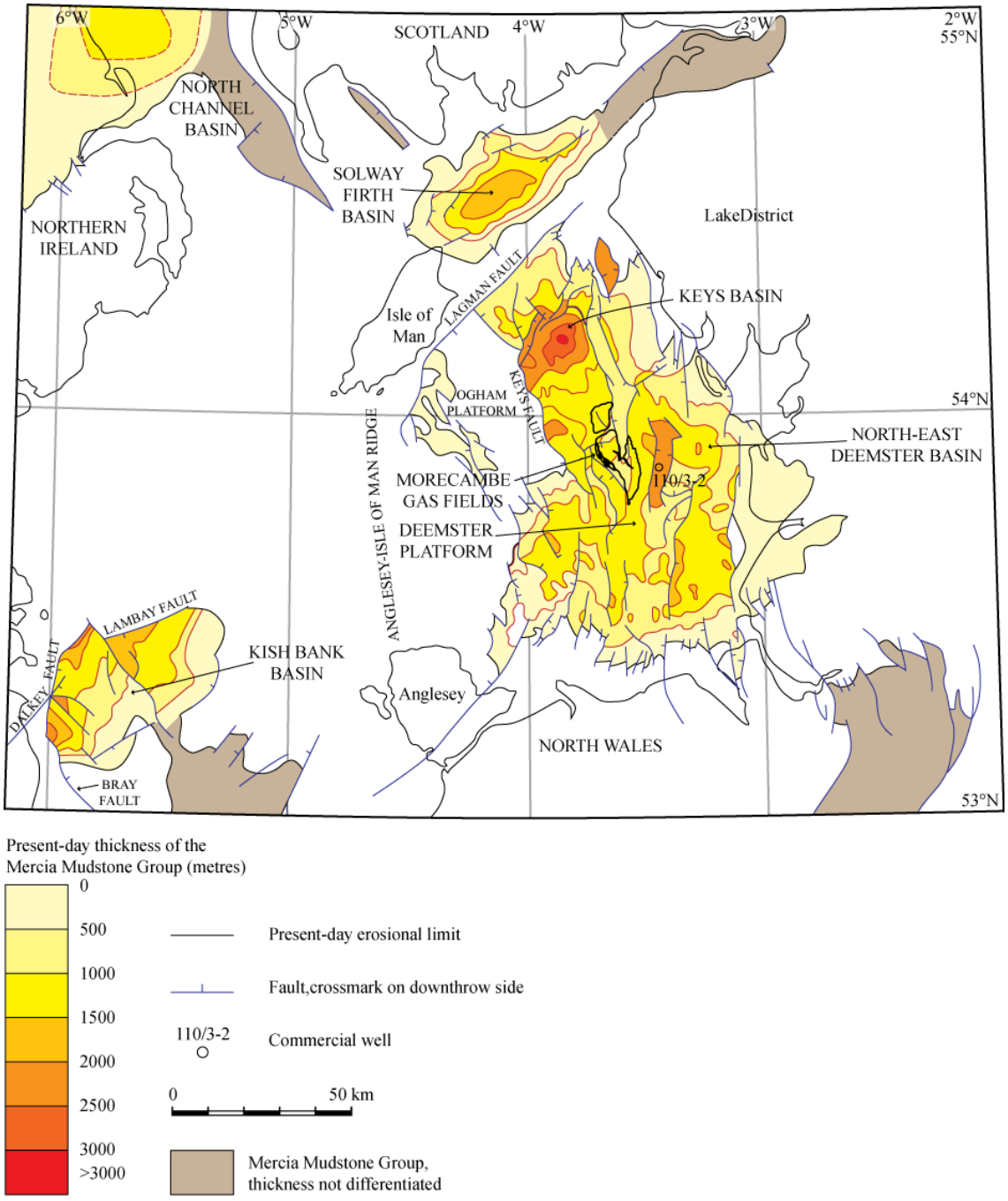

Figure 2.22 Distribution and Thickness of the Mercia Mudstone Group within the East Irish Sea Basin. After Jackson et al. (1995).

2.6. SUMMARY

In summary, a high quality depleted gas reservoir has intrinsic properties including porosity, permeability, and significant reservoir volume. Similar properties are necessary for a high quality CO_2 storage reservoir, with the produced gas resulting in a substantial CO_2 storage capacity remaining. Reservoir sandstones deposited within fluvial and aeolian environments such as those of the Hewett Gas Field of the Southern North Sea and the Morecambe North and South Gas Fields of the East Irish Sea Basin have high quality reservoir properties: tectonism and compaction has not destroyed the porosity and permeability. The Hewett Gas Field has an anticlinal trap, and is sealed vertically by the Dowsing Dolomitic Formation of the Haisborough Group. The Morecambe South Gas Field also has an anticlinal trap, whereas the Morecambe North Gas Field has a rotated fault block trapping mechanism. Both the Morecambe Fields are sealed vertically by the Mercia Mudstone Group. All of the reservoirs analysed within this thesis have successfully stored hydrocarbons over geological timescales. Chapters 4, 5, and 6, will assess whether the reservoirs have the potential to host CO_2, and will attempt to determine their theoretical and effective CO_2 storage capacities.

3 Data and Methodology

3.1. INTRODUCTION

This chapter introduces the methods that will be used within chapters 4, 5 and 6 to estimate the theoretical and effective CO_2 storage capacity of both water drive and depletion drive gas reservoirs for carbon dioxide storage. The methods include (1) 3-D seismic interpretation and structural modelling (including fault seal analysis) of the individual reservoirs, (2) an integrated analysis of historical production and pressure datasets, and (3) studies of the properties of reservoir fluids, including phase behaviour and the gas deviation factor. A workflow of the methodology is displayed in Figure 3.1.

3-D seismic interpretation allows greater understanding of the subsurface geology and is essential for assessing whether a depleted gas reservoir can be used for CO_2 storage. It encompasses the 3-D mapping of stratigraphy (particularly of reservoirs and cap rocks), and structure (trap geometries and mechanisms including faults). Well-calibrated seismic interpretation ensures accurate interpretation across faults and through areas of low seismic resolution. Fault interpretation and analysis of fault seal integrity are of particular importance to CO_2 storage within depleted gas reservoirs.

Analysis of production and pressure datasets gathered routinely throughout the productive lifetimes of gas reservoirs can be used to analyse the dynamic behaviour of reservoirs, in particular the aquifer performance within a reservoir (Pletcher, 2002), and can be used to predict their behaviour throughout their CO_2 storage lifetimes (Bachu et al., 2004). Production and pressure datasets can reveal evidence of compartmentalisation within a gas reservoir, or evidence of pressure and/or fluid communication with a neighbouring reservoir. Compartmentalisation may make a reservoir uneconomical for development for CO_2 storage due to the

necessity of drilling many new wells (Holloway, 2005). Reservoirs in pressure and/or fluid communication with neighbouring reservoirs may still be utilisable for CO_2 storage, however, their dynamic behaviour needs to be well understood and appropriately managed throughout injection.

Pressure and production datasets can also be used to analyse the driving mechanism that has resulted in gas production. Material balance methods can be used to reveal evidence of depletion drive reservoirs (where the natural reservoir pressure is the driving force of gas flow to the surface (Hagoort, 1988)) and water drive reservoirs (where water (aquifer) influx is the major driving force of gas flow to the surface (Hagoort, 1988)). Depletion drive reservoirs should simply re-pressurise during CO_2 injection, whereas CO_2 will have to displace formation water during CO_2 injection in water drive reservoirs.

Another important consideration for CO_2 storage is the phase behaviour of the residual gas – injected CO_2 mix. The phase behaviour of natural gas is a prime consideration in the development and management of gas reservoirs (Danesh, 1998), ergo the phase behaviour of CO_2 within the subsurface will be of prime importance throughout the CO_2 storage lifetimes of gas reservoirs. The behaviour of a fluid at reservoir and surface conditions is determined by its chemical composition and the prevailing temperature and pressure (Danesh, 1998).

Reservoir fluids exist as vapour or liquid phases. A phase is defined as a part of a system, which is physically distinct from other parts by definite boundaries (Danesh, 1998). Phase behaviour is governed by the state of equilibrium – no changes will occur with time if the system remains at constant temperature and pressure (Danesh, 1998). Production of hydrocarbons, and injection of CO_2, results in a departure from equilibrium conditions and so it is important to determine the expected changes in phase behaviour of the pure components and/or multicomponent mixtures.

Examination of phase behaviour relies upon analysis of pure components and multicomponent mixtures; therefore it is necessary to consider the gas deviation factor (Z) of real gases. The gas deviation factor is a correction factor for the deviation of real gases from ideal gas behaviour, and is related to pressure-volume-temperature (PVT) behaviour expressed by the Real Gas Law (see section

3.6.1. and equation 3.17). For ideal gases the Z-factor is equal to unity, however, real gases rarely exhibit ideal gas properties. At elevated temperatures and pressures, the departure from ideal gas behaviour increases. It is therefore an important consideration for CO_2 injection where there will be continual increases in reservoir pressure.

Estimates of theoretical and effective CO_2 storage capacity are dependent upon the accuracy of input parameters to the equations used (see Chapter 1, section 1.6.). Some parameters, such as initial reservoir pressure, have well constrained values; other parameters, such as porosity, show a wide range of variability across the reservoir. Previous CO_2 storage capacity estimation in some gas reservoirs have seen average values used for parameters that show a wide range of variability (e.g. Bentham (2006) and Brook et al. (2003)). This study will include ranges of variability for the relevant parameters to obtain a range of expected CO_2 storage capacity estimates for the reservoirs considered within this thesis.

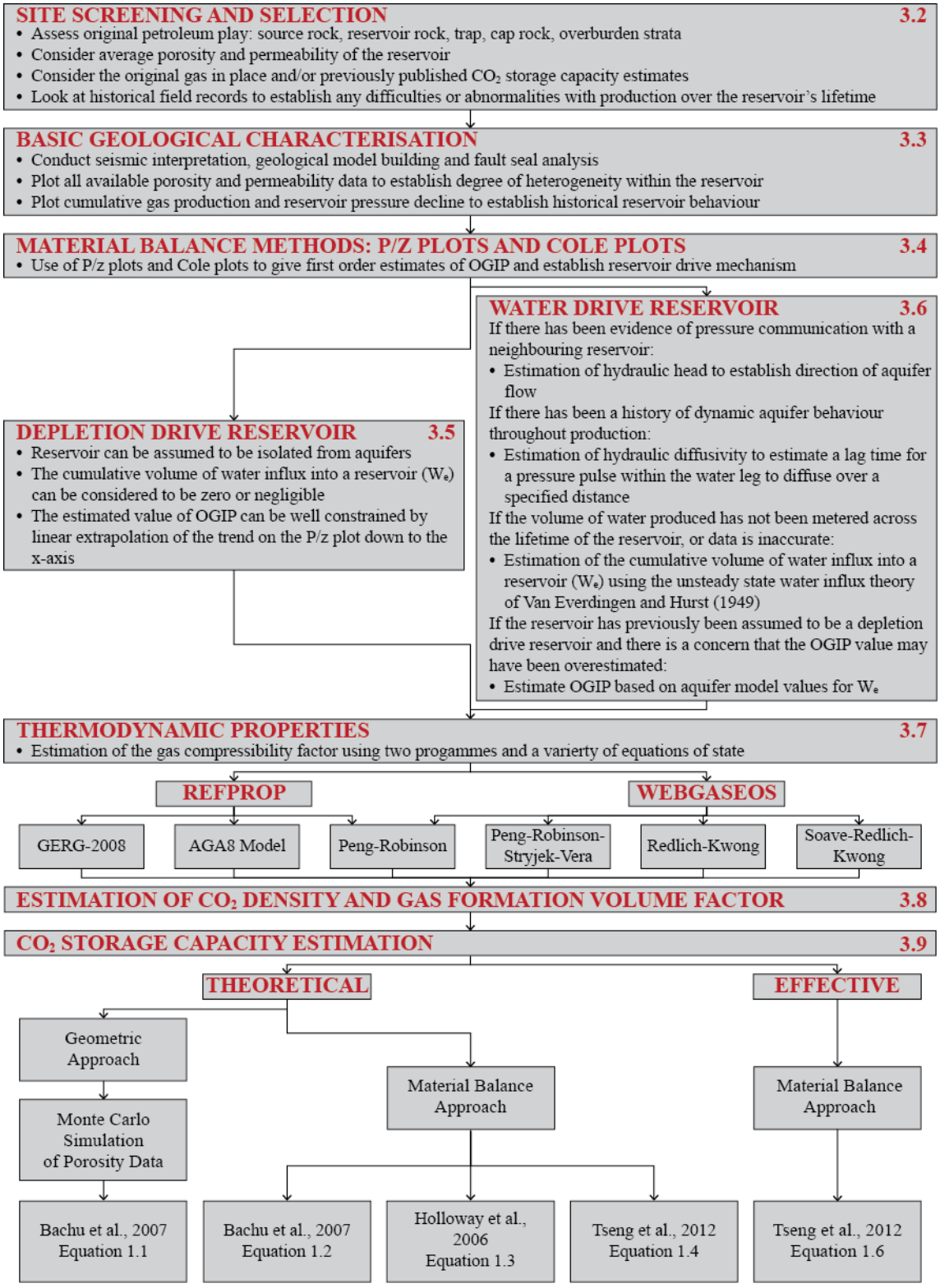

Figure 3.1 A workflow of the methodology developed within this study to evaluate depleted gas reservoirs with respect to CO_2 storage. The numbers in red to the right of the sub-headings refer to the relevant sections within this chapter

3.2. SITE SCREENING AND SELECTION

Site screening is used to assess the original petroleum system in terms of its individual play elements. Details of the source rock, reservoir rock, trap, cap rock and overburden are considered as to their suitability for ensuring secure CO_2 storage within the depleted hydrocarbon reservoir. The average porosity and permeability of the reservoir rock will be considered here to establish the degree of connectivity within the reservoir rock. The original gas in place, volume of recovered reserves, and any published CO_2 storage capacity estimates will be used to assess the storage potential of the site. Historical field records will be used to provide an insight as to any difficulties or abnormalities in production over the reservoir's lifetime.

3.3. BASIC GEOLOGICAL CHARACTERISATION

3.3.1. 3-D SEISMIC INTERPRETATION

Three-dimensional seismic interpretation is used here to map subsurface geological structure and to contribute to the understanding of reservoir behaviour (as described in section 3.1) in order to develop the offshore reservoirs for carbon dioxide storage. The acquired 3-D seismic data is processed to remove unwanted energy (such as multiples (section 3.2.2.)) and to place the required events in the correct location (Bacon et al., 2003). It is necessary to understand how the data has been acquired and how it has been processed to determine accurate geometries and/or structures, particularly with respect to CO_2 capacity estimation.

3.3.1.1. 3-D SEISMIC ACQUISITION

Acquisition of marine seismic reflection surveys involve an acoustic source (such as an air, water or steam gun) to generate compressional waves. In terms of marine seismic acquisition only P-waves are transmitted, fluids being unable to transmit S-waves. The source is usually towed behind a boat along with pressure sensitive receivers (normally hydrophones) to record the reflections from

subsurface geological interfaces, such as lithological or fluid changes, diagenetic features and fault planes (Bacon et al., 2003; Brown, 2011; Kearey et al., 2002) (see Figure 3.2). The time taken for a signal to leave the source and reflect back to the receiver gives an indication as to the depth of a subsurface interface and the changes in rock properties through the subsurface stratigraphy.

At a geological interface there is usually a change in rock properties (including bulk rock density) resulting in a change in velocity propagation of the P-wave through the stratigraphy (Kearey et al., 2002). The energy within a seismic pulse is split into transmitted and reflected pulses, the relative amplitudes of which are governed by the velocities and densities of the two layers, and the angle of incidence on the interface (Kearey et al., 2002). The relative proportions of energy transmitted and reflected are determined by the contrast in acoustic impedance (Z) across the interface (Kearey et al., 2002). Acoustic impedance is the product of rock or sediment density (ρ) and P-wave velocity through the rock or sediment (v) (see equation 3.1):

$$Z = \rho v \tag{3.1}$$

There are many advantages using 3-D seismic datasets for interpretation over 2-D seismic datasets. 2-D lines are often widely spaced, which results in difficulties in interpreting geological structure, especially faults and other complex structures (Bacon et al., 2003), (see Figure 3.3).

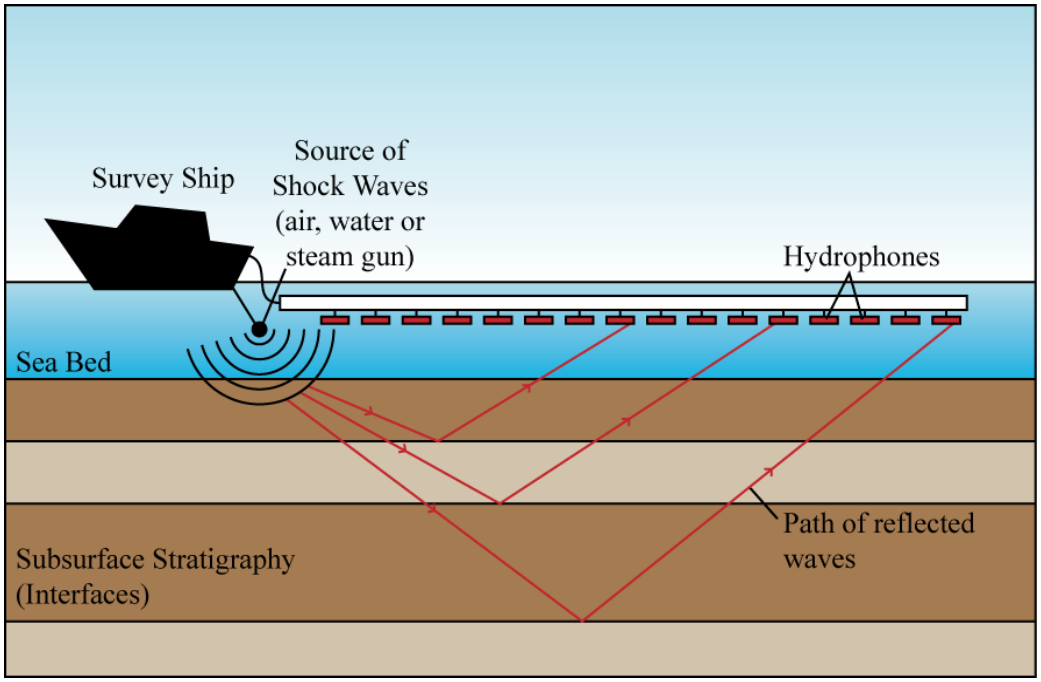

Figure 3.2 Schematic diagram of marine seismic acquisition. The acoustic source emits compressional waves which are reflected from subsurface interfaces and detected by receivers (hydrophones) back at the surface. Adapted from Bacon et al. (2003).

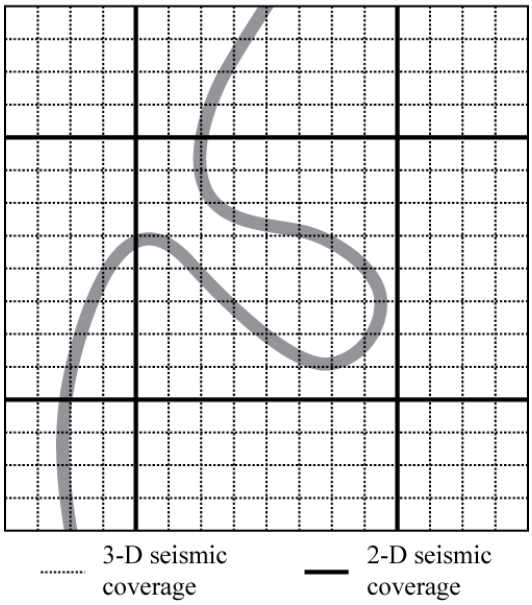

Figure 3.3 Schematic demonstrating the advantage of 3-D seismic coverage over 2-D seismic coverage when interpreting geological structure. It is not possible to observe the meander loop using the 2-D seismic dataset, however, the complexity of the structure can be interpreted in much more detail using the 3-D seismic dataset. After Brown (2011).

3.3.1.2. 3-D SEISMIC PROCESSING

A number of necessary processing steps are applied to the acquired data prior to seismic interpretation. Processing allows rearrangement, filtering and migration of recorded data to image the subsurface. A basic seismic processing sequence is shown in Figure 3.4 and explained below.

Prior to processing, data are displayed in columns of seismic traces at different offsets (step 1 of Figure 3.4) (Yilmaz and Doherty, 1987). The seismic traces are converted to a convenient format to be used throughout the processing sequence (Yilmaz and Doherty, 1987). Seismic traces are also edited prior to processing (step 2 of Figure 3.4). Noisy traces and traces with transient glitches or monofrequency signals are deleted, and polarity reversals, corrected (Yilmaz and Doherty, 1987). A gain recovery function is applied to the data to correct for amplitude effects (Yilmaz and Doherty, 1987). Finally, the field geometry is incorporated to the data (Yilmaz and Doherty, 1987). This is an important step in order to avoid processing problems later on.

Seismic processing begins with deconvolution. Deconvolution improves temporal resolution through compression of the effective source wavelet to a spike (Yilmaz and Doherty, 1987). Spiking deconvolution results in more high frequency energy, however, this also includes an increase in high frequency noise (Yilmaz and Doherty, 1987). Therefore, filtering may be necessary after deconvolution.

The next step is common midpoint (CMP) sorting, or common depth point (CDP) sorting, where the data is transformed from shot-receiver to mid-point offset coordinates, and requires field geometry information (Yilmaz and Doherty, 1987). Seismic data acquisition is recorded in shot receiver (s,g) coordinates, the geometry of which is shown in Figure 3.5. Seismic data processing requires transformation of the data to midpoint-offset (y,h) coordinates through the sorting of the data into CMP gathers (step 3 of Figure 3.4). The individual traces are assigned to the midpoint between the shot and receiver locations associated with that trace. Traces with the same midpoint location are grouped together into CMP gathers (see Figure 3.6).

Seismic multiples may occur when a ray path returns to the surface having been reflected more than once within the subsurface (see Figure 3.7) (Bacon et al., 2003). Processing attempts to remove these multiple reflections, however, this is not always possible. If so, seismic multiples can be easily identified within the final displayed data as regularly spaced, lower amplitude, repeating reflections.

A velocity analysis on CMP gathers often follows resulting in a measure of signal coherency (Yilmaz and Doherty, 1987). The velocity field is often used in normal moveout (NMO) correction of CMP gathers. During this process, traces become stretched in a time-varying manner, causing frequency distortion (Yilmaz and Doherty, 1987). To avoid degradation, particularly of shallow events, the distorted zone is deleted (or muted) prior to stacking (step 4 of Figure 3.4). Finally, a CMP stack is obtained by lining up traces (step 5 of Figure 3.4) and summing over the offset (step 6 of Figure 3.4).

Following the stacking of CMP gathers, further processing steps include predictive deconvolution (compression) which can be effective in suppressing reverberations or short period multiples (step 7 of Figure 3.4) (Yilmaz and Doherty, 1987). Filtering can suppress noisy frequency bands and a gain function may be applied to bring up weak reflections (Yilmaz and Doherty, 1987). Finally, dipping events can be migrated from their recorded position to their true subsurface locations (Bacon et al., 2003) before the data can finally be displayed (step 8 of Figure 3.4) and interpreted (step 9 of Figure 3.4).

There are many options available in the migration process and the final algorithm used may be selected according to the required accuracy of the results and the cost (Bacon et al., 2003). Accuracy is determined by issues such as the largest dip that can be properly migrated and the frequency content of the final displayed data (Bacon et al., 2003). The migration of data can occur either before or after stacking, and the choice is dependent on the velocity regime and the subsurface dip ranges within the data (Bacon et al., 2003). Further information on seismic data processing is provided by Yilmaz and Doherty (1987) and Bacon et al. (2003).

The data made available for use within this thesis was supplied already processed, with limited information on the exact procedure followed; however, a

key step during processing of the datasets was post-stack-time-migration. Seismic traces in this thesis are displayed using the Society of Exploration Geophysicists (SEG) normal convention, i.e. positive standard polarity. A downward increase in acoustic impedance is displayed as a positive wavelet, and a downward decrease in acoustic impedance is displayed as a negative wavelet (see Figure 3.8) (Bacon et al., 2003). An understanding of seismic polarity is essential for correlating data.

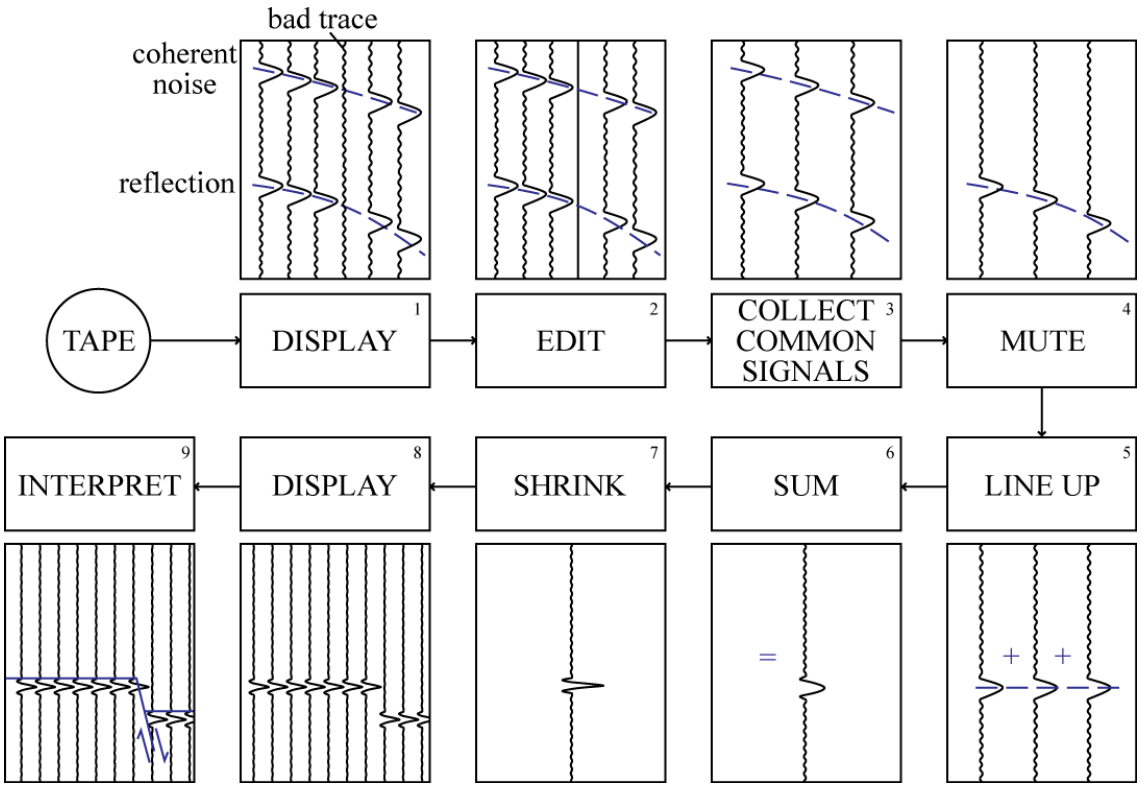

Figure 3.4 A basic seismic processing sequence. The acquired data is recorded on tape and displayed. The data is then edited – this may result in the removal of bad traces.

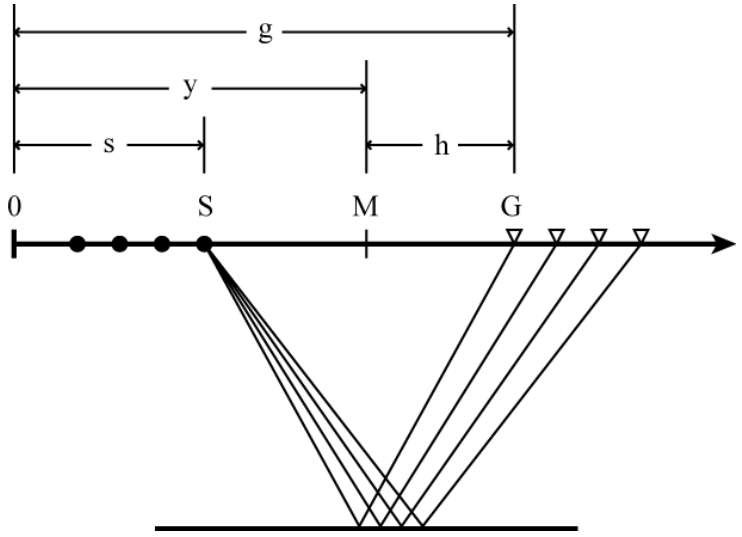

Figure 3.5 Seismic data acquisition is done in shot-receiver (s,g) coordinates. The ray paths shown are associated with a planar horizontal reflector from a shotpoint, S, to several receiver locations, G. The processing coordinates, midpoint-(half) offset, (y,h) are defined in terms of (s,g): y=(g+s)/2, h=(g-s)/2. The shot axis here points opposite the profiling direction, which is to the left. After Yilmaz and Doherty (1987).

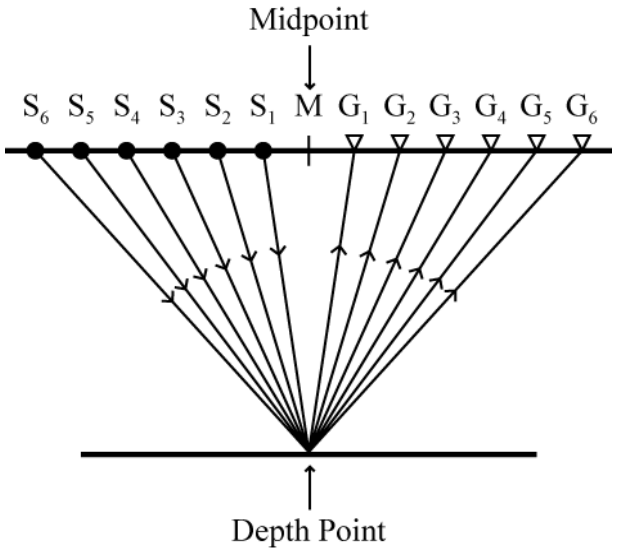

Figure 3.6 Seismic data processing is done in midpoint-offset (y,h) coordinates. The ray paths shown are associated with a single CMP gather. A CMP gather is identical to a CDP gather if the depth point were on a horizontally flat reflector and if the medium above were horizontally layered. After Yilmaz and Doherty (1987).

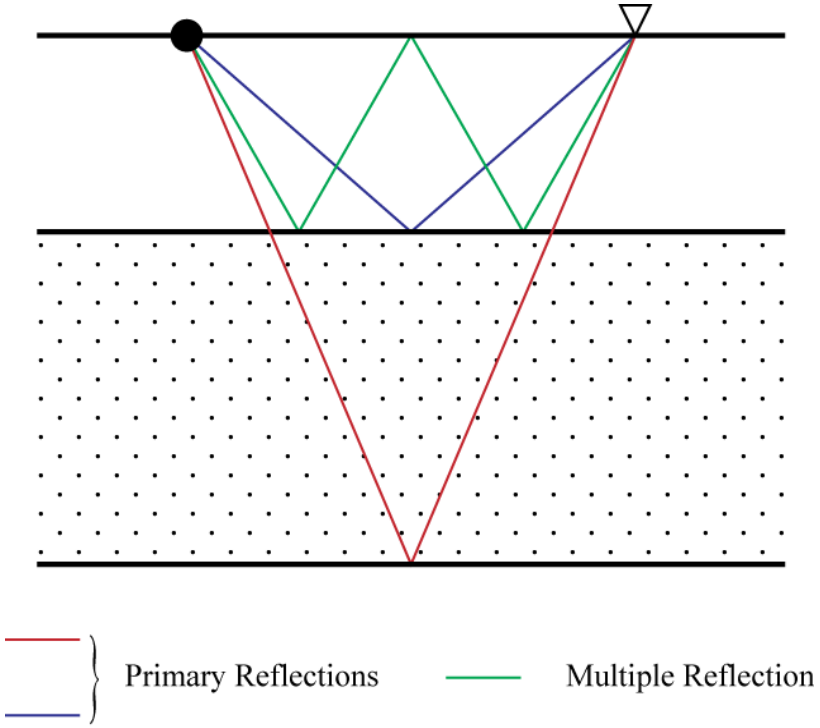

Figure 3.7 Primary and multiple reflections. The red and blue events are primary reflections which have a single reflection along the ray path. The green event has multiple reflections and in this case is the first order multiple of the blue event. The timing of the green event may be similar to underlying primary events, and if not removed through processing, it may obscure the deeper reflectivity. After Bacon et al. (2003).

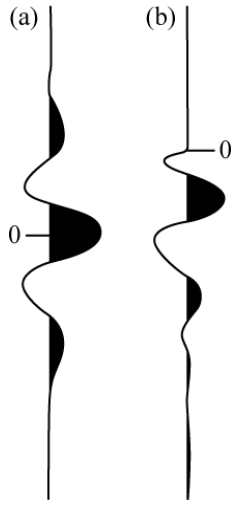

Figure 3.8 Positive Standard Polarity (Society of Exploration Geophysicists normal convention). For a positive reflection (a) the centre of the positive symmetrical (zero-phase) wavelet is a peak, (b) a minimum-phase wavelet begins with a trough. After Sheriff (1995).

3.3.1.3. SEISMIC RESOLUTION

Seismic resolution is the ability to distinguish separate geological features. Seismic wave frequency (number of waves per unit time) governs both vertical and horizontal resolution of seismic data, confining observable geological structure on seismic (Bacon et al., 2003). Wave frequency tends to decrease with depth due to the attenuation of waves resulting in decreasing seismic resolution with depth.

For two vertically-situated geological features to be resolvable on seismic as two separate events there must be a minimum vertical distance between them. At a spacing of greater than one-quarter of the wavelength of the seismic source the features will be resolvable as two separate events. However, at a spacing less than one-quarter of the wavelength (λ), constructive interference of reflections results in one, high amplitude event being resolvable on seismic. This is known as the Rayleigh Criterion, or tuning thickness, and represents the minimum vertical resolvable detail on seismic:

$$Vertical\ resolution = \lambda/4 \tag{3.2}$$

Likewise, for two horizontally-situated geological features to be resolvable on seismic as two separate events there must be a minimum horizontal distance between them. This is defined by the Fresnel zone (Bacon et al., 2003) and can be approximated by:

$$Horizontal\ resolution = \lambda/2 \tag{3.3}$$

3.3.1.4. SEISMIC REFLECTION INTERPRETATION

3-D seismic reflection data in this study were interpreted using SeisWorks within Landmark Openworks, a modern seismic interpretation tool used widely within the oil and gas industry. One 3-D seismic survey has been interpreted over the Hewett Unit within the Southern North Sea.

Seismic interpretation involves the interpretation of structural and stratigraphic geological features (Brown, 2011). Seismic horizons are usually the first surfaces to be interpreted. A seismic horizon is an imaginary surface within the subsurface, usually representing a chronostratigraphic surface in a time seismic reflection survey (Brown, 2011). Horizons are interpreted on intersecting lines using the autotracker tool within SeisWorks to track either maximum or minimum amplitudes. This builds up a grid of interpreted lines. It is not necessary to interpret every line within a 3-D seismic dataset, however, it is good practice to increase the number of interpretations in areas of structural complexity. When a horizon has been interpreted appropriately manually, SeisWorks can be used to auto-pick more horizon seed points by interpolation between interpretations, to build a horizon surface, or time structure map. Often, interpretations will begin from a well pick of a unit of interest within the survey. An example of these well-to-seismic ties within the Hewett Unit Seismic Survey is shown in Appendix A.

The Hewett Unit Seismic Survey is located within the Southern North Sea approximately 16 kms NE offshore Bacton on the Norfolk coastline within a water depth of between 22-38 m. It covers an area of 958 km^2 and has 925 lines and 1657 traces at a spacing of 25 m in both directions. The survey was provided by Tullow Oil and made available for use by Durham University. These data have been processed using a standard sequence of steps including post-stack time migration. The dominant frequency between a depth of 0-1000 metres below sea floor (mbsf) is within the range of 40 to 50 Hertz, giving a vertical resolution of ~10 m and a horizontal resolution of ~25 m. Seismic horizons mapped in the survey were correlated with well data, made available by ENI.

3.3.1.5. WELL DATA AND DEPTH CONVERSION

There are a considerable number of exploration and production wells within the Southern North Sea dataset. Well data has been made available from ENI within the Southern North Sea. The well data is used within this thesis to allow accurate seismic horizon correlations particularly within faulted regions.

The seismic project was depth-converted within TrapTester, interpretation software for mapping and modelling reservoir structure. When using a seismic project in time it is necessary to depth-convert it to use all the functionality within TrapTester, and more importantly, to estimate CO_2 storage capacity. The process requires the use of time-depth curves from well data to create a 3-D velocity model and can be refined with the use of pseudo-wells.

Figure 3.9 shows an example of time-depth curves that may be present within a seismic project. As can be seen, there is considerable spread in the data. Some of the time-depth curves which have a linear trend may be erroneous. The depth-conversion module within TrapTester allows the user to select the time-depth curves to be incorporated into the depth-conversion process. Therefore, if any time-depth curves show erroneous profiles, they can be omitted from the final depth converted project. TrapTester also allows the user to define extrapolation points (one shallow and one deep) to enable extrapolation of time-depth curves beyond the well data range to ensure smooth depth conversion of all project data.

Omitting the erroneous time-depth curves from the depth-converted model results in a significant decrease in the spread of data in Figure 3.9. It is unlikely the spread of data will contribute to erroneous CO_2 storage capacity estimates. The only storage capacity equation that relies upon use of the data directly from the model is the method of Bachu et al. (2007), (see Chapter 1, equation 1.1). The method requires the reservoir area and thickness to be calculated. The reservoir area will not be affected by the time-depth conversion in TrapTester using these data, however, the reservoir thickness might be. Instead, reservoir thickness can be calculated from composite logs from several wells.

Pseudo-wells can also be included to control the depth-conversion process. This allows the inclusion of additional information in data sparse regions. The trajectory of the pseudo well should then be defined, i.e. the top and base X and Y values and the trajectory path as defined by depth (assuming the project is already in depth). The created well can then be displayed within the volume editor and/or well editor together with horizon and fault picks.

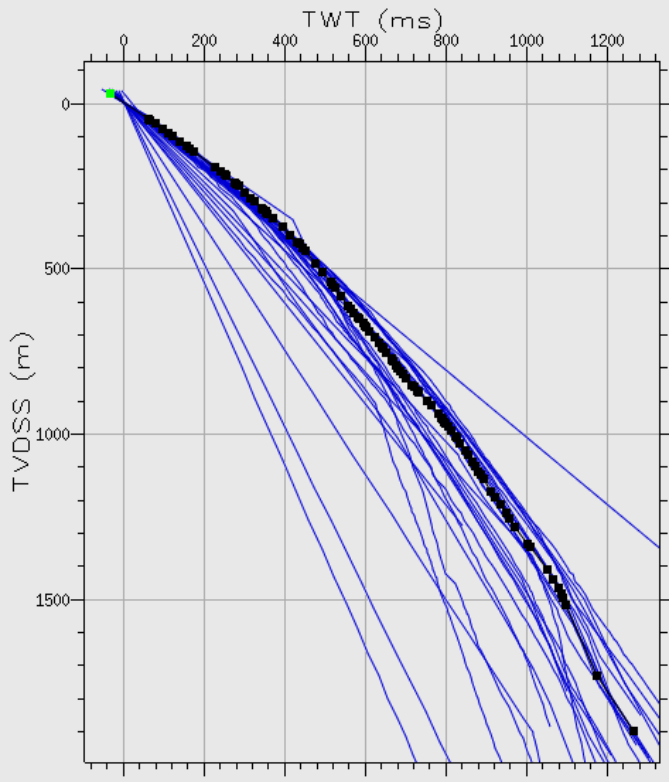

Figure 3.9 Time-depth curves of well data within TrapTester.

3.3.2. 3-D STRUCTURAL MODELLING

Within this thesis, the horizon interpretations made within Landmark Openworks were imported into Badley Geoscience's TrapTester 6.0 for fault interpretation, structural modelling and fault seal analysis using the algorithms for SGR (equations 3.7 and 3.8). The probability of sealing along faults critical for the secure storage of carbon dioxide is considered within the results following chapters 4, 5 and 6.

Most seismic interpretation focuses on detailed horizon surface mapping (Freeman et al., 1998). Detailed fault interpretation is often neglected or is not combined with horizon interpretation to produce a consistent three-dimensional model (Freeman et al., 1998). The resulting fault planes may not have true geometries modelled as would be possible if interpreted using software such as TrapTester, where fault attributes and horizon polygons can be easily displayed and edited. This is particularly important when assessing the lateral sealing capabilities

of faults, as is described in greater detail below through the process fault seal analysis.

To accurately define the three-dimensional geometry of a fault plane, information from each of the intersected interpreted horizons within a structural model needs to be incorporated. The most widely accepted approach is to view the throw pattern on the fault surface and to analyse the likely causes of variations in this pattern (Figure 3.10).

The displacement pattern for a single, ideal, blind fault surface within an isotropic material is well documented (Barnett et al., 1987; Needham et al., 1996; Watterson, 1986). Greatest displacement occurs in the centre of the fault and decreases outwards in all directions to zero at the tip, marked by an elliptical tip line (Figure 3.10). Horizon displacement is zero at the tip line and increases towards the centre of the fault (Figure 3.10). Many naturally occurring faults show close comparison to this ideal model (Needham et al., 1996). Minor deviations from the ideal occur, for example, due to lithological contrasts, mechanical differences between layers and seismic velocity variations (Needham et al., 1996). More complex deviations occur, for example, where faults interact (Needham et al., 1996). Figure 3.11 illustrates the variations in fault displacement where splay faults interact with master faults. Fault throw on the master fault increases towards the branchline, and remains high at the branchline with intersecting faults.

3.3.3. FAULT SEAL ANALYSIS

Once an accurate horizon and fault framework has been constructed, fault seal can be considered. It is necessary to estimate the sealing capability of critical faults (such as those that structurally close a reservoir) to ensure secure storage of CO_2. There are two main categories of fault seal: (1) reservoir against non-reservoir in which case the juxtaposition of permeable rocks against non-permeable rocks provides a sealing mechanism; and (2) reservoir against reservoir in which case the fault itself must provide a barrier to fluid migration, (see Figure 3.12) (Yielding et al., 1997). Detailed seismic mapping and well analysis is required to

decipher between the two categories of fault seal (Freeman et al., 1998; Yielding et al., 1997).

The first phase of fault seal analysis requires the identification of reservoir juxtaposed areas on the fault surface. This usually involves the construction of Allan diagrams (Allan, 1989) as an attribute on the fault surface and uses information from mapped horizons and a refined reservoir stratigraphy defined by isochores at the fault surface (Yielding et al., 1997)), (see, Figure 3.13).

The second phase of fault seal analysis assesses the likelihood a continuous impermeable membrane (e.g. clay or shale smear) exists along the fault plane in regions of sand-sand juxtaposition (Yielding et al., 1997). There are several published methods of fault seal estimation. It is possible to assess seal integrity through clay smear potential, CSP (Bouvier et al., 1989), generalised smear factor, GSF (Yielding et al., 1997), shale smear factor, SSF (Lindsay et al., 1993), or shale gouge ratio, SGR (Yielding et al., 1997). In general, gouge ratio methods are used to model fault zone composition, whereas smear factors model the morphology of clay or shale smears within the fault zone.

The first major research into clay smear includes studies such as that of Weber et al. (1978). The study focusses on observations of faulting within interbedded sand-shale sequences. Experiments and outcrop studies reveal clay smear within normal fault shear zones. Clay smear is at its thickest at the source bed, and thins towards the centre of offset.

Bouvier et al. (1989) estimate the likelihood of clay smearing within reservoir-juxtaposed regions of faults, otherwise known as clay smear potential, CSP (see equation 3.4). The CSP represents the relative amount of clay smeared from individual shale source beds at a certain point along a fault plane (Yielding et al., 1997), see Figure 3.14. CSP is greater when there are thicker shale source beds and greater numbers of them.

$$CSP = \sum \frac{(Shale\ bed\ thickness)^2}{Distance\ from\ source\ bed} \tag{3.4}$$

The study of Lehner and Pilaar (1996) states that the volume of clay or shale entrained into the fault gouge from a particular layer is proportional to the square of its thickness. Therefore, equation 3.4 has shale bed thickness raised to the power of 2. Yielding et al. (1997) proposed that a generalised smear factor (GSF) can be defined, based on the CSP, which has dimensions of distance (see Figure 3.14):

$$Smear\ factor = \sum \frac{(Shale\ bed\ thickness)^n}{(Distance\ from\ source\ bed)^m} \tag{3.5}$$

where, exponents n and m are additional variables, the values for which originate from experimental models or outcrop studies (Yielding et al., 1997).

The studies of Lindsay et al. (1993) predict the likelihood of a continuous smear of clay or shale in reservoir juxtaposed areas of faults (see Figure 3.14). They define the shale smear factor, SSF, as:

$$SSF = \frac{Fault\ throw}{Shale\ layer\ thickness} \tag{3.6}$$

The shale gouge ratio (SGR) is used to estimate the net clay or shale percentage in the entire slipped interval (Yielding et al., 1997). It is, therefore, a lithology-dependent attribute (Yielding et al., 1997) and, within sand-shale sequences, gives an indication of the proportion of shale or clay minerals entrained in the fault gouge during slip (Freeman et al., 1998; Yielding et al., 1997). It is important to note that proportions of shale or clay will vary across the fault surface therefore faults cannot be simply characterised as either sealing or nonsealing (Yielding et al., 1997). It is a measure of fault zone composition (Yielding et al., 2011). Figure 3.14 illustrates how the SGR is calculated at a given point on a fault surface for explicit shale beds. The following equation relates the total shale bed thickness within the column of rock that has slipped:

$$SGR = \frac{\sum(shale\ bed\ thickness)}{fault\ throw} \times 100\% \tag{3.7}$$

If reservoir zones are known rather than individual beds the net contribution of fine-grained material from each zone can be related to the clay content and thickness. The corresponding equation is:

$$SGR = \frac{\sum(zone\ thickness) \times (zone\ clay\ fraction)}{fault\ throw} \times 100\% \tag{3.8}$$

As shale content of the wall rocks increases, so does the proportion of shale entrained into the fault rock, and the higher the capillary entry pressure.

The algorithms defined in equations 3.4 to 3.8 require calibration – the resulting values of the are not conclusively a prediction of the likelihood of seal capacity (Yielding et al., 2010). For shale smear factor, the continuity of the smear from upthrown to downthrown side is measured (see Figure 3.14) (Yielding et al., 2010). When SSF is <4-5, smear is continuous, and the fault is likely to seal; when SSF is increased above 5, smear is discontinuous, and the fault is unlikely to seal (Yielding et al., 2010).

For clay smear potential, the probability of fault seal increases with increasing CSP until a "saturation" value is reached, after which fault seal probability plateaus (Yielding et al., 2010). A publication by Jev et al. (1993) states that a CSP value above 30 is representative of fault seal (Yielding et al., 2010).

A similar relationship is observed with the shale gouge ratio: the probability of fault seal increases with increasing SGR until a "saturation" value is reached (Yielding et al., 2010). At SGR values of >50% it is likely that fault rock is dominated by clay smear, thus capillary properties of clay smears should be representative of the fault surface (Yielding et al., 2010). Where SGR values <20% prevail, fault rock is likely to be dominated by disaggregation zones or cataclasites, and therefore their properties will be characteristic of the fault surface (Yielding et al., 2010). Fault surfaces with SGR values between 20% and 50% may only have a

small volume of phyllosilicate material – some clay/shale smears may be discontinuous (Yielding et al., 2010). For the purposes of this thesis, the SGR is estimated along fault planes critical for secure CO_2 storage due to its estimation of net shale/clay percentage in the entire slipped interval (Yielding et al., 1997).

A study by Yielding et al. (2011) noted a lack of evidence in the literature for subsurface faults to act as seals for CO_2. Instead, faulted hydrocarbon traps, naturally rich in CO_2, are used as analogues to assess whether faults may act as barriers or conduits for CO_2 flow (Yielding et al., 2011). The initial gas composition within one of the analysed traps included 50% CO_2 (Yielding et al., 2011). The study demonstrated that it is possible for top seals and fault seals in a CO_2-rich reservoir to remain intact over geological timescales (ca. 50 Ma) (Yielding et al., 2011).

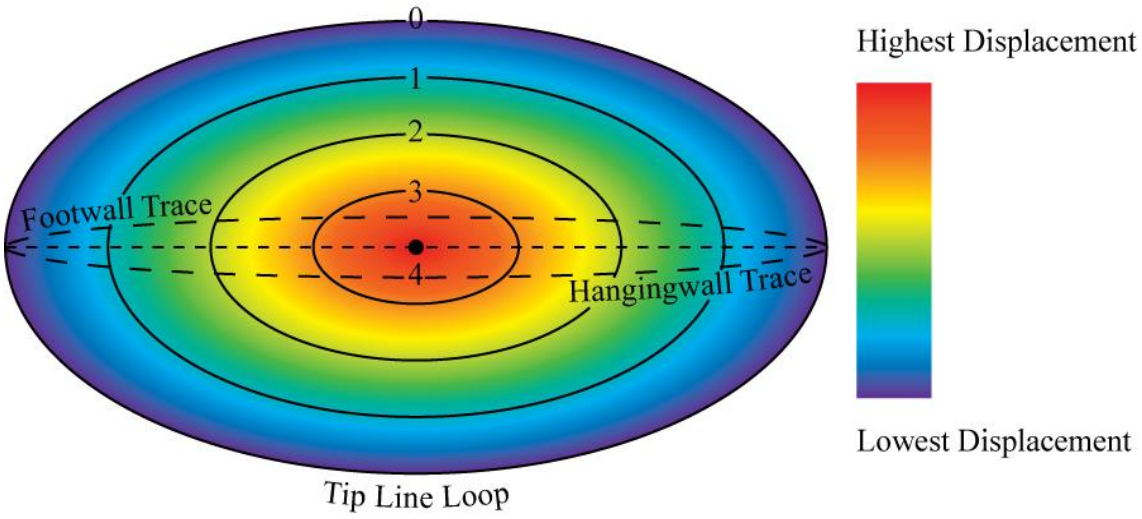

Figure 3.10 Schematic displacement contour diagram for an idealised fault plane viewed perpendicular to the fault surface. The tip line has an elliptical form and displacement increases towards the centre of the fault. The horizon separation also increases towards the centre. Adapted from Barnett et al. (1987) and Needham et al. (1996).

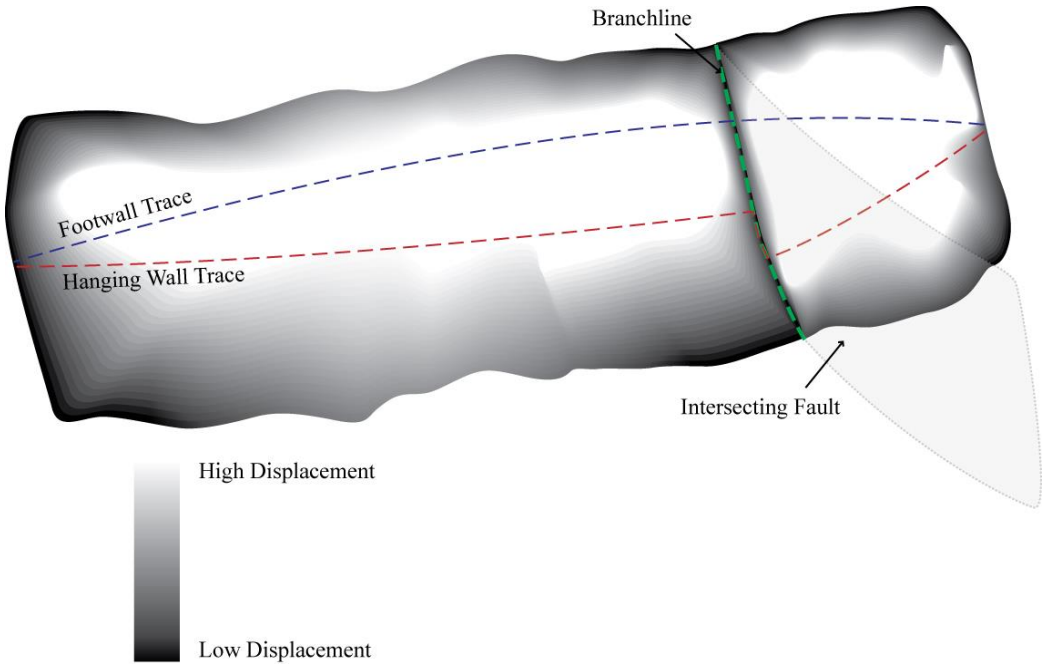

Figure 3.11 Throw attribute modelled on a fault plane where an intersecting fault cuts hanging wall strata but not footwall strata (see the footwall and hanging wall traces). The branchline marks the intersection of the main fault with the fault cutting hanging wall strata. Adapted from Needham et al. (1996).

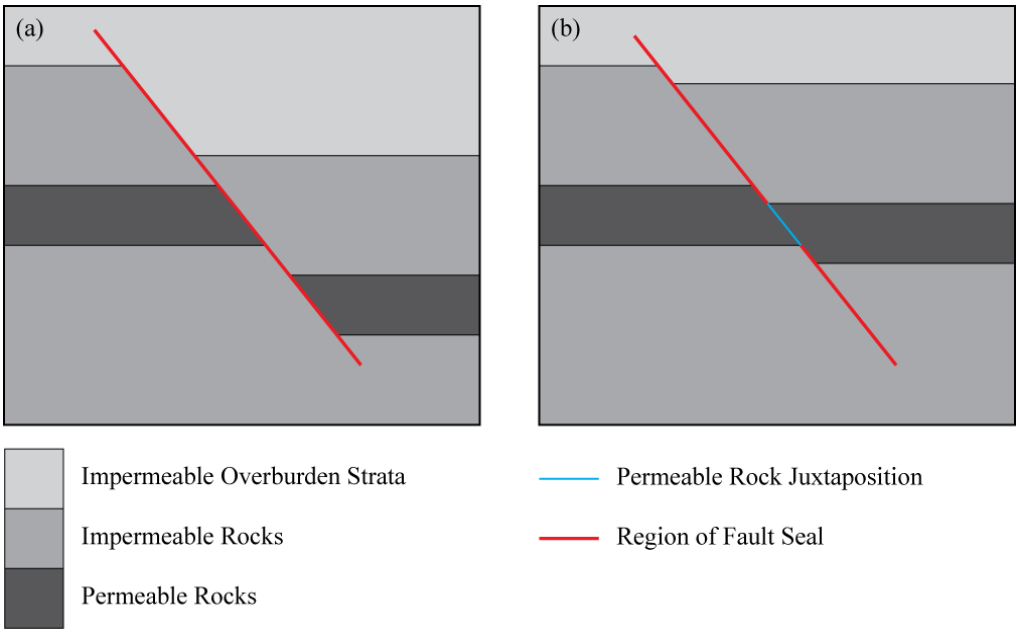

Figure 3.12 The two categories of fault seal: (a) reservoir against non-reservoir in which the juxtaposition of permeable rocks against non-permeable rocks provides a sealing mechanism, and (b) reservoir against reservoir in which case the fault itself must provide a barrier to fluid flow in order to seal.

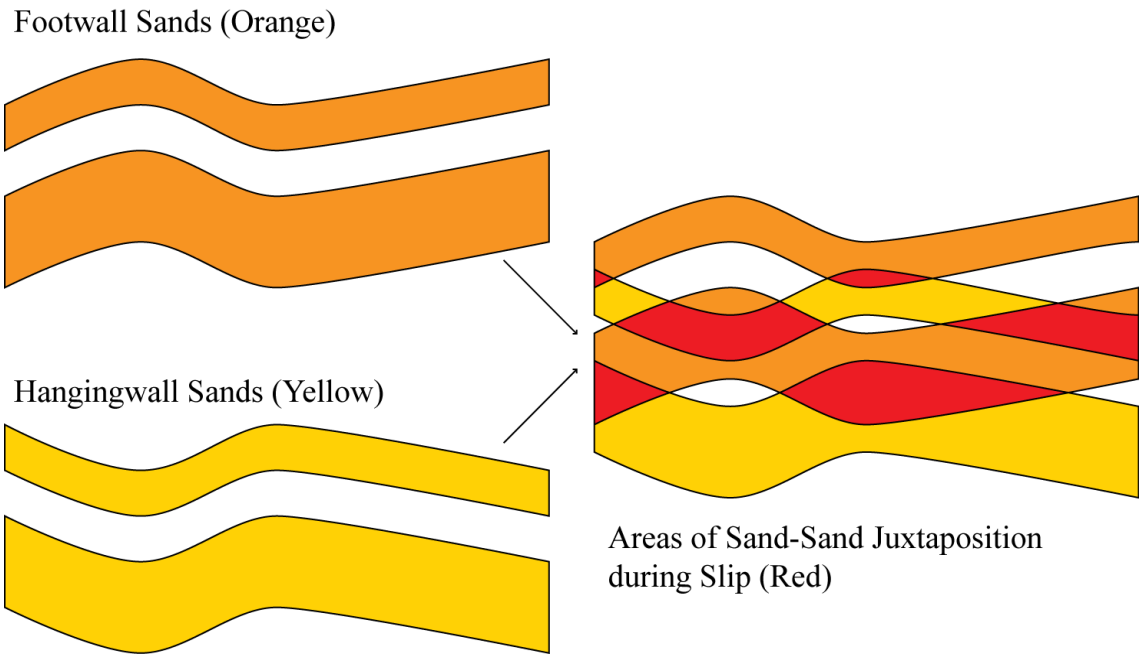

Figure 3.13 A simple Allan Diagram (after Allan (1989)). The footwall sands within the footwall rock are shown independently in orange. Likewise, the hanging wall sands within the hanging wall rock are shown independently in yellow. When superimposed on top of each other as they would be across-fault, it is possible to visualise areas of sand-sand juxtaposition (shown in red). These are areas in the fault-rock which may act as conduits to fluid flow – their seal integrity will need to be assessed through calculation of the shale gouge ratio. If the surrounding rock in the footwall and hanging wall is impermeable, it will pose a barrier to fluid flow across-fault when juxtaposed to a sand unit.

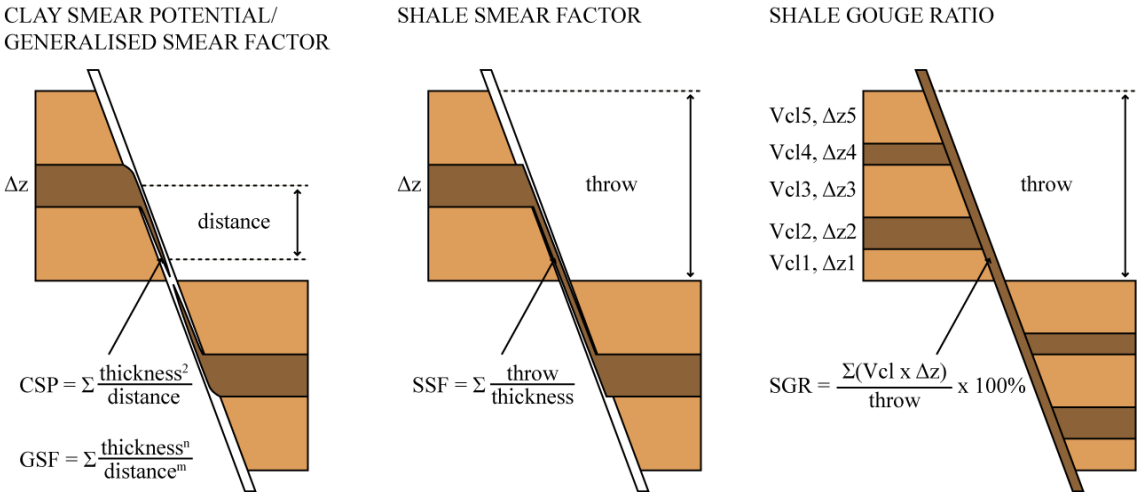

Figure 3.14 Fault seal algorithms for estimating the likelihood of clay entrainment in the fault gouge zone. Clay smear potential (CSP) is the sum of (thickness^2/distance) for shale beds (Bouvier et al., 1989). Generalised smear factor (GSF) is based on the CSP, but the CSP has dimensions of distance (Yielding et al., 1997). It is the sum of the source-bed thickness divided by smear distance (Yielding et al., 1997). Both CSP and GSF methods model the morphology of shear-type smears with distance (Yielding et al., 1997). The shale smear factor (SSF) is equal to the sum of throw divided by source-bed thickness (Lindsay et al., 1993). The SSF method models the morphology of abrasion smears (Yielding et al., 1997). The shale gouge ratio (SGR) estimates fault rock composition through measurement of the proportion of phyllosilicate material within the slipped rock interval. The figure shows the calculation for a sequence of reservoir zones, where Δz is reservoir zone thickness and Vcl is the clay volume fraction in the zone. After Freeman et al. (1998), Yielding et al. (1997), and Yielding et al. (2010); redrawn by Jolley et al. (2007).

3.3.4. POROSITY AND PERMEABILITY DATA

All porosity and permeability data (petrophysical characteristics) from the reservoir will be plotted on a series of graphs to establish the degree of heterogeneity within the reservoir. A graph of porosity versus permeability will be used to establish connectivity and overall reservoir quality. The porosity and permeability data will then be analysed individually. Both suites of data will be plotted on a boxplot to establish where the main body (50%) of data lies within the population. Both suites of data will also be assigned a best-fit probability distribution. The Anderson-Darling (A-D) test will then be used to assess the goodness-of-fit of the dataset to that particular probability distribution. This information can later be combined with Monte Carlo simulation to estimate CO_2 storage capacity.

3.3.5. PRODUCTION AND PRESSURE DEPLETION DATA

Analysis of routinely collected production and pressure data gives an insight into the dynamic behaviour of the reservoirs during their productive lifetimes, especially with respect to water drive (e.g. Agarwal et al. (1965), Archer and Wall (1986), Bruns et al. (1965), Chierici et al. (1967), Dake (1978), Hagoort (1988), Payne (1996), Pletcher (2002), and Tehrani (1985)). This information has been used to assess their expected behaviour during and following their storage lifetime.

Through plotting the cumulative production data against elapsed time since the onset of production it is possible to see the relative size of the storage site in terms of its hydrocarbon volume, and how the rate of production has changed over its lifetime. If pressure depletion against the same time period is plotted it is possible to see first-order results of how the reservoir has behaved in response to production. If any problems have been encountered during the productive lifetime of the reservoir they will become apparent through combined analysis of the production and pressure depletion graphs, especially if they result in a cessation of production over a certain time period. For example, it will be apparent if a major producing well has watered-out (been overcome with water production) and it has

been necessary to drill another well to replace it. Or, it will be apparent if it has been necessary to shut-in a reservoir (stop production from wells and close them) and/or reduce the production of the reservoir to seasonal production allowing time for the reservoir to re-pressurise slightly, for example through aquifer (water) influx, before production restarts.

More importantly, the use of material balance methods can be used to distinguish the reservoir drive mechanism of the gas reservoir, i.e. depletion drive or water drive. Depletion drive and water drive reservoirs have been previously defined in section 3.1. Depletion drive reservoirs (including volumetric reservoirs) are often left at extremely low pressure at the end of production. As such, any injected CO_2 is expected to simply re-pressurise the reservoir.

Conversely, water drive reservoirs are more complicated. The effect of gas production is to induce water influx into the reservoir; hence injected CO_2 is likely to have to displace formation water if the reservoir is to be used for storage. However, the volume of formation water that it is necessary to displace is dependent on the cumulative volume of water that has migrated into the reservoir throughout production. If the rate of water influx was equal to the rate of gas production, reservoir pressure will be maintained throughout the productive lifetime of the field. If the rate of water influx was less than the rate of gas production, pressure depletion will occur in the gas reservoir over the productive lifetime of the field. This implies there is a certain volume of utilisable pore space for CO_2 available immediately without the need for displacement of formation waters. This obviously has a direct effect on CO_2 storage capacity: it is necessary for there to be a sufficient volume of pore space outside the storage trap for the displaced formation waters to migrate to. Also, injected volumes of CO_2 need to be closely monitored to ensure CO_2 does not migrate outside of the trap with the displaced formation waters.

3.4. MATERIAL BALANCE METHODS: P/Z PLOTS AND COLE PLOTS

The use of material balance methods can be used to accurately evaluate reservoir behaviour, particularly with reference to aquifer performance (Archer and Wall, 1986; Bruns et al., 1965; Dake, 1978; Hagoort, 1988; Pletcher, 2002). The material balance equation is a volume balance which equates the total production to the difference between the initial volume of hydrocarbons in the reservoir and the current volume (Dake, 1978). The equation is commonly used to estimate the original gas in place and reservoir performance during production (King, 1993). For depletion drive reservoirs (i.e. a reservoir with insignificant volume of, or no water influx) compressibility of gas will exceed compressibility of the reservoir pore volume. Thus, the initial gas volume at the initial pressure will be equal to the remaining gas volume at lower pressure (Archer and Wall, 1986). Therefore:

$$\frac{P}{Z} = \frac{P_i}{Z_i}\left(1 - \frac{G_P}{G}\right) \tag{3.9}$$

After Archer and Wall (1986)

where, P is reservoir pressure, Z is the gas deviation factor, G_p is the cumulative volume of produced gas, G is the original gas in place, and the subscript "*i*" refers to initial conditions

Equation 3.6 can be arranged in linear form:

$$\frac{P}{Z} = \left(-\frac{P_i}{Z_i G}\right) G_p + \frac{P_i}{Z_i} \tag{3.10}$$

After Archer and Wall (1986)

A plot of P/Z against the cumulative volume of produced gas (G_p) has two significant intercepts: (a) $P/Z = P_i/Z_i$ at $G_p = 0$, and (b) $G_p = G$ at $P/Z = 0$ (Archer and Wall, 1986).

For gas reservoirs that experience either aquifer influx or aquifer depletion, the material balance must be re-written as:

$$G(B_{gi}) = (G - G_p)B_g + W_e - W_pB_w \tag{3.11}$$

After Archer and Wall (1986)

Equation 3.11 can be re-arranged as:

$$\frac{G_pB_g}{B_g - B_{gi}} = G + \frac{W_e - W_pB_w}{B_g - B_{gi}} \tag{3.12}$$

After Pletcher (2002)

where, B_g is the gas formation volume factor, W_e is the cumulative volume of water influx, W_p is the cumulative volume of produced water, B_w is the formation volume factor for water, and the subscript "*i*" refers to initial conditions.

As described, the material balance equation is suited to depletion drive reservoirs. However, there are difficulties in solving the equation for reservoirs experiencing water drive, i.e. where a reduction in reservoir pressure (throughout production) leads to an expansion of aquifer water resulting in aquifer (water) influx into the reservoir (Dake, 1978). In both depletion and water drive reservoirs extrapolation of the material balance plot (P/Z vs. Gp) can be used to determine the original gas in place (OGIP), (see Figure 3.15 (a)). However, this estimate will be erroneously high in water drive reservoirs. The Cole Plot (Pletcher, 2002) enables distinction between depletion and water drive reservoirs: when plotted on a graph, depletion drive reservoirs display a positive linear trend, whereas water drive reservoirs show a curve, and the shape of the curve identifies the strength of the water drive (weak, moderate or strong), (see Figure 3.15 (b)).

The Cole Plot (Cole, 1969) involves plotting the left side of equation 3.12 on the y-axis vs. cumulative gas production on the x-axis (Pletcher, 2002). For depletion drive reservoirs (i.e. reservoirs with no aquifer influx) the term (W_e-W_pB_w)/(B_g-B_{gi}) goes to zero and the points plot linearly with the y-intercept equal

to G (the original gas in place). However, within water-drive reservoirs, this term is no longer equal to zero and points plot with a curved trend. Where a weak water drive is present, the term on the far right hand side of equation 3.12, $W_e - W_pB_w/B_g - B_{gi}$, decreases with time because the denominator (gas expansion) increases faster than the numerator (net water influx). Therefore the resulting plot will have a negative slope that progresses towards the OGIP as production continues (Wang and Teasdale, 1987). For moderate and strong water drive the shape of the curve on the Cole plot is dependent on the gas formation volume factor which, in turn, is dependent on both W_e and the cumulative volume of produced gas, G_p. Figure 3.15 (b) shows Cole plot curves shapes as a function of aquifer strength, based on plots by Dake (1978).

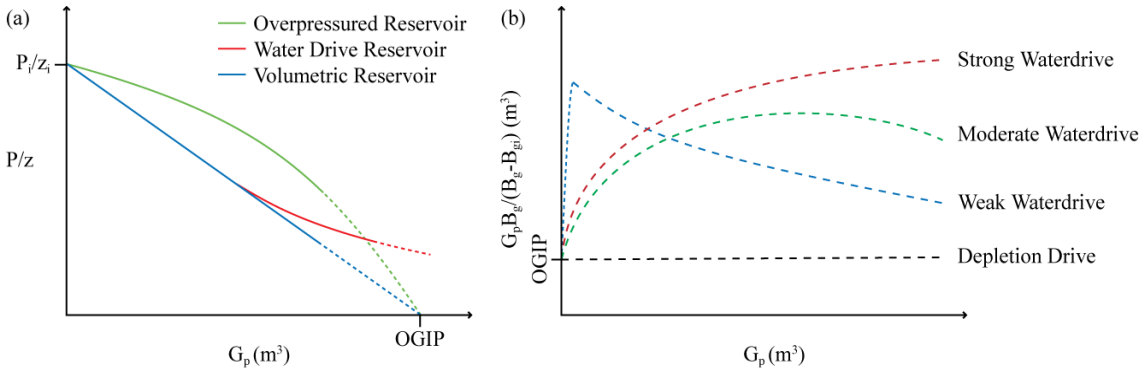

Figure 3.15 Material Balance Methods. (a) The original material balance method of pressure divided by gas compressibility factor against cumulative gas production. The major trends are shown on the graph for an over-pressured reservoir, a water drive reservoir and a volumetric reservoir. Due to the difficulties in solving the original material balance equation within water drive reservoirs, the water drive trend is often difficult to decipher on this graph from a volumetric reservoir trend. Instead a Cole Plot (b) can provide a clear distinction between water drive and volumetric (depletion) drive reservoirs.

3.5. DEPLETION DRIVE RESERVOIRS

Depletion drive reservoirs are generally considered to be isolated from aquifers. As such, the cumulative volume of water influx into a reservoir (W_e) can be considered to be zero or negligible. The estimated volume of original gas in

place (OGIP) can be well constrained by linear extrapolation of the trend on the P/z plot down to the x-axis.

3.6. WATER DRIVE RESERVOIRS

Water drive gas reservoirs are often associated with complex dynamic behaviour throughout their productive lifetimes (Dake, 1978; Hagoort, 1988). Gas production from a water drive reservoir results in an ever increasing reduction in reservoir pressure leading to an expansion of aquifer water, inducing aquifer (water) influx into the reservoir (Dake, 1978). This implies there is fluid communication outside of the reservoir within the immediate aquifer, as well as the potential for a neighbouring field to be in communication.

It is important to be able to estimate the volume of water remaining in a gas reservoir post-production as this will directly affect the volume of pore space available for CO_2 storage, and this is not necessarily equivalent to the volume of original gas in place. As such, it is necessary to establish a rate of water influx to, or displacement from, the storage reservoir. These estimates can be used to determine the volume of formation water that may be displaced during CO_2 injection.

The cumulative volume of water influx (W_e) to a reservoir can be estimated using the material balance equation (equation 3.11). However, required parameters for estimation include the cumulative volume of produced water (W_p) and the gas formation volume factor for water (B_w). If the water produced from the reservoir has never been metered over its lifetime, it is not possible to measure W_e with equation 3.11. Instead indirect methods of calculation will need to be used, as are outlined in the following sections 3.5.1. to 3.5.3.

There are up to four methods necessary to establish the volume of original gas in place and cumulative volume of aquifer influx (W_e) for water drive reservoirs:

1. If there has been evidence of pressure communication with a neighbouring reservoir from the historical production and pressure data it

is necessary to estimate the hydraulic head within both reservoirs and establish the direction of aquifer flow.

2. If there has been a history of dynamic aquifer behaviour throughout production it is necessary to estimate the hydraulic diffusivity to estimate a lag time for a pressure pulse within the water leg to diffuse over a specified distance.
3. If the volume of water produced from the wells has not been metered across the lifetime of the reservoir, or data is inaccurate, then it is necessary to estimate the cumulative volume of water influx into a reservoir (W_e) using the unsteady state water influx theory of Van Everdingen and Hurst (1949).
4. If the reservoir has previously been assumed to be a depletion drive reservoirs and there is a concern that the OGIP value may have been overestimated in the published literature or industry data and OGIP estimate must be made based on the aquifer model values for W_e (step 3).

3.6.1.1. HISTORICAL AQUIFER BEHAVIOUR THROUGHOUT PRODUCTIONESTIMATION OF HYDRAULIC HEAD

In order to understand aquifer behaviour throughout production, and to predict behaviour throughout and following the storage lifetime of the reservoir, it is necessary to measure hydraulic (or piezometric) head, H_{res}. Calculation of the hydraulic heads within neighbouring communicating reservoirs allows the estimation of direction of aquifer movement (see Figure 3.16). Aquifer movement will be from the reservoir with the higher head value, to the reservoir with the lower head value (Figure 3.16). Depending on production rates and lifetimes of the reservoirs involved, the direction of aquifer movement may change. The hydraulic head is a measurement of liquid pressure above a geometric datum, z. Ideally, hydraulic head measurements should be determined for individual reservoirs, both initially and throughout their productive lifetimes, from a deeper arbitrary datum point, z, using the following equation:

$$H_{res} = \frac{P}{\rho_w . g} + z_{res} \tag{3.13}$$

After Ingebritsen and Sanford (1999)

where ρ_w is the density of water, g is gravitational acceleration, and z_{res} is the height above an arbitrary datum point, z.

In order to predict how the storage reservoir will behave during carbon dioxide injection it is once again necessary to consider the head values at the end of production, immediately prior to the storage phase. If the storage reservoir is found to be in communication with a neighbouring field with a lower hydraulic head value, as the pressure increases within the storage reservoir its hydraulic head value will also increase resulting in aquifer movement away from the storage reservoir. This may not be a disadvantage to storage within the reservoir as the displaced water will allow a greater volume of carbon dioxide to be stored. However, the volume of carbon dioxide injected will have to be managed extensively to ensure it does not migrate out of the storage reservoir with the displaced water.

If the storage reservoir is found to be in communication with a neighbouring field with a higher hydraulic head value, initially during injection aquifer movement will remain from the aquifer, into the storage reservoir, except local to the injection wells. As the pressure within the storage reservoir increases with carbon dioxide injection, the hydraulic head value will increase. There may come a point where the hydraulic head value has increased so much that it exceeds the hydraulic head value of the communicating reservoir. In this case a reversal in aquifer movement will occur and once again the volume of carbon dioxide injected will have to be managed extensively to ensure it does not migrate out of the storage reservoir with the displaced water.

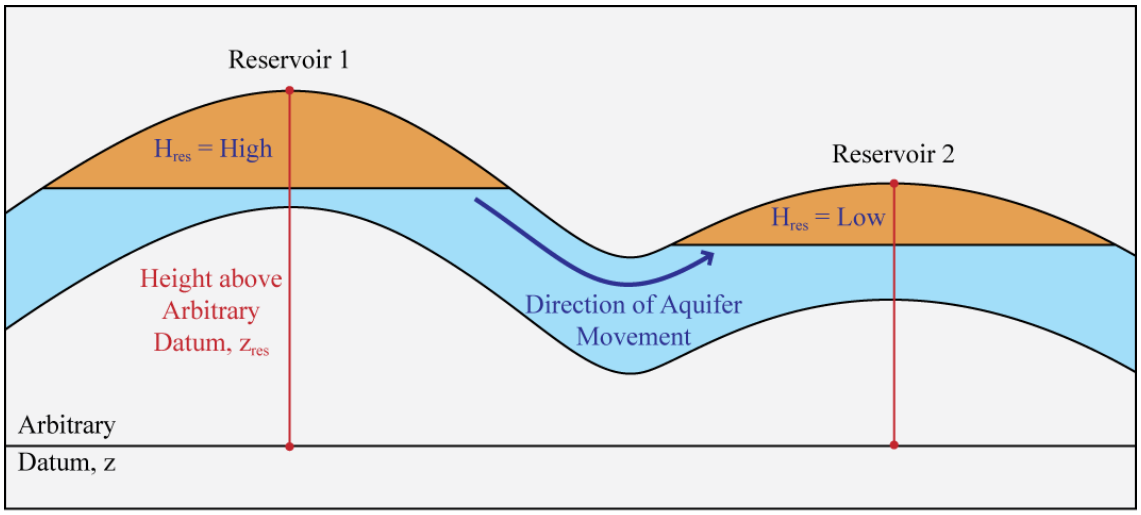

Figure 3.16 The relation of hydraulic head to the direction of aquifer movement. Hydraulic head is an estimate of liquid pressure above a deeper arbitrary datum, z. Within a petroleum system, the direction of aquifer movement can be determined between two reservoirs that share a common aquifer: during production movement will be from the reservoir with the higher head value to the reservoir with the lower head value. Prior to production, hydraulic heads will be in equilibrium, implying a higher pressure in the deeper Reservoir 2 compared with the shallower Reservoir 1.

3.6.1.2. ESTIMATION OF HYDRAULIC DIFFUSIVITY

Hydraulic diffusivity, κ_ϕ, is the ratio of hydraulic conductivity to the volume of water that a unit volume of saturated soil or rock releases from storage per unit decline in hydraulic head (Goudie, 1985). It is a parameter that combines transmission characteristics and storage properties (Goudie, 1985). If there are two reservoirs in communication through a shared aquifer, the diffusion distance, Δx, between them can be measured and hydraulic diffusivity estimated to give an order-of-magnitude estimate for the characteristic diffusion time, Δt, for a pressure change within one reservoir to influence the pressure within the other reservoir, via the equation:

$$\Delta t = \Delta x^2 / \kappa_\phi \tag{3.14}$$

Hydraulic diffusivity can be estimated with the following equation:

$$\kappa_\phi = \frac{k}{\mu \times \phi \times (c_{res} + c_{fluid})} \tag{3.15}$$

(after Wibberley (2002))

where, k is the permeability, μ is fluid viscosity, ϕ is porosity, and c_{res} and c_{fluid} is the bulk compressibility of the reservoir rock and reservoir fluid respectively.

Parameters to equation 3.15, such as permeability and porosity, generally show a vast range of heterogeneity within reservoir and aquifer rocks. Normally an average value for such parameters would be used in equation 3.15 to estimate hydraulic diffusivity. However, accuracy can be improved upon if the entire range of variability of such parameters is taken into consideration. This can be achieved through Monte Carlo simulation (Shonkwiler and Mendivil, 2009).

Monte Carlo simulation analyses risk for any parameter displaying natural uncertainty, through use of a probability distribution, for example, a normal distribution or bell curve. Random sampling takes place from the selected probability distributions for each variable, and is repeated thousands of times for accuracy. The outcome is a probability distribution showing the most likely results.

3.6.1.3. ESTIMATION OF THE CUMULATIVE VOLUME OF AQUIFER INFLUX INTO A RESERVOIR (W_e)

When the volume of water produced has not been metered across the productive lifetime of a reservoir, or the data is considered to be inaccurate or incomplete, it is necessary to estimate values for W_e using aquifer modelling. The unsteady state water influx theory of Van Everdingen and Hurst (1949) is used here to model both radial and linear, infinite and finite aquifers, and produce more accurate estimates of W_e.

3.6.1.4. ESTIMATION OF ORIGINAL GAS IN PLACE (OGIP)

In some cases, the published or industry values of OGIP may be inaccurate if the reservoir drive mechanism (i.e. water drive) has been previously incorrectly identified as depletion drive. The following equation is used here to estimate OGIP based on the aquifer model values for OGIP:

$$OGIP = \frac{G_p - W_e E}{1 - E/E_i} \tag{3.16}$$

3.7. THERMODYNAMIC PROPERTIES

3.7.1. GAS COMPRESSIBILITY FACTOR ESTIMATION AND CO_2 STORAGE IMPLICATIONS

The gas compressibility factor or Z-factor, (see Chapter 1, section 1.6.), is the correction factor for the deviation of a real gas from ideal behaviour at given pressures and temperatures. Estimation of the gas compressibility factor (or Z-factor) is highly complex, not only for pure substances but particularly for gas mixtures. Within this thesis, the reservoirs considered for carbon dioxide storage have variable residual volumes of their own individual natural gas mixtures. It is therefore necessary to calculate individual Z-factors based on the reservoirs' individual compositions.

Recently, computer software has been developed to allow estimation of the thermophysical properties of individual fluids based around various built-in equations of state. The software used within this thesis include RefProp (developed by the National Institute of Standards and Technology, NIST) which uses the Peng-Robinson (Peng and Robinson, 1976), GERG-2008 (Kunz and Wagner, 2012), and AGA8 Model (Starling and Savidge, 1992) equations of state to model the thermophysical properties of fluids. A second, but less rigorous tool used within this thesis is WebGasEOS, an online tool provided by the Lawrence Berkeley National Laboratory, and uses the Peng-Robinson (Peng and Robinson, 1976), Peng-Robinson-Stryjek-Vera (Stryjek and Vera, 1986), Redlich-Kwong (Redlich and Kwong, 1949) and Soave-Redlich-Kwong (Soave, 1972) equations of state. The tool has only a limited list of components (ten in total) that can form a gas mix: methane, ethane, propane, hydrogen sulphide, carbon dioxide, nitrogen, oxygen, water, ethanol and hydrogen. Therefore, hydrocarbons with carbon chains longer than three cannot be input to a gas mix. This restricts its application – the majority of natural gas compositions will contain hydrocarbons such as butane, pentane, hexane, etc.

The software allows input of temperature, pressure and gas composition (as well as other more complex parameters within RefProp), along with a choice of

equation of state for calculation of gas properties. In this way, it is possible to produce estimates of gas compressibility factors under the same reservoir conditions using different equations of state and compare the different results.

These results can be input into calculations to estimate the carbon dioxide storage capacity of the individual reservoirs, the details of which are described in the following section. In order to estimate the theoretical and/or effective CO_2 storage capacity with any accuracy, it is necessary to understand and use different equations of state in gas compressibility factor estimation.

3.7.1.1. PROPERTIES OF PURE SUBSTANCES

As we have seen in Chapter 1, section 1.6., some methods of theoretical and effective storage capacity estimation rely on predicting the gas compressibility factor, Z. This Z-factor, can be estimated with the use of equations of state.

Equations of state are frequently used to define the state of matter (distinct phases such as solid, liquid, gas and plasma) under a constrained set of physical conditions including temperature, pressure, volume or internal energy. Their applications include the description of fluid properties, fluid mixtures and solids.

An equation of state relates pressure, temperature and specific volume of a substance (Çengel and Boles, 2011). Historically, there have been many attempts to determine fluid properties including Boyle's Law (Boyle, 1662), Charles' Law, 1787 (later formulated by Gay-Lussac (1802)) and Dalton's Law of Partial Pressures (Dalton, 1801). However, it was not until the ideal gas law was defined by Émile Clapeyron (Clapeyron, 1834) that the first statement of an equation of state was ascertained:

$$PV = RT \tag{3.17}$$

where, P is the absolute pressure, V is the specific volume, R is the universal gas constant and T is the absolute temperature. Absolute pressure is measured relative to absolute vacuum (i.e. absolute zero pressure). Absolute temperature is on a scale where 0 is taken as absolute zero, such as the Kelvin scale. Specific

volume is the ratio of a substance's volume to its mass and is the reciprocal of density.

The ideal gas law unites Boyle's Law and Charles' Law into one expression and is one of the most basic equations of state to relate gas and liquid densities to temperatures and pressures. It is approximately accurate for weakly polar gases (molecules that have weak electrical poles resulting from bonding) at low pressures and moderate temperatures. However, inaccuracies are abundant at higher pressures and lower temperatures and the equation is unable to anticipate condensation from a gas to a liquid.

Gases that obey the ideal-gas relation are termed ideal gases. In practice, the ideal-gas relation closely approximates P-V-T behaviour of real gases at low densities, however, real gases tend to deviate from ideal-gas behaviour significantly at states near the saturation region and the critical point. This deviation from ideal-gas behaviour at a given temperature and pressure can be accurately accounted for by the introduction of a correction factor called the gas deviation factor (Z):

$$Z = PV/RT \tag{3.18}$$

For real gases, Z can be greater or less than unity. The farther away Z is from unity, the more the gas deviates from ideal-gas behaviour.

As previously stated, the ideal and real gas equations accurately predict fluid properties at low pressures and moderate temperatures – but how is it possible to define a low pressure or a moderate temperature? 100 °C may be a low temperature for many substances, such as carbon, magnesium, aluminium, etc., which are solids at this temperature, however, it is not a low temperature for substances such as nitrogen, methane, carbon dioxide, etc. These three substances (nitrogen, methane and carbon dioxide) are well over their critical temperature at 100 °C (see Chapter 1, section 1.4.) and are either gases or supercritical fluids depending on the pressure. As such, the pressure or temperature of a substance is high or low relative to its critical temperature or pressure (the point at which no phase boundaries exist), (Çengel and Boles, 2011).

Gases behave differently at a given temperature and pressure. However, *reduced* temperature and pressure can be defined as actual temperature and pressure normalised to the *critical* temperatures and pressures (see equation 3.19) (Çengel and Boles, 2011). The reduced values of temperature and pressure for different pure gases ensure that their individual properties can be compared:

$$P_R = \frac{P}{P_{cr}} \quad and \quad T_R = \frac{T}{T_{cr}} \tag{3.19}$$

where, P_R is the reduced pressure and T_R is the reduced temperature. All fluids, when compared at the same reduced temperature and reduced pressure, have approximately the same gas compressibility factor (Z-factor) and all deviate from ideal gas behaviour to about the same degree – this is known as the principle of corresponding states (Archer and Wall, 1986; Çengel and Boles, 2011). The principle of corresponding states can be applied to gas mixtures of light hydrocarbons with a reasonable degree of accuracy, therefore correlations of the compressibility factor with reduced pressure for isotherms of reduced temperature (Standing-Katz correlations (Standing and Katz, 1942), (see Figure 3.17)) are widely accepted in estimations of gas reservoir behaviour (Archer and Wall, 1986).

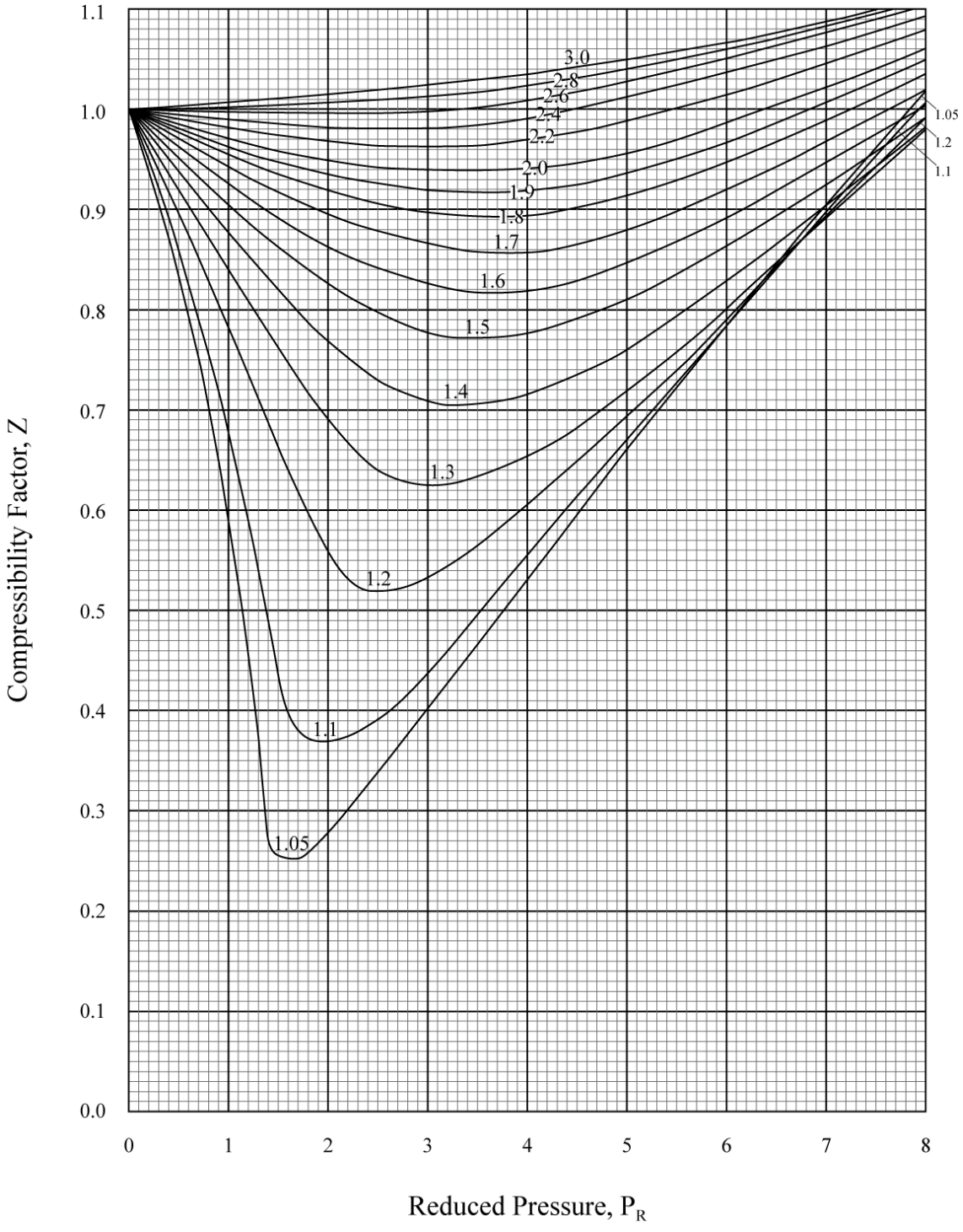

Figure 3.17 Standing-Katz Correlation of the Gas Compressibility Factor (Z) against Reduced Pressure for Isotherms of Reduced Temperature. After Standing and Katz (1942).

3.7.1.2. PROPERTIES OF GAS MIXTURES

Estimation of the fluid properties of a gas mixture is not as simple as for pure substances. If the critical pressure and critical temperature of the gas mixture is known, the Standing-Katz chart (Standing and Katz, 1942) can be used. However, the process of empirically determining the critical properties of a gas mix is extremely complex. Also for any degree of accuracy, it is often more appropriate to estimate fluid properties through use of alternative equations of state (see section 3.6.2.3).

In order to use equations of state to determine fluid properties, it is necessary to know the composition of the mixture (below), as well as the properties of the individual components (see section 3.6.2.1. and 3.6.2.2.). This can be done either through molar analysis (by specifying the number of moles of each component) or through gravimetric analysis (by specifying the mass of each component).

Within a given gas mixture, the mass of the mixture, m_m, is the sum of the masses of the individual components, and the mole number of the mixture, N_m, is the sum of the mole numbers of the individual components:

$$m_m = \sum_{i=1}^{k} m_i \quad and \quad N_m = \sum_{i=1}^{k} N_i \tag{3.20}$$

The ratio of the mass of a component to the mass of the mixture is called the mass fraction, mf, and the ratio of the mole number of a component to the mole number of the mixture is called the mole fraction, y:

$$mf_i = \frac{m_i}{m_m} \quad and \quad y_i = \frac{N_i}{N_m} \tag{3.21}$$

The sum of the mass fraction of mole fractions for a mixture is equal to 1:

$$\sum_{i=1}^{k} mf_i = 1 \quad and \quad \sum_{i=1}^{k} y_i = 1 \tag{3.22}$$

3.7.1.2.1. P-V-T BEHAVIOUR OF GAS MIXTURES: IDEAL AND REAL GASES

An ideal gas is defined as a gas whose molecules are spaced far apart so that the behaviour of the molecule is not influence by the presence of other molecules – a situation encountered at low densities. Real gases approximate this behaviour closely when they are at a low pressure or a high temperature relative to their critical point values.

When two or more ideal gases are mixed, the behaviour of a molecule normally is not influenced by the presence of other similar or dissimilar molecules, and therefore a non-reacting mixture of ideal gases also behaves as an ideal gas. When a gas mixture consists of real (non-ideal) gases, however, the prediction of the P-V-T behaviour of the mixture becomes rather involved

Prediction of P-V-T behaviour is usually based on two models: Dalton's law of additive pressures and Amagat's law of additive volumes. Dalton's law of additive pressures: the pressure of a gas mixture is equal to the sum of the pressures each gas would exert if it existed alone at the mixture temperature and volume. Amagat's law of additive volumes: the volume of a gas mixture is equal to the sum of the volumes each gas would occupy if it existed alone at the mixture temperature and pressure.

Dalton's and Amagat's laws hold exactly for ideal-gas mixtures, but only approximately for real gas mixtures. This is due to intermolecular forces that may be significant for real gases at high densities. For ideal gases, these two laws are identical and give identical results.

3.7.1.2.2. PROPERTIES OF GAS MIXTURES: IDEAL AND REAL GASES

The mass of a gas mixture is equal to the sum of the masses of the individual components. This is an example of an extensive property and a similar rule can be applied to the total internal energy, enthalpy and entropy of an ideal or real gas mixture. For example:

Consider a gas mixture of 6 kmol methane and 3 kmol ethane. If the methane has a mass of 2 kg and ethane has a mass of 3 kg, the total mass of the gas mixture will be 5 kg.

$$2\ kg + 3\ kg = 5\ kg \tag{3.23}$$

The temperature of a gas mixture is an example of an intensive property and is calculated by adopting an averaging scheme per unit mass or unit mole of the components of an ideal or real gas mixture. The internal energy, enthalpy and entropy per unit mass or per unit mole of the gas mixture can be calculated by dividing by the mass or mole number of the mixture. For example:

Consider the same gas mixture of 6 kmol methane and 3 kmol ethane. The temperature of the methane is 25 °C and the temperature of the ethane is 30 °C. If we multiply the number of moles of methane and ethane by their respective temperatures and add the calculated values together, then divide by the total number of moles, we arrive at a gas mixture temperature of 26.67 °C (see equation 3.24):

$$\frac{(6 \times 25) + (3 \times 30)\ kmol\ °C}{6 + 3\ kmol} = \frac{240\ kmol\ °C}{9\ kmol} = 26.67\ °C \tag{3.24}$$

3.7.1.2.3. EQUATIONS OF STATE FOR ESTIMATION OF FLUID PROPERTIES

The ideal and real gas equations of state are extremely simple, however, their range of applicability is limited. As such, it is useful to consider alternative equations of state that represent the P-V-T behaviour of substances over a larger region with a higher degree of accuracy and fewer limitations. The Van der Waals

equation of state (Waals, 1873) was the first equation to produce more accurate results than those predicted by the ideal gas law (equation 3.25):

$$\left(P + \frac{a}{v^2}\right)(v - b) = RT \tag{3.25}$$

As for other cubic equations (meaning the equation can be rearranged as a cubic function of molar volume, V_m) the Van der Waals equation consists of an attraction parameter, a, and a repulsion parameter, b. The Van der Waals equation of state was the first equation to attempt to describe the attractions (of intermolecular forces) and repulsions (the volume occupied by the gas molecules per unit mass) between molecules through the attraction and repulsion parameters:

$$Attraction\ term, a = \frac{27R^2T_{cr}^2}{64P_{cr}} \tag{3.26}$$

$$Repulsion\ term, b = \frac{RT_{cr}}{8P_{cr}} \tag{3.27}$$

where, T_{cr} is the critical temperature and P_{cr} is the critical pressure.

Van der Waals is now only used to demonstrate the advancement of the study of equations of state as it has now been superseded in accuracy by alternative, more modern equations of state (Çengel and Boles, 2011). The Redlich-Kwong (Redlich and Kwong, 1949) and Soave-Redlich-Kwong (Soave, 1972) equations of state are extensions of Van der Waals and provide more accurate results with only a slight increase in complexity.

Due to the extent of inaccuracies in estimating fluid properties using the ideal gas law and Van der Waals equations, the equations have been omitted for use in this study. Nonetheless, they are important to acknowledge as they provide the basis from which modern methods have been developed. A major inaccuracy of the ideal gas law is in estimation of fluid properties (including gas compressibility factor) above the critical point. The Van der Waals equation of state is an improvement upon this; however, it is inaccurate at the vapour-liquid equilibrium.

Due to the nature of CO_2 storage within low pressure depleted gas reservoirs, it will be important to predict fluid properties at the vapour-liquid equilibrium line (as the reservoir is re-pressurised with CO_2) and past the critical point (where CO_2 will be present in the reservoir as a supercritical fluid).

Currently there are numerous published equations of state to calculate fluid properties at various pressures and temperatures, but no single equation of state exists that can precisely estimate properties of all substances under all conditions. In light of this, there are certain methods published which offer a reasonably accurate estimation of fluid properties specifically within natural gas reservoirs. These methods include: Peng-Robinson (Peng and Robinson, 1976), GERG-2008 (Kunz and Wagner, 2012), AGA8 Model (Starling and Savidge, 1992), Peng-Robinson-Stryjek-Vera (Stryjek and Vera, 1986), Redlich-Kwong (Redlich and Kwong, 1949) and Soave-Redlich-Kwong (Soave, 1972). These equations of state have been used to estimate both natural gas properties and CO_2 properties within the selected storage sites with particular emphasis on the compressibility factor.

The Peng-Robinson equation of state (Peng and Robinson, 1976) is another example of a cubic equation of state:

$$P = \frac{RT}{V_m - b} - \frac{a(T)}{V_m(V_m + b) + b(V_m - b)} \tag{3.28}$$

Where, a(T) is the attraction term as a function of temperature.

Applying equation 3.20 at the critical point, we have:

$$a(T_{cr}) = \frac{0.457235R^2T_{cr}^2}{P_{cr}} \tag{3.29}$$

$$b(T_{cr}) = \frac{0.077796RT_{cr}}{P_{cr}} \tag{3.30}$$

$$Z_c = 0.307 \tag{3.31}$$

At temperatures other than the critical, we let:

$$a(T) = a(T_c).\alpha(T_r, \omega) \tag{3.32}$$

$$b(T) = b(T_c) \tag{3.33}$$

where $\alpha(T_r, \omega)$ is a dimensionless function of reduced temperature and acentric factor, and equals unity at the critical temperature.

For all substances examined, the relationship between α and T_r can be linearized by the following equation:

$$\alpha^{0.5} = 1 + \kappa(1 - T_r^{0.5}) \tag{3.34}$$

where, κ is a constant characteristic of each substance. These constants have been correlated against the acentric factors. The resulting equation is:

$$\kappa = 0.37464 + 1.54226\omega - 0.26992\omega^2 \tag{3.35}$$

Like the Van der Waals equation of state (Waals, 1873), the Peng-Robinson equation of state (Peng and Robinson, 1976) consists of an attraction term (defined in equation 3.28) and a repulsion term (defined in equation 3.29). In particular, the model is able to provide fairly accurate results for fluid properties in proximity to the critical point, notably in estimations of compressibility factor and liquid density; therefore it is a very useful equation for this study. Another useful quality of the equation is that it is highly suited for the estimation of fluid properties within the natural gas environment due to its effectiveness with non-polar fluids, of which hydrocarbons (and carbon dioxide) make up a large number.

The Peng-Robinson-Stryjek-Vera equation of state (Stryjek and Vera, 1986) is a modification to the Peng-Robinson equation of state (equation 3.28). The first modification (PRSV1) is to the attraction term, which significantly improves the model's accuracy by introducing an adjustable pure component parameter and by modifying the polynomial fit of the acentric factor. However it is still fairly unreliable in phase-equilibrium calculations:

$$\kappa = \kappa_0 + \kappa_1(1 + T_r^{0.5})(0.7 - T_r) \tag{3.36}$$

$$\kappa_0 = 0.378893 + 1.489715\omega - 0.171318\omega^2 + 0.019655\omega^3 \tag{3.37}$$

where, κ_1 is an adjustable pure component parameter.

A subsequent modification (PRSV2) further improves the model's accuracy by introducing two additional pure component parameters to the previously modified attraction term, so that equation 3.31 becomes:

$$\kappa = \kappa_0 + [\kappa_1 + \kappa_2(\kappa_3 - T_r)(1 - T_r^{0.5})](1 + T_r^{0.5})(0.7 - T_r) \tag{3.38}$$

It is particularly useful for the estimation of vapour-liquid equilibrium, however, it is unreliable above the critical point as estimations of the alpha function become erratic. Hence, it is advisable to substitute other equations to determine alpha at temperatures and pressures above the critical point.

The Redlich-Kwong equation of state (Redlich and Kwong, 1949) as previously stated is a continuation of the Van der Waals equation of state (Waals, 1873), (equation 3.39).

$$P = \frac{RT}{V_m - b} - \frac{a}{V_m(V_m + b)T^{0.5}} \tag{3.39}$$

$$a = \frac{0.42748 R^2 T_{cr}^{2.5}}{P_{cr}} \tag{3.40}$$

$$b = \frac{0.08662 R T_{cr}}{P_{cr}} \tag{3.41}$$

The Redlich-Kwong equation of state (Redlich and Kwong, 1949) improves accuracy considerably in comparison to other published equations of the time even though it is reasonably simple. However, it is unable to calculate vapour-liquid equilibria to any degree of accuracy due to its poor estimation of the liquid phase. Nonetheless, it can be applied to the estimation of gas phase properties when the reduced pressure is less than 50 % of the reduced temperature.

The Soave-Redlich-Kwong equation of state (Soave, 1972) is a modification to the Redlich-Kwong equation of state (Redlich and Kwong, 1949), (equation 3.39).

$$P = \frac{RT}{V_m - b} - \frac{a(T)}{V_m(V_m + b)} \tag{3.42}$$

At the critical temperature:

$$a(T_{cr}) = \frac{0.42747 R^2 T_{cr}^2}{P_{cr}} \tag{3.43}$$

$$b(T_{cr}) = \frac{0.08664 R T_{cr}}{P_{cr}} \tag{3.44}$$

At temperatures other than the critical temperature, we let:

$$a(T) = a(T_{cr})\alpha(T) \tag{3.45}$$

where, α(T) is an adimensional factor which becomes unity at the critical temperature.

The relationship between α and T_r can be linearized by the following equation:

$$\alpha^{0.5} = 1 - m_i(1 - T_r^{0.5}) \tag{3.46}$$

$$m_i = \frac{\alpha^{0.5}(0.7) - 1}{1 - (0.7)^{0.5}} \tag{3.47}$$

The parameter, m_i, is connected directly with the acentric factors, ω, of the substances. The alpha function is designed to fit hydrocarbon vapour pressure data and performs comparably well to that of the Peng-Robinson equation of state. However, the Peng-Robinson equation of state is generally considered to be superior in the estimation of liquid densities, particularly in non-polar substances such as hydrocarbons.

There is no single equation of state in existence that is accurate in the description of thermodynamic properties over the entire fluid region (i.e. gas phase, liquid phase and supercritical region). As such, the GERG-2008 equation of state (Kunz and Wagner, 2012) was specifically developed as a wide-range equation of state to predict the phase behaviour and thermodynamic properties of natural gas mixtures and similar mixtures. It spans the entire fluid region including the vapour-liquid equilibrium states for mixtures of 21 specified components: methane, nitrogen, carbon dioxide, ethane, propane, n-Butane, isobutane, n-Pentane, isopentane, n-Hexane, n-Heptane, n-Octane, n-Nonane, n-Decane, hydrogen, hydrogen sulphide, carbon monoxide, water, oxygen, argon and helium. Its range of validity extends between 90 and 450 K and pressures of up to 35 MPa, where the most accurate experimental data of the thermal and caloric properties are represented to within their accuracy. It also has an extended range from 60 to 700 K and up to 70 MPa. GERG-2008 will be adopted as an ISO Standard (ISO 20765-2/3) for natural gases. The equation itself is extremely complex – full details can be found within Kunz and Wagner (2012). Its basic structure is detailed below:

$$\alpha(\delta,\tau,\bar{x}) = \alpha^{o}(\rho,T,\bar{x}) + \sum_{i=1}^{N} x_i \alpha_{0i}^{r}(\delta,\tau) + \Delta\alpha^{r}(\delta,\tau,\bar{x}) \tag{3.48}$$

$$\alpha = a/RT \tag{3.49}$$

$$\delta = \rho/\rho_r(\bar{x}) \tag{3.50}$$

$$\tau = T_r(\bar{x})/T \tag{3.51}$$

where, α is the reduced Helmholtz free energy (as estimated using equation 3.49). The Helmholtz free energy is a thermodynamic potential that measures "useful" work obtainable from a closed thermodynamic system at a constant temperature; δ is the reduced density of the mixture (as estimated using equation 3.50); τ is the reduced temperature of the mixture (as estimated using equation 3.51); $\bar{x}$ is the composition (mole fractions) of the mixture; x is the mole fraction of a pure substance within the mixture; ρ is the density of the mixture; $\rho_r(\bar{x})$ is the reducing function of density, only dependent on the composition of the mixture; $T_r(\bar{x})$ is the reducing function of temperature, only dependent on the composition of the mixture; and T is the temperature of the mixture. The first term of equation 3.48 is the ideal gas part, the second term is the contribution of the pure substances, and the third term is the departure function.

The AGA8-DC92 equation of state (Starling and Savidge, 1992) is valid only within the gas phase specific to the natural gas environment. Once again, it is a very complex equation of state which includes 58 polynomial terms and polynomial terms in combination with exponential functions requiring 860 different parameters. Full details of the equation can be found within Starling and Savidge (1992).

The AGA8-DC92 equation of state was designed for accurate estimation of the compressibility factor, therefore it is a key equation of state to use within this study. It is more limited than GERG-2008 within the homogenous gas region,

liquid phase and vapour-liquid equilibrium states. Once again, 21 components can be incorporated within a gas mixture, although the concentration range is more limited than GERG-2008. However, the AGA8-DC92 equation of state still covers a wide range of temperatures between 143 – 673 K and pressures up to 280 MPa. There are uncertainties in the prediction of fluid properties in natural gas mixtures between temperatures of 250 – 270 K. At higher temperatures (up to 290 K) any uncertainties are restricted to pressures lower than 12 MPa. There are also large uncertainties for gas mixtures containing higher fractions of nitrogen, carbon dioxide, ethane, or heavier alkanes at low temperatures.

The AGA8-DC92 equation of state overall is considerably more accurate than many of the methods previously stated, except the GERG-2008 equation of state. However, due to its restricted capabilities in estimation of fluid properties within lower pressure and temperature environments the accuracy of results within sites selected for evaluation within this study may not be completely reliable.

3.8. ESTIMATION OF CO_2 DENSITY AND GAS FORMATION VOLUME FACTOR

CO_2 density will be estimated within this thesis using both RefProp (Lemmon et al., 2013) and WebGasEOS (Reagan and Oldenburg, 2006), using the same equations of state as mentioned in the previous section.

The gas formation volume factor can be estimated using either of the two equations below, after Archer and Wall (1986):

$$B_g = \frac{reservoir\ volume}{standard\ condition\ volume} \tag{3.52}$$

$$B_g = \frac{P_{sc}}{T_{sc}} \times T_{res} \times \frac{z_{res}}{P_{res}} \tag{3.53}$$

Again, the value for z_{res} in equation 3.53 will be estimated using both RefProp (Lemmon et al., 2013) and WebGasEOS (Reagan and Oldenburg, 2006).

3.9. CO_2 STORAGE CAPACITY ESTIMATION

The theoretical CO_2 storage capacity of the reservoirs assessed within this thesis will be estimated using the equations of Bachu et al. (2007), equation 1.1 and 1.2, Holloway et al. (2006), equation 1.3 and Tseng et al. (2012), equation 1.4. The effective CO_2 storage capacity will be estimated using the equation of Tseng et al. (2012), equations 1.6 and 1.7.

The method of Bachu et al. (2007), equation 1.1 is a geometric approach to storage capacity estimation. The method requires the porosity of a reservoir to be input into the storage capacity equation. Previous studies have used a single, average value for reservoir porosity, despite porosity data showing a large degree of heterogeneity. This thesis will use Monte Carlo simulation to attempt to honour all available porosity data for the reservoirs being assessed. This will result in a range of potential storage capacity for the individual reservoirs.

All other methods (both theoretical and effective) are based on the material balance approach. This approach requires the input of parameters that are generally well constrained and show little variability.

3.10. SUMMARY

The methods outlined above are now used within Chapters 4, 5 and 6 to assess individual reservoir suitability for carbon storage. Water drive gas reservoirs where water production has not been metered will utilise all the described methods within this chapter to estimate aquifer behaviour and CO_2 storage capacity. Depletion drive gas reservoirs and water drive gas reservoirs where water production has been metered will utilise all the methods described here, except for the methods listed in section 3.5 where aquifer behaviour is estimated using indirect methods. This is an unnecessary step for depletion drive reservoirs which tend to be isolated and have not experienced aquifer influx throughout their productive lifetimes. For water drive gas reservoirs where water production has been metered, this step is an unnecessary step as the material balance equation (equation 3.11) can

be used to accurately constrain aquifer behaviour throughout the productive lifetime of the reservoir.

4 The Hewett Lower Bunter Reservoir: Geological Characterisation for Carbon Dioxide Storage and Storage Capacity Estimation within a High Quality Depleted Gas Reservoir without a Water Drive

4.1. INTRODUCTION

There is substantial variation in both theoretical and effective storage capacity estimation within depleted gas reservoirs (Bradshaw et al., 2007). Theoretical storage capacity estimations rely on knowledge of reservoir geometry and petrophysics (i.e. a STOOIP-based approach such as that of Bachu et al. (2007); Chapter 1, equation 1.1), or the principle that a variable proportion of the pore space occupied by the recoverable hydrocarbon reserves will be available for CO_2 storage (i.e. due to gas compressibility at reservoir conditions, such as the methods of Bachu et al. (2007), Holloway et al. (2006) and Tseng et al. (2012); Chapter 1, equations 1.2, 1.3 and 1.4, respectively). Estimates of the effective storage capacity rely on determining a number of coefficients that take account of, for example, mobility and buoyancy of CO_2 (Bachu et al., 2007) to reduce the theoretical storage capacity (for example, the method of Bachu et al. (2007); Chapter 1, equation 1.5). An alternative approach is to use material balance methods that take account of residual hydrocarbon and injected CO_2 mixtures within the reservoir (for example, the method of Tseng et al. (2012); Chapter 1, equations 1.6 and 1.7). All of these methods rely on accurate determination of CO_2 density, whilst material balance-based methods require accurate determination of the gas compressibility factor (Z-factor). In turn, CO_2 densities, gas formation volume factor (B_g) and/or Z-factors are governed by the chosen equation of state

(see section 3.6 of Chapter 3). The aims of this chapter are: (a) to investigate the effects that geometric (e.g. gross rock volume), petrophysical (e.g. porosity, water saturation, recovery factor, net to gross) and thermodynamic (e.g. equation of state) properties have on estimations of theoretical and effective CO_2 storage capacity (Table 4.1); and (b) to investigate the variability of the resulting storage capacity estimations that arises due to the different approaches outlined above.

We use a four-way dip-closed, depletion drive gas reservoir in the Southern North Sea – the Lower Bunter Sandstone reservoir of the Hewett Gas Field (Figure 4.1) – as a case study, which provides the starting point for subsequent chapters that investigate reservoirs characterized by more complex structures and/or depletion through water drive. In depletion drive reservoirs, the lack of aquifer influx means that any fluid added or removed can be accounted for either through injection or production, as will be demonstrated by the material balance plots below (section 4.4.3.1). An additional advantage of this reservoir is the abundance of data (e.g. 3D seismic reflection data; wireline logs; petrophysical data; production curves) and its well-understood volumetric production history (Hagoort, 1988) (Figure 4.2). Furthermore, published theoretical storage capacity estimates for the entire Hewett Gas Field (including the Upper and Lower Bunter and Zechsteinkalk reservoirs) display significant variation (see below).

This study will constrain the input parameters to both the theoretical and effective storage capacity estimates. In particular, explicit use of different equations of state to model gas compressibility factors of natural gas and CO_2, and CO_2 density has not previously been applied to the Hewett Lower Bunter Sandstone reservoir with respect to carbon storage. Moreover, this study will be the first of its kind for effective CO_2 storage capacity estimation within the Hewett Lower Bunter Sandstone reservoir.

ABBREVIATION	DEFINITION	APPROACH TO BETTER CONSTRAIN INPUT PARAMETER TO CO_2 STORAGE CAPACITY EQUATIONS	CO_2 STORAGE CAPACITY EQUATIONS THAT WILL BENEFIT
A	Reservoir/play area	Static 3D structural modelling	1.1
B_g	Gas formation volume factor or gas expansion factor. Is equal to the produced gas volume at reservoir conditions divided by the produced gas volume at standard conditions	Investigate with a variety of equations of state	1.3; 1.4
B_{gas}	Gas formation volume factor in the reservoir at the end of production	Investigate with a variety of equations of state	1.4
B_{iCO2}	CO_2 formation volume factor at initial reservoir conditions	Investigate with a variety of equations of state	1.4
F_{IG}	Fraction of injected gas	Historical field records; limited on data, unable to constrain further	1.2
G_{phc}	Volume of produced hydrocarbons	Standard value; unable to constrain further	1.4; 1.7
h	Reservoir height/thickness	Static 3D structural modelling, analysis of well data	1.1
OGIP or G_{ihc}	Original gas in place, or, volume of initial hydrocarbons	Historical field records, extrapolation of material balance (P/z) plots	1.2; 1.7
P_{ihc}	Pressure at initial reservoir conditions	Standard value; unable to constrain further	1.7
P_r	Reservoir pressure	Historical pressure data; unable to constrain further	1.2; 1.7
$P_{reshc/CO2}$	Pressure of residual hydrocarbon/carbon dioxide mix	Investigate with a variety of equations of state	1.7
P_s	Surface pressure	Standard value; unable to constrain further	1.2; 1.7
R_f	Recovery factor	Material balance methods to better constrain OGIP and up to date production data	1.1; 1.2

ABBREVIATION	DEFINITION	APPROACH TO BETTER CONSTRAIN INPUT PARAMETER TO CO_2 STORAGE CAPACITY EQUATIONS	CO_2 STORAGE CAPACITY EQUATIONS THAT WILL BENEFIT
S_w	Water Saturation	Historical field records; limited on data, unable to constrain further	1.1
T_r	Reservoir temperature	Historical field records; limited on data, unable to constrain further	1.2; 1.7
T_s	Surface temperature	Standard value; unable to constrain further	1.2; 1.7
V_{GAS} or URR	Volume of ultimate recoverable reserves	Material balance methods to better constrain OGIP	1.3
V_{iw}	Volume of injected water	Historical field records; limited on data, unable to constrain further	1.1
V_{pw}	Volume of produced water	Historical field records; limited on data, unable to constrain further	1.1
z_{gas}	Gas deviation factor in the reservoir at the end of production	Investigate with a variety of equations of state	1.4
z_{iCO2}	CO_2 gas deviation factor at initial reservoir conditions	Investigate with a variety of equations of state	1.4
z_{ihc}	Gas deviation factor at initial reservoir conditions	Investigate with a variety of equations of state	1.7
Z_r	Reservoir compressibility	Investigate with a variety of equations of state	1.2; 1.4; 1.7
$z_{reshc/CO2}$	Gas deviation factor of residual hydrocarbon/carbon dioxide mix	Investigate with a variety of equations of state	1.7
Z_s	Surface compressibility	Standard value; unable to constrain further	1.2; 1.7
ρ_{CO2r}	Density of carbon dioxide at reservoir conditions	Investigate with a variety of equations of state	1.1; 1.2; 1.3; 1.4; 1.6
Φ	Reservoir porosity	Analysis of core data and use of historical field records; Monte Carlo Simulation	1.1

Table 4.1 Approaches to be taken to improve the accuracy of input parameters to storage capacity equations

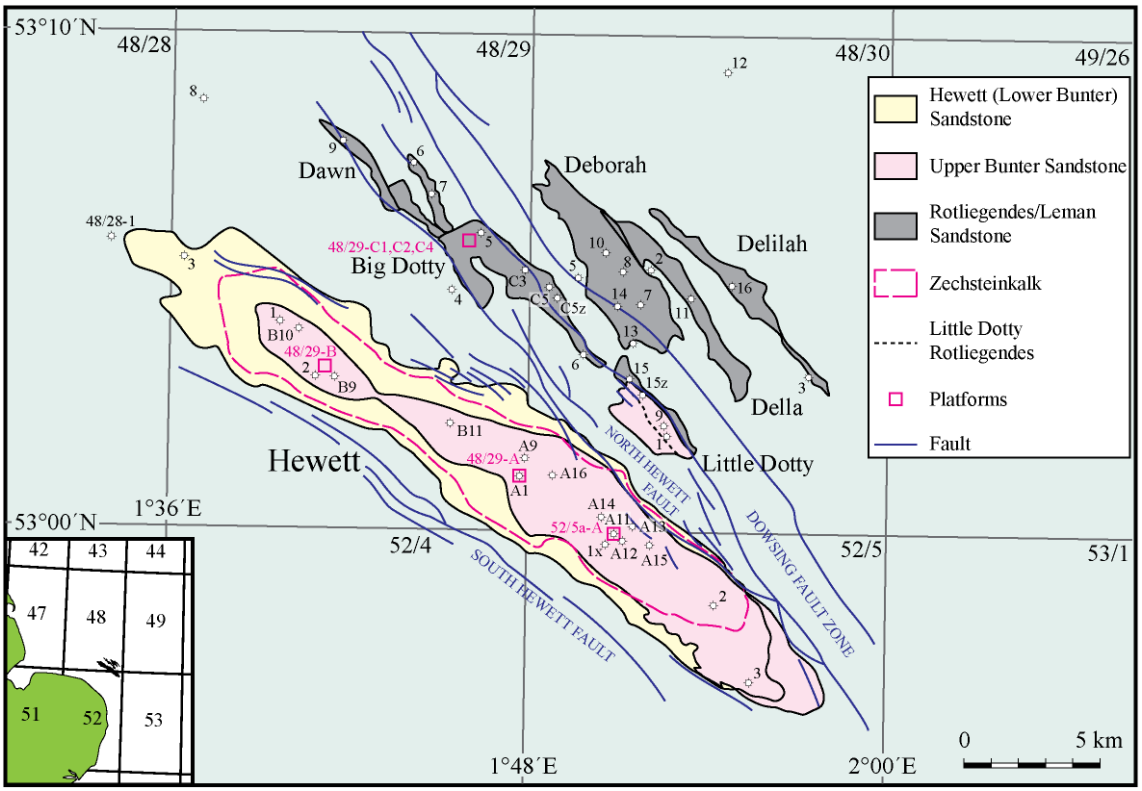

Figure 4.1 Location and structure of the Hewett Unit, UK Southern North Sea. Only major faults and their trends are displayed. The original gas-water contacts of the reservoir play areas are shown. Wells and platforms are displayed for reference. Adapted from Cooke-Yarborough and Smith (2003).

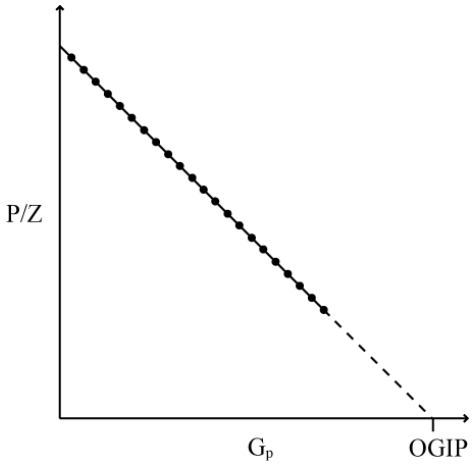

Figure 4.2 Material balance schematic plot (P/Z) for a volumetric reservoir. The original gas in place (OGIP) can be estimated by linear extrapolation of the trend observed on the P/Z plot, down to the x-axis (P/Z=0). Accuracy of the OGIP increases as depletion progresses. Its accuracy will also directly affect the estimated recovery factor, R_f, as $R_f = G_p/OGIP$. Adapted from Dake (1978) and Hagoort (1988).

4.2. PUBLISHED CO_2 STORAGE CAPACITY ESTIMATES

Previously published theoretical storage capacity estimates for the entire Hewett Gas Field (comprising both the Hewett Upper and Lower Bunter reservoirs and the Zechsteinkalk reservoir) have varied by a factor of 3.7 (Bentham, 2006; Brook et al., 2003; E.ON, 2009; Holloway, 1996; Holloway et al., 2006) (see Table 4.2) which equates to a difference in storage capacity of 294.26 Mt CO_2, or a difference in the storage lifetime of 30.5 years at the proposed post-demonstrator injection rate of 26,400 tonnes/day (BakerRDS, 2011b).

In contrast to the Hewett Lower Bunter reservoir, the Hewett Upper Bunter reservoir has experienced a moderate water drive (Chapter 5). Different approaches have been used to account for water drive and depletion drive reservoirs. For example, the Gestco study of Brook et al. (2003) did not account for possible post-production water influx in their theoretical CO_2 storage capacity calculations. A later study by Bentham (2006) attempted to address this issue by determining the reservoir drive mechanism within each *field* – not each reservoir. In depletion drive gas fields, it was assumed that 90% of the available pore space could be occupied by CO_2; in water drive gas fields, 65%; and in gas fields with both depletion and water drive production mechanisms (such as Hewett), 77.5%. Therefore, the theoretical storage capacities predicted by Brook et al. (2003) were reduced by these percentages, depending on the reservoir drive mechanism. This approach can be applied quickly to a group of reservoirs, but as will be demonstrated throughout this and the following chapters, do not yield a particularly accurate representation of theoretical storage capacity.

There are few studies that have estimated the theoretical storage capacity for solely the Hewett Lower Bunter Sandstone reservoir. However, published figures vary by a factor of 1.3 (E.ON, 2009; Grewcock, 2009; Holloway et al., 2006), equating to a storage capacity difference of 63 Mt, or a storage lifetime difference of 6.5 years at the proposed post-demonstrator injection pressure.

AUTHOR	TITLE	THEORETICAL/EFFECTIVE CO_2 STORAGE CAPACITY ESTIMATION?	EQUATION	CALCULATED CO_2 STORAGE CAPACITY (Mt)	WHICH RESERVOIRS?
Bentham, 2006	Tyndall Centre for Climate Change Research: An Assessment of Carbon Sequestration Potential in the UK - Southern North Sea Case Study	Theoretical	$V_{CO2} = \left(V_{GAS}(stp)/B_g\right).\rho_{CO2}$	108.24	Entire Hewett Gas Field
Brook et al., 2003	BGS: GESTCO Case Study 2a-1: Storage Potential of the Bunter Sandstone in the UK sector of the Southern North Sea and the adjacent onshore area of Eastern England	Theoretical	$V_{CO2}(tonnes) = (Ah\phi.\rho_{CO2}).0.4$	139.66	Entire Hewett Gas Field
Grewcock, 2009	CO2 Storage - An Oil Industry Perspective	Theoretical	Unknown	300.00	Hewett Lower Bunter Sandstone Reservoir
Holloway et al., 2006	Industrial Carbon Dioxide Emissions and Carbon Dioxide Storage Potential in the UK	Theoretical	$M_{CO2} = \left(V_{GAS}(stp)/B_g\right).\rho_{CO2}$	383.00	Entire Hewett Gas Field
E.ON, 2009	Capturing Carbon, Tackling Climate Change: A Vision for a CCS Cluster in the South East	Theoretical	$M_{CO2} = \left(V_{GAS}(stp)/B_g\right).\rho_{CO2}$	383.00	Entire Hewett Gas Field
Holloway, 1996	Final report of the Joule II Project No CT92-0031: The Underground Disposal of Carbon Dioxide	Theoretical	$M_{CO2} = \left(V_{GAS}(stp)/B_g\right).\rho_{CO2}$	402.50	Entire Hewett Gas Field

Table 4.2 Overview of Hewett Gas Field published theoretical CO_2 storage capacities and methods used

4.3. THE ORIGINAL PETROLEUM PLAY

The regional geological setting of the Hewett Gas Field as a whole has been previously summarised in Chapter 2. The major properties that have previously made the Hewett Lower Bunter sandstone reservoir a successful petroleum play are now summarised within Table 4.3 and the following sections 4.3.1 to 4.3.4. It is widely accepted that successful CO_2 storage sites share many of the same geological characteristics as successful hydrocarbon plays including (1) sufficient CO_2 storage capacity and injectivity capabilities, (2) a cap rock or confining unit with adequate sealing integrity, and (3) should be situated within a stable tectonic environment (IPCC, 2005). This assumption is particularly appropriate to CO_2 storage in depleted gas reservoirs, such as the Hewett Lower Bunter Sandstone reservoir. The petroleum play elements are therefore summarised below, before a more detailed analysis of the geometric and petrophysical properties of this reservoir.

4.3.1. THE HEWETT LOWER BUNTER SANDSTONE RESERVOIR

The Hewett Lower Bunter Sandstone is a thick sandstone unit within the Bröckelshiefer Member (cf. Figure 4.3 and Figure 4.4). The lithology of the sandstone has previously been described in detail in Chapter 2. It is only developed within the southern part of the basin, adjacent to the London-Brabant Platform ((Johnson et al., 1994), see Figure 4.3). The Hewett Lower Bunter Sandstone reservoir is considered to be a good quality sandstone with high porosity and permeability values (as will be later described in detail in section 4.4.2.1.).

4.3.2. TRAP

The Hewett Lower Bunter trap is considered to be a four-way dip-closed structural trap according to the Hewett Field records. This structure will be investigated further within the 3-D seismic interpretation and structural modelling of the datasets provided.

OVERBURDEN STRATA	
Geological Formation	Cromer Knoll Group
Depositional Environment	Marine
Depositional Facies	Shallow marine
Age	Lower Cretaceous
Geological Formation	Lias Group
Depositional Environment	Marine
Depositional Facies	Marine shelf
Age	Lower Jurassic
Geological Formation	Haisborough Group
Depositional Environment	Terrestrial and transitional
Depositional Facies	Sabkha, restricted marine and flood plain
Age	Triassic
Geological Formation	Bacton Group
Depositional Environment	Terrestrial
Depositional Facies	Alluvial fan and overbank deposits
Age	Triassic
DIRECT CAP ROCK	
Geological Formation	Bunter Shale Formation, Bacton Group
Depositional Environment	Terrestrial
Depositional Facies	Lacustrine, flood plain
Age	Lower Triassic, Scythian
Average Thickness (m)	300
TRAP	
Structure	Structural anticline, four-way dip closure
Depth to crest (m)	1227.1
Initial gas column (m)	118.6
Initial gas-water contact (m)	1345.7
RESERVOIR	
Geological Formation	Lower Bunter (Hewett) Sandstone
Depositional Environment	Alluvial
Age	Lower Triassic, Scythian
Lateral extent/play area (m^2)	140,000,000
Average Thickness (m)	41.15
Net/gross ratio	0.88
Average Porosity (%)	23
Average Permeability (mD)	1000
Average hydrocarbon saturation (%)	80
Irreducible water saturation (%)	20
Isolated or underlain by aquifer?	Isolated
PETROLEUM/FIELD CHARACTERISTICS	
Formation volume factor (stand. cond./res. cond.)	140
Original gas in place (m^3)	5.95E+10
Initial pressure (MPa)	13.686
Reservoir temperature (°C)	52.2
Recovery factor	0.978

Table 4.3 Hewett Lower Bunter Sandstone Reservoir properties. Adapted from Cooke-Yarborough and Smith (2003).

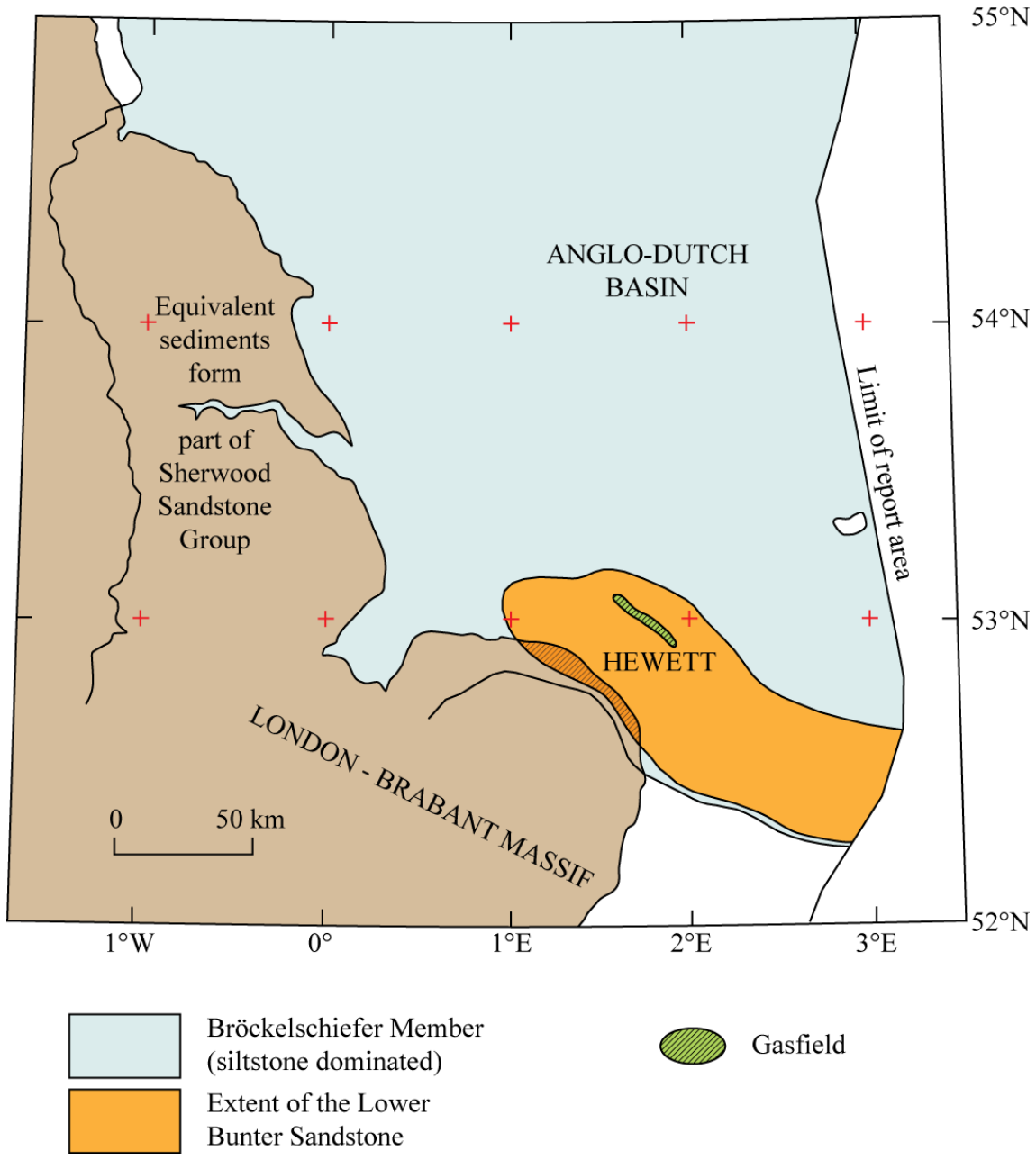

Figure 4.3 Distribution of the Bröckelshiefer Member and the Hewett Lower Bunter Sandstone Formation. Adapted from Cameron et al. (1992).

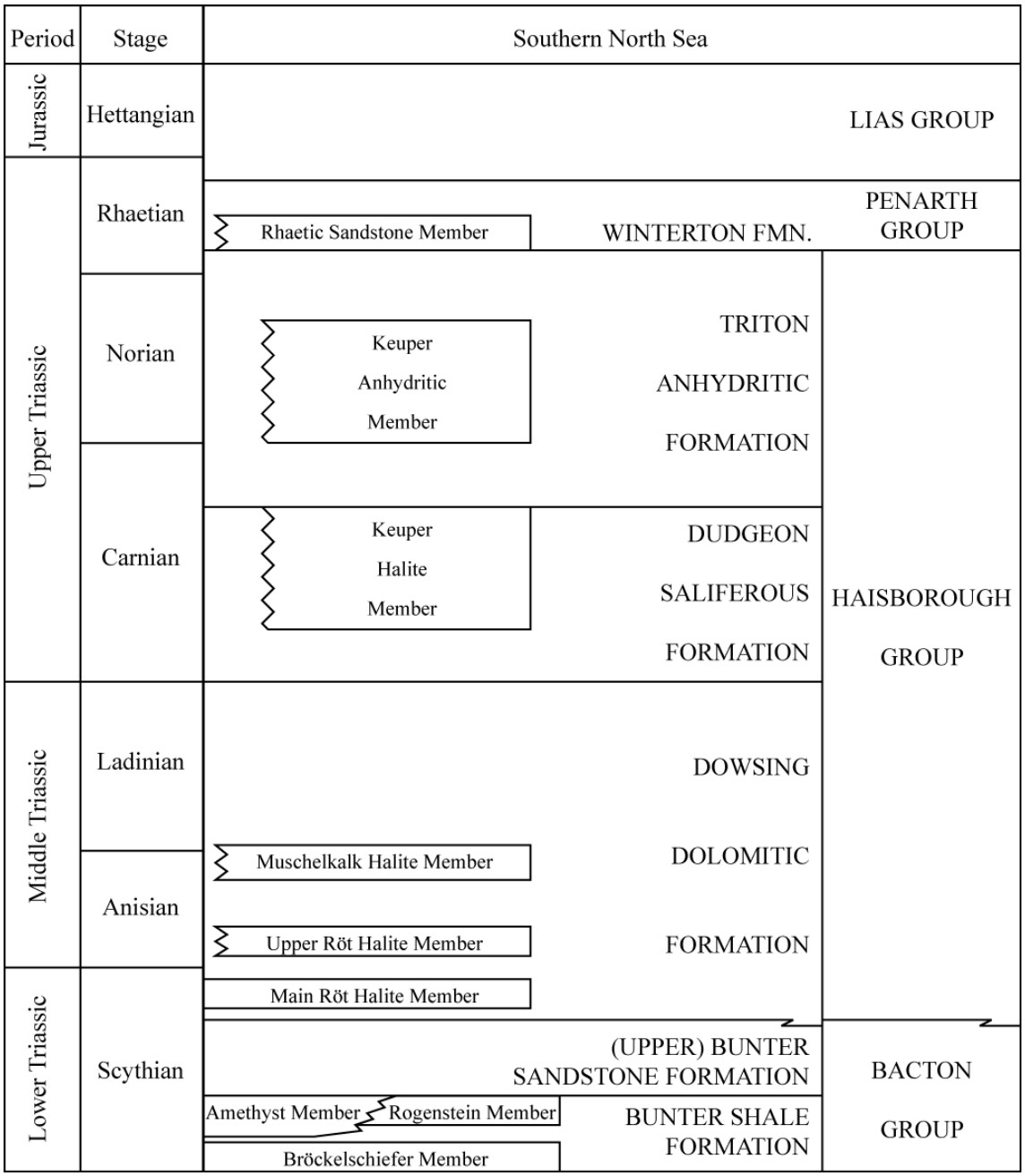

Figure 4.4 Southern North Sea lithostratigraphy. The Lower Bunter Sandstone occurs within the Bröckelshiefer Member of the Bunter Shale Formation. Adapted from Cameron et al. (1992).

4.3.3. DIRECT CAP ROCK

The Bunter Shale Formation of the Bacton Group forms the direct cap rock to the Hewett Lower Bunter Sandstone reservoir. The lithology of the Bunter Shale Formation has previously been described in detail in Chapter 2. Within the Hewett Unit itself, and regionally within the Southern North Sea, the Bunter Shale Formation maintains an almost constant thickness (averaging at 230 m within the Hewett Gas Field). Unfortunately, cap rock laboratory data does not exist for the Bunter Shale Formation. Instead, analogue studies have been used to assess cap rock integrity (BakerRDS, 2010). In this study, the best candidate for an analogue to Hewett was considered to be Block P and Q offshore Netherlands where the Solling and Rot cap rocks are composed of thin shale interbeds and inter-laminations with very fine grained sandstone. A variety of capillary entry pressures were observed ranging between 5.52-137.9 MPa air-mercury at laboratory conditions in samples with porosities of between 1.3-4.2 %. In Hewett, this would support a gas column height of between 92-2305 m – substantial since the reservoir thickness is 41.14 m.

The Bunter Shale Formation has provided a proven reliable hydrocarbon seal over geological time scales with no evidence of gas having entered or migrated through the cap rock. Evidence for this comes from the 3-D seismic dataset where there have been no observations of structures such as gas chimneys penetrating through the cap rock. Therefore, it is likely that at initial reservoir conditions the buoyancy pressure of the hydrocarbons did not exceed the minimum capillary entry pressure of the Bunter Shale Formation cap rock (BakerRDS, 2010). Due to lack of laboratory analysis on the Bunter Shale Formation it must be considered that the minimum capillary entry pressure of the cap rock is that of the buoyancy pressure of the hydrocarbons at initial reservoir conditions, although this is unlikely and the minimum capillary entry pressure is expected to be higher. Under this scenario, the maximum CO_2 column height the Hewett Lower Bunter Sandstone reservoir could support would be 24.5 m, approximately 50 % of the original hydrocarbon column height (BakerRDS, 2010). However, a study by Naylor et al. (2011) indicated the CO_2 columns could be one to two times that of the original gas column, as

supercritical CO_2 is much more dense than methane and therefore has a much lower buoyancy pressure.

4.3.4. OVERBURDEN STRATA

The Hewett Upper Bunter Sandstone Reservoir of the Bacton Group directly overlies the Bunter Shale Formation. Above this reservoir is a direct cap rock to the Hewett Upper Bunter Sandstone reservoir: the Haisborough Group. The Haisborough Group has a thickness of approximately 420 m within the Hewett Gas Field and is composed of three formations: the Triton Anhydritic Formation, the Dudgeon Saliferous Formation and the Dowsing Dolomitic Formation. These have previously been described in detail in Chapter 2.

The Haisborough Group is overlain by a thin (ca. 30 m) claystone and sandstone unit of the Winterton Formation. This is the only unit within the overburden which is not considered to be a sealing unit. The remaining ~390 m of overburden consists of more claystone units which provide more sealing units (Cooke-Yarborough and Smith, 2003).

4.4. GEOMETRIC, PETROPHYSICAL AND PRODUCTION CHARACTERISTICS

4.4.1. 3-D SEISMIC INTERPRETATION RESULTS

Well-calibrated 3-D seismic data was acquired by Tullow Oil and made available to Durham University, as previously described in Chapter 3. Seismic data coverage includes the entire Hewett Unit of the UK Southern North Sea (comprising the Hewett Gas Field and six surrounding "D" fields: Little Dotty, Big Dotty, Dawn, Deborah, Delilah and Della – see Figure 4.1). The dataset was interpreted in the time domain, and has processing in the form of post stack time migration applied to it – for further details, see Chapter 3.

The 3-D seismic dataset of the Hewett Unit was interpreted using Landmark SeisWorks for horizon interpretation, and TrapTester 6.0 for 3-D structural

modelling. Interpretation has revealed the four-way dip-closed anticlinal structure of the Hewett Lower Bunter reservoir. A cross-section of the 3-D seismic data within TrapTester is shown in Figure 4.5. The cross-section cuts through the Hewett Gas Field anticline in a NE-SW orientation at the widest part of the reservoir.

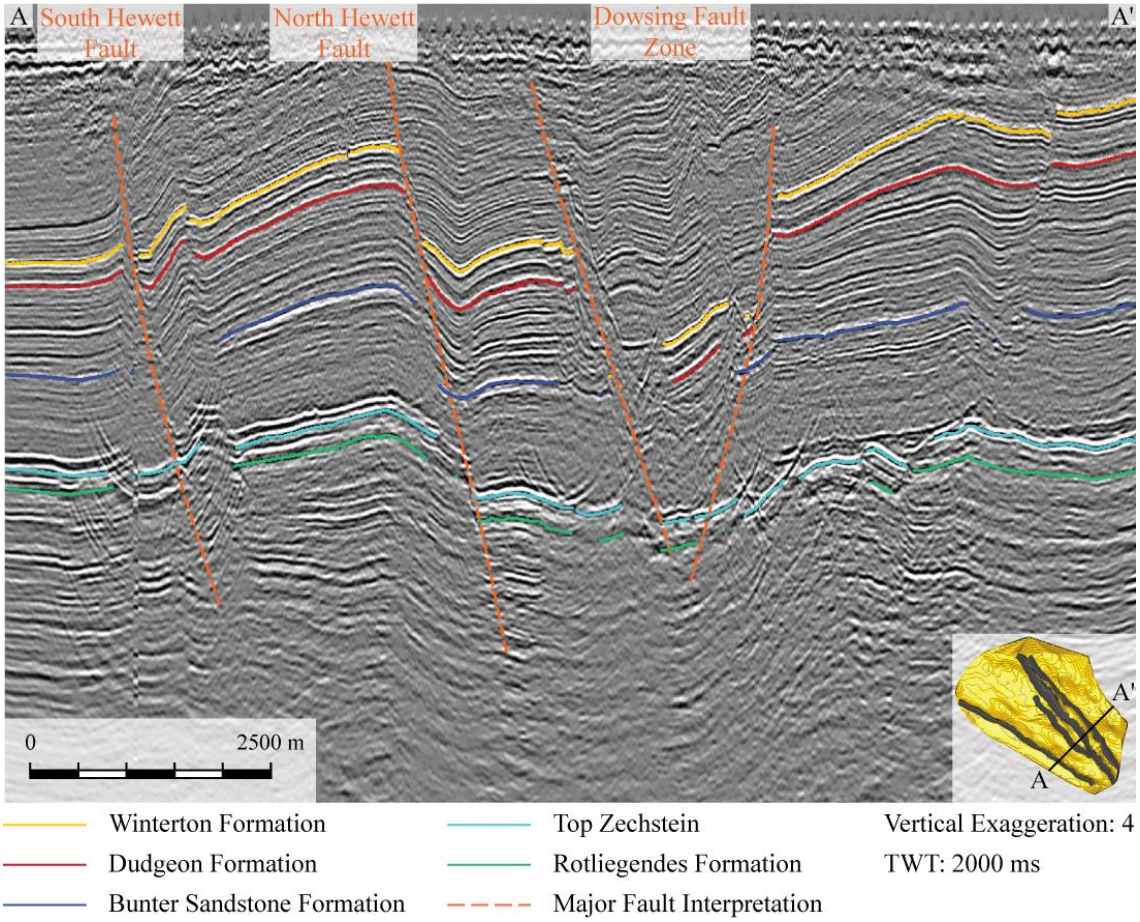

Figure 4.5 Cross-section through the structural anticlines of the Hewett Gas Field and surrounding "D" fields. The Hewett Field anticline is visible on section between the South Hewett Fault and North Hewett Fault. The Little Dotty Field structure is visible between the North Hewett Fault and the eastern bounding fault of the Dowsing Fault Zone. The Big Dotty and Dawn Fields lie within the same situation further north. The Della, Deborah and Delilah Fields are situated to the west of the Dowsing Fault Zone, but lie further north of the cross-section.

Unfortunately it was not possible to interpret the top surface of the Lower Bunter Sandstone within SeisWorks: the unit is located between the top Upper Bunter Sandstone Formation horizon and the Top Zechstein horizon and is affected

by poor seismic resolution. Instead, a horizon surface was automatically constructed within TrapTester. Based on average well data from IHS, the Lower Bunter Sandstone horizon was scaled between the mapped Upper Bunter Sandstone and Top Zechstein, at a point 92.2% down from the top of the interval, and can be seen in Figure 4.6. Fault polygons of the modelled horizon can be displayed on fault surfaces, alongside the fault polygons of mapped surfaces. An example of this is shown on a major fault within the Hewett Unit (see Figure 4.7).

A horizon surface was also created for the overlying Bunter Shale Formation (direct cap rock to the Lower Bunter Sandstone). The horizon was scaled to occur 42.7% below the mapped Upper Bunter Sandstone Formation horizon based on well data from IHS.

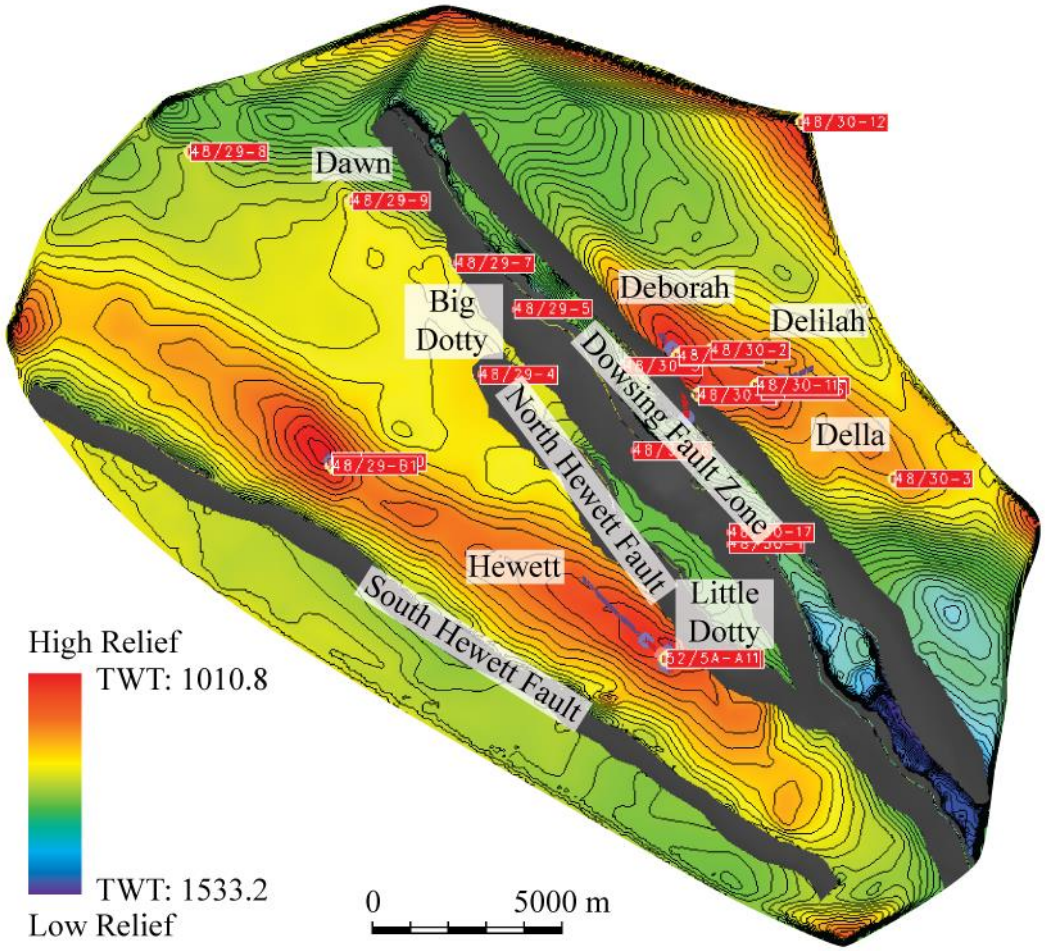

Figure 4.6 Automated time structure surface of the Lower Bunter Sandstone Formation within the Hewett Unit. The field locations and major faults are displayed.

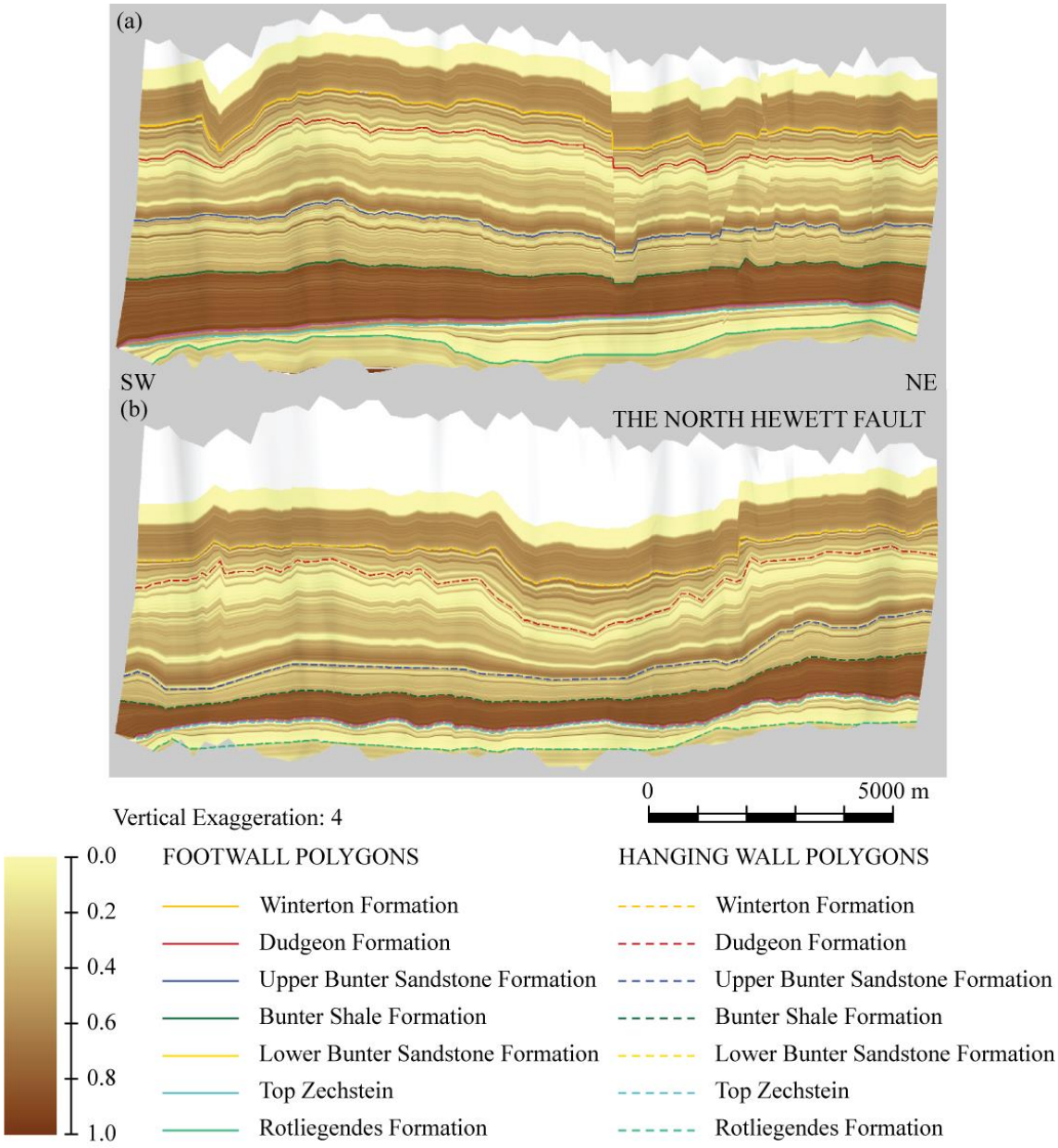

Figure 4.7 Modelled isochore surfaces on the North Hewett Fault, Hewett Unit. (a) Attribute displayed along the fault is the Vshale within the footwall. Both seismic and marker footwall polygons are displayed, (b) Attribute displayed along the fault is the Vshale within the hanging wall. Both seismic and marker footwall polygons are displayed. Mapped seismic polygons are those of the Winterton Formation, Dudgeon Formation, Upper Bunter Sandstone Formation, Top Zechstein and Rotliegendes Formation. Isochore polygons are those of the Bunter Shale Formation and the Lower Bunter Sandstone Formation.

The computed horizon of the Top Lower Bunter Sandstone Formation (Figure 4.6) reveal there are four major faults that cut through the stratigraphy, from west to east: the South Hewett Fault, North Hewett Fault, and the two major faults bounding the Dowsing Fault Zone. These are extensive basement-cutting faults that penetrate up through much of the Triassic and Jurassic stratigraphy but do not reach the surface. They have developed from ancient Hercynian faults as they still have the typical NW-SE trend preserved. They are listric faults which once formed as normal faults in an extensional structural regime, but have undergone inversion when regional transpression took place (Cooke-Yarborough and Smith, 2003).

As can be seen from the time structure maps produced within Landmark SeisWorks (see Appendix B), due to the vast amount of faulting, coupled with inversion that has taken place within the region, there were difficulties in horizon interpretation due to poor seismic resolution as indicated by the gaps present within the horizons. Interpretation was improved within TrapTester 6.0 where it is possible to model horizon polygons directly onto fault planes where there is difficulty in automated interpretation. This allows horizons to be interpreted directly up to the fault planes, and makes for a robust, "watertight" 3-D structural model.

Vertical seal is fairly well established from the stratigraphic column (Figure 4.4) and well data (including composite logs). From Figure 4.6 and Figure 4.8 it is possible to see the anticlinal structure of the Hewett Field. It is very obvious from the model that the reservoir is at least three-way dip closed. The only dubious area is on the central eastern flank of the reservoir where the North Hewett Field is in close proximity. On closer inspection of the structural model it is possible to see that the anticlinal structure closes the field before the North Hewett Fault cuts through the strata (see Figure 4.8). This geometry may be due to normal drag from the North Hewett Fault. Ultimately, the Hewett Lower Bunter Sandstone reservoir can be shown to be a four-way dip closed anticlinal structure.

As previously stated, within Table 4.1, the purpose of the structural modelling of the Hewett Lower Bunter Sandstone reservoir was not only to assess

the trapping mechanism of the structure, but also to estimate the reservoir play area and reservoir height.

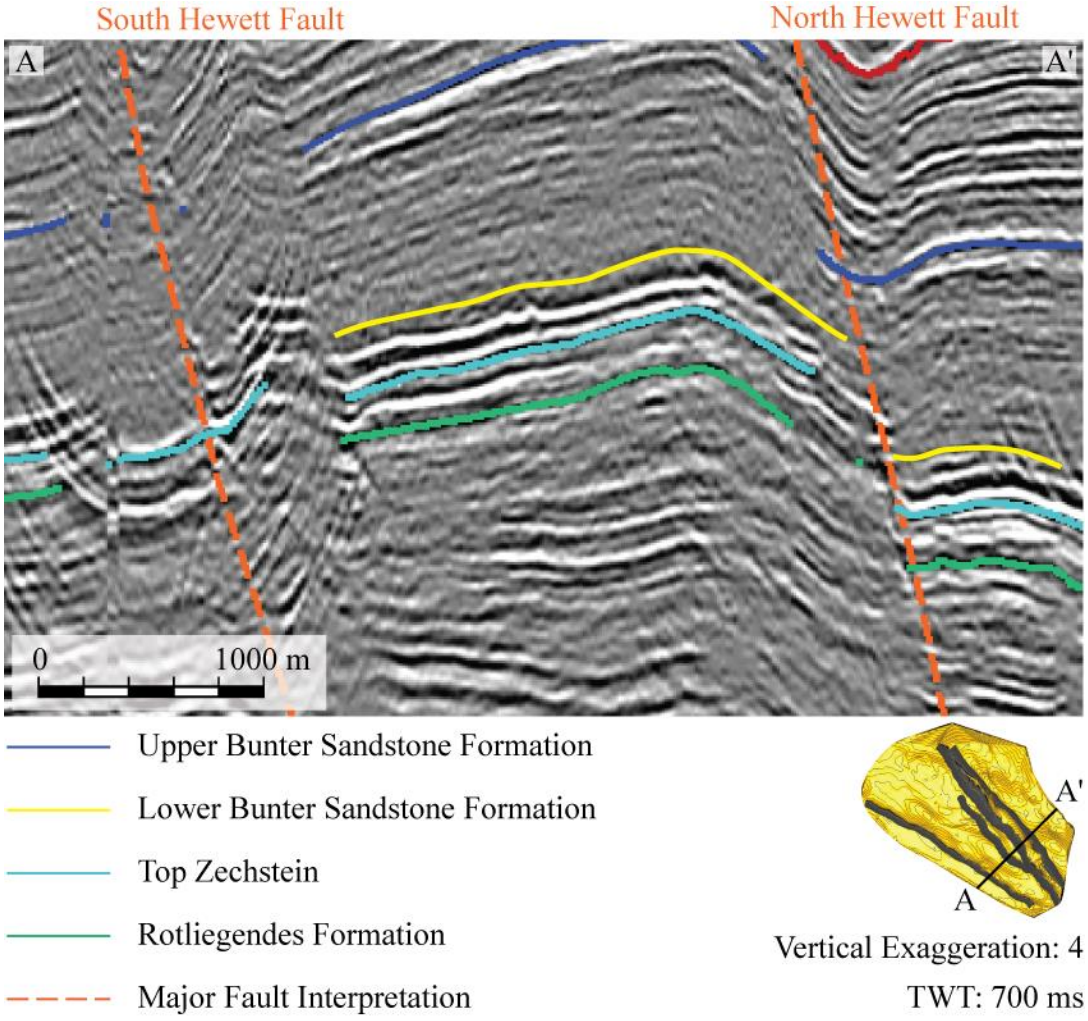

Figure 4.8 Anticlinal structure of the Hewett Lower Bunter Sandstone reservoir in the vicinity of the North Hewett Fault on the central eastern flank of the reservoir.

The reservoir play area was estimated within TrapTester by picking the gas water contact (at 1060 ms) on the automated Lower Bunter Sandstone Formation marker horizon. The play area was estimated to be 74,888,440 m^2.

The reservoir height was estimated using the Hewett well data, made available to Durham University by ENI and IHS. Few wells had stratigraphic tops information (i.e. the depth at which the top of a lithology is found to occur within a well). The top and base of the Lower Bunter Sandstone Formation in each well was found, results are shown in Table 4.4.

	WELL							
	048/29-01	048/29-B01	048/29-02	048/29-A01	052/05a-01	052/05a-02	052/05a-03	AVERAGE
Depth of Top of Hewett Lower Bunter Sandstone Formation (m)	1274	1227	1252	1257	1250	1298	1341	1271
Depth of Base of Hewett Lower Bunter Sandstone Formation (m)	1296	1287	1309	1321	1279	1344	1372	1315
Thickness of the Hewett Lower Bunter Sandstone Formation (m)	22	60	57	64	29	46	31	44

Table 4.4 Depth to the top and base of the Lower Bunter Sandstone Formation from wells within the Hewett Field.

4.4.2. PETROPHYSICAL CHARACTERISTICS

4.4.2.1. POROSITY AND PERMEABILITY DATA

The following graphs and boxplots (Figure 4.9 to Figure 4.13) represent the plotted porosity and permeability dataset of the Hewett Lower Bunter Sandstone reservoir made available to Durham University by IHS. The graph (Figure 4.9) shows a positive linear correlation with increasing porosity and permeability values, with an r^2 value of 0.3198. Through application of the Pearson correlation it is possible to test whether a significant correlation exists in the population (Gravetter and Wallnau, 1999). The critical r value for a sample size of 717 and a significance level of 0.0005 for a one tailed probability (i.e. it is known the direction of correlation is positive) is 0.104. Therefore, the calculated r value for the porosity and permeability correlation of 0.565 exceeds the critical value and can be considered as significant. Regionally the Lower Bunter Sandstone Formation becomes interbedded with the base of the Bunter Shale Formation within its upper limits. However, within the Hewett Gas Field the sand is relatively clean, hence the good reservoir properties (Cameron et al., 1992).

Generally, an average value for porosity would be input into CO_2 storage capacity estimates. However, it is important to note that sandstone reservoirs show a degree of heterogeneity, which is apparent in the porosity data for the Hewett Field. These data can be described in several ways. A boxplot of the data can illustrate where the main body (50%) of data lies through consideration of quartiles, and to highlight any outliers within the data population. Furthermore, Monte Carlo simulation allows consideration of the entire data population to evaluate whether it originated from a specific probability distribution (Stephens, 1974).

The boxplot of the porosity data for the Hewett Lower Bunter Sandstone reservoir is shown in Figure 4.10. The main body (50%) of data ranges between 11.75% (Q1) and 24.00% (Q3) porosity, and the median value (Q2) is 18.07%. Outliers are any value that lie more than 1.5 times the length of the box from either end of the box, i.e. if a data point is below $Q_1 - 1.5 \times \text{IQR}$ or above $Q_3 + 1.5 \times \text{IQR}$ it lies too far away from the central values to be reasonable. The IQR is the

interquartile range and is equal to $Q_3 - Q_1$. For the Hewett Lower Bunter Sandstone reservoir porosity dataset outliers would be any values below -6.63% or above 42.38%. As can be seen from the boxplot in Figure 4.10 these data range between 1.80% and 33.10% therefore there are no outliers. Another important point to note is that it is not possible to have a negative value for porosity.

As previously stated, Monte Carlo simulation can also be used to analyse the data population. The Anderson-Darling (A-D) test assesses the goodness-of-fit of the dataset to a specific probability distribution (Stephens, 1974). The closer the A-D value is to 1, the better the fit of a data to a probability distribution. Wells with core analysis (porosity and permeability) data include, 048/30-01, 048/30-07, 048/30-13, 048/29-03, 048/29-08, 052/05-01 and 052/05-03 (see Figure 4.1 for locations).

The resulting best-fit distribution is a Weibull distribution, shown in Figure 4.11. The resulting Anderson-Darling value for the dataset was 3.876, therefore the fit of the data to the probability distribution is poor. The A-D P-value tests for normality – if the P-value is <0.05 then the result is not normal; if the P-value is >0.05 then the result is normal and the data follow a specified distribution. In this case the P-value for the Weibull distribution is 0.00 therefore these data do not follow a specified distribution. However, compared to the other available distributions, the Weibull is the best fit of the porosity data.

Only porosity data are necessary for CO_2 storage capacity estimation (Chapter 1, equations 1.1 to 1.7). However, permeability is still an important rock property to analyse during geological characterisation as it illustrates the degree of pore connectivity within a reservoir. The boxplot of the permeability data for the Hewett Lower Bunter Sandstone reservoir is shown in Figure 4.12. The main body (50%) of data ranges between 14.53 mD (Q1) and 1043.36 mD (Q3), with a median value (Q2) of 195.48 mD. Outliers within the Hewett Lower Bunter Sandstone reservoir permeability dataset are any values below -1528.72 mD or above 2586.61 mD. As such, 86 outliers were found to be present in the permeability dataset on the right hand side of the data range in Figure 4.12. It is possible to see that the 86 outliers are spread over a wide range of permeability, indicated by the black boxes plotted outside of the boxplot on Figure 4.12. Once again it is important to note

that it is not possible to have a negative value for permeability, therefore the whisker on the left hand side of the boxplot is limited to 0.00 mD.

Average (mean) permeability values of the Hewett Lower Bunter Sandstone reservoir are 958.10 mD, based upon data from the same wells with porosity information. The logarithmic histogram of permeability (Figure 4.13) shows there to be a high number of instances as permeability increases, however, as has been demonstrated through use of the boxplot in Figure 4.12, the higher values are spread over a vast range of permeability, up to 9930.00 mD.

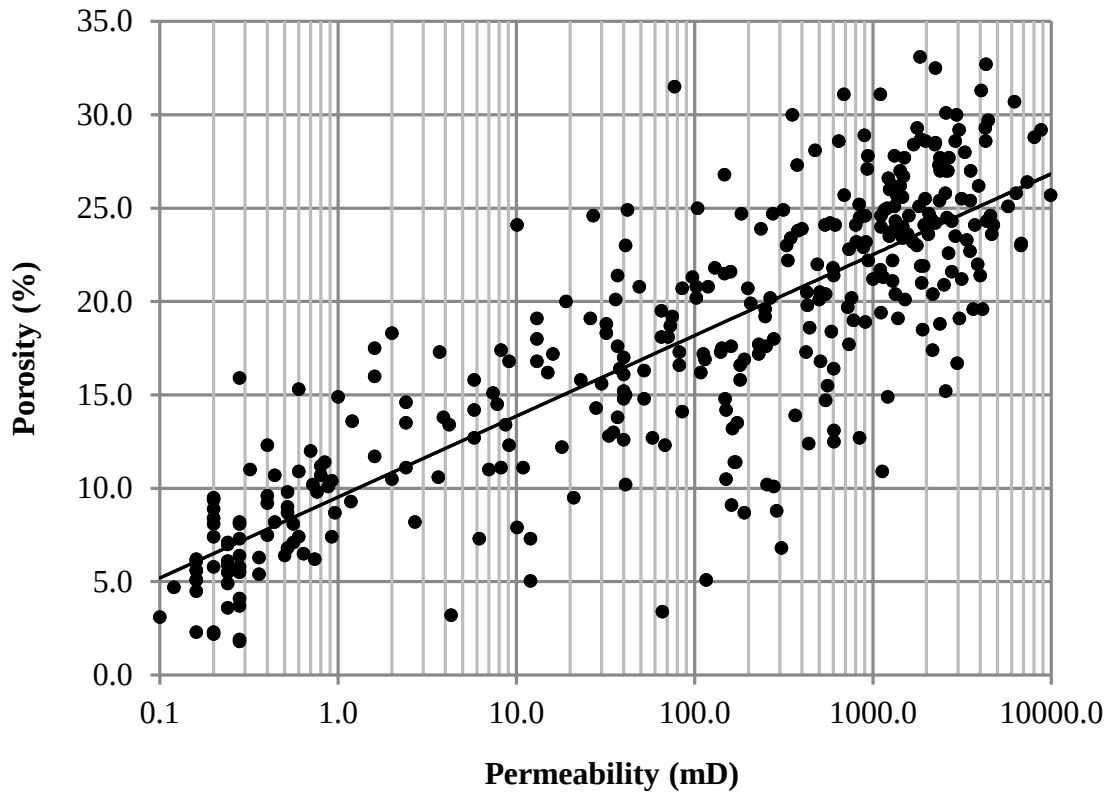

Figure 4.9 Hewett Lower Bunter Sandstone Reservoir Quality

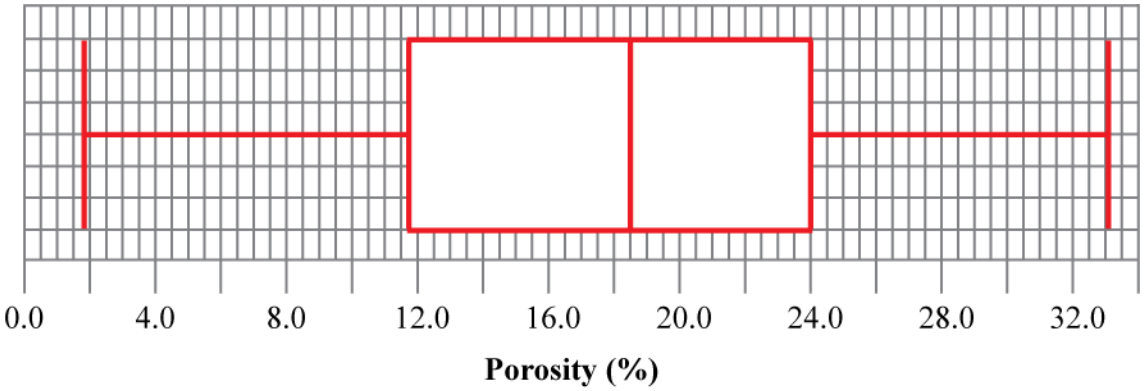

Figure 4.10 Hewett Lower Bunter Sandstone Reservoir boxplot for porosity. Boxplots are used to highlight the quartiles (the three points in a ranked dataset that divide the data into four equal groups), including the median (Q2), to present a spread of data. The "box" is drawn from the lower quartile (Q1) to the upper quartile (Q3) with the median drawn within the box. The box represents the inter-quartile range (Q3-Q1) and encompasses the middle half (50%) of the data. The porosity data plotted here lie within 1.5 times the IQR either side of the upper and lower quartiles, therefore the "whiskers" on the boxplot are drawn to the highest and lowest values within the dataset. Boxplots are a measure of statistical dispersion and are the most significant basic robust measure of scale.

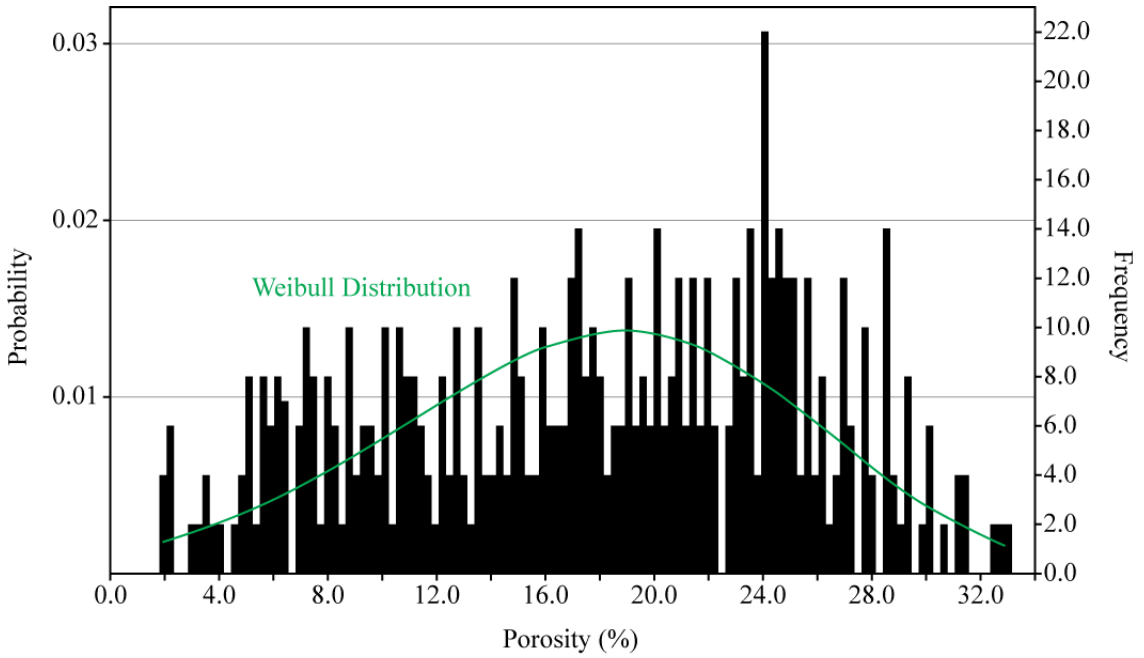

Figure 4.11 Histogram of Hewett Lower Bunter Sandstone Reservoir porosity based on 717 values

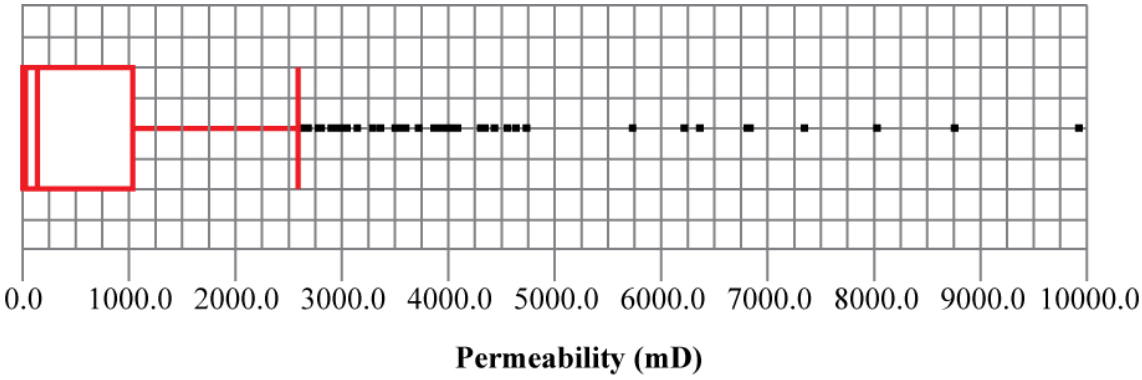

Figure 4.12 Hewett Lower Bunter Sandstone Reservoir boxplot for permeability. The permeability data plotted here do not lie within 1.5 times the IQR of the upper quartile, but are within 1.5 times the IQR of the lower quartile. Therefore, the whisker on the right hand side of the boxplot represents the upper quartile plus 1.5 times the IQR, whereas the whisker on the left hand side (although obscured by the box) is limited to 0.00 mD as it is not possible to have a negative value for permeability. A total of 86 outliers have been plotted on the boxplot on the right hand side. As can be seen, they are spread over a wide range indicating that higher values of permeability are possible within the Hewett Lower Bunter Sandstone reservoir, however, the likelihood is that overall reservoir permeability will be similar to that defined by the IQR.

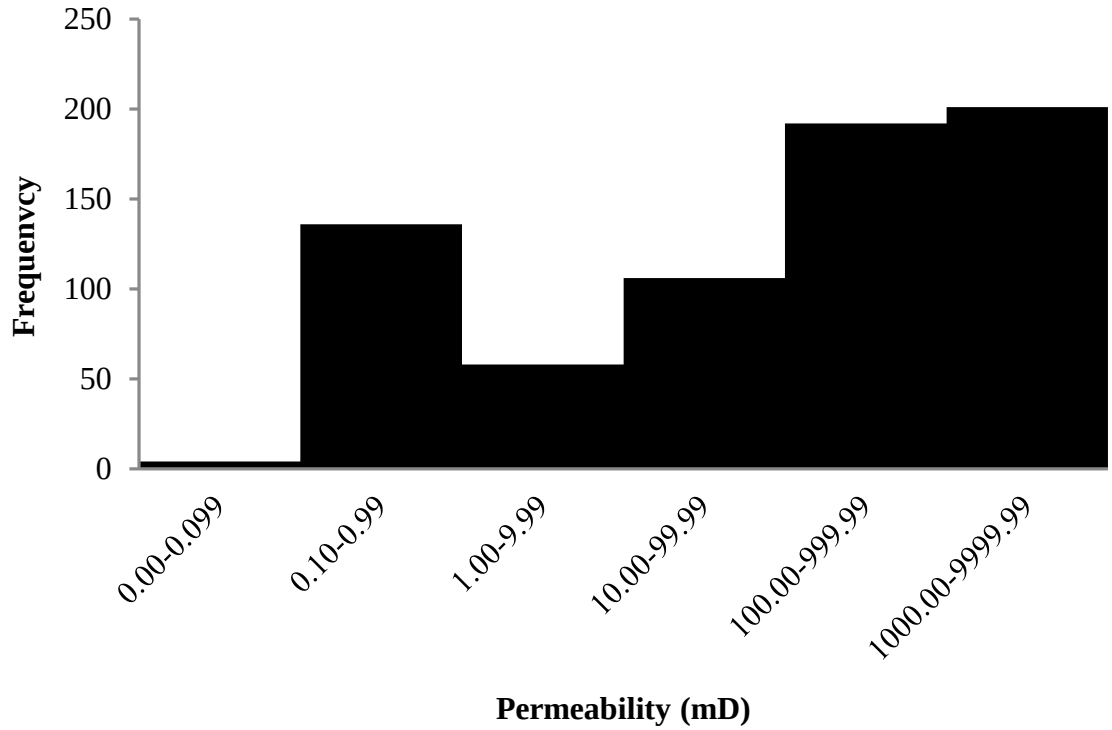

Figure 4.13 Histogram of Hewett Lower Bunter Sandstone Reservoir Permeability.

4.4.3. GAS PRODUCTION AND ASSOCIATED PRESSURE DECLINE

The Hewett Lower Bunter Sandstone reservoir has produced natural gas since 12 July 1969. The last recorded volume of produced gas was in 2002 at 58.021 billion cubic metres, based on the production data made available to Durham University by ENI. Production has continued past 2002 meaning this is not the final cumulative volume of produced gas, however, this data has not been made available to Durham University. The gas production data from all the productive wells (including 048/29-A1, A2, A3, A4, A5, A6, A7 and A8, 052/05a-A1, A4, A6, A7, A8, A9 and A10, and 048/29-B1, B2, B3, B4, B5, B6, B7 and B8) have been plotted in Figure 4.14, which shows a moderate but increasing rate of production for approximately 3 years following the reservoir coming online in 1969. The rate of production then rapidly increased between 1972-1977 to reach a peak of 4.55E+09 m^3/year. Rate of production began to slow gradually from 1977 onwards, and past 1990 production effectively continued at a low but reasonably steady rate of 3.58E+08 m^3/year.

The pressure history of the reservoir has also been plotted alongside the gas production data in Figure 4.14, from well 048/29-A1. The associated pressure decline due to production has a similar but opposite trend to that of gas production. For the three years following the onset of production in 1969 the rate of pressure decline was moderate but increasing. Between 1972 and 1982 there was a high rate of pressure decline with a peak rate of 0.859 MPa/year. From 1982 onwards, this rate of decline decreased and once again, from 1990 onwards the rate of decline continued at a low but reasonably steady rate of 0.0948 MPa/year.

It is important to note the degree of error in the pressure dataset. The reservoir pressures are Repeat Formation Tester (RFT) measurements. RFT data is wireline data that measures formation pressure versus depth in the borehole. It is generally used to measure the initial reservoir pressure, and pressure throughout the productive lifetime during times of reservoir shut-in (i.e. no production). It can also be used to detect the gas-water contact.

Initial pressures within the Hewett Lower Bunter Sandstone reservoir were taken over 40 years ago. Very early RFT tools used strain gauges, which are less

accurate than tools used within approximately the last 20 years which use a Hewlett Packard quartz gauge, making them in general an order of magnitude more accurate. Strain gauge accuracy is 0.18% and quartz gauge accuracy is 0.025%. Therefore, the pressure data recorded over the entire lifetime of the Hewett Lower Bunter Sandstone reservoir will be reasonably accurate; however, the first 20 years of measurement may be slightly reduced in accuracy in comparison to the later measurements.

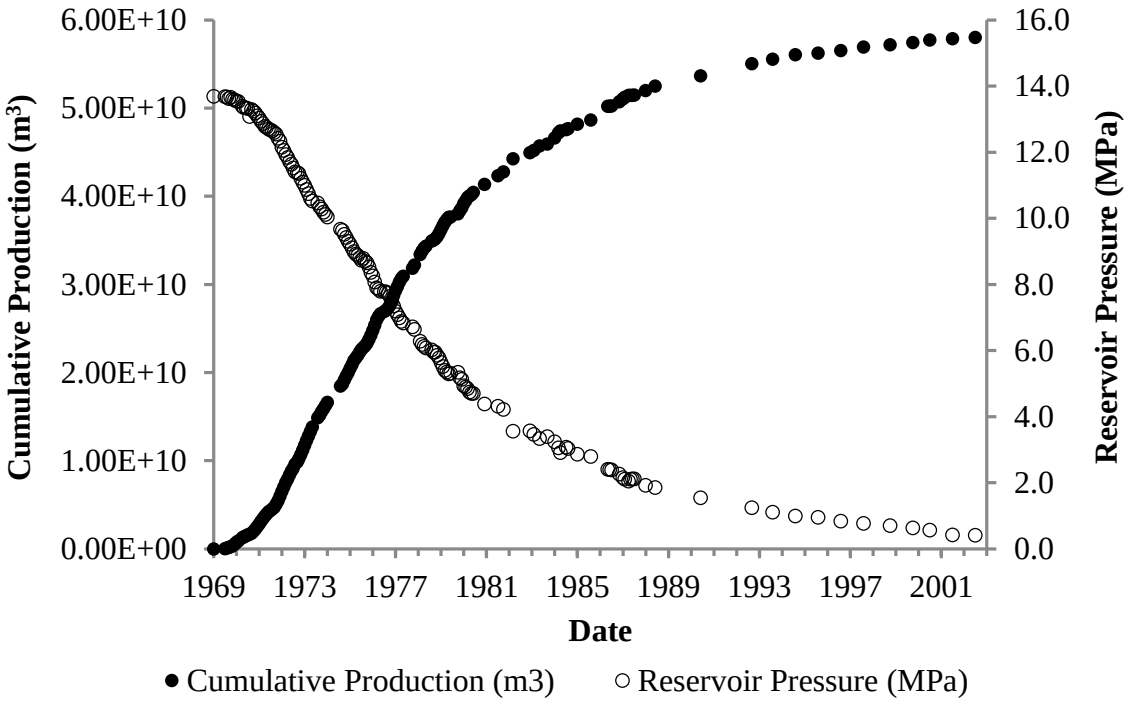

Figure 4.14 Hewett Lower Bunter Sandstone Reservoir cumulative production and reservoir pressure data, based on production data from ENI.

4.4.3.1. MATERIAL BALANCE METHODS

Material balance methods have been previously described in Chapter 3. They are used here to validate the observation of a lack of water encroachment in the Hewett Lower Bunter Sandstone reservoir throughout its productive lifetime. They are also used to better constrain the recovery factor, original gas in place and the ultimate recoverable reserves, which are necessary parameters for CO_2 storage capacity estimation.

The material balance plot of the Hewett Lower Bunter Sandstone reservoir data is shown in (Figure 4.15). The method requires estimation of the Z-factor. Z-factor values have been provided within the data made available to Durham University by ENI, however, it is unknown how the values were determined. As such, Z-factor values have been estimated using RefProp and the Peng-Robinson equation of state for the Hewett Lower Bunter Sandstone reservoir initial gas composition and the resulting P/Z plot has been plotted alongside that of the industry calculated results. The trends differ only slightly: the RefProp estimated P/Z results plot slightly lower than the industry calculated values at the beginning of production, however, the two datasets converge as the reservoir becomes more depleted. Both datasets conform extremely well to a linear trend throughout production until the limit of the original volume of gas in place. The reservoir is therefore interpreted to be a depletion drive reservoir based on the results of this graph when compared to Figure 3.15 (a).

The Cole Plot (Pletcher, 2002) of the same data is shown in Figure 4.17. It is necessary to estimate the gas formation volume factor, B_g, when constructing a Cole Plot. There are two possible methods to estimate B_g, described in section 4.5.2. Equation 4.2 describes method 1 and equation 4.3 describes method 2. Once again, it is also necessary to estimate Z-factor values. The values have been estimated as before: both the industry calculated Z-factor values (of unknown method) have been used alongside Z-factor values estimated using RefProp and the Peng-Robinson equation of state for the Hewett Lower Bunter Sandstone reservoir initial gas composition. All four trends confirm the depletion drive status of the reservoir as it shows an overall linear trend when compared to Figure 4.16 (b). Any amount of water drive, however small, produces a curved trend when plotted on a Cole Plot (see Figure 4.16). The scatter observed on the graph shortly after the onset of production may have manifested due to even small errors in pressure measurement early on in the Hewett Lower Bunter Sandstone reservoir's production history (Pletcher, 2002). If a pressure gradient existed in the reservoir, wells in different locations will record different pressures under reasonable shut-in times (Payne, 1996). Pressure can also be influenced by a well's previous

production rate (Payne, 1996). This often occurs following the onset of production until the reservoir becomes settled in and rate of production becomes more stable.

Now the Hewett Lower Bunter Sandstone reservoir has been confirmed to be a depletion drive reservoir it is possible to make more accurate estimations of the recovery factor, original gas in place and the volume of ultimate recoverable reserves. A value for the original gas in place is easily obtainable for a depletion drive reservoir and involves linear extrapolation of the trend line(s) on Figure 4.15 until it intersects the x-axis. For the Hewett Lower Bunter Sandstone reservoir, the extrapolated linear trend crosses the x-axis at 59.465 billion cubic metres.

The recovery factor can now be properly constrained and is defined as the volume of produced gas divided by the original gas in place, multiplied by 100%. The last recorded volume of produced gas was 58.021 billion cubic metres, giving a recovery factor of 97.6%, based on production data from ENI.

The volume of ultimate recoverable reserves will be similar to the value for the original gas in place for the Hewett Lower Bunter Sandstone reservoir due to it being confirmed as a depletion drive reservoir. Ultimate recoverable reserves refer to the volume of technically and economically recoverable gas. Therefore, as the gas is being produced through depletion drive (i.e. it does not rely on any other driving force, such as water influx), it is expected that virtually all the gas in the reservoir can be produced.

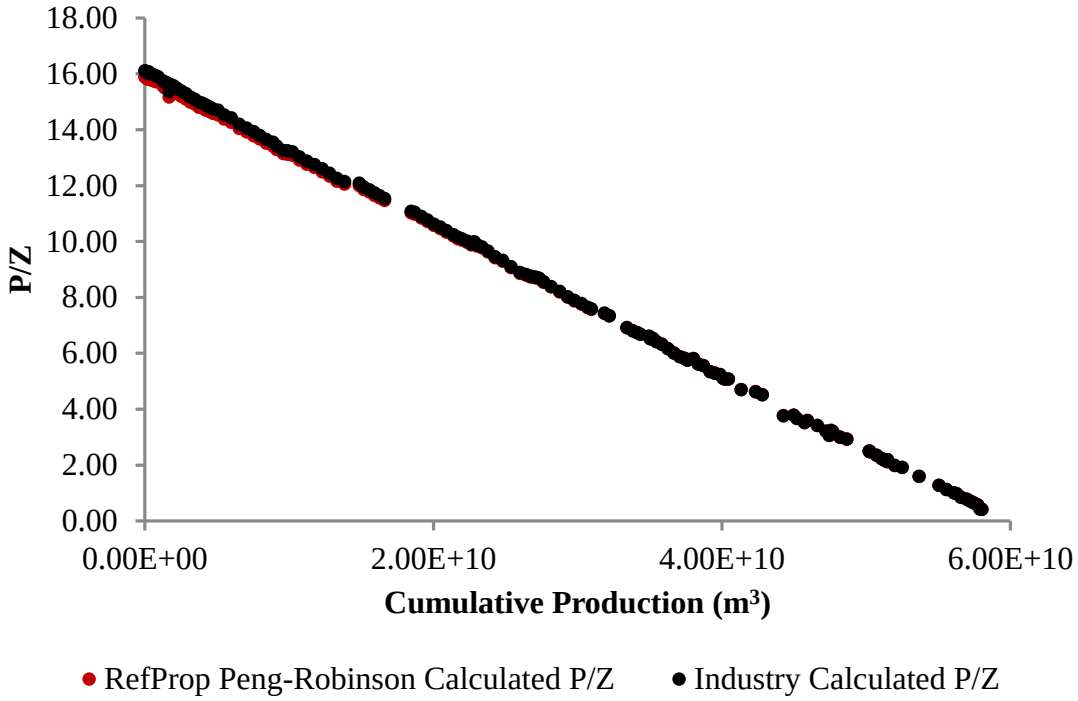

Figure 4.15 Hewett Lower Bunter Sandstone Reservoir material balance plot. Industry calculated Z-factor values (method unknown) have been used as well as Z-factor values estimated using RefProp and the Peng-Robinson equation of state for the Hewett Lower Bunter Sandstone reservoir initial gas composition.

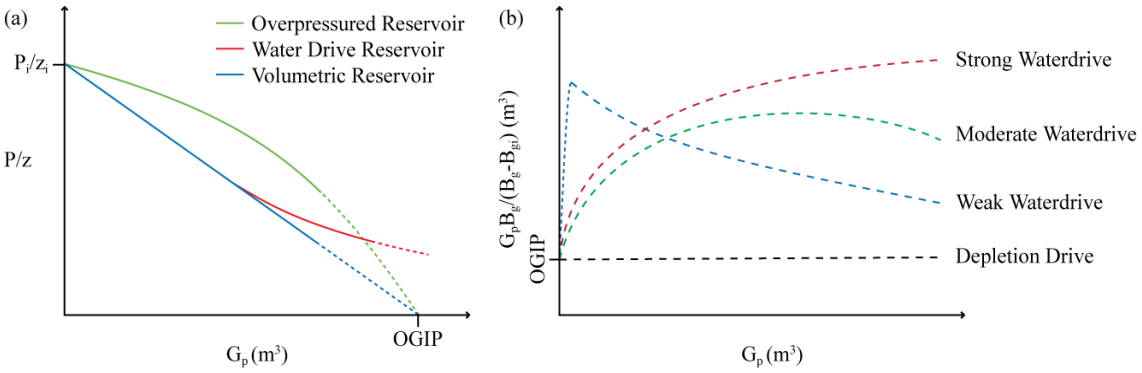

Figure 4.16 Material Balance Methods. (a) The original material balance method of pressure divided by gas compressibility factor against cumulative gas production. The major trends are shown on the graph for an over-pressured reservoir, a water drive reservoir and a volumetric reservoir. Due to the difficulties in solving the original material balance equation within water drive reservoirs, the water drive trend is often difficult to decipher on this graph from a volumetric reservoir trend. Instead a Cole Plot (b) can provide a clear distinction between water drive and volumetric (depletion) drive reservoirs.

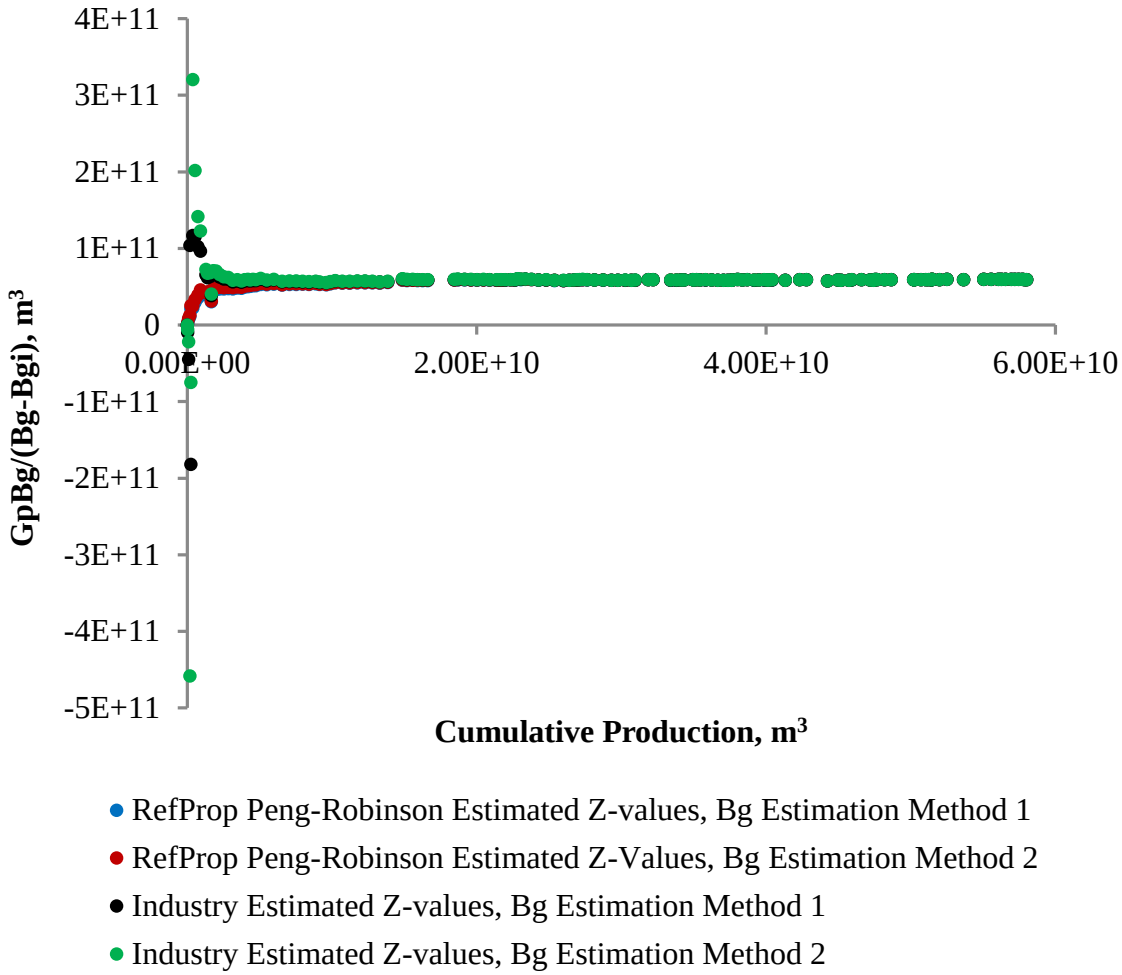

Figure 4.17 Hewett Lower Bunter Sandstone Reservoir Cole Plots. It is necessary to determine Z-factor values to calculate the gas formation volume factor (B_g) within the Cole Plot equation (see Chapter 3, equation 3.12). Industry calculated Z-factor values (unknown method) are used as well as Z-factor values estimated using RefProp software and the Peng-Robinson equation of state. There are also two methods of B_g estimation (see section 4.5.2., equations 4.2 and 4.3). Equation 4.2 describes method 1 and equation 4.3 describes method 2.

4.5. ESTIMATION OF RESERVOIR FLUID COMPRESSIBILITY AND IMPLICATIONS FOR CO_2 STORAGE CAPACITY ESTIMATION

Reservoir fluids are compressible, and at constant reservoir temperature it is possible to define isothermal compressibility as a positive term, c, as follows:

$$c = -\frac{1}{V}\left(\frac{\delta V}{\delta P}\right)_T \tag{4.1}$$

(Archer and Wall, 1986)

Where, V is the original volume, P is the pressure and the subscript, T, denotes constant reservoir temperature.

Gas compressibility is significantly greater than those of liquid hydrocarbons, which in turn are greater than those of reservoir waters (Archer and Wall, 1986). It is therefore important to consider gas compressibility variation when estimating the CO_2 storage capacity of depleted gas reservoirs as any variation will have a direct effect on utilisable storage capacity.

Gas is produced from the reservoir when the fluid expands from the initial reservoir pressure to a lower abandonment pressure (Archer and Wall, 1986). Prediction of gas behaviour can be calculated using various equations of state. The particular equation of state used depends on the environment that is being considered (in this case, the natural gas environment) and the individual limitations of the equation of state used (e.g. pressure and temperature limits).

Estimations of the gas compressibility factor (or Z-factor) were made using both RefProp (Lemmon et al., 2013) and the Lawrence Berkeley National Laboratory online calculator, WebGasEOS (Reagan and Oldenburg, 2006). Both RefProp (Lemmon et al., 2013) and WebGasEOS (Reagan and Oldenburg, 2006) were used for Z-factor estimation so that several equations of state could be used for analysis.

The calculated results of the Z-factor were input into both methods for calculating theoretical CO_2 storage capacity (for example, Bachu et al. (2007), Holloway et al. (2006) and Tseng et al. (2012)) and effective CO_2 storage capacity (for example, Tseng et al. (2012)). Through the variation of both estimations of Z-factor using various equations of state and the methods used to calculate CO_2 storage capacity, a range of results were produced.

4.5.1. GAS COMPRESSIBILITY FACTOR ESTIMATION

4.5.1.1. REFPROP ESTIMATIONS OF GAS COMPRESSIBILITY FACTOR

RefProp (Lemmon et al., 2013) was used to investigate Z-factor variability of several gas compositions (see Table 4.5) at constant temperature, whilst varying pressure and the equation of state used (Figure 4.18). The temperature was maintained at the initial reservoir temperature of 52.2 °C (325.372 K) as real-time temperature variation data was not available for the Hewett Lower Bunter Sandstone reservoir. Pressure was varied between the initial reservoir pressure of 13.686 MPa and the final reservoir pressure of 0.414 MPa. Gas compressibility factors were produced for three different equations of state: Peng-Robinson (Peng and Robinson, 1976), GERG-2008 (Kunz and Wagner, 2012) and the AGA8 Model (Starling and Savidge, 1992). The suitability of these equations of state to the natural gas environment and their individual limitations has been discussed previously in Chapter 3. Graphs of the results are displayed in Figure 4.18, and the main results to be used in the methods of storage capacity estimation are summarised in Table 4.6.

	MOLE FRACTION					
	Initial	20% CO_2	40% CO_2	60% CO_2	80% CO_2	99% CO_2
	HEWETT LOWER BUNTER INITIAL GAS COMPOSITION					
Methane	0.921300	0.737040	0.552780	0.368520	0.184260	0.009213
Ethane	0.035600	0.028480	0.021360	0.014240	0.007120	0.000356
Propane	0.008500	0.006800	0.005100	0.003400	0.001700	0.000085
i-Butane	0.001600	0.001280	0.000960	0.000640	0.000320	0.000016
n-Butane	0.002200	0.001760	0.001320	0.000880	0.000440	0.000022
i-Pentane	0.001000	0.000800	0.000600	0.000400	0.000200	0.000010
n-Pentane	0.000800	0.000640	0.000480	0.000320	0.000160	0.000008
Heavy HC	0.005200	0.004160	0.003120	0.002080	0.001040	0.000052
Carbon Dioxide	0.000200	0.200160	0.400120	0.600080	0.800040	0.990002
Nitrogen	0.023600	0.018880	0.014160	0.009440	0.004720	0.000236
TOTAL	**1.000000**	**1.000000**	**1.000000**	**1.000000**	**1.000000**	**1.000000**
	PURE METHANE					
Methane	1.00	0.80	0.60	0.40	0.20	0.01
Carbon Dioxide	0.00	0.20	0.40	0.60	0.80	0.99
TOTAL	**1.00**	**1.00**	**1.00**	**1.00**	**1.00**	**1.00**
	GAS MIX 1 COMPOSITION					
Methane	0.8500	0.6800	0.5100	0.3400	0.1700	0.0085
Ethane	0.0500	0.0400	0.0300	0.0200	0.0100	0.0005
Propane	0.0200	0.0160	0.0120	0.0080	0.0040	0.0002
Nitrogen	0.0800	0.0640	0.0480	0.0320	0.0160	0.0008
Carbon Dioxide	0.0000	0.2000	0.4000	0.6000	0.8000	0.9900
TOTAL	**1.0000**	**1.0000**	**1.0000**	**1.0000**	**1.0000**	**1.0000**
	GAS MIX 2 COMPOSITION					
Methane	0.7000	0.5600	0.4200	0.2800	0.1400	0.0070
Ethane	0.2300	0.1840	0.1380	0.0920	0.0460	0.0023
Propane	0.0500	0.0400	0.0300	0.0200	0.0100	0.0005
Nitrogen	0.0200	0.0160	0.0120	0.0080	0.0040	0.0002
Carbon Dioxide	0.0000	0.2000	0.4000	0.6000	0.8000	0.9900
TOTAL	**1.0000**	**1.0000**	**1.0000**	**1.0000**	**1.0000**	**1.0000**
	PURE CARBON DIOXIDE					
Carbon Dioxide	1.00					
TOTAL	**1.00**					

Table 4.5 Gas mixture compositions used in RefProp (Lemmon et al., 2013) and WebGasEOS (Reagan and Oldenburg, 2006) modelling of fluid properties

Figure 4.18 shows the variability of the gas compressibility factor with the particular equation of state used for the gas compositions shown. In general, the Peng-Robinson equation of state (Peng and Robinson, 1976) predicts a higher degree of gas compressibility at lower pressures than the GERG-2008 (Kunz and Wagner, 2012) and AGA8-DC92 Model (Starling and Savidge, 1992) equations of state. At higher pressures, the opposite occurs, and the GERG-2008 equation of state (Kunz and Wagner, 2012) estimates a higher degree of gas compressibility, with the AGA8-DC92 Model (Starling and Savidge, 1992) tending towards the predicted trend of the GERG-2008 equation of state (Kunz and Wagner, 2012) but at a slightly lower degree of compressibility. However, when there is 1 mol% natural gas and 99 mol% CO_2 within the Hewett Lower Bunter reservoir (i.e. in graphs (a) to (d)) the gas compressibility factor prediction of the AGA8-DC92 Model (Starling and Savidge, 1992) is largely similar to that of the GERG-2008 equation of state (Kunz and Wagner, 2012), both with a large difference in estimated gas compressibility factor to that predicted by the Peng-Robinson equation of state (Peng and Robinson, 1976) at higher pressures.

Figure 4.18 (a) shows the likely gas compressibility factor in the Hewett Lower Bunter Sandstone reservoir as it is re-pressurised with CO_2, calculated using the initial reservoir gas composition as defined in Table 4.5. Currently the reservoir is at low pressure (ca. 0.414 MPa) and has a composition of 100 mol% natural gas. As the reservoir is re-pressurised with CO_2, due to the residual volume of natural gas within the reservoir (ca. < 1.44 × 109 m3 or 45.9 Mt oil equivalent) the Hewett Lower Bunter Sandstone reservoir is expected to reach a composition of approximately 50 mol% CO_2, equating to a pressure of 3.1 MPa, after just 12 years of injection at a low rate of 6,600 tonnes/day (Baker-RDS, 2011b). For the remaining 28 years of the planned injection lifetime, the rate of injection is expected to increase to 26,400 tonnes/day (Baker-RDS, 2011b), therefore the predicted scenario of 1 mol% residual gas to 99 mol% CO_2 will be established early on in the injection lifetime of the Hewett Lower Bunter Sandstone reservoir. This would result in a high degree of gas compressibility within the reservoir (Figure 4.18), implying an efficient use of utilisable pore space for CO_2 storage.

Figure 4.18 (b) shows the likely gas compressibility factor under Hewett Lower Bunter Sandstone reservoir conditions for pure methane, with increasing mol% of pure CO_2. The major trends are very similar to that of Figure 4.18 (a) however, the Hewett Lower Bunter Sandstone reservoir initial gas composition is slightly more compressible than that of pure methane. Similarly, Figure 4.18 (c) and (d) show gas compressibility variation using Gas Mix 1 and Gas Mix 2 compositions respectively (as defined in Table 4.5). Both these gas compositions are more compressible than that of the actual Hewett Lower Bunter Sandstone reservoir composition. Figure 4.18 (e) shows the compressibility of pure CO_2 under Hewett Lower Bunter pressure and temperature conditions for comparison. It can be seen that CO_2, as has been demonstrated in graphs (a) to (d), is a highly compressible reservoir fluid.

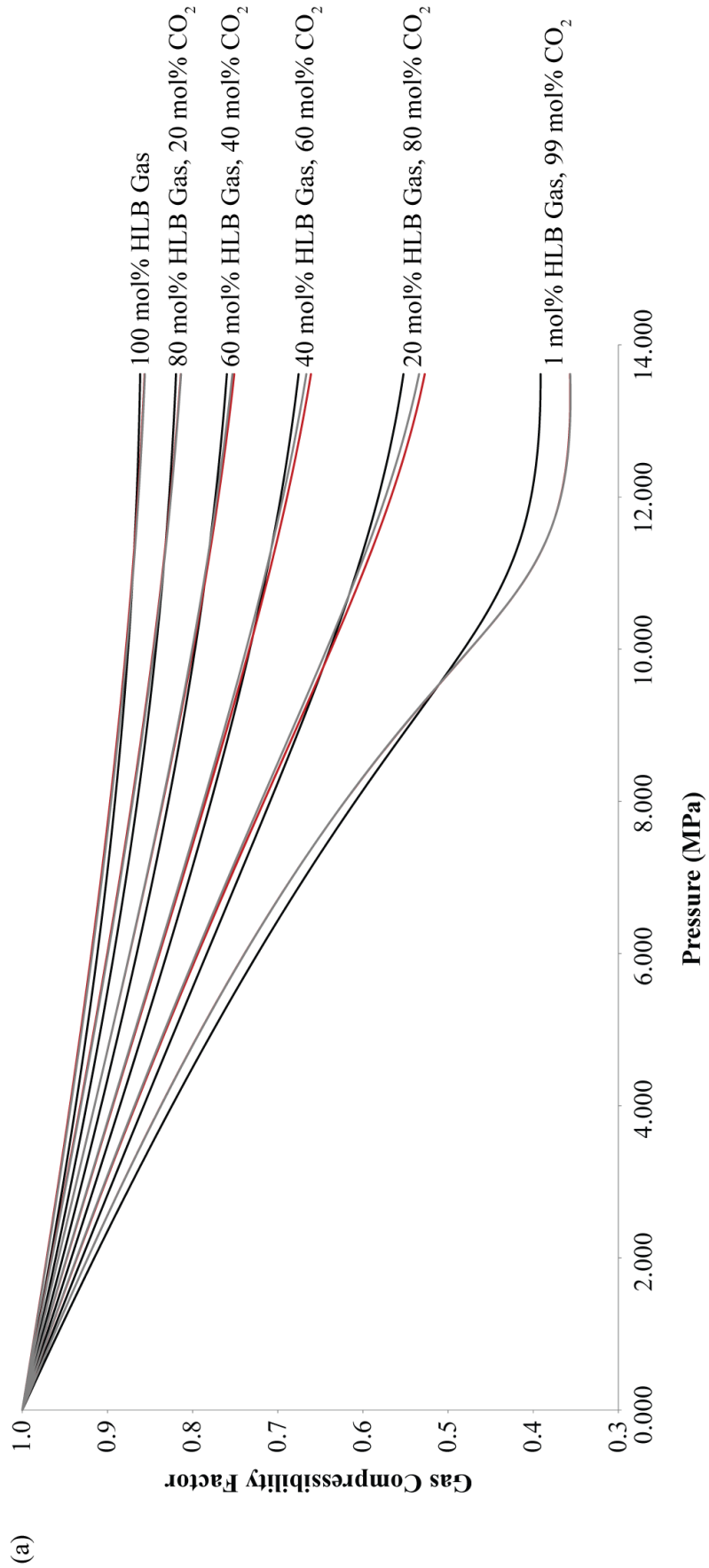
Peng-Robinson
GERG-2008
AGA8 Model
100 mol% HLB Gas
80 mol% HLB Gas, 20 mol% CO2
60 mol% HLB Gas, 40 mol% CO2
40 mol% HLB Gas, 60 mol% CO2
20 mol% HLB Gas, 80 mol% CO2
1 mol% HLB Gas, 99 mol% CO2
Gas Compressibility Factor
1.0
0.9
0.8
0.7
0.6
0.5
0.4
0.3
0.000
2.000
4.000
6.000
8.000
10.000
12.000
14.000
Pressure (MPa)

(a)

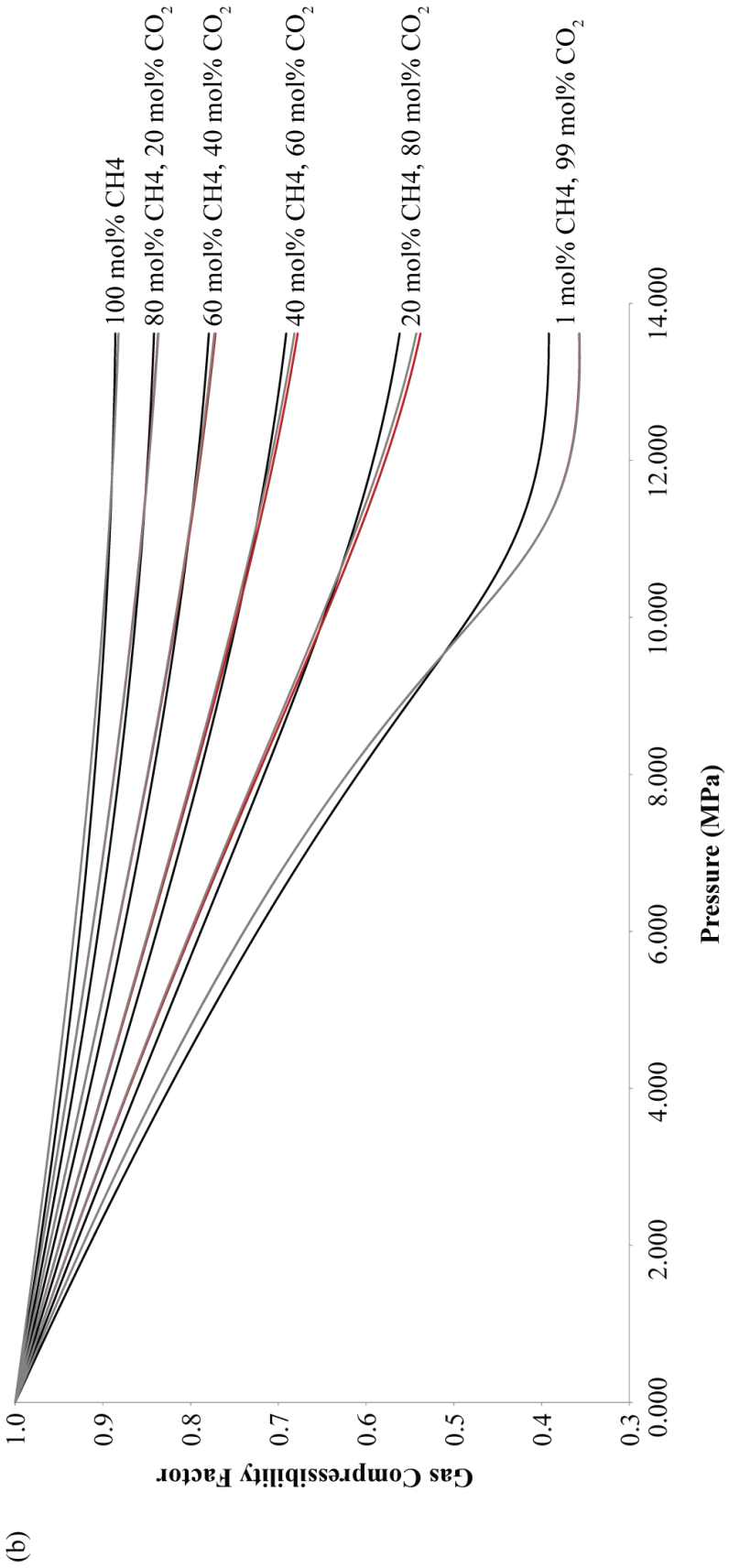
100 mol% CH4
80 mol% CH4, 20 mol% CO2
60 mol% CH4, 40 mol% CO2
40 mol% CH4, 60 mol% CO2
20 mol% CH4, 80 mol% CO2
1 mol% CH4, 99 mol% CO2
Gas Compressibility Factor
1.0
0.9
0.8
0.7
0.6
0.5
0.4
0.3
0.000
2.000
4.000
6.000
8.000
10.000
12.000
14.000
Pressure (MPa)

(b)

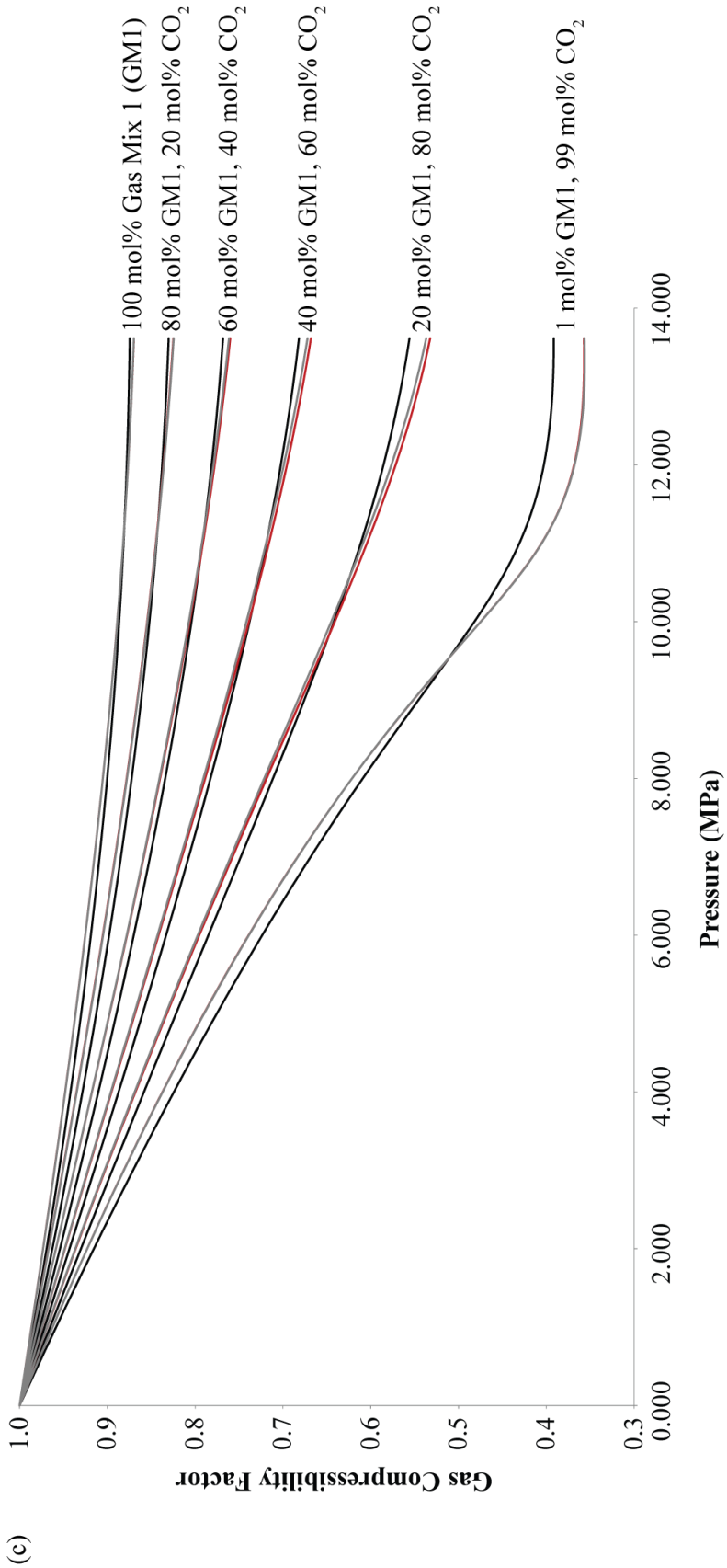
100 mol% Gas Mix 1 (GM1)
80 mol% GM1, 20 mol% CO_2
60 mol% GM1, 40 mol% CO_2
40 mol% GM1, 60 mol% CO_2
20 mol% GM1, 80 mol% CO_2
1 mol% GM1, 99 mol% CO_2
Gas Compressibility Factor
1.0
0.9
0.8
0.7
0.6
0.5
0.4
0.3
0.000
2.000
4.000
6.000
8.000
10.000
12.000
14.000
Pressure (MPa)

(c)

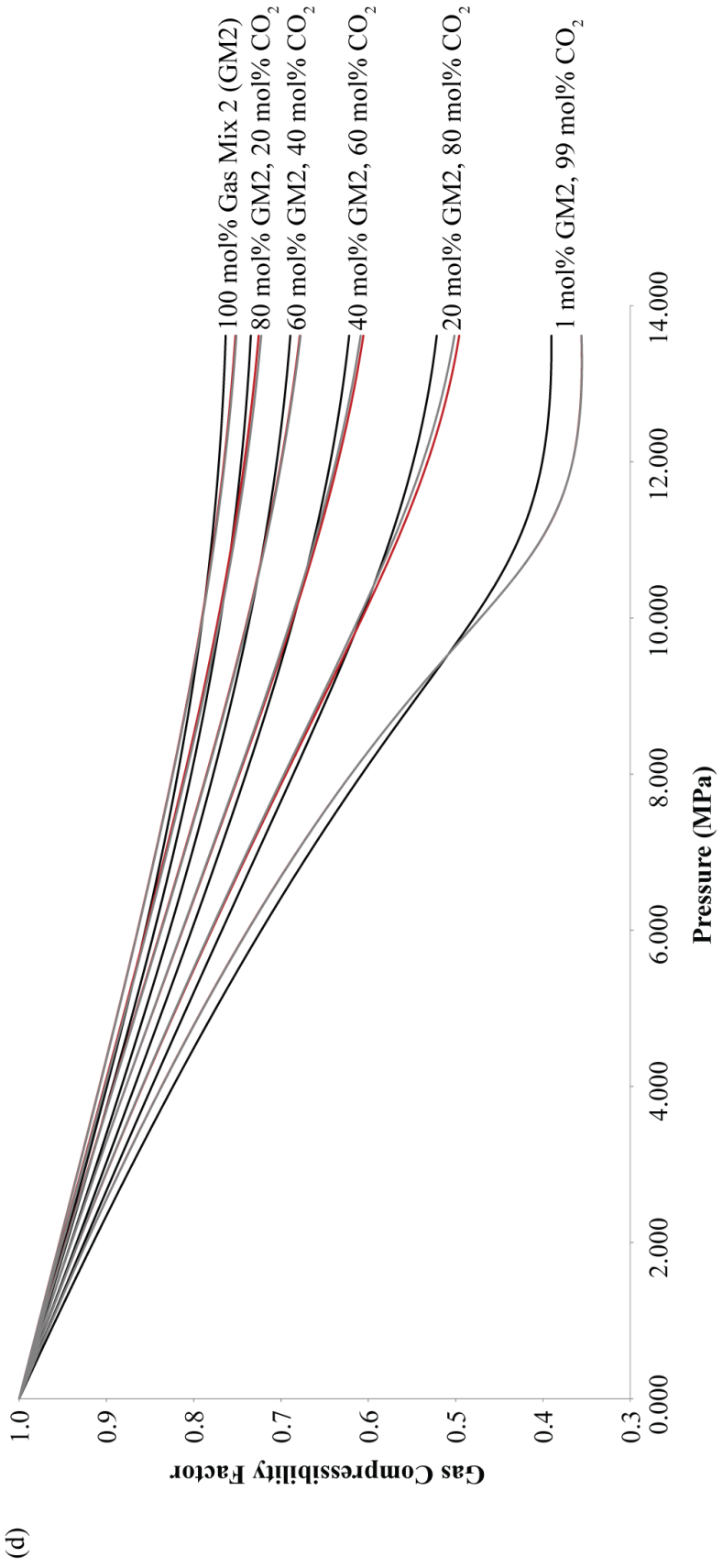
100 mol% Gas Mix 2 (GM2)
80 mol% GM2, 20 mol% CO_2
60 mol% GM2, 40 mol% CO_2
40 mol% GM2, 60 mol% CO_2
20 mol% GM2, 80 mol% CO_2
1 mol% GM2, 99 mol% CO_2
Gas Compressibility Factor
1.0
0.9
0.8
0.7
0.6
0.5
0.4
0.3
0.000
2.000
4.000
6.000
8.000
10.000
12.000
14.000
Pressure (MPa)

(d)

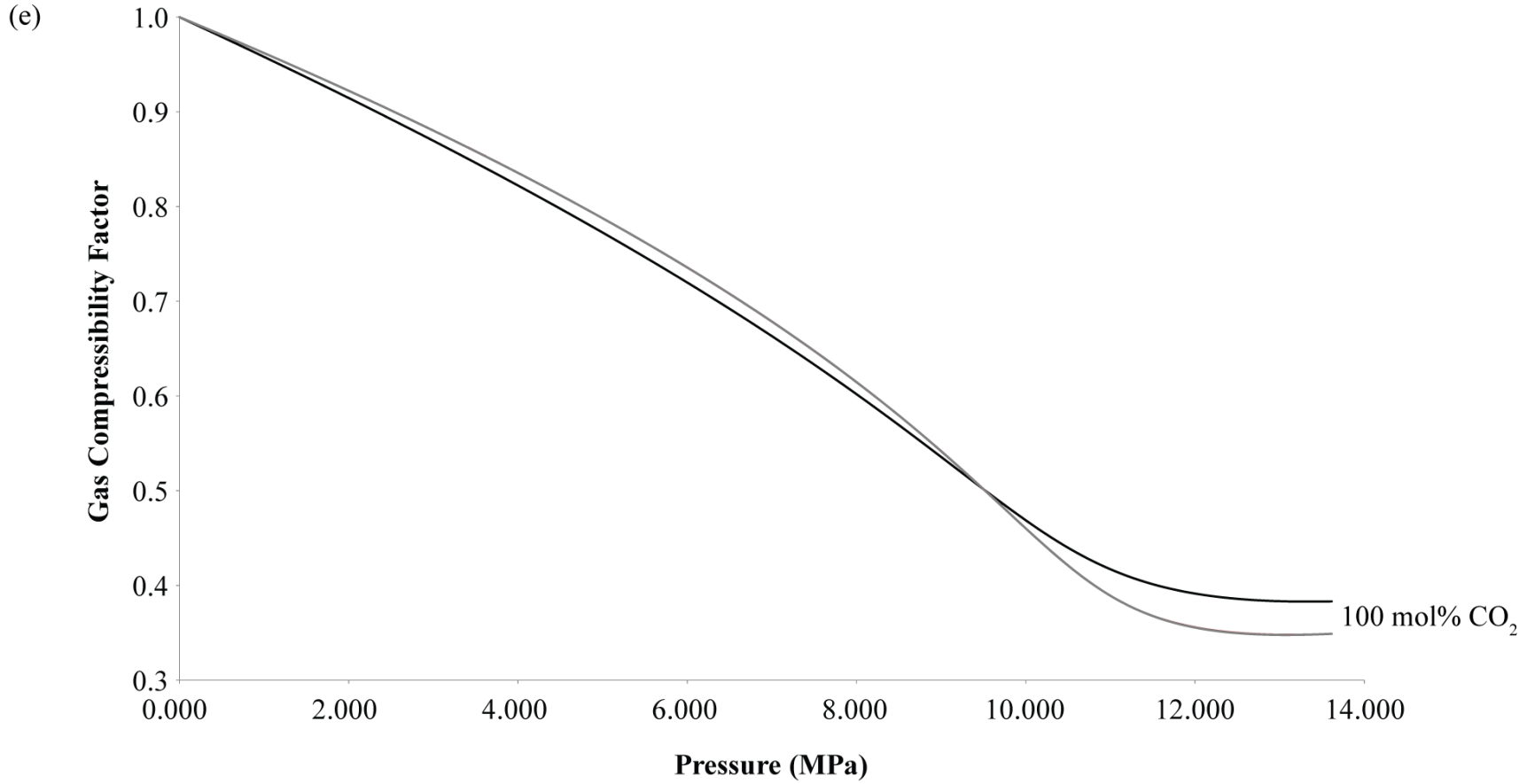

Figure 4.18 Hewett Lower Bunter Sandstone Reservoir Gas Compressibility Factor variation with pressure at constant temperature (52.2 °C) using the Peng-Robinson, GERG-2008 and AGA8 Model Equations of State and different gas compositions, modelled in RefProp (Lemmon et al., 2013). (a) Hewett Lower Bunter Sandstone reservoir initial gas composition with increasing mol% CO_2; (b) Pure methane with increasing mol% CO_2; (c) Gas mix 1 (as defined in Table 4.5) with increasing mol% CO_2; (d) Gas mix 2 (as defined in Table 4.5) with increasing mol% CO_2; (e) Pure CO_2.

EQUATION OF STATE	PARAMETER	UNITS	HLB INITIAL GAS COMPOSITION	PURE METHANE	GAS MIX 1	GAS MIX 2
Peng-Robinson	z_{iCO2}	Dimensionless	0.383	0.383	0.383	0.383
	z_{ihc}	Dimensionless	0.861	0.886	0.875	0.763
	z_{gas}	Dimensionless	0.993	0.994	0.993	0.989
	ρCO_2	kg/m^3	580.79	580.79	580.79	580.79
GERG-2008	z_{iCO2}	Dimensionless	0.349	0.349	0.349	0.349
	z_{ihc}	Dimensionless	0.856	0.882	0.870	0.752
	z_{gas}	Dimensionless	0.994	0.995	0.994	0.990
	ρCO_2	kg/m^3	637.45	637.45	637.45	637.45
AGA8 Model	z_{iCO2}	Dimensionless	0.349	0.349	0.349	0.349
	z_{ihc}	Dimensionless	0.856	0.882	0.870	0.751
	z_{gas}	Dimensionless	0.994	0.995	0.994	0.990
	ρCO_2	kg/m^3	637.42	637.42	637.42	637.42

Table 4.6 Summary of RefProp (Lemmon et al., 2013) Estimated Isoproperties for various Equations of State

4.5.1.2. WEBGASEOS ESTIMATIONS OF GAS COMPRESSIBILITY FACTOR

WebGasEOS (Reagan and Oldenburg, 2006), the online tool for computing gas properties created by the Lawrence Berkeley National Laboratories, was used to estimate the gas compressibility factor of the gas mixtures (Table 4.5) using alternative equations of state including Peng-Robinson (Peng and Robinson, 1976), Peng-Robinson-Stryjek-Vera (Stryjek and Vera, 1986), Redlich-Kwong (Redlich and Kwong, 1949) and Soave-Redlich-Kwong (Soave, 1972). There are a limited number of species that can be included in the gas mixture analysis, and as not all the components of the initial gas composition within the Hewett Lower Bunter Sandstone reservoir were included, it was not possible to simulate results for this mixture. The species lacking in the WebGasEOS tool (Reagan and Oldenburg, 2006), but present in the Hewett Lower Bunter Sandstone reservoir initial gas composition include i-Butane, n-Butane, i-Pentane and hexane. However, estimations of the gas compressibility factor were predicted for the pure methane, gas mix 1, gas mix 2 and pure carbon dioxide fluids.

Graphs of the results are shown in Figure 4.19 and a summary of the main isoproperties for input into the storage capacity estimation methodologies are displayed in Table 4.7.

EQUATION OF STATE	PARAMETER	UNITS	PURE METHANE	GAS MIX 1	GAS MIX 2
Peng-Robinson	z_{iCO2}	Dimensionless	0.378	0.378	0.378
	z_{ihc}	Dimensionless	0.862	0.853	0.739
	z_{gas}	Dimensionless	0.993	0.993	0.988
	ρCO_2	kg/m^3	588.28	588.28	588.28
Peng-Robinson-Stryjek-Vera	z_{iCO2}	Dimensionless	0.378	0.378	0.378
	z_{ihc}	Dimensionless	0.863	0.854	0.740
	z_{gas}	Dimensionless	0.993	0.993	0.988
	ρCO_2	kg/m^3	588.57	588.57	588.57
Redlich-Kwong	z_{iCO2}	Dimensionless	0.388	0.388	0.388
	z_{ihc}	Dimensionless	0.883	0.868	0.759
	z_{gas}	Dimensionless	0.995	0.994	0.990
	ρCO_2	kg/m^3	574.54	574.54	574.54
Soave-Redlich-Kwong	z_{iCO2}	Dimensionless	0.411	0.411	0.411
	z_{ihc}	Dimensionless	0.905	0.893	0.783
	z_{gas}	Dimensionless	0.995	0.995	0.991
	ρCO_2	kg/m^3	542.03	542.03	542.03

Table 4.7 Summary of WebGasEOS (Reagan and Oldenburg, 2006) Estimated Isoproperties for various Equations of State.

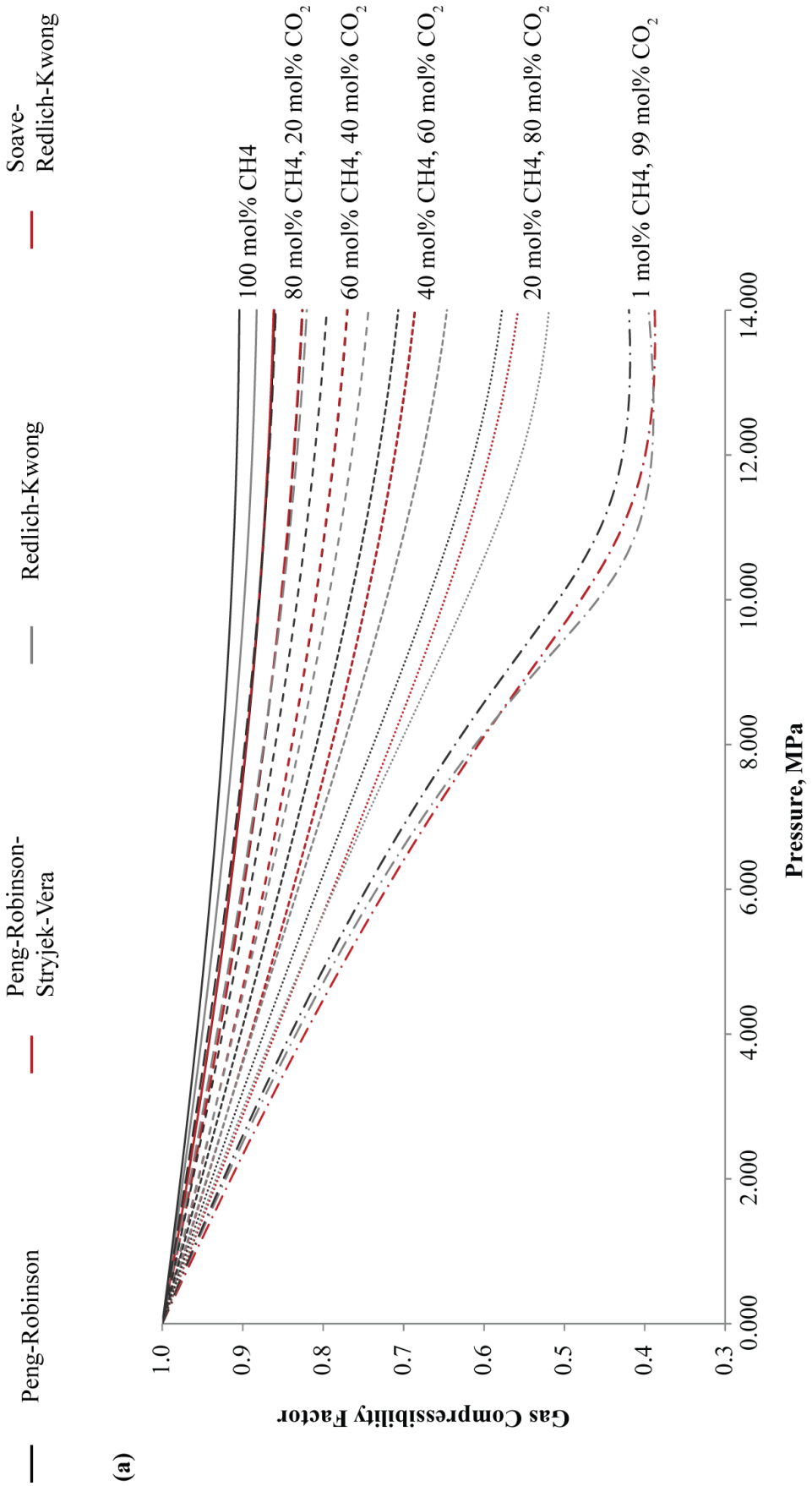
(a)
Peng-Robinson
Peng-Robinson-Stryjek-Vera
Redlich-Kwong
Soave-Redlich-Kwong
100 mol% CH4
80 mol% CH4, 20 mol% CO2
60 mol% CH4, 40 mol% CO2
40 mol% CH4, 60 mol% CO2
20 mol% CH4, 80 mol% CO2
1 mol% CH4, 99 mol% CO2
Gas Compressibility Factor
1.0
0.9
0.8
0.7
0.6
0.5
0.4
0.3
0.000
2.000
4.000
6.000
8.000
10.000
12.000
14.000
Pressure, MPa

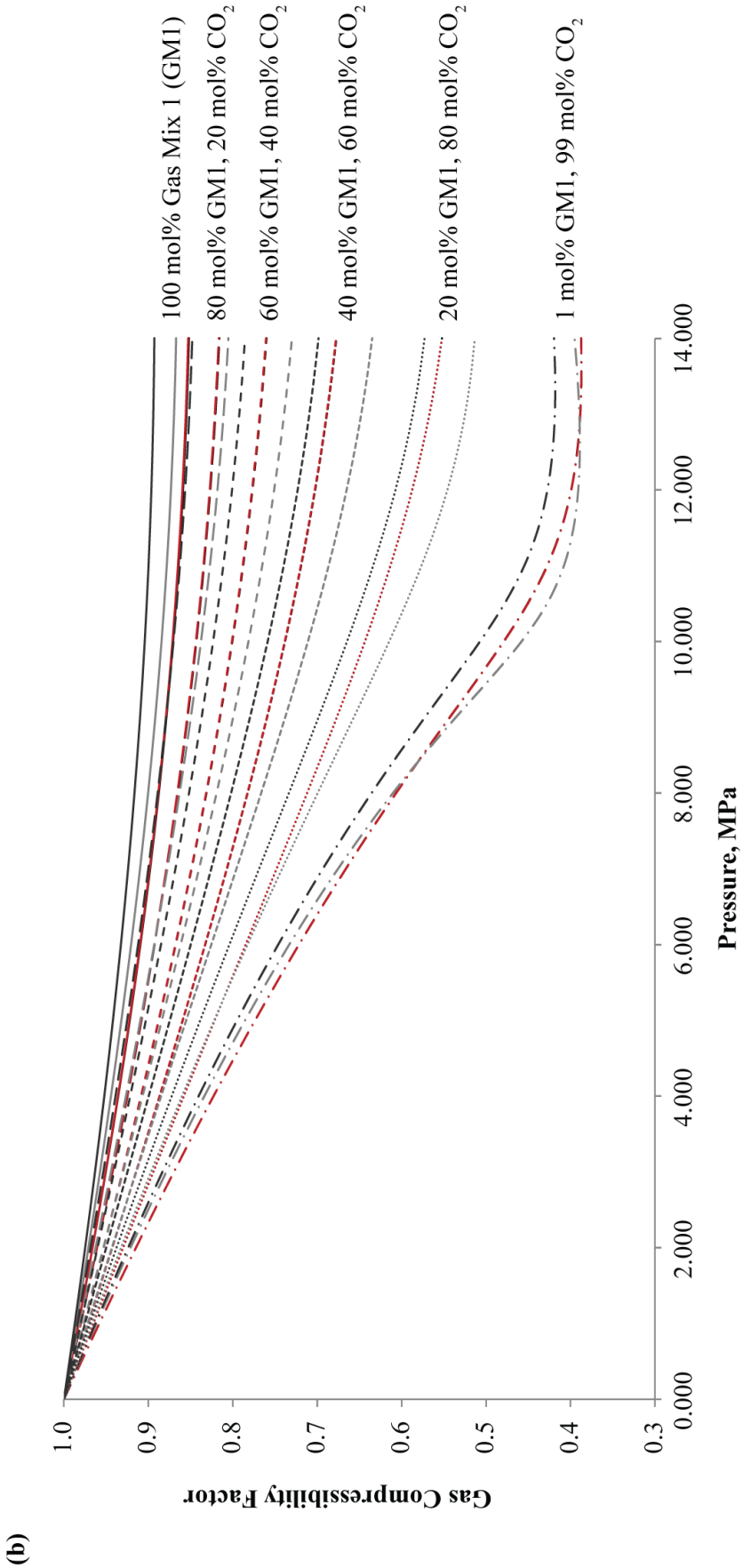
100 mol% Gas Mix 1 (GM1)
80 mol% GM1, 20 mol% CO2
60 mol% GM1, 40 mol% CO2
40 mol% GM1, 60 mol% CO2
20 mol% GM1, 80 mol% CO2
1 mol% GM1, 99 mol% CO2
Gas Compressibility Factor
1.0
0.9
0.8
0.7
0.6
0.5
0.4
0.3
0.000
2.000
4.000
6.000
8.000
10.000
12.000
14.000
Pressure, MPa

(a)

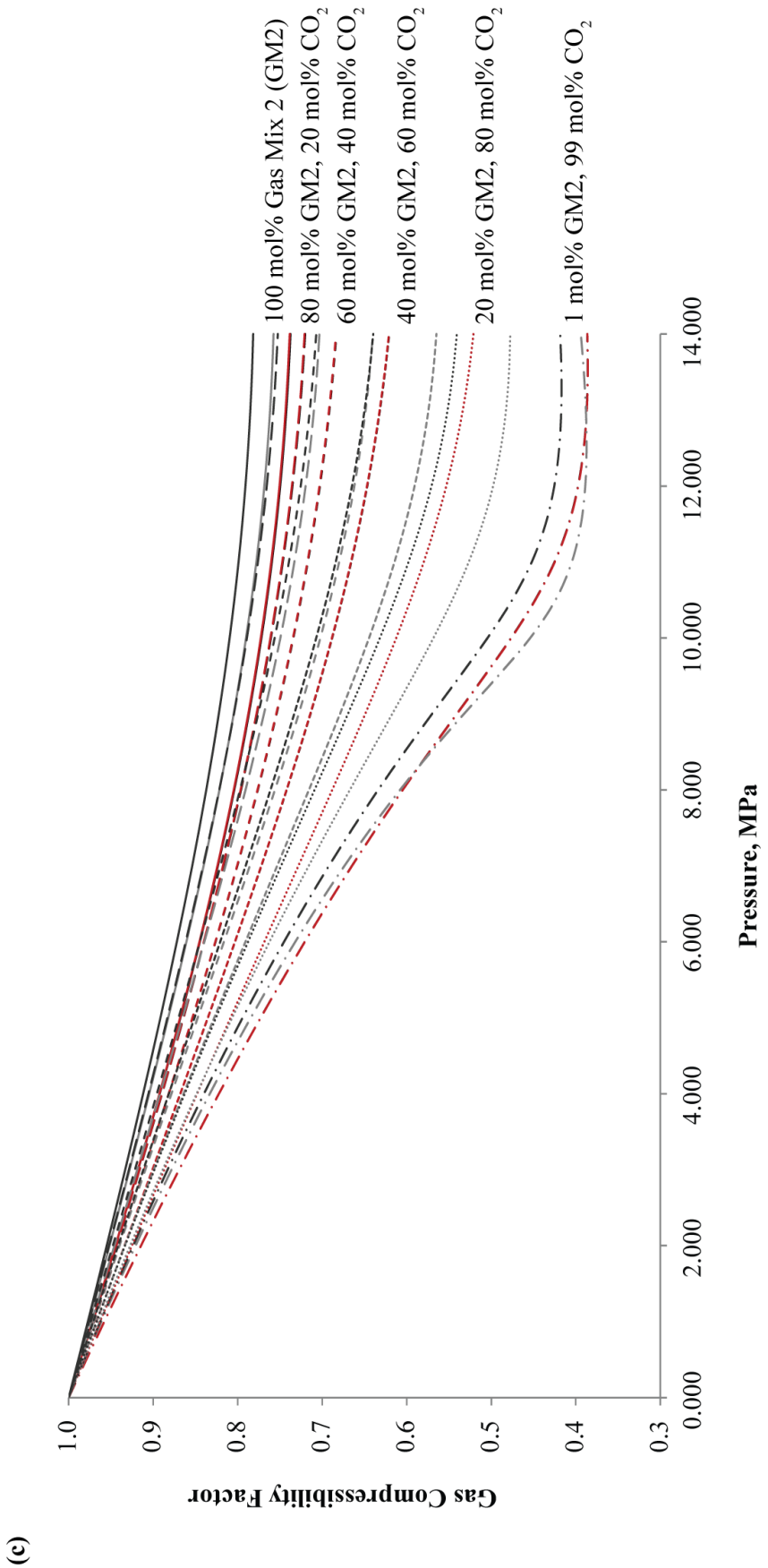
100 mol% Gas Mix 2 (GM2)
80 mol% GM2, 20 mol% CO2
60 mol% GM2, 40 mol% CO2
40 mol% GM2, 60 mol% CO2
20 mol% GM2, 80 mol% CO2
1 mol% GM2, 99 mol% CO2
Gas Compressibility Factor
1.0
0.9
0.8
0.7
0.6
0.5
0.4
0.3
0.000
2.000
4.000
6.000
8.000
10.000
12.000
14.000
Pressure, MPa

(c)

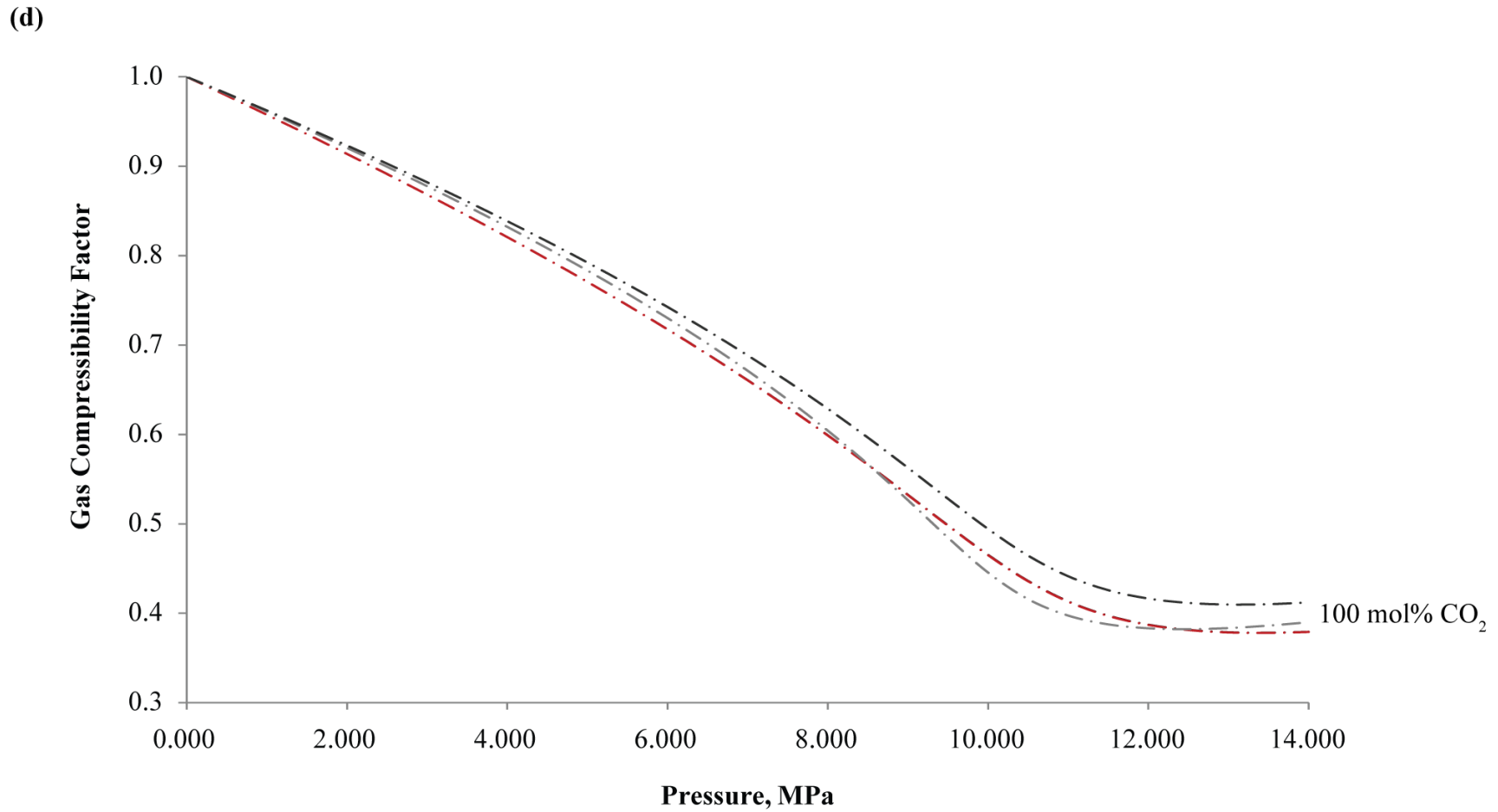

Figure 4.19 Hewett Lower Bunter Sandstone Reservoir Gas Compressibility Factor variation with pressure at constant temperature (52.2 °C) using the Peng-Robinson, Peng-Robinson-Stryjek-Vera, Redlich-Kwong and Soave-Redlich-Kwong Equations of State and different gas compositions, modelled in WebGasEOS (Reagan and Oldenburg, 2006). (a) Pure methane with increasing mol% CO_2; (b) Gas mix 1 (as defined I Table 4.5) with increasing mol% CO_2; (c) Gas mix 2 (as defined in Table 4.5) with increasing mol% CO_2; (d) Pure CO_2.

Figure 4.19 once again shows the variability of the gas compressibility factor with the particular equation of state used, as estimated in WebGasEOS (Reagan and Oldenburg, 2006) for the gas compositions shown in Table 4.7, excluding the Hewett Lower Bunter Sandstone reservoir initial gas composition. Equations of state used for modelling include Peng Robinson (Peng and Robinson, 1976), Peng-Robinson-Stryjek-Vera (Stryjek and Vera, 1986), Redlich-Kwong (Redlich and Kwong, 1949) and Soave-Redlich-Kwong (Soave, 1972).

The Soave-Redlich-Kwong equation of state (Soave, 1972) always predicts a much lower gas compressibility than the other equations of state within WebGasEOS (Reagan and Oldenburg, 2006). The Redlich-Kwong equation of state (Redlich and Kwong, 1949) predicts a low, but higher compressibility than that of Soave-Redlich-Kwong (Soave, 1972), when there is a higher mole percent of natural gas within the gas composition. However, when there is > 40 mol% CO_2 in the gas composition, the Redlich-Kwong equation of state (Redlich and Kwong, 1949) predicts the highest gas compressibilities out of all the equations of state modelled in WebGasEOS (Reagan and Oldenburg, 2006).

The Peng-Robinson (Peng and Robinson, 1976) and Peng-Robinson-Stryjek-Vera (Stryjek and Vera, 1986) equations of state always predict very similar curves for the temperature and pressure conditions modelled here. At 100 mol% natural gas, they predict the highest compressibility. However, when there is > 40 mol% CO_2 in the gas composition, they predict a compressibility curve that tends to lie between those estimated using the Redlich-Kwong (Redlich and Kwong, 1949) and Soave-Redlich-Kwong (Soave, 1972) equations of state.

There is some variability with gas compositions consisting of 80 mol% CO_2. At lower pressures (below ~ 8 MPa at 52.2 °C), the curve predicted with the Redlich-Kwong equation of state (Redlich and Kwong, 1949) estimates lower gas compressibilities than those predicted by the Peng-Robinson (Peng and Robinson, 1976) and Peng-Robinson-Stryjek-Vera (Stryjek and Vera, 1986) equations of state. The curves crossover at pressures between 5-6 MPa for all graphs in Figure 4.19 (a) to (d) with a gas composition of 80 mol% CO_2.

Similarly, for the gas composition of 99 mol% CO_2, this crossover occurs at a slightly higher pressure of just > 8 MPa, where the curve estimated using the

Redlich-Kwong equation of state (Redlich and Kwong, 1949) dips below those of the Peng-Robinson (Peng and Robinson, 1976) and Peng-Robinson-Stryjek-Vera (Stryjek and Vera, 1986) equations of state. However, as the pressure further increases there is yet another crossover of the Redlich-Kwong curve (Redlich and Kwong, 1949) back above those of the Peng-Robinson (Peng and Robinson, 1976) and Peng-Robinson-Stryjek-Vera (Stryjek and Vera, 1986) equations of state. This once again occurs in all the graphs in Figure 4.19 (a) to (d).

The results of both sections 4.5.1.1. and 4.5.1.2. show the degree of variability in Z-factor estimation. As such, this variability will need to be included in CO_2 storage capacity estimation.

4.5.2. GAS FORMATION VOLUME FACTOR ESTIMATION

The gas formation volume factor (B_g) is used to relate the volume of a fluid phase existing at reservoir conditions of temperature and pressure to its equivalent volume at standard conditions (Archer and Wall, 1986). It can be estimated through two main methods:

$$B_g = \frac{reservoir\ volume}{standard\ condition\ volume} \tag{4.2}$$

$$B_g = \frac{P_{sc}}{T_{sc}} \times T_{res} \times \frac{z_{res}}{P_{res}} \tag{4.3}$$

(Archer and Wall, 1986)

The gas formation volume factor has been calculated within the Hewett Lower Bunter Sandstone reservoir throughout its productive lifetime. Method 1 (equation 4.2) involves use of the real gas equation (Chapter 3, equation 3.16) and therefore relies upon estimation of the gas compressibility factor, Z. Method 2 (equation 4.3) also relies upon estimation of the Z-factor. For each method, Z-factors have been calculated within RefProp (Lemmon et al., 2013) using the initial Hewett Lower Bunter Sandstone reservoir gas composition and a variety of

equations of state: Peng-Robinson (Peng and Robinson, 1976), GERG-2008 (Kunz and Wagner, 2012), and AGA8-DC92 (Starling and Savidge, 1992). These results have been plotted and can be compared to the industry calculated Z-factor, and resulting estimated gas formation volume factors. The results have been estimated under the initial reservoir temperature conditions of 325.372 K, whilst varying pressure. The results are shown in Figure 4.20. As can be seen from Figure 4.20, the difference between the results of the two methods and the various equations of state used are negligible. This implies that estimates of the gas formation volume factor are very well constrained within the Hewett Lower Bunter Sandstone reservoir, and can be treated with confidence when used within CO_2 storage capacity calculations.

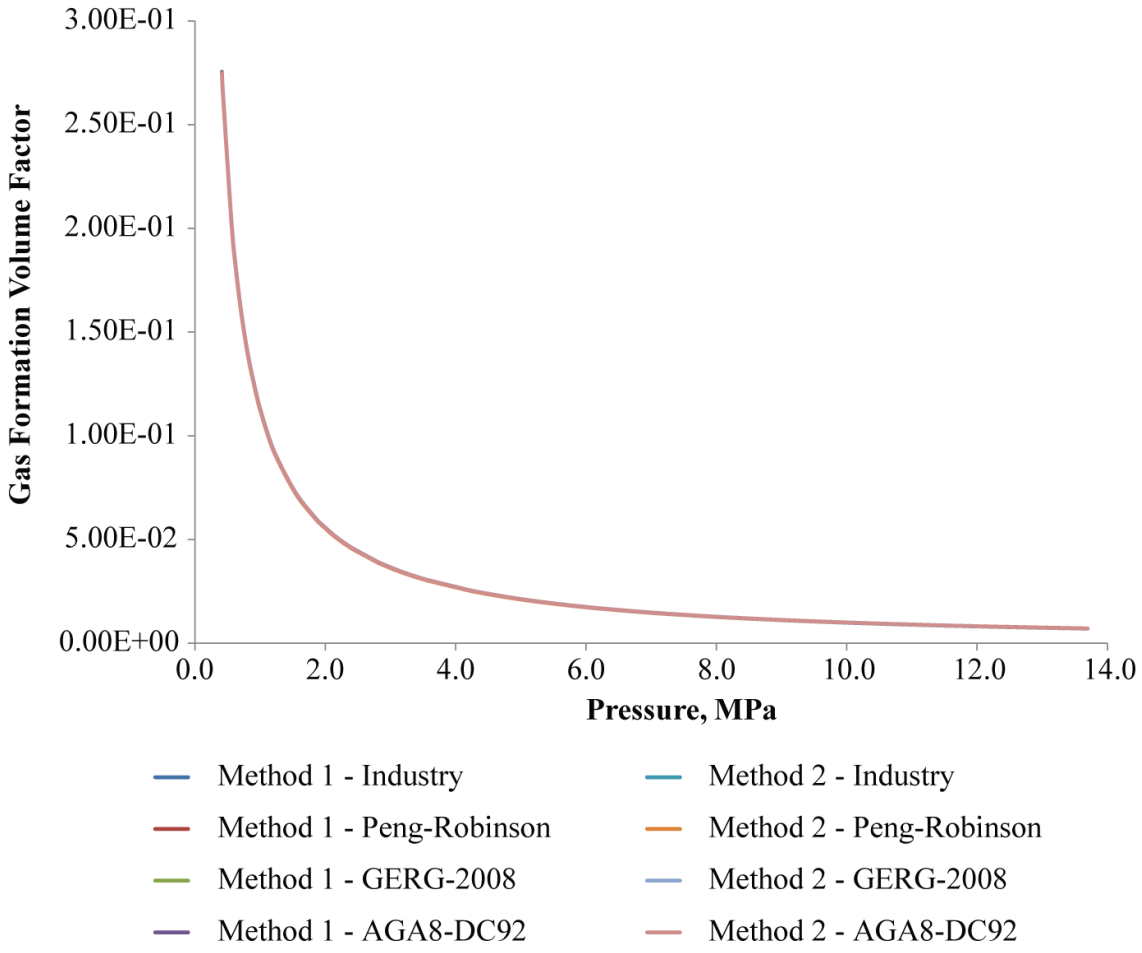

Figure 4.20 Estimation of the gas formation volume factor within the Hewett Lower Bunter Sandstone reservoir using two main methods of calculation and a variety of equations of state and under initial reservoir temperature conditions of 325.372 K. The gas compressibility factor, necessary for calculation of the gas formation volume factor (B_g) was estimated using RefProp (Lemmon et al., 2013). Three equations of state were used: Peng-Robinson (Peng and Robinson, 1976), GERG-2008 (Kunz and Wagner, 2012), and the AGA8-DC92 Model (Starling and Savidge, 1992). These values were compared back to industry calculated values.

4.5.3. ESTIMATION OF CO_2 DENSITY

CO_2 density has been estimated within RefProp (Lemmon et al., 2013) using three equations of state: Peng-Robinson (Peng and Robinson, 1976), GERG-2008 (Kunz and Wagner, 2012), and the AGA8-DC92 Model (Starling and Savidge, 1992). The results were estimated under the initial reservoir temperature conditions of 325.372 K, whilst varying pressure. The results are shown in Figure 4.21.

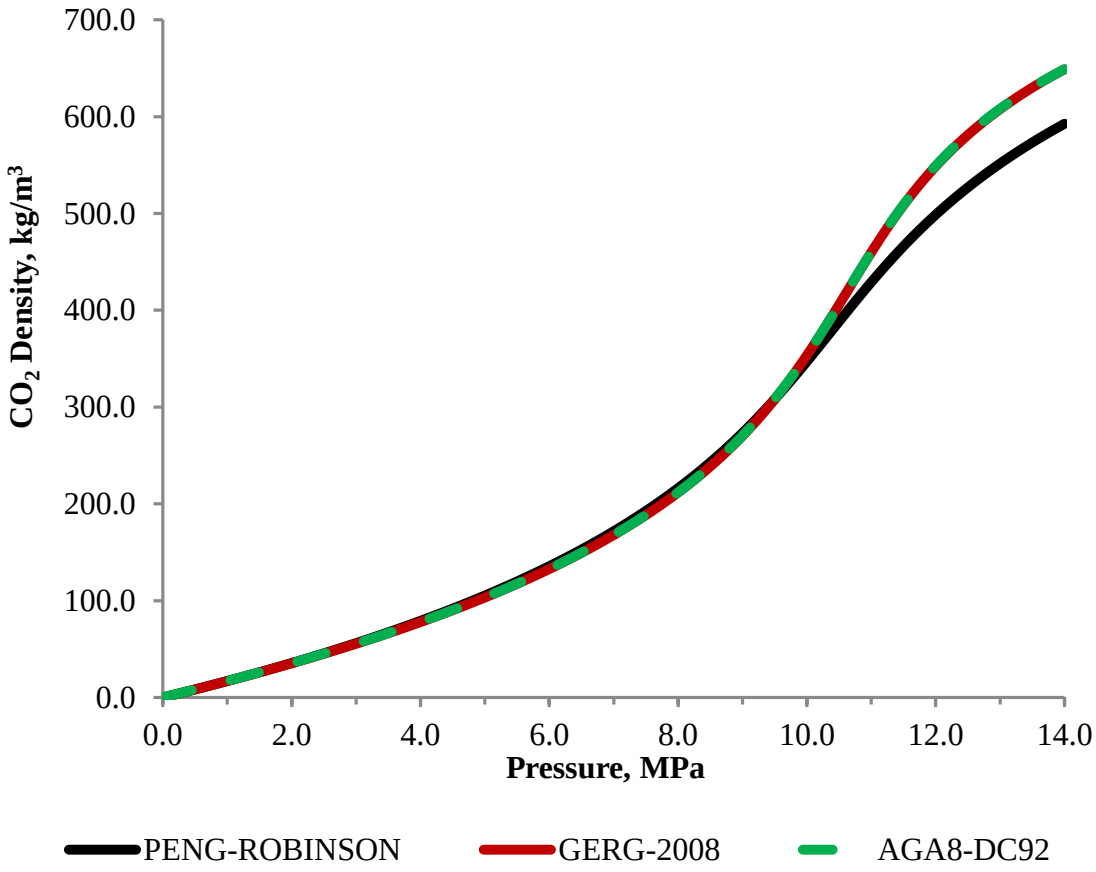

Figure 4.21 Estimations of CO_2 density with pressure within the Hewett Lower Bunter Sandstone reservoir under initial reservoir temperature conditions of 325.372 K. Results have been estimated using RefProp (Lemmon et al., 2013) and various equations of state: Peng-Robinson (Peng and Robinson, 1976), GERG-2008 (Kunz and Wagner, 2012), and the AGA8-DC92 Model (Starling and Savidge, 1992).

The results in Figure 4.21 show that CO_2 density increases with pressure. The GERG-2008 (Kunz and Wagner, 2012) and AGA8-DC92 (Starling and Savidge, 1992) equations of state predict very similar CO_2 densities throughout the pressure range shown. The Peng-Robinson equation of state (Peng and Robinson, 1976) predicts very similar CO_2 densities at low pressure, however, above ~10 MPa, the trend diverges from that of the GERG-2008 (Kunz and Wagner, 2012) and AGA8-DC92 (Starling and Savidge, 1992) equations of state, and predicted CO_2 densities are lower.

4.5.4. STORAGE CAPACITY ESTIMATION RESULTS

The estimates of the parameters outlined above, including gas compressibility factor, CO_2 density and gas formation volume factor, for the individual gas compositions were used to calculate both theoretical and effective storage capacities of the Hewett Lower Bunter Sandstone reservoir using various published methods.

4.5.4.1. THEORETICAL CO_2 STORAGE CAPACITY ESTIMATES

Theoretical CO_2 storage capacity estimates of the Hewett Lower Bunter Sandstone reservoir (previously defined in Chapter 1 and section 4.2 of this chapter) use methods (re-stated in Table 4.8) provided by Bachu et al. (2007), Holloway et al. (2006), and Tseng et al. (2012).

The Hewett Lower Bunter Sandstone reservoir has produced over 58 billion cubic metres of natural gas over its entire productive lifetime, equating to a mass of 43.5 Mt Hewett Lower Bunter Sandstone reservoir gas at standard conditions.

The geometric-based approach of Bachu et al. (2007), Table 4.8, equation 1.1, requires the use of parameters that have natural variability within a sandstone reservoir, such as porosity, reservoir area and reservoir height. As such, Monte Carlo simulation has been used to reduce the risk of storage capacity estimates produced using this method.

Porosity data was taken from well data made available to Durham University by IHS and assigned a best-fit probability distribution, found to be a Weibull

distribution, within Oracle Crystal Ball software (Figure 4.11). Both reservoir area and reservoir height were assigned uniform distributions due to limited data from wells, i.e. there is an equal chance of obtaining a value between 66-83 km^2 for reservoir area, and 18-64 m for reservoir height.

Monte Carlo simulation then produced the results (probability distributions) illustrated in Figure 4.22. Alongside the simulated forecast values in Table 4.9, the results illustrate the vast amount of variability in CO_2 storage capacity estimation. The average range between minimum and maximum storage capacity estimates for the Hewett Lower Bunter Sandstone reservoir is 1010 Mt CO_2. As such the mean CO_2 storage capacity values have been plotted alone in Figure 4.23. Error bars on the figure show the minimum, maximum, P10 and P90 values, i.e. the extent of variance. The minimum, P10, P50 (median), mean, P90 and maximum values for the probability distributions are shown in Table 4.9.

A sensitivity plot of the method of Bachu et al. (2007), Table 4.8, equation 1.1, shows that the theoretical CO_2 storage capacity results are most sensitive to porosity, followed by reservoir height and reservoir area (see Figure 4.24).

Theoretical CO_2 storage capacity results by Bachu et al. (2007), Table 4.8, equation 1.2; Holloway et al. (2006), Table 4.8, equation 1.3; and Tseng et al. (2012), Table 4.8, equation 1.4, are based upon the principle that a variable proportion of the pore space occupied by the recoverable reserves will be available for CO_2 storage. The parameters required within the methods are well constrained values which do not show variability.

Final results are displayed in Figure 4.25 and Table 4.10. Mean values of the probability distributions for the Hewett Lower Bunter Sandstone reservoir are plotted on Figure 4.25 and stated in Table 4.10 to represent CO_2 storage capacity estimates for the method of Bachu et al. (2007), Table 4.8, equation 1.1. The theoretical CO_2 storage capacity estimates of all the methods used are comparable, ranging between 241 and 309 Mt CO_2 for the Hewett Lower Bunter Sandstone reservoir initial gas composition (see Table 4.10). In general, the highest estimates are predicted by the method of Tseng et al. (2012), Table 4.8, equation 1.4, and the lowest estimates by the method of Holloway et al. (2006), Table 4.8, equation 1.3,

except for Gas Mix 2, where the method of Bachu et al. (2007), Table 4.8, equation 1.2 predicts the lowest CO_2 storage capacity estimates.

In general, the GERG-2008 equation of state (Kunz and Wagner, 2012) always predicts the highest estimate of theoretical CO_2 storage capacity, closely followed by the AGA8-DC92 Model (Starling and Savidge, 1992). When compared to the results of the Peng-Robinson equation of state (Peng and Robinson, 1976) estimated using RefProp (Lemmon et al., 2013), the results predicted using the GERG-2008 equation of state (Kunz and Wagner, 2012) are ~9.6% greater (see Table 4.10). The Soave-Redlich-Kwong equation of state (Soave, 1972) always predicts the lowest estimate of theoretical CO_2 storage capacity. When compared to the results of the Peng-Robinson equation of state (Peng and Robinson, 1976) estimated using RefProp (Lemmon et al., 2013), the results predicted using the Soave-Redlich-Kwong equation of state (Soave, 1972) are ~6.1% lower (see Table 4.10). These results are discussed in section 4.6.3.

STORAGE CAPACITY EQUATION	AUTHOR	EQUATION NUMBER
$M_{CO_2t} = \rho_{CO_2r}\left[R_f Ah\varphi(1 - S_w) - V_{iw} + V_{pw}\right]$	Bachu et al. (2007)	(1.1)
$M_{CO_2t} = \rho_{CO_2r} R_f (1 - F_{IG}) OGIP \left[\frac{(P_s Z_r T_r)}{(P_r Z_s T_s)}\right]$	Bachu et al. (2007)	(1.2)
$M_{CO_2t} = \left(\frac{V_{GAS}[stp]}{B_{igas}} . \rho_{CO_2r}\right)$	Holloway et al. (2006)	(1.3)
$M_{CO_2t} = \frac{\rho_{CO_2r}\left(G_{phc} . B_{gas}\right)}{B_{iCO_2}} = \frac{\rho_{CO_2r}\left(G_{phc} . z_{gas}\right)}{z_{iCO_2}}$	Tseng et al. (2012)	(1.4)
$M_{CO_2e} = C_m C_b C_h C_w C_a M_{CO_2t} \equiv C_e M_{CO_2t}$	Bachu et al. (2007)	(1.5)
$M_{injCO2} = \rho_{CO2r} . G_{injCO2}$	Tseng et al. (2012)	(1.6)
$G_{injCO2} = G_{phc} - G_{ihc} + \frac{P_{reshc/CO2}}{z_{reshc/CO2}}\left(\frac{z_{ihc}}{P_{ihc}} G_{ihc} - W_e \frac{T_{sc}}{P_{sc} T}\right)$	Tseng et al. (2012)	(1.7)

Table 4.8 Storage Capacity Equations previously introduced in Chapter 1. See Chapter 1 for definition of symbols

RefProp, Peng-Robinson Equation of State

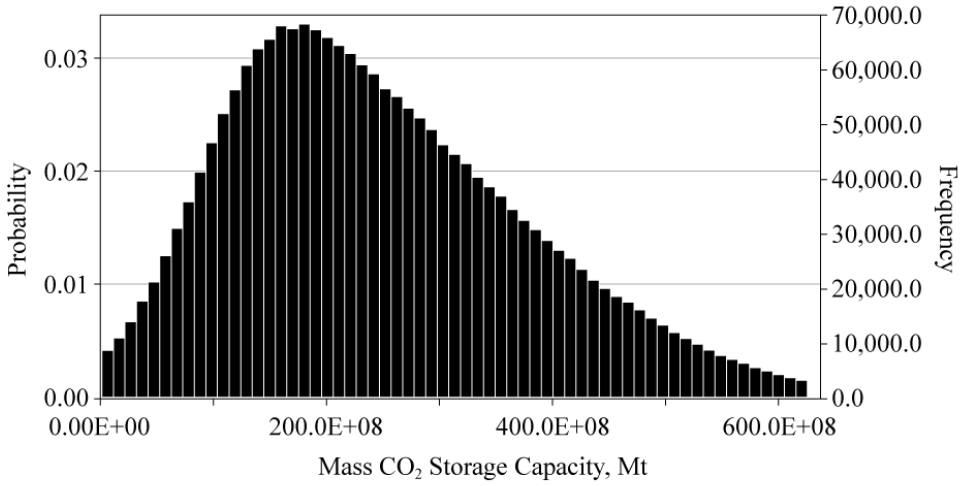

RefProp, GERG-2008 Equation of State

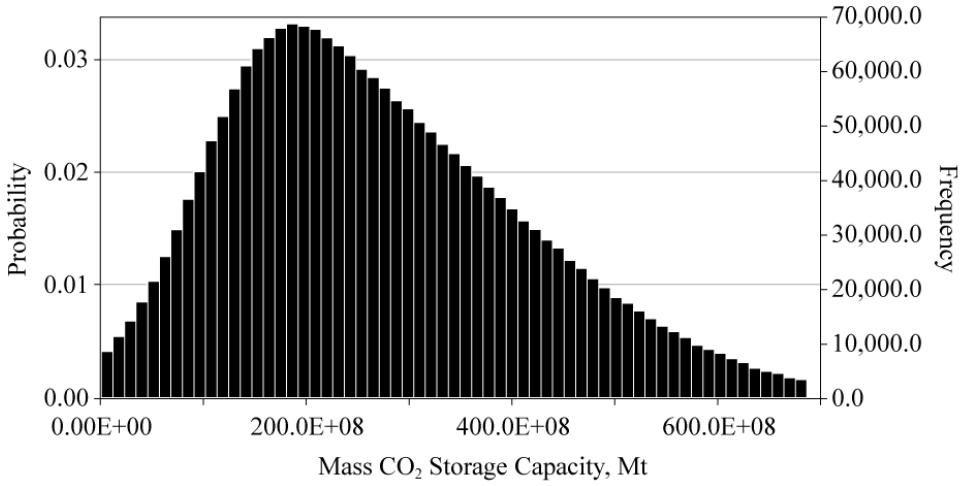

RefProp, AGA8-DC92 Equation of State

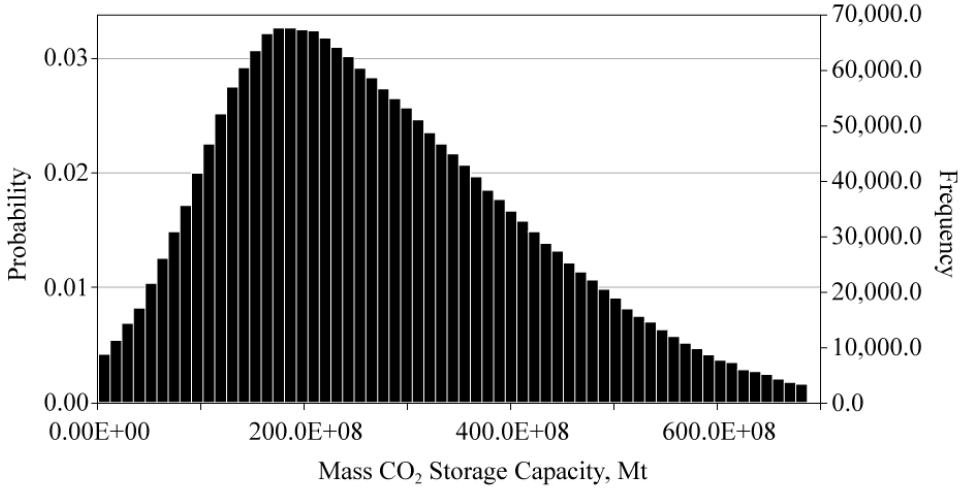

WebGasEOS, Peng-Robinson Equation of State

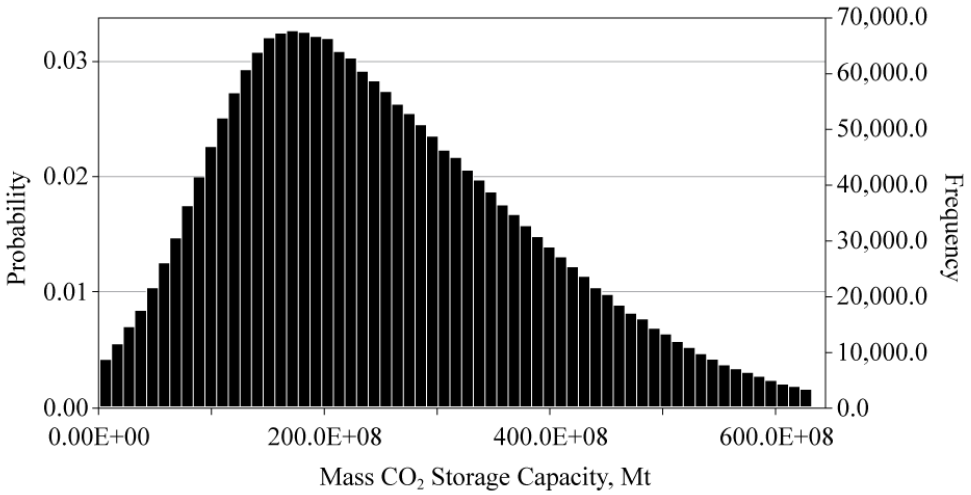

WebGasEOS, Peng-Robinson-Stryjek-Vera Equation of State

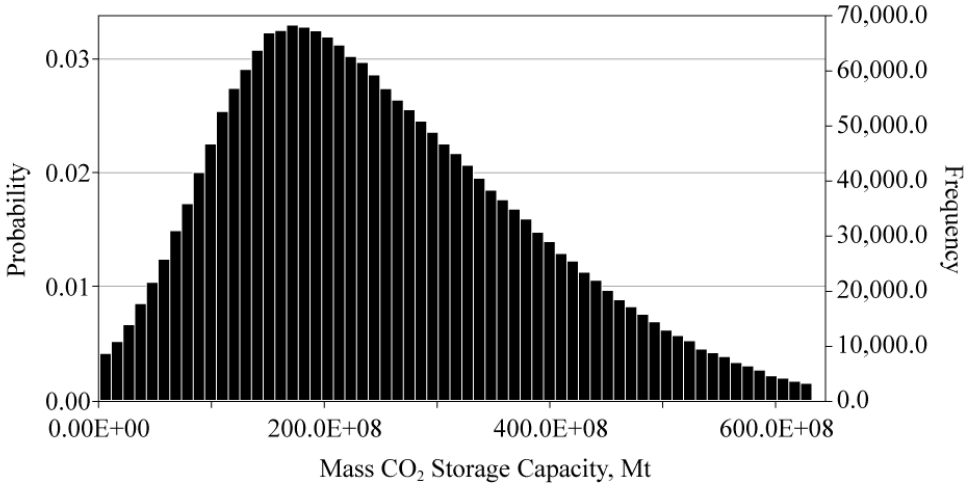

WebGasEOS, Redlich-Kwong Equation of State

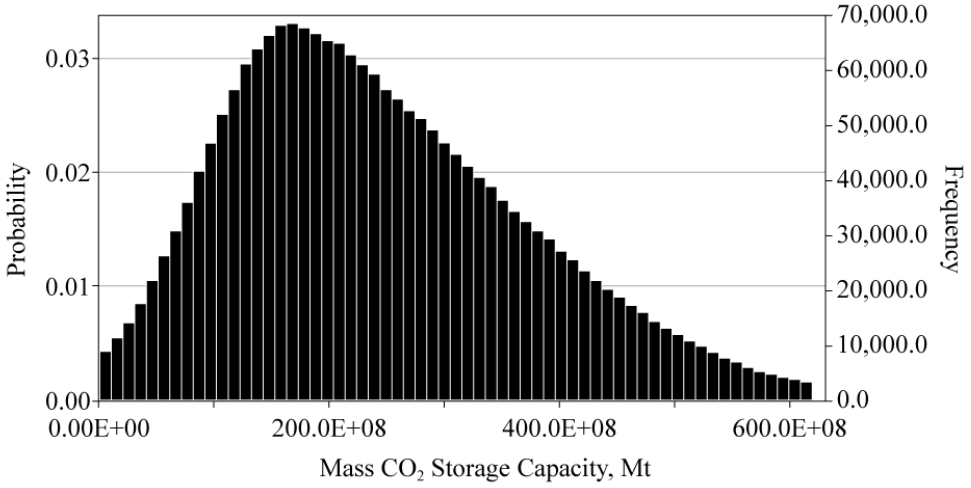

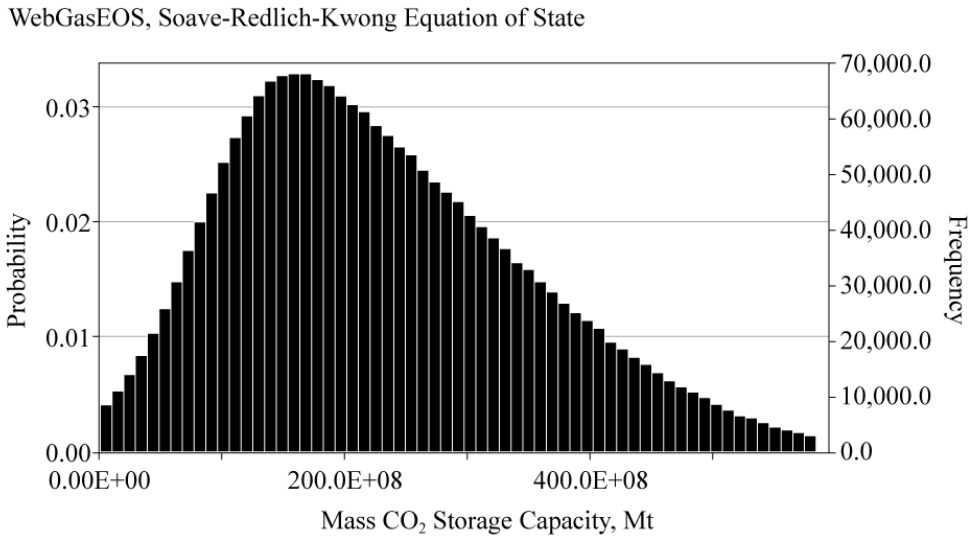

Figure 4.22 Monte Carlo Simulation probability distribution results of mass CO_2 storage capacity within the Hewett Lower Bunter Sandstone reservoir using the method of Bachu et al. (2007) Table 4.8, equation 1.1 and varying the equation of state used. Results computed using Oracle Crystal Ball software.

MODELLING SOFTWARE	EQUATION OF STATE	MINIMUM	P10	MEDIAN (P50)	MEAN	P90	MAXIMUM
RefProp	Peng-Robinson	0.004330	92.30	229.00	249.00	437.00	993.00
	GERG-2008	0.001290	101.00	251.00	274.00	480.00	1030.00
	AGA8 Model	0.003200	101.00	251.00	274.00	480.00	1100.00
WebGasEOS	Peng-Robinson	0.000257	93.50	232.00	253.00	442.00	1000.00
	Peng-Robinson-Stryjek-Vera	0.001620	93.60	232.00	253.00	443.00	1020.00
	Redlich-Kwong	0.000629	91.30	226.00	247.00	432.00	1020.00
	Soave-Redlich-Kwong	0.000331	86.10	214.00	233.00	408.00	907.00

Table 4.9 Monte Carlo Simulation forecast values for the Hewett Lower Bunter Sandstone reservoir using Oracle Crystal Ball software. Results in Mt CO_2.

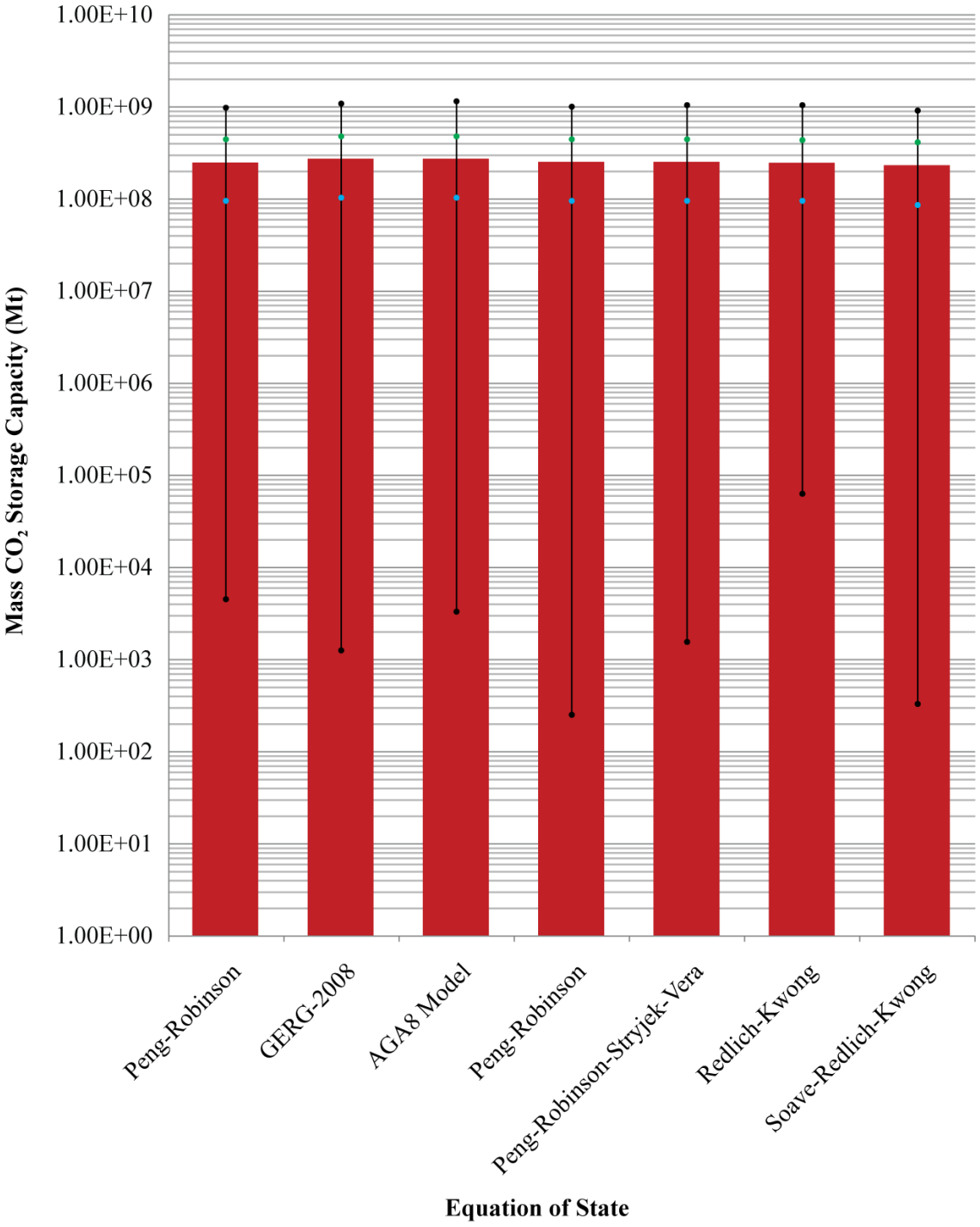

Figure 4.23 Theoretical CO_2 storage capacity of the Hewett Lower Bunter Sandstone reservoir estimated using the method of Bachu et al. (2007), Table 4.8, equation 1.1. The red columns plotted are the mean values, and the error bars shown have the minimum and maximum values plotted (black circles), alongside the P10 values (blue circles) and P90 values (green circles) as calculated from the probability distribution curves estimated through Monte Carlo Simulation (results displayed in Figure 4.22).

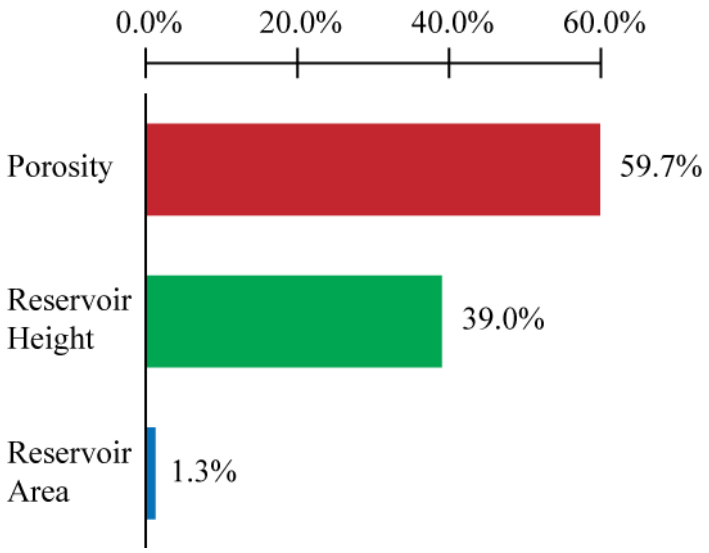

Figure 4.24 Sensitivity analysis run on the method of Bachu et al. (2007) Table 4.8, equation 1.1, throughout Monte Carlo Simulation. The results of the final probability distribution of the mass CO_2 storage capacity of the Hewett Lower Bunter Sandstone reservoir (see Figure 4.22 and Figure 4.23) are most sensitive to porosity, followed by the reservoir height and the reservoir area.

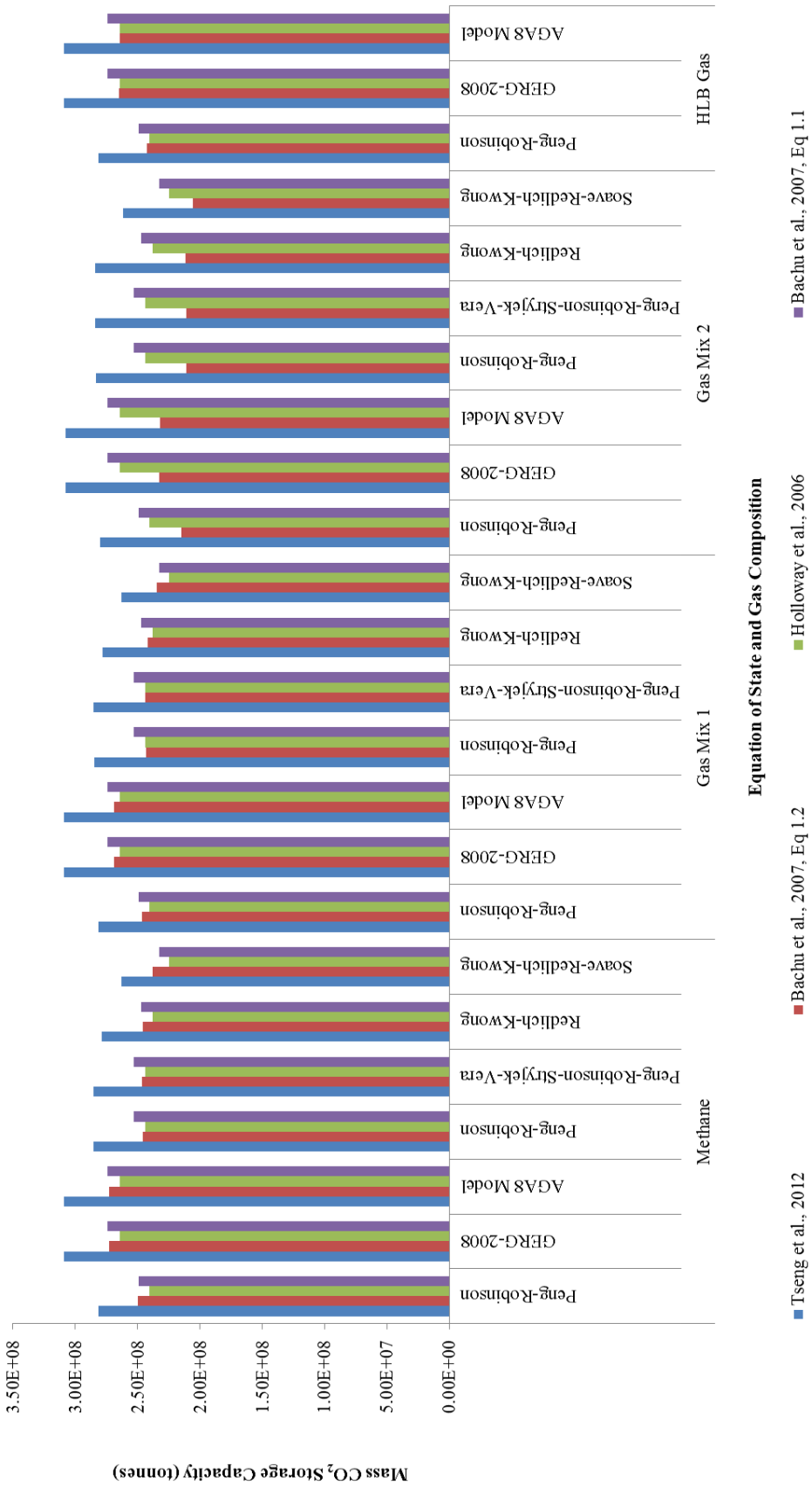

Figure 4.25 Estimated Theoretical CO_2 Storage Capacity of the Hewett Lower Bunter Sandstone reservoir using the methods of Bachu et al. (2007), Holloway et al. (2006) and Tseng et al. (2012).

	METHANE						
	REFPROP			WEBGASEOS			
	PR	GERG-2008	AGA8 Model	PR	PRSV	RK	SRK
Tseng et al., 2012	2.82E+08	3.09E+08	3.09E+08	2.85E+08	2.85E+08	2.79E+08	2.63E+08
% of Peng-Robinson (RefProp)	*100.0*	*109.8*	*109.8*	*101.2*	*101.3*	*98.9*	*93.4*
Bachu et al., 2007, Eq 1.2	2.50E+08	2.73E+08	2.73E+08	2.46E+08	2.46E+08	2.46E+08	2.38E+08
% of Peng-Robinson (RefProp)	*100.0*	*109.3*	*109.3*	*98.5*	*98.7*	*98.7*	*95.3*
Holloway et al., 2006	2.41E+08	2.64E+08	2.64E+08	2.44E+08	2.44E+08	2.38E+08	2.25E+08
% of Peng-Robinson (RefProp)	*100.0*	*109.8*	*109.7*	*101.3*	*101.3*	*98.9*	*93.3*
Bachu et al., 2007, Eq 1.1	2.49E+08	2.74E+08	2.74E+08	2.53E+08	2.53E+08	2.47E+08	2.33E+08
% of Peng-Robinson (RefProp)	*100.0*	*110.0*	*110.0*	*101.6*	*101.6*	*99.2*	*93.6*
Average Percentage Variation	100.0	109.7	109.7	100.7	100.7	98.9	93.9

	GAS MIX 1						
	REFPROP			WEBGASEOS			
	PR	GERG-2008	AGA8 Model	PR	PRSV	RK	SRK
Tseng et al., 2012	2.82E+08	3.09E+08	3.09E+08	2.85E+08	2.85E+08	2.78E+08	2.63E+08
% of Peng-Robinson (RefProp)	*100.0*	*109.8*	*109.8*	*101.2*	*101.3*	*98.9*	*93.4*
Bachu et al., 2007, Eq 1.2	2.46E+08	2.69E+08	2.69E+08	2.43E+08	2.44E+08	2.42E+08	2.35E+08
% of Peng-Robinson (RefProp)	*100.0*	*109.1*	*109.1*	*98.8*	*98.9*	*98.2*	*95.3*
Holloway et al., 2006	2.41E+08	2.64E+08	2.64E+08	2.44E+08	2.44E+08	2.38E+08	2.25E+08
% of Peng-Robinson (RefProp)	*100.0*	*109.8*	*109.7*	*101.3*	*101.3*	*98.9*	*93.3*
Bachu et al., 2007, Eq 1.1	2.49E+08	2.74E+08	2.74E+08	2.53E+08	2.53E+08	2.47E+08	2.33E+08
% of Peng-Robinson (RefProp)	*100.0*	*110.0*	*110.0*	*101.6*	*101.6*	*99.2*	*93.6*
Average Percentage Variation	100.0	109.7	109.7	100.7	100.8	98.8	93.9

	GAS MIX 2						
	REFPROP			WEBGASEOS			
	PR	GERG-2008	AGA8 Model	PR	PRSV	RK	SRK
Tseng et al., 2012	2.80E+08	3.08E+08	3.08E+08	2.84E+08	2.84E+08	2.84E+08	2.62E+08
% of Peng-Robinson (RefProp)	*100.0*	*109.9*	*109.8*	*101.2*	*101.3*	*101.3*	*93.4*
Bachu et al., 2007, Eq 1.2	2.15E+08	2.33E+08	2.32E+08	2.11E+08	2.11E+08	2.11E+08	2.06E+08
% of Peng-Robinson (RefProp)	*100.0*	*108.1*	*107.9*	*98.1*	*98.2*	*98.3*	*95.7*
Holloway et al., 2006	2.41E+08	2.64E+08	2.64E+08	2.44E+08	2.44E+08	2.38E+08	2.25E+08
% of Peng-Robinson (RefProp)	*100.0*	*109.8*	*109.7*	*101.3*	*101.3*	*98.9*	*93.3*
Bachu et al., 2007, Eq 1.1	2.49E+08	2.74E+08	2.74E+08	2.53E+08	2.53E+08	2.47E+08	2.33E+08
% of Peng-Robinson (RefProp)	*100.0*	*110.0*	*110.0*	*101.6*	*101.6*	*99.2*	*93.6*
Average Percentage Variation	100.0	109.4	109.4	100.5	100.6	99.4	94.0

	HLB INITIAL GAS COMPOSITION		
	REFPROP		
	PR	GERG-2008	AGA8 Model
Tseng et al., 2012	2.81E+08	3.09E+08	3.09E+08
% of Peng-Robinson (RefProp)	*100.0*	*109.8*	*109.8*
Bachu et al., 2007, Eq 1.2	2.43E+08	2.65E+08	2.65E+08
% of Peng-Robinson (RefProp)	*100.0*	*109.1*	*109.0*
Holloway et al., 2006	2.41E+08	2.64E+08	2.64E+08
% of Peng-Robinson (RefProp)	*100.0*	*109.8*	*109.7*
Bachu et al., 2007, Eq 1.1	2.49E+08	2.74E+08	2.74E+08
% of Peng-Robinson (RefProp)	*100.0*	*110.0*	*110.0*
Average Percentage Variation	100.0	109.7	109.7

Table 4.10 Percentage variation of theoretical CO_2 storage capacity estimation using the methods of Bachu et al. (2007), Holloway et al. (2006), and Tseng et al. (2012) and various equations of state when compared to the results given by the RefProp (Lemmon et al., 2013) estimated Peng-Robinson (Peng and Robinson, 1976) storage capacity estimate for the different gas compositions. PR is the Peng-Robinson equation of state (Peng and Robinson, 1976), PRSV is the Peng-Robinson-Stryjek-Vera equation of state (Stryjek and Vera, 1986), RK is the Redlich-Kwong equation of state (Redlich and Kwong, 1949), and SRK is the Soave-Redlich-Kwong equation of state (Soave, 1972).

4.5.4.2. EFFECTIVE CO_2 STORAGE CAPACITY ESTIMATES

Effective CO_2 storage capacity was estimated using the method of Tseng et al. (2012), Table 4.8, equations 1.6 and 1.7, for a reservoir that experiences no water drive. Results are displayed in Figure 4.26 and Table 4.11. Unfortunately, due to the limited number of parameters that can be input into the WebGasEOS online tool (Reagan and Oldenburg, 2006), the Hewett Lower Bunter Gas Composition could only be modelled using RefProp software (Lemmon et al., 2013). However, the results show an effective storage capacity within the Hewett Lower Bunter Sandstone reservoir ranging between 240 and 261 Mt CO_2 depending on the equation of state used and based on the initial gas composition. These results are discussed in section 4.6.3.

As for theoretical CO_2 storage capacity estimation, the GERG-2008 equation of state (Kunz and Wagner, 2012), closely followed by the AGA8-DC92 Model (Starling and Savidge, 1992) always predicts the highest storage capacities, whereas the Soave-Redlich-Kwong (Soave, 1972) equation of state predicts the lowest storage capacities (see Table 4.11). When compared to the results of the Peng-Robinson equation of state (Peng and Robinson, 1976) estimated using RefProp (Lemmon et al., 2013), the results predicted using the GERG-2008 equation of state (Kunz and Wagner, 2012) are ~8.4% greater, and the results predicted using the Soave-Redlich-Kwong equation of state (Soave, 1972) are ~4.4% lower (see Table 4.11).

4.5.5. COMPARISON WITH PUBLISHED CO_2 STORAGE CAPACITY ESTIMATES FOR THE HEWETT LOWER BUNTER SANDSTONE RESERVOIR

Holloway et al., (2006) and E.ON. (2009) have estimated the theoretical storage capacity of the Hewett Lower Bunter Sandstone reservoir to be 237 Mt CO_2. Estimates of storage capacity were made using the equation of Holloway et al., (2006), Table 4.8, equation 1.3, in both cases. The results predicted within this study using this equation predict theoretical storage capacities within the range 225-

264 Mt CO_2, depending on the particular equation of state used. Information on the equation of state used within the studies of Holloway et al., (2006) and E.ON. (2009) have not been included, however the prediction within this study of 238 Mt CO_2 made using the Redlich-Kwong equation of state in WebGasEOS (Reagan and Oldenburg, 2006) agrees most favourably with their predictions.

Baker-RDS in their joint report with E.ON. to the Kingsnorth Carbon Capture and Storage Project have also estimated the theoretical storage capacity of the Hewett Lower Bunter Sandstone reservoir at 205.8 Mt CO_2 (BakerRDS, 2011a). This is based on limiting the pressure to 12.21 MPa at the crest of the field (BakerRDS, 2011a). The limiting pressure is derived from the hydrostatic pressure at the crest of the reservoir and is recommended so as not to breach the cap rock seal (BakerRDS, 2011a). The theoretical storage capacity result is lower than those estimated using the methods in this study due to the pressure limitation.

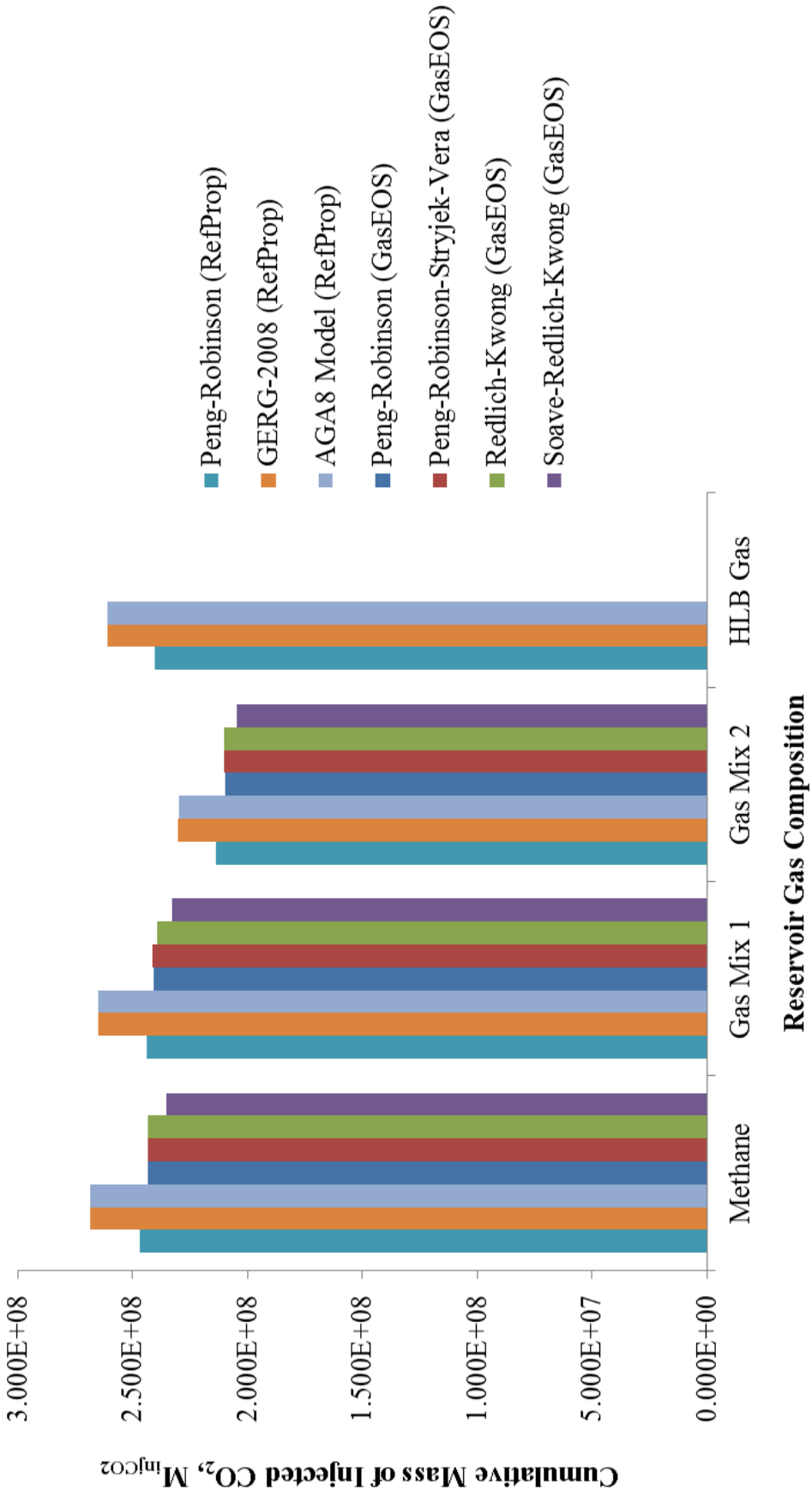

Figure 4.26 Estimated effective CO_2 storage capacity using the method of Tseng et al. (2012) and modelled with both RefProp (Lemmon et al., 2013) and the online tool by the Lawrence Berkeley National Laboratories, WebGasEOS (Reagan and Oldenburg, 2006).

	REFPROP			WEBGASEOS			
	PR	GERG-2008	AGA8 Model	PR	PRSV	RK	SRK
METHANE	2.47E+08	2.68E+08	2.68E+08	2.43E+08	2.44E+08	2.43E+08	2.35E+08
% of Peng-Robinson (RefProp)	*100.0*	*108.8*	*108.8*	*98.6*	*98.7*	*98.7*	*95.5*
GAS MIX 1	2.44E+08	2.65E+08	2.65E+08	2.41E+08	2.41E+08	2.39E+08	2.33E+08
% of Peng-Robinson (RefProp)	*100.0*	*108.6*	*108.7*	*98.8*	*99.0*	*98.2*	*95.5*
GAS MIX 2	2.14E+08	2.30E+08	2.30E+08	2.10E+08	2.10E+08	2.10E+08	2.05E+08
% of Peng-Robinson (RefProp)	*100.0*	*107.8*	*107.6*	*98.1*	*98.3*	*98.3*	*95.8*
HLB GAS	2.40E+08	2.61E+08	2.61E+08				
% of Peng-Robinson (RefProp)	*100.0*	*108.6*	*108.5*				
Average Percentage Variation	100.0	108.4	108.4	98.5	98.7	98.4	95.6

Table 4.11 Percentage variation of effective CO_2 storage capacity estimation using the method of Tseng et al. (2012) and various equations of state when compared to the results given by the RefProp (Lemmon et al., 2013) estimated Peng-Robinson (Peng and Robinson, 1976) storage capacity estimate for the different gas compositions. PR is the Peng-Robinson equation of state (Peng and Robinson, 1976), PRSV is the Peng-Robinson-Stryjek-Vera equation of state (Stryjek and Vera, 1986), RK is the Redlich-Kwong equation of state (Redlich and Kwong, 1949), and SRK is the Soave-Redlich-Kwong equation of state (Soave, 1972).

4.6. DISCUSSION

4.6.1. SUMMARY

The observations over the productive lifetime of the Hewett Lower Bunter Sandstone reservoir and the results of the combined analysis of the various datasets have shown that the reservoir has the potential to be a good quality storage site for CO_2. Production from the reservoir has been simple and predictable with no water influx from adjacent aquifers throughout the productive lifetime hindering well performance.

The reservoir is considered to offer a considerable storage capacity for CO_2. The methods described above have given a range of possible CO_2 storage capacities for the reservoir. Theoretical storage capacity methods of Bachu et al., (2007), Holloway et al., (2006) and Tseng et al. (2012) have yielded results in the order of hundreds of megatons of CO_2. Effective storage capacities of Tseng et al., (2012) have further constrained these initial estimates yielding slightly lower results in the order of hundreds of megatons of CO_2.

4.6.2. IMPACT OF EQUATION OF STATE ON STORAGE CAPACITY ESTIMATION

Six equations of state were used in the investigation of CO_2 storage capacity within the Hewett Lower Bunter Sandstone reservoir. Estimation with RefProp (Lemmon et al., 2013) utilised equations of state predicted by the Peng-Robinson (Peng and Robinson, 1976), GERG-2008 (Kunz and Wagner, 2012) and AGA8-DC92 Model (Starling and Savidge, 1992). Estimation with WebGasEOS (Reagan and Oldenburg, 2006) used the Peng-Robinson (Peng and Robinson, 1976), Peng-Robinson-Stryjek-Vera (Stryjek and Vera, 1986), Redlich-Kwong (Redlich and Kwong, 1949) and Soave-Redlich-Kwong (Soave, 1972) equations of state.

The variability between the method and equations of state used to estimate theoretical CO_2 storage capacity within the Hewett Lower Bunter Sandstone reservoir are shown in Figure 4.25 and Table 4.10. For the Hewett Lower Bunter

Sandstone reservoir initial gas composition, the minimum theoretical CO_2 storage capacity is estimated at 241 Mt CO_2 predicted by equation 1.3 (Holloway et al., 2006) and using the Peng-Robinson equation of state (Peng and Robinson, 1976). The maximum theoretical CO_2 storage capacity is estimated at 309 Mt tonnes CO_2, predicted by equation 1.4 (Tseng et al., 2012) and using the GERG-2008 equation of state (Kunz and Wagner, 2012). This equates to a total difference of 68 Mt CO_2 between the particular method of storage capacity and equation of state used.

Similarly, Figure 4.26 and Table 4.11 show the results of effective CO_2 storage capacity estimation. For the Hewett Lower Bunter Sandstone reservoir initial gas composition, minimum effective CO_2 storage capacity estimates range between 240 Mt CO_2 (as predicted using the Peng-Robinson equation of state (Peng and Robinson, 1976)) and 261 Mt CO_2 (as predicted using the GERG-2008 equation of state (Kunz and Wagner, 2012)).

Table 4.10 and Table 4.11 also show the percentage variation of theoretical and effective CO_2 storage capacity estimates, respectively, from the resulting estimate predicted by the Peng-Robinson equation of state (Peng and Robinson, 1976) using RefProp (Lemmon et al., 2013). Percentage variation was compared to Peng-Robinson (Peng and Robinson, 1976) of RefProp (Lemmon et al., 2013) for three reasons: (1) the Peng-Robinson equation of state (Peng and Robinson, 1976) can be modelled in both RefProp (Lemmon et al., 2013) and WebGasEOS (Reagan and Oldenburg, 2006), therefore, results are comparable; (2) equations of state can be modelled within RefProp (Lemmon et al., 2013) up with a high degree of accuracy – results can be modelled up to 12 significant figures; and (3) the Peng-Robinson equation of state (Peng and Robinson, 1976) has been established since 1976 and has been used extensively in the oil and gas industry for many years due to its performance.

It is useful to compare the percentage variation of CO_2 storage capacity estimation whilst varying the method and the particular equation of state used. As has been previously stated the GERG-2008 equation of state tends to predict the highest storage capacity estimates and the Soave-Redlich-Kwong the lowest storage capacity estimates for both theoretical and effective methods. However, what is particularly interesting to note is that the CO_2 storage capacity estimates vary by

almost the same percentage when the gas composition changes. For example, in Figure 4.10 the percentage variation of capacity estimates of the AGA8-DC92 Model are all around 112%, even while the gas composition alters between pure methane, gas mix 1, gas mix 2 and the Hewett Lower Bunter Sandstone reservoir initial gas composition.

Unfortunately, the limitations of WebGasEOS mean that storage capacity estimates for the Hewett Lower Bunter Sandstone reservoir initial gas composition cannot be modelled. Therefore, it is necessary to use RefProp to estimate storage capacity with any reasonable degree of accuracy within the Hewett Lower Bunter Sandstone reservoir. As such, it is important to understand the limitations of the equations of state used within the software.

The GERG-2008 (Kunz and Wagner, 2012) and AGA8 Model (Starling and Savidge, 1992) equations of state were specifically developed for natural gas environments, which also include CO_2, therefore they are optimised for use within storage complexes being considered for carbon storage. The Peng-Robinson (Peng and Robinson, 1976) equation of state has been utilised for many years within the oil and gas industry, however, the GERG-2008 (Kunz and Wagner, 2012) and AGA8 Model (Starling and Savidge, 1992) equations of state are considered to supersede the performance of the Peng Robinson (Peng and Robinson, 1976) equation of state particularly at the vapour-liquid equilibrium, an important factor in carbon storage as CO_2 is to be stored as a supercritical fluid (see Figure 4.27). The vapour-liquid equilibrium is marked by the Vapour Liquid Saturation curve on Figure 4.27.

A comparison of the performance of the GERG-2008 (Kunz and Wagner, 2012) and Peng-Robinson (Peng and Robinson, 1976) equations of state is shown in Figure 4.28. The GERG-2008 equation of state (Kunz and Wagner, 2012) has an improved performance at higher temperatures and pressures, better reflecting the results from experimental data than the Peng-Robinson equation of state (Peng and Robinson, 1976). The higher pressure and temperature region of 90-450 K and up to 35 MPa (Kunz and Wagner, 2012) reflect the Hewett Lower Bunter Sandstone reservoir initial pre-production conditions. These conditions are likely to prevail once again post-CO_2 injection. As such, it is likely that the GERG-2008 equation

of state (Kunz and Wagner, 2012) is one of the best equations of state to use in the modelling of fluid properties with respect to CO_2 storage within depleted gas reservoirs.

The GERG-2008 equation of state (Kunz and Wagner, 2012) has greater accuracy than that of the AGA8-DC92 equation of state (Starling and Savidge, 1992) within multi-component mixtures, as are dealt with here, particularly for temperatures below 290 K and for mixtures of unusual composition (Kunz and Wagner, 2012), i.e. a depleted gas reservoir containing a residual gas mixture being re-pressurised with increasing volumes of CO_2. The GERG-2008 equation of state (Kunz and Wagner, 2012) also performs better than the AGA8-DC92 equation of state (Starling and Savidge, 1992) over the entire fluid region – the region of interest for this study, i.e. in the homogenous gas, liquid and supercritical regions and for vapour-liquid equilibrium states (Kunz and Wagner, 2012). The GERG-2008 equation of state (Kunz and Wagner, 2012) is able to represent the most accurate experimental data for gas-phase and gas-like supercritical densities to within their low experimental uncertainty (Kunz and Wagner, 2012), unlike the AGA8-DC92 equation of state (Starling and Savidge, 1992), again a key region of interest in this study. Accuracy is within 0.05-0.1% for temperatures down to 250 K and at pressures up to 30 MPa (Kunz and Wagner, 2012).

In summary, the AGA8-DC92 (Starling and Savidge, 1992) and GERG-2008 (Kunz and Wagner, 2012) equations of state show major improvements in accuracy of the prediction of fluid properties compared to the Peng-Robinson equation of state (Peng and Robinson, 1976). However, the GERG-2008 equation of state (Kunz and Wagner, 2012) supersedes the accuracy of the AGA8-DC92 equation of state (Starling and Savidge, 1992) particularly in the description of gas-phase and gas-like supercritical densities of natural gas mixtures containing: (1) high fractions of nitrogen, (2) high fractions of carbon dioxide, (3) high fractions of ethane, (4) substantial amounts of ethane, propane and heavier hydrocarbons, (5) high fractions of hydrogen, (6) considerable amounts of carbon monoxide, or (7) noticeable fractions of oxygen (Kunz and Wagner, 2012).

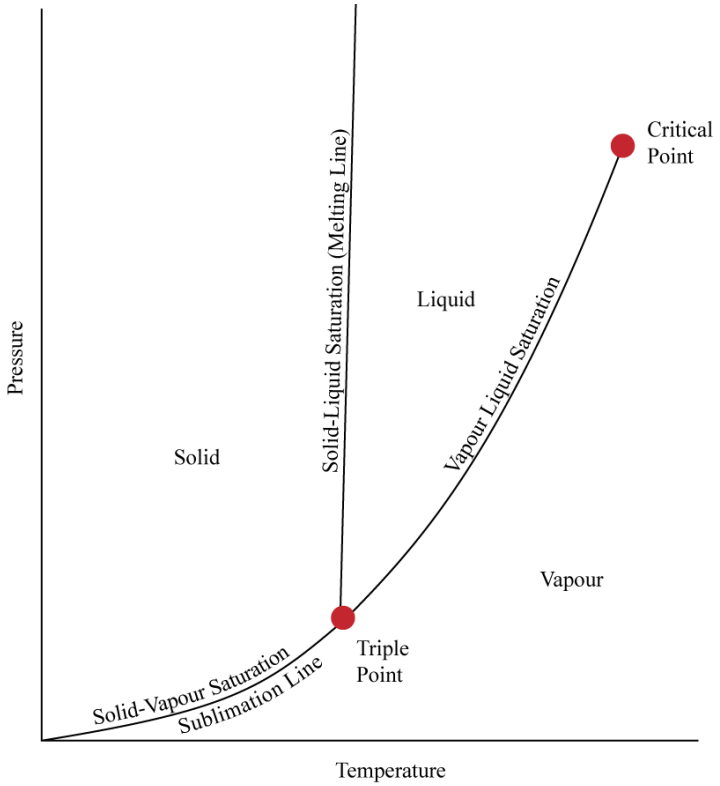

Figure 4.27 Schematic pressure-temperature graph for a pure substance.

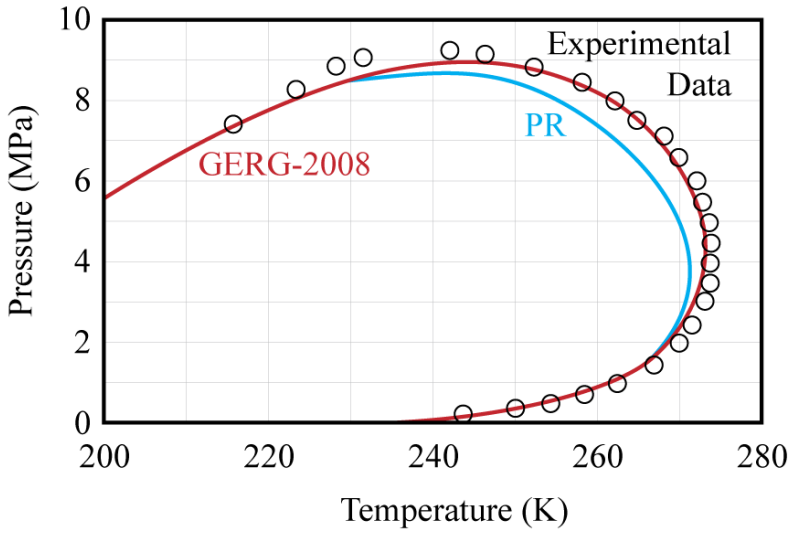

Figure 4.28 P-T graph showing the vapour liquid phase boundary of a 12 component synthetic natural gas mixture illustrating a comparison of the performance of the Peng-Robinson (Peng and Robinson, 1976) and GERG-2008 (Kunz and Wagner, 2012) equations of state with experimental dew-point data in regions of high pressure and temperature. The high pressures and temperatures reflect the initial reservoir conditions within the Hewett Lower Bunter Sandstone reservoir. After Kunz and Wagner (2012).

4.6.3. IMPACT OF CO_2 STORAGE CAPACITY METHOD ON ESTIMATES

The theoretical storage capacity estimation methods of Bachu et al. (2007), Table 4.8, equations 1.1 and 1.2, Holloway et al. (2006), Table 4.8, equation 1.3, and Tseng et al. (2012), Table 4.8, equation 1.4, have differing degree of complexity. The methods of Bachu et al. (2007), Table 4.8, equations 1.1 and 1.2, and Holloway et al. (2006), Table 4.8, equation 1.3, are basic and do not require the input of a particular gas composition. The method of Bachu et al. (2007), Table 4.8, equation 1.1, is based around the geometry of the reservoir which is quite often difficult to constrain with any degree of accuracy due to the heterogeneous nature of a gas reservoir. The method of Holloway et al. (2006), Table 4.8, equation 1.3, is similar, however it is based around the volume of recoverable reserves in the reservoir and so does not rely on accurate geometric constraints. However, the method still does not allow the input of a particular gas composition into the equation.

The method of Bachu et al. (2007), Table 4.8, equation 1.2, is slightly more complex, and allows the input of a particular gas composition through its estimation of the gas compressibility factor in the reservoir. However, the method does not require estimation of the gas compressibility of CO_2, only CO_2 density at initial reservoir conditions.

The theoretical and effective CO_2 storage capacity estimation methods of Tseng et al., (2012), Table 4.8, equations 1.4, 1.6 and 1.7, are vastly more complex and involve estimation of the gas compressibility factors and gas formation volume factors of both the natural gas and CO_2 at the beginning and end of production at reservoir conditions. The density of CO_2 at initial pre-production conditions is also factored into the estimation.

The results show that the estimates of theoretical storage capacity achieved using the method of Bachu et al. (2007), Table 4.8, equation 1.1, show a great deal of variance. As previously stated, this method of estimation relies upon accurate representation of the geometry of the depleted gas reservoir. This is constrained through geological characterisation of the reservoir. However, there is the potential

for variability of the parameters used. Parameters such as the recovery factor, CO_2 density at reservoir conditions, volume of injected water and volume of produced water can generally be accurately constrained. However, difficulties lie in constraining parameters such as reservoir area, reservoir height and porosity.

Within this study, reservoir area has been calculated during seismic interpretation and is based on the area of the original gas-water contact. This is only an approximate estimate as the seismic horizon this has been estimated from is not a user mapped surface – it has been created within TrapTester by scaling it to occur beneath a user mapped horizon, based on well data (see section 4.4.1.).

The value used for reservoir thickness is also an approximation based on average well data. Over the entire field (i.e. an area of ~74,888,440 m^2) there are only nine wells with tops information that could be used to make this approximation.

Porosity shows a high degree of variability. Previously, in section 4.4.2.1., Monte Carlo simulation has been used to model the porosity data. In the case of the Hewett Lower Bunter Sandstone reservoir the data was shown to most closely resemble a Weibull distribution, however, the fit of the data to the probability distribution was shown to be poor. The Anderson-Darling P-value was 0.00 showing these data do not follow a specified distribution. The difficulty of modelling geological data to probability distributions is apparent throughout this study.

The method of effective CO_2 storage capacity estimation of Tseng et al. (2012), Table 4.8, equations 1.6 and 1.7, has been used here to further constrain the theoretical CO_2 storage capacity estimate of the same author. It is likely that this method will give the most accurate representation of storage capacity within the Hewett Lower Bunter Sandstone reservoir due to the increased number of parameters required, the majority of which can be accurately constrained. However, caution must be taken with the above estimates for theoretical and effective CO_2 storage capacities within a depleted gas reservoir. All the above methods do not account for cap rock or fault seal integrity, i.e. capillary entry pressures are not considered in their estimation.

4.6.4. THE USE OF MONTE CARLO SIMULATION WITHIN CO_2 STORAGE CAPACITY EQUATIONS

This study has attempted to improve upon previous work (such as that of Bentham (2006), Brook et al. (2003), Holloway et al. (2006) and Kirk (2006)) by attempting to honour all available porosity data within the geometric method of CO_2 storage capacity estimation of Bachu et al. (2007), Chapter 1, equation 1.1. The porosity data was assigned a best-fit probability distribution which was truncated at 0% porosity (as it is not possible to have a negative measurement for porosity). Monte Carlo simulation was then run thousands of times over which allowed repeated random sampling of the assigned probability distribution to input porosity values into the storage capacity equation. This produced a substantial range of variation in the resulting storage capacity estimates.

The primary issue with this method is that it was not possible to assign a probability distribution which fit the porosity data with any degree of confidence. When the Anderson-Darling P-value test was applied, which tests for normality, the resulting P-value was equal to 0.00, i.e. the data do not follow a specified distribution. Therefore, it is not appropriate to conduct Monte Carlo simulation that samples from this distribution to estimate CO_2 storage capacity.

As such, until a better solution can be incorporated into the CO_2 storage capacity method of Bachu et al. (2007), Chapter 1, equation 1.1, which attempts to honour all available porosity data for a reservoir, it is most likely better to use mean porosity values.

4.7. CONCLUSIONS

The integrated analysis of reservoir structure, petrophysical characterisation and thermodynamic behaviour of the Hewett Lower Bunter Sandstone reservoir has shown the potential for it to be a good quality CO_2 storage site. Its productive lifetime has shown the reservoir to be simple and predictable in its behaviour, with no water encroachment hindering well performance. The depletion drive status of the Hewett Lower Bunter Sandstone reservoir has been proven through the use of

material balance methods including Cole plots. As such, the reservoir is one of the best to develop methods to better constrain input parameters to CO_2 storage capacity estimation methods – its depletion drive status means that any fluid added or removed from the reservoir can be accounted for through production or injection, meaning dynamic reservoir behaviour is simple to understand, and projections of future behaviour throughout CO_2 injection and after should be easily ascertainable with a certain degree of confidence.

Overall, the best equation of state for estimating fluid properties within natural gas environments being re-pressurised with large volumes of CO_2 was found to be the GERG-2008 equation of state (Kunz and Wagner, 2012), with the results from the AGA8-DC92 equation of state (Starling and Savidge, 1992) showing close comparison. The methods of CO_2 storage capacity estimation found to best represent that of the Hewett Lower Bunter Sandstone reservoir were the theoretical and effective methods of Tseng et al. (2012). The estimated theoretical CO_2 storage capacity of the Hewett Lower Bunter Sandstone reservoir was found to be 309 Mt CO_2 using the method of Tseng et al. (2012) and the GERG-2008 equation of state (Kunz and Wagner, 2012). The estimated effective CO_2 storage capacity of the Hewett Lower Bunter Sandstone reservoir was found to be 261 Mt CO_2 using the method of Tseng et al. (2012) and the GERG-2008 equation of state (Kunz and Wagner, 2012). However, caution must be taken when considering these estimates – they represent a maximum estimate within the Hewett Lower Bunter Sandstone reservoir and do not take into account other geological limitations such as cap rock integrity or fault seal integrity, i.e. estimation of capillary entry pressure.

5 The Hewett Upper Bunter Reservoir: Geological Characterisation for Carbon Dioxide Storage and Storage Capacity Estimation within a High Quality Depleted Gas Reservoir with a Water Drive

5.1. INTRODUCTION

True depletion drive reservoirs (i.e. those that experience no rock compaction and no aquifer influx) such as the Hewett Lower Bunter Sandstone reservoir (Chapter 4) are rare in occurrence (Hagoort, 1988). They can be represented by the expression:

$$\begin{matrix} Initial\ gas\ volume \\ at\ initial\ pressure \end{matrix} = \begin{matrix} Remaining\ gas\ volume \\ at\ lower\ pressure \end{matrix}$$

hence,

$$G(B_{gi}) = (G - G_p)B_g \tag{5.1}$$

(Archer and Wall, 1986)

Parameters have been previously defined in Chapter 3, section 3.4.1.

However, the majority of gas reservoirs experience some degree of water drive: production typically induces aquifer influx to the reservoir. The cumulative volume of water influx at reservoir conditions, W_e, is an important parameter within

water drive reservoirs. It gives an indication of aquifer strength and governs reservoir performance. On a material balance plot (P/z vs. G_p) field data will typically deviate from linearity as a result of water influx (increasing pressure support and W_e) or aquifer depletion (decreasing pressure support and W_e by fluid transport to another reservoir) (Archer and Wall, 1986). The material balance equation can be re-written as:

$$G(B_{gi}) = (G - G_p)B_g + W_e - W_p B_w \tag{5.2}$$

(Archer and Wall, 1986)

Estimation of W_e is not only important for the geological characterisation of water drive reservoirs, but also for theoretical and effective CO_2 storage capacity estimation. The methods of Tseng et al. (2012) are used once again to estimate effective storage capacity via the following equations in Table 5.1:

STORAGE CAPACITY EQUATION	EQUATION NUMBER
$M_{injCO2} = \rho_{CO2r} . G_{injCO2}$	(1.6)
$G_{injCO2} = G_{phc} - G_{ihc} + \frac{P_{reshc/CO2}}{z_{reshc/CO2}} \left(\frac{z_{ihc}}{P_{ihc}} G_{ihc} - W_e \frac{T_{sc}}{P_{sc} T} \right)$	(1.7)

Table 5.1 Effective CO_2 storage capacity equations of Tseng et al. (2012) previously introduced in Chapter 1.

As can be seen, equation 1.7 in Table 5.1 requires a value for W_e to calculate the effective volume of CO_2, the result of which is a key parameter within equation 1.6 of Table 5.1.

The Hewett Upper Bunter Sandstone reservoir of the Hewett Gas Field, UK Southern North Sea is adopted as a case study to further develop the methods in Chapter 4, but for a depleted gas reservoir with a water drive. The reservoir is advantageous for the further development of methods due to its abundance of data and its well-understood production history. The reservoir is more complex than the Hewett Lower Bunter Sandstone reservoir (Chapter 4) not only in terms of water drive but also in terms of trap closure (structure), being three-way dip closed with fault closure on one flank. Further methods developed include analysis of fault seal integrity with interpretation of potential fluid migration pathways out of the reservoir. These analyses may indicate connectivity between the Hewett Upper Bunter Sandstone reservoir and neighbouring reservoirs through a shared aquifer (i.e. the Bunter aquifer). If so, the nature of the connectivity will be investigated through analysis of reservoir hydraulic heads. Additionally, aquifer influx rates are estimated (through calculation of hydraulic diffusivity), thus giving an indication on the rate of natural re-pressurisation of the Hewett Upper Bunter Sandstone reservoir with aquifer waters. This is necessary to assess the volume of available pore space for CO_2 currently unoccupied by water.

Theoretical and effective storage capacity estimations for the Hewett Upper Bunter Sandstone reservoir will be calculated (as for Chapter 4). Once again, the methods of Bachu et al., (2007), Chapter 1, equations 1.1 and 1.2, Holloway et al., (2006), Chapter 1, equation 1.3, and Tseng et al., (2012) Chapter 1, equations 1.4, 1.6 and 1.7, will be used for estimation. The effects that (a) geometric, petrophysical, productive behaviour and thermodynamic properties have on estimations of theoretical and effective CO_2 storage capacity, and (b) the variability of the resulting storage capacity estimations that arise due to the different approaches outlined above, will again be investigated.

This study is the first of its kind to provide methods for estimating aquifer influx rates within water drive depleted gas reservoirs where produced water, W_p, has not been metered, through estimation of hydraulic diffusivity. Furthermore, the study will quantify a range of values for effective CO_2 storage capacity based upon chosen equations of state within the Hewett Upper Bunter Sandstone reservoir for the first time.

5.2. PUBLISHED CO_2 STORAGE CAPACITY ESTIMATES

Previous published theoretical storage capacity estimates for the entire Hewett Gas Field have been described in Chapter 4, section 4.2, with an overview in Table 4.1. There are few studies that have estimated the theoretical storage capacity for the Hewett Upper Bunter Sandstone reservoir. Holloway et al., (2006) and E.ON. (2009) have estimated the theoretical storage capacity of the reservoir to be 122 Mt CO2. This equates to a storage lifetime of just over 12.5 years at the post-demonstrator injection pressure of 26,400 tonnes/day proposed for the underlying Hewett Lower Bunter Sandstone reservoir.

5.3. THE ORIGINAL PETROLEUM PLAY

The regional geological setting of the Hewett Gas Field has been described in Chapter 2. The distribution and thickness of the Upper Bunter Sandstone Formation within the Southern North Sea is illustrated in Figure 5.1. Table 5.2 summarises the major geological properties of the Hewett Upper Bunter Sandstone reservoir as a productive petroleum field. The original petroleum play characteristics are summarised below, before a more detailed analysis of the geometric, petrophysical properties and productive characteristics of the reservoir.

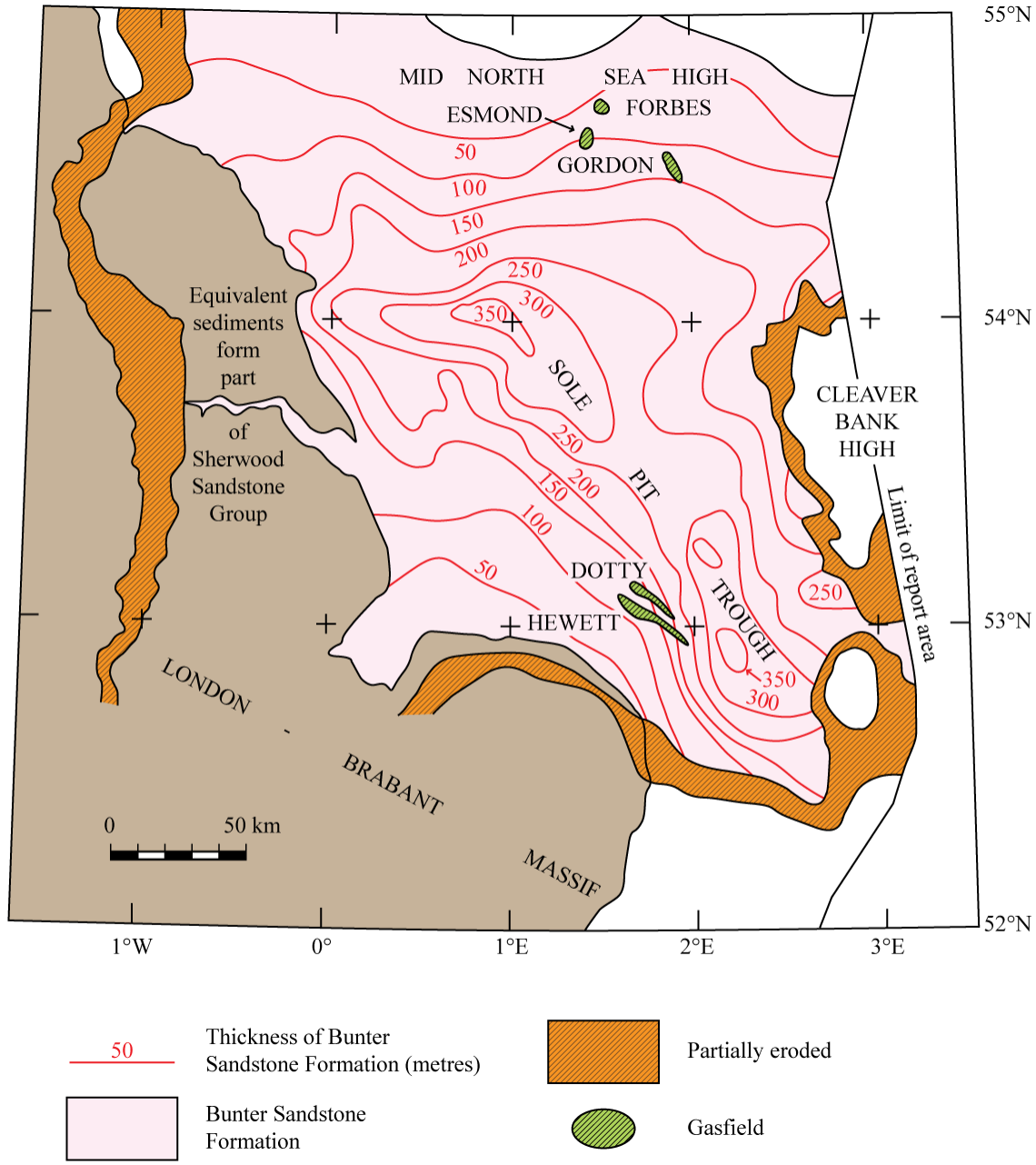

Figure 5.1 Distribution and thickness of the Bunter Sandstone Formation. Adapted from Cameron et al. (1992).

5.3.1. THE HEWETT UPPER BUNTER SANDSTONE RESERVOIR

The Hewett Upper Bunter Sandstone reservoir is located within the Hewett Field of the Southern North Sea, stratigraphically higher than the Hewett Lower Bunter Sandstone reservoir (Figure 5.2). The reservoir consists of a thick sequence of coarse grained fluvial sandstones interbedded with mudstones. The lithology and structure of the Hewett Upper Bunter Sandstone Formation has been described previously in Chapter 2. However, it has formed as an amalgamation of several alluvial fans originating from onshore the east coast of the UK and the London-Brabant Platform to the south. It is thickest (350 m) in the Sole Pit Trough, but thins towards the London-Brabant Platform, Cleaver Bank High and Mid North Sea High (see Figure 5.1) (Cameron et al., 1992).

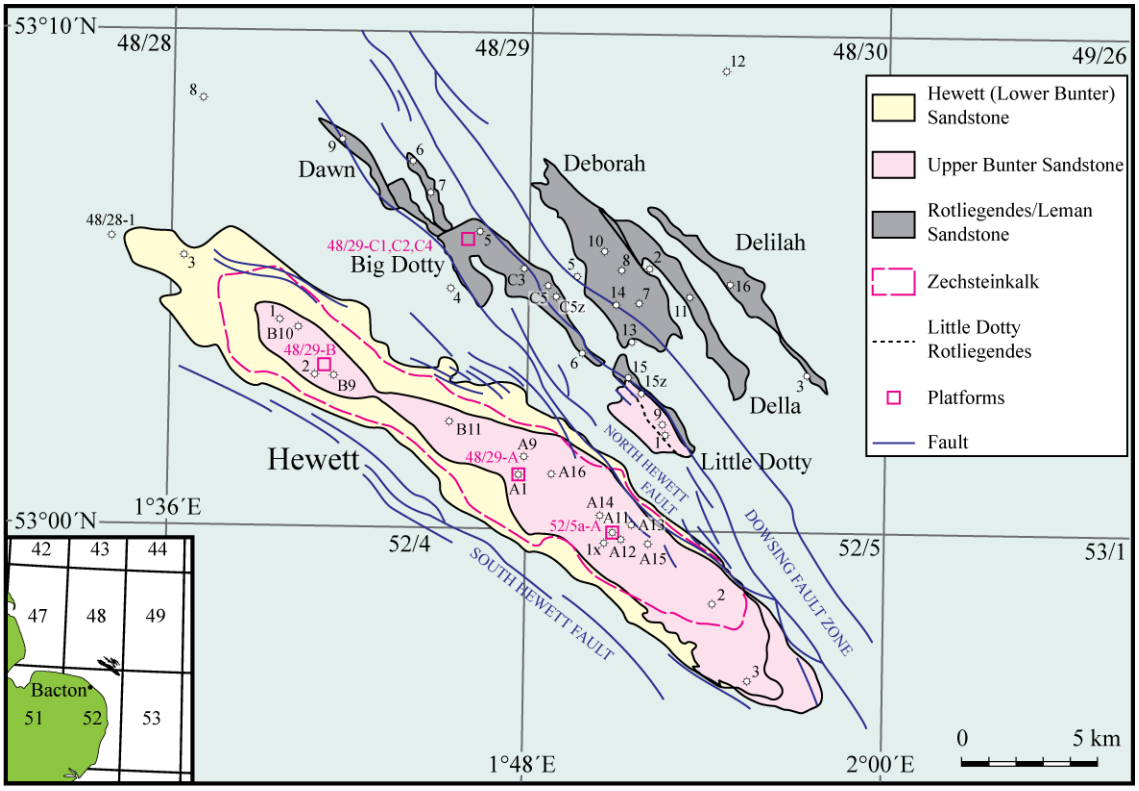

Figure 5.2 Location and structure of the Hewett Unit, UK Southern North Sea. Only major faults and their trends are displayed. The original gas-water contacts of the reservoir play areas are shown. Wells and platforms are displayed for reference. Adapted from Cooke-Yarborough and Smith (2003).

The Hewett Upper Bunter Sandstone reservoir has produced natural gas since it came online in 1973. The reservoir is underlain by the regional Bunter aquifer and has experienced water influx associated with production. During the late 1980s the degree of water influx was so high there was a high risk of the Hewett Upper Bunter Sandstone reservoir watering out (Cooke-Yarborough and Smith, 2003). However, following the onset of production from the neighbouring Little Dotty Upper Bunter Sandstone reservoir in 1986 water influx to the Hewett Upper Bunter Sandstone reservoir slowed, and by 1990 effectively stopped (Cooke-Yarborough and Smith, 2003).

As such, the dynamic behaviour of the Bunter aquifer and the Hewett and Little Dotty Upper Bunter Sandstone reservoirs needs to be better understood in order to gain accurate estimations of W_e (previously described in section 5.1). An understanding of observed behaviour throughout the productive lifetime of the Hewett Unit (encompassing the Hewett Gas Field and surrounding six 'D' fields, see Figure 5.2) will be used to support predictions of behaviour during the storage lifetime of the Hewett Upper Bunter Sandstone reservoir. This will help to ensure effective and secure storage of CO_2.

5.3.2. TRAP

The Hewett Upper Bunter Sandstone trap is three-way dip-closed to the north, west and south according to the Hewett Field records. The trap is closed by the North Hewett Fault on the central eastern flank. This structure is investigated further within the 3D seismic interpretation and structural modelling of the datasets provided (see section 5.4.1.).

5.3.3. DIRECT CAP ROCK

The Dowsing Dolomitic Formation of the Haisborough Group forms the direct cap rock to the Hewett Upper Bunter reservoir. The lithology of the Dowsing Dolomitic Formation has previously been described in detail in Chapter 2. The cap rock has an average thickness of 162.7 m over much of the Hewett anticline. The

average thickness was calculated from well data made available to Durham University by IHS. The Dowsing Dolomitic Formation thins towards the south-east of the anticline within Quad 52 to an average of 103.7 m.

The Dowsing Dolomitic Formation has provided a proven reliable hydrocarbon seal over geological time scales with no evidence of gas having entered or migrated through the cap rock as indicated by the absence of structures such as gas chimneys penetrating through the reservoir and cap rock on the 3-D seismic dataset.

5.3.4. OVERBURDEN STRATA

The Dudgeon Saliferous Formation and the Triton Anhydritic Formation of the Haisborough Group directly overlie the Dowsing Dolomitic Formation, with a total thickness of approximately 420 m directly above the Hewett Gas Field. Above this lie the Penarth Group and the Lias Group, previously described in Chapter 2.

Overburden Strata	
Geological Formation	Cromer Knoll Group
Depositional Environment	Marine
Depositional Facies	Shallow marine
Age	Lower Cretaceous
Geological Formation	Lias Group
Depositional Environment	Marine
Depositional Facies	Marine shelf
Age	Lower Jurassic
Geological Formation	Haisborough Group
Depositional Environment	Terrestrial and transitional
Depositional Facies	Sabkha, restricted marine and flood plain
Age	Triassic
Direct Cap Rock	
Geological Formation	Dowsing Formation, Haisborough Group
Depositional Environment	Terrestrial
Depositional Facies	Alluvial, flood plain
Age	Lower – Middle Triassic, Anisian - Ladinian
Average Thickness (m)	143
Trap	
Structure	Structural anticline, three-way dip closure, fault closure along central eastern flank
Depth to crest (m)	790
Initial gas column (m)	130
Initial gas-water contact (m)	920
Reservoir	
Geological Formation	(Upper) Bunter Sandstone Formation
Depositional Environment	Alluvial
Age	Lower Triassic
Lateral extent/play area (m^2)	60,000,000
Average Thickness (m)	165.5
Net/gross ratio	0.96
Average Porosity (%)	21
Average Permeability (mD)	500
Average hydrocarbon saturation (%)	78
Irreducible water saturation (%)	22
Isolated or underlain by aquifer?	Underlain by aquifer
Petroleum/Field Characteristics	
Formation volume factor (stand. cond./res. cond.)	97
Original gas in place (m^3)	3.84E+10
Initial pressure (MPa)	9.391
Reservoir temperature (°C)	42.2
Recovery factor	0.898

Table 5.2 Hewett Upper Bunter Sandstone Reservoir Properties (adapted from Cooke-Yarborough and Smith (2003))

5.4. GEOMETRIC, PETROPHYSICAL AND PRODUCTION CHARACTERISTICS

5.4.1. 3-D SEISMIC INTERPRETATION RESULTS

The same well-calibrated 3-D seismic dataset used for interpretation of the Hewett Lower Bunter Sandstone reservoir was used for the Upper Bunter Sandstone reservoir. The details of the dataset have previously been described in Chapter 4, section 4.4.1.

Once again, the 3-D seismic dataset of the Hewett Unit was interpreted using Landmark SeisWorks for horizon interpretation and TrapTester 6.0 for 3-D structural modelling. Laterally continuous reflectors of the Winterton Formation, Dudgeon Saliferous Formation, top Bunter Sandstone Formation, Zechsteinkalk and the Rotliegendes Sandstone Formation were interpreted within the 3-D seismic volume to produce a series of time structure maps. Stratigraphic control was provided by the formation tops within well 048/29-A01. The time structure map of the Bunter Sandstone Formation is shown in Figure 5.3.

It is apparent the North Hewett Fault plays a role in the secure storage of CO_2 within the Hewett Upper Bunter Sandstone reservoir, therefore the fault seal integrity was analysed within TrapTester 6.0. Fault polygons were constructed for major faults and important minor faults throughout the 3-D seismic volume, using methods developed by Bretan (1992, 1992b), Childs et al. (2003), Freeman et al. (1990), Needham et al. (1996), Walsh et al. (2003) and Walsh and Watterson (1988).

Juxtaposition analysis along the North Hewett Fault (Figure 5.4) shows that the Hewett Upper Bunter Sandstone reservoir interval is not self-juxtaposed across the majority of the fault from the southeast to northwest. In fact, the reservoir in this region is juxtaposed against sealing unit of the Haisborough Group. However, within 2 km of the northwest lateral tip of the North Hewett Fault, sand-sand juxtaposition occurs with the Bunter Sandstone Formation self-juxtaposed.

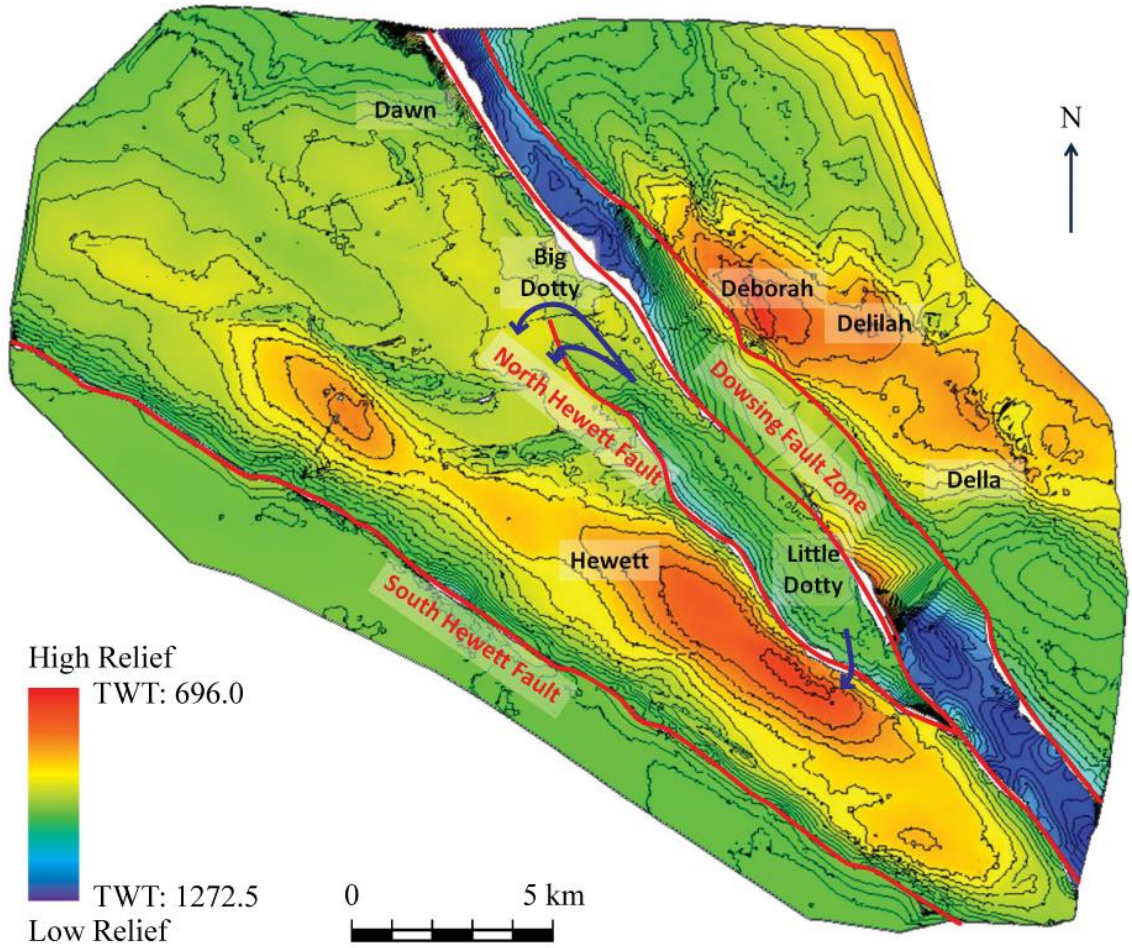

Figure 5.3 Annotated Time Structure Map of the Top Bunter Sandstone Formation within the Hewett Unit. Potential pressure communication pathways, via the regional Bunter aquifer, are illustrated as dark blue arrows. Interpreted in TrapTester.

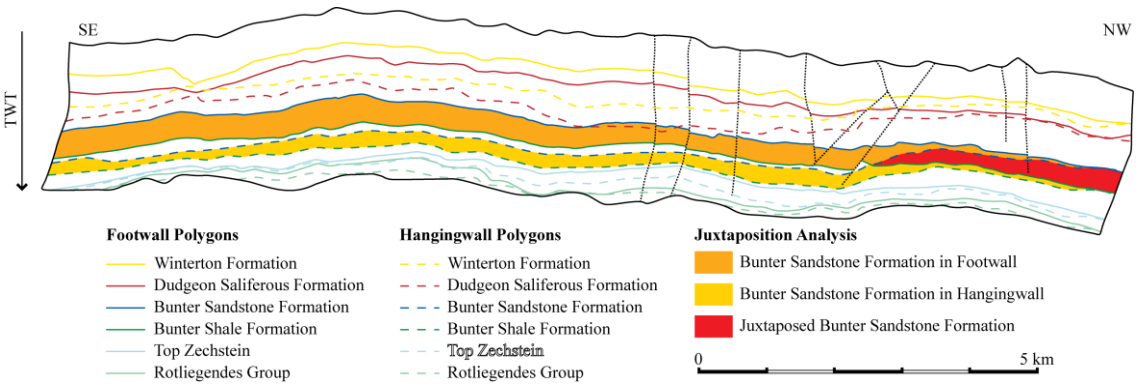

Figure 5.4 Juxtaposition analysis of the North Hewett Fault.

The juxtaposition of sand upon sand at the northwest tip of the North Hewett Fault implies that there is the potential for fluid flow and pressure communication through this area. Fault seal analysis has been used to assess the shale gouge ratio of areas of juxtaposition through estimation of the volume of phyllosilicate minerals predicted to be entrained into the fault gouge during slip. Generally, it is suggested that fault gouges with SGR values of > 50 will act as a barrier to fluid flow and/or pressure communication. However, SGR values <20 are considered to be too low to indicate any possibility of fault seal. SGR values between 20-50 indicate that some seal is possible, becoming increasingly likely as SGR increases (Yielding et al., 2010). Fault seal analysis of the juxtaposed region of the North Hewett Fault reveals values of shale gouge ratio between 0 and 50, therefore there are regions where the SGR is too low to indicate any possibility of fault seal.

5.4.1.1. IDENTIFIED PRESSURE COMMUNICATION PATHWAYS

These results demonstrate two major pressure communication pathways are likely to exist between the Hewett Upper Bunter Sandstone reservoir and the neighbouring Little Dotty Upper Bunter Sandstone reservoir through the shared Bunter aquifer: a simple pathway around the NW tip of the North Hewett Fault and a more complex pathway through the final 2 km of the NW tip of the North Hewett Fault (see Figure 5.3 and Figure 5.4).

Juxtaposition analysis shows that the Hewett Upper Bunter Sandstone reservoir does not appear to be self-juxtaposed across the southeast section of the North Hewett Fault. However, there is a large uncertainty in the position of the top Bunter Sandstone reflector in the hanging wall of the North Hewett Fault, close to the branchline with the western bounding fault of the Dowsing Fault Zone (Figure 5.3). This region lies within a 3 km radius of the Little Dotty Field and suffers from poor seismic resolution and velocity effects such as pushdown of seismic reflectors. In part, this decrease in seismic resolution is likely to result from the structural complexity associated with the branchline between two major fault zones: the North Hewett Fault and Dowsing Fault Zone (see Figure 5.3). As such seismic picks are poorly constrained within this region and the top Bunter pick in the

hanging wall of the Dowsing Fault Zone has been projected directly onto the hanging wall of the North Hewett Fault giving rise to spuriously large throws on the North Hewett Fault in this very localised region (see Figure 5.5). Correcting for this effect results in self-juxtaposition of the Upper Bunter Sandstone interval with a potential overlap of between 120 and 210 m (see Figure 5.5). Thus, there is the potential for a third pressure communication pathway across the south-eastern part of the North Hewett Fault in the vicinity of the branch line with the Dowsing Fault Zone: an effect that is explored further within section 5.4.2.3. The North Hewett Fault structurally closes the Hewett Upper Bunter Sandstone reservoir within this region. However, there is no evidence of hydrocarbons having previously migrated through the juxtaposed region, and CO_2 storage will still be possible within the reservoir as the juxtaposed region is below the initial gas-water-contact of 920.5 m.

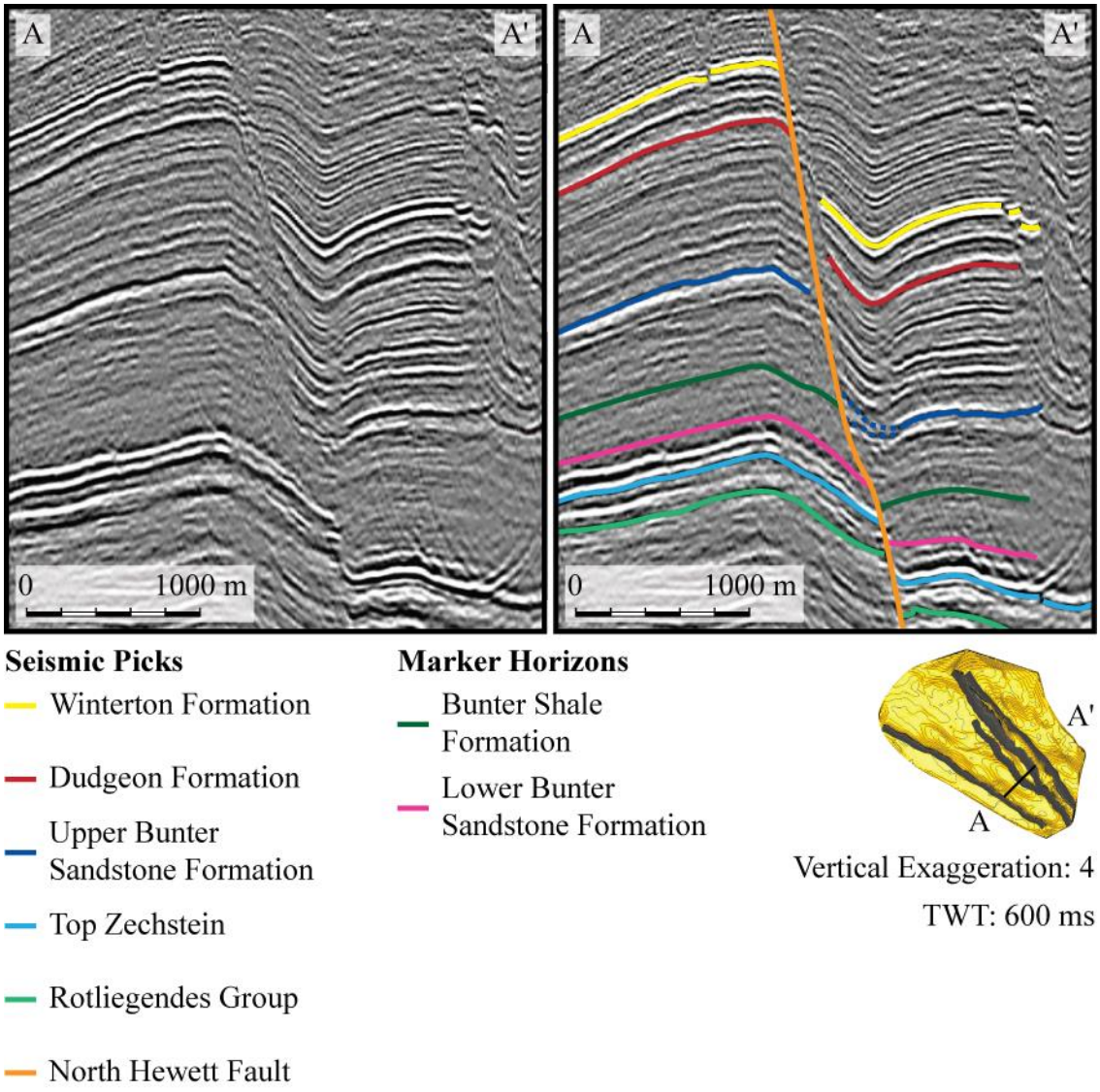

Figure 5.5 Seismic cross-section within the vicinity of the Little Dotty Upper Bunter Sandstone reservoir and the Dowsing Fault Zone shown both with and without interpretations. It is possible to observe the poor seismic resolution and pushdown of seismic reflectors on the right hand side of the North Hewett Fault (orange interpretation). The Bunter Sandstone Formation seismic pick (dark blue interpretation) is poorly constrained within the hanging wall as indicated by the dashed lines. The original interpretation is indicated by the lower dashed line which gave rise to spuriously large throws on the North Hewett Fault in this localised region. Correcting for this effect results in the interpretation indicated by the upper dashed line and self-juxtaposition of the Upper Bunter Sandstone interval, thus creating a third communication pathway across the south-eastern part of the North Hewett Fault. Interpretations made within TrapTester.

5.4.2. PETROPHYSICAL CHARACTERISTICS

The following graphs and boxplots (Figure 5.6 to Figure 5.10) illustrate the porosity and permeability dataset of the Hewett Upper Bunter Sandstone reservoir made available to Durham University by IHS. The graph of sandstone porosity versus permeability (Figure 5.6) shows a positive correlation as porosity and permeability increase, with an r^2 value of 0.2978. Through application of the Pearson correlation it is possible to test whether a correlation exists in the population (Gravetter and Wallnau, 1999). The critical r value for a sample size of 1138 and a significance level of 0.0005 for a one tailed probability is 0.104. Therefore, the calculated r value for the porosity and permeability correlation of 0.546 exceeds the critical value and can be considered as significant.

As previously described in Chapter 4, generally an average value for porosity would be input into CO_2 storage capacity equations. However, due to the heterogeneous nature of sandstone reservoirs, a better understanding of the porosity dataset can be achieved through measuring statistical dispersion, i.e. through use of boxplots and Monte Carlo simulation of the dataset.

The boxplot of the porosity data for the Hewett Upper Bunter Sandstone reservoir is shown in Figure 5.7. The main body (50%) of the data ranges between 15.65% (Q1) and 24.21% (Q3) porosity. The IQR is the interquartile range, and is calculated by subtracting the lower quartile (Q1) from the upper quartile (Q3). The median value (Q2) is 20.06%. Outliers for the dataset are any values that occur below 2.81% and above 37.05% porosity. The porosity data range between 3.50% and 37.10%; therefore there are only two outliers in the whole dataset, both of which are plotted on the right hand side of the boxplot (Figure 5.7). In this case, the whiskers are plotted showing the limits of $Q_1 - 1.5 \times \text{IQR}$ on the left hand side and $Q_3 + 1.5 \times \text{IQR}$ on the right hand side of the boxplot, so that the outliers of the porosity dataset can be easily observed on Figure 5.7.

The porosity dataset for the Hewett Lower Bunter Sandstone reservoir was then analysed via Monte Carlo simulation. Wells with core analysis (porosity and permeability) data for the Hewett Upper Bunter Sandstone reservoir include, 048/30-01, 048/30-02, 048/30-09, 048/30-13, 048/29-01, 048/29-05, 048/29-05,

048/29-08 and 052/05-01 (see for Figure 5.3 locations). The resulting best-fit distribution shows a beta distribution (see Figure 5.8). The Anderson-Darling value for the dataset was 0.6493 therefore the fit of the data to the probability distribution is reasonable. The A-D P-value tests for normality – if the P-value is <0.05 then the result is not normal; if the P-value is >0.05 then the result is normal and the data follow a specified distribution. In this case, the P-value for the Beta distribution is 0.00 therefore these data do strictly not follow a specified distribution. Nevertheless, compared to the other available distributions, the Beta distribution is the best fit of the porosity data.

As for the Hewett Lower Bunter Sandstone reservoir, only porosity data are necessary for CO_2 storage capacity estimation within a water drive reservoir. However, permeability is still an important rock property to analyse as it is a measurement of the reservoir's ability to transmit fluids. The boxplot for permeability Figure 5.9 shows the main body (50%) of data ranges between 43.00 mD (Q1) and 907.50 mD (Q3), with a median value (Q2) of 262.44 mD. Outliers within the Hewett Upper Bunter Sandstone reservoir permeability dataset are any values below -1253.75 mD and above 2204.25 mD. It is not possible to have a negative value for permeability, therefore, the whisker is limited to 0.00 mD on the left hand side of the boxplot. However, there are a total of 128 outliers on the right hand side of the boxplot. As such, the limit of the whisker on the right hand side of the boxplot represents the upper quartile plus 1.5 times the IQR, i.e. 2204.25 mD, so that it is possible to view the outliers in Figure 5.9.

The logarithmic histogram of permeability data (Figure 5.10) shows there to be a high number of instances as permeability increases. However, as has been demonstrated through use of the boxplot in Figure 5.9, the higher values of permeability are spread over a vast range, up to 8130.00 mD.

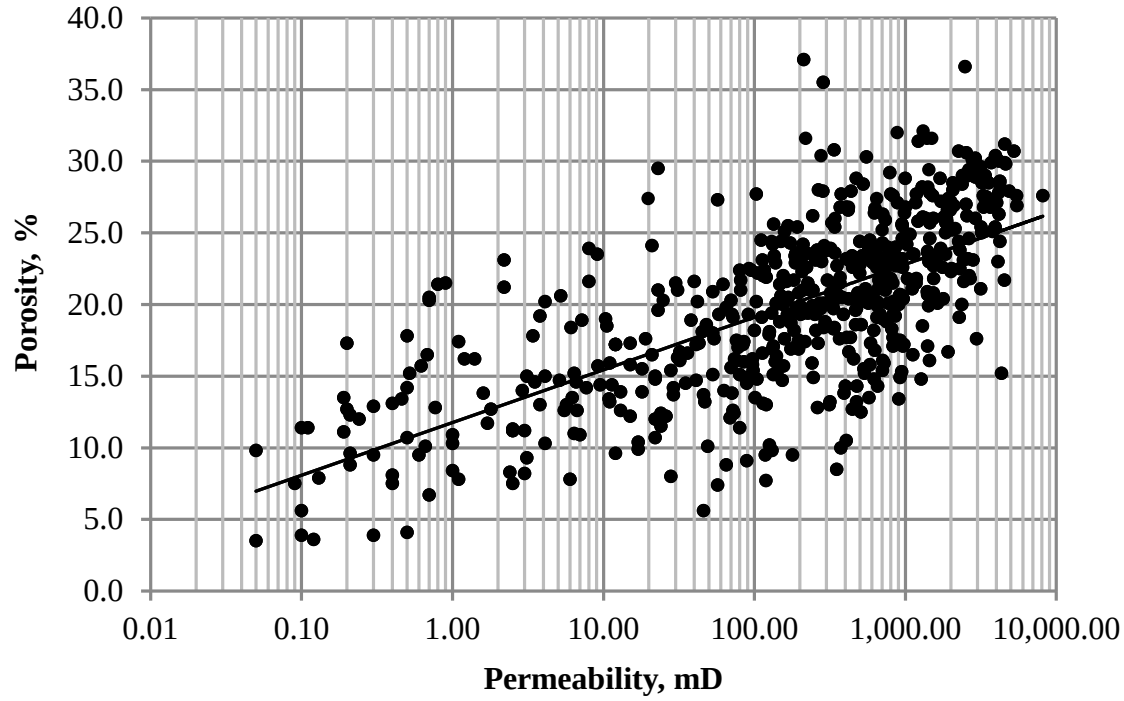

Figure 5.6 Hewett Upper Bunter Sandstone Reservoir Quality

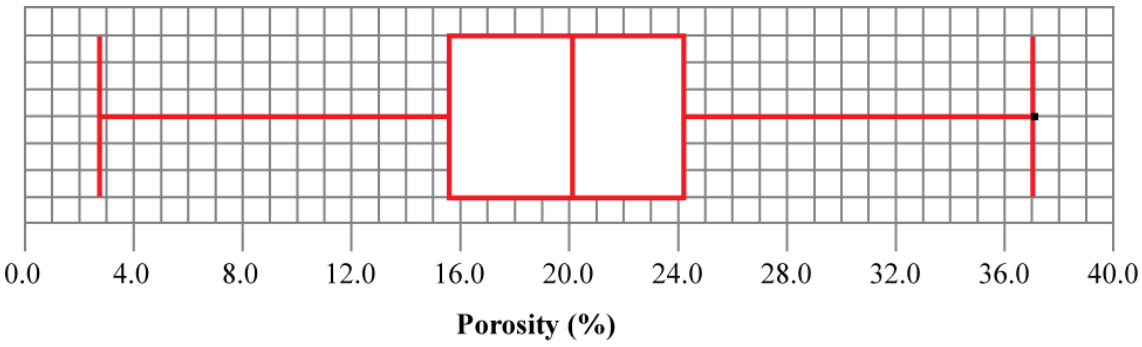

Figure 5.7 Hewett Upper Bunter Sandstone Reservoir Boxplot for porosity. The limit of the whisker on the left hand side of the boxplot is at 1.5 times the IQR minus the lower quartile, and on the right hand side is 1.5 times the IQR plus the upper quartile. As such the two outliers on the right hand side of the boxplot can be observed. The two outliers are extremely close to the upper limit of the values that are assumed to be reasonable, i.e. within 0.05% porosity.

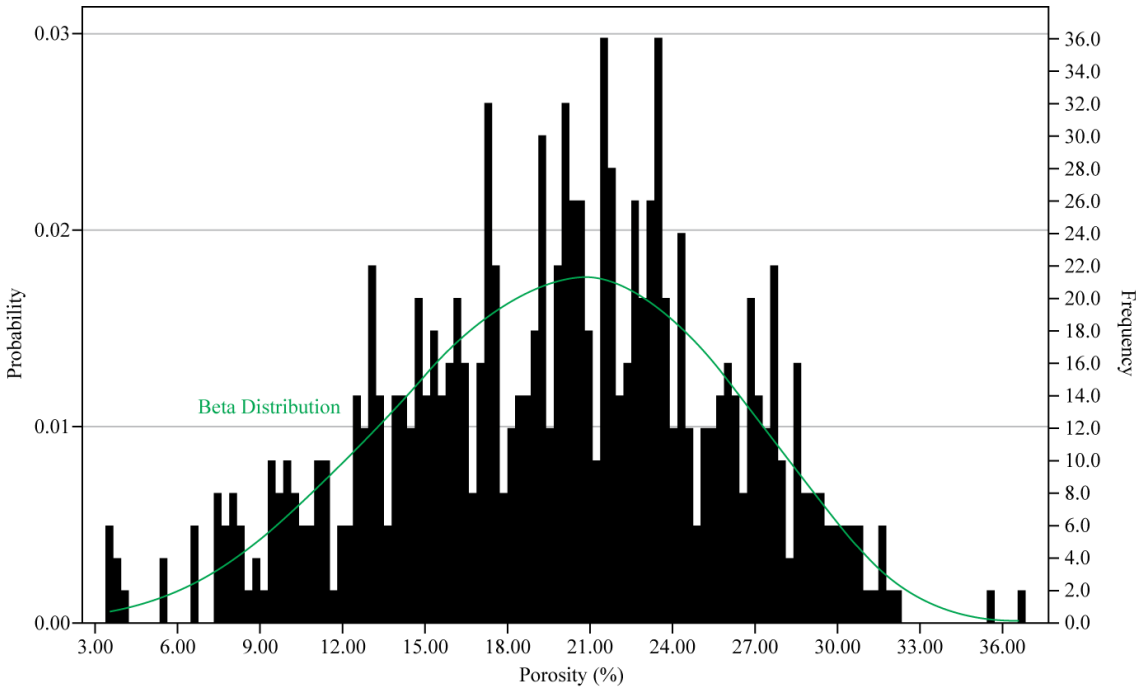

Figure 5.8 Histogram of Hewett Upper Bunter Sandstone Reservoir Porosity

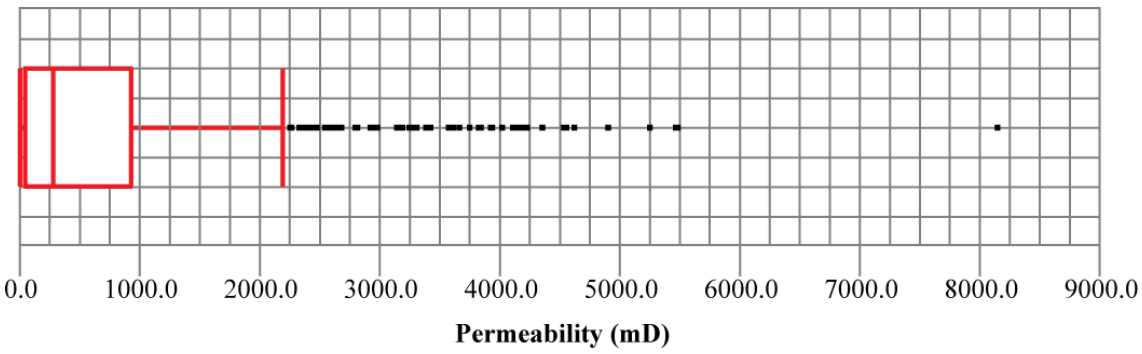

Figure 5.9 Hewett Upper Bunter Sandstone Reservoir Boxplot for permeability. The permeability data plotted here do not lie within 1.5 times the IQR of the upper quartile, but are within 1.5 times the IQR of the lower quartile. Therefore, the whisker on the right hand side of the boxplot represents the upper quartile plus 1.5 times the IQR, whereas the whisker on the left hand side is limited to 0.00 mD as it is not possible to have a negative value for permeability. A total of 128 outliers have been plotted on the boxplot on the right hand side. As can be seen, they are spread over a wide range indicating that higher values of permeability are possible within the Hewett Upper Bunter Sandstone reservoir, however, the likelihood is that overall reservoir permeability will be similar to that defined by the IQR.

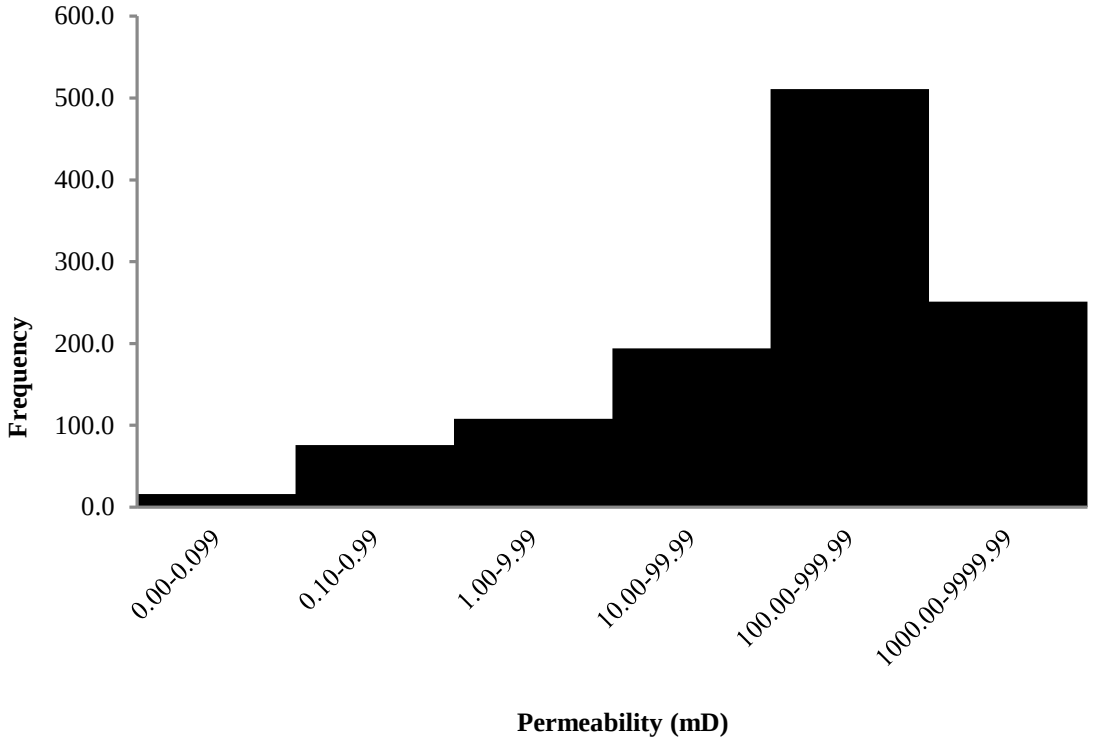

Figure 5.10 Histogram of Hewett Upper Bunter Sandstone Reservoir Permeability

5.4.3. GAS PRODUCTION AND ASSOCIATED PRESSURE DECLINE

The Hewett Upper Bunter Sandstone reservoir has been in production since September 1973. The original volume of gas in place was estimated to be 38.398 billion cubic metres and over 89.8% of this gas has been recovered (34.481 billion cubic metres), based on the production data made available to Durham University by ENI. Production has continued after 2002 meaning this is not the final cumulative volume of produced gas; however, this data has not been made available to Durham University.

The gas production data for the Hewett Upper Bunter Sandstone reservoir between 1973 and 2002 has been plotted in Figure 5.11 from all productive wells (including 052/05a-A1, A4, A5, A6, A7, A8, A9 and A10). From the onset of production in 1973 the reservoir showed an immediate rapid rate of production of 1.28E+10 m^3/year until 1982. The rate of production began to gradually drop from 1982 onwards, marked by a curve in the production trend on Figure 5.11. Between

1982 and 1989 the rate of production slowed, with an average rate of 9.17E+08 m^3/year. From 1989 until the end of the available data in 2002 the rate of production once again slowed to a lower average rate of production of 1.57E+08 m^3/year.

The pressure history of the Hewett Upper Bunter Sandstone reservoir has also been plotted alongside the gas production data in Figure 5.11 from well 052/05a-A1. Following the onset of production in 1973 the reservoir pressure declined from an initial pressure of 9.391 MPa to 3.358 MPa in 1982, giving an average rate of depletion of 0.670 MPa/year. Between 1982 and 1989 the rate of pressure depletion slowed to an average rate of 0.275 MPa/year. From 1989 until the end of the available data in 2002, the rate of pressure depletion once again fell to an average rate of 0.0719 MPa/year.

It is apparent, particularly in the later life of the Hewett Upper Bunter reservoir (from 1990 onwards), that the pressure fluctuated about the expected trend. Fluctuation was the direct result of well shut-in (i.e. periods of time where there was no production from the reservoir). This produced subtle steps in the cumulative production trend, however the pressure depletion trend was much more affected. A period of shut-in allowed the Hewett Upper Bunter Sandstone reservoir to partially re-pressurise through water influx from the regional Bunter aquifer, hence the five pressure increases observed between April 1991 to October 1991, September 1993 to October 1994, October 1995 to October 1996, April 1997 to December 1997 and June 2001 to July 2002 (Figure 5.11). Individual rates of pressure increase are displayed in Table 5.3. Following a period of shut-in the reservoir pressure increased slightly and production continued at a slightly higher rate for a brief period of time whilst the pressure depleted again as the rate of production was higher than the rate of aquifer influx.

As for the Hewett Lower Bunter Sandstone reservoir (Chapter 4) it is important to note the degree of error in the pressure dataset. Once again, the reservoir pressures are Repeat Formation Tester (RFT) measurements, and the timescale over which pressures are measured within the Hewett Upper Bunter Sandstone reservoir are similar to those of the Hewett Lower Bunter Sandstone reservoir (i.e. over a period of ~ 40 years). As such the RFT tools used at the

beginning of production will have used strain gauges with an accuracy of 0.18% and later measurements (within the last 20 years) will have used a Hewlett Packard quartz gauge with an accuracy of 0.025%. Therefore, pressure data recorded over the entire lifetime of the Hewett Upper Bunter Sandstone reservoir will be reasonably accurate. It is important to note that the accuracy of the pressure readings will be increased as the pressures begin to fluctuate around the expected trend in the later life of the Hewett Upper Bunter reservoir as previously outlined (see Figure 5.11).

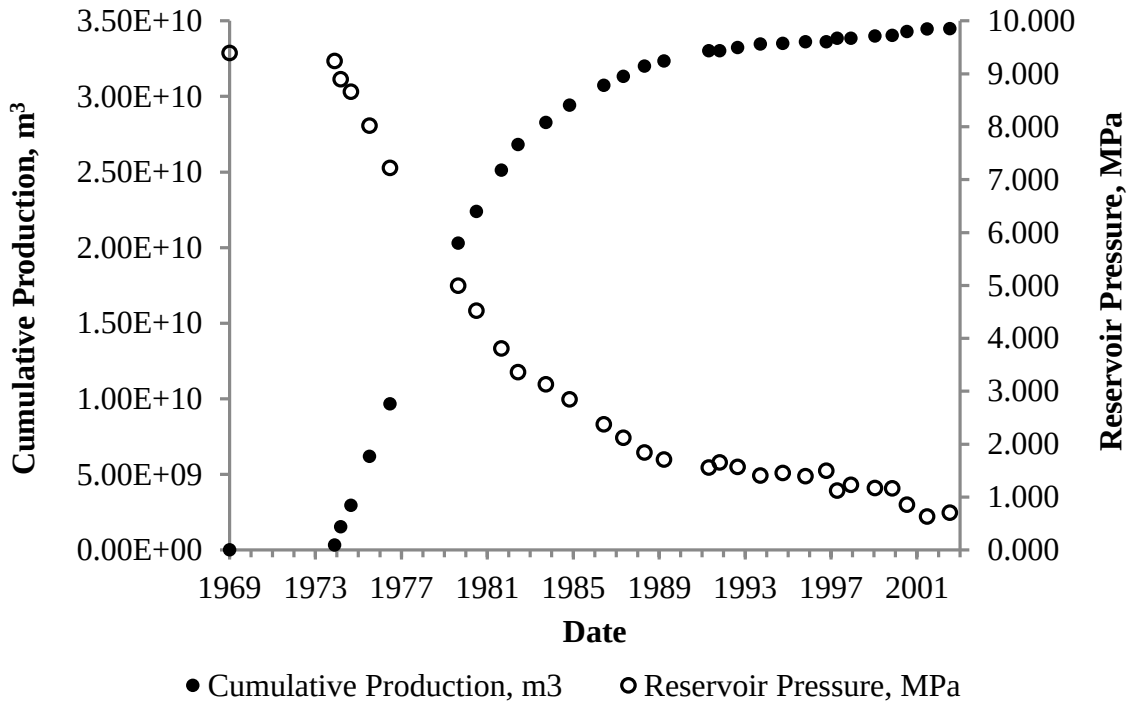

Figure 5.11 Hewett Upper Bunter Sandstone Reservoir Cumulative Production and Pressure Depletion Data.

SHUT-IN TIME PERIOD	DAYS	INITIAL PRESSURE (MPa)	FINAL PRESSURE (MPa)	RATE OF PRESSURE INCREASE (MPa/day)
26/04/1991 – 26/10/1991	183	1.558	1.655	0.0005
18/09/1993 – 02/10/1994	379	1.407	1.455	0.0001
26/10/1995 – 14/10/1996	354	1.393	1.496	0.0003
17/04/1997 – 03/12/1997	230	1.124	1.227	0.0004
24/06/2001 – 14/07/2002	385	0.634	0.703	0.0002

Table 5.3 Shut-in time periods with associated reservoir pressure increases within the Hewett Upper Bunter Sandstone reservoir.

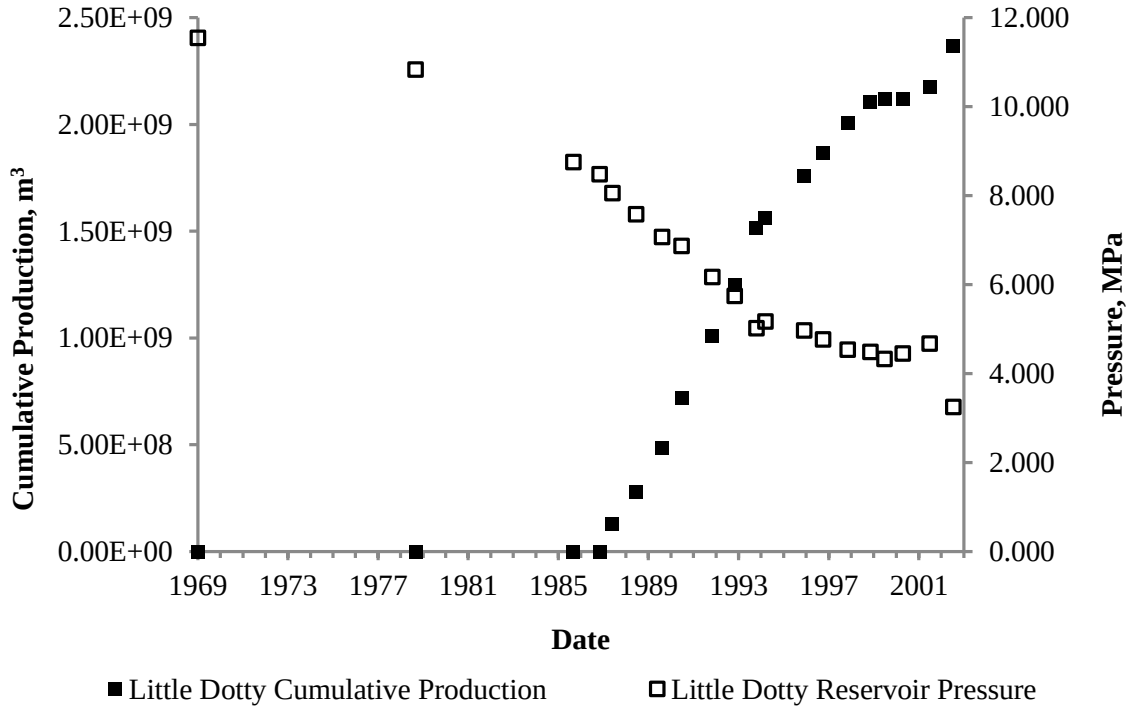

Figure 5.12 Little Dotty Upper Bunter Sandstone Reservoir Cumulative Production and Pressure Depletion Data

As described in section 5.3.1., the Hewett Upper Bunter Sandstone reservoir is underlain by the regional Bunter aquifer and as such has experienced water drive throughout its productive lifetime. This suggests there is connectivity between the two reservoirs via the underlying regional Bunter aquifer. As such, it is necessary to analyse the gas production and pressure decline data of the Little Dotty Upper Bunter Sandstone reservoir alongside that of the Hewett Upper Bunter Sandstone reservoir.

The gas production data for the Little Dotty Upper Bunter Sandstone reservoir has been plotted in Figure 5.12. From the onset of production in 1986 the reservoir showed an immediate rapid rate of production of 2.16E+08 m^3/year until 1993. Between 1993 and 1998 the rate of production slowed, with an average rate of 1.20E+08 m^3/year. Between 1998 and 2000 the rate of production effectively plateaus with an average rate of 5.00E+06 m^3/year. Production within the Little Dotty Upper Bunter Sandstone reservoir has been from one well, 048/30-09. This well was shut-in during March 1999 due to excessive water production. The well was modified so that it could produce with a higher watercut and was brought back online in March 2001. This explains the plateau observed in the production data between 1998 and 2000 as there was a period where no gas was produced. However, normal production resumed afterwards and between 2000 until the end of the available data in 2002 the rate of production increased to an average rate of production of 1.25E+08 m^3/year.

The pressure history of the Little Dotty Upper Bunter Sandstone reservoir has also been plotted alongside the gas production data in Figure 5.12. The most striking part of the graph is reflected in the pressure depletion data. The initial pre-production reservoir pressure within the Little Dotty Upper Bunter Sandstone reservoir was 11.549 MPa. A significant pressure drop of 3.068 MPa can be observed within the Little Dotty Upper Bunter Sandstone reservoir between 1969 and 1986, i.e. throughout the time period *before* production began from the Little Dotty Upper Bunter Sandstone reservoir. This could be caused by leakage or "fugitive emissions" from the Little Dotty exploration well, although the volume liberated to cause such a large pressure drop would be necessarily high. However, the pressure drop has been attributed to production from the Hewett Upper Bunter

Sandstone reservoir by Cooke-Yarborough and Smith (2003) as both reservoirs are underlain by the regional Bunter aquifer. This is consistent with the cumulative production data (Figure 5.12) if the point at which cumulative production is equal to zero in 1979 is taken at face value. Accepting the model proposed by Cooke-Yarborough and Smith (2003), material balance methods can be applied in section 5.4.3.1.

The pressure depletion data from 1986 to 1992 (Figure 5.12) shows a rapid rate of decline averaging at 0.455 MPa/year. There was a shut-in period between 1993-1994 with a total pressure increase of 0.152 MPa. Between 1994 and 1999 pressure depletion continued at an average rate of 0.158 MPa/year. During the shut-in period in well 048/30-09 between 1999 and 2001 there was a pressure increase rate of 0.172 MPa/year, however this was followed by a rapid depletion rate from 2001 to 2002 (extent of data made available) averaging at 1.420 MPa/year.

Figure 5.13 displays the production and pressure data from both the Hewett and Little Dotty Upper Bunter Sandstone reservoirs displayed in Figure 5.11 and Figure 5.12 alongside each other. It can be seen how small in size the Little Dotty Upper Bunter Sandstone reservoir is in comparison with that of the Hewett Upper Bunter Sandstone reservoir. Despite this, the reservoir pressure depletion data reveals the responsive nature of both the Hewett and Little Dotty Upper Bunter Sandstone reservoirs to any change in either reservoir brought about by production. This relationship will be further explored in the following sections, 5.4.3.1 through 5.4.3.5 of this chapter.

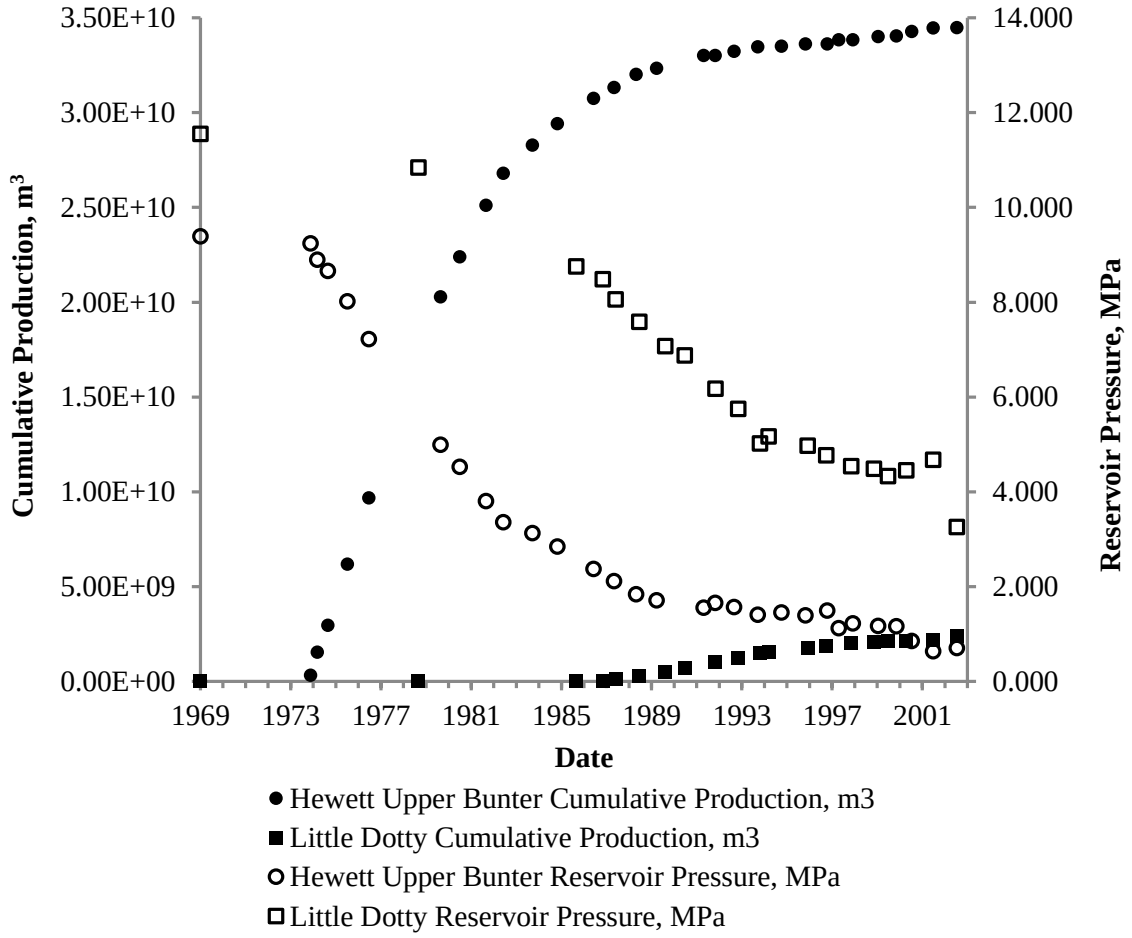

Figure 5.13 Hewett and Little Dotty Upper Bunter Sandstone Cumulative Production and Pressure Depletion Data

5.4.3.1. MATERIAL BALANCE METHODS

Material balance methods have been previously described in Chapter 3. They are used here to estimate aquifer strength in both the Hewett and Little Dotty Upper Bunter Sandstone reservoirs. The use of Cole Plots here will allow accurate characterisation of strong, moderate or weak water drive reservoirs (Bruns et al., 1965; Chierici et al., 1967; Dake, 1978; Pletcher, 2002; Tehrani, 1985; Vega and Wattenbarger, 2000).

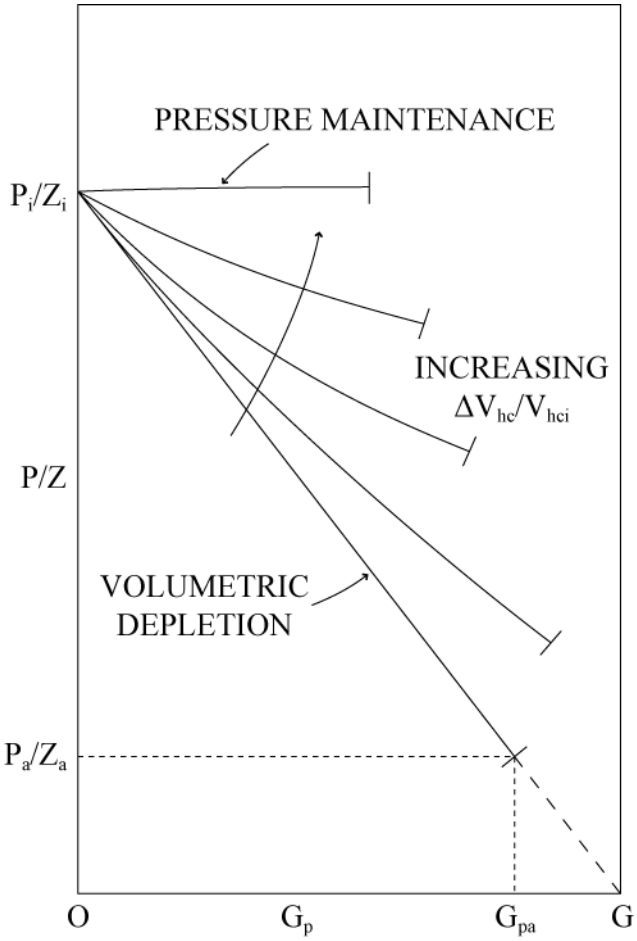

Figure 5.14 Material balance (P/Z) as a function of cumulative production (G_p) for various values of hydrocarbon pore volume ratio, i.e. current hydrocarbon pore volume divided by initial hydrocarbon pore volume ($\Delta V_{hc}/V_{hci}$). After Hagoort (1988)

Figure 5.14 shows the difference in P/Z plot trends between a volumetric (or depletion drive) reservoir as previously described for the Hewett Lower Bunter Sandstone reservoir in Chapter 4, and alternative scenarios where a reservoir receives varying degrees of pressure support (for example, through aquifer influx). An accurate estimation of OGIP can be obtained for depletion drive reservoirs through linear extrapolation of the trend on the P/Z plot. However, this is not possible within reservoirs that receive pressure support as the P/Z trend curves away from the x-axis as production continues. If OGIP is estimated within a reservoir that receives pressure support, but the model assumes a depletion drive trend, the resulting OGIP value will be an over-estimate.

The material balance graph for the Hewett Upper Bunter Sandstone reservoir (Figure 5.15 (a)) appears to show a linear trend and as such, has been determined by industry to be a depletion drive reservoir (see Figure 5.16 (a)). The industry estimated OGIP value is 38.398 billion cubic metres of natural gas, and therefore the estimated recovery factor is 89.8%. However, in comparison with the results of the material balance for the Hewett Lower Bunter Sandstone reservoir (Chapter 4), it is apparent that the data fluctuates about a strict linear trend. In addition, towards the end of the reservoir lifetime, there is a tail-off of the data from a linear trend as the abandonment pressure is approached. (The abandonment pressure is reached when the production rate drops below the rate specified within the gas contract (Dake, 1978)).

When these data are presented on the Cole plot (Figure 5.17 (a)), it is clear the Hewett Upper Bunter Sandstone reservoir has experienced moderate water drive throughout its productive lifetime (see Figure 5.16 (b)). This is consistent with a water influx ranging between 15 and 50% of the reservoir volume (Hagoort, 1988). At the start of production, as the volume of produced hydrocarbons increases, $G_pB_g/(B_g-B_{gi})$ increases at a decreasing rate, such as the shape of the graph at this point is concave down, increasing. Towards the end of the productive lifetime of the reservoir, when the volume of produced hydrocarbons is close to the volume specified by the OGIP the rate of $G_pB_g/(B_g-B_{gi})$ decreases at an increasing rate, resulting in a concave down, decreasing shaped curve on the graph (Figure 5.17 (a)).

As such, it is likely that the industry estimated OGIP of 38.398 billion cubic metres is incorrect if the OGIP value has been estimated assuming a depletion drive reservoir instead of a water drive reservoir (see Figure 5.14). To check this estimate it is possible to use equation 5.3 to estimate a value for the cumulative volume of water influx into the Hewett Upper Bunter Sandstone reservoir, W_e, throughout its productive lifetime up until 2002 (last recorded data):

$$W_e = \frac{G_p - OGIP(1 - E/E_i)}{E} \tag{5.3}$$

(After Dake (1978))

where, E is the gas expansion factor and the subscript, *i*, denotes initial conditions.

The estimated value of W_e using equation 5.3 is -0.215 billion cubic metres. This is further evidence to suggest that the industry estimated value for OGIP is incorrect – if the Hewett Upper Bunter Sandstone reservoir has a water drive as the Cole Plot suggests (Figure 5.17 (a)), the estimated value for W_e should be positive. This will be investigated further in section 5.4.3.5.

In comparison, the P/Z plot of the Little Dotty Upper Bunter Sandstone appears to show a concave up trend (see red dashed line on Figure 5.15 (b)) consistent with that of a water drive reservoir (Figure 5.16 (a)). It could be argued that the trend is also linear, however considering the OGIP of 2.83E+09 m^3, it is likely the actual data curves away from a linear trend (see blue dashed line on Figure 5.15 (b)) and so the reservoir is unlikely to be volumetric (Figure 5.16 (a)).

When the data are displayed on a Cole plot (Figure 5.17 (b)), it is apparent that the reservoir experiences strong water drive (see Figure 5.16 (b)). This is consistent with a water influx in excess of 50% of the reservoir volume (Hagoort, 1988) which is to be expected: despite being connected to the same regional aquifer as that of the Hewett Upper Bunter Sandstone reservoir, the Little Dotty reservoir has a volume approximately 7% of that of Hewett. At the start of production, as the volume of produced hydrocarbons increases, $G_pB_g/(B_g-B_{gi})$ increases at a

decreasing rate, resulting in a concave down, increasing curve on the graph (Figure 5.17 (b)) similar to that of the moderate water drive. However, towards the end of production, $G_pB_g/(B_g-B_{gi})$ settles into a steadily increasing rate with increasing volumes of produced hydrocarbons, so that the curve produced is still concave down, increasing in shape (Figure 5.17 (b)). The main difference between strong and moderate water drive curves is the lack of tail off observed in the strong water drive trend as the OGIP is approached (Figure 5.15 (b)).

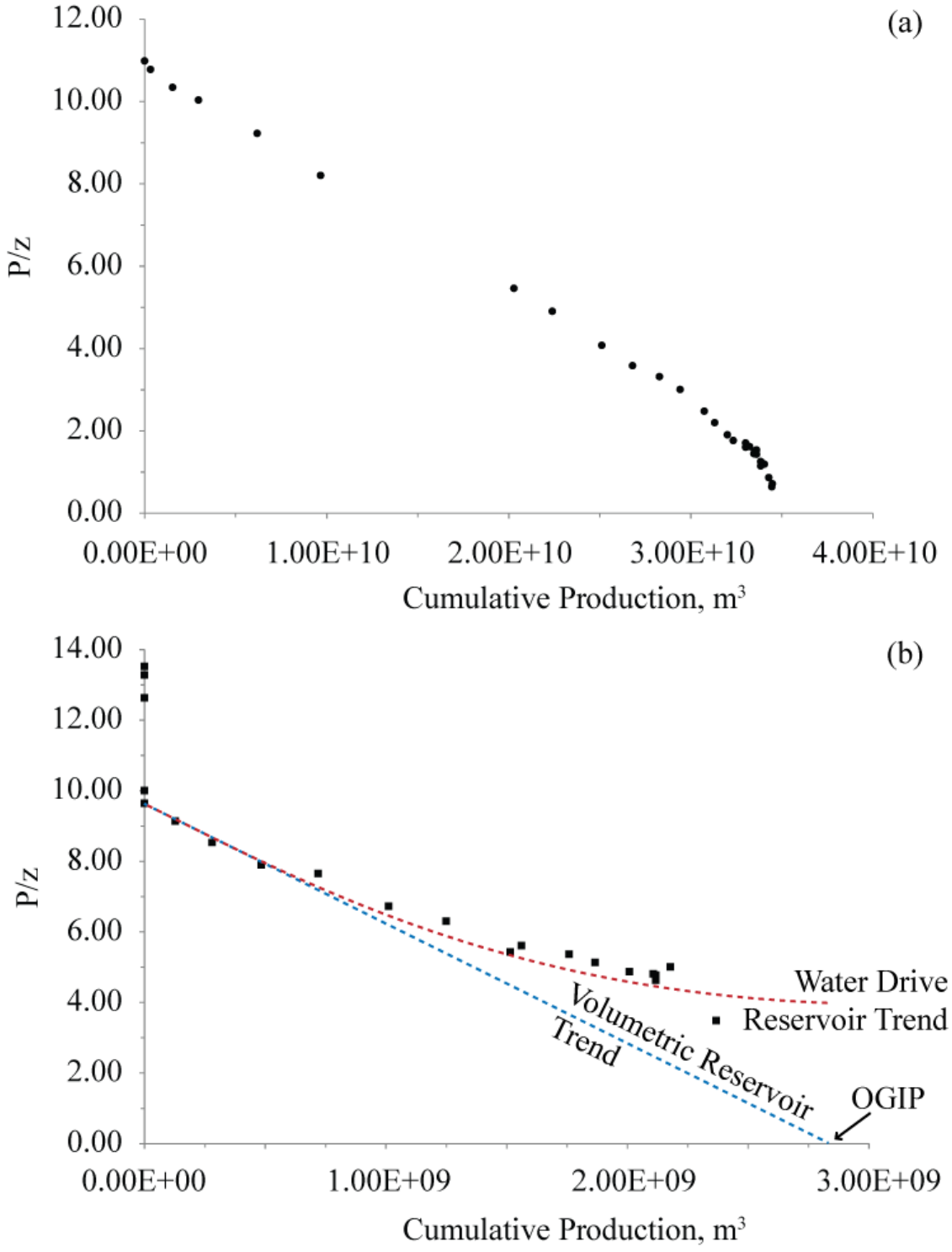

Figure 5.15 Material Balance Plots of Production and Pressure Data for (a) the Hewett Upper Bunter Sandstone Reservoir, and (b) the Little Dotty Upper Bunter Sandstone Reservoir. OGIP is the industry estimate of original gas in place, based on linear extrapolation of the P/z data.

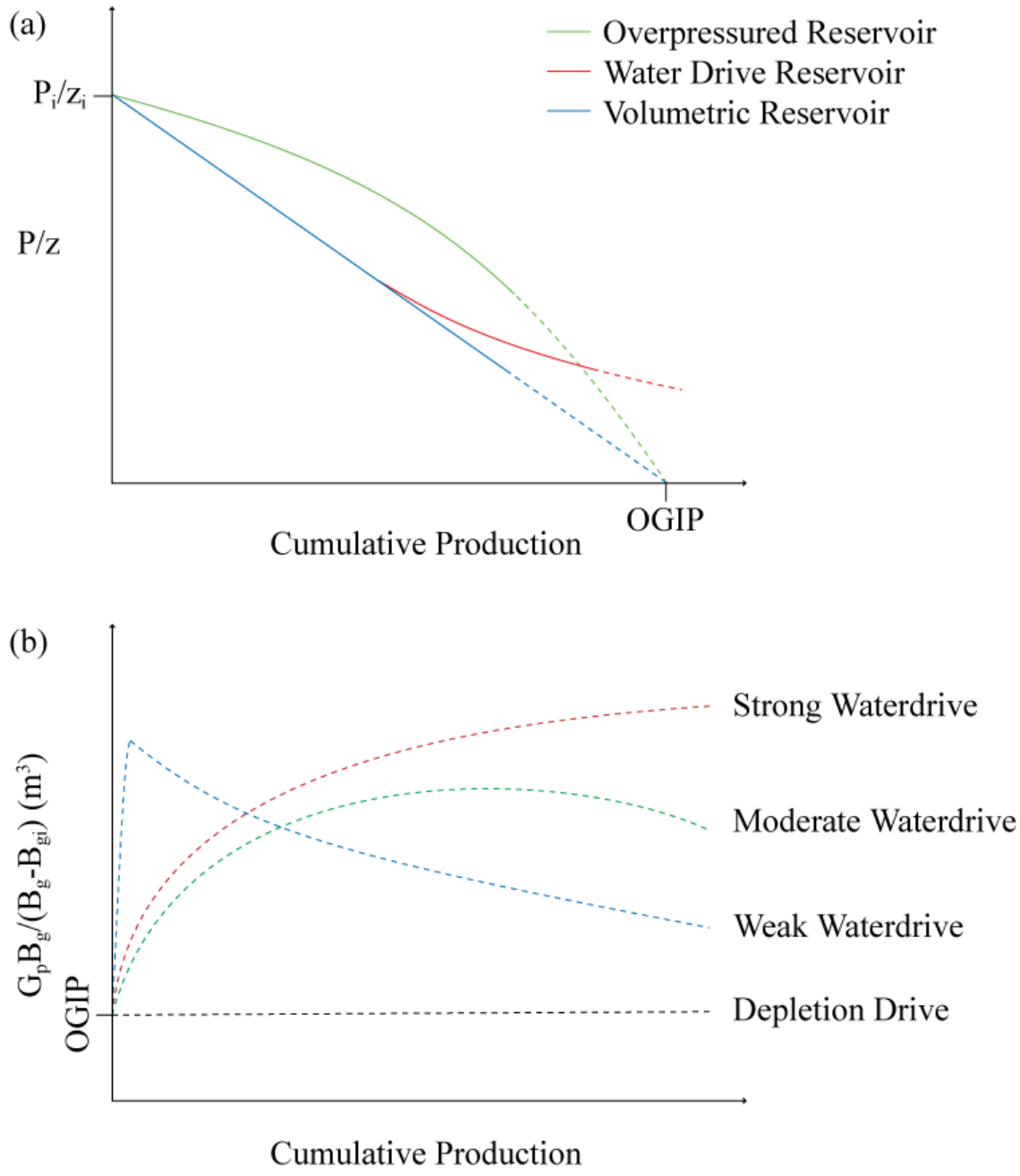

Figure 5.16 (a) Typical Material Balance Plot Trends for Overpressured, Water Drive and Depletion Drive Reservoirs, and (b) Cole plot curve shapes as a function of aquifer strength. Adapted from Pletcher (2002).

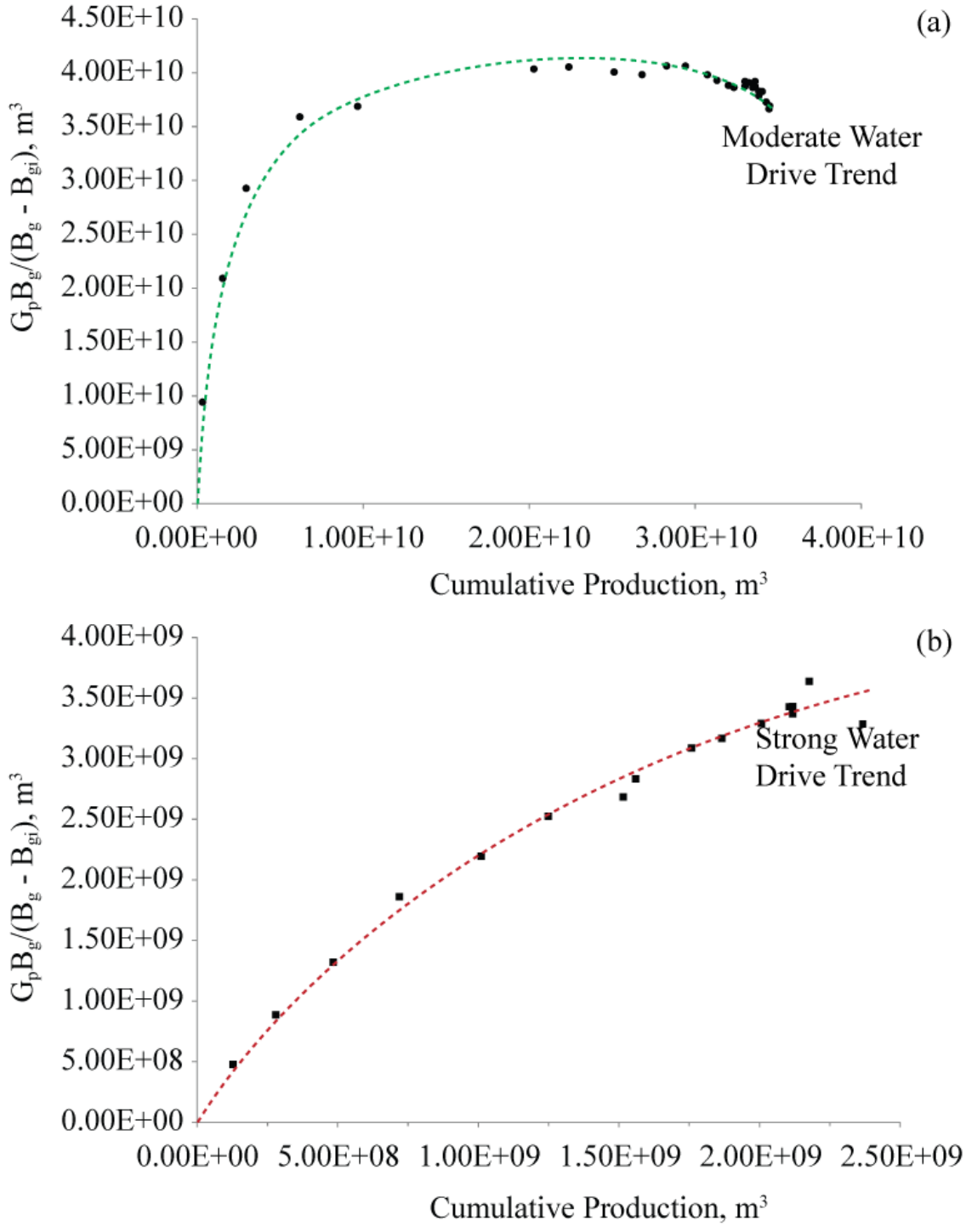

Figure 5.17 Cole Plots of Production and Pressure Data for (a) the Hewett Upper Bunter Sandstone Reservoir, and (b) the Little Dotty Upper Bunter Sandstone Reservoir

5.4.3.2. ESTIMATION OF HYDRAULIC HEAD AND CONCEPTUAL MODEL OF AQUIFER BEHAVIOUR

A conceptual model to explain the pressure communication between the Hewett and Little Dotty Upper Bunter Sandstone reservoirs via the regional Bunter aquifer during gas production has been developed. The hydraulic (or piezometric) head (a measurement of liquid pressure above a geometric datum) for the two reservoirs, both initially and throughout their productive lifetimes has been determined (Figure 5.18). The initial hydraulic heads, H_{res}, of the Hewett and Little Dotty Upper Bunter Sandstone reservoirs were calculated (based on their initial gas water contacts) from a deeper arbitrary datum point, z, of 1434 m near the base of the Upper Bunter Sandstone formation within Little Dotty, using the equation:

$$H_{res} = \frac{P}{\rho_w . g} + z_{res} \qquad (5.4)$$

Adapted from Ingebritsen and Sanford (1999)

where, ρ_w is water density, g is gravitation acceleration and z_{res} is the height above the datum point, z. Through calculation of the hydraulic heads in both the Hewett and Little Dotty Upper Bunter Sandstone reservoirs, it is possible to estimate the direction of aquifer movement.

In 1967, the hydraulic head in both the Hewett and Little Dotty Upper Bunter Sandstone reservoirs had similar values (see Figure 5.19), consistent with a low pre-production hydraulic gradient across the western part of the regional Bunter aquifer local to the Hewett Unit. As previously stated, production commenced from the Hewett Upper Bunter Sandstone reservoir in 1973 causing reservoir pressure to decline. As hydraulic head is directly affected by changes in pressure, a decline in the hydraulic head within both the Hewett and non-producing Little Dotty Upper Bunter Sandstone reservoirs resulted (Figure 5.19). It can be seen that the decline in head within the Hewett reservoir exceeded the decline in head within the then non-producing Little Dotty Upper Bunter Sandstone reservoir (Figure 5.19). This observation demonstrates an increase in hydraulic gradient between the two reservoirs and is consistent with the movement of formation water through the

shared Bunter aquifer from Little Dotty (H_{res} = high) towards the Hewett Upper Bunter Sandstone reservoir (H_{res} = low). This simple model provides an explanation for the pressure decline in Little Dotty prior to the onset of production in 1986. After 1986, the hydraulic head in the Little Dotty Upper Bunter Sandstone reservoir continued to fall, whilst the rate of decline in the Hewett Upper Bunter Sandstone reservoir decreased, re-establishing the low hydraulic gradient between the two reservoirs towards the end of production (Figure 5.19). During 2002 the hydraulic heads in both reservoirs were almost equal.

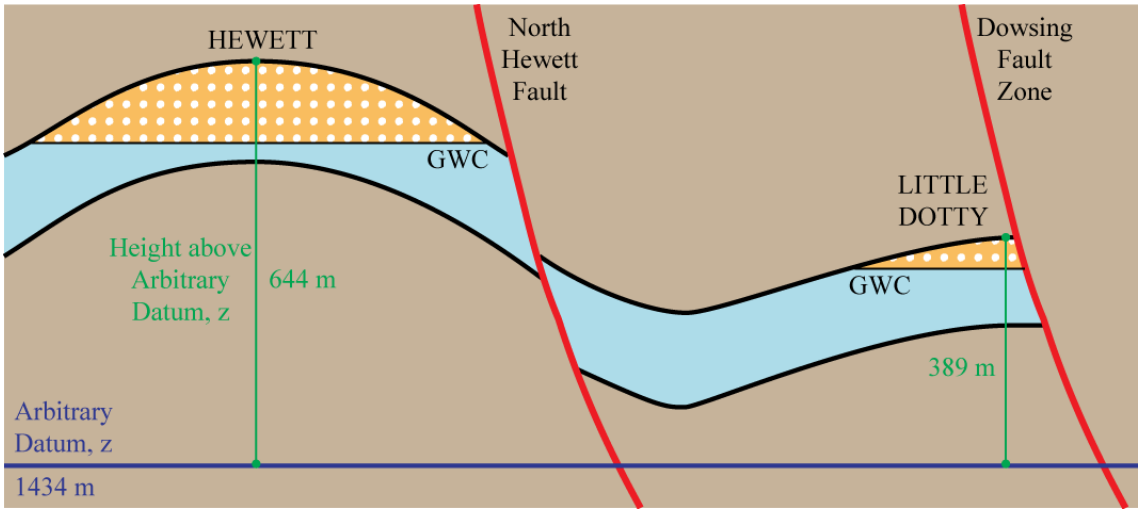

Figure 5.18 Schematic diagram of the Upper Bunter Sandstone Formation showing the arbitrary datum point and measurements for hydraulic head calculations (Equation 5.4) within the Hewett and Little Dotty Upper Bunter Sandstone reservoirs

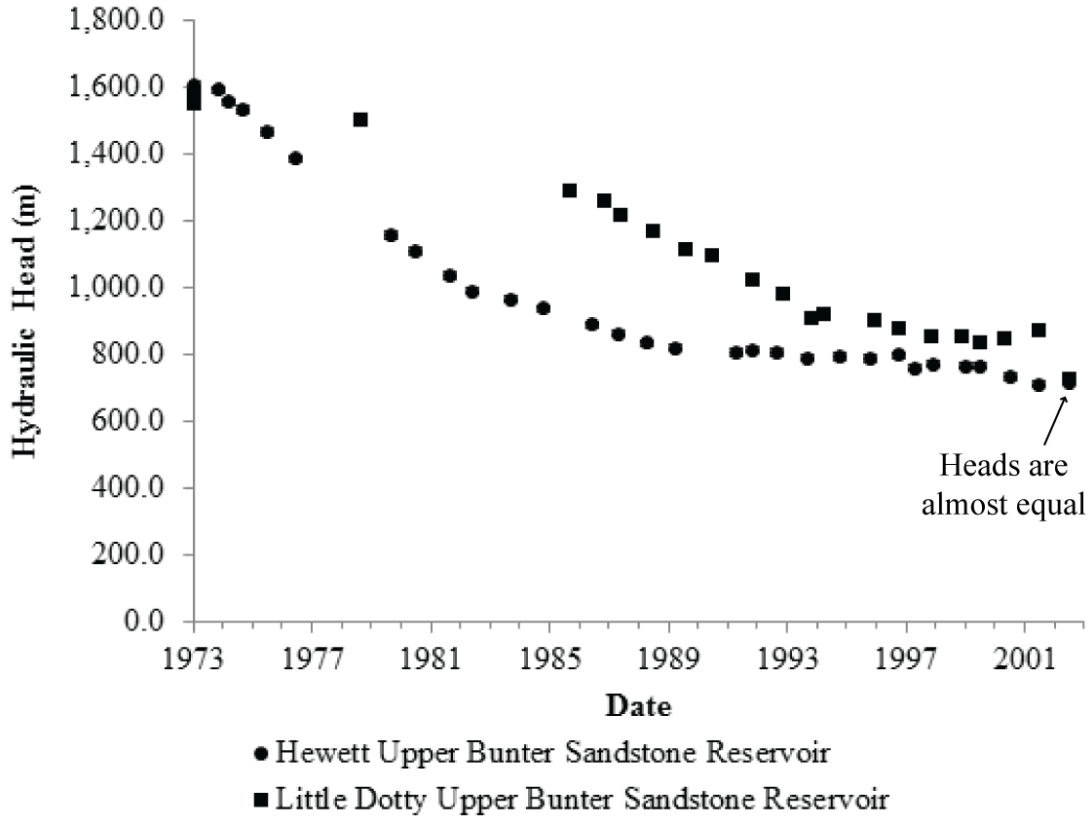

Figure 5.19 Hydraulic head variation within the Hewett and Little Dotty Upper Bunter Sandstone reservoirs over their respective productive lifetimes using Equation 5.4. The two reservoirs were in equilibrium prior to the onset of production. Production from the Hewett Upper Bunter Sandstone reservoir resulted in perturbation of the Bunter aquifer as the hydraulic head in Hewett dropped. Following the onset of production of from the Little Dotty Upper Bunter Sandstone reservoir in 1986, the hydraulic head gradients in both reservoirs moved towards a second state of equilibrium (where the heads will be equal) but at a lower pressure due to the liberation of natural gas through production. Nearing the end of production, the heads were almost equal.

5.4.3.3. HYDRAULIC DIFFUSIVITY

The results of the structural and fault seal analysis have revealed three potential pathways for pressure communication between the Hewett and Little Dotty Upper Bunter Sandstone reservoirs through the underlying regional Bunter aquifer. However, a key question arising from these results is whether the main pathway for pressure communication and fluid flow is either through the sand-sand juxtaposed areas in the northwest and/or southeast, or around the northwest tip of the North Hewett Fault.

Monte Carlo simulation was used to estimate hydraulic diffusivity, κ_ϕ, of the regional Bunter aquifer based on the permeability, k, porosity, ϕ, measured in wells, the estimated brine viscosity, μ, and bulk compressibility for matrix and fluid, c_{res} and c_{fluid}, respectively, where:

$$\kappa_\phi = \frac{k}{\mu \times \phi \times (C_{res} + C_{fluid})} \tag{5.5}$$

Adapted from Wibberley (2002)

Monte Carlo simulation analyses risk for any parameter displaying natural uncertainty through use of a probability distribution, for example, a normal distribution or bell curve. Random sampling takes place from the selected probability distributions for each variable, and is repeated thousands of times for accuracy. The outcome is a probability distribution showing the most likely results.

The hydraulic diffusivity was used to evaluate an order-of-magnitude estimate for the characteristic diffusion time (Δt) for a pressure change within the Hewett Upper Bunter Sandstone reservoir to influence the pressure within the Little Dotty Upper Bunter Sandstone reservoir through the medium of the regional Bunter aquifer:

$$\Delta t = \Delta x^2 / \kappa_\phi \tag{5.6}$$

where, Δx is the characteristic diffusion distance.

Results are shown in Figure 5.20 and Table 5.4. The mean of the simulated results gave a hydraulic diffusivity of 0.026 m^2/s. Based upon analysis of the 3-D structural model, the diffusion distance from Little Dotty to Hewett around the northwest tip of the North Hewett Fault has been estimated at approximately 18 km long. Using this estimate with equation 5.6, the characteristic diffusion time would be in the order of hundreds to thousands of years (see Table 5.5).

From the measured pressure changes (Figure 5.13) it is clear that the pressure in the Little Dotty Upper Bunter Sandstone reservoir was perturbed by the pressure decline in the Hewett Upper Bunter Sandstone reservoir over a 13 year period between 1973 when the Hewett Upper Bunter Sandstone reservoir first came online and 1986 when the Little Dotty Upper Bunter Sandstone reservoir commenced production. If this pressure decline was solely associated with pressure diffusion away from Little Dotty around the northwest tip of the North Hewett Fault, the estimated lag time (in the order of hundreds of years) would be far too long to achieve the rapid pressure decline observed in the Little Dotty Upper Bunter Sandstone reservoir prior to production in 1986 (see Figure 5.13). The observed decadal timescale implies that a shorter migration pathway for pressure diffusion and communication from Little Dotty, across the North Hewett Fault and into the Hewett Field, e.g. across the south-eastern section of the North Hewett Fault, adjacent to the branchline with the neighbouring Dowsing Fault Zone. Substitution of a shorter diffusion pathway of 3.5 km (the approximate distance from Little Dotty to the Hewett Field across the North Hewett Fault), yields a characteristic diffusion time in the order of years (see Table 5.5); a result that is more consistent with the historical pressure data (Figure 5.13). It is therefore suggested that pressure communication, due to self-juxtaposition of the regional Bunter aquifer across the south-eastern end of the north Hewett Fault was the most likely pathway, even when taking into account the possible reduction in hydraulic diffusivity of the fault zone.

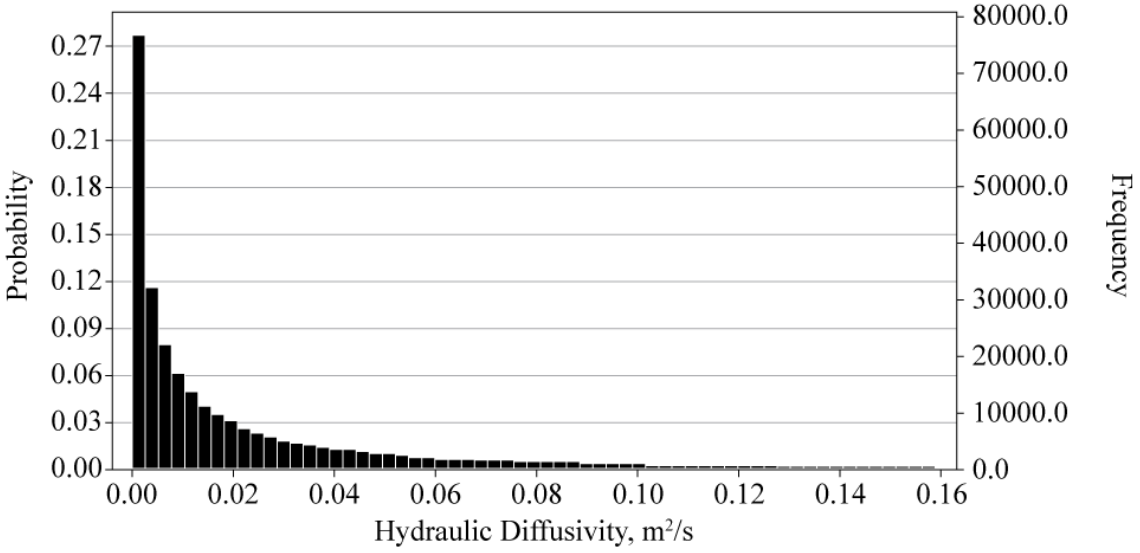

Figure 5.20 Hewett Upper Bunter Sandstone reservoir forecast chart for hydraulic diffusivity modelled using Oracle Crystal Ball Software.

RESERVOIR	MINIMUM	P10	MEDIAN (P50)	MEAN	P90	MAXIMUM
HEWETT UPPER BUNTER SANDSTONE	3.27E-11	4.45E-04	9.04E-03	2.60E-02	6.92E-02	1.37E+00

Table 5.4 Hydraulic diffusivity (m^2/s) estimates from Monte Carlo simulation in Oracle Crystal Ball software for the Hewett Upper Bunter Sandstone reservoir

PARAMETER	UNITS	HEWETT UPPER BUNTER SANDSTONE RESERVOIR		HEWETT UPPER BUNTER SANDSTONE RESERVOIR	
		MEAN	MEDIAN	MEAN	MEDIAN
HYDRAULIC DIFFUSIVITY	m^2/s	2.60E-02	9.04E-03	2.60E-02	9.04E-03
AQUIFER LENGTH	m	18000.00	18000.00	3500.00	3500.00
DIFFUSION DISTANCE	m^2	3.24E+08	3.24E+08	1.23E+07	1.23E+07
TIME	secs	1.24E+10	3.58E+10	4.70E+08	1.35E+09
TIME	years	394.47	1135.91	14.91	42.95

Table 5.5 Estimation of characteristic diffusion time for a pressure pulse to propagate along various aquifer lengths within the Hewett Upper Bunter Sandstone reservoir based on hydraulic diffusivity estimates. Results estimated using equation 5.6.

Over the entire productive lifetime of the Hewett Upper Bunter Sandstone reservoir (ca. 40 years) the distance over which aquifer movement has occurred is between ~ 3-6 km based on the mean and median hydraulic diffusivity estimates (see Table 5.6).

PARAMETER	UNITS	HEWETT UPPER BUNTER SANDSTONE RESERVOIR	
		MEAN	MEDIAN
HYDRAULIC DIFFUSIVITY	m^2/s	2.60E-02	9.04E-03
TIME	years	40.00	40.00
TIME	secs	1.26E+09	1.26E+09
DIFFUSION DISTANCE	m^2	3.29E+07	1.14E+07
AQUIFER LENGTH	m	5731.82	3377.77

Table 5.6 Estimations of aquifer length within the Hewett Upper Bunter Sandstone reservoir based on mean and median hydraulic diffusivity estimates.

5.4.3.4. ESTIMATION OF THE CUMULATIVE VOLUME OF WATER INFLUX INTO THE HEWETT UPPER BUNTER SANDSTONE RESERVOIR

We have seen in equation 5.2 in the introduction of this chapter (section 5.1) that the material balance equation for a water drive reservoir can be written as in Table 5.7.

EQUATION	EQUATION NUMBER
$G(B_{gi}) = (G - G_p)B_g + W_e - W_pB_w$	(5.2)

Table 5.7 Restatement of equation 5.2, the material balance equation for a reservoir that experiences a water drive. After Archer and Wall (1986)

It follows that a linear equation can be solved by assuming values of W_e to *force* linearity:

$$\frac{G_pB_g + W_pB_w}{B_g - (B_{gi})} = \left[\frac{1}{B_g - B_{gi}}\right]W_e + G \qquad (5.7)$$

After Archer and Wall (1986)

The relationship between the assumed W_e values and reservoir pressure at the gas water contact can be used to characterise aquifer performance, i.e. steady state, pseudo steady state or unsteady state. The production terms ($G_pB_g + W_pB_w$) are denoted as F, and the volume expansion term ($B_g - B_{gi}$) as E_x, the material balance equation becomes:

$$F = W_e + GE_x \qquad (5.8)$$

Or expressed linearly:

$$\frac{F}{E_x} = \frac{W_e}{E_x} + G \tag{5.9}$$

The evaluation of W_e then becomes a forcing exercise (see Figure 5.21):

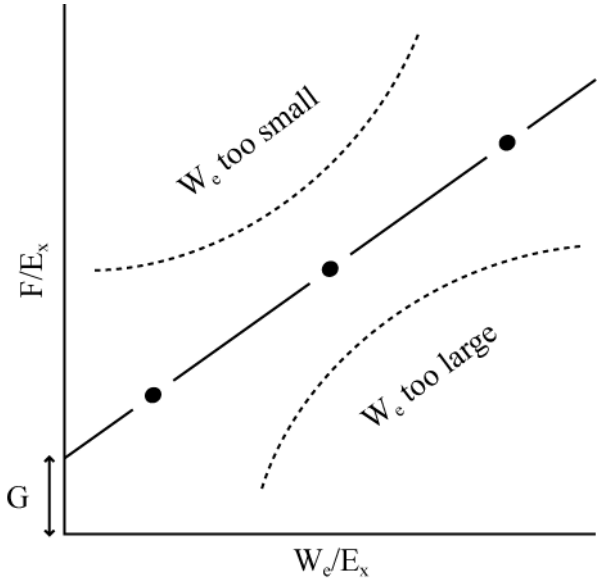

Figure 5.21 Assessing aquifer performance through assuming values of W_e. After Archer and Wall (1986).

Unfortunately it was not possible to obtain reliable results via this method as the necessary production parameter, W_p (cumulative volume of produced water) was unknown for the Hewett Upper Bunter Sandstone reservoir.

Instead, the unsteady state water influx theory of Van Everdingen and Hurst (1949) was used to estimate the cumulative volume of water influx, W_e, from the regional Bunter aquifer, into the Hewett Upper Bunter Sandstone reservoir. Throughout the study, the Hewett Upper Bunter Sandstone reservoir was considered to be a bounded aquifer rather than infinite, as the Southern North Sea stratigraphy is substantially faulted, and based on the results of Table 5.6, pressure changes within the Hewett Upper Bunter Sandstone reservoir only perturb pressures within

the regional aquifer waters up to ca. 6 km away over the productive lifetime of 40 years.

Aquifers can be characterised as radial or linear. In terms of the Hewett Upper Bunter Sandstone reservoir, the aquifer type was unknown, therefore both radial and linear models were evaluated.

For a radial aquifer, the following equation can be used to estimate the cumulative volume of water influx, W_e, into the Hewett Upper Bunter Sandstone reservoir:

$$W_e = U\Delta P W_D(t_D) \tag{5.10}$$

where U is the aquifer constant, ΔP is the pressure change over the time interval being assessed and $W_D(t_D)$ is the dimensionless cumulative water influx function.

For a radial aquifer, U is defined by the following equation:

$$U = 2\pi f \varphi h \left(c_{res} + c_{fluid}\right) {r_o}^2 \tag{5.11}$$

where, f is a constant used for aquifers which subtend angles of less than 360° and is defined by equation 5.12, ϕ is porosity, h is aquifer height, c_{res} is the matrix compressibility, c_{fluid} is the fluid (water) compressibility, and r_o^2 is the square of the reservoir radius. The constant, *f*, can be estimated using the following equation:

$$f = \frac{(encroachment\ angle)°}{360°} \tag{5.12}$$

The dimensionless cumulative water influx function, $W_D(t_D)$, is determined from graphs, after Van Everdingen and Hurst (1949), in Dake (1978), by reading off the value for W_D which corresponds to the point where dimensionless time, t_D, intersects the relevant curve for the dimensionless radius, r_{eD} (see Figure 5.22 and Figure 5.23). Dimensionless time, t_D, and dimensionless radius, r_{eD}, are determined using the following equations:

$$t_D = \frac{kt}{\varphi\mu(c_{res} + c_{fluid}){r_o}^2} \tag{5.13}$$

$$r_{eD} = \frac{r_e}{r_o} \tag{5.14}$$

where, k is permeability, t is time, μ is viscosity and r_e is the external boundary radius.

It is possible to check the W_D value estimated from the graphs (Figure 5.22 and Figure 5.23) using equation 5.13. In cases of bounded aquifers, irrespective of the geometry, there is a value of t_D for which the dimensionless water influx reaches a constant maximum value. The value is dependent upon the geometry as defined in equation 5.15:

$$Radial\ W_D(\max) = \frac{1}{2}({r_{eD}}^2 - 1) \tag{5.15}$$

For a linear aquifer, equation 5.8 can again be used to calculate W_e. However, the aquifer constant, U, is defined by the following equation:

$$U = wLh\varphi(c_{res} + c_{fluid}) \tag{5.16}$$

where, w is aquifer width and L is the aquifer length.

The equation for dimensionless time, t_D, is also modified to:

$$t_D = \frac{kt}{\varphi\mu(c_{res} + c_{fluid})L^2} \tag{5.17}$$

The dimensionless cumulative water influx function, W_Dt_D, is determined from Figure 5.22. For the example of the linear aquifer, however, values of W_D are determined by reading off where t_D intersects the line, "finite linear aquifer". It is

again possible to check the estimated W_D value: for a linear aquifer the maximum value for W_D is equal to 1.

The results for the Hewett Upper Bunter Sandstone reservoir are shown in Table 5.8. For the example of a finite radial aquifer, the constant, *f*, was calculated to be 0.5, as the encroachment angle was estimated as 180° due to the reservoir geometry. The Hewett Upper Bunter Sandstone reservoir is fault bounded to the east by the North Hewett Fault and the South Hewett Fault also runs nearby, parallel to the western flank of the anticline. This implies flow can occur in a N-S orientation (see Figure 5.24). Linear aquifer geometry is shown in Figure 5.25.

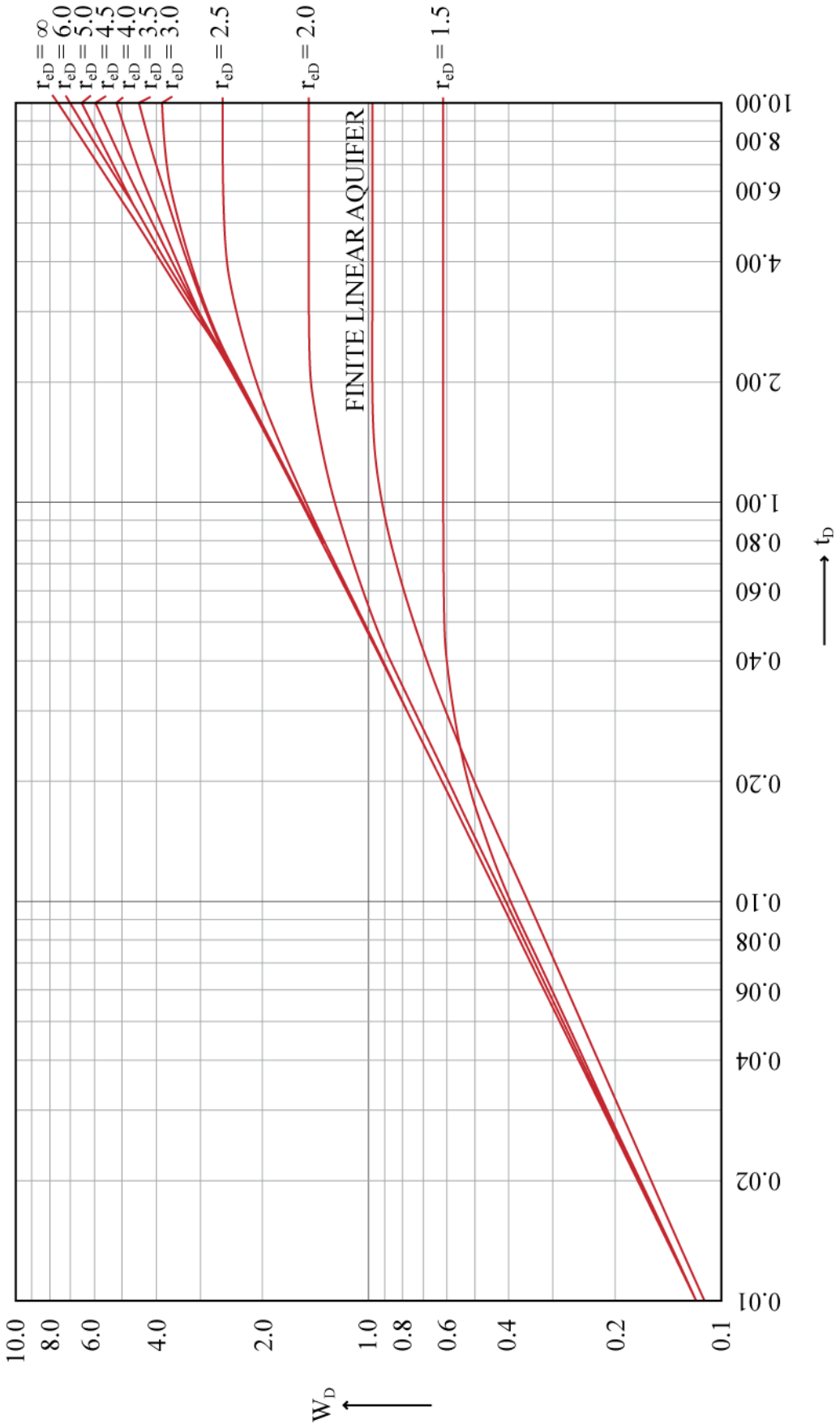

Figure 5.22 Dimensionless water influx for radial and linear flow. After Van Everdingen and Hurst (1949), in Dake (1978).

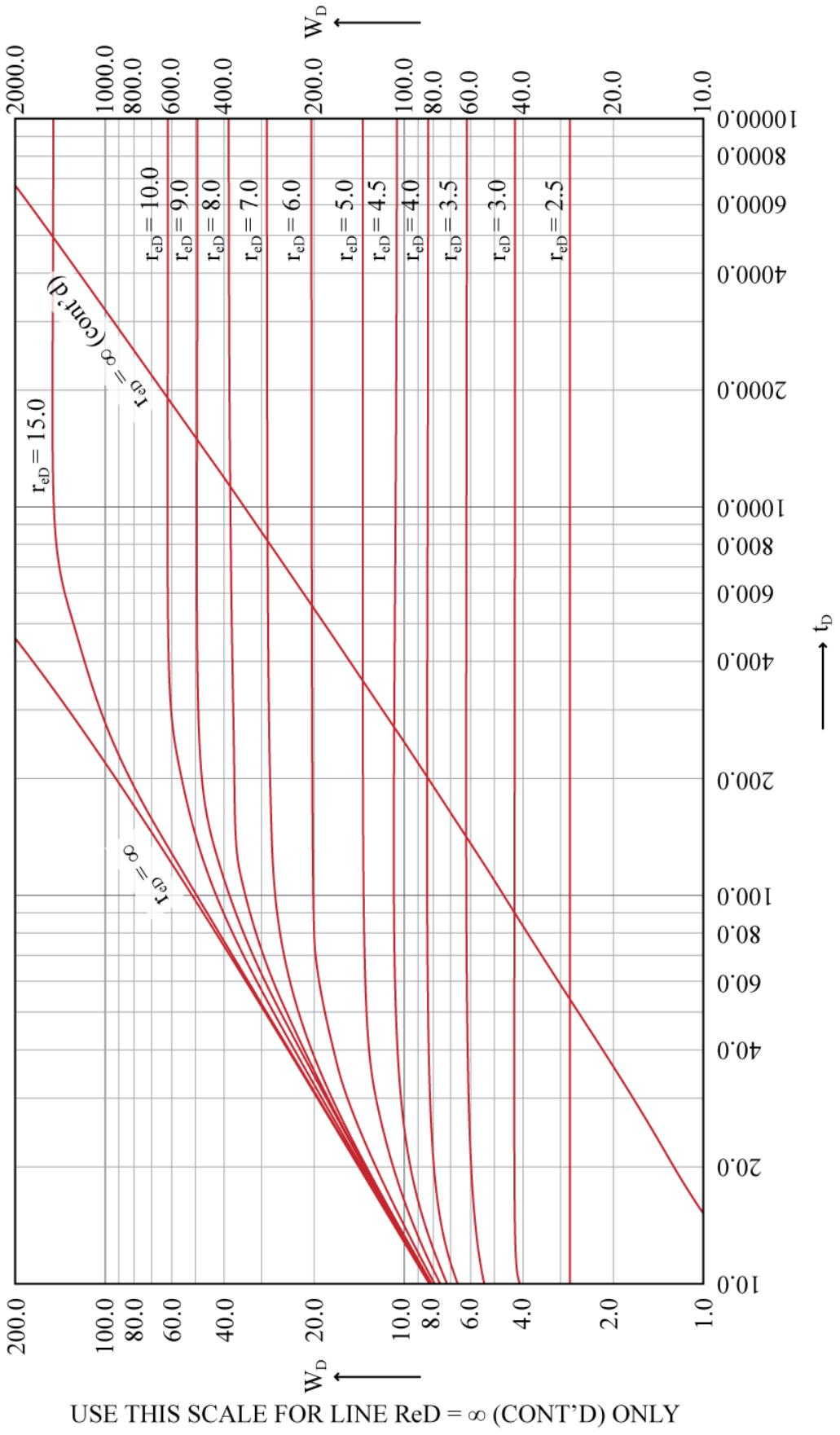

Figure 5.23 Dimensionless water influx for radial and linear flow. After Van Everdingen and Hurst (1949), in Dake (1978).

(a) FINITE RADIAL AQUIFER

PARAMETER	MEAN
f	0.50
t_D	682.00
U	0.13
R_{eD}	6.73
$W_D(t_D)$	22.15
W_e (m^3)	1.70E+07
Radial W_D (max)	22.158

(b) FINITE LINEAR AQUIFER

PARAMETER	MEAN
t_D	20.80
U	0.70
$W_D(t_D)$	1.00
W_e (m^3)	4.19E+06
Linear W_D (max)	1.00

Table 5.8 Results of the Van Everdingen and Hurst (1949) unsteady state water influx theory for the Hewett Upper Bunter Sandstone reservoir, as (s) a finite radial aquifer, and (b) a finite linear aquifer

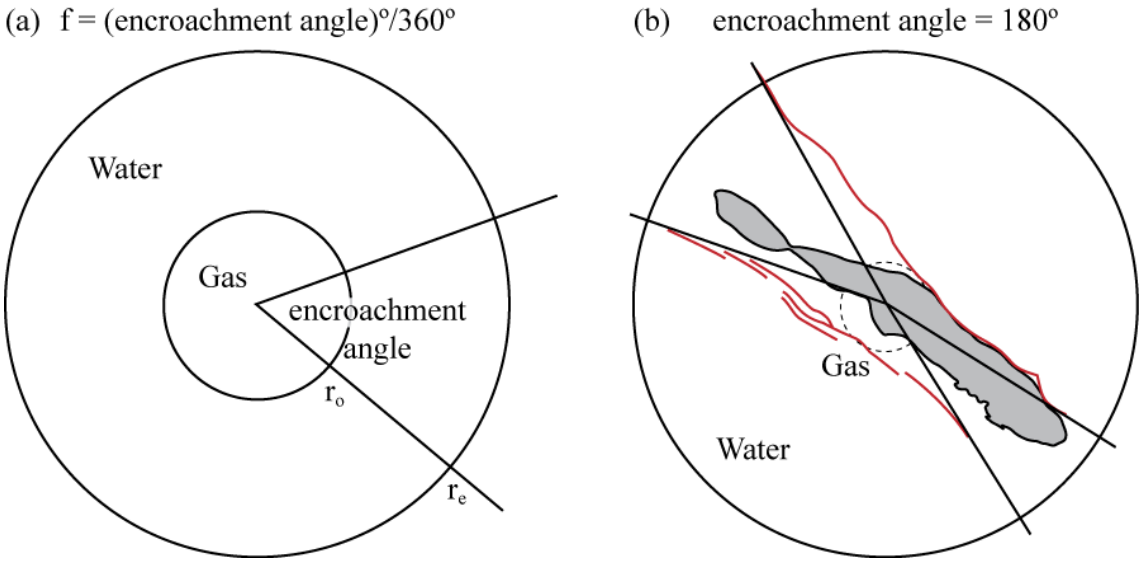

Figure 5.24 Radial aquifer geometry (a) schematic, (b) the Hewett Upper Bunter Sandstone reservoir. The Hewett Upper Bunter Sandstone reservoir outline can be observed in (b) with the bounding faults (red) to the east and west. The encroachment angle is 180° with water influx from both the north and south.

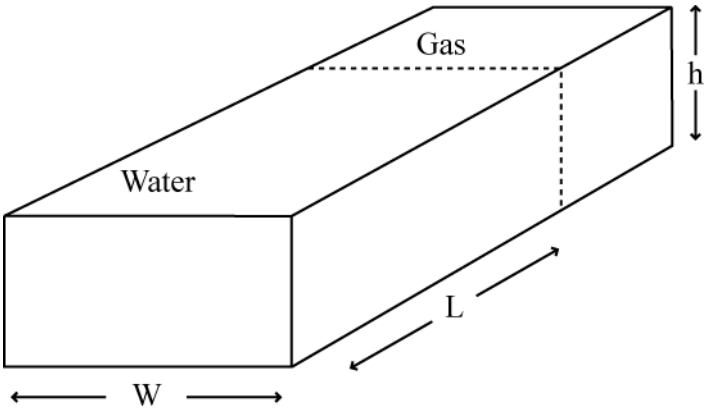

Figure 5.25 Linear aquifer geometry schematic. After Dake (1978).

5.4.3.5. ESTIMATING OGIP BASED ON AQUIFER MODELS

We have seen in section 5.4.3.1. that the industry estimated OGIP value of 38.398 billion cubic metres for the Hewett Upper Bunter Sandstone reservoir may be incorrect due to the reservoir experiencing a moderate water drive and the corresponding estimated value of W_e (the cumulative volume of water influx into the reservoir) being negative. Using the mean estimates of W_e obtained using the finite radial and linear aquifer models (Table 5.8) it is possible to obtain values of OGIP through rearranging equation 5.3:

$$OGIP = \frac{G_p - W_e E}{1 - E/E_i} \tag{5.18}$$

(After Dake (1978))

Estimates of OGIP were obtained using mean W_e values calculated from the finite radial and linear aquifer models, and a "base case" aquifer model whose values represent the average of the two (radial and linear) mean values of W_e. Results are shown in Table 5.9 and show that OGIP estimates are reduced by a maximum of 1.6 billion cubic metres of natural gas, compared with the original industry estimate. These calculations strongly suggest that the industry estimated OGIP value of 38.398 billion cubic metres is too large. As such, the revised estimates of OGIP will be input to both theoretical and effective CO_2 storage capacity equations in section 5.5.4., as they are considered to provide a more accurate basis for storage capacity estimation within the Hewett Upper Bunter Sandstone reservoir.

PARAMETER	ABBREVIATION	UNITS	VALUE
Cumulative Volume of Gas Produced	G_p	m^3	3.448E+10
Gas Expansion Factor	E	Dimensionless	6.408
Initial Gas Expansion Factor	E_i	Dimensionless	97.000
Finite Radial Aquifer Mean Cumulative Volume of Water Influx	W_e Radial Mean	m^3	1.700E+07
Finite Radial Aquifer Mean Original Gas In Place Estimate	**OGIP Radial Mean**	**m^3**	**3.680E+10**
Finite Linear Aquifer Mean Cumulative Volume of Water Influx	W_e Linear Mean	m^3	4.190E+06
Finite Linear Aquifer Mean Original Gas In Place Estimate	**OGIP Linear Mean**	**m^3**	**3.689E+10**
Base Case Cumulative Volume of Water Influx	W_e Base Case	m^3	1.060E+07
Base Case Original Gas In Place Estimate	**OGIP Base Case**	**m^3**	**3.685E+10**

Table 5.9 Estimates of original gas in place (OGIP) using equation 5.18 and based on mean W_e values (cumulative volume of water influx into a reservoir) from aquifer models (section 5.4.3.4.).

5.5. ESTIMATION OF RESERVOIR FLUID COMPRESSIBILITY AND IMPLICATIONS FOR CO_2 STORAGE CAPACITY ESTIMATION

As for the Hewett Lower Bunter Sandstone reservoir, estimations of the gas compressibility factor (or Z-factor) of the Hewett Upper Bunter Sandstone gas composition were made using both RefProp (Lemmon et al., 2013) and the Lawrence Berkeley National Laboratory online calculator, WebGasEOS (Reagan and Oldenburg, 2006) enabling several equations of state to be utilised for analysis.

The calculated results of the Z-factor were input into both methods for calculating theoretical (including Bachu et al. (2007), Holloway et al. (2006) and Tseng et al. (2012)) and effective CO_2 storage capacity (including Tseng et al. (2012)), as before in Chapter 4. Once again, through the variation of both estimation of Z-factor, the utilisation of several equations of state and the different methods used to calculate CO_2 storage capacity, a range of results were produced.

5.5.1. GAS COMPRESSIBILTY FACTOR ESTIMATION

5.5.1.1. REFPROP ESTIMATIONS OF GAS COMPRESSIBILITY FACTOR

RefProp (Lemmon et al., 2013) was used to investigate Z-factor variability of the gas compositions stated in Table 5.10 at constant temperature, whilst varying pressure and the equation of state used (Figure 5.26). The temperature was maintained once again at the initial reservoir temperature of 42.2 °C (315.372 K) within the Hewett Upper Bunter Sandstone reservoir as data encompassing temperature change through time was not available. Pressure was varied between the initial reservoir pressure of 9.391 MPa and the final reservoir pressure of 0.703 MPa. Gas compressibility factors were produced for three different equations of state: Peng-Robinson (Peng and Robinson, 1976), GERG-2008 (Kunz and Wagner, 2012) and the AGA8 Model (Starling and Savidge, 1992). Graphs of the results are displayed in Figure 5.26 and the main results to be used in the methods of storage capacity estimation are summarised in Table 5.11.

	MOLE FRACTION					
	Initial	20% CO_2	40% CO_2	60% CO_2	80% CO_2	99% CO_2
HEWETT UPPER BUNTER INITIAL GAS COMPOSITON						
Methane	0.8319	0.665520	0.499140	0.332760	0.166380	0.008319
Ethane	0.0532	0.042560	0.031920	0.021280	0.010640	0.000532
Propane	0.0214	0.017120	0.012840	0.008560	0.004280	0.000214
i-Butane	0.0021	0.001680	0.001260	0.000840	0.000420	0.000021
n-Butane	0.0015	0.001200	0.000900	0.000600	0.000300	0.000015
i-Pentane	0.0008	0.000640	0.000480	0.000320	0.000160	0.000008
Heavy HC	0.0041	0.003280	0.002460	0.001640	0.000820	0.000041
Hydrogen Sulphide	0.0002	0.000160	0.000120	0.000080	0.000040	0.000002
Carbon Dioxide	0.0008	0.200640	0.400480	0.600320	0.800160	0.990008
Nitrogen	0.0840	0.067200	0.050400	0.033600	0.016800	0.000840
TOTAL	**1.0000**	**1.0000**	**1.0000**	**1.0000**	**1.0000**	**1.0000**
PURE METHANE						
Methane	1.00	0.80	0.60	0.40	0.20	0.01
Carbon Dioxide	0.00	0.20	0.40	0.60	0.80	0.99
TOTAL	**1.00**	**1.00**	**1.00**	**1.00**	**1.00**	**1.00**
GAS MIX 1						
Methane	0.85	0.6800	0.5100	0.3400	0.1700	0.0085
Ethane	0.05	0.0400	0.0300	0.0200	0.0100	0.0005
Propane	0.02	0.0160	0.0120	0.0080	0.0040	0.0002
Nitrogen	0.08	0.0640	0.0480	0.0320	0.0160	0.0008
Carbon Dioxide	0.00	0.2000	0.4000	0.6000	0.8000	0.9900
TOTAL	**1.00**	**1.0000**	**1.0000**	**1.0000**	**1.0000**	**1.0000**
GAS MIX 2						
Methane	0.70	0.5600	0.4200	0.2800	0.1400	0.0070
Ethane	0.23	0.1840	0.1380	0.0920	0.0460	0.0023
Propane	0.05	0.0400	0.0300	0.0200	0.0100	0.0005
Nitrogen	0.02	0.0160	0.0120	0.0080	0.0040	0.0002
Carbon Dioxide	0.00	0.2000	0.4000	0.6000	0.8000	0.9900
TOTAL	**1.00**	**1.0000**	**1.0000**	**1.0000**	**1.0000**	**1.0000**
PURE CARBON DIOXIDE						
Carbon Dioxide	1.00					
TOTAL	**1.00**					

Table 5.10 Gas mixture compositions used in RefProp (Lemmon et al., 2013) and WebGasEOS (Reagan and Oldenburg, 2006) modelling of fluid properties.

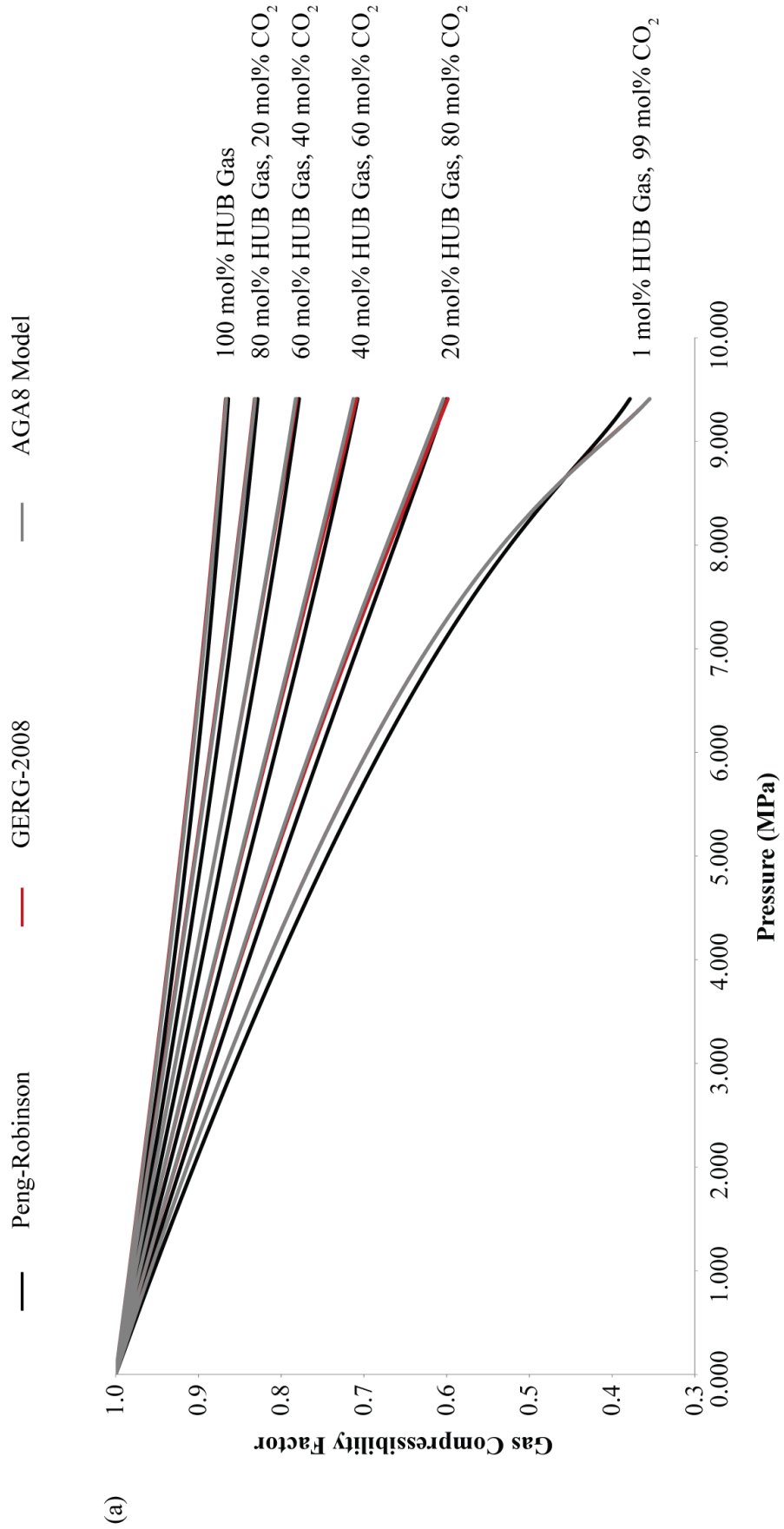
Peng-Robinson
GERG-2008
AGA8 Model
100 mol% HUB Gas
80 mol% HUB Gas, 20 mol% CO2
60 mol% HUB Gas, 40 mol% CO2
40 mol% HUB Gas, 60 mol% CO2
20 mol% HUB Gas, 80 mol% CO2
1 mol% HUB Gas, 99 mol% CO2
Gas Compressibility Factor
1.0
0.9
0.8
0.7
0.6
0.5
0.4
0.3
0.000
1.000
2.000
3.000
4.000
5.000
6.000
7.000
8.000
9.000
10.000
Pressure (MPa)

(a)

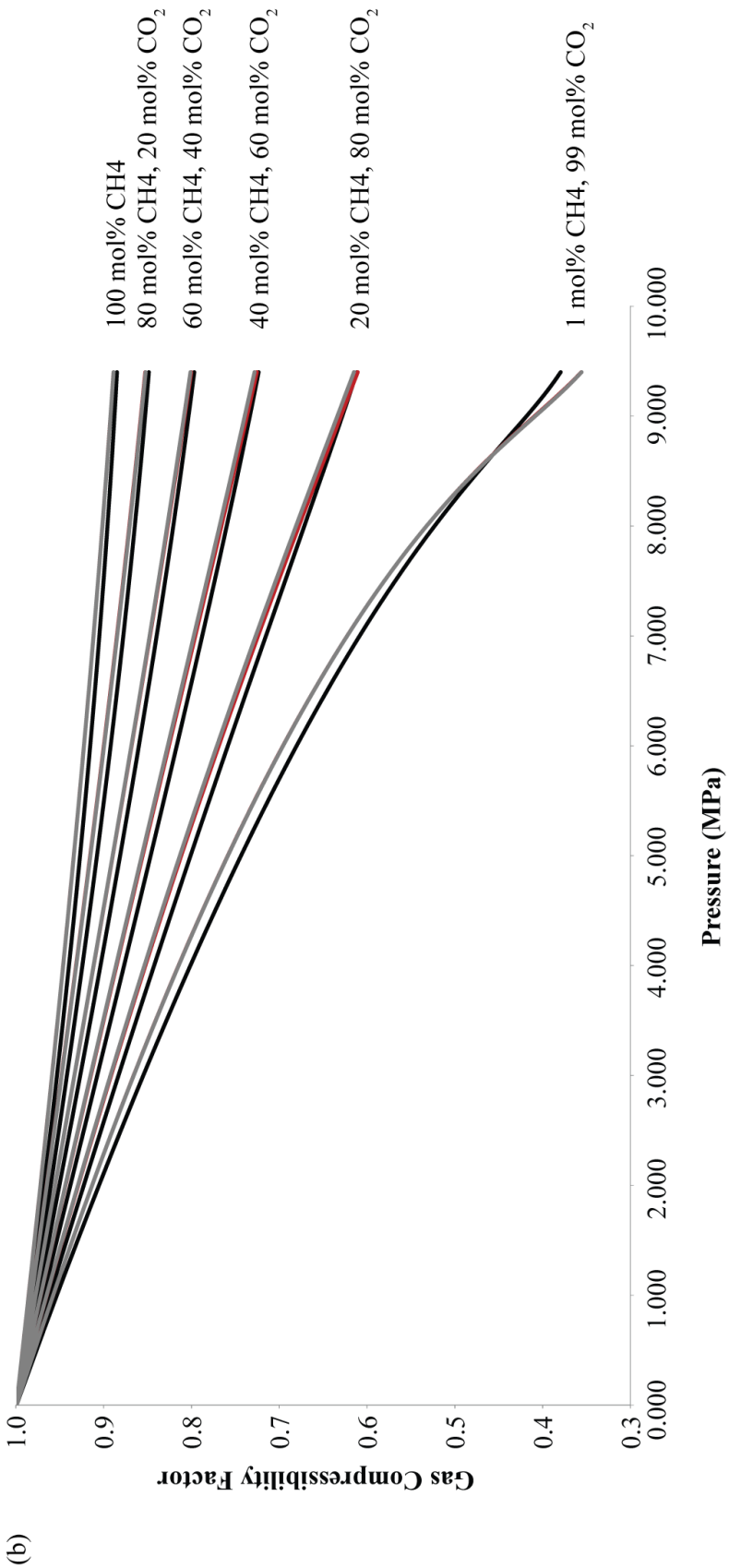
100 mol% CH4
80 mol% CH4, 20 mol% CO2
60 mol% CH4, 40 mol% CO2
40 mol% CH4, 60 mol% CO2
20 mol% CH4, 80 mol% CO2
1 mol% CH4, 99 mol% CO2
Gas Compressibility Factor
Pressure (MPa)
1.0
0.9
0.8
0.7
0.6
0.5
0.4
0.3
0.000
1.000
2.000
3.000
4.000
5.000
6.000
7.000
8.000
9.000
10.000

(b)

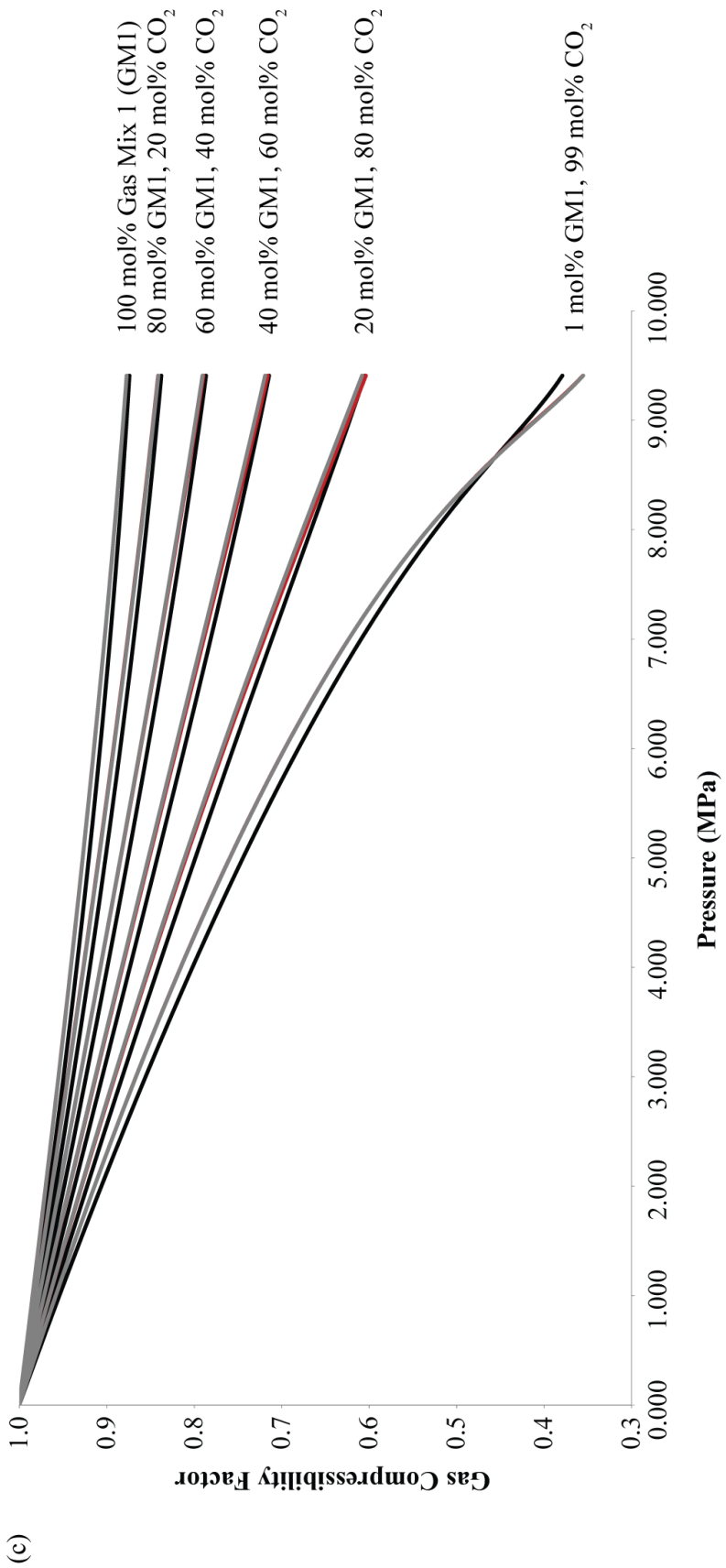
100 mol% Gas Mix 1 (GM1)
80 mol% GM1, 20 mol% CO2
60 mol% GM1, 40 mol% CO2
40 mol% GM1, 60 mol% CO2
20 mol% GM1, 80 mol% CO2
1 mol% GM1, 99 mol% CO2
Gas Compressibility Factor
1.0
0.9
0.8
0.7
0.6
0.5
0.4
0.3
0.000
1.000
2.000
3.000
4.000
5.000
6.000
7.000
8.000
9.000
10.000
Pressure (MPa)

(c)

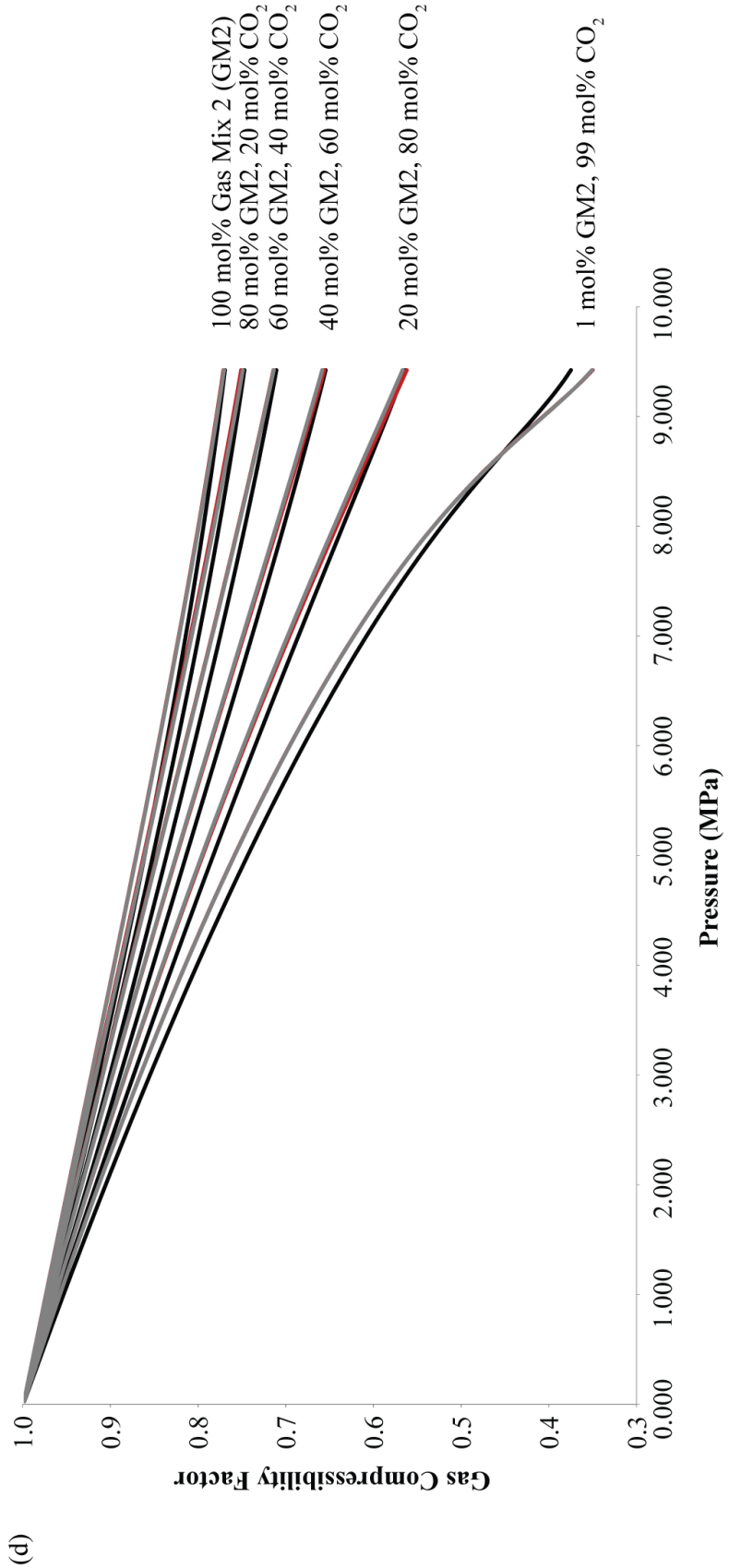
(d)
Gas Compressibility Factor
1.0
0.9
0.8
0.7
0.6
0.5
0.4
0.3
0.000
1.000
2.000
3.000
4.000
5.000
6.000
7.000
8.000
9.000
10.000
Pressure (MPa)
100 mol% Gas Mix 2 (GM2)
80 mol% GM2, 20 mol% CO2
60 mol% GM2, 40 mol% CO2
40 mol% GM2, 60 mol% CO2
20 mol% GM2, 80 mol% CO2
1 mol% GM2, 99 mol% CO2

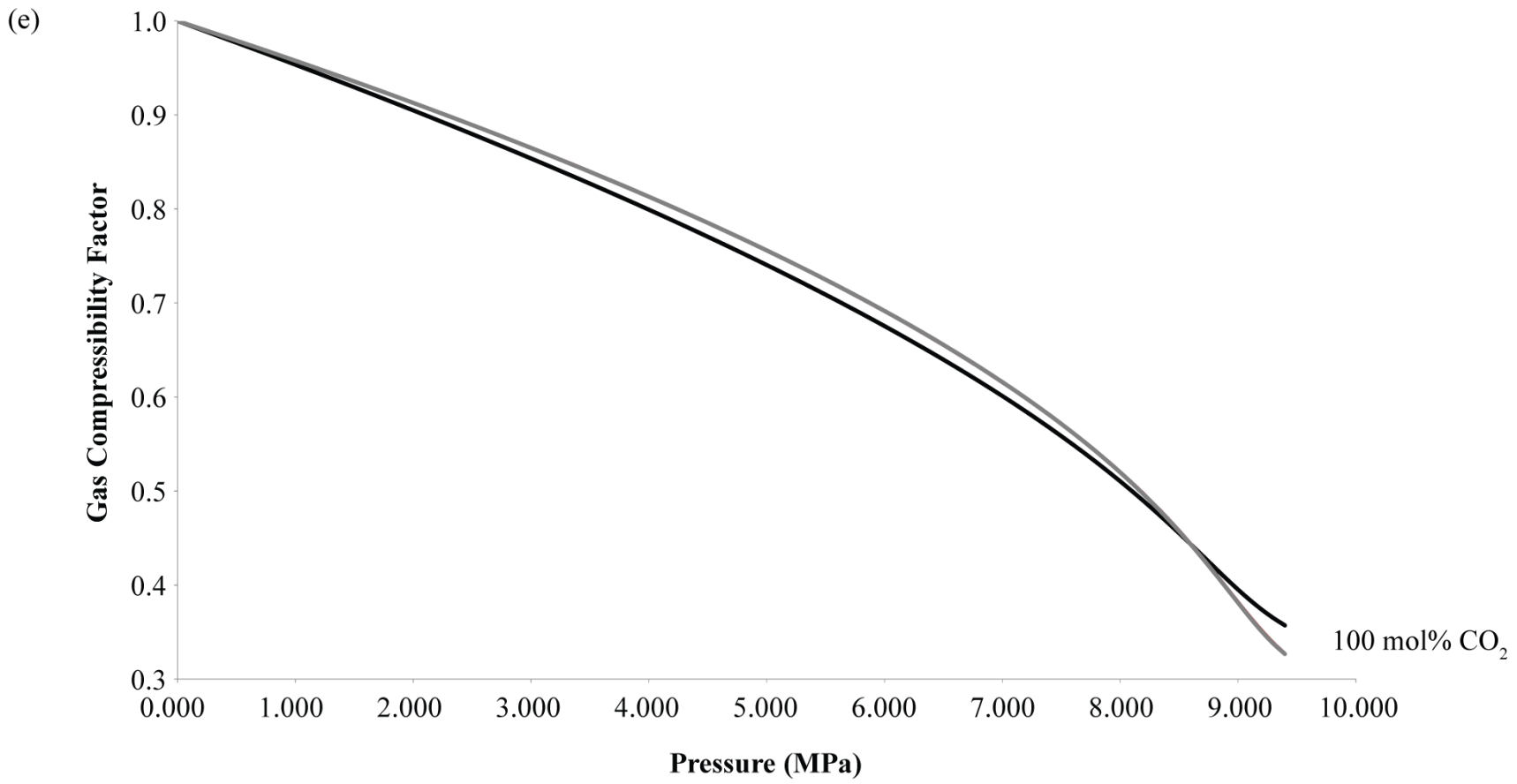

Figure 5.26 Hewett Upper Bunter Sandstone Reservoir Gas Compressibility Factor variation with pressure at constant temperature (42.2 °C) using the Peng-Robinson, GERG-2008 and AGA8 Model Equations of State and different gas compositions, modelled in RefProp (Lemmon et al., 2013). (a) Hewett Upper Bunter Sandstone reservoir initial gas composition with increasing mol% CO_2; (b) Pure methane with increasing mol% CO_2; (c) Gas mix 1 (as defined in Table 5.10) with increasing mol% CO_2; (d) Gas mix 2 (as defined in Table 5.10) with increasing mol% CO_2; (e) Pure CO_2.

EQUATION OF STATE	PARAMETER	UNITS	HUB INITIAL GAS COMPOSITION	PURE METHANE	GAS MIX 1	GAS MIX 2
Peng-Robinson	z_{iCO2}	Dimensionless	0.357	0.357	0.357	0.357
	z_{ihc}	Dimensionless	0.864	0.885	0.874	0.770
	z_{gas}	Dimensionless	0.987	0.989	0.987	0.979
	ρCO_2	kg/m^3	441.41	441.41	441.41	441.41
GERG-2008	z_{iCO2}	Dimensionless	0.327	0.327	0.327	0.327
	z_{ihc}	Dimensionless	0.867	0.889	0.877	0.772
	z_{gas}	Dimensionless	0.988	0.990	0.989	0.982
	ρCO_2	kg/m^3	482.11	482.11	482.11	482.11
AGA8 Model	z_{iCO2}	Dimensionless	0.327	0.327	0.327	0.327
	z_{ihc}	Dimensionless	0.866	0.889	0.877	0.771
	z_{gas}	Dimensionless	0.988	0.990	0.989	0.982
	ρCO_2	kg/m^3	482.20	482.20	482.20	482.20

Table 5.11 Summary of RefProp (Lemmon et al., 2013) Estimated Isoproperties for various Equations of State.

Figure 5.26 shows the variability of the gas compressibility factor with the particular equation of state used for the gas compositions shown. In general, the Peng-Robinson equation of state (Peng and Robinson, 1976) predicts a higher degree of gas compressibility for all gas mixes with increasing mole percentages of CO_2. When there is 99 mol% CO_2 within the reservoir, gas compressibility factor estimations of the Peng-Robinson equation of state (Peng and Robinson, 1976) predict a lower compressibility than those of the GERG-2008 (Kunz and Wagner, 2012) and AGA8 Model (Starling and Savidge, 1992) equations of state at pressures of ≥ 9 MPa.

For reservoir compositions between 0 and 80 mol% CO_2 there is a divergence in estimation of gas compressibility factor as pressure increases, with the Peng-Robinson equation of state (Peng and Robinson, 1976) predicting the highest degree of gas compressibility and in general the AGA8 Model equation of state (Starling and Savidge, 1992) predicting the lowest degree. At pressures greater than 5 MPa, gas compressibility factor estimations start to converge again and are almost consistent at 9.391 MPa (initial pre-production pressure of the Hewett Upper Bunter Sandstone reservoir).

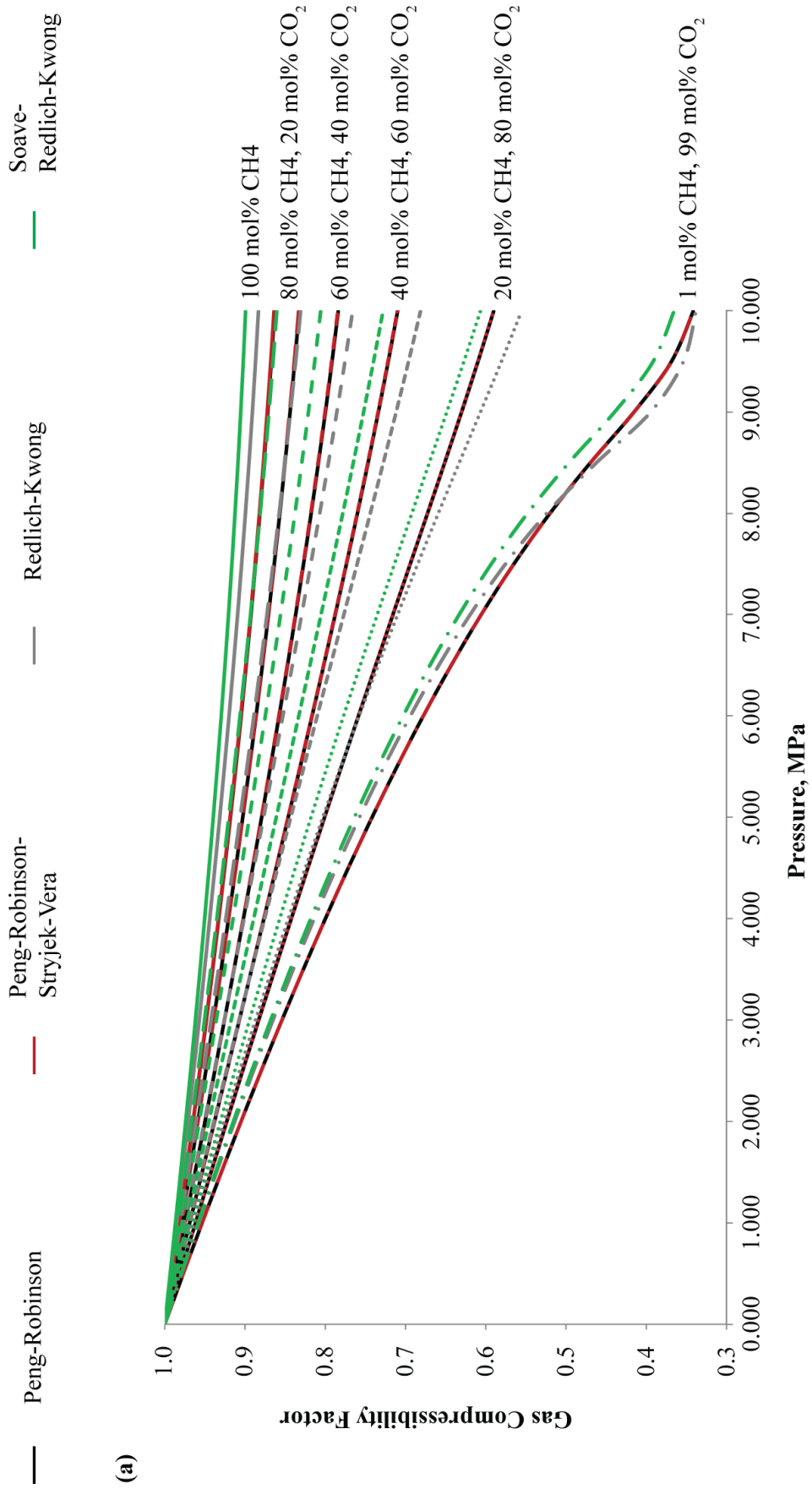
(a)
Peng-Robinson
Peng-Robinson-Stryjek-Vera
Redlich-Kwong
Soave-Redlich-Kwong
100 mol% CH4
80 mol% CH4, 20 mol% CO2
60 mol% CH4, 40 mol% CO2
40 mol% CH4, 60 mol% CO2
20 mol% CH4, 80 mol% CO2
1 mol% CH4, 99 mol% CO2
Gas Compressibility Factor
1.0
0.9
0.8
0.7
0.6
0.5
0.4
0.3
0.000
1.000
2.000
3.000
4.000
5.000
6.000
7.000
8.000
9.000
10.000
Pressure, MPa

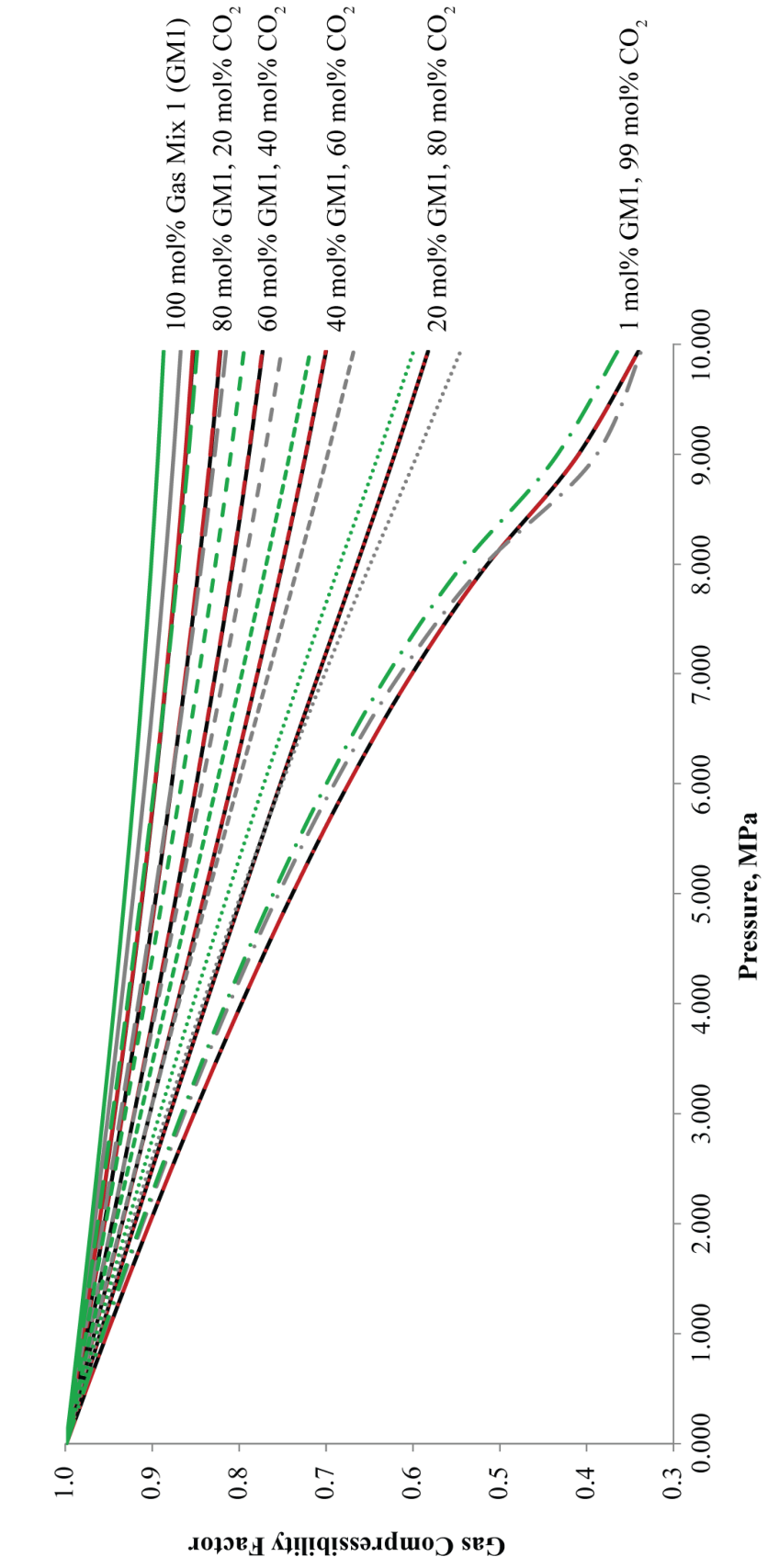
100 mol% Gas Mix 1 (GM1)
80 mol% GM1, 20 mol% CO2
60 mol% GM1, 40 mol% CO2
40 mol% GM1, 60 mol% CO2
20 mol% GM1, 80 mol% CO2
1 mol% GM1, 99 mol% CO2
Gas Compressibility Factor
1.0
0.9
0.8
0.7
0.6
0.5
0.4
0.3
0.000
1.000
2.000
3.000
4.000
5.000
6.000
7.000
8.000
9.000
10.000
Pressure, MPa

(b)

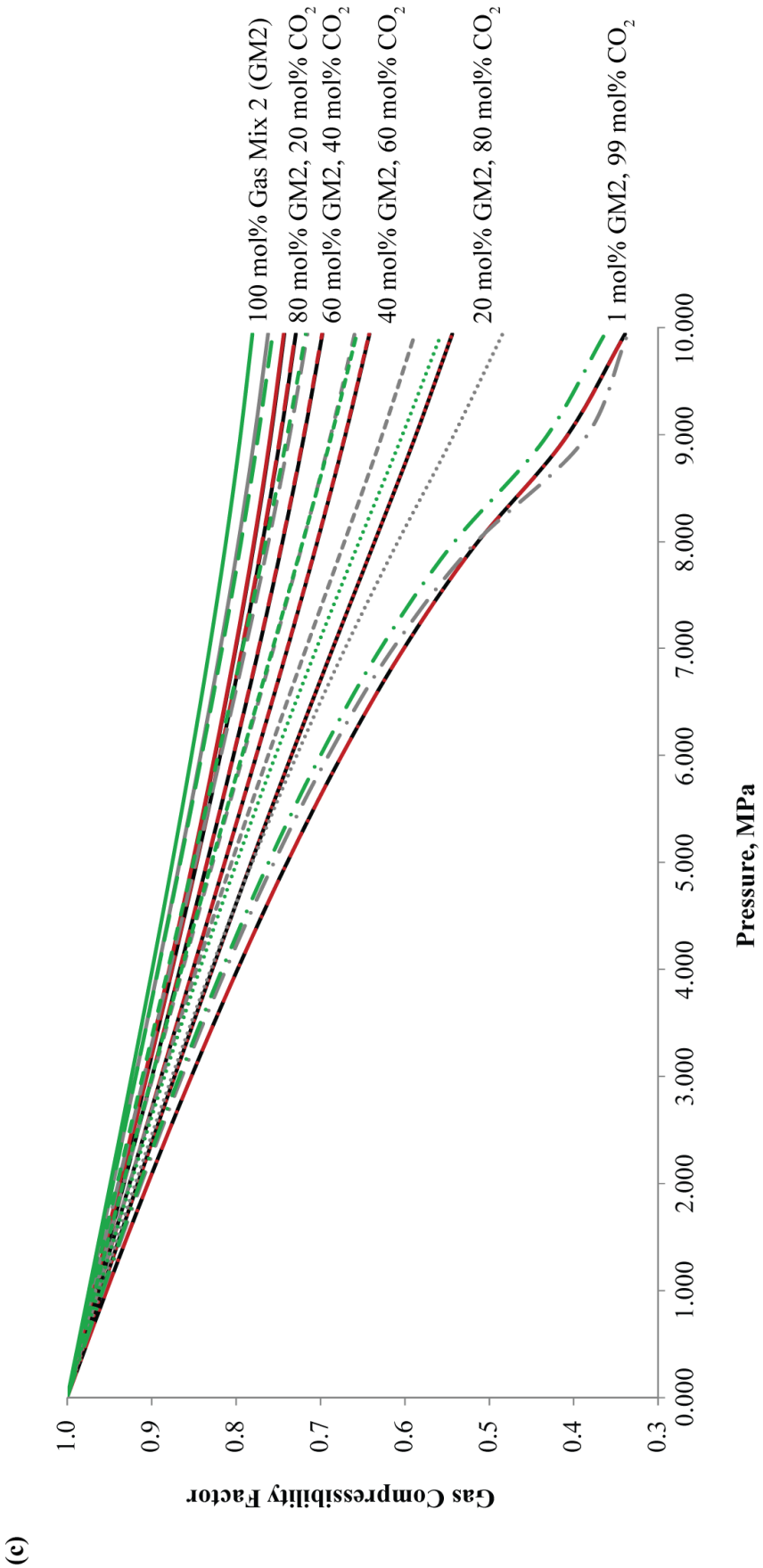
100 mol% Gas Mix 2 (GM2)
80 mol% GM2, 20 mol% CO2
60 mol% GM2, 40 mol% CO2
40 mol% GM2, 60 mol% CO2
20 mol% GM2, 80 mol% CO2
1 mol% GM2, 99 mol% CO2
Gas Compressibility Factor
1.0
0.9
0.8
0.7
0.6
0.5
0.4
0.3
0.000
1.000
2.000
3.000
4.000
5.000
6.000
7.000
8.000
9.000
10.000
Pressure, MPa

(c)

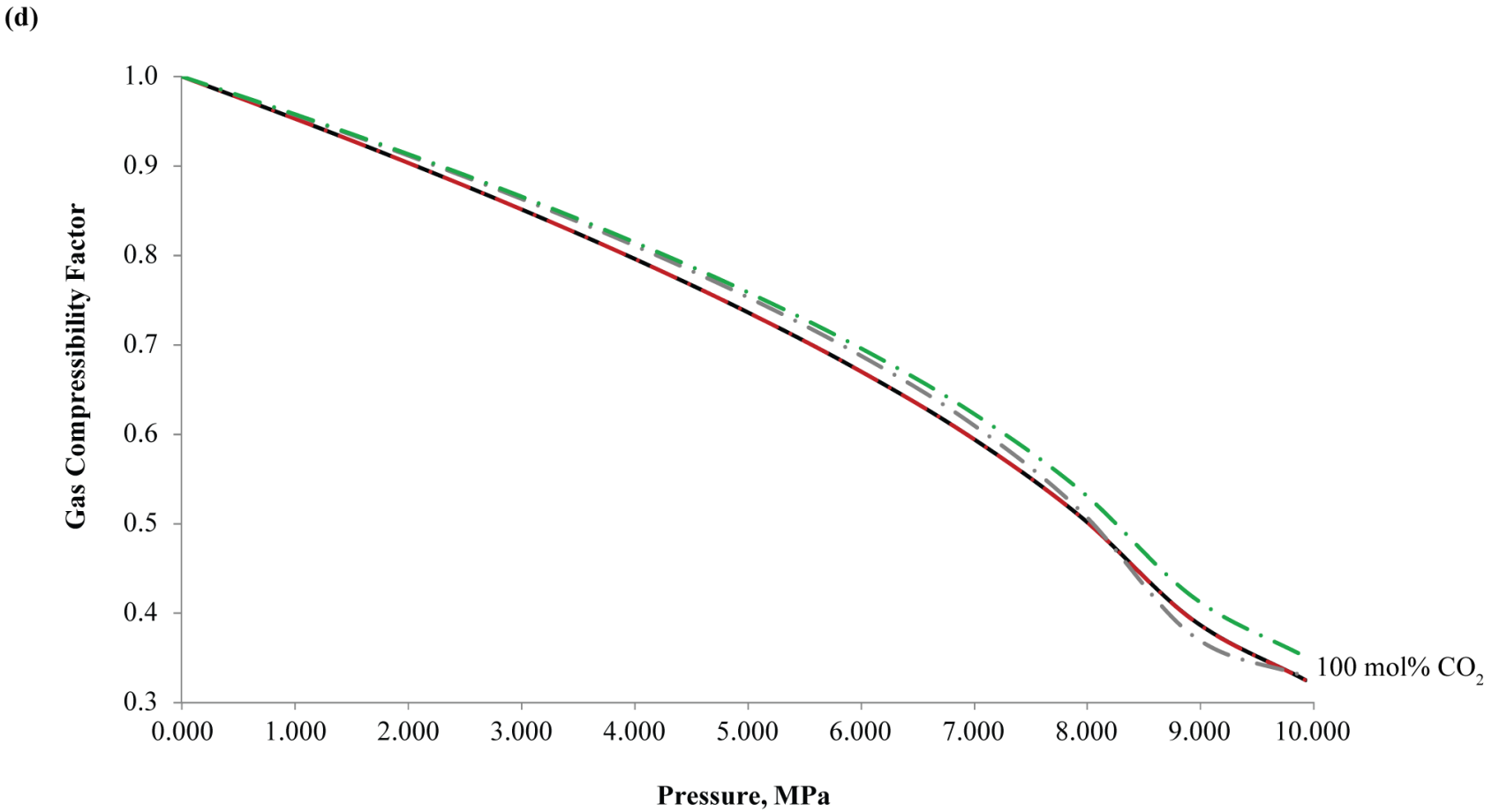

Figure 5.27 Hewett Upper Bunter Sandstone Reservoir Gas Compressibility Factor variation with pressure at constant temperature (42.2 °C) using the Peng-Robinson, Peng-Robinson-Stryjek-Vera, Redlich-Kwong and Soave-Redlich-Kwong Equations of State and different gas compositions, modelled in WebGasEOS (Reagan and Oldenburg, 2006). (a) Pure methane with increasing mol% CO_2; (b) Gas mix 1 (as defined in Table 5.10) with increasing mol% CO_2; (c) Gas mix 2 (as defined in Table 5.10) with increasing mol% CO_2; (d) Pure CO_2

EQUATION OF STATE	PARAMETER	UNITS	PURE METHANE	GAS MIX 1	GAS MIX 2
Peng-Robinson	z_{iCO2}	Dimensionless	0.354	0.354	0.354
	z_{ihc}	Dimensionless	0.868	0.859	0.753
	z_{gas}	Dimensionless	0.987	0.986	0.978
	ρCO_2	kg/m^3	445.57	445.57	445.57
Peng-Robinson-Stryjek-Vera	z_{iCO2}	Dimensionless	0.353	0.353	0.353
	z_{ihc}	Dimensionless	0.869	0.860	0.753
	z_{gas}	Dimensionless	0.987	0.986	0.978
	ρCO_2	kg/m^3	445.91	445.91	445.91
Redlich-Kwong	z_{iCO2}	Dimensionless	0.344	0.344	0.344
	z_{ihc}	Dimensionless	0.888	0.873	0.772
	z_{gas}	Dimensionless	0.990	0.988	0.981
	ρCO_2	kg/m^3	457.82	457.82	457.82
Soave-Redlich-Kwong	z_{iCO2}	Dimensionless	0.379	0.379	0.379
	z_{ihc}	Dimensionless	0.903	0.892	0.789
	z_{gas}	Dimensionless	0.991	0.990	0.982
	ρCO_2	kg/m^3	416.40	416.40	416.40

Table 5.12 Summary of WebGasEOS (Reagan and Oldenburg, 2006) Estimated Isoproperties for various Equations of State.

5.5.1.2. WEBGASEOS ESTIMATIONS OF GAS COMPRESSIBILITY FACTOR

WebGasEOS (Reagan and Oldenburg, 2006) was used as for the Hewett Lower Bunter Sandstone reservoir to estimate the gas compressibility factor of the gas mixtures (Table 5.10) using alternative equations of state including Peng-Robinson (Peng and Robinson, 1976), Peng-Robinson-Stryjek-Vera (Stryjek and Vera, 1986), Redlich-Kwong (Redlich and Kwong, 1949), and Soave-Redlich-Kwong (Soave, 1972). Once again, due to the limited number of species that can be included in the gas mixture analysis, and the lack of integral components to the Hewett Upper Bunter Sandstone reservoir gas composition, it was not possible to simulate results for this mixture. Species lacking in the WebGasEOS tool, but present in the Hewett Upper Bunter Sandstone reservoir gas composition include i-Butane, n-Butane, i-Pentane and hexane. However, estimations of the gas compressibility factor were predicted for pure methane, gas mix 1, gas mix 2 and pure carbon dioxide fluids, making these results comparable with those of the Hewett Lower Bunter Sandstone reservoir (Chapter 4) and the results of the RefProp analysis of these fluids within the Hewett Upper Bunter Sandstone reservoir (this chapter).

Graphs of the results are shown in Figure 5.27 and a summary of the main isoproperties for input into the storage capacity estimation methodologies are displayed in Table 5.12.

Figure 5.27 shows the variability of the gas compressibility factor with equation of state used as estimated in WebGasEOS for the gas compositions shown in Table 5.10, excluding the Hewett Upper Bunter Sandstone reservoir initial gas composition. Equations of state used for modelling include Peng Robinson (Peng and Robinson, 1976), Peng-Robinson-Stryjek-Vera (Stryjek and Vera, 1986), Redlich-Kwong (Redlich and Kwong, 1949) and Soave-Redlich-Kwong (Soave, 1972).

As for the Hewett Lower Bunter Sandstone reservoir, the Soave-Redlich-Kwong equation of state (Soave, 1972) always predicts a much lower gas compressibility than the other equations of state within WebGasEOS. The Redlich-Kwong equation of state (Redlich and Kwong, 1949) predicts a low, but higher

compressibility than that of Soave-Redlich-Kwong (Soave, 1972), when there is a higher mole percent of natural gas within the gas composition. However, when there is > 40 mol% CO_2 in the gas composition, the Redlich-Kwong equation of state (Redlich and Kwong, 1949) predicts the highest gas compressibilities out of all the equations of state modelled in WebGasEOS.

The Peng-Robinson (Peng and Robinson, 1976) and Peng-Robinson-Stryjek-Vera (Stryjek and Vera, 1986) equations of state always predict very similar curves for the temperature and pressure conditions modelled here. At 100 mol% natural gas, they predict the highest compressibility. However, when there is > 40 mol% CO_2 in the gas composition, they predict a compressibility curve that tends to lie between those estimated using the Redlich-Kwong (Redlich and Kwong, 1949) and Soave-Redlich-Kwong (Soave, 1972) equations of state.

There is some variability with gas compositions consisting of 80 mol % CO_2. At lower pressures (below ~ 6 MPa at 42.2 °C), the curve predicted with the Redlich-Kwong equation of state (Redlich and Kwong, 1949) estimates lower gas compressibilities than those predicted by the Peng-Robinson (Peng and Robinson, 1976) and Peng-Robinson-Stryjek-Vera (Stryjek and Vera, 1986) equations of state. The curves crossover at pressures between 5.5-6 MPa for all graphs in Figure 5.27 (a) to (d) with a gas composition of 80 mol% CO_2.

Similarly, for the gas composition of 99 mol% CO_2, this crossover occurs at a slightly higher pressure of between 8-8.5 MPa, where the curve estimated using the Redlich-Kwong equation of state (Redlich and Kwong, 1949) dips below those of the Peng-Robinson (Peng and Robinson, 1976) and Peng-Robinson-Stryjek-Vera (Stryjek and Vera, 1986) equations of state. However, as the pressure further increases the Redlich-Kwong equation of state (Redlich and Kwong, 1949) begins to converge with the Peng-Robinson (Peng and Robinson, 1976) and Peng-Robinson-Stryjek-Vera (Stryjek and Vera, 1986) equations of state in graphs (a) to (d). In graph (d) alone, showing the gas compressibility factor of pure CO_2, the curves in fact crossover at just below 10 MPa (greater than the initial reservoir pressure of the Hewett Upper Bunter Sandstone reservoir).

5.5.2. GAS FORMATION VOLUME FACTOR ESTIMATION

The gas formation volume factor has been calculated within the Hewett Upper Bunter Sandstone reservoir throughout its productive lifetime using the equations previously defined in Chapter 4, see Table 5.13.

GAS FORMATION VOLUME FACTOR EQUATION	EQUATION NUMBER
$B_g = \frac{reservoir\ volume}{standard\ condition\ volume}$	(4.2)
$B_g = \frac{P_{sc}}{T_{sc}} \times T_{res} \times \frac{z_{res}}{P_{res}}$	(4.3)

Table 5.13 Gas formation volume factor equations as stated previously in Chapter 4. After Archer and Wall (1986).

The results of the two methods have been plotted and can be compared to the industry calculated Z-factor provided by ENI, and resulting estimated gas formation volume factors. The results have been estimated under the initial reservoir temperature condition of 315.372 K, whilst varying pressure. The results are shown in Figure 5.28.

As can be seen from Figure 5.28, the difference between the results of the two methods and the various equations of state are negligible. This implies that estimates of the gas formation volume factor are very well constrained within the Hewett Upper Bunter Sandstone reservoir, and can be treated with confidence when used within CO_2 storage capacity calculations.

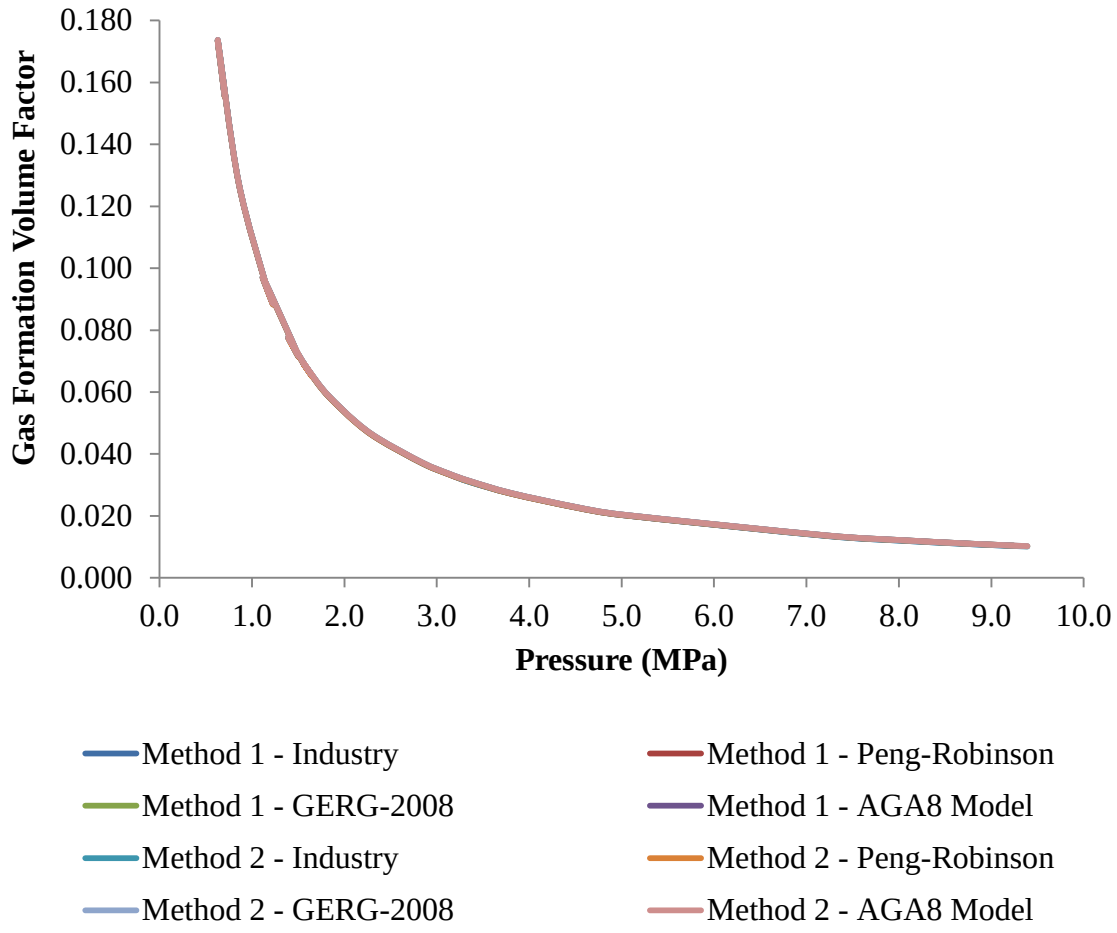

Figure 5.28 Estimation of the gas formation volume factor within the Hewett Upper Bunter Sandstone reservoir using two main methods of calculation and a variety of equations of state, under initial temperature conditions of 315.372 K. The gas compressibility factor, necessary for the calculation of the gas formation volume factor (B_g) was estimated using RefProp (Lemmon et al., 2013). Three equations of state were used: Peng-Robinson (Peng and Robinson, 1976), GERG-2008 (Kunz and Wagner, 2012), and the AGA8-DC92 Model (Starling and Savidge, 1992). These values were compared back to industry calculated values.

5.5.3. ESTIMATION OF CO_2 DENSITY

CO_2 density has been estimated within RefProp (Lemmon et al., 2013) using three equations of state: Peng-Robinson (Peng and Robinson, 1976), GERG-2008 (Kunz and Wagner, 2012), and the AGA8-DC92 Model (Starling and Savidge, 1992). The results were estimated under the initial reservoir temperature conditions of 315.372 K, whilst varying pressure. The results are shown in Figure 5.29.

The results show that CO_2 density increases with pressure. All three equations of state predict very similar CO_2 densities between 0.0 and 8.8 MPa. However, between 8.8 and 10.0 MPa, i.e. the end of the displayed pressure range, the GERG-2008 (Kunz and Wagner, 2012) and AGA8-DC92 (Starling and Savidge, 1992) equations of state continue to predict very similar CO_2 densities, however, the Peng-Robinson (Peng and Robinson, 1976) equation of state diverges away from the other two, predicting lower CO_2 densities.

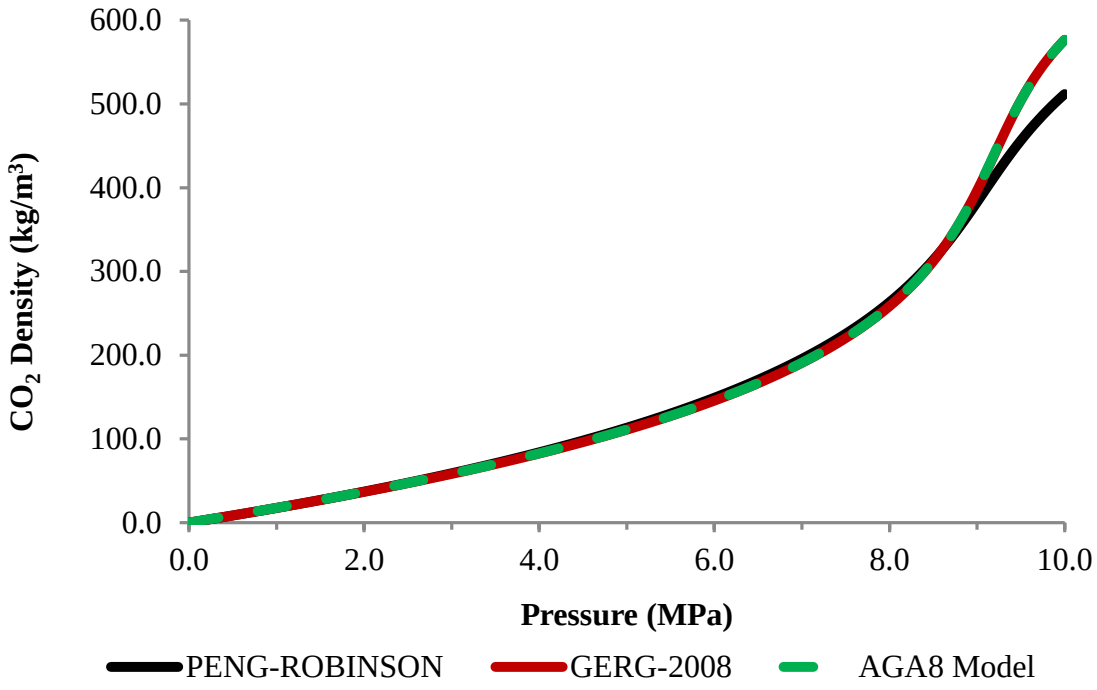

Figure 5.29 Estimations of CO_2 density with pressure within the Hewett Upper Bunter Sandstone reservoir under initial reservoir temperature conditions of 315.372 K. Results have been estimated using RefProp (Lemmon et al., 2013) and various equations of state: Peng-Robinson (Peng and Robinson, 1976), GERG-2008 (Kunz and Wagner, 2012), and the AGA8-DC92 Model (Starling and Savidge, 1992).

5.5.4. STORAGE CAPACITY ESTIMATION RESULTS

The estimates of gas compressibility factor and density for the individual gas compositions were used to calculate both theoretical and effective storage capacities of the Hewett Upper Bunter Sandstone reservoir using various published methods.

5.5.4.1. THEORETICAL CO_2 STORAGE CAPACITY ESTIMATES

Theoretical CO_2 storage capacity estimates of the Hewett Upper Bunter Sandstone reservoir (previously defined in Chapter 1 and Chapter 4) were estimated using methods (restated in Table 4.8) provided by Bachu et al. (2007), Holloway et al. (2006), and Tseng et al. (2012).

The Hewett Upper Bunter Sandstone reservoir has produced over 34.5 billion cubic metres of natural gas over its entire productive lifetime, equating to a mass of 27.6 Mt Hewett Upper Bunter Sandstone reservoir gas at standard conditions.

As previously stated in Chapter 4, the geometric-based approach of Bachu et al. (2007), Table 4.8, equation 1.1, requires the use of parameters that have natural variability within a sandstone reservoir, such as porosity, reservoir area and reservoir height. As such, Monte Carlo simulation has been used to reduce the risk of storage capacity estimates produced using this method.

Porosity data was again taken from well data made available to Durham University by IHS and assigned a best-fit probability distribution, found to be a Beta distribution, within Oracle Crystal Ball software (Figure 5.8). Both reservoir area and reservoir height were assigned uniform distributions due to limited data from wells, i.e. there is an equal chance of obtaining a value between 67-82 km^2 for reservoir area, and 99-193 m for reservoir height.

Monte Carlo simulation was then used to produce the results (probability distributions) illustrated in Figure 5.30 using a recovery factor based on the industry estimated OGIP value. Simulated forecast values based on the probability distributions are displayed in Table 5.15 (a) showing the minimum, P10, P50

(median), mean, P90 and maximum values for the porosity distributions using the industry estimated OGIP estimate. Monte Carlo simulation was also used to produce tabulated forecast values of storage capacity estimates using recovery factors based on the OGIP estimates from the finite radial aquifer model, finite linear aquifer model and the "base case" aquifer model. These results are displayed in Table 5.15 (b), (c) and (d), respectively, again showing the minimum, P10, P50 (median), mean, P90 and maximum values. Once again, the results illustrate the vast amount of variability in CO_2 storage capacity estimation using the method of Bachu et al. (2007): the average range between minimum and maximum storage capacity estimates for the Hewett Upper Bunter Sandstone reservoir of all the models is 1786.6 Mt CO_2.

The mean CO_2 storage capacity values for the industry estimated aquifer model have been plotted alone in Figure 5.31. Error bars on the figure show the minimum, maximum, P10 and P90 values, i.e. the extent of variance within the industry estimated aquifer model storage capacity results. A sensitivity plot of the method of Bachu et al. (2007), Table 4.8, equation 1.1, shows that the theoretical CO_2 storage capacity results are most sensitive to porosity, followed by reservoir height and reservoir area (see Figure 5.32).

Theoretical storage capacity results by Bachu et al. (2007), Table 4.8, equation 1.2; Holloway et al. (2006), Table 4.8, equation 1.3; and Tseng et al. (2012), Table 4.8, equation 1.4, are based upon the principle that a variable proportion of the pore space occupied by the recoverable reserves will be available for CO_2 storage. The majority of parameters required within the methods are well constrained values which do not show variability. However, as has been demonstrated in section 5.4.3., the industry estimated OGIP value may be incorrect and this will affect the storage capacity estimates of Bachu et al. (2007), Table 4.8, equation 1.2, both in terms of the recovery factor, R_f, and the OGIP value, and the storage capacity estimates of Holloway et al. (2006), Table 4.8, equation 1.3, in terms of the OGIP value. However, the theoretical CO_2 storage capacity method of Tseng et al. (2012), Table 4.8, equation 1.4, is unaffected, consisting only of parameters with well constrained values which do not show variability. As such, the four aquifer models (industry estimated, finite radial, finite linear and base case)

have been used once again to provide estimates of OGIP to assess the variability of theoretical CO_2 storage capacity within the Hewett Upper Bunter Sandstone reservoir.

The final results are displayed in Figure 5.33. The columns on the bar chart represent the base case aquifer model results and the error bars reflect the results of the finite radial and linear aquifer models. The industry estimated aquifer model results are plotted as circles for comparison.

As for the Hewett Lower Bunter Sandstone reservoir (Chapter 4) the mean values for the probability distributions for the Hewett Upper Bunter Sandstone reservoir are plotted on Figure 5.33 and stated in Table 5.16 to represent CO_2 storage capacity estimates for the method of Bachu et al. (2007), Table 4.8, equation 1.1. For the alternative methods the final resulting storage capacity estimate is displayed in Figure 5.33 and stated in Table 5.16.

Table 5.16 shows theoretical CO_2 storage capacity estimates for the Hewett Upper Bunter Sandstone reservoir for different gas compositions: (a) pure methane, (b) gas mix 1 (as defined in Table 5.10), (c) gas mix 2 (as defined in Table 5.10), and (d) the Hewett Upper Bunter Sandstone reservoir initial gas composition. Table 5.16 also states the estimated theoretical storage capacities of the four methods, and for each of the four aquifer models. Capacity estimates vary according to the equation of state used and the tool/software used to model them, i.e. WebGasEOS (Reagan and Oldenburg, 2006) or RefProp (Lemmon et al., 2013). The percentage variation of the storage capacity estimates from the RefProp (Lemmon et al., 2013) estimated Peng-Robinson equation of state (Peng and Robinson, 1976) is also displayed.

The theoretical CO_2 storage capacity estimates of the methods of Bachu et al. (2007), Table 4.8, equation 1.2; Holloway et al. (2006), Table 4.8, equation 1.3; and Tseng et al. (2012), Table 4.8, equation 1.4 are comparable, ranging between 155 and 195 Mt CO_2 for the Hewett Upper Bunter Sandstone reservoir initial gas composition (see Table 5.16 (d)). In contrast, the results of the method of Bachu et al. (2007), Table 4.8, equation 1.1 give much higher storage capacity estimates, ranging between 794 and 903 Mt CO_2 for the Hewett Upper Bunter Sandstone reservoir initial gas composition (Table 5.16 (d)).

In general the highest theoretical CO_2 storage capacity estimates are predicted by the method of Bachu et al. (2007), Table 4.8, equation 1.1 and the lowest estimates by the method of Bachu et al. (2007), Table 4.8, equation 1.2. The GERG-2008 equation of state (Kunz and Wagner, 2012) always predicts the highest estimate of theoretical CO_2 storage capacity, closely followed by the AGA8-DC92 Model (Starling and Savidge, 1992). When compared to the results of the Peng-Robinson equation of state (Peng and Robinson, 1976) estimated using RefProp (Lemmon et al., 2013), the results predicted using the GERG-2008 equation of state (Kunz and Wagner, 2012) are ~9.3% greater (see Table 5.16). The Soave-Redlich-Kwong equation of state (Soave, 1972) always predicts the lowest estimate of theoretical CO_2 storage capacity. When compared the results of the Peng-Robinson equation of state (Peng and Robinson, 1976) estimated using RefProp (Lemmon et al., 2013), the results predicted using the Soave-Redlich-Kwong equation of state (Soave, 1972) are ~5.1% lower (see Table 5.16). These results are discussed in section 5.6.3.

STORAGE CAPACITY EQUATION	AUTHOR	EQUATION NUMBER
$M_{CO_2t} = \rho_{CO_2r}\left[R_f Ah\varphi(1-S_w) - V_{iw} + V_{pw}\right]$	Bachu et al. (2007)	(1.1)
$M_{CO_2t} = \rho_{CO_2r} R_f (1-F_{IG}) OGIP \left[\frac{(P_s Z_r T_r)}{(P_r Z_s T_s)}\right]$	Bachu et al. (2007)	(1.2)
$M_{CO_2t} = \left(\frac{V_{GAS}[stp]}{B_{igas}} . \rho_{CO_2r}\right)$	Holloway et al. (2006)	(1.3)
$M_{CO_2t} = \frac{\rho_{CO_2r}(G_{phc} . B_{gas})}{B_{iCO_2}} = \frac{\rho_{CO_2r}(G_{phc} . z_{gas})}{z_{iCO_2}}$	Tseng et al. (2012)	(1.4)
$M_{CO_2e} = C_m C_b C_h C_w C_a M_{CO_2t} \equiv C_e M_{CO_2t}$	Bachu et al. (2007)	(1.5)
$M_{injCO2} = \rho_{CO2r} . G_{injCO2}$	Tseng et al. (2012)	(1.6)
$G_{injCO2} = G_{phc} - G_{ihc} + \frac{P_{reshc/CO2}}{z_{reshc/CO2}}\left(\frac{z_{ihc}}{P_{ihc}} G_{ihc} - W_e \frac{T_{sc}}{P_{sc} T}\right)$	Tseng et al. (2012)	(1.7)

Table 5.14 Storage Capacity Equations previously introduced in Chapter 1. See Chapter 1 for definition of symbols

RefProp, Peng-Robinson Equation of State

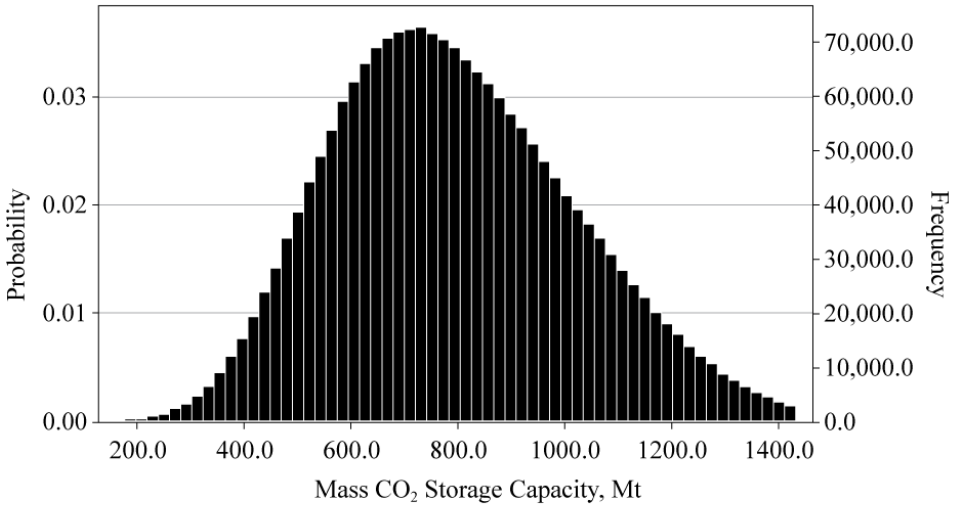

RefProp, GERG-2008 Equation of State

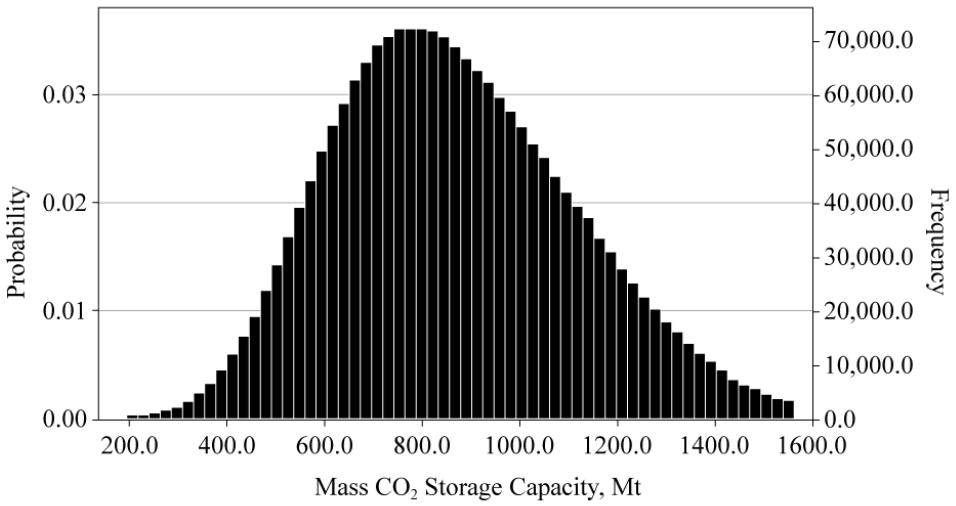

RefProp, AGA8-DC92 Equation of State

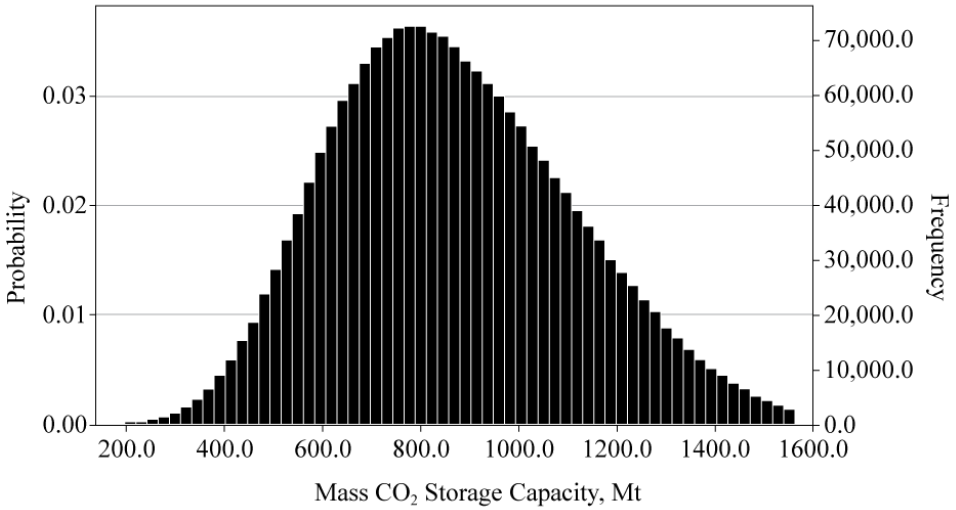

WebGasEOS, Peng-Robinson Equation of State

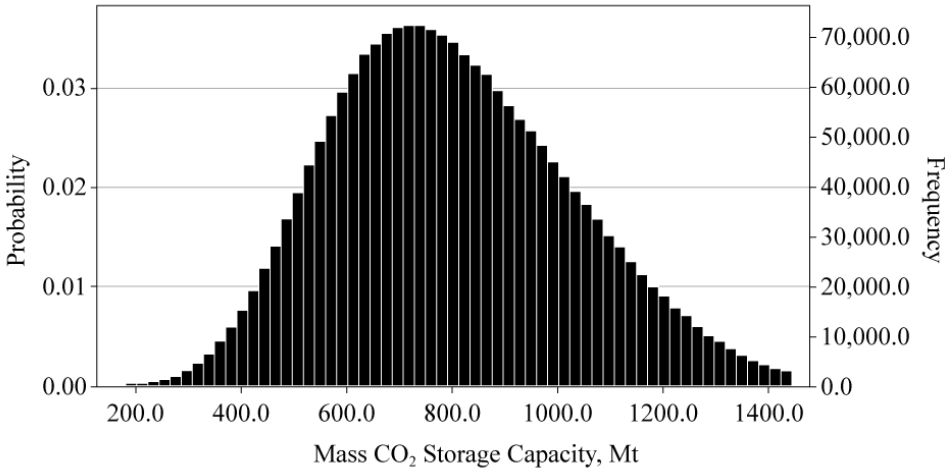

WebGasEOS, Peng-Robinson-Stryjek-Vera Equation of State

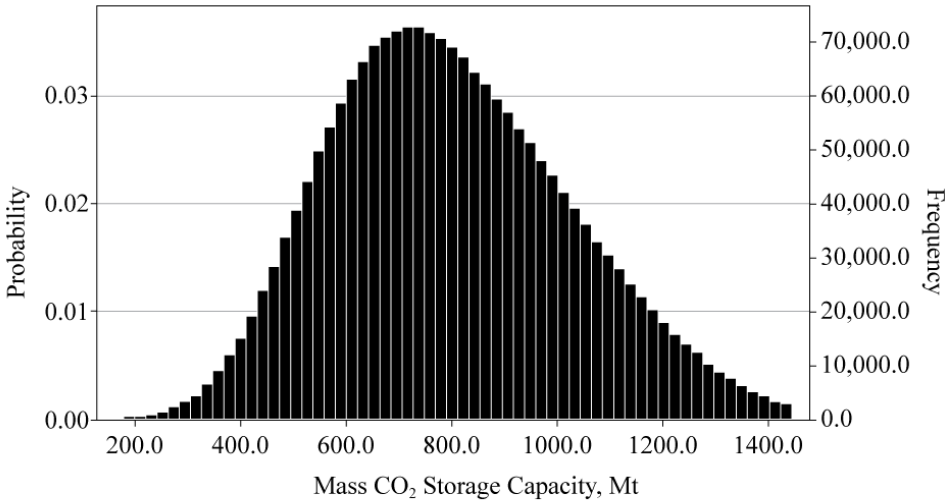

WebGasEOS, Redlich-Kwong Equation of State

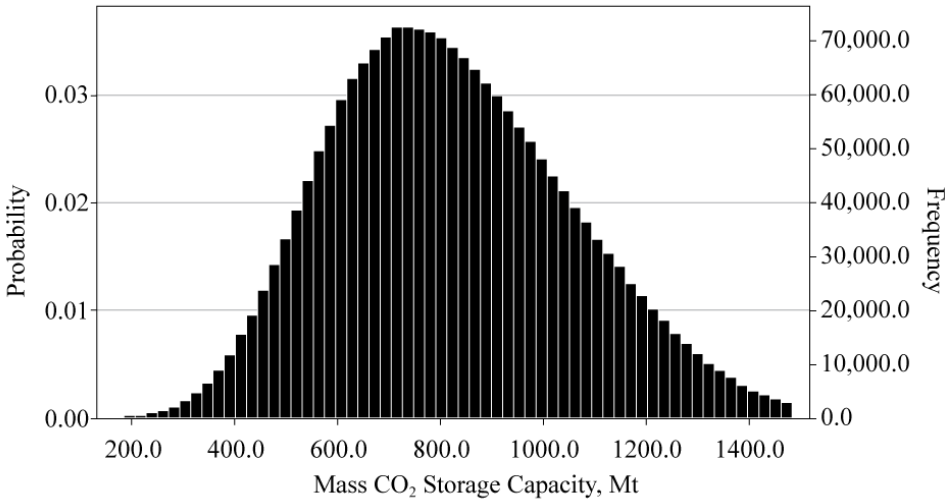

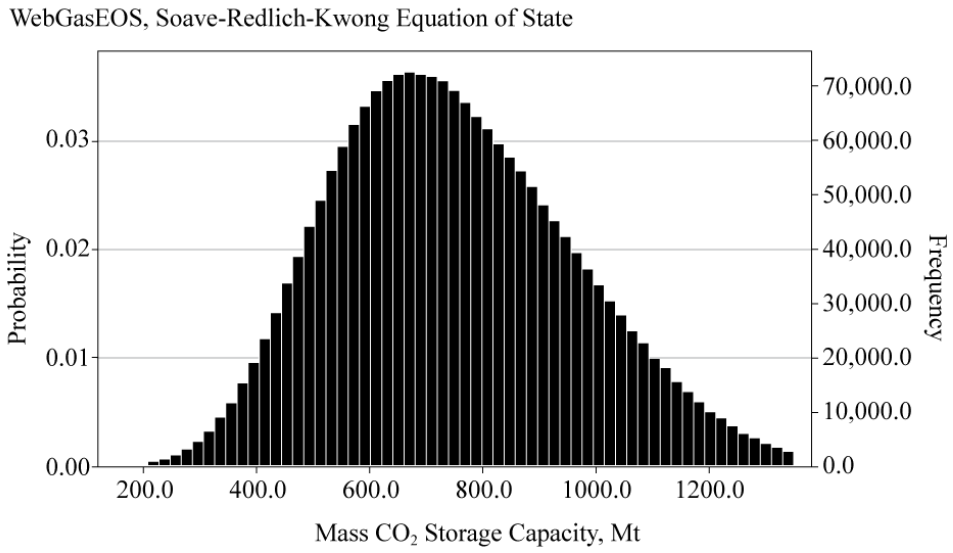

Figure 5.30 Monte Carlo Simulation probability distribution results of mass CO_2 storage capacity within the Hewett Upper Bunter Sandstone reservoir using the method of Bachu et al. (2007) Table 4.8, equation 1.1 and varying the equation of state used. The results shown use the industry estimated value of OGIP. Results computed using Oracle Crystal Ball software.

(a) Aquifer Model based on Indutry Estimated OGIP Value

MODELLING SOFTWARE	EQUATION OF STATE	MINIMUM	P10	MEDIAN (P50)	MEAN	P90	MAXIMUM
RefProp	Peng-Robinson	84.11	512.98	774.14	793.73	1104.99	1787.06
	GERG-2008	103.28	560.51	845.66	867.03	1206.85	1975.12
	AGA8 Model	121.89	560.76	845.53	867.00	1207.15	2013.12
WebGasEOS	Peng-Robinson	93.22	518.19	781.76	801.56	1115.89	1814.94
	Peng-Robinson-Stryjek-Vera	98.97	518.69	782.25	802.03	1116.82	1774.55
	Redlich-Kwong	129.71	532.52	803.34	823.54	1146.37	1853.85
	Soave-Redlich-Kwong	94.09	484.40	730.64	749.04	1042.68	1680.68

(b) Finite Radial Aquifer Model

MODELLING SOFTWARE	EQUATION OF STATE	MINIMUM	P10	MEDIAN (P50)	MEAN	P90	MAXIMUM
RefProp	Peng-Robinson	100.48	534.17	806.66	826.88	1151.39	1874.84
	GERG-2008	91.97	583.52	880.82	902.98	1257.47	2049.43
	AGA8 Model	97.61	583.40	881.29	903.41	1257.98	2086.13
WebGasEOS	Peng-Robinson	112.37	539.40	814.43	835.00	1162.74	1873.34
	Peng-Robinson-Stryjek-Vera	119.82	539.72	814.99	835.54	1163.80	1882.98
	Redlich-Kwong	107.50	554.08	836.89	857.96	1195.04	1939.86
	Soave-Redlich-Kwong	108.21	503.75	760.90	780.17	1087.15	1746.41

(c) Finite Linear Aquifer Model

MODELLING SOFTWARE	EQUATION OF STATE	MINIMUM	P10	MEDIAN (P50)	MEAN	P90	MAXIMUM
RefProp	Peng-Robinson	95.14	533.20	805.26	825.51	1149.78	1857.07
	GERG-2008	129.24	582.26	878.95	901.05	1254.84	2014.07
	AGA8 Model	114.17	582.48	879.04	901.28	1255.09	2040.83
WebGasEOS	Peng-Robinson	111.73	537.86	812.52	833.02	1160.27	1860.55
	Peng-Robinson-Stryjek-Vera	91.93	538.72	812.99	833.58	1160.79	1889.04
	Redlich-Kwong	123.85	552.68	834.88	855.88	1191.89	1926.53
	Soave-Redlich-Kwong	96.33	502.92	759.44	778.69	1083.98	1803.90

(d) Base Case Aquifer Model

MODELLING SOFTWARE	EQUATION OF STATE	MINIMUM	P10	MEDIAN (P50)	MEAN	P90	MAXIMUM
RefProp	Peng-Robinson	100.85	533.42	805.45	825.69	1149.99	1864.50
	GERG-2008	119.16	582.78	879.67	901.88	1256.20	2024.98
	AGA8 Model	112.91	582.98	880.13	902.33	1256.59	1995.55
WebGasEOS	Peng-Robinson	102.64	538.75	813.26	833.77	1160.82	1867.12
	Peng-Robinson-Stryjek-Vera	109.25	539.03	814.14	834.73	1162.60	1828.98
	Redlich-Kwong	104.82	553.77	836.06	857.05	1193.33	1954.11
	Soave-Redlich-Kwong	115.41	503.75	760.32	779.48	1085.47	1736.13

Table 5.15 Monte Carlo Simulation forecast values for the Hewett Upper Bunter Sandstone reservoir using Oracle Crystal Ball software, for (a) the aquifer model based on the industry estimated OGIP value, (b) the finite radial aquifer model, (c) the finite linear aquifer model, and (d) the base case aquifer model. Results in Mt CO_2.

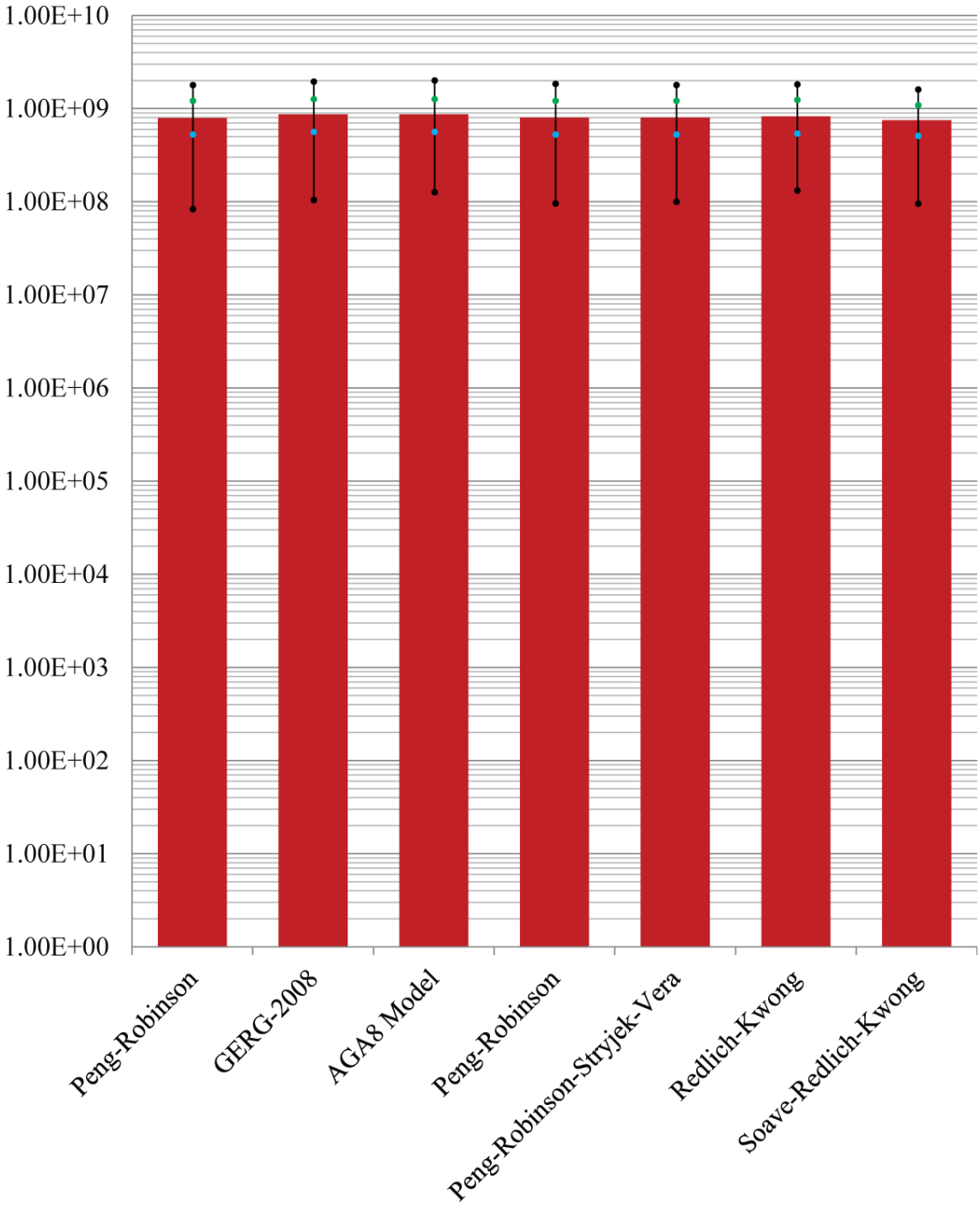

Figure 5.31 Theoretical CO_2 storage capacity of the Hewett Upper Bunter Sandstone reservoir estimated using the method of Bachu et al. (2007), Table 4.8, equation 1.1. The results shown use the industry estimate value of OGIP. The red columns plotted are the mean values, and the error bars shown have the minimum and maximum values plotted (black circles), alongside the P10 values (blue circles) and P90 values (green circles) as calculated from the probability distribution curves estimated through Monte Carlo Simulation (results displayed in Figure 5.30).

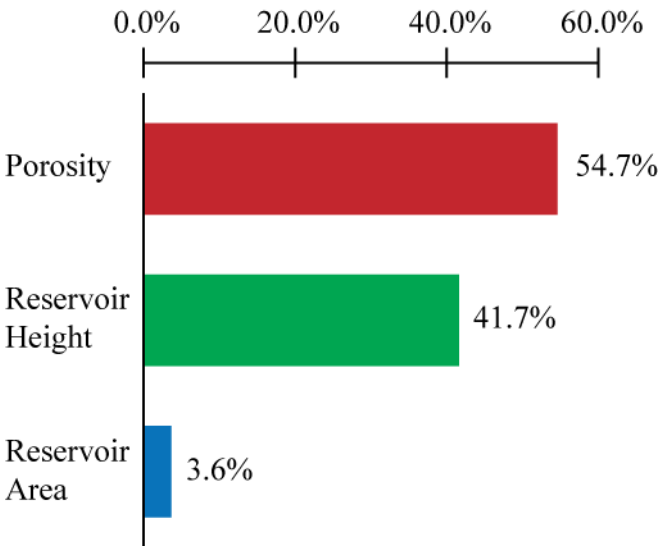

Figure 5.32 Sensitivity analysis run on the method of Bachu et al. (2007) Table 4.8, equation 1.1, throughout Monte Carlo Simulation. The results shown are based on the method using the industry estimated value of OGIP. The results of the final probability distribution of the mass CO_2 storage capacity of the Hewett Upper Bunter Sandstone reservoir (see Figure 5.30 and Figure 5.31) are most sensitive to porosity, followed by the reservoir height and the reservoir area.

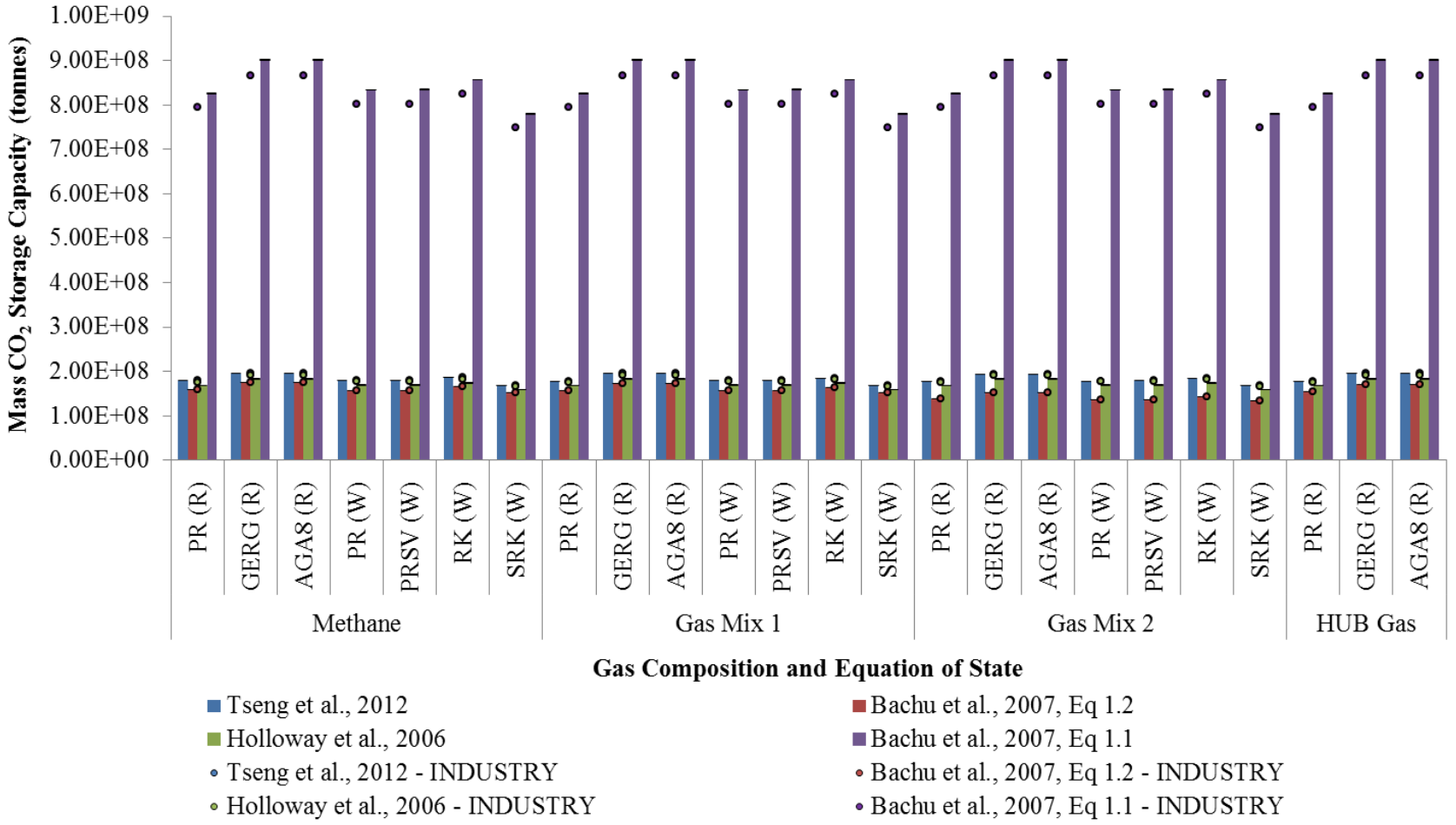

Figure 5.33 Estimated Theoretical CO_2 Storage Capacity of the Hewett Upper Bunter Sandstone reservoir using the methods of Bachu et al. (2007), Holloway et al. (2006) and Tseng et al. (2012). The columns represent the base case aquifer model results and the error bars reflect the results of the finite radial and linear aquifer models. The results using the industry estimated value of OGIP are plotted as circles for comparison.

GAS COMPOSITION	MODELLING TOOL	EQUATION OF STATE	AQUIFER MODEL	Tseng et al., 2012	% of Peng-Robinson (RefProp)	Bachu et al., 2007, Eq 1.2	% of Peng-Robinson (RefProp)	Holloway et al., 2006	% of Peng-Robinson (RefProp)	Bachu et al., 2007, Eq 1.1	% of Peng-Robinson (RefProp)	Average Percentage Variation
METHANE	REFPROP	PR	I	1.79E+08	100.0	1.59E+08	100.0	1.75E+08	100.0	7.94E+08	100.0	100.0
			R	1.79E+08	100.0	1.59E+08	100.0	1.67E+08	100.0	8.27E+08	100.0	100.0
			L	1.79E+08	100.0	1.59E+08	100.0	1.68E+08	100.0	8.26E+08	100.0	100.0
			B	1.79E+08	100.0	1.59E+08	100.0	1.68E+08	100.0	8.26E+08	100.0	100.0
		GERG	I	1.95E+08	108.9	1.75E+08	110.1	1.91E+08	109.1	8.67E+08	109.2	109.3
			R	1.95E+08	108.9	1.75E+08	110.1	1.83E+08	109.6	9.03E+08	109.2	109.4
			L	1.95E+08	108.9	1.75E+08	110.1	1.83E+08	108.9	9.01E+08	109.1	109.3
			B	1.95E+08	108.9	1.75E+08	110.1	1.83E+08	108.9	9.02E+08	109.2	109.3
		AGA8	I	1.95E+08	108.9	1.75E+08	110.1	1.91E+08	109.1	8.67E+08	109.2	109.3
			R	1.95E+08	108.9	1.75E+08	110.1	1.83E+08	109.6	9.03E+08	109.2	109.4
			L	1.95E+08	108.9	1.75E+08	110.1	1.83E+08	108.9	9.01E+08	109.1	109.3
			B	1.95E+08	108.9	1.75E+08	110.1	1.83E+08	108.9	9.02E+08	109.2	109.3
	WEBGASEOS	PR	I	1.80E+08	100.6	1.58E+08	99.4	1.76E+08	100.6	8.02E+08	101.0	100.4
			R	1.80E+08	100.6	1.58E+08	99.4	1.69E+08	101.2	8.35E+08	101.0	100.5
			L	1.80E+08	100.6	1.58E+08	99.4	1.69E+08	100.6	8.33E+08	100.8	100.3
			B	1.80E+08	100.6	1.58E+08	99.4	1.69E+08	100.6	8.34E+08	101.0	100.4
		PRSV	I	1.80E+08	100.6	1.58E+08	99.4	1.77E+08	101.1	8.02E+08	101.0	100.5
			R	1.80E+08	100.6	1.58E+08	99.4	1.69E+08	101.2	8.36E+08	101.1	100.6
			L	1.80E+08	100.6	1.58E+08	99.4	1.70E+08	101.2	8.34E+08	101.0	100.5
			B	1.80E+08	100.6	1.58E+08	99.4	1.69E+08	100.6	8.35E+08	101.1	100.4
		RK	I	1.85E+08	103.4	1.66E+08	104.4	1.81E+08	103.4	8.24E+08	103.8	103.7
			R	1.85E+08	103.4	1.66E+08	104.4	1.74E+08	104.2	8.58E+08	103.7	103.9
			L	1.85E+08	103.4	1.66E+08	104.4	1.74E+08	103.6	8.56E+08	103.6	103.7
			B	1.85E+08	103.4	1.66E+08	104.4	1.74E+08	103.6	8.57E+08	103.8	103.8
		SRK	I	1.69E+08	94.4	1.53E+08	96.2	1.65E+08	94.3	7.49E+08	94.3	94.8
			R	1.69E+08	94.4	1.53E+08	96.2	1.58E+08	94.6	7.80E+08	94.3	94.9
			L	1.69E+08	94.4	1.53E+08	96.2	1.58E+08	94.0	7.79E+08	94.3	94.7
			B	1.69E+08	94.4	1.53E+08	96.2	1.58E+08	94.0	7.79E+08	94.3	94.7

(a) Pure Methane

GAS COMPOSITION	MODELLING TOOL	EQUATION OF STATE	AQUIFER MODEL	Tseng et al., 2012	% of Peng-Robinson (RefProp)	Bachu et al., 2007, Eq 1.2	% of Peng-Robinson (RefProp)	Holloway et al., 2006	% of Peng-Robinson (RefProp)	Bachu et al., 2007, Eq 1.1	% of Peng-Robinson (RefProp)	Average Percentage Variation
GAS MIX 1	REFPROP	PR	I	1.79E+08	100.0	1.57E+08	100.0	1.75E+08	100.0	7.94E+08	100.0	100.0
			R	1.79E+08	100.0	1.57E+08	100.0	1.67E+08	100.0	8.27E+08	100.0	100.0
			L	1.79E+08	100.0	1.57E+08	100.0	1.68E+08	100.0	8.26E+08	100.0	100.0
			B	1.79E+08	100.0	1.57E+08	100.0	1.68E+08	100.0	8.26E+08	100.0	100.0
		GERG	I	1.95E+08	108.9	1.72E+08	109.6	1.91E+08	109.1	8.67E+08	109.2	109.2
			R	1.95E+08	108.9	1.72E+08	109.6	1.83E+08	109.6	9.03E+08	109.2	109.3
			L	1.95E+08	108.9	1.72E+08	109.6	1.83E+08	108.9	9.01E+08	109.1	109.1
			B	1.95E+08	108.9	1.72E+08	109.6	1.83E+08	108.9	9.02E+08	109.2	109.2
		AGA8	I	1.95E+08	108.9	1.72E+08	109.6	1.91E+08	109.1	8.67E+08	109.2	109.2
			R	1.95E+08	108.9	1.72E+08	109.6	1.83E+08	109.6	9.03E+08	109.2	109.3
			L	1.95E+08	108.9	1.72E+08	109.6	1.83E+08	108.9	9.01E+08	109.1	109.1
			B	1.95E+08	108.9	1.72E+08	109.6	1.83E+08	108.9	9.02E+08	109.2	109.2
	WEBGASEOS	PR	I	1.80E+08	100.6	1.56E+08	99.4	1.76E+08	100.6	8.02E+08	101.0	100.4
			R	1.80E+08	100.6	1.56E+08	99.4	1.69E+08	101.2	8.35E+08	101.0	100.5
			L	1.80E+08	100.6	1.56E+08	99.4	1.69E+08	100.6	8.33E+08	100.8	100.3
			B	1.80E+08	100.6	1.56E+08	99.4	1.69E+08	100.6	8.34E+08	101.0	100.4
		PRSV	I	1.80E+08	100.6	1.56E+08	99.4	1.77E+08	101.1	8.02E+08	101.0	100.5
			R	1.80E+08	100.6	1.56E+08	99.4	1.69E+08	101.2	8.36E+08	101.1	100.6
			L	1.80E+08	100.6	1.56E+08	99.4	1.70E+08	101.2	8.34E+08	101.0	100.5
			B	1.80E+08	100.6	1.56E+08	99.4	1.69E+08	100.6	8.35E+08	101.1	100.4
		RK	I	1.85E+08	103.4	1.63E+08	103.8	1.81E+08	103.4	8.24E+08	103.8	103.6
			R	1.85E+08	103.4	1.63E+08	103.8	1.74E+08	104.2	8.58E+08	103.7	103.8
			L	1.85E+08	103.4	1.63E+08	103.8	1.74E+08	103.6	8.56E+08	103.6	103.6
			B	1.85E+08	103.4	1.63E+08	103.8	1.74E+08	103.6	8.57E+08	103.8	103.6
		SRK	I	1.69E+08	94.4	1.51E+08	96.2	1.65E+08	94.3	7.49E+08	94.3	94.8
			R	1.69E+08	94.4	1.51E+08	96.2	1.58E+08	94.6	7.80E+08	94.3	94.9
			L	1.69E+08	94.4	1.51E+08	96.2	1.58E+08	94.0	7.79E+08	94.3	94.7
			B	1.69E+08	94.4	1.51E+08	96.2	1.58E+08	94.0	7.79E+08	94.3	94.7

(b) Gas Mix 1

GAS COMPOSITION	MODELLING TOOL	EQUATION OF STATE	AQUIFER MODEL	Tseng et al., 2012	% of Peng-Robinson (RefProp)	Bachu et al., 2007, Eq 1.2	% of Peng-Robinson (RefProp)	Holloway et al., 2006	% of Peng-Robinson (RefProp)	Bachu et al., 2007, Eq 1.1	% of Peng-Robinson (RefProp)	Average Percentage Variation
GAS MIX 2	REFPROP	PR	I	1.77E+08	100.0	1.38E+08	100.0	1.75E+08	100.0	7.94E+08	100.0	100.0
			R	1.77E+08	100.0	1.38E+08	100.0	1.67E+08	100.0	8.27E+08	100.0	100.0
			L	1.77E+08	100.0	1.38E+08	100.0	1.68E+08	100.0	8.26E+08	100.0	100.0
			B	1.77E+08	100.0	1.38E+08	100.0	1.68E+08	100.0	8.26E+08	100.0	100.0
		GERG	I	1.94E+08	109.6	1.51E+08	109.4	1.91E+08	109.1	8.67E+08	109.2	109.3
			R	1.94E+08	109.6	1.51E+08	109.4	1.83E+08	109.6	9.03E+08	109.2	109.4
			L	1.94E+08	109.6	1.51E+08	109.4	1.83E+08	108.9	9.01E+08	109.1	109.3
			B	1.94E+08	109.6	1.51E+08	109.4	1.83E+08	108.9	9.02E+08	109.2	109.3
		AGA8	I	1.94E+08	109.6	1.51E+08	109.4	1.91E+08	109.1	8.67E+08	109.2	109.3
			R	1.94E+08	109.6	1.51E+08	109.4	1.83E+08	109.6	9.03E+08	109.2	109.4
			L	1.94E+08	109.6	1.51E+08	109.4	1.83E+08	108.9	9.01E+08	109.1	109.3
			B	1.94E+08	109.6	1.51E+08	109.4	1.83E+08	108.9	9.02E+08	109.2	109.3
	WEBGASEOS	PR	I	1.79E+08	101.1	1.37E+08	99.3	1.76E+08	100.6	8.02E+08	101.0	100.5
			R	1.79E+08	101.1	1.37E+08	99.3	1.69E+08	101.2	8.35E+08	101.0	100.6
			L	1.79E+08	101.1	1.37E+08	99.3	1.69E+08	100.6	8.33E+08	100.8	100.5
			B	1.79E+08	101.1	1.37E+08	99.3	1.69E+08	100.6	8.34E+08	101.0	100.5
		PRSV	I	1.79E+08	101.1	1.37E+08	99.3	1.77E+08	101.1	8.02E+08	101.0	100.6
			R	1.79E+08	101.1	1.37E+08	99.3	1.69E+08	101.2	8.36E+08	101.1	100.7
			L	1.79E+08	101.1	1.37E+08	99.3	1.70E+08	101.2	8.34E+08	101.0	100.6
			B	1.79E+08	101.1	1.37E+08	99.3	1.69E+08	100.6	8.35E+08	101.1	100.5
		RK	I	1.84E+08	104.0	1.44E+08	104.3	1.81E+08	103.4	8.24E+08	103.8	103.9
			R	1.84E+08	104.0	1.44E+08	104.3	1.74E+08	104.2	8.58E+08	103.7	104.1
			L	1.84E+08	104.0	1.44E+08	104.3	1.74E+08	103.6	8.56E+08	103.6	103.9
			B	1.84E+08	104.0	1.44E+08	104.3	1.74E+08	103.6	8.57E+08	103.8	103.9
		SRK	I	1.67E+08	94.4	1.34E+08	97.1	1.65E+08	94.3	7.49E+08	94.3	95.0
			R	1.67E+08	94.4	1.34E+08	97.1	1.58E+08	94.6	7.80E+08	94.3	95.1
			L	1.67E+08	94.4	1.34E+08	97.1	1.58E+08	94.0	7.79E+08	94.3	95.0
			B	1.67E+08	94.4	1.34E+08	97.1	1.58E+08	94.0	7.79E+08	94.3	95.0

(c) Gas Mix 2

GAS COMPOSITION	MODELLING TOOL	EQUATION OF STATE	AQUIFER MODEL	Tseng et al., 2012	% of Peng-Robinson (RefProp)	Bachu et al., 2007, Eq 1.2	% of Peng-Robinson (RefProp)	Holloway et al., 2006	% of Peng-Robinson (RefProp)	Bachu et al., 2007, Eq 1.1	% of Peng-Robinson (RefProp)	Average Percentage Variation
HEWETT UPPER BUNTER GAS	REFPROP	PR	I	1.78E+08	100.0	1.55E+08	100.0	1.75E+08	100.0	7.94E+08	100.0	100.0
			R	1.78E+08	100.0	1.55E+08	100.0	1.67E+08	100.0	8.27E+08	100.0	100.0
			L	1.78E+08	100.0	1.55E+08	100.0	1.68E+08	100.0	8.26E+08	100.0	100.0
			B	1.78E+08	100.0	1.55E+08	100.0	1.68E+08	100.0	8.26E+08	100.0	100.0
		GERG	I	1.95E+08	109.6	1.70E+08	109.7	1.91E+08	109.1	8.67E+08	109.2	109.4
			R	1.95E+08	109.6	1.70E+08	109.7	1.83E+08	109.6	9.03E+08	109.2	109.5
			L	1.95E+08	109.6	1.70E+08	109.7	1.83E+08	108.9	9.01E+08	109.1	109.3
			B	1.95E+08	109.6	1.70E+08	109.7	1.83E+08	108.9	9.02E+08	109.2	109.3
		AGA8	I	1.95E+08	109.6	1.70E+08	109.7	1.91E+08	109.1	8.67E+08	109.2	109.4
			R	1.95E+08	109.6	1.70E+08	109.7	1.83E+08	109.6	9.03E+08	109.2	109.5
			L	1.95E+08	109.6	1.70E+08	109.7	1.83E+08	108.9	9.01E+08	109.1	109.3
			B	1.95E+08	109.6	1.70E+08	109.7	1.83E+08	108.9	9.02E+08	109.2	109.3

(d) The Hewett Upper Bunter Sandstone Reservoir Initial Gas Composition

Table 5.16 Percentage deviation of theoretical CO_2 storage capacity estimation using the methods of Bachu et al. (2007), Holloway et al. (2006), and Tseng et al. (2012) and various equations of state when compared to the results given by the RefProp (Lemmon et al., 2013) estimated Peng-Robinson (Peng and Robinson, 1976) storage capacity estimate for the different gas compositions: (a) pure methane, (b) gas mix 1 (as defined in Table 5.10), (c) gas mix 2 (as defined in Table 5.10), and (d) the Hewett Upper Bunter Sandstone reservoir initial gas composition. PR is the Peng-Robinson equation of state (Peng and Robinson, 1976), PRSV is the Peng-Robinson-Stryjek-Vera equation of state (Stryjek and Vera, 1986), RK is the Redlich-Kwong equation of state (Redlich and Kwong, 1949), and SRK is the Soave-Redlich-Kwong equation of state (Soave, 1972). The storage capacity estimates are shown for the different aquifer models: I is the result calculated using the industry estimated OGIP value, R is the finite radial aquifer model, L is the finite linear radial model and B is the base case aquifer model.

5.5.4.2. EFFECTIVE CO_2 STORAGE CAPACITY ESTIMATES

Effective CO_2 storage capacity was estimated using the methods of Tseng et al. (2012), Table 4.8, equations 1.6 and 1.7, for a reservoir that experiences water drive. Results are displayed in Figure 5.34 and Table 5.17. The graph (Figure 5.34) is similar to that for theoretical CO_2 storage capacity (Figure 5.33) in that the columns on the bar chart represent the base case aquifer model results and the error bars reflect the results of the finite radial and linear aquifer models. The results of the aquifer model based on the industry estimated value of OGIP are also plotted as circles for comparison.

Table 5.17 is similar to Table 5.16 in that it shows the effective CO_2 storage capacity estimates for the Hewett Upper Bunter Sandstone reservoir for different gas compositions: pure methane, gas mix 1 (as defined in Table 5.10), gas mix 2 (as defined in Table 5.10) and the Hewett Upper Bunter Sandstone reservoir initial gas composition. Table 5.17 also states the estimated effective CO_2 storage capacities for each of the four aquifer models. Capacity estimates vary according to the equation of state used and the tool/software used to model them, i.e. WebGasEOS (Reagan and Oldenburg, 2006) or RefProp (Lemmon et al., 2013). The percentage variation of the storage capacity estimates from the RefProp (Lemmon et al., 2013) estimated Peng-Robinson equation of state (Peng and Robinson, 1976) is also displayed.

Due to the limitations of the WebGasEOS online tool (Reagan and Oldenburg, 2006) the Hewett Upper Bunter Sandstone reservoir initial gas composition could only be modelled using RefProp software (Lemmon et al., 2013). The results modelled in RefProp (Lemmon et al., 2013) for the Hewett Upper Bunter Sandstone reservoir show an effective storage capacity ranging between 135 and 150 Mt CO_2 for the finite radial, finite linear and base case aquifer models. In comparison, the effective storage capacity using the industry estimated aquifer model gives higher estimates between 228 and 245 Mt CO_2. These results are further discussed in section 5.6.3.

Again, the GERG-2008 equation of state (Kunz and Wagner, 2012), closely followed by the AGA8 Model (Starling and Savidge, 1992) always predicts the

highest storage capacities, whereas the Soave-Redlich-Kwong (Soave, 1972) equation of state predicts the lowest storage capacities.

5.5.5. COMPARISON WITH PUBLISHED CO_2 STORAGE CAPACITY ESTIMATES FOR THE HEWETT UPPER BUNTER SANDSTONE RESERVOIR

Holloway et al., (2006) and E.ON. (2009) have estimated the theoretical storage capacity of the Hewett Upper Bunter Sandstone reservoir to be 122 Mt CO_2. Estimates of storage capacity were made using the equation of Holloway et al., (2006), Table 4.8, equation 1.3 in both cases.

The results predicted within this study using this equation predict theoretical storage capacities within the range 155-195 Mt CO_2, depending on the particular equation of state used. Information on the equation of state used within the studies of Holloway et al., (2006) and E.ON. (2009) have not been included, however the prediction within this study of 155 Mt CO_2 made using the method of Bachu et al. (2007), Table 4.8, equation 1.2, and the Peng-Robinson equation of state (Peng and Robinson, 1976) in RefProp (Lemmon et al., 2013) agrees most favourably with their predictions, although it is a much higher prediction (see Table 5.16 (d)).

The effective CO_2 storage capacity estimate of 135 Mt CO_2 made using the method of Tseng et al. (2012), Table 4.8, equation 1.6 and 1.7, and the Peng-Robinson equation of state (Peng and Robinson, 1976) in RefProp (Lemmon et al., 2013), and based on the finite radial aquifer model, agrees more favourably with their predictions, however the estimate is still high (see Table 5.17).

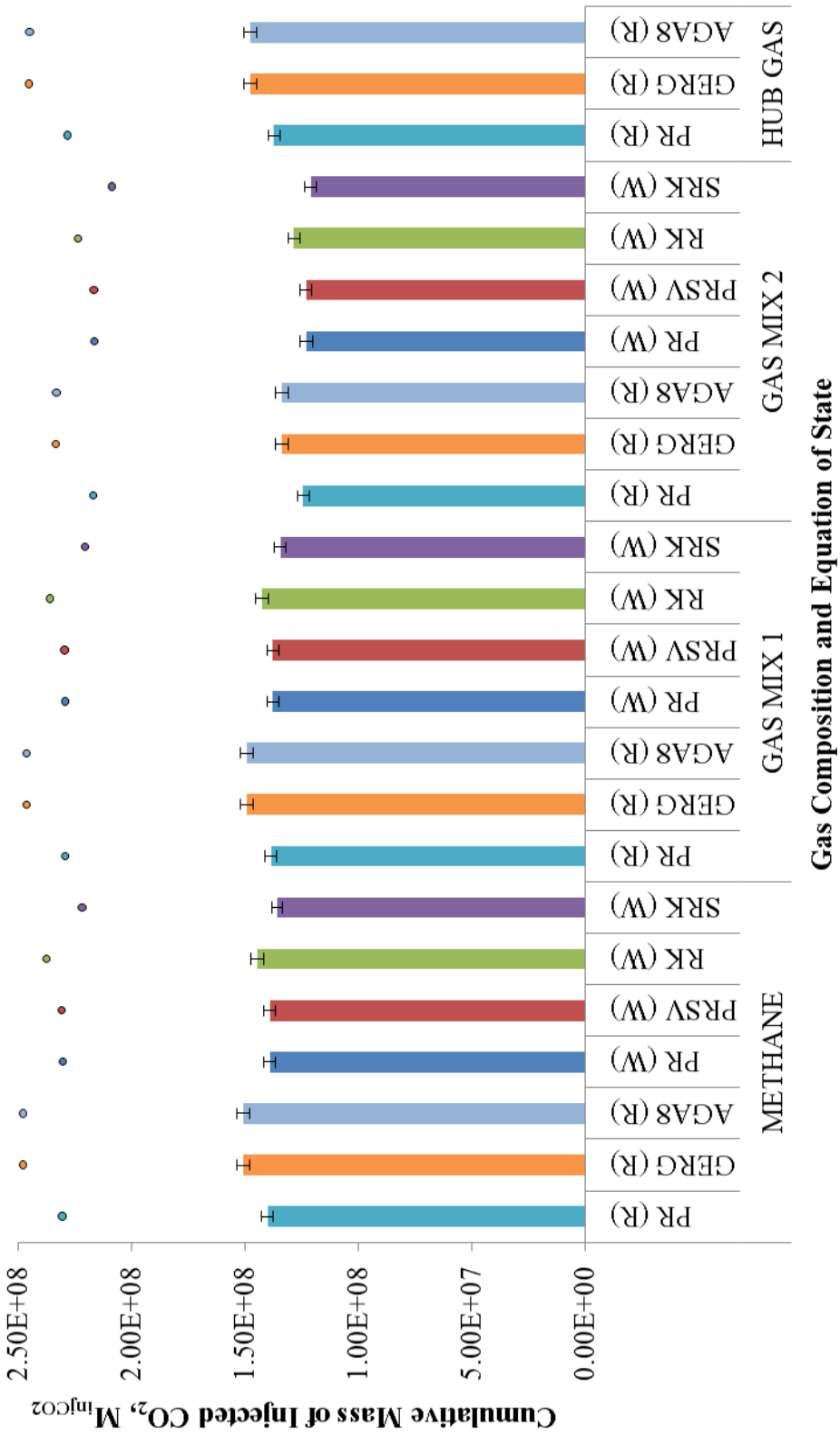

Figure 5.34 Estimated effective CO_2 storage capacity using the method of Tseng et al. (2012) and modelled with both RefProp (Lemmon et al., 2013) and the online tool by the Lawrence Berkeley National Laboratories, WebGasEOS (Reagan and Oldenburg, 2006). The columns represent the base case aquifer model results and the error bars reflect the results of the finite radial and linear aquifer models. The results of the aquifer model based on the industry estimated OGIP value are plotted as circles for comparison.

		REFPROP			WEBGASEOS			
		PR	GERG	AGA8	PR	PRSV	RK	SRK
METHANE	INDUSTRY	2.31E+08	2.48E+08	2.48E+08	2.30E+08	2.31E+08	2.38E+08	2.22E+08
	% of Peng-Robinson (RefProp)	*100.0*	*107.4*	*107.4*	*99.9*	*100.0*	*103.0*	*96.2*
	RADIAL	1.38E+08	1.48E+08	1.48E+08	1.36E+08	1.37E+08	1.42E+08	1.33E+08
	% of Peng-Robinson (RefProp)	*100.0*	*107.6*	*107.6*	*99.1*	*99.2*	*103.2*	*97.0*
	LINEAR	1.43E+08	1.54E+08	1.54E+08	1.42E+08	1.42E+08	1.47E+08	1.38E+08
	% of Peng-Robinson (RefProp)	*100.0*	*107.6*	*107.6*	*99.2*	*99.3*	*103.2*	*96.9*
	BASE CASE	1.40E+08	1.51E+08	1.51E+08	1.39E+08	1.39E+08	1.45E+08	1.36E+08
	% of Peng-Robinson (RefProp)	*100.0*	*107.6*	*107.6*	*99.2*	*99.3*	*103.2*	*96.9*
GAS MIX 1	INDUSTRY	2.29E+08	2.46E+08	2.46E+08	2.29E+08	2.30E+08	2.36E+08	2.21E+08
	% of Peng-Robinson (RefProp)	*100.0*	*107.4*	*107.4*	*100.0*	*100.1*	*102.9*	*96.2*
	RADIAL	1.36E+08	1.46E+08	1.46E+08	1.35E+08	1.35E+08	1.40E+08	1.32E+08
	% of Peng-Robinson (RefProp)	*100.0*	*107.6*	*107.6*	*99.3*	*99.4*	*102.8*	*97.0*
	LINEAR	1.41E+08	1.52E+08	1.52E+08	1.40E+08	1.40E+08	1.45E+08	1.37E+08
	% of Peng-Robinson (RefProp)	*100.0*	*107.6*	*107.6*	*99.3*	*99.5*	*102.8*	*96.9*
	BASE CASE	1.39E+08	1.49E+08	1.49E+08	1.38E+08	1.38E+08	1.43E+08	1.34E+08
	% of Peng-Robinson (RefProp)	*100.0*	*107.6*	*107.6*	*99.3*	*99.4*	*102.8*	*97.0*
GAS MIX 2	INDUSTRY	2.17E+08	2.33E+08	2.33E+08	2.16E+08	2.17E+08	2.24E+08	2.09E+08
	% of Peng-Robinson (RefProp)	*100.0*	*107.6*	*107.5*	*99.8*	*99.9*	*103.1*	*96.3*
	RADIAL	1.22E+08	1.31E+08	1.31E+08	1.20E+08	1.21E+08	1.26E+08	1.19E+08
	% of Peng-Robinson (RefProp)	*100.0*	*107.7*	*107.6*	*98.8*	*98.9*	*103.3*	*97.4*
	LINEAR	1.27E+08	1.37E+08	1.37E+08	1.26E+08	1.26E+08	1.31E+08	1.24E+08
	% of Peng-Robinson (RefProp)	*100.0*	*107.7*	*107.6*	*98.9*	*99.0*	*103.2*	*97.3*
	BASE CASE	1.24E+08	1.34E+08	1.34E+08	1.23E+08	1.23E+08	1.28E+08	1.21E+08
	% of Peng-Robinson (RefProp)	*100.0*	*107.7*	*107.6*	*98.8*	*99.0*	*103.2*	*97.3*
HUB GAS	INDUSTRY	2.28E+08	2.45E+08	2.45E+08				
	% of Peng-Robinson (RefProp)	*100.0*	*107.4*	*107.4*				
	RADIAL	1.35E+08	1.45E+08	1.45E+08				
	% of Peng-Robinson (RefProp)	*100.0*	*107.6*	*107.5*				
	LINEAR	1.40E+08	1.50E+08	1.50E+08				
	% of Peng-Robinson (RefProp)	*100.0*	*107.6*	*107.5*				
	BASE CASE	1.37E+08	1.48E+08	1.48E+08				
	% of Peng-Robinson (RefProp)	*100.0*	*107.6*	*107.5*				
	Average Percentage Variation	100.0	107.6	107.6	99.3	99.4	103.1	96.9

Table 5.17 Percentage deviation of effective CO_2 storage capacity estimation using the method of Tseng et al. (2012) and various equations of state when compared to the results given by the RefProp (Lemmon et al., 2013) estimated Peng-Robinson (Peng and Robinson, 1976) storage capacity estimate for the different gas compositions: pure methane, gas mix 1 (as defined in Table 5.10), gas mix 2 (as defined in Table 5.10) and the Hewett Upper Bunter Sandstone reservoir initial gas composition. PR is the Peng-Robinson equation of state (Peng and Robinson, 1976), PRSV is the Peng-Robinson-Stryjek-Vera equation of state (Stryjek and Vera, 1986), RK is the Redlich-Kwong equation of state (Redlich and Kwong, 1949), and SRK is the Soave-Redlich-Kwong equation of state (Soave, 1972). The storage capacity estimates are shown for the different aquifer models: I is the aquifer model based on the industry estimated OGIP value, R is the finite radial aquifer model, L is the finite linear aquifer modal and B is the base case aquifer model.

5.6. DISCUSSION

5.6.1. SUMMARY

The observations over the productive lifetime of the Hewett Upper Bunter Sandstone reservoir, and the results of the combined analysis of the various datasets have shown that the reservoir has the potential to be a good quality storage site for CO_2. However, the key to ensuring effective storage of CO_2 within a water drive reservoir is to understand the internal dynamics of the storage system in detail particularly through the combined analysis of data sets gathered during production.

The Hewett Upper Bunter Sandstone reservoir has experienced complexity in its production with wells coming close to watering out through vast quantities of aquifer influx during the 1980s. However, good reservoir management with production initiating from the neighbouring Little Dotty upper Bunter Sandstone reservoir in 1986 meant that the water level in the Hewett Upper Bunter Sandstone reservoir stabilised and even dropped in later years (Cooke-Yarborough and Smith, 2003).

Despite this, compared to the Hewett Lower Bunter Sandstone reservoir (Chapter 4) the Hewett Upper Bunter Sandstone reservoir offers a smaller, but still significant storage capacity for CO_2 storage. The methods described in section 5.5.2 have given a range of possible CO_2 storage capacities for the reservoir. Theoretical storage capacity methods of Bachu et al. (2007) and Holloway et al. (2006) have yielded results in the order of hundreds of megatons of CO_2. The effective CO_2 storage capacity method of Tseng et al. (2012) has further constrained these results, however they still remain in the order of hundreds of megatons of CO_2.

5.6.2. ADVANTAGES OF INTEGRATED APPROACH TO CHARACTERISATION OF A WATER DRIVE RESERVOIR

The Hewett Upper Bunter Sandstone reservoir is much more complex than the Hewett Lower Bunter Sandstone reservoir in terms of its connectivity to the Little Dotty Upper Bunter Sandstone reservoir. Three potential pressure communication pathways have been found between the Hewett Upper Bunter Sandstone reservoir and the local Little Dotty Upper Bunter Sandstone reservoir via the regional Bunter aquifer: two pathways around and through the NW lateral tip of the North Hewett Fault and one pathway near the SE branchline. At least two of these pathways would not have been identified without the integration of structural, stratigraphic and production data.

The North Hewett Fault has had an important role in the closure of the central eastern flank of the Hewett Upper Bunter Sandstone reservoir which is juxtaposed against sealing unit and this region of the fault will continue to play an important role in the effective storage of CO_2 within the reservoir. However, the NW and SE sections of the fault that have been identified as plausible pressure communication pathways did not play a role in the effective storage of natural gas – they are located beneath the initial gas water contact.

In order to predict how the Hewett Upper Bunter Sandstone reservoir will respond to injection of CO_2 it is important to consider the relative changes in hydraulic head between the Hewett and Little Dotty Upper Bunter Sandstone reservoirs. Hydraulic head, H_{res}, was previously calculated in section 5.4.3.4 from an arbitrary datum point, z, of 1434 m (near the base of the Upper Bunter Sandstone Formation within the vicinity of Little Dotty) using equation 5.6. Both the Hewett and Little Dotty Upper Bunter Sandstone reservoirs had similar pre-production hydraulic head values, i.e. the Bunter aquifer local to the Hewett Unit was in equilibrium prior to production with no net direction of flow. Following the onset of production from the Hewett Upper Bunter Sandstone reservoir in 1973, hydraulic head declined in Hewett, exceeding the decline observed in the non-producing Little Dotty Upper Bunter Sandstone reservoir: this resulted in a perturbed aquifer no longer in equilibrium and implies movement of formation water through the

shared Bunter aquifer was from Little Dotty towards the Hewett Upper Bunter Sandstone reservoir. This trend correlates well with observations by Cooke-Yarborough and Smith (2003) that the gas-water contact rose progressively following the onset of production within the Hewett Upper Bunter Sandstone reservoir.

When the Little Dotty Upper Bunter Sandstone reservoir came online in 1986 its hydraulic head accelerated in its decline and rapidly approached a similar value to that of Hewett by the early to mid-1990s, continuing until the end of the dataset in 2002. It can be inferred that the aquifer is becoming less perturbed and is nearing equilibrium once again but at a lower pressure due to the loss of gas through production. However, if the hydraulic head value for the Hewett Upper Bunter Sandstone reservoir were to exceed that of the Little Dotty Upper Bunter Sandstone reservoir a reversal in the direction of aquifer flow could occur.

Further re-pressurisation due to aquifer influx is likely to decline post-production (Hagoort, 1988), therefore pressure is likely to remain low prior to CO_2 injection. Pressure, and therefore the hydraulic head, in the Hewett Upper Bunter Sandstone reservoir is expected to rise on injection above that of the Little Dotty Upper Bunter Sandstone reservoir and so the direction of aquifer flow will be reversed, i.e. formation water will flow from the Hewett Upper Bunter Sandstone reservoir to the Little Dotty Upper Bunter Sandstone reservoir.

Key questions arising from this study are based around the role of the Little Dotty Upper Bunter Sandstone reservoir in secure CO_2 storage within the Hewett Upper Bunter Sandstone reservoir. We have seen that the resulting re-pressurisation of the Hewett Upper Bunter Sandstone reservoir during CO_2 storage could induce a fluid flow reversal in the regional Bunter aquifer from Hewett into the Little Dotty Upper Bunter Sandstone reservoir. However, if the Little Dotty Upper Bunter Sandstone reservoir could be re-pressurised either through contemporaneous CO_2 or, to minimise risk, through water injection, the head value of the Little Dotty reservoir could be managed so that it remains higher than that of the Hewett Upper Bunter Sandstone reservoir. This would mean that the direction of aquifer flow would remain the same, from the Little Dotty Upper Bunter Sandstone reservoir to the Hewett Upper Bunter Sandstone reservoir.

5.6.3. THE USE OF AQUIFER MODELS FOR THE CORRECT ESTIMATION OF ORIGINAL GAS IN PLACE WITHIN A WATER DRIVE RESERVOIR

Throughout this study, it has been apparent that the industry-estimated original gas in place (OGIP) of 38.397 billion cubic metres of natural gas for the Hewett Upper Bunter Sandstone reservoir was too high. Evidence to suggest this has come from the use of equation 5.3 to estimate the cumulative volume of water influx into the reservoir (W_e) over the productive lifetime up until 2002 (the last recorded data for the reservoir). The W_e value obtained using the industry estimated OGIP was negative.

However, it is well established that the Hewett Upper Bunter Sandstone reservoir experiences a water drive. Evidence comes from historical observations of Cooke-Yarborough and Smith (2003). Further evidence for a water drive is apparent in the Cole Plot of the Hewett Upper Bunter Sandstone reservoir (Figure 5.17 (a)) which shows a trend indicative of a moderate water drive.

As such, finite radial and linear aquifer models have been used to estimate the cumulative volume of water influx (W_e) into the Hewett Upper Bunter Sandstone reservoir. Equation 5.3 was rearranged to equation 5.18 to estimate the original gas in place of the Hewett Upper Bunter Sandstone reservoir based on the estimated W_e values produced from the finite radial, finite linear and base case aquifer models. The OGIP estimates obtained are likely to be more representative of the Hewett Upper Bunter Sandstone reservoir and the W_e values are positive so they represent the cumulative volume of water influx into the reservoir more accurately.

When the estimated OGIP values were input into the theoretical CO_2 storage capacity method of Tseng et al. (2012), Table 4.8, equation 1.4, the results based on all four aquifer models did not vary. This method does not include the OGIP as a parameter, or any other parameter that extends from an OGIP estimate, such as the recovery factor, R_f. There method itself is based on well constrained parameters that do not show variability.

The theoretical CO_2 storage capacity method of Bachu et al. (2007), Table 4.8, equation 1.1, requires estimation of the recovery factor, R_f. The recovery factor is equal to the cumulative volume of gas produced divided by the original gas in place, therefore it is dependent on the accurate estimation of the OGIP. As it is likely that the industry estimated OGIP value was over-estimated, a low value for the recovery factor is produced – theoretically, it means a larger of volume of hydrocarbons was estimated to exist in the reservoir than actually are present. As such, the resulting industry estimated theoretical CO_2 storage capacity is lower than those predicted by the finite radial, finite linear and base case aquifer models (see Figure 5.33).

The theoretical CO_2 storage capacity method of Holloway et al. (2006), Table 4.8, equation 1.3, requires estimation of the OGIP. As this was over-estimated using the industry value, the resulting storage capacity estimated using the industry OGIP value is higher than those predicted by the finite radial, finite linear and base case aquifer models (see Figure 5.33).

The theoretical CO_2 storage capacity method of Bachu et al. (2007), Table 4.8, equation 1.2, requires both the recovery factor and OGIP to be estimated. As for the method of Bachu et al. (2007), Table 4.8, equation 1.1, the recovery factor is based on a value for OGIP which has been over-estimated by industry. Therefore a low value for the recovery factor would result in a lower storage capacity estimate. However, the method also requires estimation of the OGIP as a separate necessary parameter. The result is that the storage capacity estimate obtained using the industry estimated OGIP value is, in fact, slightly higher than those estimated using the finite radial, finite linear and base case aquifer models (see Figure 5.33).

The effective CO_2 storage capacity method of Tseng et al. (2012), Table 4.8, equation 1.7, requires estimation of the OGIP and W_e. As the OGIP was previously over-estimated using the industry value, this resulted in a negative value for W_e (see section 5.4.3.1.). Despite this, the resulting industry estimated effective CO_2 storage capacities were much greater than those estimated using the finite radial, finite linear and base case aquifer models (see Figure 5.34).

5.6.4. IMPACT OF EQUATION OF STATE AND METHOD APPLIED ON STORAGE CAPACITY ESTIMATION

As for the Hewett Lower Bunter Sandstone reservoir (Chapter 4), six equations of state were used in the investigation of CO_2 storage capacity within the Hewett Upper Bunter Sandstone reservoir. Estimation with RefProp utilised equations of state predicted by the Peng-Robinson (Peng and Robinson, 1976), GERG-2008 (Kunz and Wagner, 2012) and AGA8 Model (Starling and Savidge, 1992). Estimation with WebGasEOS used the Peng-Robinson (Peng and Robinson, 1976) again, Peng-Robinson-Stryjek-Vera (Stryjek and Vera, 1986), Redlich-Kwong (Redlich and Kwong, 1949) and Soave-Redlich-Kwong (Soave, 1972) equations of state.

The variability between the various equations of state in both theoretical and effective storage capacity estimation are shown in Figure 5.33 and Figure 5.34 respectively for the four gas compositions modelled: pure methane, Gas Mix 1, Gas Mix 2 and the Hewett Upper Bunter Sandstone reservoir initial gas composition. Table 5.16 and Table 5.17 show the percentage deviation of the storage capacity estimates away from the RefProp estimated theoretical and effective storage capacity estimates using the Peng-Robinson equation of state (Peng and Robinson, 1976). This equation of state was used for comparison as it can also be modelled within WebGasEOS and therefore results from both programs are comparable.

In general, the GERG-2008 equation of state (Kunz and Wagner, 2012), closely followed by the AGA8 Model (Starling and Savidge, 1992) always predicts the highest storage capacities, whereas the Soave-Redlich-Kwong (Soave, 1972) equation of state predicts the lowest storage capacities.

The GERG-2008 (Kunz and Wagner, 2012) and AGA8 Model (Starling and Savidge, 1992) equations of state were specifically developed for natural gas environments, which also include CO_2, therefore they are optimised for use within storage complexes being considered for carbon storage. The Peng-Robinson (Peng and Robinson, 1976) equation of state has been utilised for many years within the oil and gas industry due to its accuracy, however, the GERG-2008 (Kunz and Wagner, 2012) and AGA8 Model (Starling and Savidge, 1992) equations of state

are considered to supersede the performance of the Peng Robinson (Peng and Robinson, 1976) equation of state particularly at the vapour-liquid equilibrium (Kunz and Wagner, 2012), an important factor in carbon storage as CO_2 is to be stored as a supercritical fluid.

Therefore, it is likely that the GERG-2008 (Starling and Savidge, 1992) and AGA8 Model (Kunz and Wagner, 2012) equations of state provide the best representation of storage capacity estimates as they have been specifically developed for the natural gas environment and is more valid, particularly within the region of the vapour-liquid equilibrium.

As for the Hewett Lower Bunter Sandstone reservoir (Chapter 4), the theoretical CO_2 storage capacity methods of Bachu et al. (2007), Table 4.8, equation 1.2, Holloway et al. (2006), Table 4.8, equation 1.3, and Tseng et al. (2012), Table 4.8, equation 1.4 show comparable, accurately constrained storage capacity results within the range 155-195 Mt CO_2 for the Hewett Upper Bunter Sandstone reservoir initial gas composition (see Table 5.16), depending on the equation of state and aquifer model used. However, the geometrically based theoretical CO_2 storage capacity method of Bachu et al. (2007), Table 4.8, equation 1.1, again predict considerably higher mean values, and as such, show a degree of variability. Mean values were found to range between 826 and 903 Mt CO_2 for the Hewett Upper Bunter Sandstone reservoir initial gas composition using the finite radial, finite linear and base case aquifer models; the average range between the highest and lowest values predicted using Monte Carlo simulation and the finite radial, finite linear and base case aquifer models was found to be 1802.4 Mt CO_2 for the Hewett Upper Bunter Sandstone reservoir initial gas composition.

Effective CO_2 storage capacity estimation using the method of Tseng et al. (2012) further constrained the estimates to within the range 123-132 Mt CO_2 for the Hewett Upper Bunter Sandstone reservoir initial gas composition depending on the equation of state used.

It is likely that the theoretical and effective CO_2 storage capacity methods of Tseng et al. (2012), Table 4.8, equations 1.4, 1.6 and 1.7, provide the most accurate estimates within the Hewett Upper Bunter Sandstone reservoir, as they require

parameters that are generally well constrained and their methods are more complex than the alternative methods within this study.

As it was necessary to assume aquifer models for the Hewett Upper Bunter Sandstone reservoir to accurately estimate the cumulative volume of water influx into the reservoir, W_e, and the OGIP (due to the over-estimation by industry), it is likely that the base case aquifer model (i.e. the mean between the finite radial and finite linear aquifer models) will yield the most accurate values for these parameters. Unfortunately, it was not possible to establish whether the finite radial or finite linear aquifer model was more representative of the Hewett Upper Bunter Sandstone reservoir. As such, it is better to use the base case aquifer model despite there being very little difference between the W_e and OGIP values estimated using the finite radial and finite linear aquifer models.

5.6.5. THE USE OF MONTE CARLO SIMULATION WITHIN CO_2 STORAGE CAPACITY EQUATIONS

This study has again attempted to improve upon previous work (such as that of Bentham (2006), Brook et al. (2003), Holloway et al. (2006) and Kirk (2006)) by attempting to honour all available porosity data within the geometric method of CO_2 storage capacity estimation of Bachu et al. (2007), Chapter 1, equation 1.1. Porosity data from the Hewett Upper Bunter Sandstone reservoir was assigned a best-fit probability distribution, truncated at 0% porosity (as it is not possible to have a negative value for porosity). Again, Monte Carlo simulation was run thousands of times over which allowed repeated random sampling of the assigned probability distribution to input porosity values into the storage capacity equation. This produced a substantial range of variation in the resulting storage capacity estimates.

Again, it was not possible to assign a probability distribution which fit the porosity data with any degree of confidence. When the Anderson-Darling P-value test was applied, which tests for normality, the resulting P-value was equal to 0.00, i.e. the data do not follow a specified distribution. Therefore, it is not appropriate

to conduct Monte Carlo simulation that samples from this distribution to estimate CO_2 storage capacity.

As such, until a better solution can be incorporated into the CO_2 storage capacity method of Bachu et al. (2007), Chapter 1, equation 1.1, which attempts to honour all available porosity data for a reservoir, it is most likely better to use mean porosity values.

5.7. CONCLUSIONS

The Hewett Upper Bunter Sandstone reservoir has proven pressure communication and fluid flow with the Little Dotty Upper Bunter Sandstone reservoir via the shared regional Bunter aquifer across three major pathways. Despite the three pathways, proven in this study to exist between the Hewett and Little Dotty Upper Bunter Sandstone reservoirs, effective management during CO_2 injection will mean that they should not affect secure storage of CO_2 within the Hewett Upper Bunter structural closure. This study provides detailed analysis of the dynamic behaviour of the two connected reservoirs through estimation of reservoir hydraulic head over their respective productive lifetimes. It then projects this behaviour during the storage lifetime of the Hewett Upper Bunter Sandstone reservoir and identifies the role of the Little Dotty Upper Bunter Sandstone reservoir during storage. Successful, secure storage of CO_2 can be achieved through careful management during CO_2 injection within the Hewett Upper Bunter Sandstone alone.

The Hewett Upper Bunter Sandstone reservoir can offer good quality storage sites for CO_2 with considerable theoretical and effective CO_2 storage capacities. The GERG-2008 equation of state is the most favourable to use as it is robust and designed for the natural gas environment. Once again, the most favourable theoretical and effective CO_2 storage capacity methods were found to be those of Tseng et al. (2012). As such, the likely theoretical CO_2 storage capacity of the Hewett Upper Bunter Sandstone reservoir is 195 Mt CO_2, and the likely effective CO_2 storage capacity is 148 Mt CO_2 using the base case aquifer model.

A final outcome of this study is that although water drive reservoirs are a great deal more complex than depletion drive reservoirs, successful characterisation is still possible even if traditionally gathered datasets are incomplete. There was a great deal of production and pressure data available for analysis from the Hewett Upper Bunter Sandstone reservoir and neighbouring Little Dotty Upper Bunter Sandstone reservoir. However, produced water was unfortunately never metered from these fields. Nevertheless, alternative methods of Van Everdingen and Hurst (1949) in Dake (1978) were used to estimate values for W_e and OGIP based on aquifer models to attempt to increase the accuracy of storage capacity equations. These methods will be tested as to their global application within similar water drive reservoirs being considered for CO_2 storage in the next chapter.

6 South and North Morecambe: Case Studies for Testing Developed Methods

6.1. INTRODUCTION

The methods developed in Chapters 4 and 5 for better constraining CO_2 storage capacity estimates within depletion drive and water drive gas reservoirs, respectively, are tested here using the East Irish Sea Triassic gas fields, South and North Morecambe as case studies Figure 6.1.

The South Morecambe Sherwood Sandstone reservoir is a partially depleted, depletion drive gas reservoir within the East Irish Sea Basin, and therefore similar to that of the Hewett Lower Bunter Sandstone reservoir of the Hewett Gas Field, Southern North Sea (Chapter 4). The South Morecambe Sherwood Sandstone reservoir lies within a structural anticline that has successfully stored hydrocarbons over geological timescales. The northern limb is fault bounded to the north, west and east. The southern limb is fault bounded to the west and dip-closed to the east.

Conversely, the North Morecambe Sherwood Sandstone reservoir is a partially depleted water drive reservoir within the East Irish Sea Basin, similar to that of the Hewett Upper Bunter Sandstone reservoir of the Hewett Gas Field, Southern North Sea (Chapter 5). The reservoir lies within a N-S trending, north-westerly dipping fault block, fault bounded to the east, west and south, and dip-closed to the north.

The previous methods developed in Chapters 4 and 5 are used here to assess the variability of storage capacity estimation within the South and North Morecambe Sherwood Sandstone reservoir. The reservoirs are first characterised according to their original petroleum properties, i.e. source rocks, reservoir rocks, trap and petroleum field characteristics. The reservoirs are then analysed separately in terms of their petrophysical characteristics and production histories (including

gas production, pressure decline, material balance methods and where relevant, aquifer behaviour), gas compressibility factors, gas formation volume factors, and CO_2 density. Finally, theoretical and effective storage capacity is estimated for the South and North Morecambe Sherwood Sandstone reservoirs. These estimates are then compared to previously published estimates.

In contrast to the Hewett Upper Bunter Sandstone reservoir (Chapter 5) it was considered unnecessary to complete a detailed 3-D fault seal analysis of the South and North Morecambe Sherwood Sandstone reservoirs for several reasons. Although there are structural trapping mechanisms within both the South and North Morecambe Sherwood Sandstone reservoirs, both reservoirs have successfully stored hydrocarbons over geological timescales. The overburden strata (ca. 670.56 m over South Morecambe (Bastin et al., 2003) and 899.16 m over the North Morecambe gas field (Cowan and Boycott-Brown, 2003)) is composed of sealing halites and mudstones of the Mercia Mudstone Group, with a thin (ca. 60 m thick) layer of Quaternary and Tertiary deposits at the surface. Therefore, the reservoir sandstones are most likely to be juxtaposed against sealing unit as the bounding faults have significant fault throws (for example, between 91.5 m and 609.6 m along the eastern bounding fault of North Morecambe (Cowan and Boycott-Brown, 2003)).

Further evidence for sealing bounding faults comes from the fact that the South and North Morecambe Sherwood Sandstone reservoirs have different reservoir pressures, gas compositions and gas water contacts. Although the South and North Morecambe Sherwood Sandstone reservoirs are separated by only a narrow graben, initial aquifer pressure in North Morecambe was 0.965 MPa less than that in South Morecambe, indicating the major basin faults are full seals (Stuart, 1993) and there is no pressure communication between the two fields.

The first gas-charge of the South and North Morecambe reservoirs occurred during the Jurassic, and was rich in CO_2 (Stuart and Cowan, 1991). During the Cimmerian, uplift caused breaching of the South Morecambe Sherwood Sandstone reservoir and a loss of hydrocarbon charge, but not in the North Morecambe Sherwood Sandstone reservoir (Stuart and Cowan, 1991). A second gas charge occurred towards the end of the Cretaceous (Stuart and Cowan, 1991), and it is this

charge that has remained within, and has been produced from, the South Morecambe Sherwood Sandstone reservoir. As such, the North Morecambe Sherwood Sandstone reservoir initial gas composition contains a greater mole percentage of naturally occurring CO_2, and also has hydrogen and helium components. This provides further evidence for the presence of full seals between the two reservoirs as the gas compositions have not mixed together forming a similar overall composition in both reservoirs.

The initial gas-water-contact within the South Morecambe reservoir was at a depth of 1140 m and for North Morecambe, 1196 m. If the two reservoirs were in communication the gas-water-contacts would be similar, providing the final evidence that a full seal exists along faults between the two reservoirs.

A final point to note is that a detailed structural model and fault seal analysis was necessary within the Hewett Upper Bunter Sandstone reservoir (Chapter 5) to understand the relation between it and the Little Dotty Upper Bunter Sandstone reservoir, as observations of potential pressure communication had been observed throughout their respective productive lifetimes. No such communication has been documented throughout the productive lifetimes of the South and North Morecambe reservoirs, either between each other or the other nearby surrounding gas fields of the East Irish Sea Basin.

As has been previously described in Chapter 2, both the South and North Morecambe reservoirs are affected by illite precipitation. Illite precipitation can destroy permeability within a sandstone reservoir. As such, it is necessary to assess the impact of illite on CO_2 storage within the South and North Morecambe Sherwood Sandstone reservoirs.

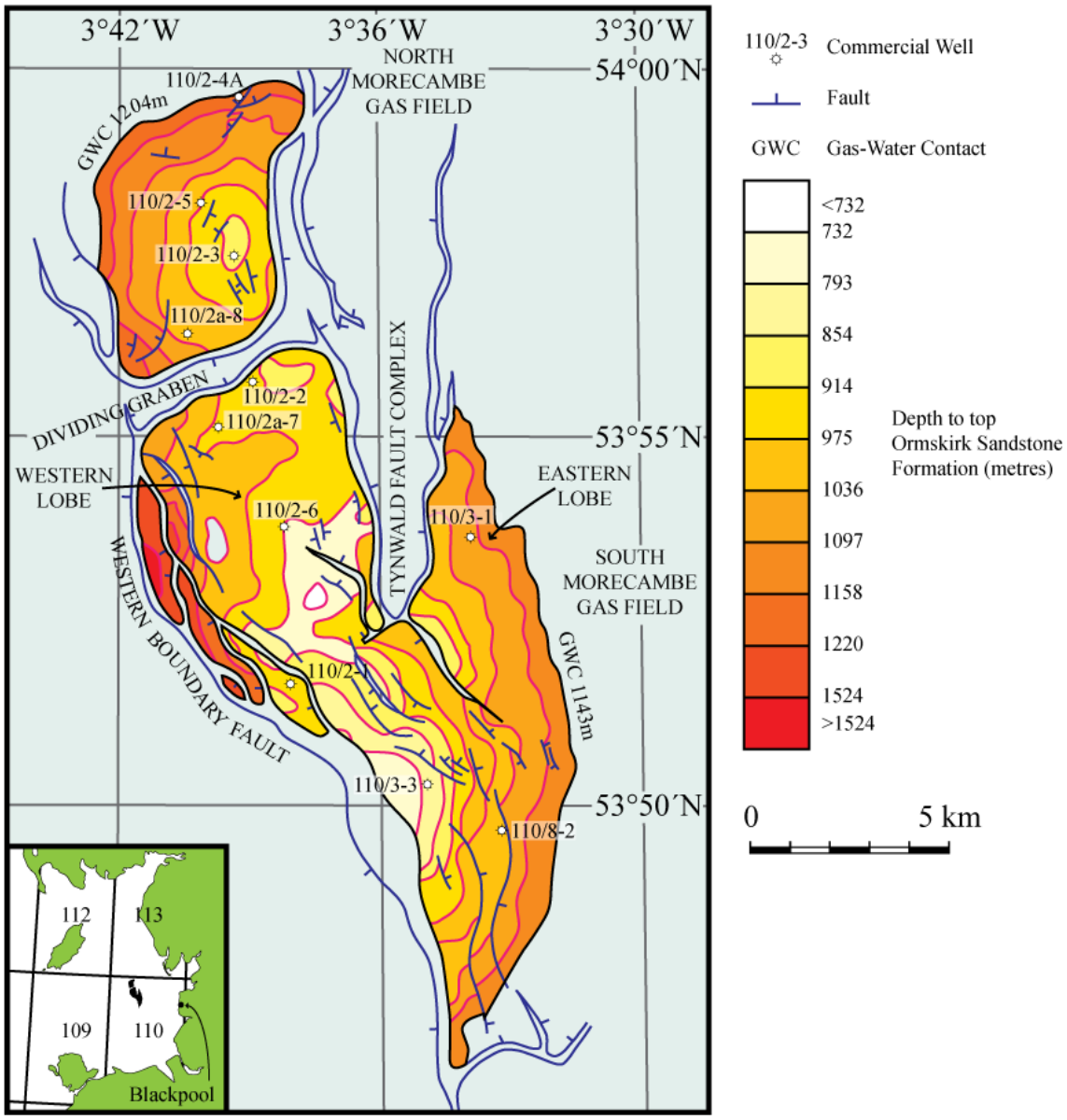

Figure 6.1 The location, structure and areal extent of the South and North Morecambe gas fields of the East Irish Sea Basin. The limit of the areal extent is defined by the original gas-water contact within each reservoir prior to production, where fault closure of the traps does not occur. After Jackson et al. (1995).

6.2. PUBLISHED STORAGE CAPACITY ESTIMATES

Previously published theoretical CO_2 storage capacity estimates for the South and North Morecambe gas fields have varied by a factor of 1.04 (see Table 6.1, (Brown et al., 2011; Coulthurst et al., 2011; Holloway et al., 2006; Kirk, 2006; Lewis et al., 2009; Shackley et al., 2004)), i.e. they are reasonably consistent in comparison with those of the Hewett Gas Field of the Southern North Sea (Chapter 4). This equates to a difference in storage capacity of 37 Mt CO_2.

Theoretical CO_2 storage capacity estimates of the South Morecambe gas field have varied by a factor of 1.12, or 86 Mt CO_2. Theoretical CO_2 storage capacity estimates of the North Morecambe gas field have varied by a factor of 1.27, or 38 Mt CO_2.

Although the previously published CO_2 storage capacity estimates seem to be better constrained than for the Hewett Gas Field of the Southern North Sea, they all use the same method of estimation: Chapter 1, equation 1.3 of Holloway et al. (2006). The following chapter will estimate the theoretical and effective CO_2 storage capacity of the South and North Morecambe Gas Fields using the alternative methods of Bachu et al. (2007), Chapter 1, equations 1.1 and 1.2, and Tseng et al. (2012), Chapter 1, equations 1.4, 1.6 and 1.7, as well as Holloway et al. (2006), Chapter 1, equation 1.3.

AUTHOR	TITLE	THEORETICAL/EFFECTIVE CO_2 STORAGE CAPACITY ESTIMATION?	EQUATION	CALCULATED CO_2 STORAGE CAPACITY (Mt)	WHICH RESERVOIRS?
Holloway et al., 2006	Industrial Carbon Dioxide Emissions and Carbon Dioxide Storage Potential in the UK	Theoretical	$M_{CO2} = (V_{GAS}(stp)/B_g).\rho_{CO2}$	1034.00	South and North Morecambe
				734.00	South Morecambe
				139.00	North Morecambe
Kirk, 2006	Potential for storage of carbon dioxide in the rocks beneath the East Irish Sea	Theoretical	$M_{CO2} = (V_{GAS}(stp)/B_g).\rho_{CO2}$	734.40	South Morecambe
				139.10	North Morecambe
Coulthurst, Taylor and Baddeley, 2011	The East Irish Sea CCS Cluster: A Conceptual Design - Technical Report	Theoretical	$M_{CO2} = (V_{GAS}(stp)/B_g).\rho_{CO2}$	997.00	South and North Morecambe
				820.00	South Morecambe
				177.00	North Morecambe
Brown et al., 2011	The East Irish Sea CCS Cluster: A Conceptual Design	Theoretical	$M_{CO2} = (V_{GAS}(stp)/B_g).\rho_{CO2}$	997.00	South and North Morecambe
				820.00	South Morecambe
				177.00	North Morecambe
Shackley and Gough, 2006	An Integrated Assessment of Carbon Dioxide Capture and Storage in the UK	Theoretical	$M_{CO2} = (V_{GAS}(stp)/B_g).\rho_{CO2}$	734.40	South Morecambe
				139.10	North Morecambe
Lewis et al., 2009	Assessment of the potential for geological storage of carbon dioxide in Ireland and Northern Ireland	Theoretical	$M_{CO2} = (V_{GAS}(stp)/B_g).\rho_{CO2}$	734.00	South Morecambe
				139.00	North Morecambe

Table 6.1 Overview of previously published storage capacity estimates for the South and North Morecambe gas fields.

6.3. THE ORIGINAL PETROLEUM PLAY

The regional geological setting of the South and North Morecambe gas fields has previously been described in Chapter 2. The major geological properties of the South and North Morecambe gas fields that have previously made them successful petroleum plays are summarised in Table 6.2 and Table 6.3, respectively, and in the following sections 6.3.1. to 6.3.5.

6.3.1. THE SOUTH MORECAMBE SHERWOOD SANDSTONE RESERVOIR

The South Morecambe Sherwood Sandstone reservoir is a thick sequence of fluvial (braided stream and sheetflood) sandstones (Stuart and Cowan, 1991) with main production from the Ormskirk Sandstone Formation and top St. Bees Sandstone Formation (see Figure 6.2 and Figure 6.3) over a gross thickness of 1463 m (Bastin et al., 2003). Chapter 2 has previously detailed the lithostratigraphy, facies associations, diagenetic stages and tectonic events following the deposition of the Sherwood Sandstone Formation within the Morecambe area of the East Irish Sea Basin.

Reservoir properties within the South Morecambe Sherwood Sandstone reservoir are governed by the abundance and distribution of authigenic platy illite. Platy illite was originally precipitated beneath a palaeo-gas-water-contact (Bastin et al., 2003). It is widespread within the northern and western areas of the South Morecambe Sherwood Sandstone reservoir, but absent along the eastern flank (Bastin et al., 2003). In the illite-free zone the reservoir enjoys reasonably good reservoir properties with high porosity and permeability values as will be demonstrated later in section 6.5.1.1.

6.3.2. THE NORTH MORECAMBE SHERWOOD SANDSTONE RESERVOIR

The North Morecambe Sherwood Sandstone reservoir is similar to the South Morecambe Sherwood Sandstone reservoir in terms of facies associations and deposition and diagenetic stages. It has previously been described in Chapter 2. The main control on reservoir performance in North Morecambe is, once again, governed by platy illite distribution which can reduce permeability by up to two orders of magnitude in affected areas (Stuart, 1993).

6.3.3. THE SOUTH AND NORTH MORECAMBE TRAPS

The South Morecambe reservoir is a structural anticline (see Figure 6.1). The northern limb is fault bounded to the north, west and east. The southern limb is fault bounded to the west and dip-closed to the east. The main dip direction is to the east.

The North Morecambe reservoir is a N-S trending, north-westerly dipping fault block, fault bounded to the east, west and south, but dip-closed to the north (see Figure 6.1). The eastern bounding fault strikes NNW-SSE and is a normal fault with a throw varying between 91.5 and 609.6 m. There are several small faults within the reservoir, however, the only significant internal fault has a 30.5 m throw and defines an easterly fault terrace which is in pressure communication with the rest of the reservoir (Cowan and Boycott-Brown, 2003).

There is a narrow graben that separates the South and North Morecambe Sherwood Sandstone reservoirs. The two bounding faults that define the graben have been found to act as full seals as previously described in section 6.1.

Due to the significant throws on the bounding faults of the North and South Morecambe Gas Fields, it is likely that the reservoirs will be juxtaposed against sealing unit as the downthrown fault blocks outside of the reservoir are composed of the sealing unit defined in Figure 6.3.

6.3.4. DIRECT CAP ROCK

The Mercia Mudstone Group forms the direct cap rock to the South and North Morecambe Sherwood Sandstone reservoirs. The Mercia Mudstone Group has previously been described in Chapter 2, consisting of evaporite cycles that include alternating mudstones and halites deposited as a result of cyclic flooding and drying. Within the region of South and North Morecambe, the group has an average thickness of 931.5 m.

The Mercia Mudstone Group has provided a proven hydrocarbon seal to the North Morecambe Sherwood Sandstone reservoir over geological time scales with no evidence of gas having entered or migrated through the cap rock. Evidence for this comes from the 3-D seismic dataset where there have been no observations of structures such as gas chimneys penetrating through the cap rock.

However, the early South Morecambe structure is likely to have been partially or wholly breached following late Cimmerian movements (late Jurassic/early Cretaceous) as a result of widespread uplift and erosion (Bushell, 1986). Due to the different gas compositions in the North and South Morecambe Sherwood Sandstone reservoirs, it is likely that hydrocarbons leaked out of the South Morecambe structure and it is also possible that meteoric waters were able to invade the structure (Bushell, 1986). Following the breaching of the South Morecambe structure further sedimentation occurred followed by a late phase gas charge during the Cretaceous/Early Tertiary as a result of a renewed burial of Carboniferous source rocks, increasing the geothermal gradient (Bushell, 1986). This second gas charge has been successfully stored within the South Morecambe Sherwood Sandstone reservoir over geological time scales with no evidence of gas having entered or migrated through the cap rock (Bushell, 1986).

Therefore, it is likely that at initial reservoir conditions the buoyancy pressure of the hydrocarbons did not exceed the minimum capillary entry pressure of the Mercia Mudstone Group. Again, no laboratory analysis data has been made available for analysis on the Mercia Mudstone Group, therefore it must be considered that the minimum capillary entry pressure of the cap rock is that of the

buoyancy pressure of the hydrocarbons at initial reservoir conditions, although this is unlikely and the minimum capillary entry pressure is expected to be higher.

6.3.5. OVERBURDEN STRATA

The Mercia Mudstone Group forms the majority of the overlying strata (see Figure 6.3). The Mercia Mudstone Group consists of various formations including the Hambleton and Singleton Mudstone Formations and Thornton Mudstone, all of which include salt members. The top ~60 m consists of Quaternary deposits, the base of which marks an unconformity.

OVERBURDEN STRATA	
Geological Formation	Lias Group
Depositional Environment	Marine
Depositional Facies	Marine shelf
Age	Lower Jurassic
Geological Formation	Penarth Group
Depositional Environment	Marine
Depositional Facies	Marine Shelf
Age	Upper Triassic, Rhaetian
DIRECT CAP ROCK	
Geological Formation	Mercia Mudstone Group
Depositional Environment	Terrestrial
Depositional Facies	Lacustrine
Age	Middle Triassic, Anisian-Norian
Average Thickness (m)	922.5
TRAP	
Structure	Structural anticline. The northern limb is fault bounded to the north, west and east. The Southern limb is fault bounded to the west and dip-closed to the east. Main dip is to the east
Depth to top structure (m)	732.0
Initial gas column (m)	411.0
Initial gas-water contact (m)	1140.0
RESERVOIR	
Geological Formation	Sherwood Sandstone Group
Depositional Environment	Terrestrial, fluvial
Age	Triassic, Lower Anisian
Lateral extent/play area (m^2)	83,800,000
Average Thickness (m)	1463.0
Net/gross ratio	0.97 (IFZ), 0.96 (IAZ)
Average Porosity (%)	12.5 (IFZ), 14.0 (IAZ)
Average Permeability (mD)	200 (IFZ), 0.8 (IAZ)
Average hydrocarbon saturation (%)	79 (IFZ), 62 (IAZ)
Irreducible water saturation (%)	21 (IFZ), 38 (IAZ)
Isolated or underlain by aquifer?	Isolated
PETROLEUM/FIELD CHARACTERISTICS	
Formation volume factor (stand. cond./res. cond.)	147.1
Original gas in place (m^3)	1.557E+11
Initial pressure (MPa)	12.831
Reservoir temperature (°C)	32.8
Recovery factor	0.93

Table 6.2 South Morecambe Sherwood Sandstone Reservoir properties. The illite-free zone is denoted by IFZ, and the illite-affected zone is denoted by IAZ. Adapted from Bastin et al. (2003).

OVERBURDEN STRATA	
Geological Formation	Lias Group
Depositional Environment	Marine
Depositional Facies	Marine shelf
Age	Lower Jurassic
Geological Formation	Penarth Group
Depositional Environment	Marine
Depositional Facies	Marine Shelf
Age	Upper Triassic, Rhaetian
DIRECT CAP ROCK	
Geological Formation	Mercia Mudstone Group
Depositional Environment	Terrestrial
Depositional Facies	Lacustrine, flood plain
Age	Middle Triassic, Anisian-Norian
Average Thickness (m)	940.5
TRAP	
Structure	N-S trending, north-westerly dipping fault block, fault bounded to the east, west and south, but dip-closed to the north
Depth to crest (m)	900.0
Initial gas column (m)	297.2
Initial gas-water contact (m)	1196.0
RESERVOIR	
Geological Formation	Sherwood Sandstone Group
Depositional Environment	Terrestrial, fluvial
Age	Triassic, Lower Anisian
Lateral extent/play area (m^2)	24,000,000
Average Thickness (m)	1500.0
Net/gross ratio	0.89 (IFL), 0.73 (IAL)
Average Porosity (%)	12.4 (IFL), 12.5 (IAL)
Average Permeability (mD)	25.00-180.00 (IFL), 0.02-1.00 (IAL)
Average hydrocarbon saturation (%)	100.0-65.0
Irreducible water saturation (%)	0.0-35.0
Isolated or underlain by aquifer?	Isolated
PETROLEUM/FIELD CHARACTERISTICS	
Formation volume factor (stand. cond./res. cond.)	142.9
Original gas in place (m^3)	3.653E+10
Initial pressure (MPa)	12.411
Reservoir temperature (°C)	33.3
Recovery factor	0.80

Table 6.3 North Morecambe Sherwood Sandstone Reservoir properties. The illite-free zone is denoted by IFZ, and the illite-affected zone is denoted by IAZ. Adapted from Cowan and Boycott-Brown (2003).

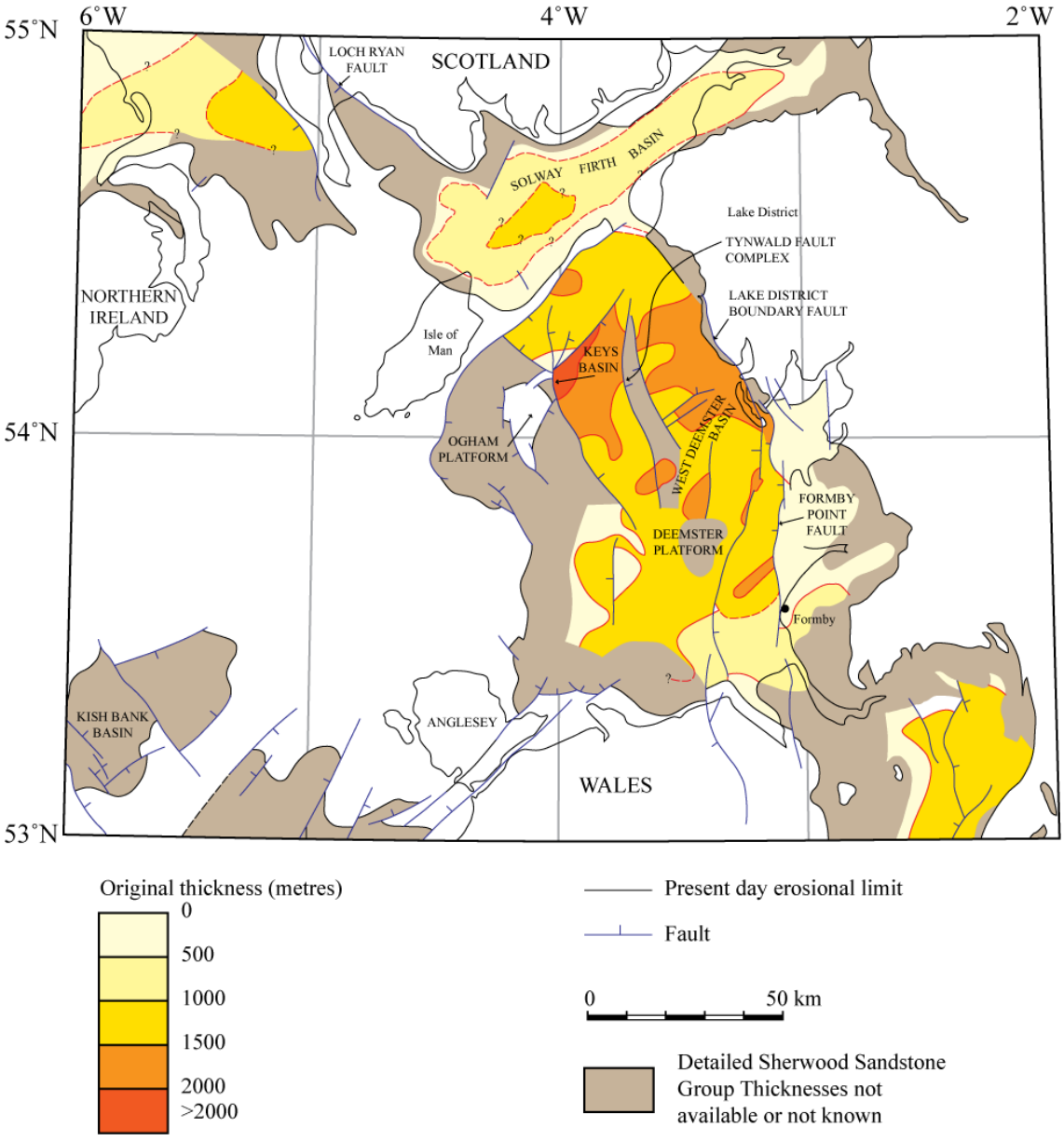

Figure 6.2 Distribution and Thickness of the Sherwood Sandstone Group within the East Irish Sea Basin. After Jackson et al. (1995).

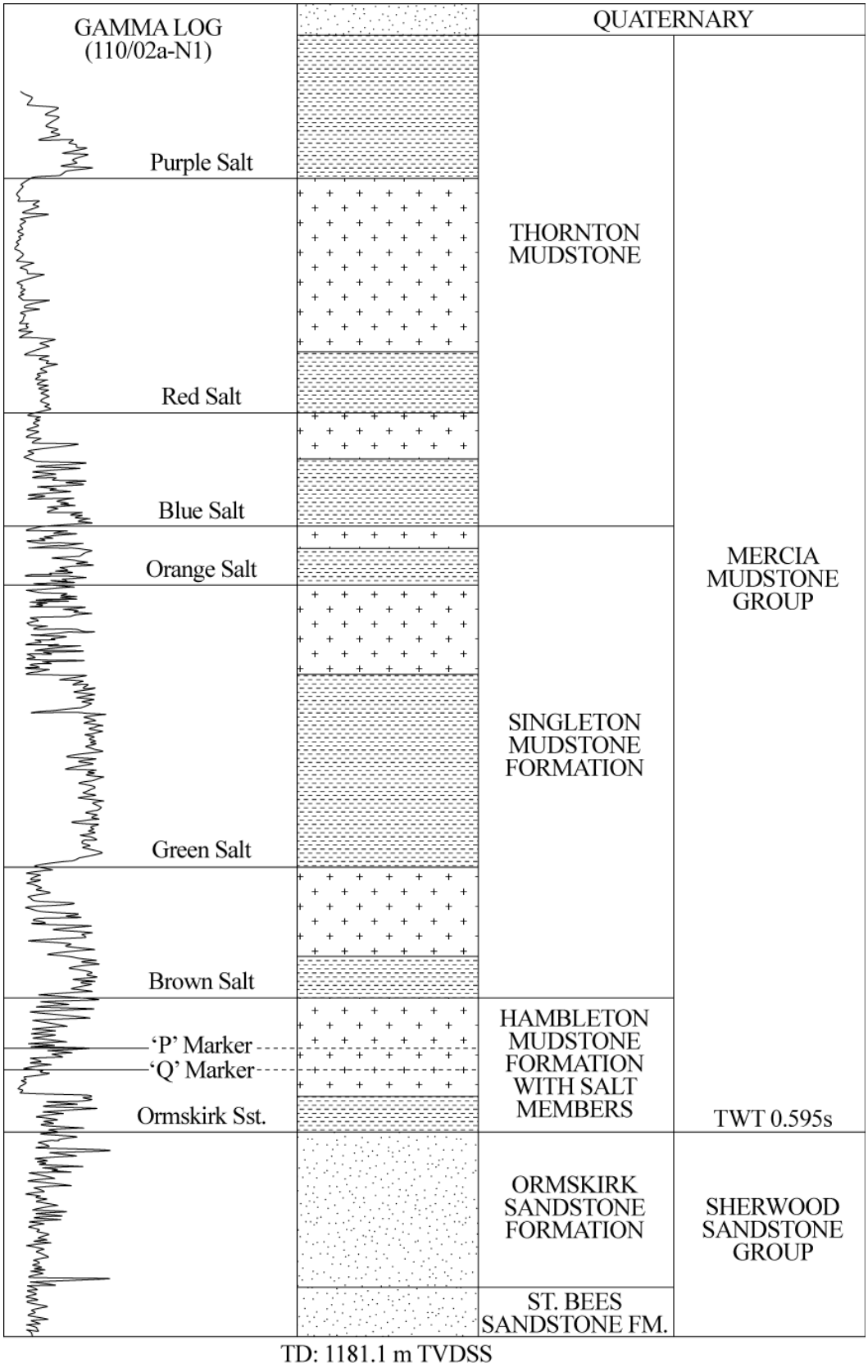

Figure 6.3 North Morecambe Field Triassic stratigraphy. After (Cowan and Boycott-Brown, 2003).

6.4. THE SOUTH MORECAMBE GAS FIELD

6.4.1. PETROPHYSICAL CHARACTERISTICS

6.4.1.1. POROSITY AND PERMEABILITY DATA

The following graphs and boxplots (Figure 6.4 to Figure 6.8) represent the plotted porosity and permeability dataset made available to Durham University by IHS. Wells with core analysis data include 110/02-01, 110/02-02, 110/02a-06, 110/02a-07, 110/02a-F01 and 110/03-01 (see Figure 6.1 for locations). Figure 6.4 (a) is a graph of porosity versus permeability for the entire South Morecambe Sherwood Sandstone reservoir, and shows a positive correlation with an r^2 value of 0.1392. Through application of the Pearson correlation (Gravetter and Wallnau, 1999), the critical r value for a sample size of 3197 and a significance level of 0.0005 for a one tailed probability (i.e. it is known the direction of correlation is positive) is 0.104. Therefore, the calculated r value for the porosity and permeability correlation of 0.373 exceeds the critical value and can be considered as significant.

Due to the reservoir being affected by illite precipitation, data from the illite free zone and illite affected zone have been analysed separately. Figure 6.4 (b) for the illite free zone shows a positive correlation with an r^2 value of 0.266. The critical r value for 1564 values is 0.104, therefore the calculated r value of 0.516 exceeds this, and the correlation can be considered significant. Figure 6.4 (c) for the illite affected zone also shows a positive correlation with an r^2 value of 0.0827. Once again, the critical r value for 1633 values is 0.104, therefore the calculated r value of 0.288 exceeds this, and the correlation can be considered significant.

Figure 6.5 shows boxplots of the porosity data of, (a) the entire South Morecambe Sherwood Sandstone reservoir and from (b) the illite free zone, and (c) illite affected zone. Porosity data from the entire South Morecambe Sherwood Sandstone reservoir (Figure 6.5 (a)) show the main body (50%) of data ranges between 9.07% (Q1) and 15.66% (Q3), with a median value (Q2) of 12.22%. Outliers were calculated to be porosity data less than -0.815% and greater than

25.545%. As such, the whisker on the left hand side of the box is limited to 0.0% (as it is not possible to have a negative value for porosity). On the right hand side of the boxplot there are a total of 15 outliers, illustrated as black boxes on the boxplot.

Porosity data from the illite free and illite affected zones were then analysed separately. The illite free zone within the South Morecambe Sherwood Sandstone reservoir (Figure 6.5 (b)) show the main body (50%) of porosity data ranges between 7.84% (Q1) and 14.26% (Q3), with a median value (Q2) of 10.82%. Outliers were calculated to be porosity data less than -1.79% and greater than 23.89%. Again, the whisker on the left hand side of the box is limited to 0.0% (as it is not possible to have a negative value for porosity). On the right hand side of the boxplot there are, once again, a total of 15 outliers.

Porosity data from the illite affected zone within the South Morecambe Sherwood Sandstone reservoir (Figure 6.5 (c)) show the main body (50%) of porosity data ranges between 10.66% (Q1) and 16.46% (Q3), with a median value (Q2) of 13.56%. Outliers were calculated to be porosity data less than 1.96% and greater than 25.16%. There are a total of 3 outliers on the left hand side of the boxplot and 17 outliers on the right hand side of the boxplot.

From the boxplots it is possible to observe that porosity is generally greater within the illite affected zone than the illite free zone. This is due to the illite free zone containing greater volumes of quartz and dolomite cements than the illite affected zone, and is a result of a breaching of the South Morecambe structure and a loss of the initial gas charge after the precipitation of platy illite (Bushell, 1986).

As for the Hewett Lower and Upper Bunter Sandstone reservoirs (Chapters 4 and 5 respectively), Monte Carlo simulation of these data, and application of the Anderson-Darling (A-D) test is used to evaluate whether the data population originated from a specific probability distribution (Stephens, 1974).

The best-fit distribution for the entire South Morecambe Sherwood Sandstone reservoir is a lognormal distribution, shown in Figure 6.6 (a). The resulting A-D value for the dataset is 1.230; therefore the fit of the data to the probability distribution is reasonable. The A-D P-value test for normality gives a result of 0.00, implying these data do not follow a specified distribution. However,

compared to the alternative distributions, the lognormal is the best fit of the porosity data.

Data from the illite free and illite affected zones of the South Morecambe Sherwood Sandstone reservoir were then analysed separately. The best-fit distribution for data from the illite free zone is a lognormal distribution, shown in Figure 6.6 (b). The A-D value for the dataset is 1.331, once again implying the fit of the data to the probability distribution is reasonable. The A-D P-value test for normality gives a result of 0.00, showing these data do not follow a specified distribution.

The best-fit distribution for data from the illite affected zone is a logistic distribution, shown in Figure 6.6 (c). The A-D value for the dataset is 3.282; therefore the fit of the data to the probability distribution is very poor. The A-D P-value test for normality gives a result of 0.00, once again showing these data do not follow a specified distribution.

As has been previously stated in Chapters 4 and 5, only porosity data are necessary for CO_2 storage capacity estimation (Chapter 1, equations 1.1 to 1.7). However, permeability is still an important rock property to analyse during geological characterisation as it illustrates the degree of pore connectivity within a reservoir. It is well documented that illite severely affects permeability (Bastin et al., 2003; Bushell, 1986; Cowan and Boycott-Brown, 2003), therefore it is essential to analyse the effect of illite in the affected zone of the South Morecambe Sherwood Sandstone reservoir.

The boxplot of permeability for the entire South Morecambe Sherwood Sandstone reservoir is shown in Figure 6.7 (a). The main body (50%) of data ranges between 0.18 mD (Q1) and 16.98 mD (Q3), with a median value (Q2) of 1.69 mD. Outliers were calculated to be permeability data less than -25.02 mD and greater than 42.18 mD. It is not possible to have a negative value for permeability therefore the whisker on the left hand side of the box has been limited to 0.00 mD. However, there are a total of 635 outliers on the right hand side of the box, up to a maximum permeability of 5728.32 mD. The outliers have not been plotted on this, or any of the other boxplots in Figure 6.7, due to their scale of distance away from the main body of data.

The boxplot of the illite free zone (Figure 6.7 (b)) shows the main body (50%) of data ranges between 0.28 mD (Q1) and 28.90 mD (Q3), with a median value (Q2) of 2.82 mD. Outliers were calculated to be permeability data less than -42.65 mD and greater than 71.83 mD. Again, it is not possible to have a negative value for permeability, therefore the whisker on the left hand side of the box is limited to 0.00 mD. However, there are a total of 345 outliers on the right hand side of the box, up to a maximum permeability of 3744.99 mD.

The boxplot of the illite affected zone (Figure 6.7 (c)) shows the main body (50%) of data ranges between 0.17 mD (Q1) and 8.52 mD (Q3), with a median value (Q2) of 1.19 mD. Outliers were calculated to be permeability data less than -12.36 mD and greater than 21.05 mD. The whisker on the left hand side of the box is limited to 0.00 mD as it is not possible to have a negative value for permeability. However, there are a total of 295 outliers on the right hand side of the box, up to a maximum permeability of 5728.32 mD. Comparison of the results in Figure 6.7 (b) and (c) show that the main body (50%) of data is located at higher permeabilities in the illite free zone (ranging between 0.28 mD and 28.90 mD) than the illite affected zone (ranging between 0.17 mD and 8.52 mD). This is to be expected as illite precipitation destroys permeability within sandstone reservoirs.

Average (mean) permeability values of the entire South Morecambe Sherwood Sandstone reservoir are 97.01 mD, the illite free zone, 129.61 mD and the illite affected zone, 65.79 mD, based upon data from the same wells listed above for porosity. The logarithmic histogram of permeability for the entire South Morecambe Sherwood Sandstone reservoir (Figure 6.8 (a)) shows there to be a high number of instances as permeability increases, however, as has been demonstrated through use of the boxplot in Figure 6.7 (a) the higher values are spread over a vast range of permeability, up to 5728.32 mD. Similar trends can be observed in Figure 6.8 (b) and (c) for the illite free and illite affected zone respectively. As previously demonstrated with the boxplots in Figure 6.7 (b) and (c), the illite free zone has a higher number of instances at higher permeabilities than that of the illite affected zone.

(a)

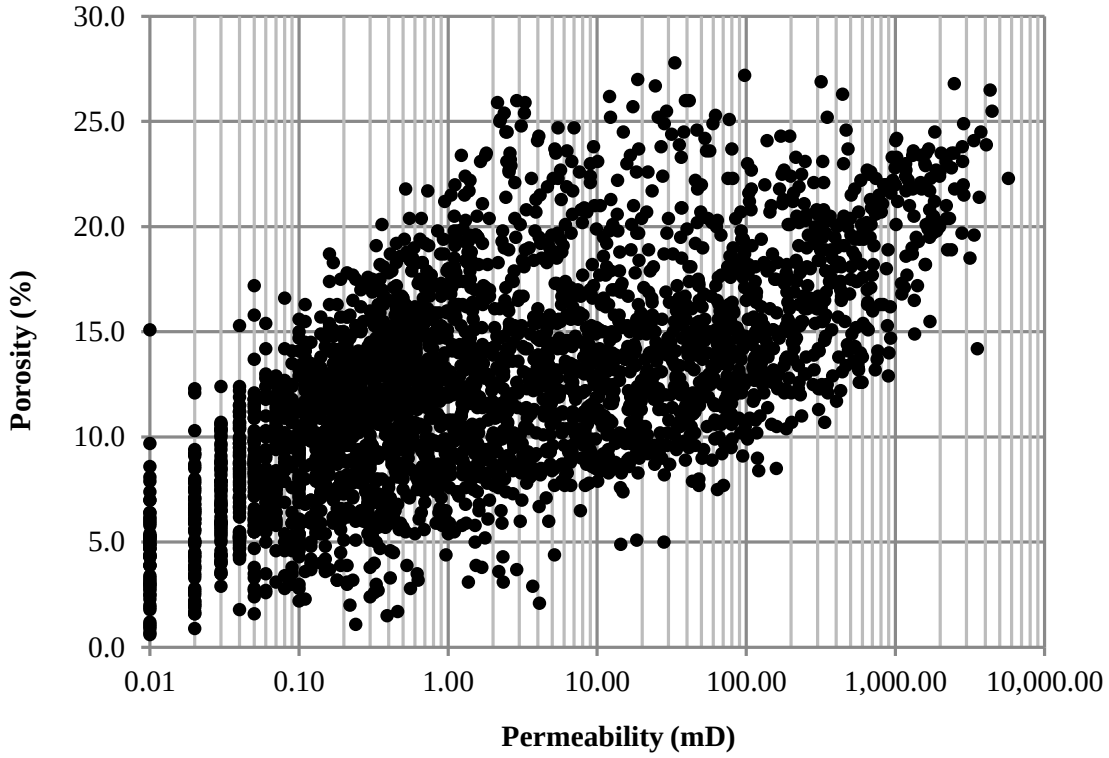
30.0
25.0
20.0
15.0
10.0
5.0
0.0
Porosity (%)
0.01
0.10
1.00
10.00
100.00
1,000.00
10,000.00
Permeability (mD)

(b)

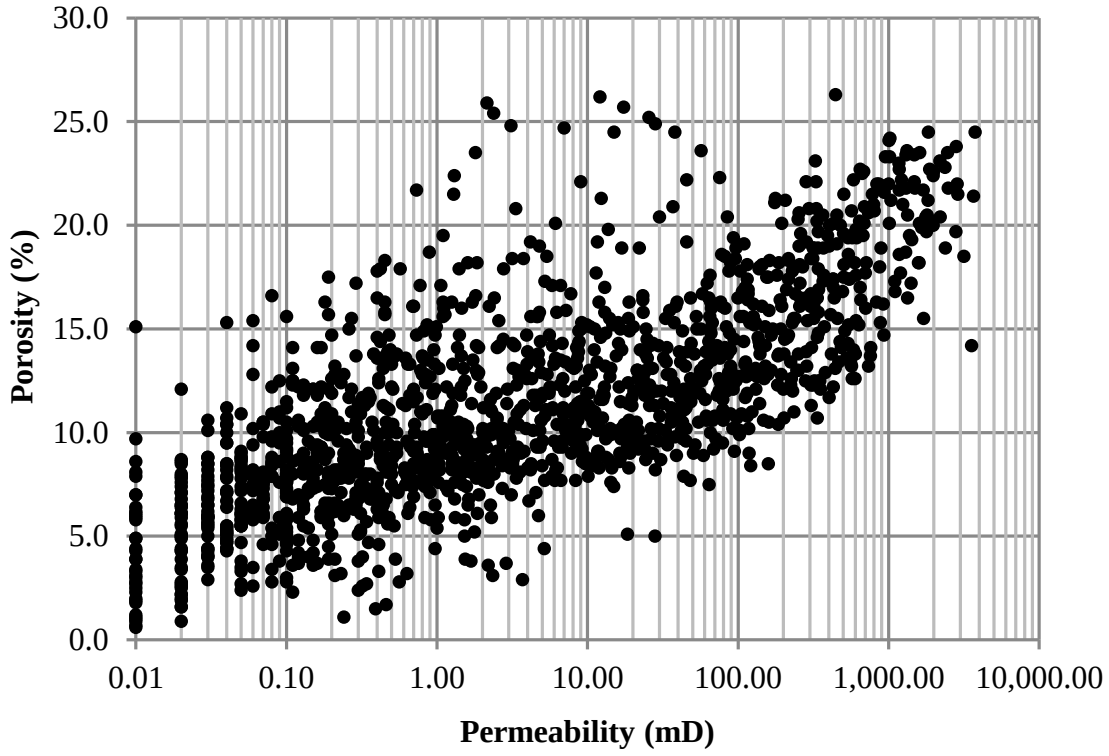
30.0
25.0
20.0
15.0
10.0
5.0
0.0
Porosity (%)
0.01
0.10
1.00
10.00
100.00
1,000.00
10,000.00
Permeability (mD)

(c)

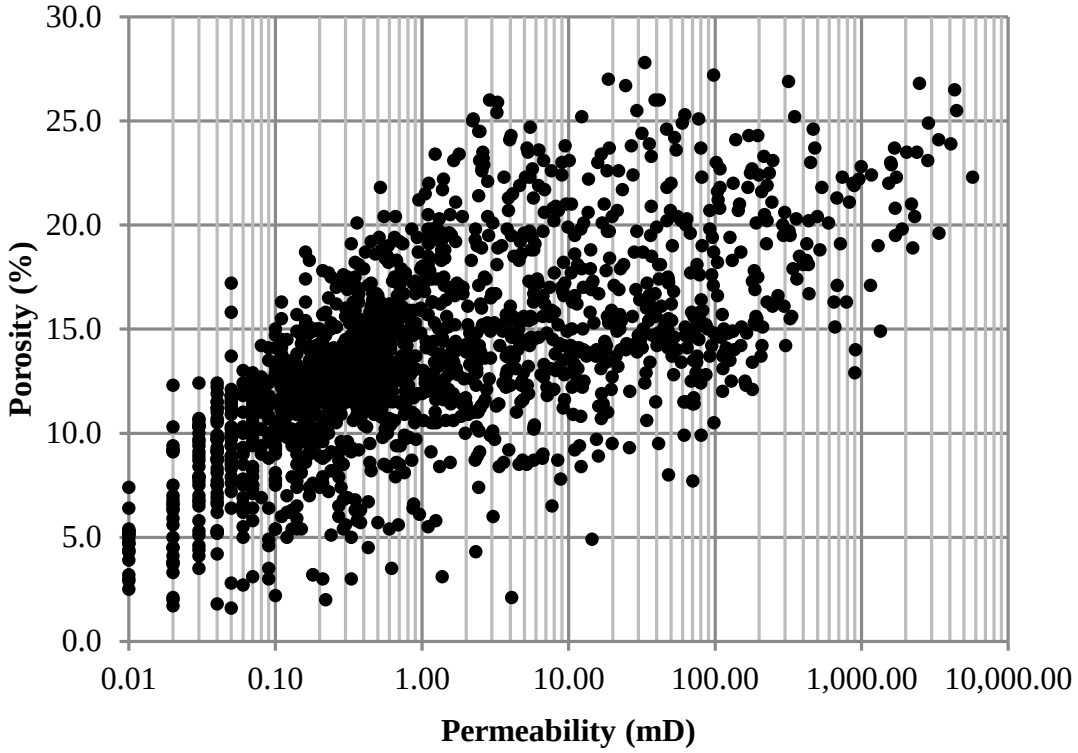

Figure 6.4 South Morecambe Sherwood Sandstone Overall Reservoir Quality for (a) the entire reservoir, (b) the illite free zone, and (c) the illite affected zone.

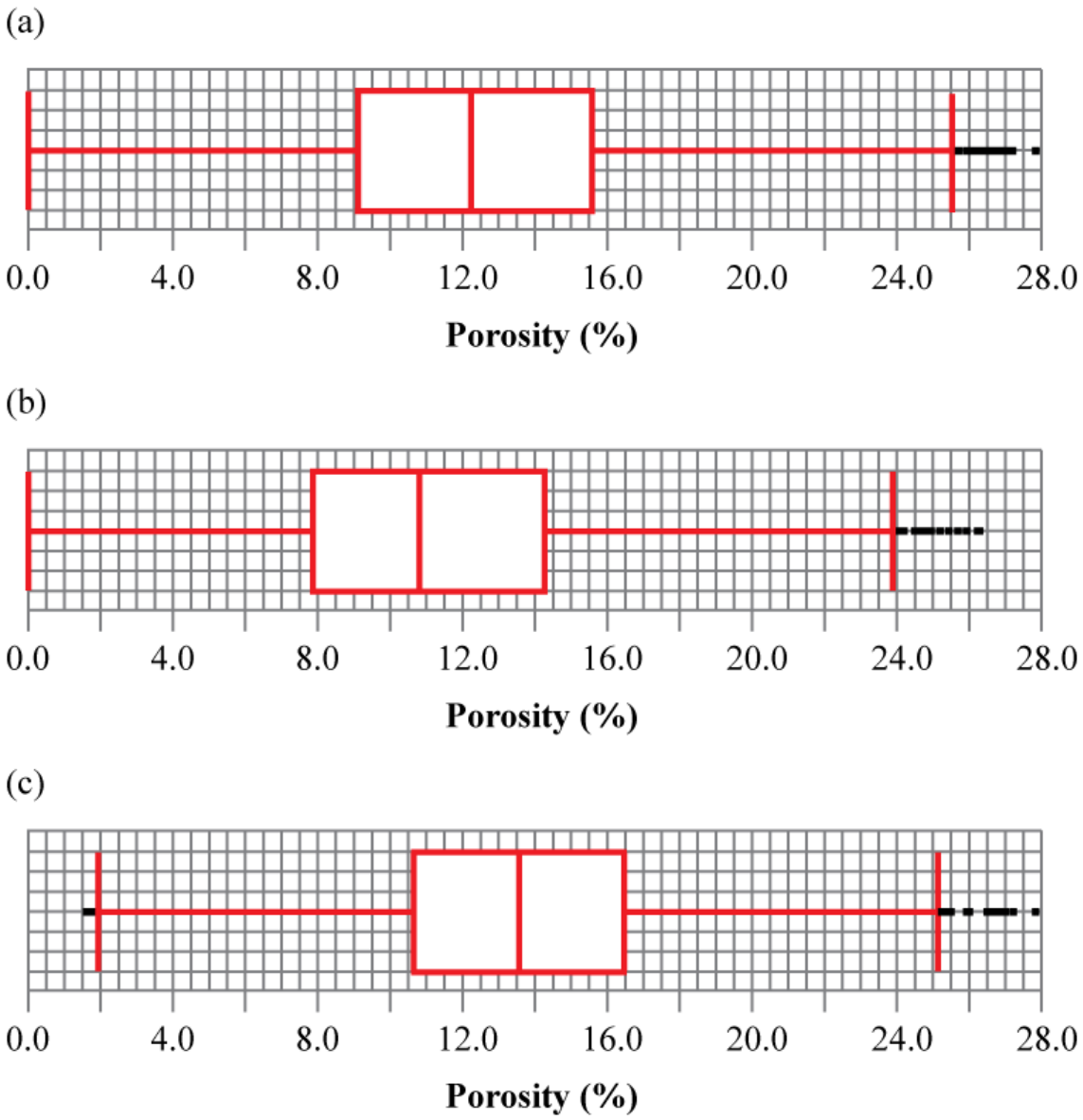

Figure 6.5 South Morecambe Sherwood Sandstone Reservoir boxplots for porosity. (a) Porosity of the reservoir overall, (b) porosity of the illite free zone within the reservoir, and (c) porosity of the illite affected zone within the reservoir.

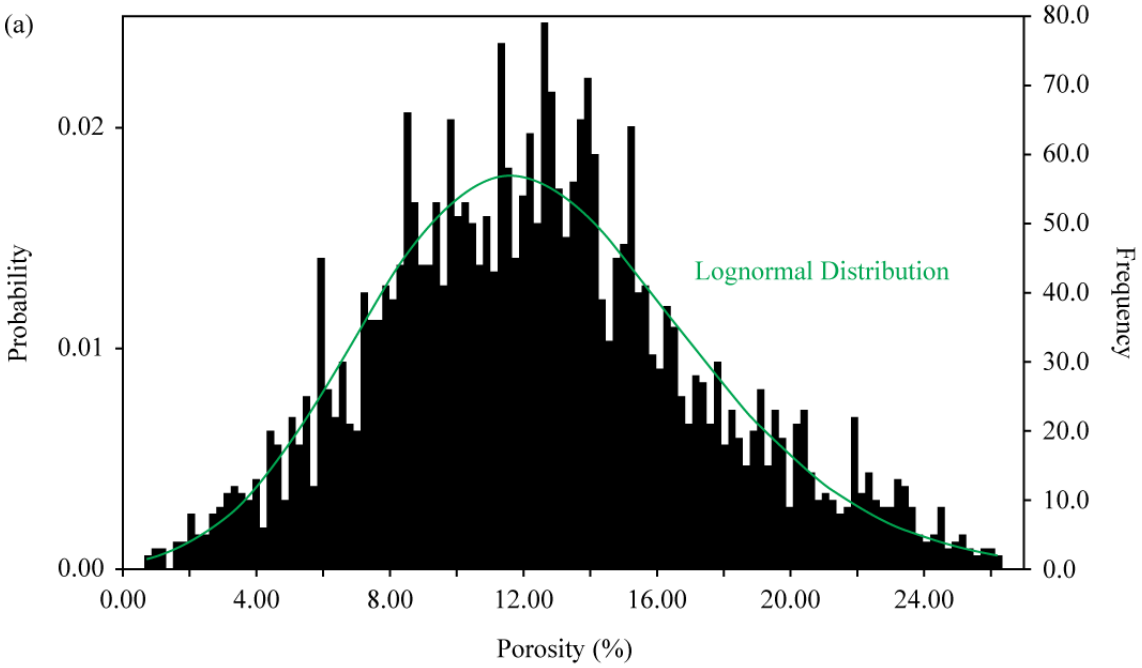
(a)
Probability
Frequency
Lognormal Distribution
Porosity (%)
0.00
0.01
0.02
0.0
10.0
20.0
30.0
40.0
50.0
60.0
70.0
80.0
0.00
4.00
8.00
12.00
16.00
20.00
24.00

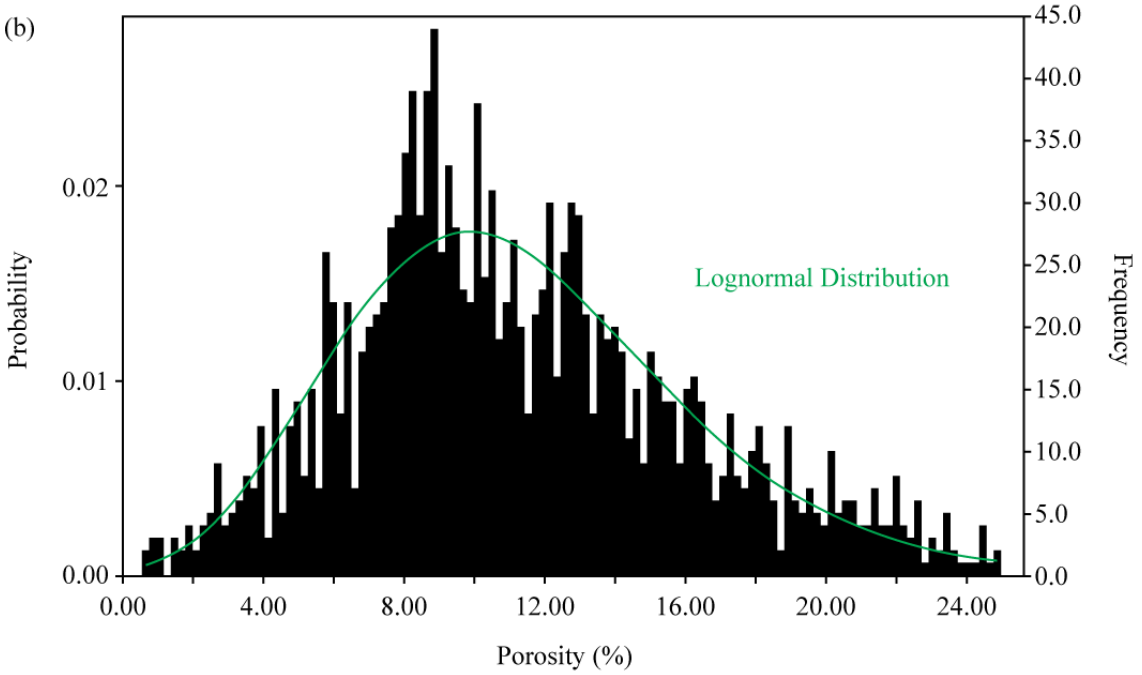
(b)
Probability
Frequency
Lognormal Distribution
Porosity (%)
0.00
0.01
0.02
0.0
5.0
10.0
15.0
20.0
25.0
30.0
35.0
40.0
45.0
0.00
4.00
8.00
12.00
16.00
20.00
24.00

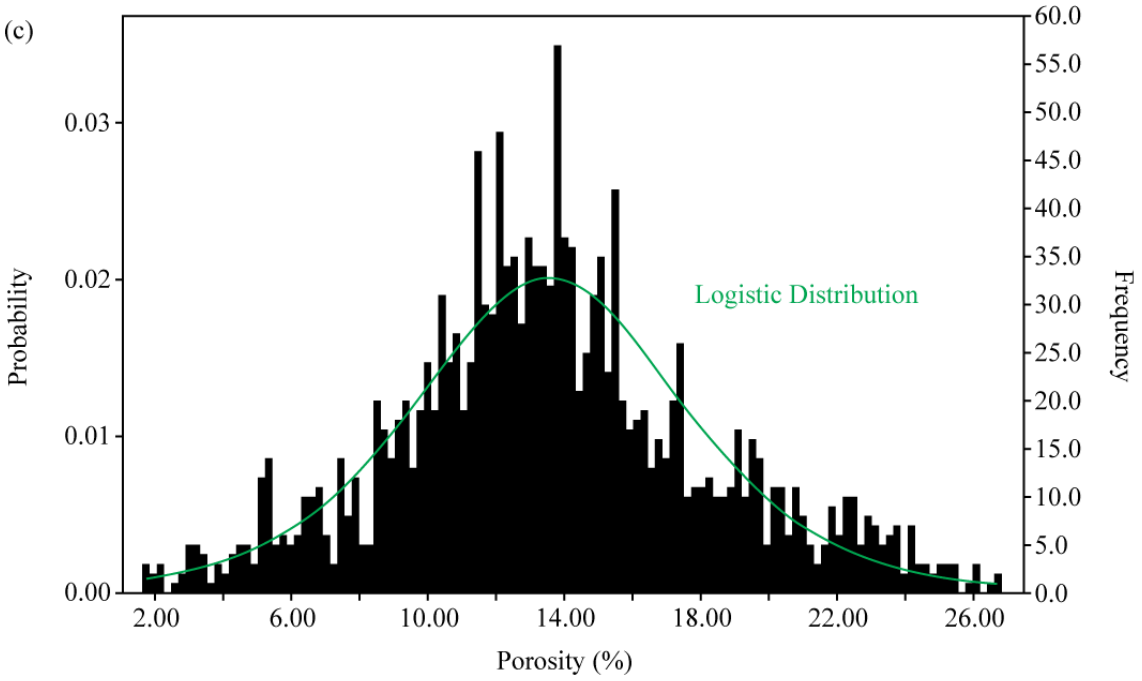

Figure 6.6 Histogram of South Morecambe Sherwood Sandstone Reservoir porosity for (a) the entire reservoir, based on 3197 values, (b) the illite free zone, based on 1564 values, and (c) the illite affected zone, based on 1633 values.

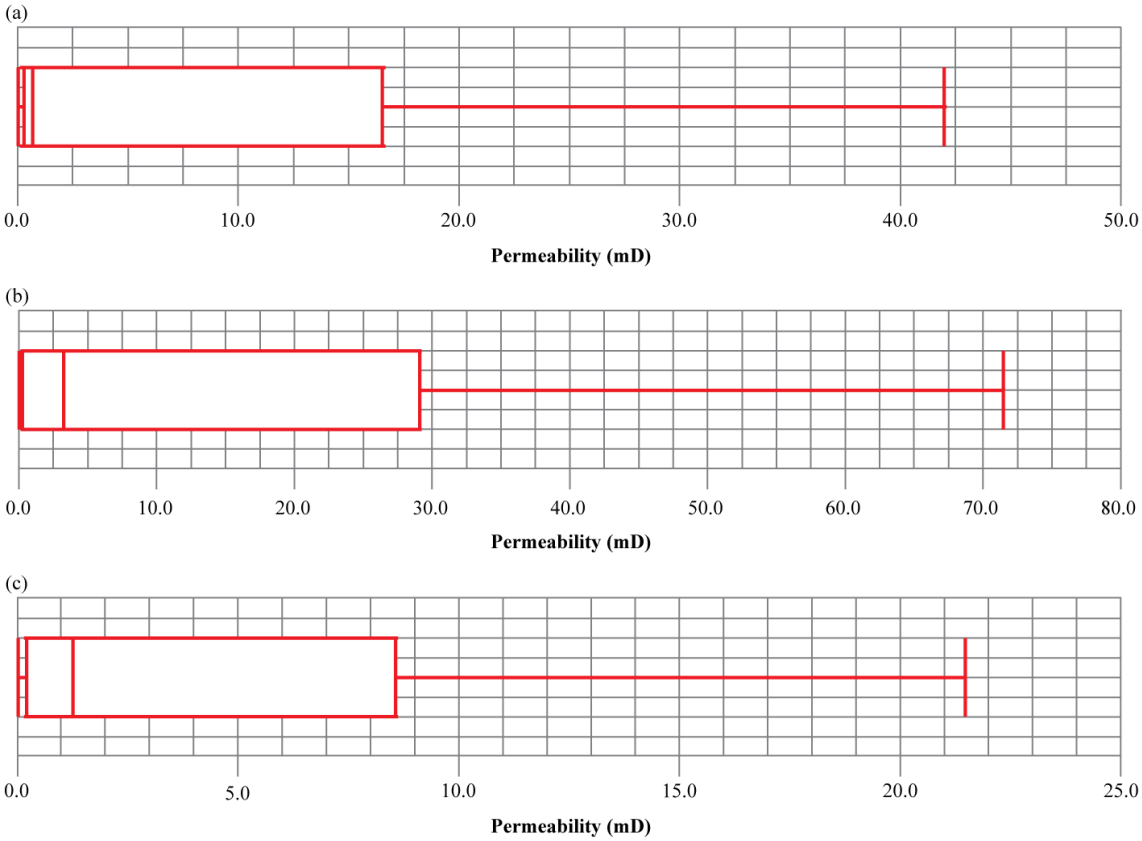

Figure 6.7 South Morecambe Sherwood Sandstone Group Reservoir boxplot for permeability for (a) the entire reservoir, (b) the illite free zone, and (c) the illite affected zone. Outliers on the right hand side of the boxplots have not been plotted on the boxplots due to their scale of distance away from the main body of data. For (a) the entire reservoir, there are a total of 635 outliers on the right hand side of the box, with a maximum permeability of 5728.32 mD. For (b) the illite free zone, there are a total of 345 outliers on the right hand side of the box, with a maximum permeability of 3744.99 mD. For (c) the illite affected zone, there are a total of 295 outliers on the right hand side of box, with a maximum permeability of 5728.32 mD.

(a)

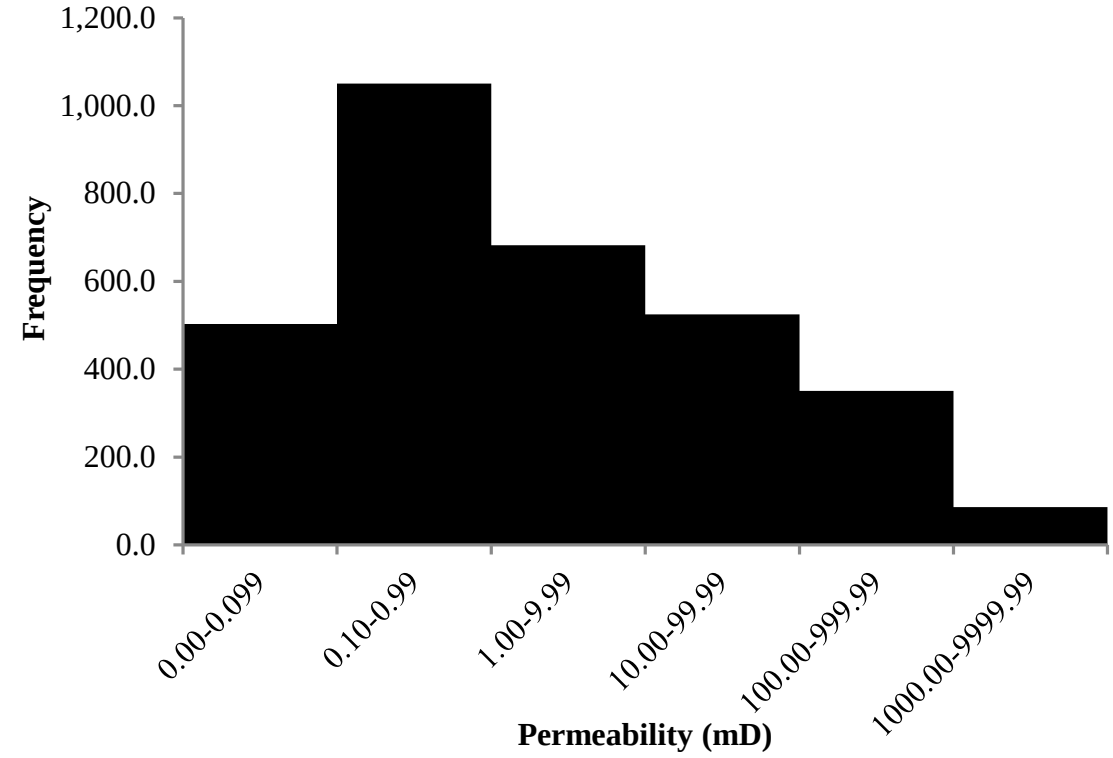
1,200.0
1,000.0
800.0
600.0
400.0
200.0
0.0
Frequency
0.00-0.099
0.10-0.99
1.00-9.99
10.00-99.99
100.00-999.99
1000.00-9999.99
Permeability (mD)

(b)

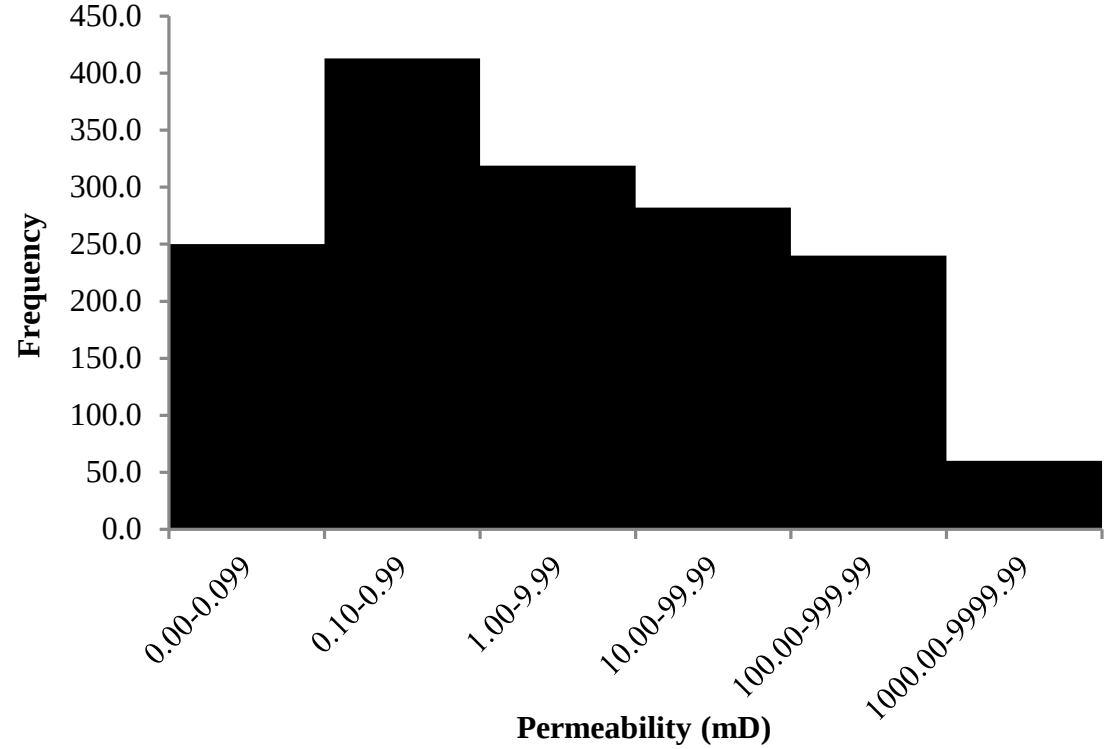
450.0
400.0
350.0
300.0
250.0
200.0
150.0
100.0
50.0
0.0
Frequency
0.00-0.099
0.10-0.99
1.00-9.99
10.00-99.99
100.00-999.99
1000.00-9999.99
Permeability (mD)

(c)

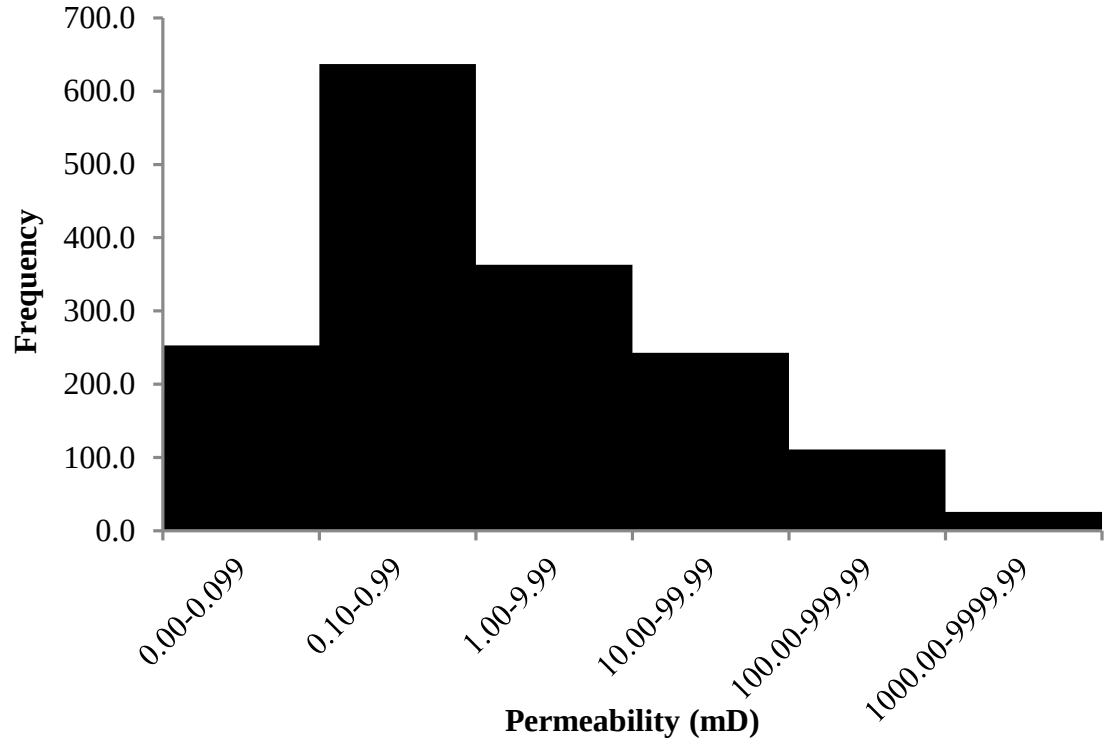

Figure 6.8 Histogram of South Morecambe Sherwood Sandstone Reservoir permeability for (a) the entire reservoir, (b) the illite free zone, and (c) the illite affected zone.

6.4.1.2. GAS PRODUCTION AND ASSOCIATED PRESSURE DECLINE

The South Morecambe Sherwood Sandstone reservoir has produced natural gas since 8 January 1985. The last recorded volume of produced gas was in December 2010 at 139.577 billion cubic metres, based on the production data received from Centrica. The gas production data, from all productive wells (including wells 110/02a-A01, A02, A03, A04, A05, A06, A07 and A08, 110/02a-C01, C02, C03, C05 and C06, 110/02a-D01, D02, D03, D04, D05, and D06, 110/02a-F01, F02, F03, F04, F05, F06 and F07, and 110/02a-H01, H02, H03, H04, H05, H06, H07 and H08) has been plotted in Figure 6.9, which shows a moderate but increasing rate of production for almost five years after the onset of production at 0.983 billion cubic metres per year. Production then rapidly increased between 1990 and 2005 at a rate of 7.53 billion cubic metres per year. The production rate decreased to 3.63 billion cubic metres per year after 2005 until the end of the

plotted dataset in 2011. At the end of 2010 the reservoir had a recovery factor of 93.6% and still has the potential for a small amount of further production.

The pressure history of the reservoir has also been plotted alongside the gas production data in Figure 6.9 from well 110/02a-A01. The associated pressure decline due to production has a similar but opposite trend to that of gas production. For the five years following the onset of production in 1985 until 1990 the rate of pressure decline was low at 0.0739 MPa/year. Pressure decline then increased between 1990 and 2005 at a rate of 0.617 MPa/year. Pressure decline began to slow after 2005 to 2011 (end of plotted dataset) to a rate of 0.286 MPa/yr. For the first 13 years of production (from 1985-1998) pressure readings were measured regularly and their trend is extremely consistent in a stepwise progression that mirrors that of cumulative production. Pressure readings taken after 1998 were more sporadic in their measurement and fluctuate around the expected trend. The stepwise changes in the production and pressure dataset are likely to be the result of periods of shut-in, i.e. periods of time where no gas was produced from the reservoir.

As for the previous pressure datasets, there will be a degree of error involved. Early readings from RFT tools will be accurate to within 0.18%. Later readings will be accurate to within 0.025%.

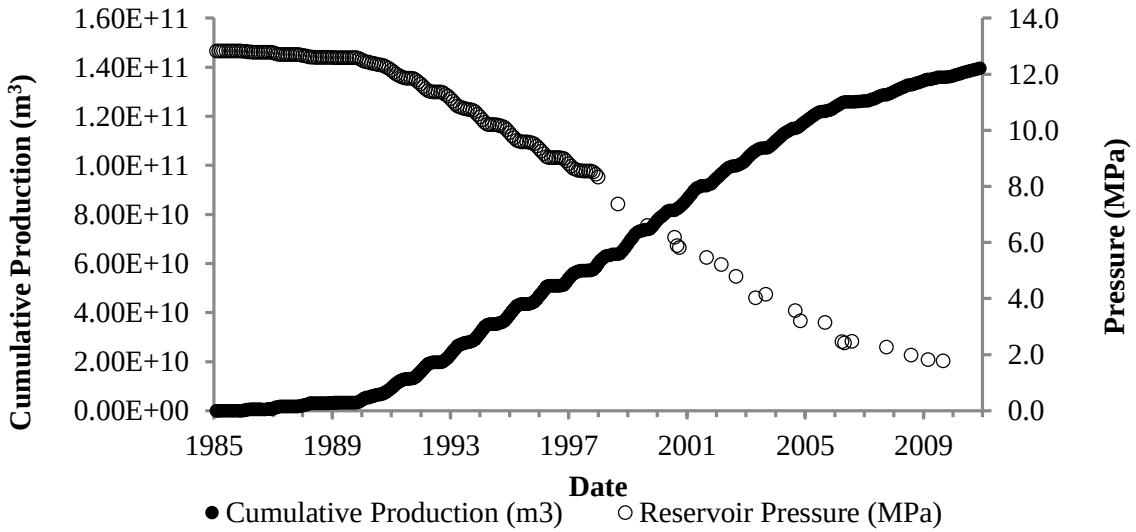

Figure 6.9 South Morecambe Sherwood Sandstone Reservoir cumulative production and pressure depletion data, based on production data from Centrica.

6.4.1.3. MATERIAL BALANCE METHODS

Material balance methods are once again used to validate the drive mechanism within the South Morecambe Sherwood Sandstone reservoir throughout its productive lifetime. The recovery factor, original gas in place and the ultimate recoverable reservoirs can also be constrained, necessary parameters for CO_2 storage capacity estimation.

The material balance plot of the South Morecambe Sherwood Sandstone reservoir (Figure 6.10) conforms extremely well to a linear trend in the first phase of production (up until ~60 billion cubic metres of natural gas have been produced). After this point, because the pressure readings are more sporadic, the resulting P/Z data is also sporadic, and the measurements fluctuate around the linear trend until the original gas in place is reached (where the trend line on Figure 6.10 intersects the x-axis). Despite the fluctuations in its later life, the South Morecambe Sherwood Sandstone reservoir is interpreted to be a depletion drive reservoir, as these data conform well to a linear trend.

The Cole Plot of the same data confirms the South Morecambe Sherwood Sandstone reservoir to be a depletion drive reservoir due to its overall linear trend on Figure 6.11. Now the South Morecambe Sherwood Sandstone reservoir has been confirmed to be a depletion drive reservoir it is possible to make more accurate estimations of the recovery factor, original gas in place and the volume of ultimate recoverable reserves. The value for the original gas in place can be determined through linear extrapolation of the trend line on Figure 6.10 until it intersects the x-axis. This occurs at 1.52E+11 m^3 for the South Morecambe Sherwood Sandstone reservoir.

The recovery factor can now be properly constrained and is defined as the volume of produced gas divided by the original gas in place, multiplied by 100%. The last recorded volume of produced gas was 139.577 billion cubic metres in December 2010, giving a recovery factor of 93.6%, based on production data from Centrica. The volume of ultimate recoverable reserves will be similar to the value for the original gas in place for the South Morecambe Sherwood Sandstone reservoir due to it being confirmed as a depletion drive reservoir.

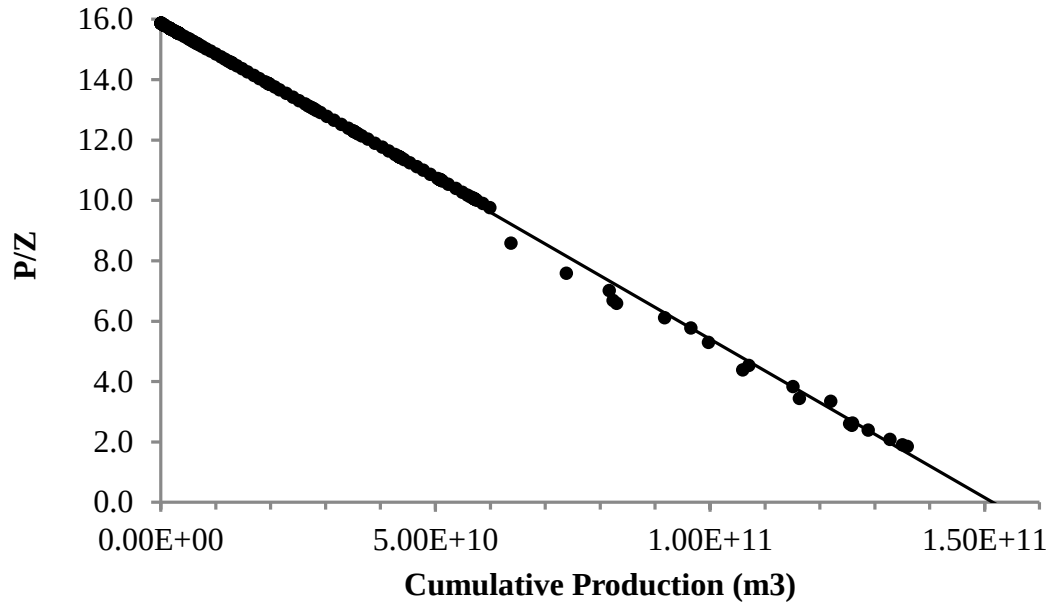

Figure 6.10 South Morecambe Sherwood Sandstone Reservoir material balance plot.

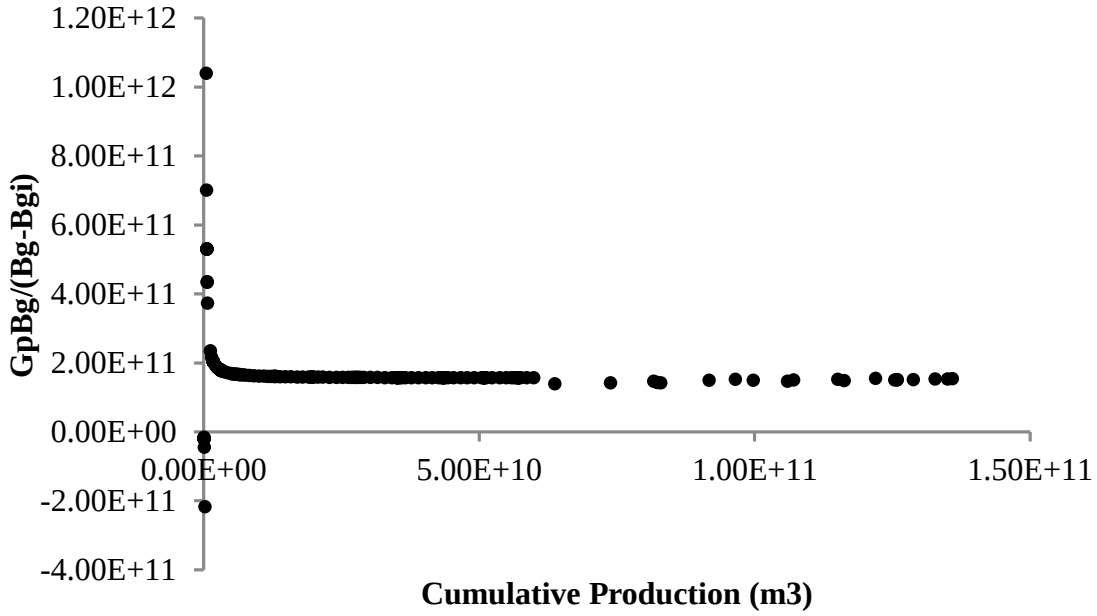

Figure 6.11 South Morecambe Sherwood Sandstone Reservoir Cole Plot.

6.4.2. ESTIMATION OF RESERVOIR FLUID COMPRESSIBILITY AND IMPLICATIONS FOR CO_2 STORAGE CAPACITY ESTIMATION

As for Chapters 4 and 5, estimations of gas compressibility factor (or Z-factor) were made using both RefProp (Lemmon et al., 2013) and the Lawrence Berkeley National Laboratory online calculator, WebGasEOS (Reagan and Oldenburg, 2006). Once again, several equations of state were used for analysis.

The calculated results of the Z-factor were input into both methods for calculating theoretical CO_2 storage capacity (for example, Bachu et al. (2007), Holloway et al. (2006), and Tseng et al. (2012)) and effective CO_2 storage capacity (for example, Tseng et al. (2012)). Through the variation of both estimations of Z-factor using various equations of state and the methods used to calculate CO_2 storage capacity, a range of results were produced.

6.4.2.1. GAS COMPRESSIBILITY FACTOR ESTIMATION

6.4.2.1.1. REFPROP ESTIMATIONS OF GAS COMPRESSIBILITY FACTOR

RefProp (Lemmon et al., 2013) was used to investigate Z-factor variability of several gas compositions (see Table 6.4) at constant temperature, whilst varying pressure and the equation of state used (Figure 6.12). The temperature was maintained at the initial reservoir temperature of 32.8 °C (305.928 K). Pressure was varied between the initial reservoir pressure of 12.831 MPa and the final reservoir pressure of 1.780 MPa. Gas compressibility factors were produced for three different equations of state: Peng-Robinson (Peng and Robinson, 1976), GERG-2008 (Kunz and Wagner, 2012) and the AGA8-DC92 Model (Starling and Savidge, 1992). Graphs of the results are displayed in Figure 6.12, and the main results to be used in the methods of storage capacity estimation are summarised in Table 6.5.

	MOLE FRACTION					
	Initial	20% CO_2	40% CO_2	60% CO_2	80% CO_2	99% CO_2
SOUTH MORECAMBE SHERWOOD SANDSTONE RESERVOIR INITIAL GAS COMPOSITION						
Methane	0.850000	0.680000	0.510000	0.340000	0.170000	0.008500
Ethane	0.045000	0.036000	0.027000	0.018000	0.009000	0.000450
Propane	0.010000	0.008000	0.006000	0.004000	0.002000	0.000100
Heavy HC	0.012000	0.009600	0.007200	0.004800	0.002400	0.000120
CO2	0.006000	0.204800	0.403600	0.602400	0.801200	0.990060
Nitrogen	0.077000	0.061600	0.046200	0.030800	0.015400	0.000770
TOTAL	**1.000000**	**1.000000**	**1.000000**	**1.000000**	**1.000000**	**1.000000**
PURE METHANE						
Methane	1.0000	0.8000	0.6000	0.4000	0.2000	0.0100
Carbon Dioxide	0.0000	0.2000	0.4000	0.6000	0.8000	0.9900
TOTAL	**1.0000**	**1.0000**	**1.0000**	**1.0000**	**1.0000**	**1.0000**
GAS MIX 1 COMPOSITION						
Methane	0.8500	0.6800	0.5100	0.3400	0.1700	0.0085
Ethane	0.0500	0.0400	0.0300	0.0200	0.0100	0.0005
Propane	0.0200	0.0160	0.0120	0.0080	0.0040	0.0002
Nitrogen	0.0800	0.0640	0.0480	0.0320	0.0160	0.0008
Carbon Dioxide	0.0000	0.2000	0.4000	0.6000	0.8000	0.9900
TOTAL	**1.0000**	**1.0000**	**1.0000**	**1.0000**	**1.0000**	**1.0000**
GAS MIX 2 COMPOSITION						
Methane	0.7000	0.5600	0.4200	0.2800	0.1400	0.0070
Ethane	0.2300	0.1840	0.1380	0.0920	0.0460	0.0023
Propane	0.0500	0.0400	0.0300	0.0200	0.0100	0.0005
Nitrogen	0.0200	0.0160	0.0120	0.0080	0.0040	0.0002
Carbon Dioxide	0.0000	0.2000	0.4000	0.6000	0.8000	0.9900
TOTAL	**1.0000**	**1.0000**	**1.0000**	**1.0000**	**1.0000**	**1.0000**
PURE CARBON DIOXIDE						
Carbon Dioxide	1.0000					
TOTAL	**1.0000**					

Table 6.4 Gas mixture compositions used in RefProp (Lemmon et al., 2013) and WebGasEOS (Reagan and Oldenburg, 2006) modelling of fluid properties.

Figure 6.12 shows the variability of the gas compressibility factor with the particular equation of state used for the gas compositions shown. As for the previous results for the Hewett Lower and Upper Bunter Sandstone reservoirs, in Chapters 4 and 5 respectively, the Peng-Robinson equation of state (Peng and Robinson, 1976) predicts a higher degree of gas compressibility at lower pressures than the GERG-2008 (Kunz and Wagner, 2012) and AGA8-DC92 Model (Starling and Savidge, 1992) equations of state. At higher pressures, the GERG-2008 equation of state (Kunz and Wagner, 2012) estimates a higher degree of gas compressibility, with the AGA8-DC92 Model (Starling and Savidge, 1992) tending towards the predicted trend of the GERG-2008 equation of state (Kunz and Wagner, 2012) but at a slightly lower degree of compressibility. Once again, when there is 1 mol% natural gas and 99 mol% CO_2 within the South Morecambe Sherwood Sandstone reservoir (i.e. in graphs (a) to (d) of Figure 6.12) the gas compressibility factor prediction of the AGA8-DC92 Model (Starling and Savidge, 1992) is largely similar to that of GERG-2008 equation of state (Kunz and Wagner, 2012), both with a large difference in estimated gas compressibility factor to that predicted by the Peng-Robinson equation of state (Peng and Robinson, 1976) at pressures ≥ 7 MPa.

Figure 6.12 (a) shows the likely gas compressibility factor in the South Morecambe Sherwood Sandstone reservoir as it is re-pressurised with CO_2. It can be observed that at a gas composition of 1 mol% South Morecambe Sherwood Sandstone initial gas and 99 mol% CO_2 it is only possible to predict fluid properties up to 7.8 MPa using the AGA8-DC92 Model. This is due to the compositional limitations of the AGA8-DC92 Model.

For all reservoir compositions between 0 and 80 mol% CO_2 there is a divergence in estimation of gas compressibility factor as pressure increases, with the Peng-Robinson equation of state (Peng and Robinson, 1976) predicting the highest degree of gas compressibility and in general the AGA8-DC92 equation of state (Starling and Savidge, 1992) predicting the lowest degree. At pressures between 8.5-11 MPa, gas compressibility factor estimations start to converge, and above these pressures begin to diverge once more.

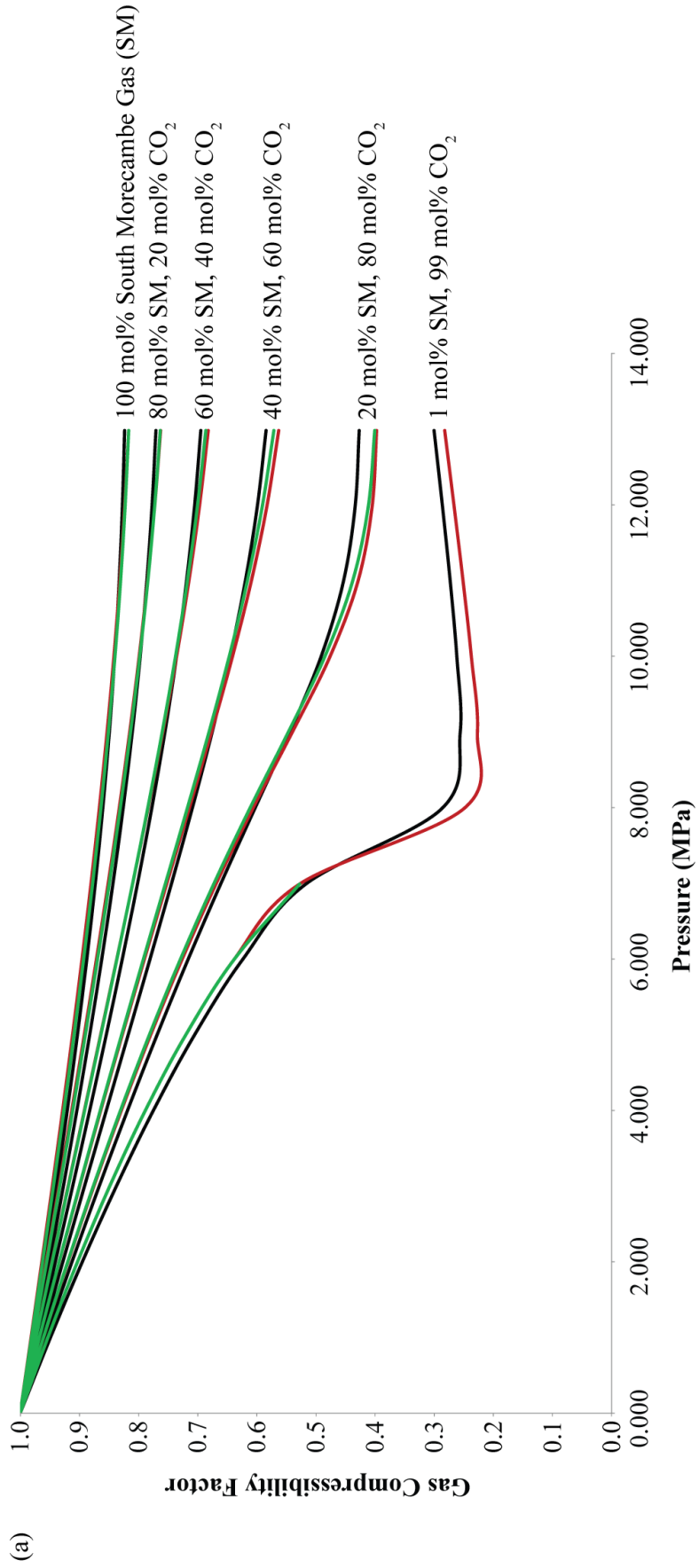
(a)
Gas Compressibility Factor
Pressure (MPa)
Peng-Robinson
GERG-2008
AGA8 Model
100 mol% South Morecambe Gas (SM)
80 mol% SM, 20 mol% CO2
60 mol% SM, 40 mol% CO2
40 mol% SM, 60 mol% CO2
20 mol% SM, 80 mol% CO2
1 mol% SM, 99 mol% CO2
1.0
0.9
0.8
0.7
0.6
0.5
0.4
0.3
0.2
0.1
0.0
0.000
2.000
4.000
6.000
8.000
10.000
12.000
14.000

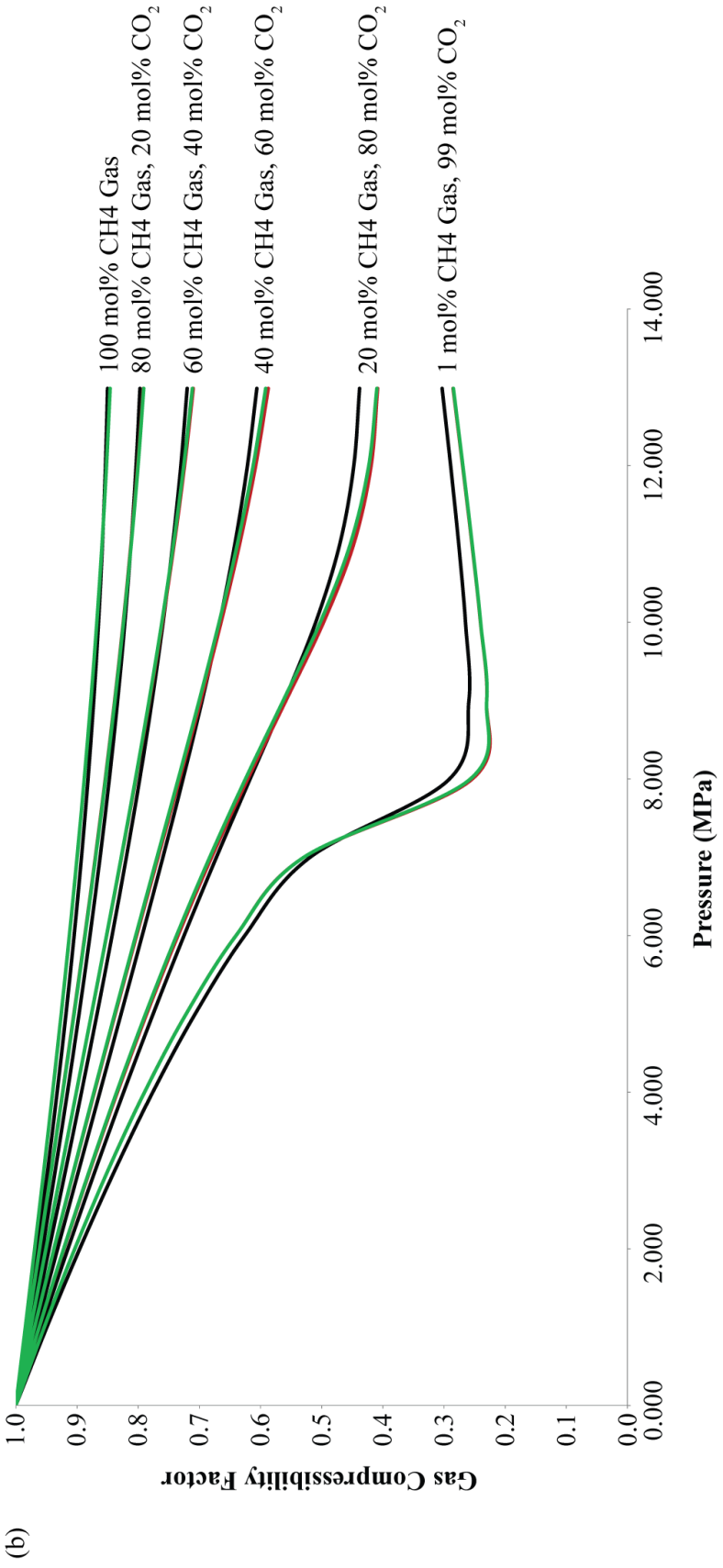
100 mol% CH4 Gas
80 mol% CH4 Gas, 20 mol% CO2
60 mol% CH4 Gas, 40 mol% CO2
40 mol% CH4 Gas, 60 mol% CO2
20 mol% CH4 Gas, 80 mol% CO2
1 mol% CH4 Gas, 99 mol% CO2
Gas Compressibility Factor
1.0
0.9
0.8
0.7
0.6
0.5
0.4
0.3
0.2
0.1
0.0
0.000
2.000
4.000
6.000
8.000
10.000
12.000
14.000
Pressure (MPa)

(b)

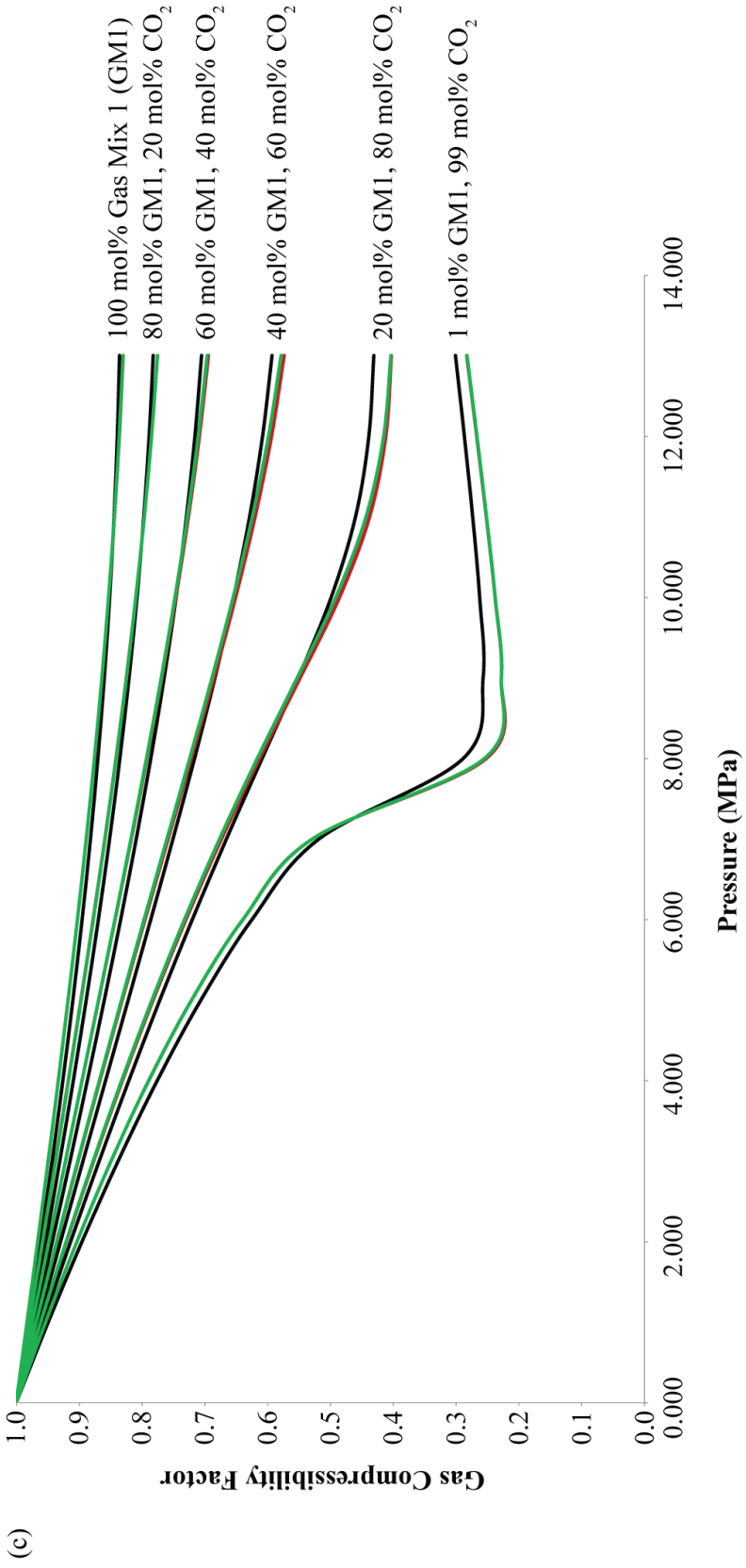
100 mol% Gas Mix 1 (GM1)
80 mol% GM1, 20 mol% CO2
60 mol% GM1, 40 mol% CO2
40 mol% GM1, 60 mol% CO2
20 mol% GM1, 80 mol% CO2
1 mol% GM1, 99 mol% CO2
Gas Compressibility Factor
Pressure (MPa)
1.0
0.9
0.8
0.7
0.6
0.5
0.4
0.3
0.2
0.1
0.0
0.000
2.000
4.000
6.000
8.000
10.000
12.000
14.000

(c)

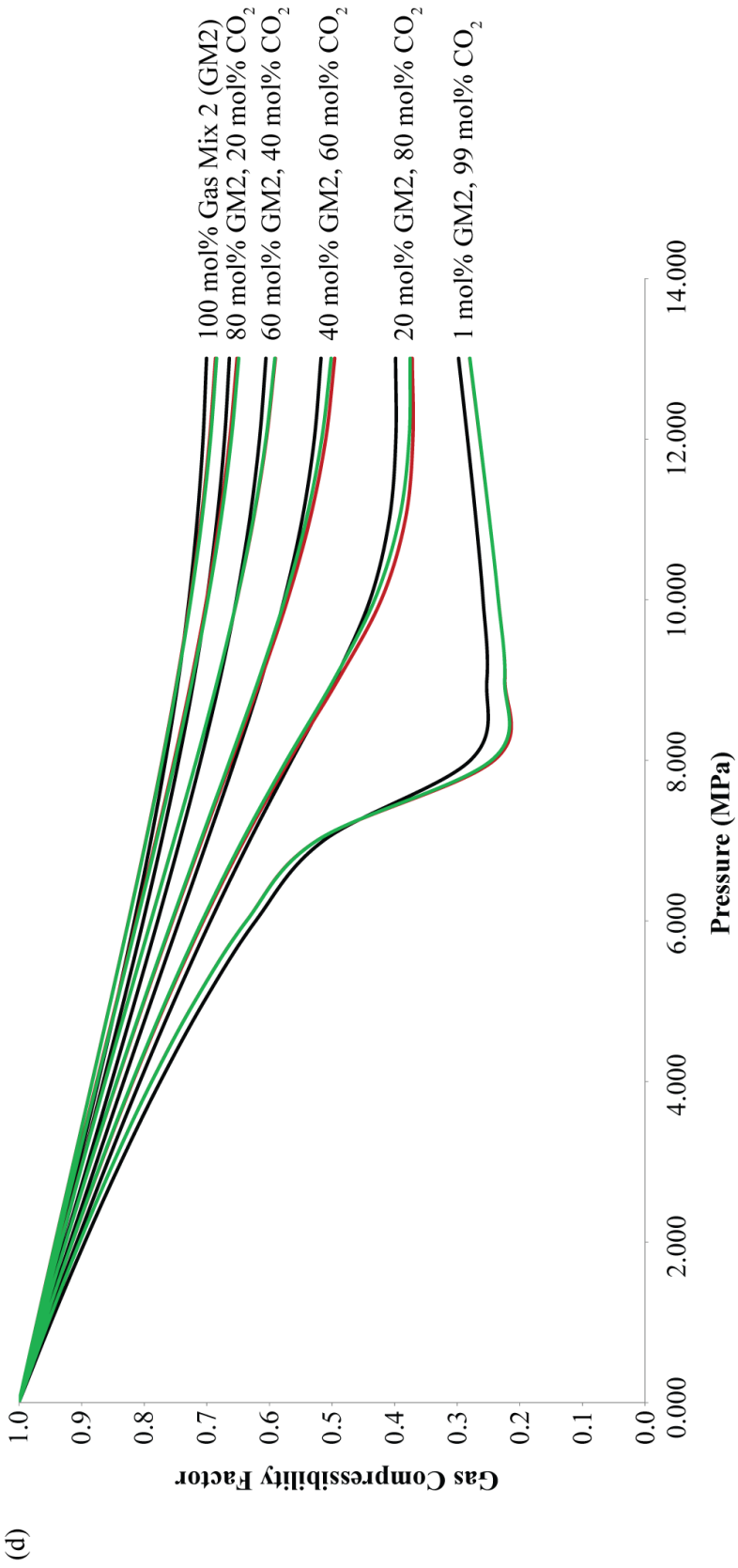
100 mol% Gas Mix 2 (GM2)
80 mol% GM2, 20 mol% CO2
60 mol% GM2, 40 mol% CO2
40 mol% GM2, 60 mol% CO2
20 mol% GM2, 80 mol% CO2
1 mol% GM2, 99 mol% CO2
Gas Compressibility Factor
1.0
0.9
0.8
0.7
0.6
0.5
0.4
0.3
0.2
0.1
0.0
0.000
2.000
4.000
6.000
8.000
10.000
12.000
14.000
Pressure (MPa)

(d)

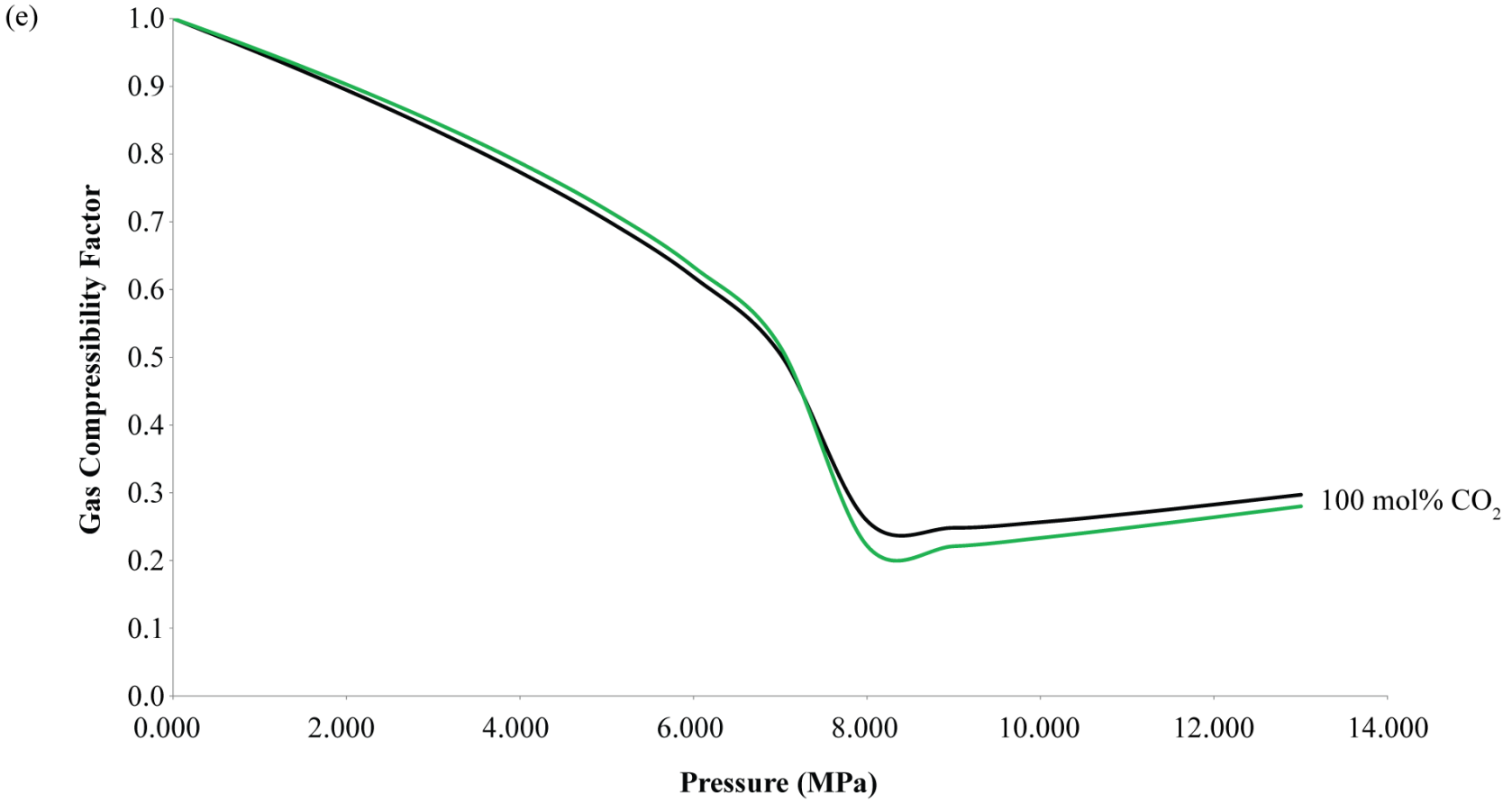

Figure 6.12 South Morecambe Sherwood Sandstone Reservoir Gas Compressibility Factor variation with pressure at constant temperature (32.8 °C) using the Peng-Robinson, GERG-2008 and AGA8 Model Equations of State and different gas compositions, modelled in RefProp (Lemmon et al., 2013). (a) South Morecambe Sherwood Sandstone Reservoir initial gas composition with increasing mol% CO_2; (b) Pure methane with increasing mol% CO_2; (c) Gas mix 1 (as defined in Table 6.4) with increasing mol% CO_2; (d) Gas mix 2 (as defined in Table 6.4) with increasing mol% CO_2; (e) Pure CO_2.

EQUATION OF STATE	PARAMETER	UNITS	SM INITIAL GAS COMPOSITION	PURE METHANE	GAS MIX 1	GAS MIX 2
Peng-Robinson	z_{iCO2}	Dimensionless	0.295	0.295	0.295	0.295
	z_{ihc}	Dimensionless	0.824	0.850	0.836	0.702
	z_{gas}	Dimensionless	0.857	0.879	0.867	0.760
	ρCO_2	kg/m^3	753.20	753.20	753.20	753.20
GERG-2008	z_{iCO2}	Dimensionless	0.277	0.277	0.277	0.277
	z_{ihc}	Dimensionless	0.818	0.847	0.831	0.689
	z_{gas}	Dimensionless	0.862	0.884	0.872	0.764
	ρCO_2	kg/m^3	800.31	800.31	800.31	800.31
AGA8 Model	z_{iCO2}	Dimensionless	0.277	0.277	0.277	0.277
	z_{ihc}	Dimensionless	0.818	0.847	0.831	0.689
	z_{gas}	Dimensionless	0.860	0.884	0.871	0.764
	ρCO_2	kg/m^3	800.34	800.34	800.34	800.34

Table 6.5 Summary of RefProp (Lemmon et al., 2013) estimated isoproperties for various equations of state.

6.4.2.1.2. WEBGASEOS ESTIMATIONS OF GAS COMPRESSIBILITY FACTOR

WebGasEOS (Reagan and Oldenburg, 2006) was used to estimate the gas compressibility factor of the gas mixtures (previously outlined in Table 6.4) using alternative equations of state including Peng-Robinson (Peng and Robinson, 1976), Peng-Robinson-Stryjek-Vera (Stryjek and Vera, 1986), Redlich-Kwong (Redlich and Kwong, 1949), and Soave-Redlich-Kwong (Soave, 1972). Once again, due to the limited number of species that can be included in the gas mixture analysis, and the lack of integral components to the South Morecambe Sherwood Sandstone reservoir gas composition, it was not possible to simulate results for this mixture. Species lacking in the WebGasEOS tool, but present in the South Morecambe Sherwood Sandstone reservoir gas composition include heavier hydrocarbons such as hexane. However, estimations of the gas compressibility factor were predicted for pure methane, gas mix 1, gas mix 2 and pure carbon dioxide fluids, making these results comparable with those of the previous chapters (4 and 5) and the results of the RefProp analysis of these fluids within the South Morecambe Sherwood Sandstone reservoir (this chapter).

Graphs of the results are shown in Figure 6.13 and a summary of the main isoproperties for input into the storage capacity estimation methodologies are displayed in Table 6.6.

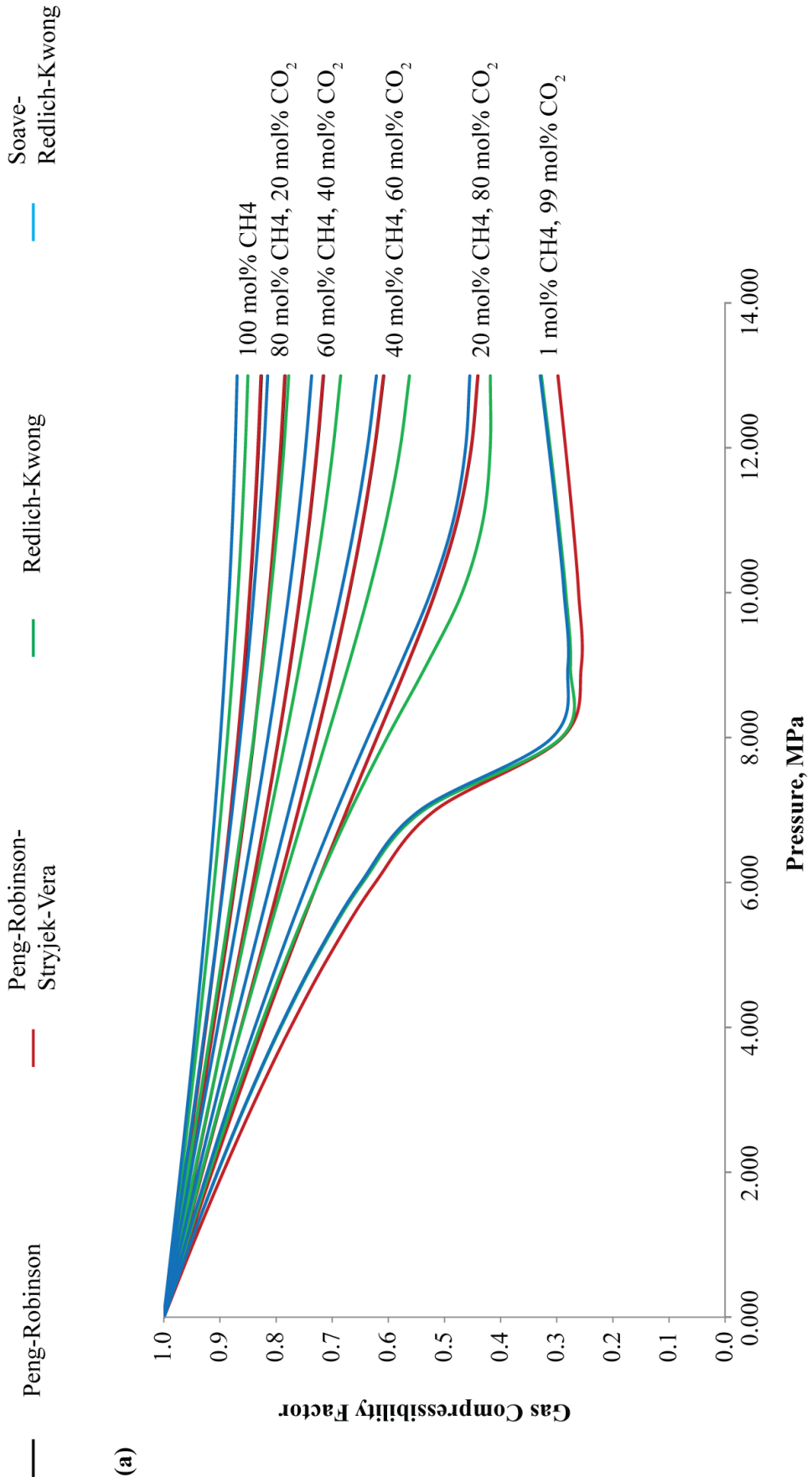
(a)
Peng-Robinson
Peng-Robinson-Stryjek-Vera
Redlich-Kwong
Soave-Redlich-Kwong
100 mol% CH4
80 mol% CH4, 20 mol% CO2
60 mol% CH4, 40 mol% CO2
40 mol% CH4, 60 mol% CO2
20 mol% CH4, 80 mol% CO2
1 mol% CH4, 99 mol% CO2
Gas Compressibility Factor
1.0
0.9
0.8
0.7
0.6
0.5
0.4
0.3
0.2
0.1
0.0
0.000
2.000
4.000
6.000
8.000
10.000
12.000
14.000
Pressure, MPa

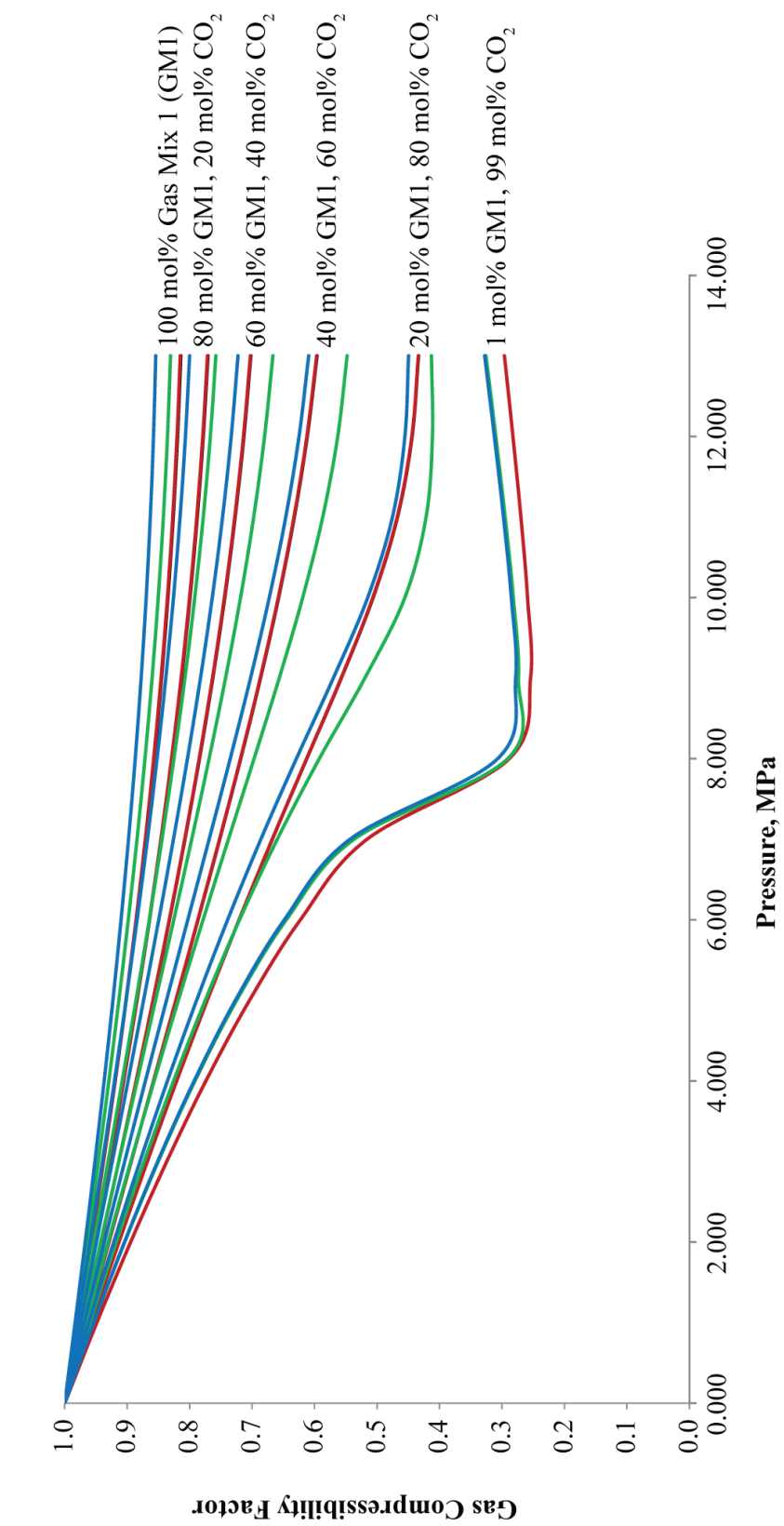
100 mol% Gas Mix 1 (GM1)
80 mol% GM1, 20 mol% CO2
60 mol% GM1, 40 mol% CO2
40 mol% GM1, 60 mol% CO2
20 mol% GM1, 80 mol% CO2
1 mol% GM1, 99 mol% CO2
Gas Compressibility Factor
1.0
0.9
0.8
0.7
0.6
0.5
0.4
0.3
0.2
0.1
0.0
0.000
2.000
4.000
6.000
8.000
10.000
12.000
14.000
Pressure, MPa

(b)

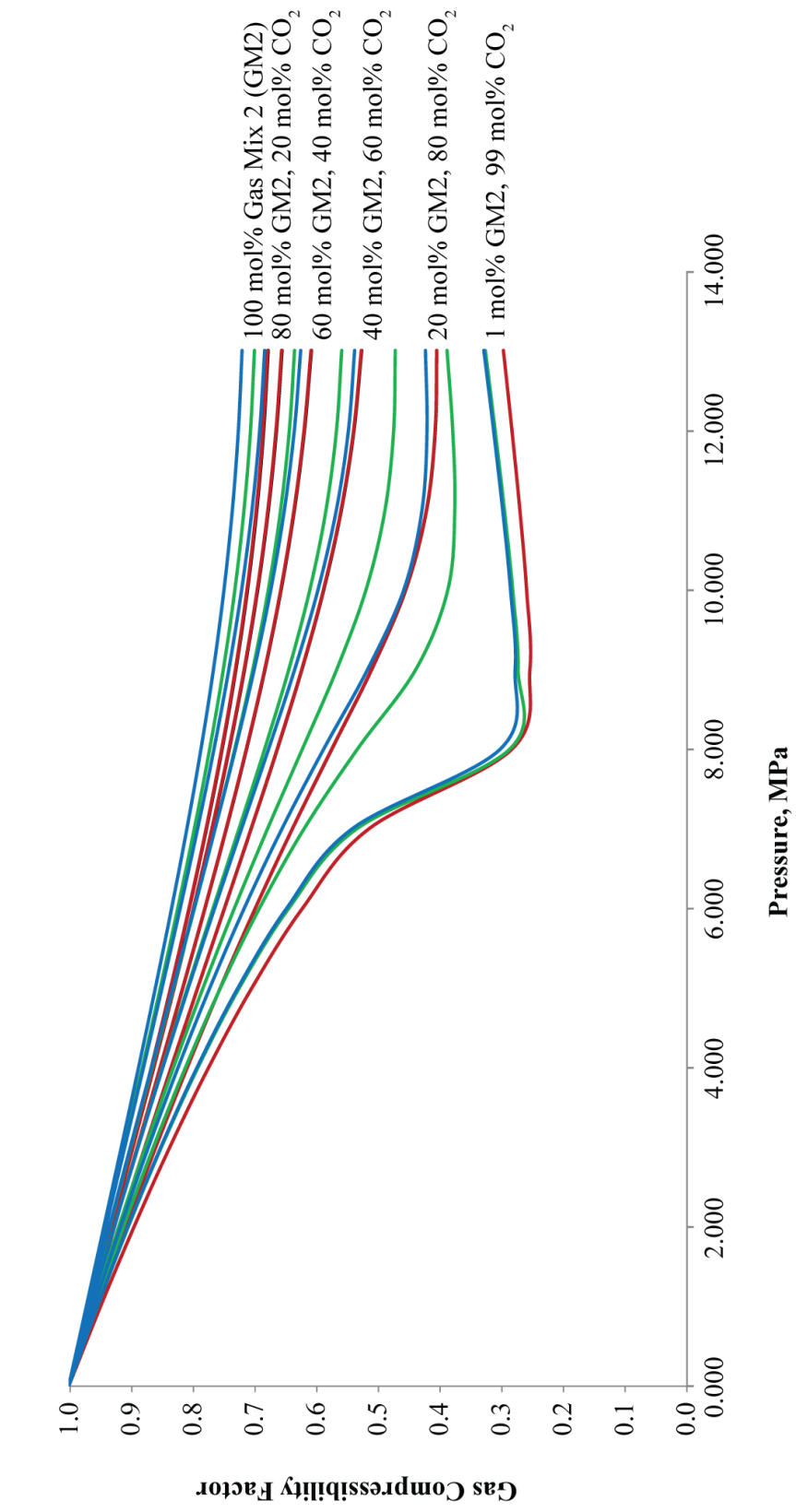
100 mol% Gas Mix 2 (GM2)
80 mol% GM2, 20 mol% CO2
60 mol% GM2, 40 mol% CO2
40 mol% GM2, 60 mol% CO2
20 mol% GM2, 80 mol% CO2
1 mol% GM2, 99 mol% CO2
Gas Compressibility Factor
1.0
0.9
0.8
0.7
0.6
0.5
0.4
0.3
0.2
0.1
0.0
0.000
2.000
4.000
6.000
8.000
10.000
12.000
14.000
Pressure, MPa

(c)

(d)

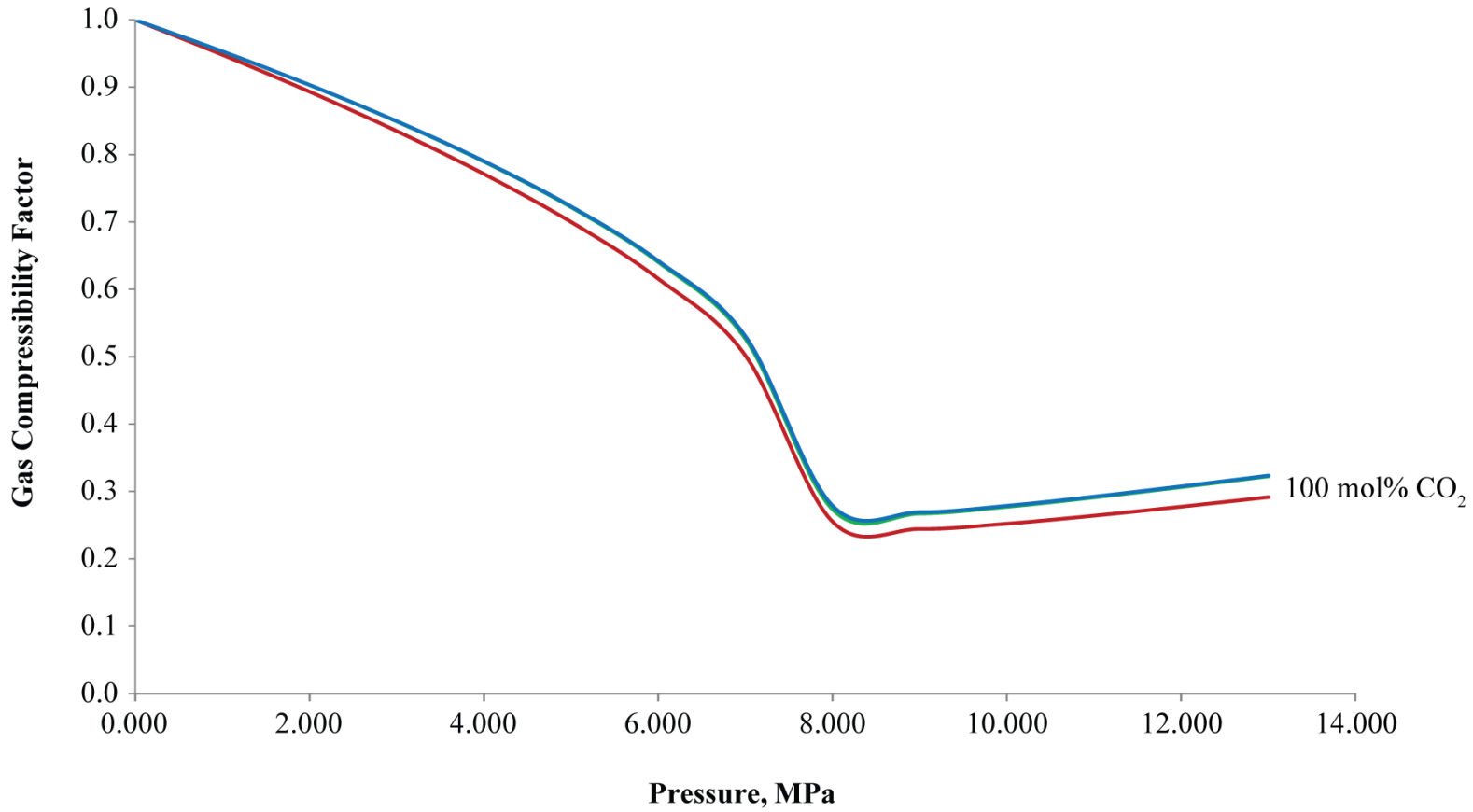

Figure 6.13 South Morecambe Sherwood Sandstone Reservoir Gas Compressibility Factor variation with pressure at constant temperature (32.8 °C) using the Peng-Robinson, Peng-Robinson-Stryjek-Vera, Redlich-Kwong and Soave-Redlich-Kwong Equations of State and different gas compositions, modelled in WebGasEOS (Reagan and Oldenburg, 2006). (a) Pure methane with increasing mol% CO_2; (b) Gas mix 1 (as defined in Table 6.4) with increasing mol% CO_2; (c) Gas mix 2 (as defined in Table 6.4) with increasing mol% CO_2; (d) Pure CO_2.

EQUATION OF STATE	PARAMETER	UNITS	PURE METHANE	GAS MIX 1	GAS MIX 2
Peng-Robinson	z_{iCO2}	Dimensionless	0.290	0.290	0.290
	z_{ihc}	Dimensionless	0.826	0.815	0.678
	z_{gas}	Dimensionless	0.863	0.853	0.744
	ρCO_2	kg/m^3	766.15	766.15	766.15
Peng-Robinson-Stryjek-Vera	z_{iCO2}	Dimensionless	0.290	0.290	0.290
	z_{ihc}	Dimensionless	0.827	0.816	0.679
	z_{gas}	Dimensionless	0.864	0.853	0.744
	ρCO_2	kg/m^3	766.17	766.17	766.17
Redlich-Kwong	z_{iCO2}	Dimensionless	0.320	0.320	0.320
	z_{ihc}	Dimensionless	0.850	0.831	0.700
	z_{gas}	Dimensionless	0.883	0.868	0.764
	ρCO_2	kg/m^3	693.13	693.13	693.13
Soave-Redlich-Kwong	z_{iCO2}	Dimensionless	0.321	0.321	0.321
	z_{ihc}	Dimensionless	0.869	0.855	0.720
	z_{gas}	Dimensionless	0.896	0.884	0.779
	ρCO_2	kg/m^3	690.78	690.78	690.78

Table 6.6 Summary of WebGasEOS Estimated Isoproperties for various Equations of State.

Figure 6.13 once again shows the variability of the gas compressibility factor with the particular equation of state used, as estimated in WebGasEOS (Reagan and Oldenburg, 2006) for the gas compositions shown in Table 6.4, excluding the South Morecambe Sherwood Sandstone reservoir initial gas composition. Equations of state used for modelling include Peng Robinson (Peng and Robinson, 1976), Peng-Robinson-Stryjek-Vera (Stryjek and Vera, 1986), Redlich-Kwong (Redlich and Kwong, 1949) and Soave-Redlich-Kwong (Soave, 1972).

As for the Hewett Lower and Upper Bunter Sandstone reservoirs (Chapters 4 and 5, respectively), the Soave-Redlich-Kwong equation of state (Soave, 1972) always predicts a much lower gas compressibility than the other equations of state within WebGasEOS. The Redlich-Kwong equation of state (Redlich and Kwong, 1949) predicts a low, but higher compressibility than that of the Soave-Redlich-Kwong equation of state (Soave, 1972) when there is no CO_2 present in the gas composition. However, at a CO_2 mol% of 20 and above, the Redlich-Kwong equation of state (Redlich and Kwong, 1949) predicts the highest gas compressibilities out of all the equations of state modelled in WebGasEOS. At 99 mol% CO_2, the Redlich-Kwong equation of state (Redlich and Kwong, 1949) predicts gas compressibilities very similar to those predicted by the Soave-Redlich-Kwong equation of state (Soave, 1972).

The Peng-Robinson (Peng and Robinson, 1976) and Peng-Robinson-Stryjek-Vera (Stryjek and Vera, 1986) equations of state produce extremely similar predictions of gas compressibility factor throughout. When there is no CO_2 present in the gas composition, the two equations of state predict gas compressibility factors greater than those predicted by the Redlich-Kwong (Redlich and Kwong, 1949) and Soave-Redlich-Kwong (Soave, 1972) equations of state. Between 20 and 80 mol% natural gas (80-20 mol% CO_2) the Peng-Robinson (Peng and Robinson, 1976) and Peng-Robinson-Stryjek-Vera (Stryjek and Vera, 1986) equations of state predict gas compressibility factors between the limits predicted by the Redlich-Kwong (Redlich and Kwong, 1949) and Soave-Redlich-Kwong (Soave, 1972) equations of state. However, when there is 99 mol% CO_2 within the gas composition, the Peng-Robinson (Peng and Robinson, 1976) and Peng-Robinson-

Stryjek-Vera (Stryjek and Vera, 1986) equations of state predict gas compressibility factors greater than those predicted using the Redlich-Kwong (Redlich and Kwong, 1949) and Soave-Redlich-Kwong (Soave, 1972) equations of state.

6.4.2.2. GAS FORMATION VOLUME FACTOR ESTIMATION

The gas formation volume factor has been calculated within the South Morecambe Sherwood Sandstone reservoir throughout its productive lifetime using the equations defined in Chapter 4 (see Table 6.7).

GAS FORMATION VOLUME FACTOR EQUATION	EQUATION NUMBER
$B_g = \frac{reservoir\ volume}{standard\ condition\ volume}$	(4.2)
$B_g = \frac{P_{sc}}{T_{sc}} \times T_{res} \times \frac{z_{res}}{P_{res}}$	(4.3)

Table 6.7 Methods of gas formation volume factors as previously defined in Chapter 4. After Archer and Wall (1986).

The results of the two methods have been plotted and can be compared to the industry calculated Z-factor provided by Centrica, and resulting estimated gas formation volume factors. The results have been estimated under the initial reservoir temperature condition of 305.928 K, whilst varying pressure. The results are shown in Figure 6.14.

As can be seen from Figure 6.14, the difference between the results of the two methods and the various equations of state are negligible. This implies that estimates of the gas formation volume factor are very well constrained within the South Morecambe Sherwood Sandstone reservoir, and can be treated with confidence when used within CO_2 storage capacity calculations.

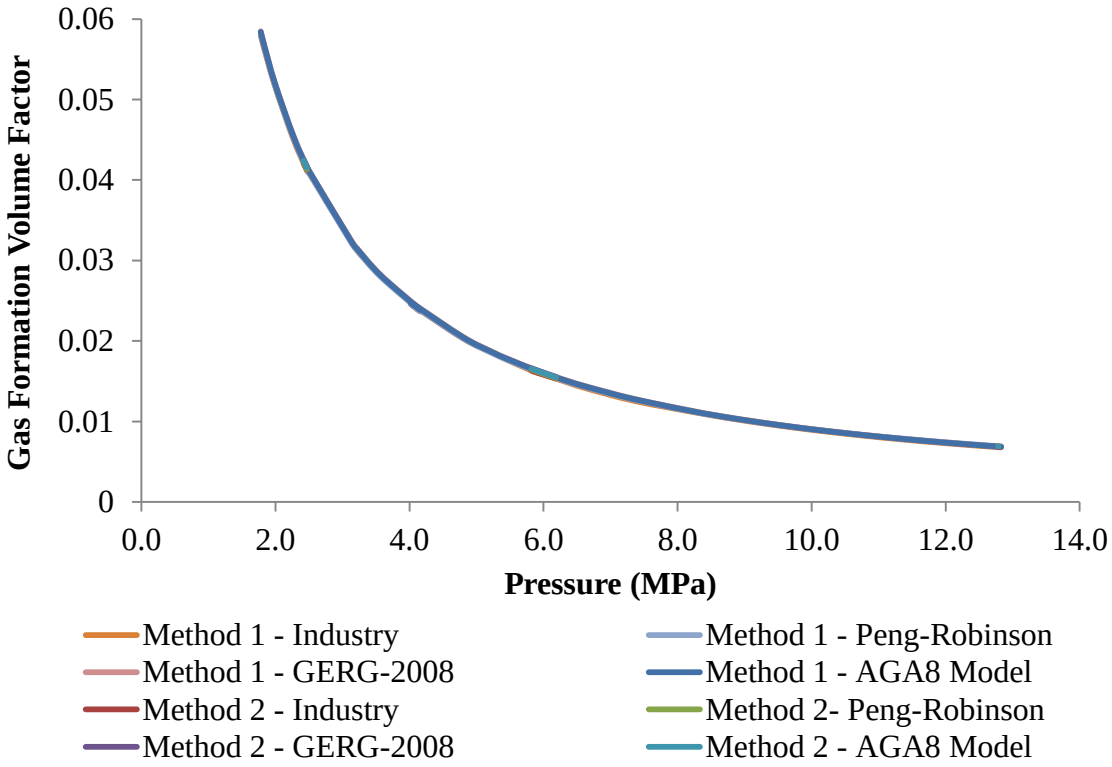

Figure 6.14 Estimation of the gas formation volume factor within the South Morecambe Sherwood Sandstone reservoir using two main methods of calculation and a variety of equations of state, under initial reservoir temperature conditions of 305.928 K. The gas compressibility factor, necessary for calculation of the gas formation volume factor (B_g) was estimated using RefProp (Lemmon et al., 2013). Three equations of state were used: Peng-Robinson (Peng and Robinson, 1976), GERG-2008 (Kunz and Wagner, 2012), and the AGA8-DC92 Model (Starling and Savidge, 1992). These values were compared back to industry calculated values.

6.4.2.3. ESTIMATION OF CO_2 DENSITY

CO_2 density has been estimated within RefProp (Lemmon et al., 2013) using three equations of state: Peng-Robinson (Peng and Robinson, 1976), GERG-2008 (Kunz and Wagner, 2012), and the AGA8-DC92 Model (Starling and Savidge, 1992). The results were estimated under the initial reservoir temperature conditions of 305.928 K, whilst varying pressure. The results are shown in Figure 6.15.

The results show that CO_2 density increases with pressure. The GERG-2008 (Kunz and Wagner, 2012) and AGA8-DC92 (Starling and Savidge, 1992) equations of state predict very similar CO_2 densities throughout the pressure range shown.

The Peng-Robinson equation of state (Peng and Robinson, 1976) predicts very similar CO_2 densities at low pressure, however, above 7.7 MPa, the trend diverges from that of the GERG-2008 (Kunz and Wagner, 2012) and AGA8-DC92 (Starling and Savidge, 1992) equations of state, and predicted CO_2 densities are lower.

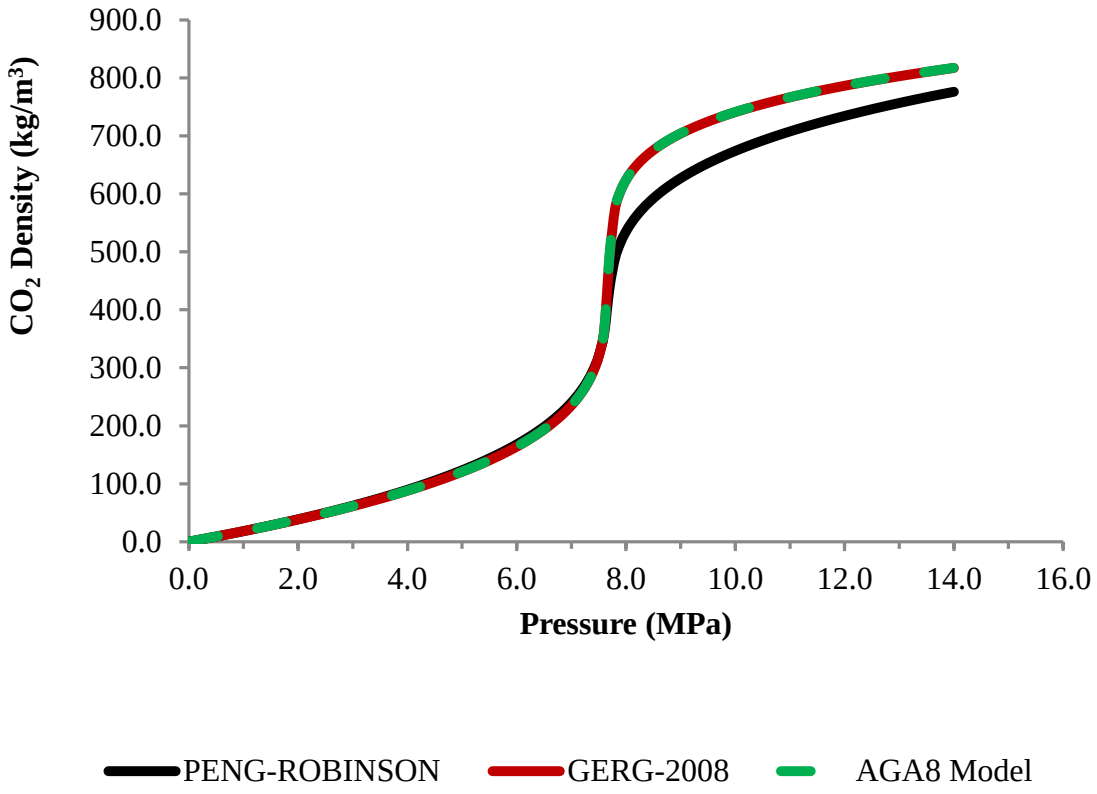

Figure 6.15 Estimations of CO_2 density with pressure within the South Morecambe Sherwood Sandstone reservoir under initial reservoir temperature conditions of 305.928 K. Results have been estimated using RefProp (Lemmon et al., 2013) and various equations of state: Peng-Robinson (Peng and Robinson, 1976), GERG-2008 (Kunz and Wagner, 2012), and the AGA8-DC92 Model (Starling and Savidge, 1992).

6.4.2.4. STORAGE CAPACITY ESTIMATION RESULTS

The estimates of the parameters outlined above, including gas compressibility factor, CO_2 density and gas formation volume factor, for the individual gas compositions were used to calculate both theoretical and effective CO_2 storage capacities of the South Morecambe Sherwood Sandstone reservoir using various published methods.

6.4.2.4.1. THEORETICAL CO_2 STORAGE CAPACITY ESTIMATES

Theoretical CO_2 storage capacity (previously defined in Chapter 1) was estimated for the South Morecambe Sherwood Sandstone reservoir using methods provided by Bachu et al. (2007), Holloway et al. (2006), and Tseng et al. (2012).

The South Morecambe Sherwood Sandstone reservoir has produced over 139.577 billion cubic metres of natural gas over its entire productive lifetime, equating to a mass of 111.8 Mt South Morecambe Sherwood Sandstone reservoir gas at standard conditions.

As in Chapters 4 and 5, for the Hewett Lower and Upper Bunter Sandstone reservoirs respectively, the geometric-based approach of Bachu et al. (2007), Table 6.8, equation 1.1, requires the use of parameters that have natural variability within a sandstone reservoir, such as porosity and reservoir height. As such, Monte Carlo simulation has been used to reduce the risk of storage capacity estimates produced using this method.

Porosity data was taken from well data made available to Durham University by IHS and assigned a best-fit probability distribution within Oracle Crystal Ball software (Figure 6.6). The best-fit probability distribution for the entire reservoir was a lognormal distribution, for the illite free zone, a lognormal distribution and for the illite affected zone, a logistic distribution. Reservoir height was assigned a uniform distribution due to limited data from wells, i.e. there is an equal chance of obtaining a value for reservoir height between 570.59 and 1469.14 m for the entire reservoir, 182.88 and 563.88 m for the illite free zone and 387.71 and 646.18 m for the illite affected zone. It was not possible to observe the variation of reservoir area as there was no data for this, therefore a standard value of 83769928 m^2 (83.770 km^2) was used for the South Morecambe Sherwood Sandstone reservoir, taken from Bastin et al. (2003).

Monte Carlo simulation then produced the results (probability distributions) illustrated in Figure 6.16 for the entire South Morecambe Sherwood Sandstone reservoir, Figure 6.17 for the illite free zone, and Figure 6.18 for the illite affected zone. Alongside the simulated forecast values in Table 6.9, Table 6.10 and Table 6.11 for the entire South Morecambe Sherwood Sandstone reservoir, illite free zone

and illite affected zone, respectively, the results illustrate the vast amount of variability in CO_2 storage capacity estimation. The average range between minimum and maximum storage capacity estimates for the entire South Morecambe Sherwood Sandstone reservoir is 11360.92 Mt CO_2, the illite free zone, 5094.79 Mt CO_2, and the illite affected zone, 5859.17 Mt CO_2. As such, the mean CO_2 storage capacity values have been plotted alone in Figure 6.19 for the entire South Morecambe Sherwood Sandstone reservoir, Figure 6.20 for the illite free zone, and Figure 6.21 for the illite affected zone. Error bars on the three figures show the minimum, maximum, P10 and P90 values, i.e. the extent of variance. The minimum, P10, P50 (median), mean, P90 and maximum values for the probability distributions are shown in Table 6.9 for the entire South Morecambe Sherwood Sandstone reservoir, Table 6.10 for the illite free zone and Table 6.11 for the illite affected zone.

A sensitivity plot of the method of (Bachu et al., 2007), Table 6.8, equation 1.1, shows that the theoretical CO_2 storage capacity results are most sensitive to porosity followed by reservoir height within the entire South Morecambe Sherwood Sandstone reservoir, the illite free zone and the illite affected zone (see Figure 6.22).

Theoretical CO_2 storage capacity results by Bachu et al. (2007), Table 6.8, equation 1.1 and 1.2; Holloway et al. (2006), Table 6.8, equation 1.3; and Tseng et al. (2012), Table 6.8, equation 1.4, are based upon the principle that a variable proportion of the pore space occupied by the recoverable reserves will be available for CO_2 storage. The parameters required within the methods are reasonably well constrained values which show little or no variability.

The final results of all the theoretical storage capacity estimation methods are displayed in Figure 6.23 and Table 6.12. Mean values of the probability distributions for the entire South Morecambe Sherwood Sandstone reservoir are plotted on Figure 6.23 and stated in Table 6.12 to represent CO_2 storage capacity estimates of the method of Bachu et al. (2007), Table 6.8, equation 1.1. The theoretical storage capacity estimates for the South Morecambe Sherwood Sandstone initial reservoir composition are comparable using the methods of Tseng et al. (2012), Table 6.8, equation 1.4, and Bachu et al. (2007), Table 6.8, equation

1.2, ranging between 312 and 329 Mt CO_2 depending on the equation of state used. Theoretical storage capacity estimates using the method of Holloway et al. (2006), Table 6.8, equation 1.3, are higher ranging between 764 and 811 Mt CO_2 depending on the equation of state used. However, the highest estimates of theoretical storage capacity within the South Morecambe Sherwood Sandstone reservoir are achieved using the method of Bachu et al. (2007), Table 6.8, equation 1.1, with mean results for the entire reservoir ranging between 2530 and 2690 Mt CO_2 depending on the equation of state used.

Again, the GERG-2008 equation of state (Kunz and Wagner, 2012) always predicts the highest estimate of theoretical CO_2 storage capacity, closely followed by the AGA8-DC92 Model (Starling and Savidge, 1992). When compared to the results of the Peng-Robinson equation of state (Peng and Robinson, 1976) estimated using RefProp (Lemmon et al., 2013), the results predicted using the GERG-2008 equation of state (Kunz and Wagner, 2012) are ~4.6% greater (see Table 6.12). The Soave-Redlich-Kwong equation of state (Soave, 1972) always predicts the lowest estimate of theoretical CO_2 storage capacity. When compared to the results of the Peng-Robinson equation of state (Peng and Robinson, 1976) estimated using RefProp (Lemmon et al., 2013), the results predicted using the Soave-Redlich-Kwong equation of state (Soave, 1972) are ~7.3% lower (see Table 6.12).

STORAGE CAPACITY EQUATION	AUTHOR	EQUATION NUMBER
$M_{CO_2t} = \rho_{CO_2r}\left[R_f Ah\varphi(1 - S_w) - V_{iw} + V_{pw}\right]$	Bachu et al. (2007)	(1.1)
$M_{CO_2t} = \rho_{CO_2r} R_f (1 - F_{IG}) OGIP \left[\frac{(P_s Z_r T_r)}{(P_r Z_s T_s)}\right]$	Bachu et al. (2007)	(1.2)
$M_{CO_2t} = \left(\frac{V_{GAS}[stp]}{B_{igas}} . \rho_{CO_2r}\right)$	Holloway et al. (2006)	(1.3)
$M_{CO_2t} = \frac{\rho_{CO_2r}(G_{phc} . B_{gas})}{B_{iCO_2}} = \frac{\rho_{CO_2r}(G_{phc} . z_{gas})}{z_{iCO_2}}$	Tseng et al. (2012)	(1.4)
$M_{CO_2e} = C_m C_b C_h C_w C_a M_{CO_2t} \equiv C_e M_{CO_2t}$	Bachu et al. (2007)	(1.5)
$M_{injCO2} = \rho_{CO2r} . G_{injCO2}$	Tseng et al. (2012)	(1.6)
$G_{injCO2} = G_{phc} - G_{ihc} + \frac{P_{reshc/CO2}}{z_{reshc/CO2}}\left(\frac{z_{ihc}}{P_{ihc}} G_{ihc} - W_e \frac{T_{sc}}{P_{sc} T}\right)$	Tseng et al. (2012)	(1.7)

Table 6.8 Storage Capacity Equations previously introduced in Chapter 1. See Chapter 1 for definition of symbols

RefProp, Peng-Robinson Equation of State

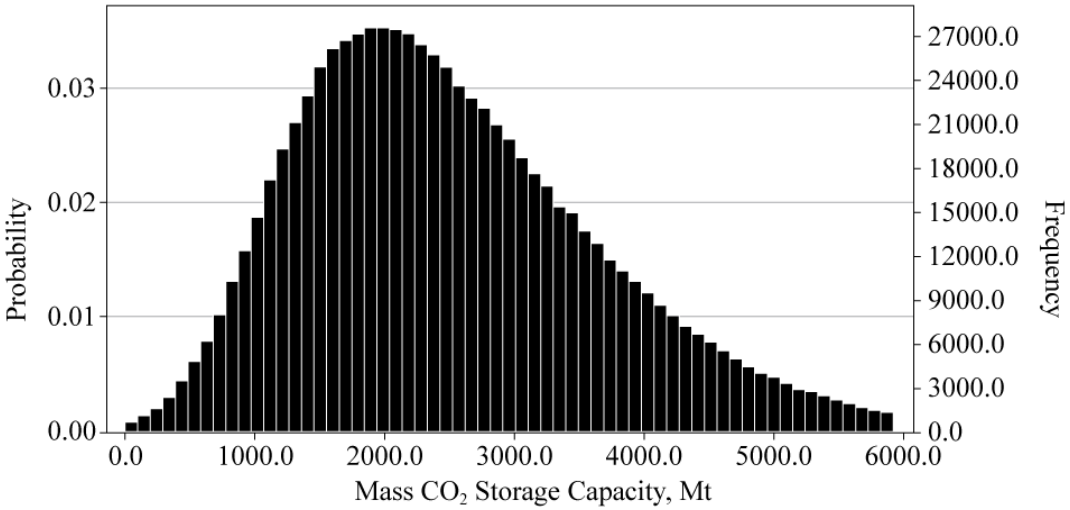

RefProp, GERG-2008 Equation of State

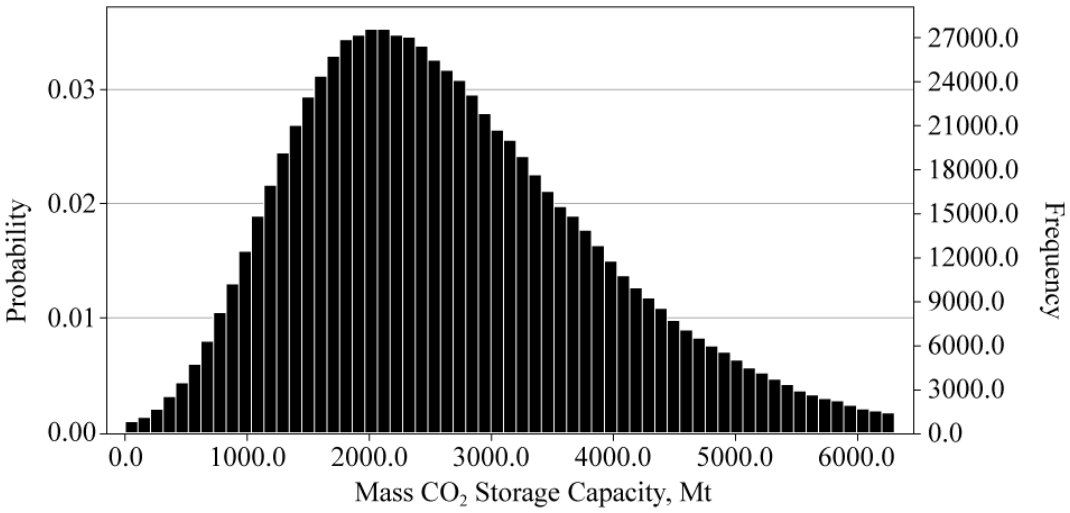

RefProp, AGA8-DC92 Equation of State

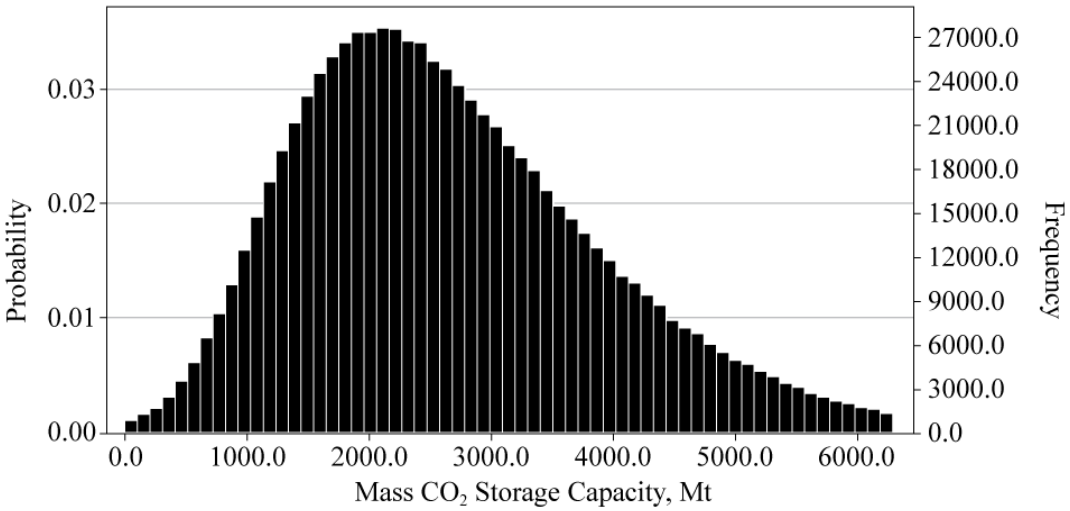

WebGasEOS, Peng-Robinson Equation of State

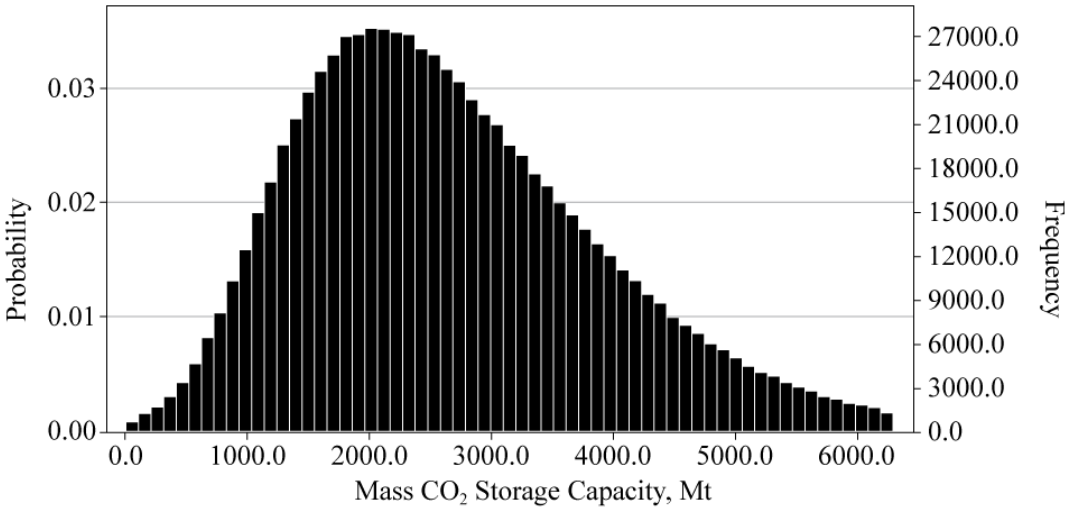

WebGasEOS, Peng-Robinson-Stryjek-Vera Equation of State

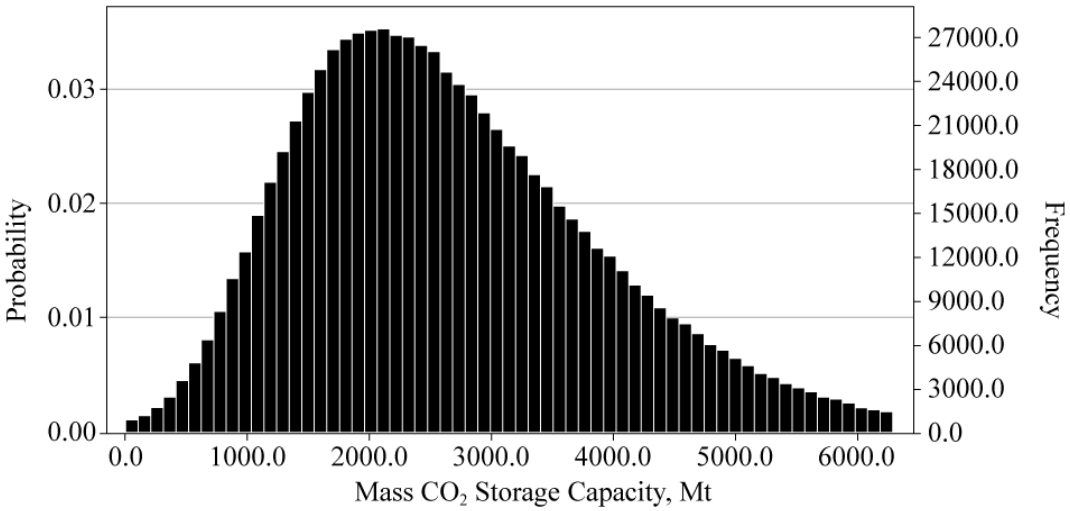

WebGasEOS, Redlich-Kwong Equation of State

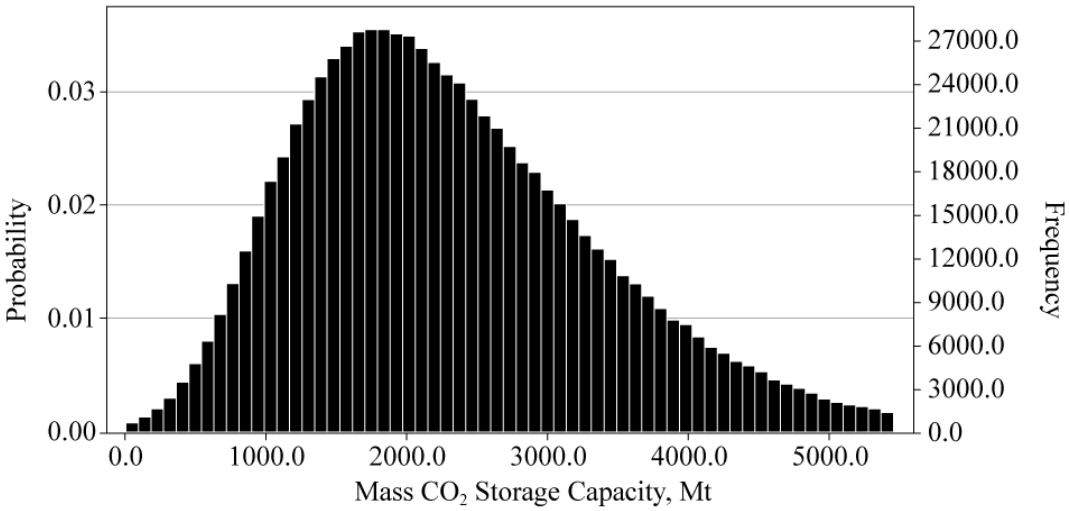

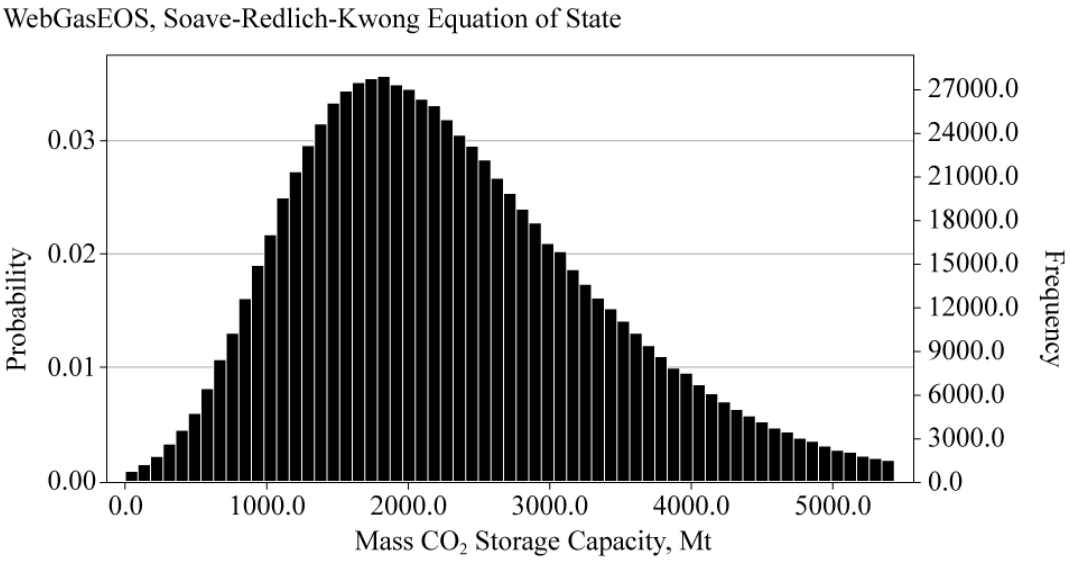

Figure 6.16 Monte Carlo Simulation probability distribution results of mass CO_2 storage capacity within the entire South Morecambe Sherwood Sandstone reservoir using the method of Bachu et al. (2007) Table 6.8, equation 1.1, and varying the equation of state used. Results computed using Oracle Crystal Ball software.

RefProp, Peng-Robinson Equation of State

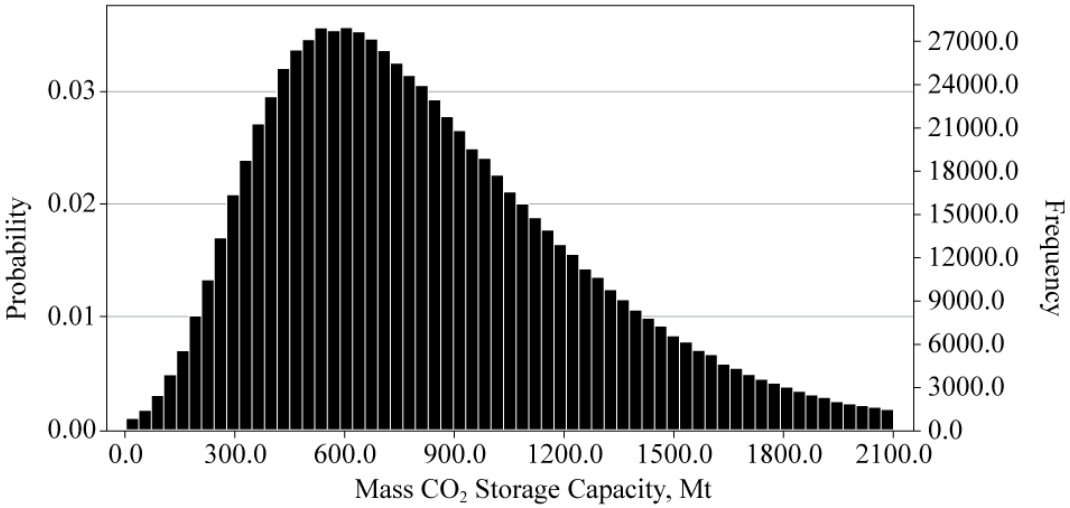

RefProp, GERG-2008 Equation of State

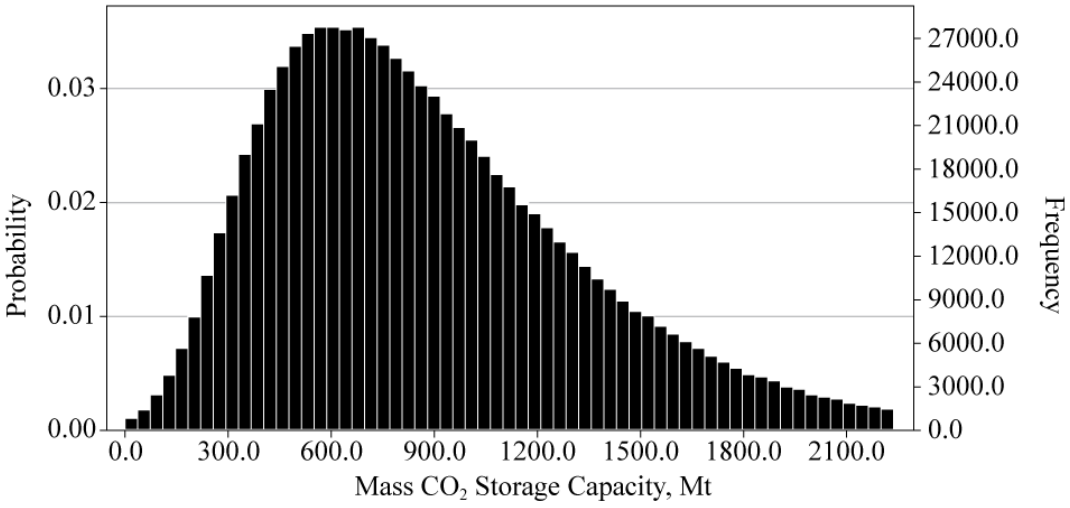

RefProp, AGA8-DC92 Equation of State

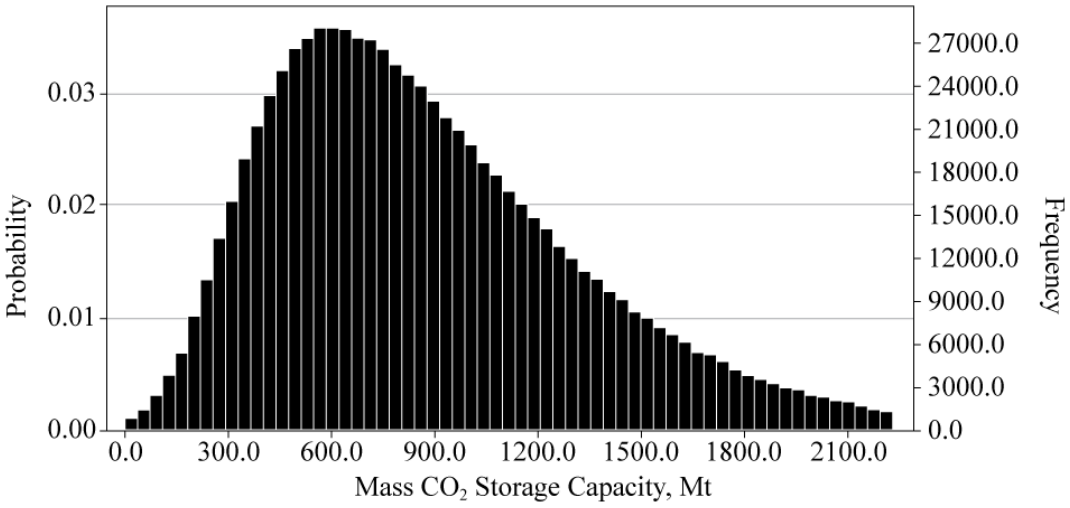

WebGasEOS, Peng-Robinson Equation of State

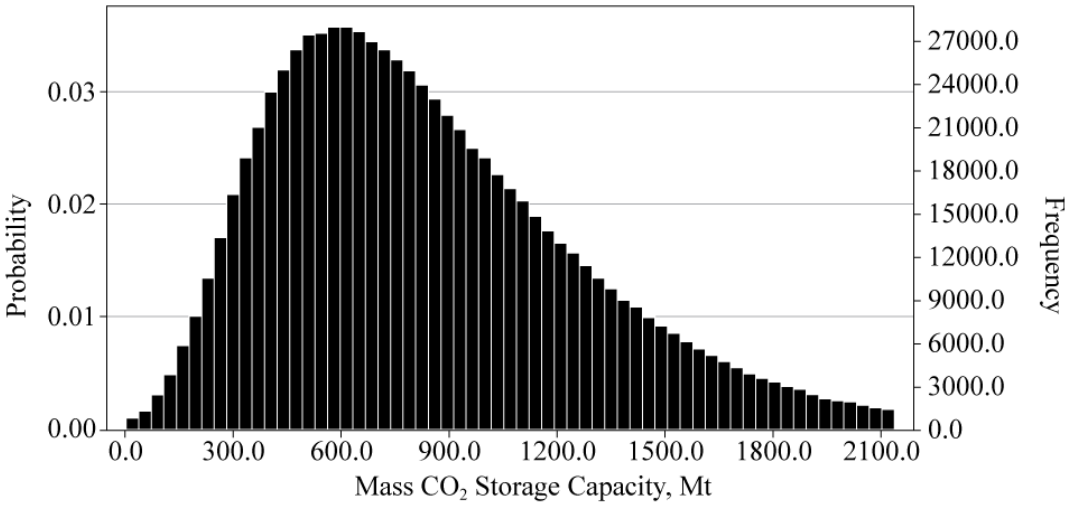

WebGasEOS, Peng-Robinson-Stryjek-Vera Equation of State

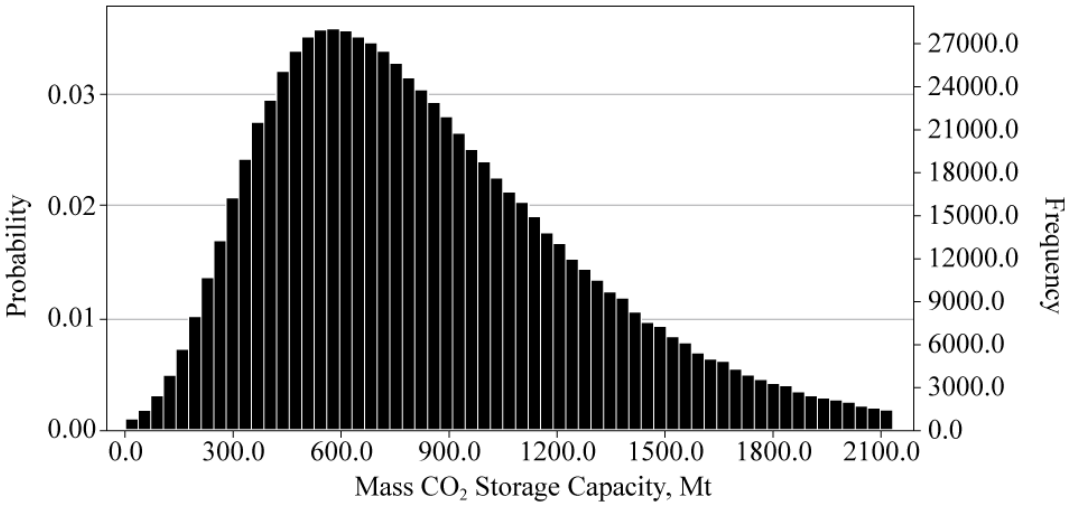

WebGasEOS, Redlich-Kwong Equation of State

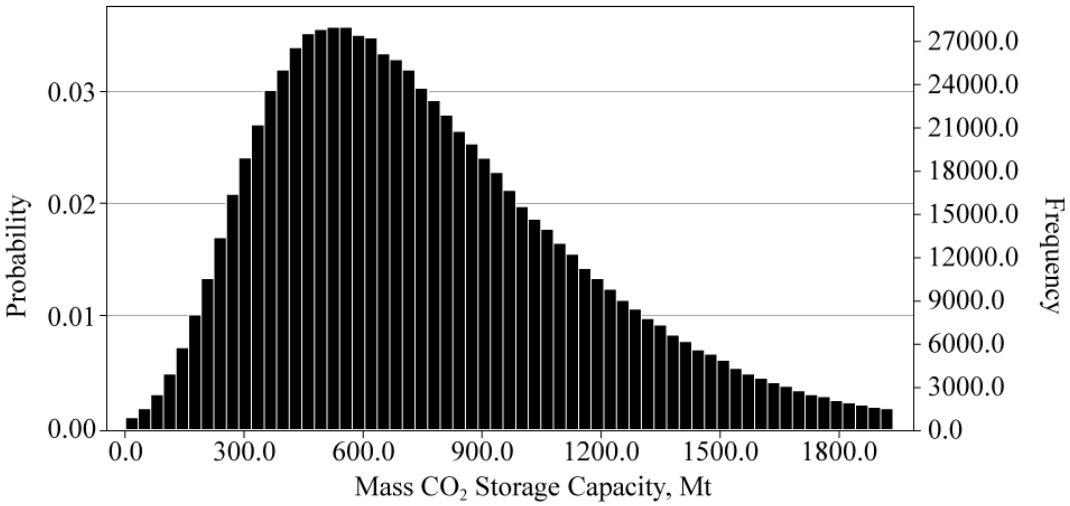

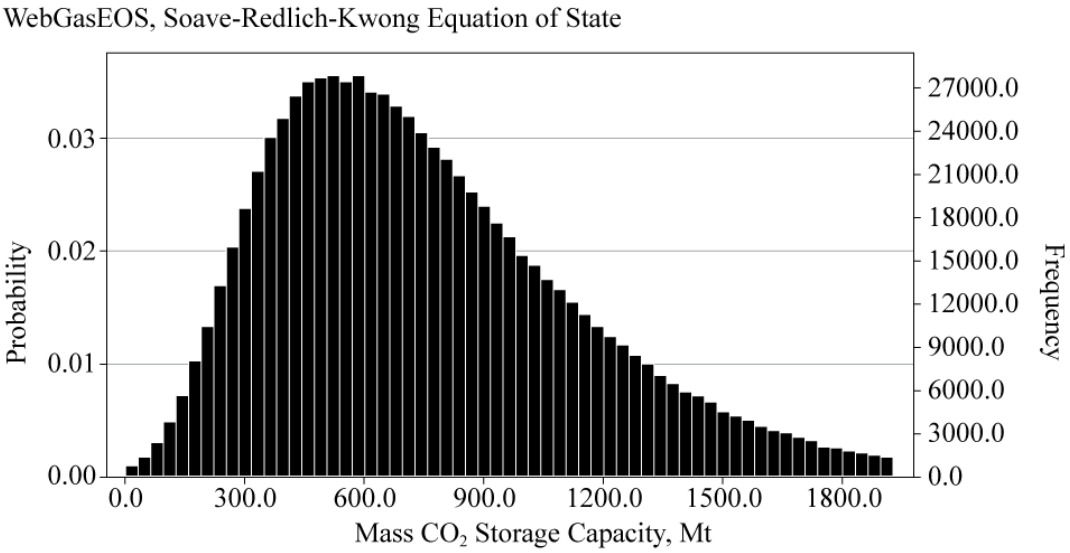

Figure 6.17 Monte Carlo Simulation probability distribution results of mass CO_2 storage capacity within the illite free zone of the South Morecambe Sherwood Sandstone reservoir using the method of Bachu et al. (2007) Table 6.8, equation 1.1, and varying the equation of state used. Results computed using Oracle Crystal Ball software.

RefProp, Peng-Robinson Equation of State

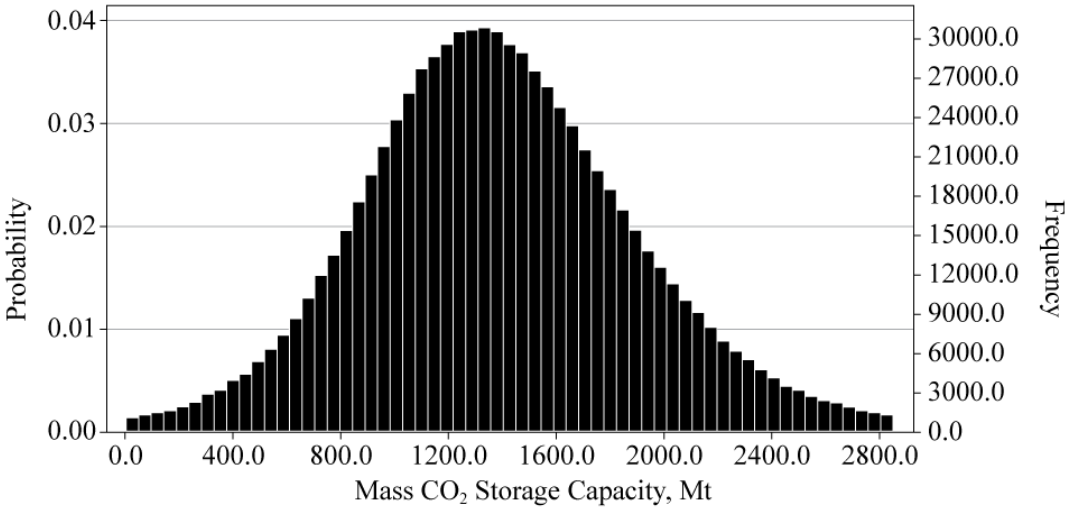

RefProp, GERG-2008 Equation of State

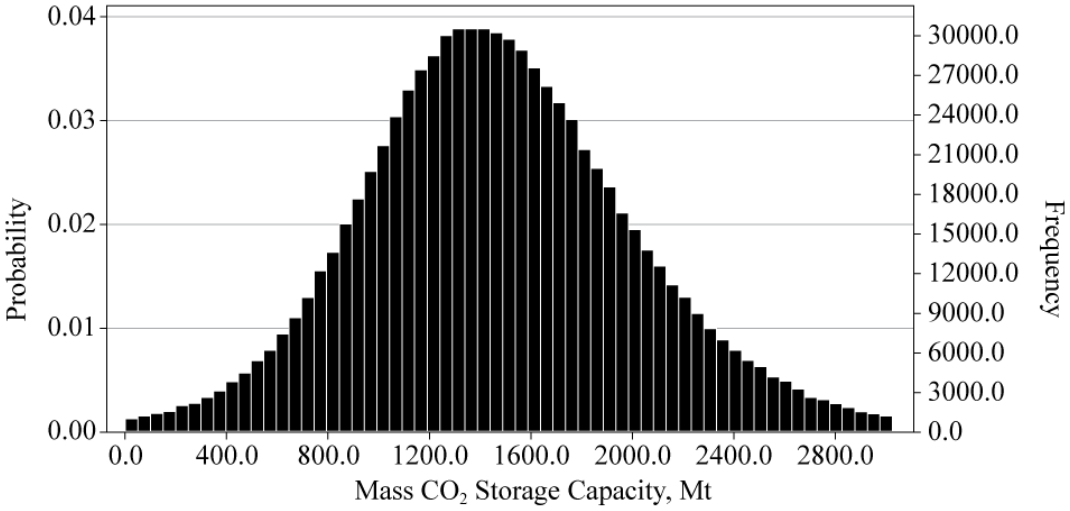

RefProp, AGA8-DC92 Equation of State

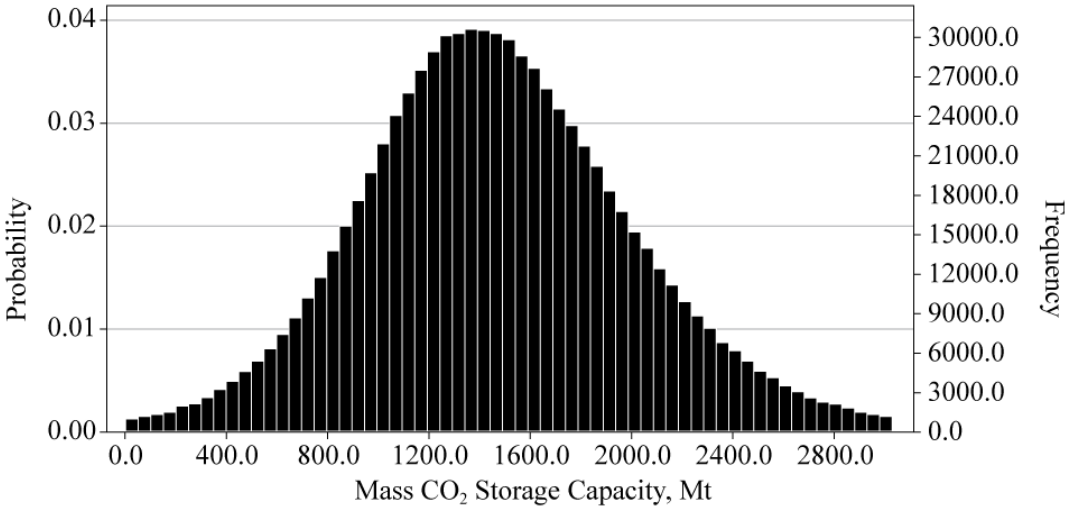

WebGasEOS, Peng-Robinson Equation of State

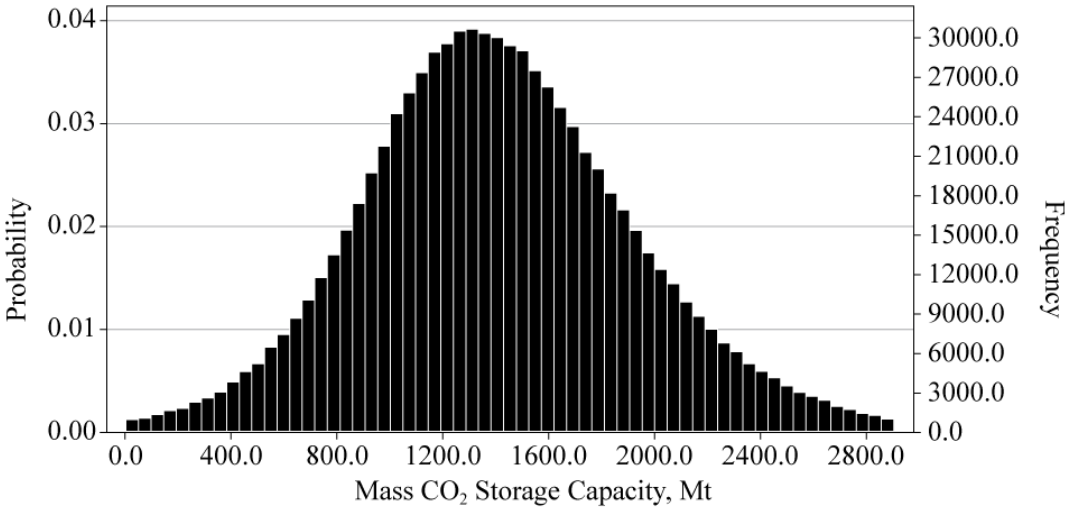

WebGasEOS, Peng-Robinson-Stryjek-Vera Equation of State

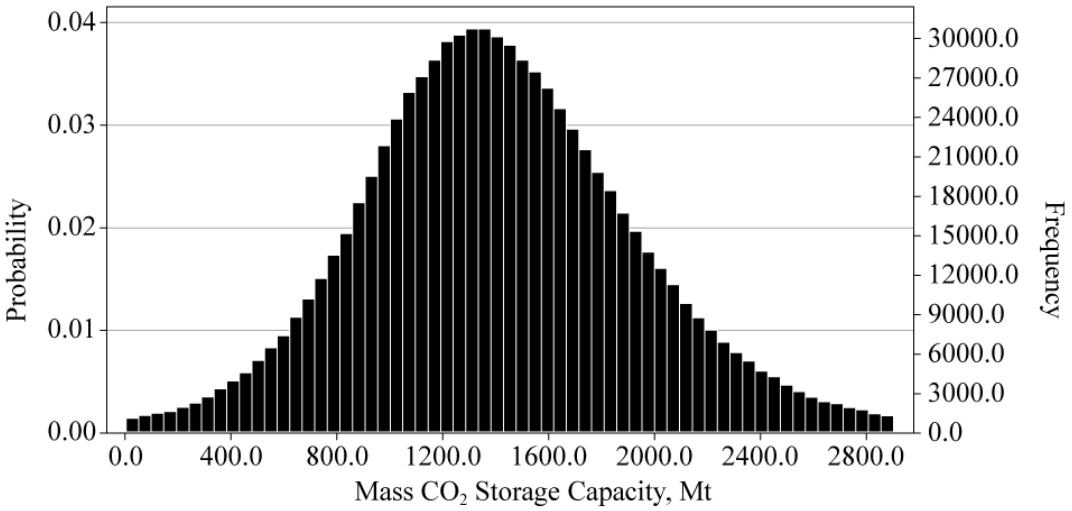

WebGasEOS, Redlich-Kwong Equation of State

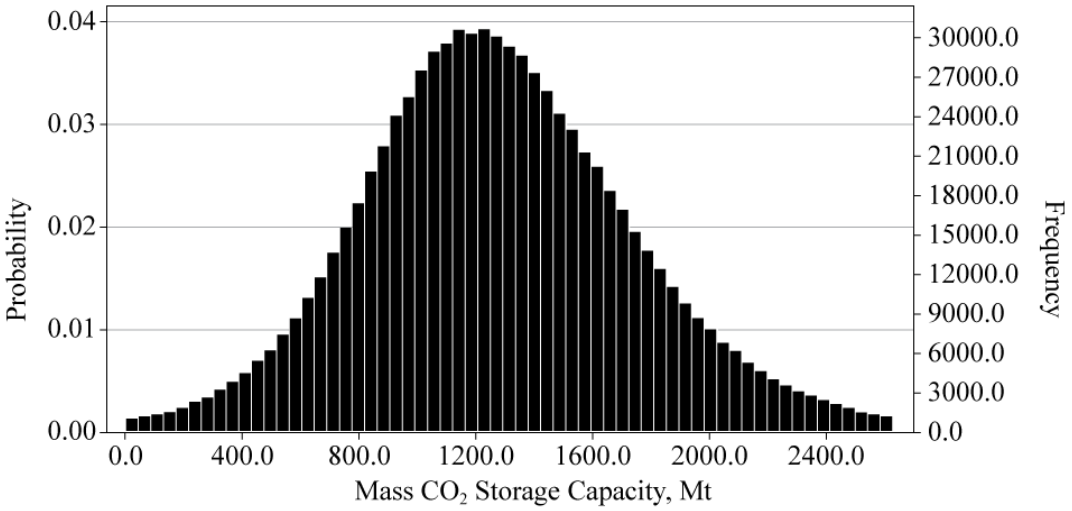

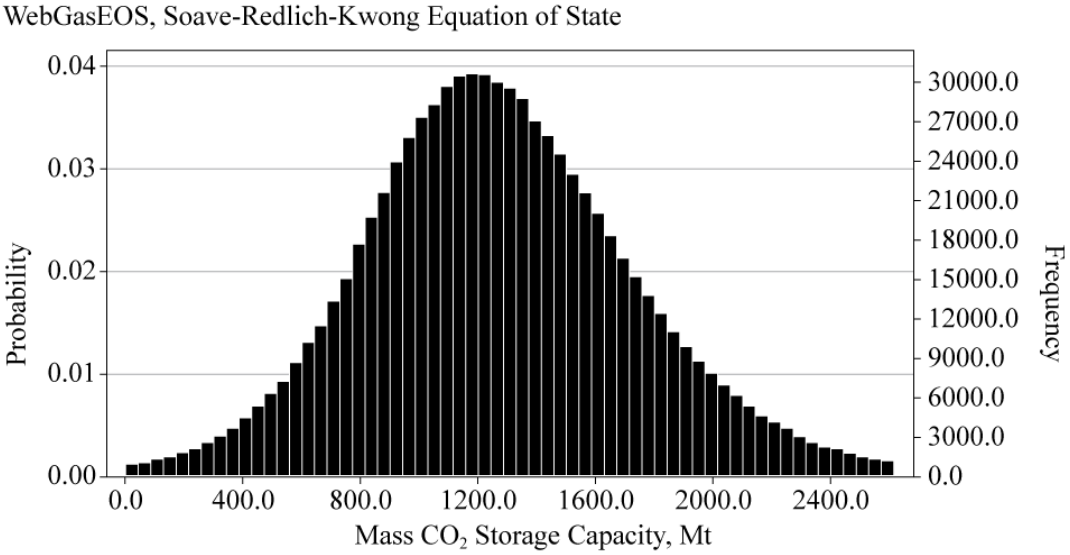

Figure 6.18 Monte Carlo Simulation probability distribution results of mass CO_2 storage capacity within the illite affected zone of the South Morecambe Sherwood Sandstone reservoir using the method of Bachu et al. (2007) Table 6.8, equation 1.1, and varying the equation of state used. Results computed using Oracle Crystal Ball software.

MODELLING SOFTWARE	EQUATION OF STATE	MINIMUM	P10	MEDIAN (P50)	MEAN	P90	MAXIMUM
RefProp	Peng-Robinson	0.11	1143.83	2351.69	2532.70	4173.31	12048.21
	GERG-2008	0.27	1215.69	2501.30	2692.24	4436.21	12116.85
	AGA8 Model	0.14	1215.32	2497.77	2691.01	4434.43	11417.04
WebGasEOS	Peng-Robinson	0.05	1163.90	2390.61	2574.63	4241.46	11323.21
	Peng-Robinson-Stryjek-Vera	0.77	1161.41	2389.12	2573.36	4245.62	11653.04
	Redlich-Kwong	0.01	1051.22	2163.11	2330.35	3839.76	10548.81
	Soave-Redlich-Kwong	0.04	1049.39	2156.65	2322.37	3827.55	10420.66

Table 6.9 Monte Carlo Simulation forecast values for the entire South Morecambe Sherwood Sandstone reservoir. Results in Mt CO_2.

MODELLING SOFTWARE	EQUATION OF STATE	MINIMUM	P10	MEDIAN (P50)	MEAN	P90	MAXIMUM
RefProp	Peng-Robinson	0.01	341.29	755.39	837.80	1446.45	4975.03
	GERG-2008	0.08	361.90	802.44	889.93	1537.58	5854.59
	AGA8 Model	0.03	363.10	801.66	889.55	1536.56	5246.29
WebGasEOS	Peng-Robinson	0.13	346.69	768.14	851.81	1470.72	5776.24
	Peng-Robinson-Stryjek-Vera	0.01	346.59	767.29	851.45	1471.30	4722.51
	Redlich-Kwong	0.01	314.00	695.32	771.27	1333.01	4719.29
	Soave-Redlich-Kwong	0.04	313.18	692.88	768.13	1326.16	4369.87

Table 6.10 Monte Carlo Simulation forecast values for the illite free zone of the South Morecambe Sherwood Sandstone reservoir. Results in Mt CO_2.

MODELLING SOFTWARE	EQUATION OF STATE	MINIMUM	P10	MEDIAN (P50)	MEAN	P90	MAXIMUM
RefProp	Peng-Robinson	0.02	771.76	1363.29	1395.11	2056.26	5786.22
	GERG-2008	0.04	820.04	1449.52	1483.66	2190.39	6112.61
	AGA8 Model	0.04	818.44	1448.78	1483.08	2186.86	6058.50
WebGasEOS	Peng-Robinson	0.00	785.04	1387.41	1420.33	2094.55	6633.61
	Peng-Robinson-Stryjek-Vera	0.04	784.37	1387.48	1420.42	2092.74	5608.37
	Redlich-Kwong	0.01	709.83	1254.34	1284.69	1894.72	5758.78
	Soave-Redlich-Kwong	0.06	708.76	1251.35	1281.43	1890.17	5056.31

Table 6.11 Monte Carlo Simulation forecast values for the illite affected zone of the South Morecambe Sherwood Sandstone reservoir. Results in Mt CO_2.

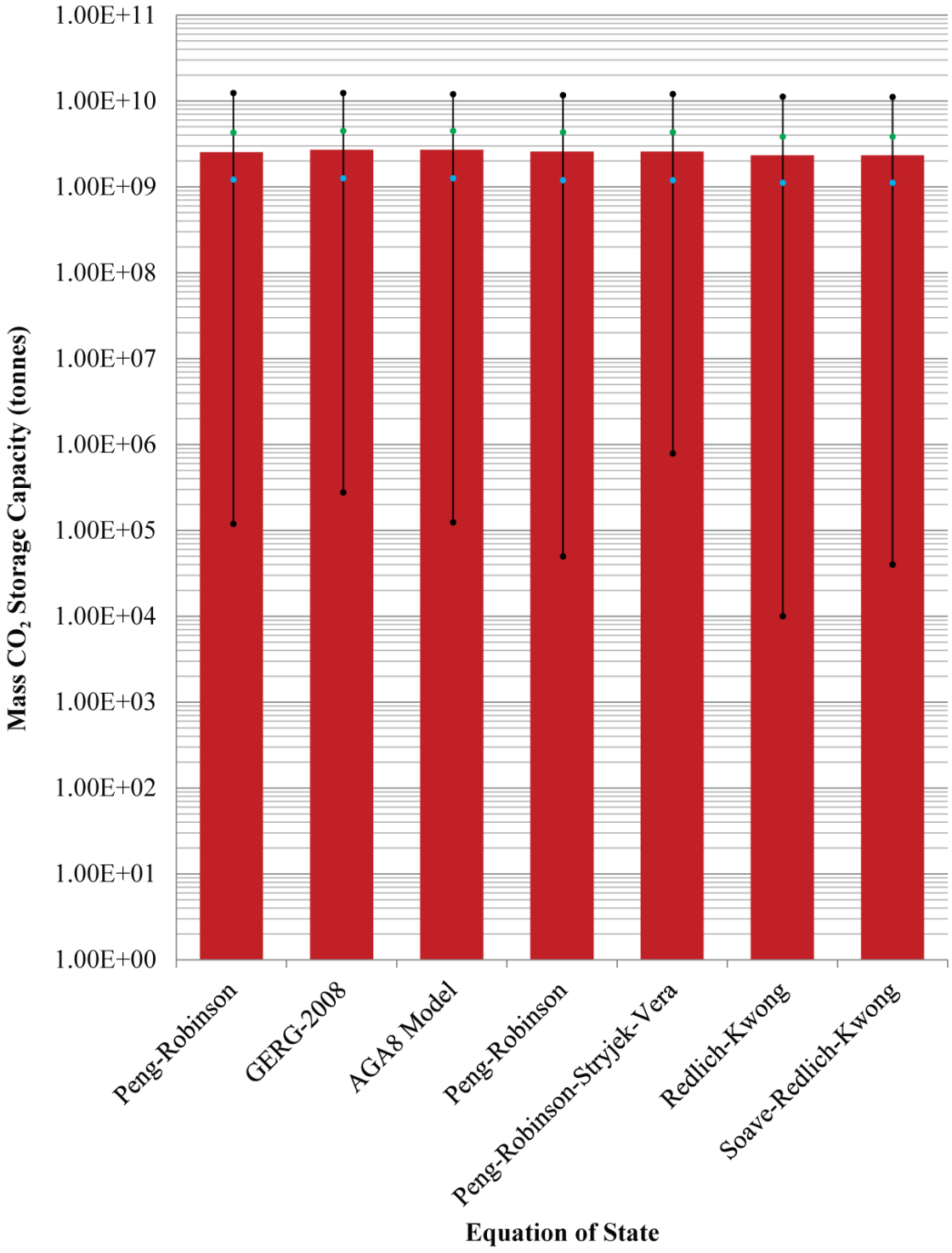

Figure 6.19 Theoretical CO_2 storage capacity of the entire South Morecambe Sherwood Sandstone reservoir estimated using the method of Bachu et al. (2007), Table 6.8, equation 1.1. The red columns plotted are the mean values, and the error bars shown have the minimum and maximum values plotted (black circles), alongside the P10 values (blue circles) and P90 values (green circles), calculated from the probability distribution curves estimated through Monte Carlo Simulation (results displayed previously in Figure 6.16).

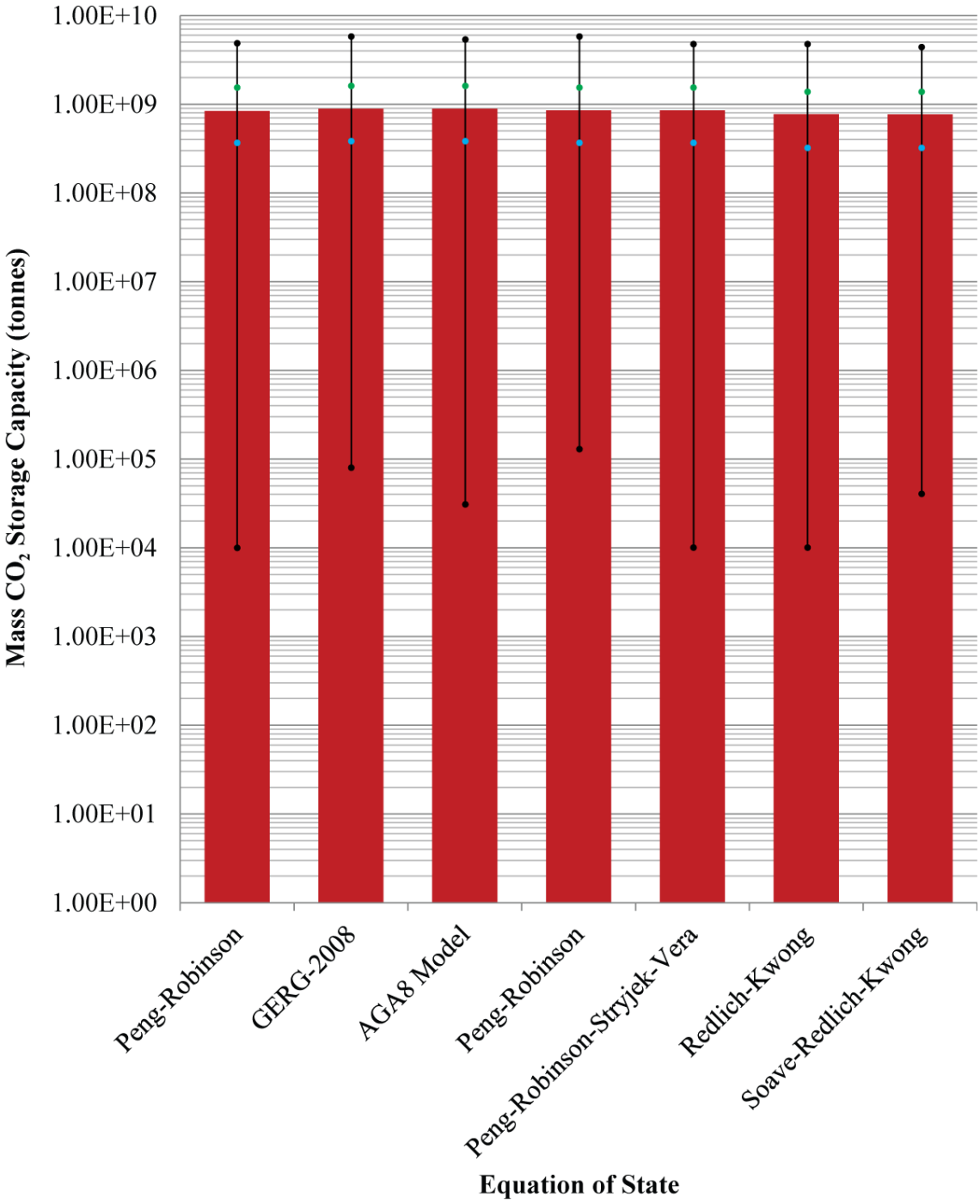

Figure 6.20 Theoretical CO_2 storage capacity of the illite free zone of the South Morecambe Sherwood Sandstone reservoir estimated using the method of Bachu et al. (2007), Table 6.8, equation 1.1. The red columns plotted are the mean values, and the error bars shown have the minimum and maximum values plotted (black circles), alongside the P10 values (blue circles) and P90 values (green circles), calculated from the probability distribution curves estimated through Monte Carlo Simulation (results displayed previously in Figure 6.17).

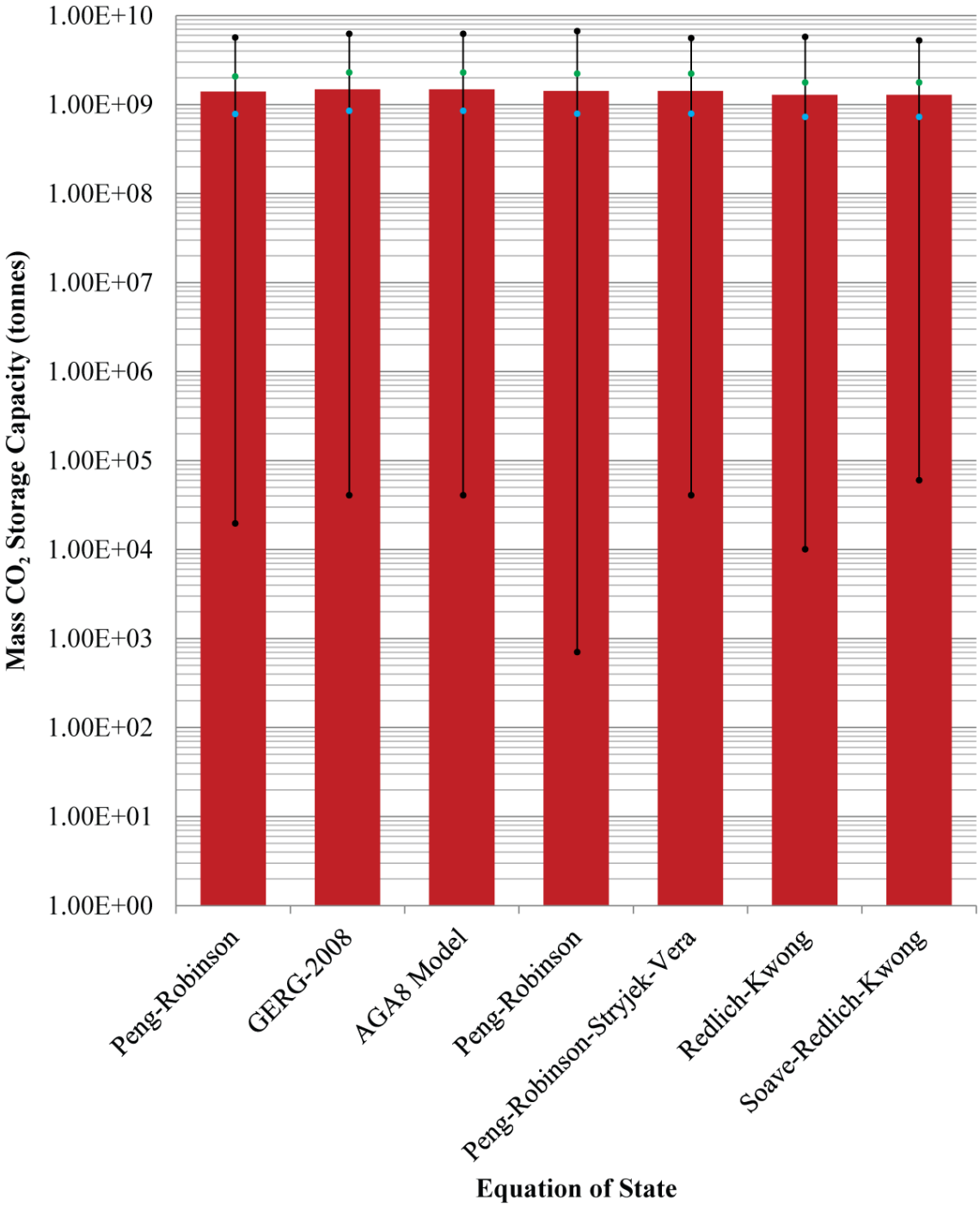

Figure 6.21 Theoretical CO_2 storage capacity of the illite free zone of the South Morecambe Sherwood Sandstone reservoir estimated using the method of Bachu et al. (2007), Table 6.8, equation 1.1. The red columns plotted are the mean values, and the error bars shown have the minimum and maximum values plotted (black circles), alongside the P10 values (blue circles) and P90 values (green circles), calculated from the probability distribution curves estimated through Monte Carlo Simulation (results displayed previously in Figure 6.18).

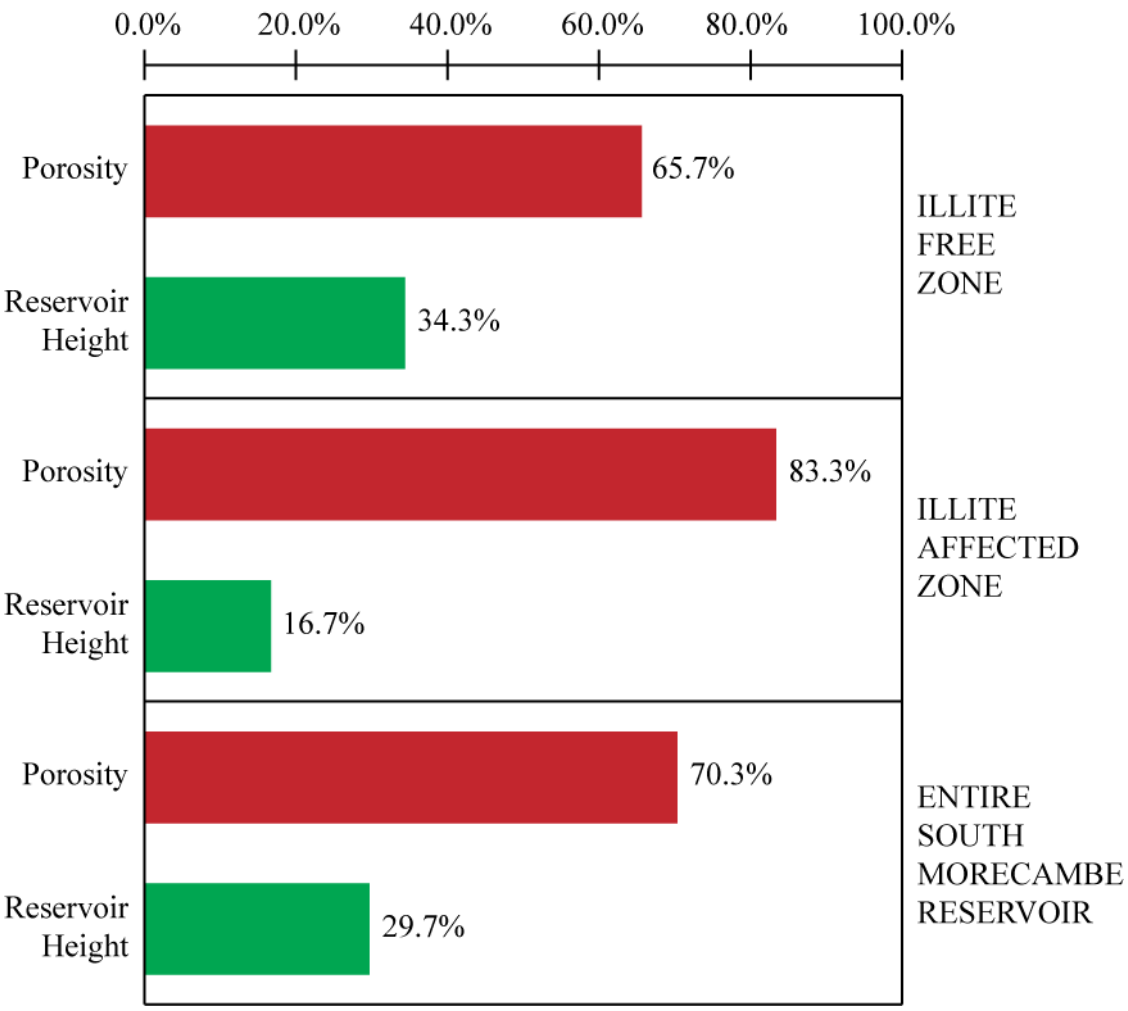

Figure 6.22 Sensitivity analysis run on the method of Bachu et al. (2007) Table 6.8, equation 1.1, throughout Monte Carlo Simulation. The results of the final probability distribution of the mass CO_2 storage capacity of the entire South Morecambe Sherwood Sandstone reservoir (Figure 6.16 and Figure 6.19), illite free zone (Figure 6.17 and Figure 6.20) and illite affected zone (Figure 6.18 and Figure 6.21), are most sensitive to porosity, followed by reservoir height.

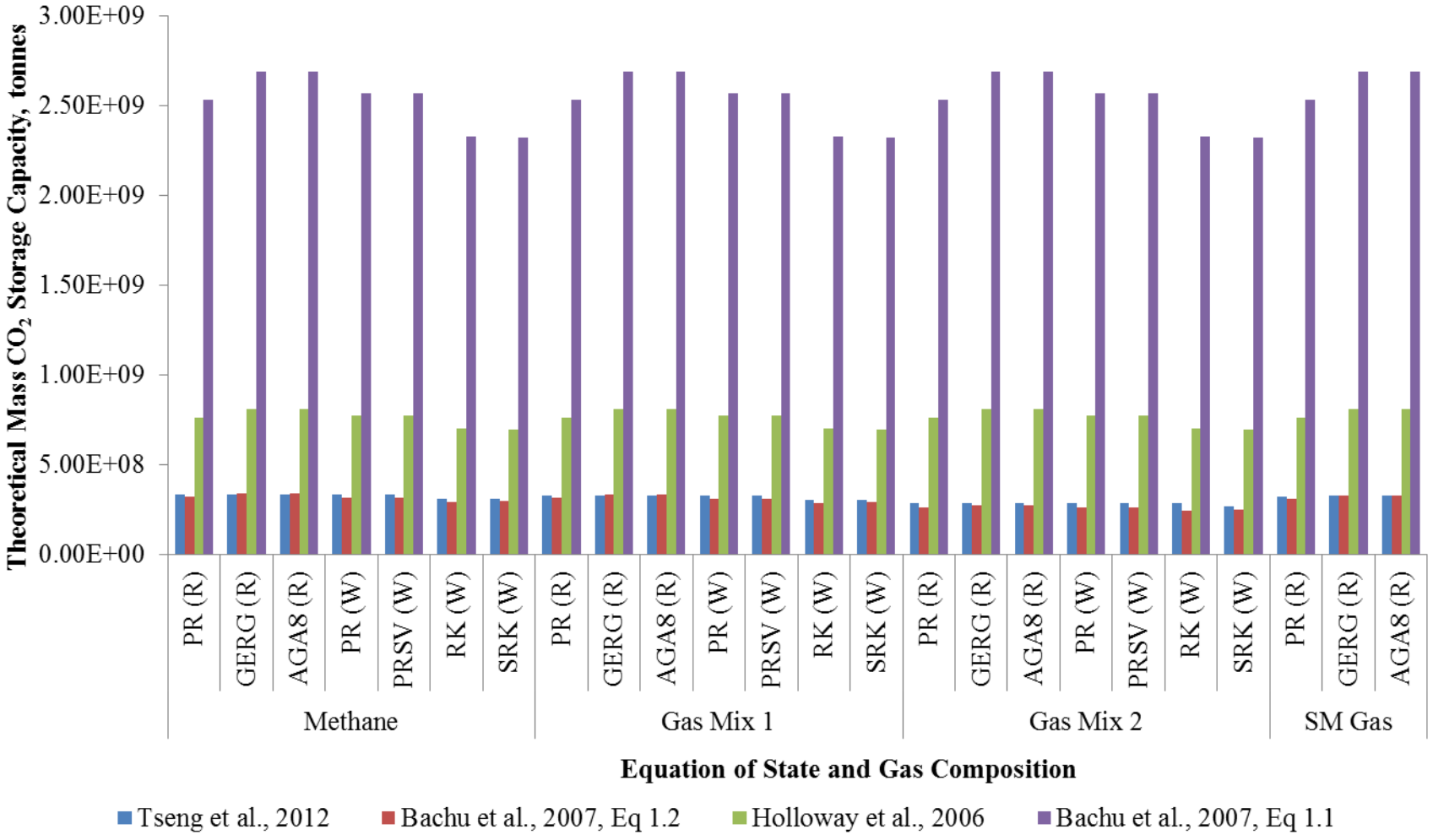

Figure 6.23 Estimated Theoretical CO_2 Storage Capacity of the South Morecambe Sherwood Sandstone reservoir using the methods of Bachu et al. (2007), Holloway et al. (2006) and Tseng et al. (2012).

	METHANE						
	REFPROP			WEBGASEOS			
	PR	GERG-2008	AGA8 Model	PR	PRSV	RK	SRK
Tseng et al., 2012	3.35E+08	3.36E+08	3.37E+08	3.34E+08	3.35E+08	3.09E+08	3.13E+08
% of Peng-Robinson (RefProp)	*100.0*	*100.6*	*100.6*	*99.9*	*100.0*	*92.4*	*93.5*
Bachu et al., 2007, Eq 1.2	3.22E+08	3.40E+08	3.40E+08	3.18E+08	3.18E+08	2.96E+08	3.02E+08
% of Peng-Robinson (RefProp)	*100.0*	*105.8*	*105.8*	*98.9*	*99.0*	*92.0*	*93.8*
Holloway et al., 2006	7.64E+08	8.11E+08	8.11E+08	7.77E+08	7.77E+08	7.03E+08	7.00E+08
% of Peng-Robinson (RefProp)	*100.0*	*106.3*	*106.3*	*101.7*	*101.7*	*92.0*	*91.7*
Bachu et al., 2007, Eq 1.1	2.53E+09	2.69E+09	2.69E+09	2.57E+09	2.57E+09	2.33E+09	2.32E+09
% of Peng-Robinson (RefProp)	*100.0*	*106.3*	*106.3*	*101.7*	*101.6*	*92.0*	*91.7*
Average Percentage Variation	100.0	104.7	104.7	100.5	100.6	92.1	92.7

	GAS MIX 1						
	REFPROP			WEBGASEOS			
	PR	GERG-2008	AGA8 Model	PR	PRSV	RK	SRK
Tseng et al., 2012	3.30E+08	3.32E+08	3.32E+08	3.30E+08	3.31E+08	3.04E+08	3.08E+08
% of Peng-Robinson (RefProp)	*100.0*	*100.5*	*100.5*	*100.1*	*100.2*	*92.1*	*93.5*
Bachu et al., 2007, Eq 1.2	3.16E+08	3.34E+08	3.34E+08	3.14E+08	3.14E+08	2.90E+08	2.97E+08
% of Peng-Robinson (RefProp)	*100.0*	*105.6*	*105.6*	*99.1*	*99.2*	*91.5*	*93.7*
Holloway et al., 2006	7.64E+08	8.11E+08	8.11E+08	7.77E+08	7.77E+08	7.03E+08	7.00E+08
% of Peng-Robinson (RefProp)	*100.0*	*106.3*	*106.3*	*101.7*	*101.7*	*92.0*	*91.7*
Bachu et al., 2007, Eq 1.1	2.53E+09	2.69E+09	2.69E+09	2.57E+09	2.57E+09	2.33E+09	2.32E+09
% of Peng-Robinson (RefProp)	*100.0*	*106.3*	*106.3*	*101.7*	*101.6*	*92.0*	*91.7*
Average Percentage Variation	100.0	104.7	104.7	100.7	100.7	91.9	92.7

	GAS MIX 2						
	REFPROP			WEBGASEOS			
	PR	GERG-2008	AGA8 Model	PR	PRSV	RK	SRK
Tseng et al., 2012	2.89E+08	2.91E+08	2.91E+08	2.88E+08	2.88E+08	2.88E+08	2.72E+08
% of Peng-Robinson (RefProp)	*100.0*	*100.5*	*100.4*	*99.6*	*99.7*	*99.7*	*94.0*
Bachu et al., 2007, Eq 1.2	2.66E+08	2.77E+08	2.76E+08	2.61E+08	2.61E+08	2.44E+08	2.50E+08
% of Peng-Robinson (RefProp)	*100.0*	*104.2*	*103.9*	*98.2*	*98.3*	*91.7*	*94.0*
Holloway et al., 2006	7.64E+08	8.11E+08	8.11E+08	7.77E+08	7.77E+08	7.03E+08	7.00E+08
% of Peng-Robinson (RefProp)	*100.0*	*106.3*	*106.3*	*101.7*	*101.7*	*92.0*	*91.7*
Bachu et al., 2007, Eq 1.1	2.53E+09	2.69E+09	2.69E+09	2.57E+09	2.57E+09	2.33E+09	2.32E+09
% of Peng-Robinson (RefProp)	*100.0*	*106.3*	*106.3*	*101.7*	*101.6*	*92.0*	*91.7*
Average Percentage Variation	100.0	104.3	104.2	100.3	100.3	93.9	92.9

	SM INITIAL GAS COMPOSITION		
	REFPROP		
	PR	GERG-2008	AGA8 Model
Tseng et al., 2012	3.26E+08	3.28E+08	3.27E+08
% of Peng-Robinson (RefProp)	*100.0*	*100.5*	*100.3*
Bachu et al., 2007, Eq 1.2	3.12E+08	3.29E+08	3.29E+08
% of Peng-Robinson (RefProp)	*100.0*	*105.4*	*105.4*
Holloway et al., 2006	7.64E+08	8.11E+08	8.11E+08
% of Peng-Robinson (RefProp)	*100.0*	*106.3*	*106.3*
Bachu et al., 2007, Eq 1.1	2.53E+09	2.69E+09	2.69E+09
% of Peng-Robinson (RefProp)	*100.0*	*106.3*	*106.3*
Average Percentage Variation	100.0	104.6	104.5

Table 6.12 Percentage variation of theoretical CO_2 storage capacity estimation using the methods of Bachu et al. (2007), Holloway et al. (2006), and Tseng et al. (2012) and various equations of state when compared to the results given by the RefProp (Lemmon et al., 2013) estimated Peng-Robinson (Peng and Robinson, 1976) storage capacity estimate for the different gas compositions. PR is the Peng-Robinson equation of state (Peng and Robinson, 1976), PRSV is the Peng-Robinson-Stryjek-Vera equation of state (Stryjek and Vera, 1986), RK is the Redlich-Kwong equation of state (Redlich and Kwong, 1949), and SRK is the Soave-Redlich-Kwong equation of state (Soave, 1972).

6.4.2.4.2. EFFECTIVE CO_2 STORAGE CAPACITY ESTIMATES

Effective CO_2 storage capacity was estimated using the method of Tseng et al. (2012), Table 6.8, equations 1.6 and 1.7, for a reservoir that experiences no water drive. Results are displayed in Figure 6.24 and Table 6.13. Unfortunately, due to the limited number of parameters that can be input into the WebGasEOS online tool (Reagan and Oldenburg, 2006), the South Morecambe Sherwood Sandstone reservoir initial gas composition could only be modelled using RefProp software (Lemmon et al., 2013). The results show an average effective storage capacity within the South Morecambe Sherwood Sandstone reservoir of between 209 and 213 Mt CO_2.

As for theoretical CO_2 storage capacity estimation, the GERG-2008 equation of state (Kunz and Wagner, 2012), closely followed by the AGA8-DC92 Model (Starling and Savidge, 1992) always predicted the highest effective CO_2 storage capacities. In contrast, the Redlich-Kwong equation of state (Redlich and Kwong, 1949) predicts the lowest effective CO_2 storage capacities (see Figure 6.24 and Table 6.13). When compared to the results of the Peng-Robinson equation of state (Peng and Robinson, 1976) estimated using RefProp (Lemmon et al., 2013), the results predicted using the GERG-2008 equation of state (Kunz and Wagner, 2012) are ~1.7% greater, and the results predicted using the Redlich-Kwong equation of state (Redlich and Kwong, 1949) are ~3.3% lower (see Table 6.13).

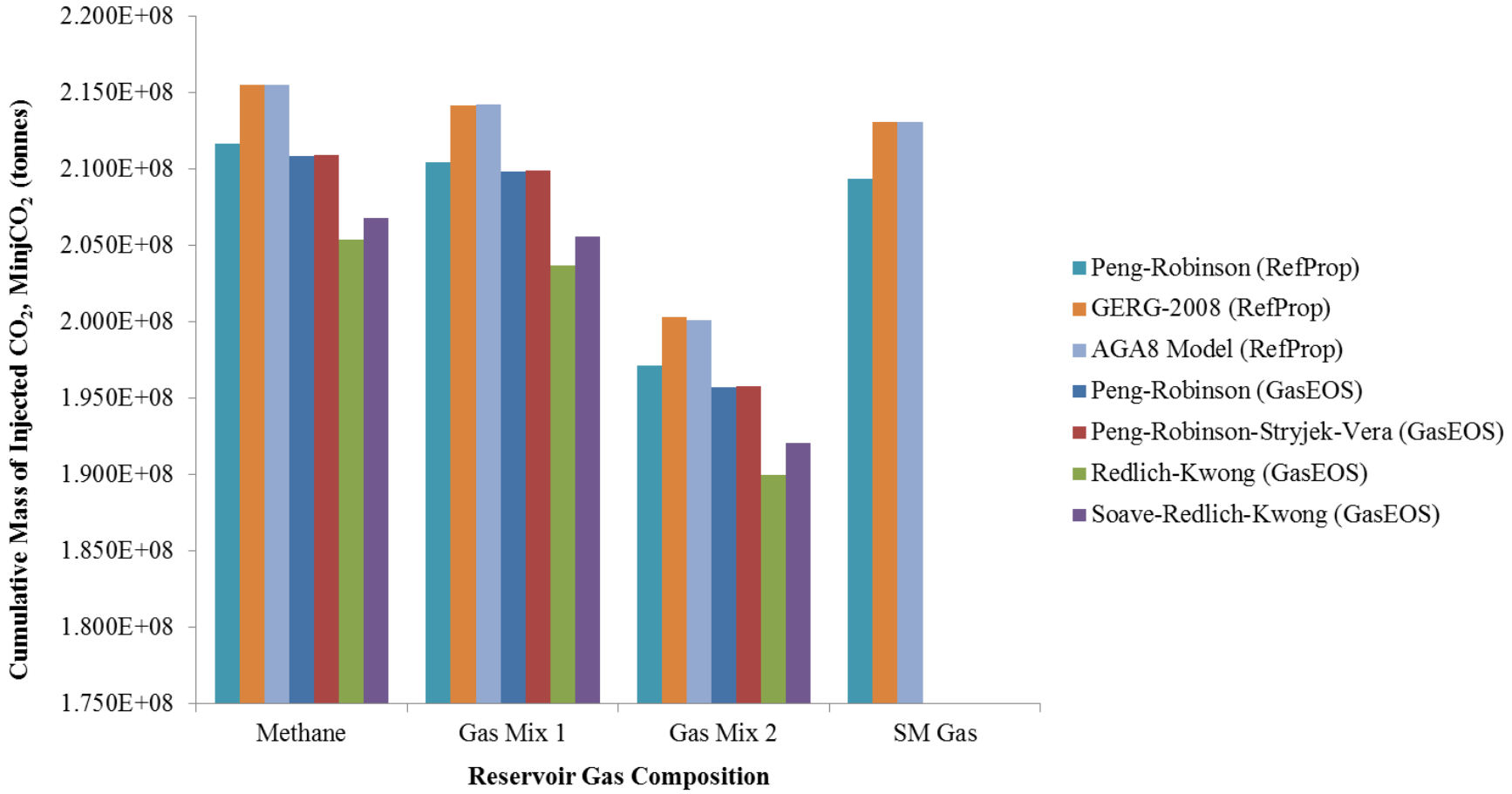

Figure 6.24 Estimated effective CO_2 storage capacity within the entire South Morecambe Sherwood Sandstone reservoir using the method of Tseng et al. (2012) and modelled with both RefProp (Lemmon et al., 2013) and the online tool by the Lawrence Berkeley National Laboratories, WebGasEOS (Reagan and Oldenburg, 2006).

	REFPROP			WEBGASEOS			
	PR	GERG-2008	AGA8 Model	PR	PRSV	RK	SRK
METHANE	2.12E+08	2.16E+08	2.15E+08	2.11E+08	2.11E+08	2.05E+08	2.07E+08
% of Peng-Robinson (RefProp)	*100.0*	*101.8*	*101.8*	*99.6*	*99.7*	*97.1*	*97.7*
GAS MIX 1	2.10E+08	2.14E+08	2.14E+08	2.10E+08	2.10E+08	2.04E+08	2.06E+08
% of Peng-Robinson (RefProp)	*100.0*	*101.8*	*101.8*	*99.7*	*99.7*	*96.8*	*97.7*
GAS MIX 2	1.97E+08	2.00E+08	2.00E+08	1.96E+08	1.96E+08	1.90E+08	1.92E+08
% of Peng-Robinson (RefProp)	*100.0*	*101.6*	*101.5*	*99.3*	*99.3*	*96.3*	*97.4*
SM GAS	2.09E+08	2.13E+08	2.13E+08				
% of Peng-Robinson (RefProp)	*100.0*	*101.8*	*101.8*				
Average Percentage Variation	100.0	101.7	101.7	99.5	99.6	96.7	97.6

Table 6.13 Percentage deviation of effective CO_2 storage capacity estimation within the entire South Morecambe Sherwood Sandstone reservoir using the method of Tseng et al. (2012) and various equations of state when compared to the results given by the RefProp (Lemmon et al., 2013) estimated Peng-Robinson (Peng and Robinson, 1976) storage capacity estimate for the different gas compositions. PR is the Peng-Robinson equation of state (Peng and Robinson, 1976), PRSV is the Peng-Robinson-Stryjek-Vera equation of state (Stryjek and Vera, 1986), RK is the Redlich-Kwong equation of state (Redlich and Kwong, 1949), and SRK is the Soave-Redlich-Kwong equation of state (Soave, 1972).

6.4.2.5. COMPARISON WITH PUBLISHED CO_2 STORAGE CAPACITY ESTIMATES FOR THE SOUTH MORECAMBE SHERWOOD SANDSTONE RESERVOIR

Previously published theoretical CO_2 storage capacity estimates for the South Morecambe Sherwood Sandstone reservoir have ranged between 734 and 820 Mt CO_2. All estimations have used the method of Holloway et al., (2006), Table 6.8, equation 1.3. Within this study, theoretical CO_2 storage capacity estimates using the same method of Holloway et al., (2006), Table 6.8, equation 1.3 produced results ranging between 764 and 811 Mt CO_2 and are therefore comparable with the published estimates. However, the results of Holloway et al., (2006), Table 6.8, equation 1.3 represent mid-range estimates for the South Morecambe Sherwood Sandstone reservoir. Estimates of Bachu et al. (2007), Table 6.8, equation 1.2 and Tseng et al. (2012), Table 6.8, equation 1.4 represent the lowest storage capacity estimates for the reservoir, ranging between 312-329 Mt CO_2 and 326-328 Mt CO_2 respectively. Conversely the estimates of Bachu et al. (2007), Table 6.8, equation 1.1, represent the highest storage capacity estimates for the reservoir, ranging between 2530-2690 Mt CO_2.

6.5. THE NORTH MORECAMBE GAS FIELD

6.5.1. PETROPHYSICAL CHARACTERISTICS

6.5.1.1. POROSITY AND PERMEABILITY DATA

The following graphs and boxplots (Figure 6.25 to Figure 6.29) represent the plotted porosity and permeability dataset for the North Morecambe Sherwood Sandstone reservoir made available to Durham University by IHS. Wells with core analysis data include 110/02-03, 110/02a-05 and 110/02a-08 (see Figure 6.1 for locations). Figure 6.25 (a) is a graph of porosity versus permeability for the entire North Morecambe Sherwood Sandstone reservoir, and shows a positive correlation with an r^2 value of 0.1273. Through application of the Pearson correlation (Gravetter and Wallnau, 1999), the critical r value for a sample size of 1340 and a significance level of 0.0005 for a one tailed probability (i.e. it is known the direction of correlation is positive) is 0.104. Therefore, the calculated r value for the porosity and permeability correlation of 0.357 exceeds the critical value and can be considered as significant.

Due to the reservoir being affected by illite precipitation, similar to that of the South Morecambe Sherwood Sandstone reservoir, data from the illite free zone and illite affected zone have been analysed separately. Figure 6.25 (b) for the illite free zone shows a positive correlation with an r^2 value of 0.3188. The critical r value for 361 values is 0.164, therefore the calculated r value of 0.564 exceeds this, and the correlation can be considered significant. Figure 6.25 (c) for the illite affected zone also shows a positive correlation with an r^2 value of 0.0013. Once again, the critical r value for 979 values is 0.104, therefore the calculated r value of 0.0361 is below this, and the correlation cannot be considered significant.

Figure 6.26 shows boxplots of the porosity data from (a) the entire North Morecambe Sherwood Sandstone reservoir and from (b) the illite free zone, and (c) illite affected zone. Porosity data from the entire North Morecambe Sherwood Sandstone reservoir (Figure 6.26 (a)) show the main body (50%) of data ranges between 8.21% (Q1) and 14.46% (Q3), with a median value (Q2) of 11.10%.

Outliers were calculated to be porosity data less than -1.165% and greater than 23.835%. As such, the whisker on the left hand side of the box is limited to 0.0% (as it is not possible to have a negative value for porosity). On the right hand side of the boxplot there are a total of 14 outliers, illustrated as black boxes on the boxplot.

Porosity data from the illite free and illite affected zones were then analysed separately. The illite free zone within the North Morecambe Sherwood Sandstone reservoir (Figure 6.26 (b)) show the main body (50%) of porosity data ranges between 11.61% (Q1) and 17.69% (Q3), with a median value (Q2) of 14.65%. Outliers were calculated to be porosity data less than 2.49% and greater than 26.81%. On the left hand side of the boxplot there are a total of 2 outliers, and on the right hand side, a total of 1 outlier.

Porosity data from the illite affected zone within the North Morecambe Sherwood Sandstone reservoir (Figure 6.26 (c)) show the main body (50%) of porosity data ranges between 7.52% (Q1) and 12.95% (Q3), with a median value (Q2) of 10.02%. Outliers were calculated to be porosity data less than -0.625% and greater than 21.095%. As such, there are a total of 20 outliers on the right hand side of the boxplot.

Once again, Monte Carlo simulation of these data, and application of the Anderson-Darling (A-D) test is used to evaluate whether the data population originated from a specific probability distribution (Stephens, 1974).

The best-fit distribution for the entire North Morecambe Sherwood Sandstone reservoir is a lognormal distribution, shown in Figure 6.27 (a). The resulting A-D value for the dataset is 1.4598; therefore the fit of the data to the probability distribution is reasonable. The A-D P-value test for normality gives a result of 0.00, implying these data do not follow a specified distribution. However, compared to the alternative distributions, the lognormal is the best fit of the porosity data.

Data from the illite free and illite affected zones of the North Morecambe Sherwood Sandstone reservoir were then analysed separately. The best-fit distribution for data from the illite free zone is a logistic distribution, shown in Figure 6.27 (b). The A-D value for the dataset is 2.2618, implying the fit of the

data to the probability distribution is very poor. The A-D P-value test for normality gives a result of 0.00, showing these data do not follow a specified distribution.

The best-fit distribution for data from the illite affected zone is a lognormal distribution, shown in Figure 6.27 (c). The A-D value for the dataset is 2.1596; therefore the fit of the data to the probability distribution is very poor. The A-D P-value test for normality gives a result of 0.00, once again showing these data do not follow a specified distribution.

Once again, the effect of illite precipitation on reservoir permeability is analysed through use of boxplots and histograms. The boxplot of permeability for the entire North Morecambe Sherwood Sandstone reservoir is shown in Figure 6.28 (a). The main body (50%) of data ranges between 0.10 mD (Q1) and 13.10 mD (Q3), with a median value (Q2) of 1.10 mD. Outliers were calculated to be permeability data less than -19.40 mD and greater than 32.60 mD. It is not possible to have a negative value for permeability therefore the whisker on the left hand side of the box has been limited to 0.00 mD. However, there are a total of 305 outliers on the right hand side of the box, up to a maximum permeability of 5900.00 mD. The outliers have not been plotted on this, or any of the other boxplots in Figure 6.28, due to their scale of distance away from the main body of data.

The boxplot of the illite free zone (Figure 6.28 (b)) shows the main body (50%) of data ranges between 6.50 mD (Q1) and 287.50 mD (Q3), with a median value (Q2) of 64.00 mD. Outliers were calculated to be permeability data less than -415.00 mD and greater than 709.00 mD. Again, it is not possible to have a negative value for permeability, therefore the whisker on the left hand side of the box is limited to 0.00 mD. However, there are a total of 29 outliers on the right hand side of the box, up to a maximum permeability of 2576.00 mD.

The boxplot of the illite affected zone (Figure 6.28 (c)) shows the main body (50%) of data ranges between 0.051 mD (Q1) and 2.214 mD (Q3), with a median value (Q2) of 0.314 mD. Outliers were calculated to be permeability data less than -3.194 mD and greater than 5.459 mD. The whisker on the left hand side of the box is limited to 0.00 mD as it is not possible to have a negative value for permeability. However, there are a total of 162 outliers on the right hand side of the box, up to a maximum permeability of 5900.000 mD. Comparison of the results in Figure 6.28

(b) and (c) show that the main body (50%) of data is located at higher permeabilities in the illite free zone (ranging between 6.50 mD and 287.5 mD) than the illite affected zone (ranging between 0.051 mD and 2.214 mD). This is to be expected as illite precipitation destroys permeability within sandstone reservoirs.

Average (mean) permeability values of the entire North Morecambe Sherwood Sandstone reservoir are 881.80 mD, the illite free zone, 247.70 mD and the illite affected zone, 22.43 mD, based upon data from the same wells listed above for porosity. The logarithmic histogram of permeability for the entire North Morecambe Sherwood Sandstone reservoir (Figure 6.29 (a)) shows there to be a high number of instances at lower permeabilites, however the number of instances decrease as permeability increases, as the higher values are spread over a vast range of permeability, up to 5900.00 mD. When the illite free zone and the illite affected zone is analysed independently, differing trends can be observed. The illite free zone (Figure 6.29 (b)) shows an increasing number of instances as permeability increases until permeability exceeds 1000 mD. Conversely, the illite affected zone (Figure 6.29 (c)) shows a high number of instances at low permeability that decrease as permeability increases.

(a)

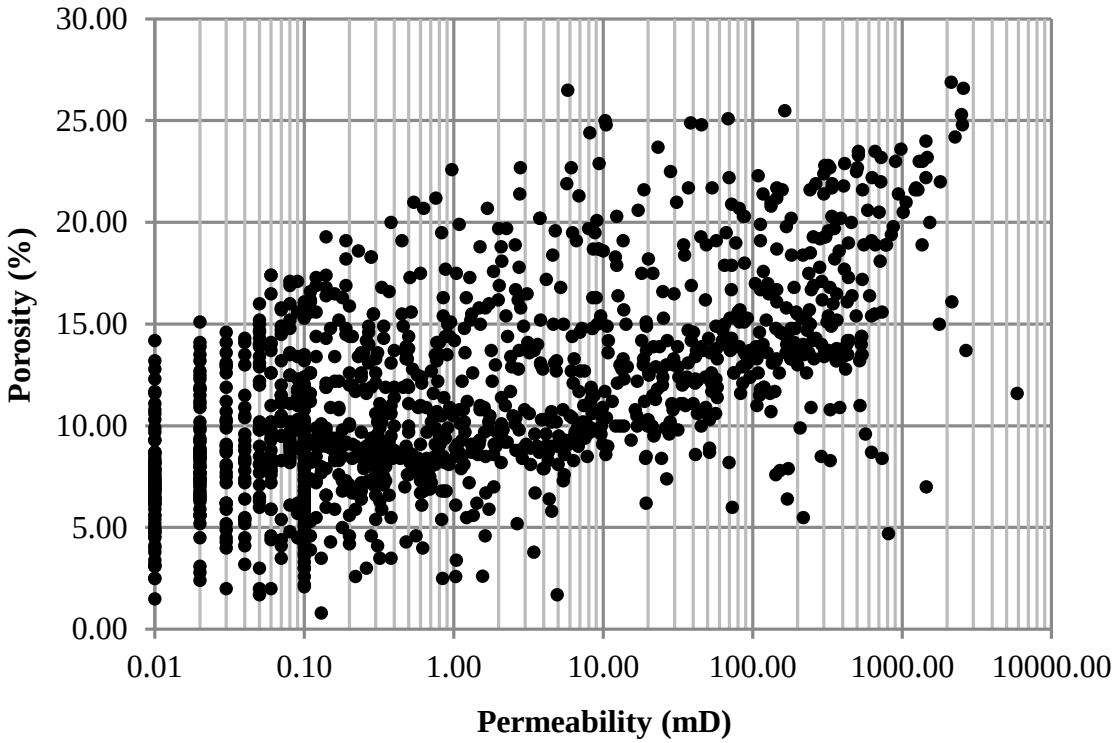

(b)

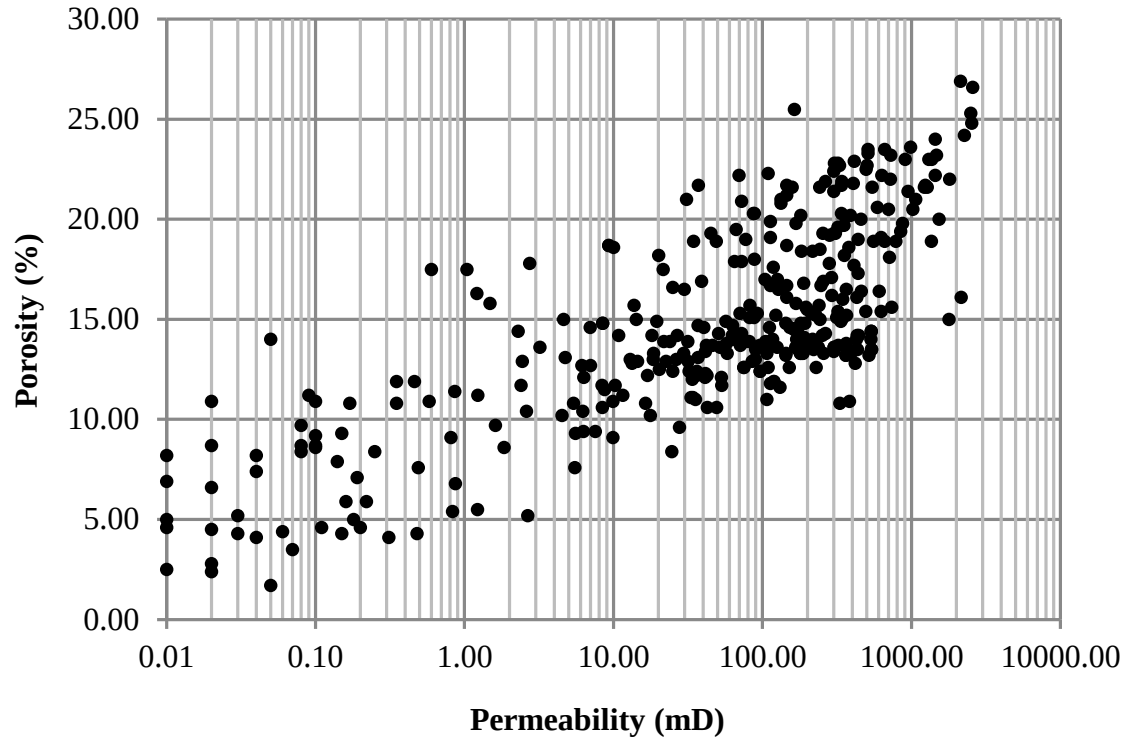

(c)

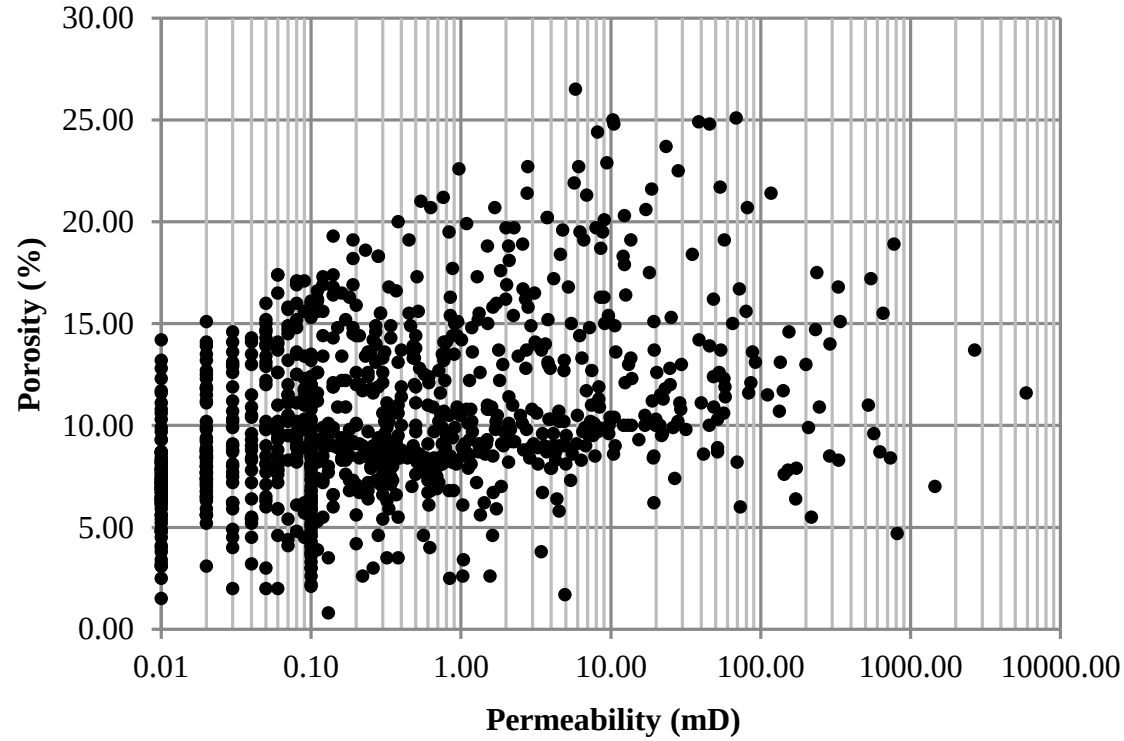

Figure 6.25 North Morecambe Sherwood Sandstone Overall Reservoir Quality for (a) the entire reservoir, (b) the illite free zone, and (c) the illite affected zone.

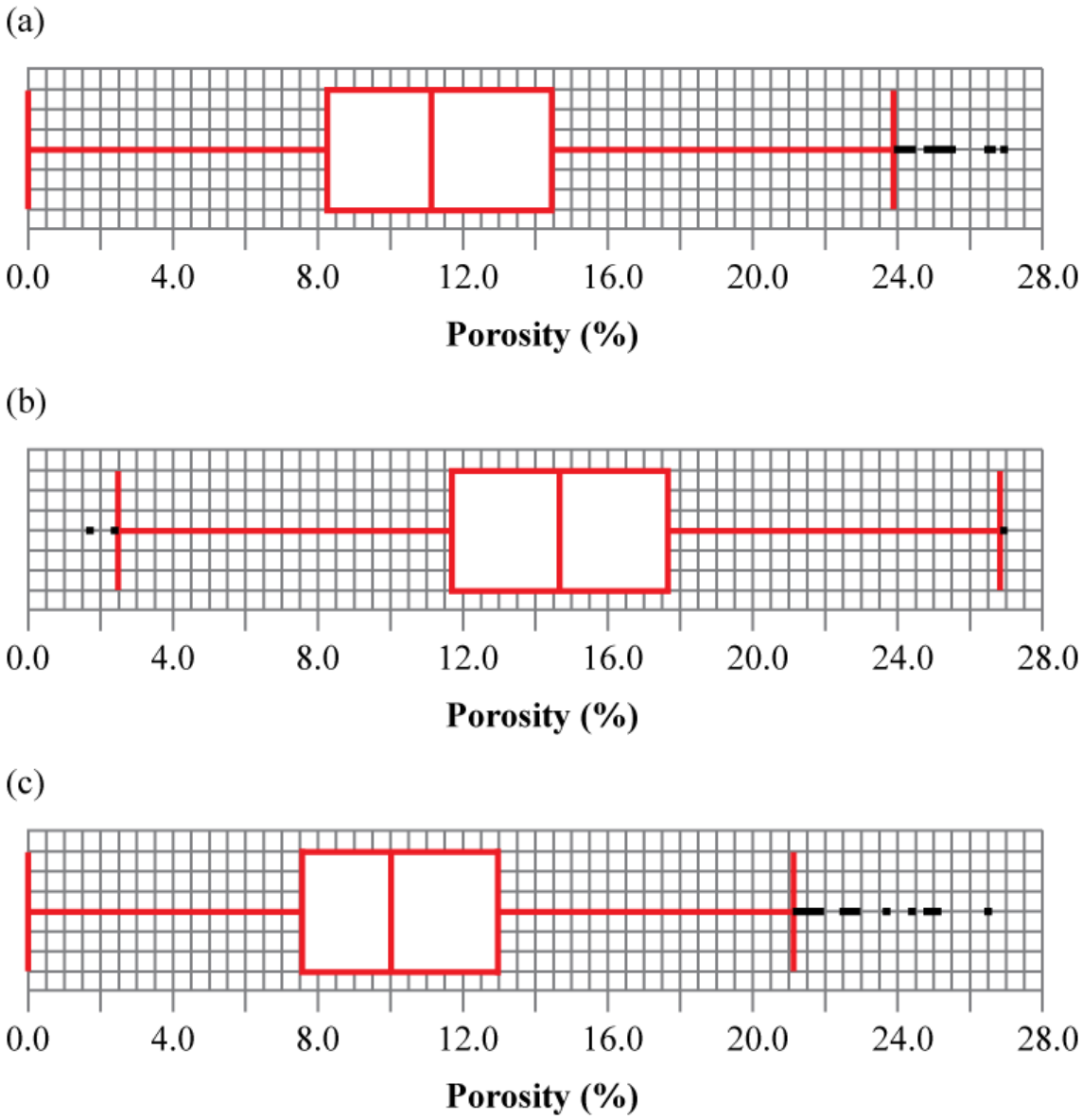

Figure 6.26 North Morecambe Sherwood Sandstone Reservoir boxplots for porosity. (a) Porosity of the reservoir overall, (b) porosity of the illite free zone within the reservoir, and (c) porosity of the illite affected zone within the reservoir.

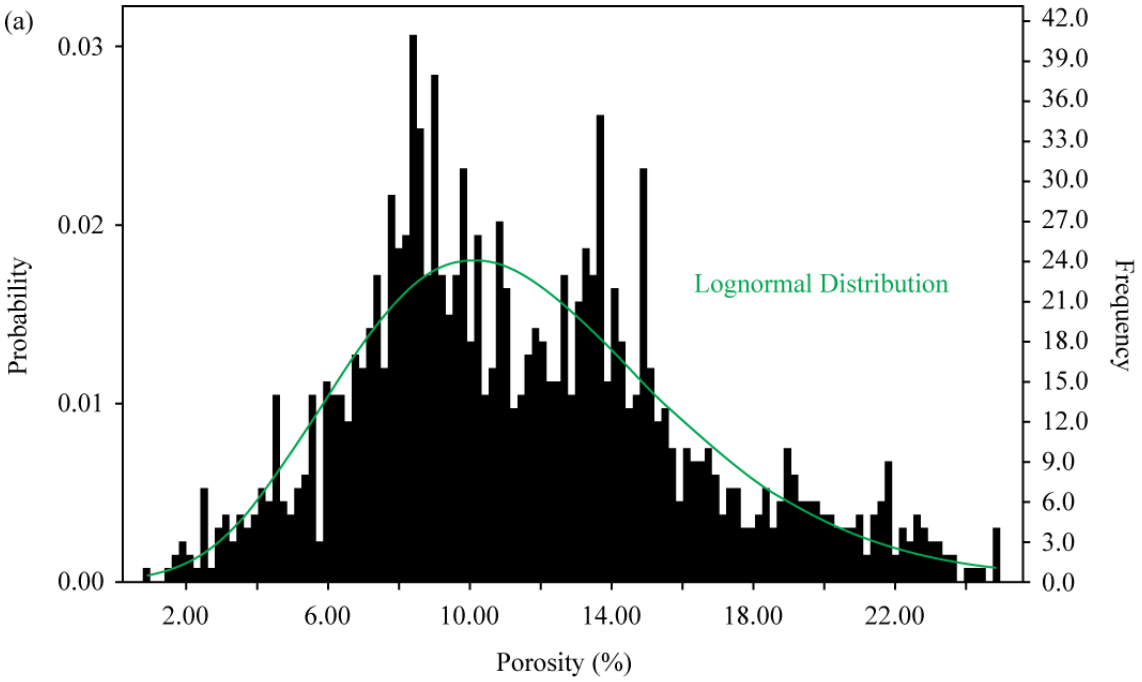
(a)
Probability
Frequency
Lognormal Distribution
Porosity (%)
0.00
0.01
0.02
0.03
0.0
3.0
6.0
9.0
12.0
15.0
18.0
21.0
24.0
27.0
30.0
33.0
36.0
39.0
42.0
2.00
6.00
10.00
14.00
18.00
22.00

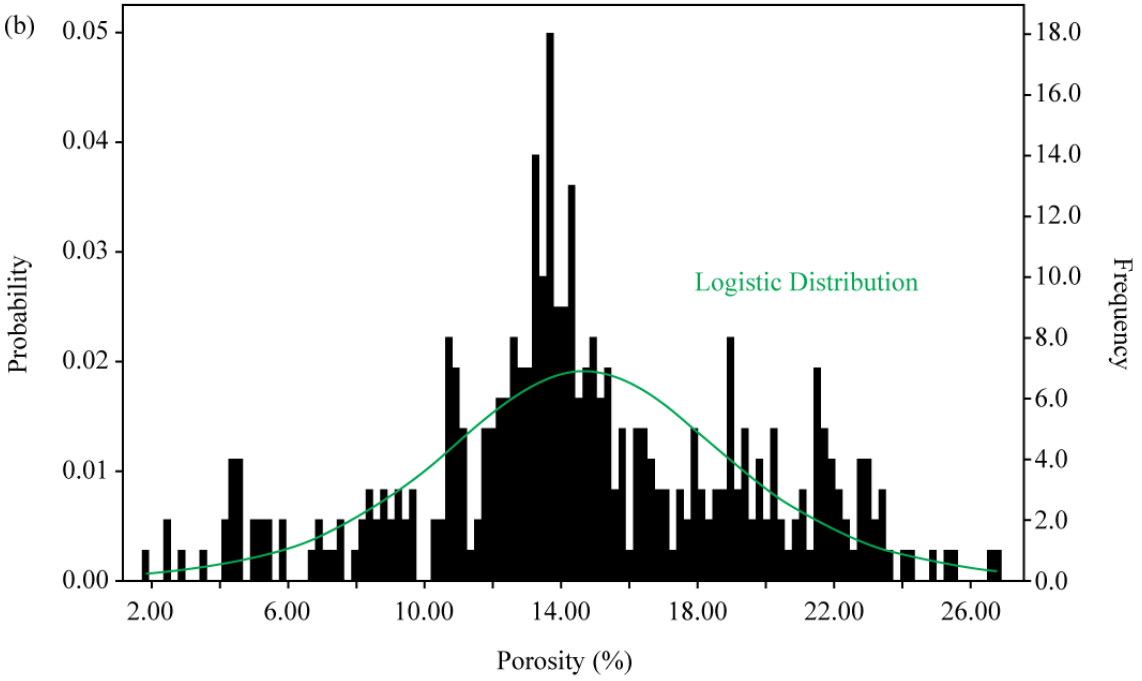
(b)
Probability
Frequency
Logistic Distribution
Porosity (%)
0.00
0.01
0.02
0.03
0.04
0.05
0.0
2.0
4.0
6.0
8.0
10.0
12.0
14.0
16.0
18.0
2.00
6.00
10.00
14.00
18.00
22.00
26.00

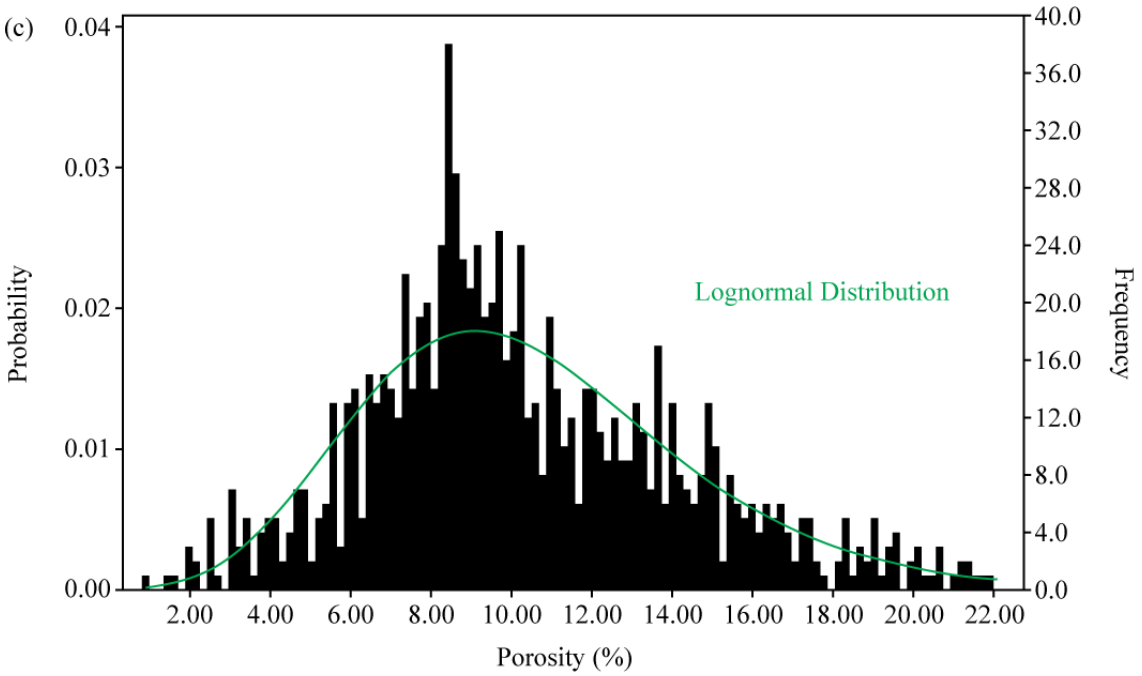

Figure 6.27 Histogram of North Morecambe Sherwood Sandstone Reservoir porosity for (a) the entire reservoir, based on 1340 values, (b) the illite free zone, based on 361 values, and (c) the illite affected zone, based on 979 values.

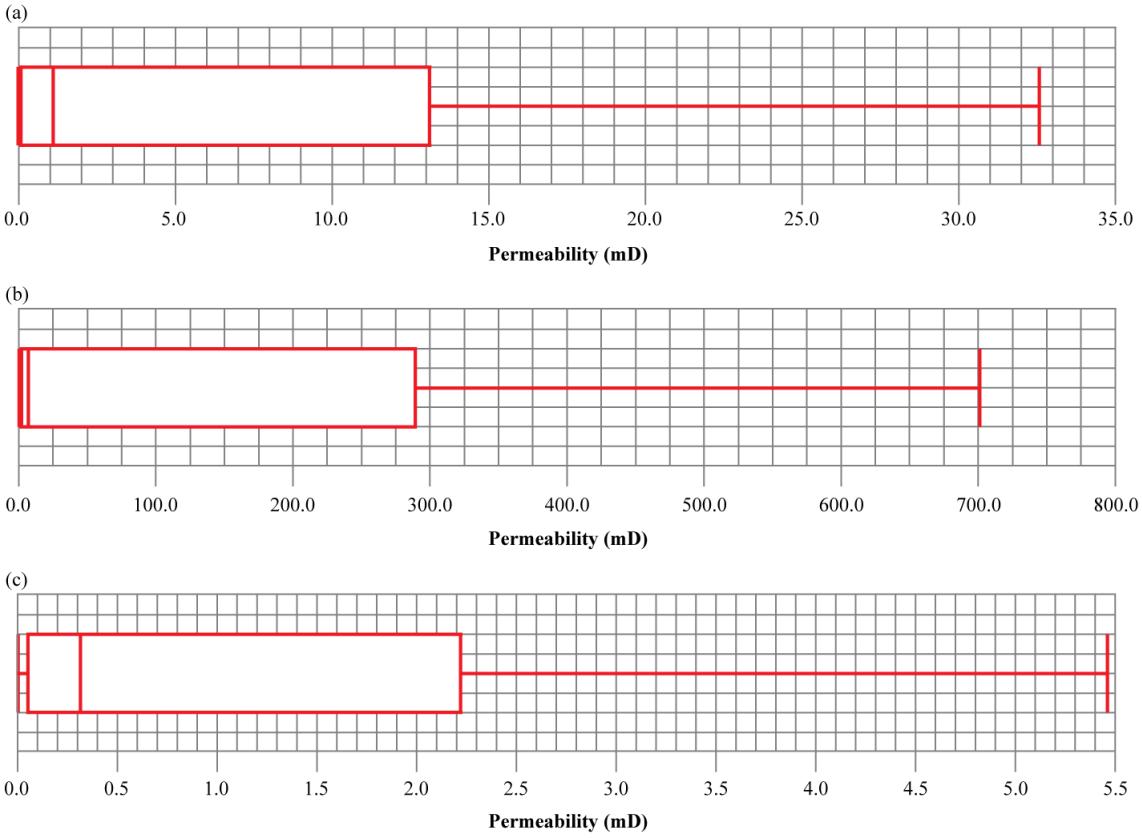

Figure 6.28 North Morecambe Sherwood Sandstone Group Reservoir boxplot for permeability for (a) the entire reservoir, (b) the illite free zone, and (c) the illite affected zone. Outliers on the right hand side of the boxplots have not been plotted on the boxplots due to their scale of distance away from the main body of data. For (a) the entire reservoir, there are a total of 305 outliers on the right hand side of the box, with a maximum permeability of 5900.00 mD. For (b) the illite free zone, there are a total of 29 outliers on the right hand side of the box, with a maximum permeability of 2576.00 mD. For (c) the illite affected zone, there are a total of 162 outliers on the right hand side of box, with a maximum permeability of 5900.00 mD.

(a)

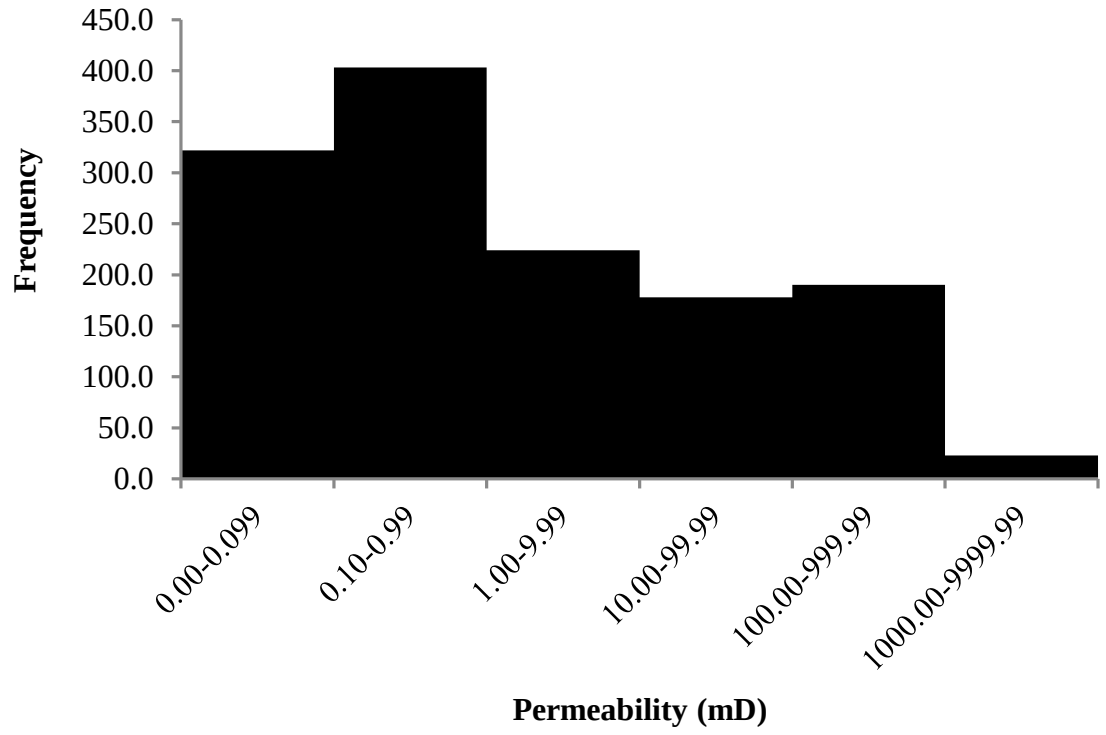
450.0
400.0
350.0
300.0
250.0
200.0
150.0
100.0
50.0
0.0
Frequency
0.00-0.099
0.10-0.99
1.00-9.99
10.00-99.99
100.00-999.99
1000.00-9999.99
Permeability (mD)

(b)

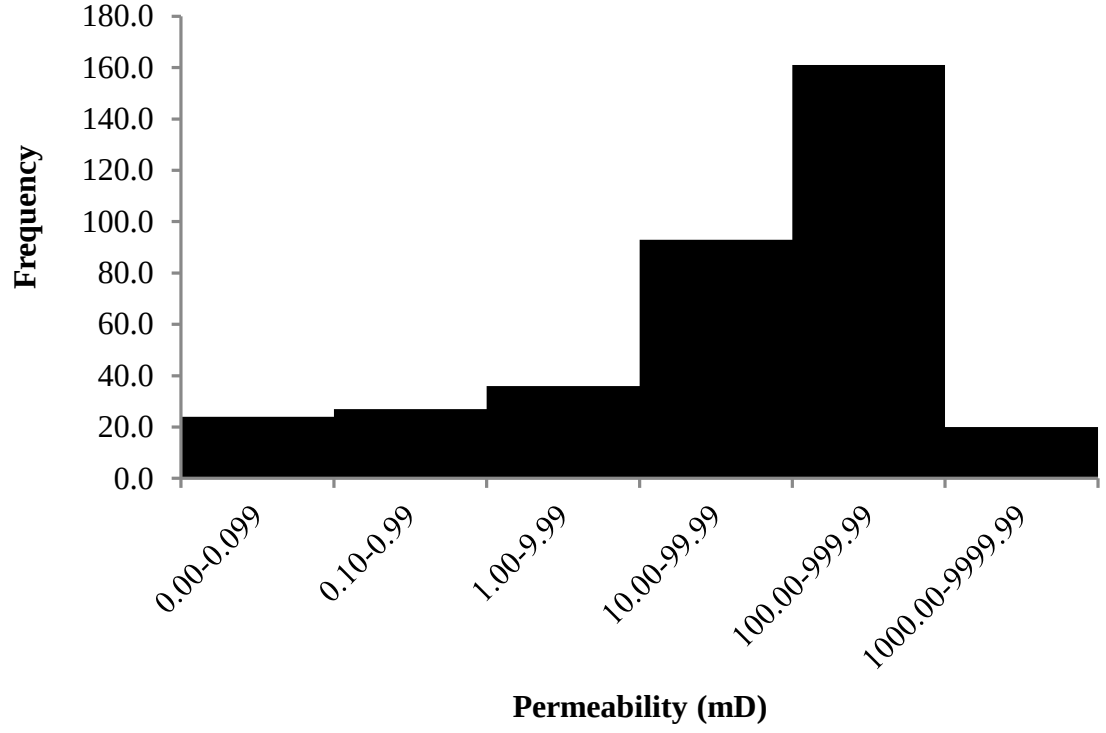
180.0
160.0
140.0
120.0
100.0
80.0
60.0
40.0
20.0
0.0
Frequency
0.00-0.099
0.10-0.99
1.00-9.99
10.00-99.99
100.00-999.99
1000.00-9999.99
Permeability (mD)

(c)

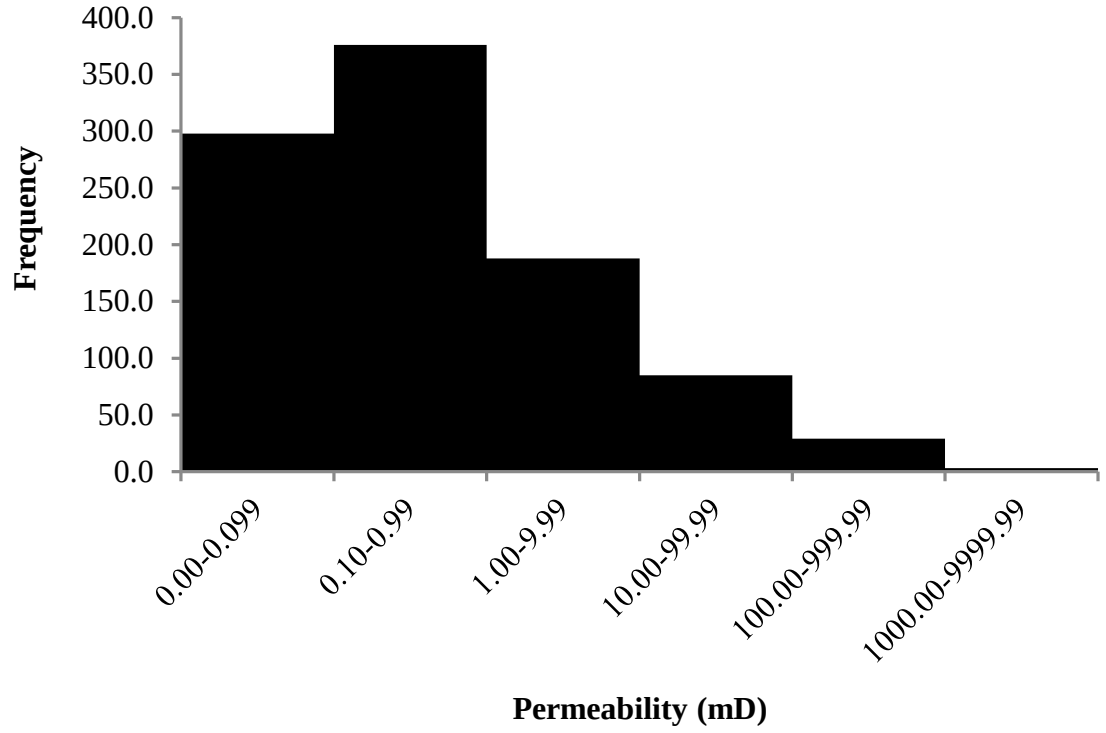

Figure 6.29 Histogram of North Morecambe Sherwood Sandstone Reservoir permeability for (a) the entire reservoir, (b) the illite free zone, and (c) the illite affected zone.

6.5.1.2. GAS PRODUCTION AND ASSOCIATED PRESSURE DECLINE

The North Morecambe Sherwood Sandstone reservoir has produced natural gas since 27 March 1994. The last recorded volume of produced gas was in February 2002 at 19.3 billion cubic metres, based on the production data received from Centrica. The gas production data from all productive wells (including wells 110/02a-N01, N02, N03, N04, N05, N06, N07, N08, N09 and N10) has been plotted in Figure 6.30, which shows an overall step-wise increase in rate of production over the nine years shown. The step-wise trend observed in the production data is likely to be due to seasonal production from the reservoir, as there are a total of eight "steps" over the field lifetime shown. Between 1994 and the end of 1998 there was an average production rate of 4.11 billion cubic metres per year, when the North Morecambe Sherwood Sandstone reservoir was online. Between 1999 and the beginning of 2002, the rate decreased to 3.57 billion cubic metres per year during the time intervals when the reservoir was online. At the end of 2002, the reservoir had a recovery factor of 52.9% and still had the potential for further production.

The pressure history of the reservoir has also been plotted alongside the gas production data in Figure 6.30 from well 110/02a-N01. The associated pressure decline due to production has a similar but opposite trend to that of gas production. The pressure declined in the North Morecambe Sherwood Sandstone reservoir in a step-wise manner, similar to the trend observed throughout production. When there is a period of no, or little, production, pressure remained constant, and in some cases even increased. When the rate of production was high, there is an associated steep decline in reservoir pressure. This observation supports the contention that the North Morecambe Sherwood Sandstone reservoir underwent seasonal production. Throughout the productive intervals over the nine year period, there was a rate of pressure decline of 2.385 MPa/year.

As for the previous pressure datasets, there will be a degree of error involved. Early readings from RFT tools will be accurate to within 0.18%. Later readings will be accurate to within 0.025%.

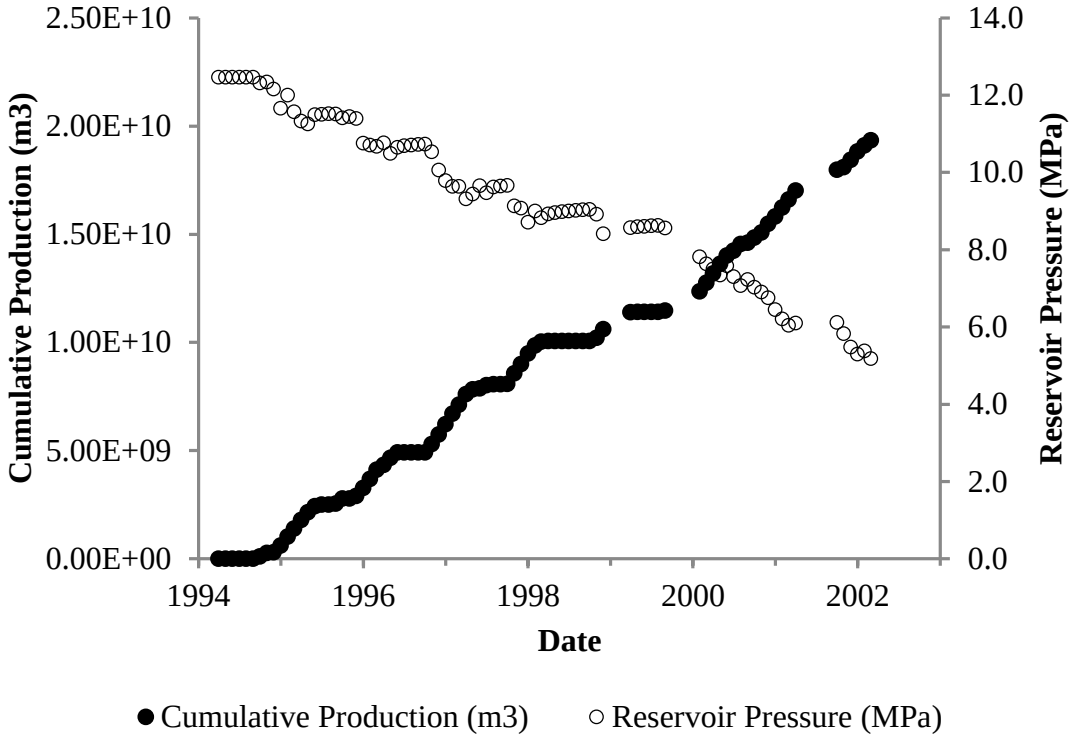

Figure 6.30 North Morecambe Sherwood Sandstone Reservoir cumulative production and pressure depletion data, based on production data from Centrica.

6.5.1.3. MATERIAL BALANCE METHODS

Material balance methods are once again used to assess if the North Morecambe Sherwood Sandstone reservoir has shown some degree of water drive throughout its productive lifetime, and if so, to estimate aquifer strength.

The material balance plot of the North Morecambe Sherwood Sandstone reservoir (Figure 6.31) fluctuates around a linear trend. Based on the trends observed on Figure 6.32, it would suggest the North Morecambe reservoir is a depletion drive reservoir. However, the Cole Plot of the reservoir (Figure 6.33) shows an overall curved trend. This suggests there is a degree of water drive within the North Morecambe Sherwood Sandstone reservoir. As can be seen, the reservoir data fluctuates around an expected curved trend. This is partially due to the seasonal production from the reservoir, as once again, the step-wise trend is reflected in the data in Figure 6.33. The reservoir is most likely to have a moderate to strong water drive. Due to the reservoir only being 52.9% depleted (based on the

OGIP value estimated by Centrica) it is not possible to see the curve dip downwards towards the end of production, which would confirm moderate water drive within the North Morecambe Sherwood Sandstone reservoir. However, it is very much apparent that the reservoir does not show a weak water drive trend, as the curve displayed is concave down, increasing, not concave up, decreasing. The reservoir is also unlikely to show strong water drive – from the production history of the reservoir there has been no information about wells taking on large volumes of water, and there is no evidence to suggest wells either have, or have been at risk of watering out.

The industry estimated OGIP value for the North Morecambe Sherwood Sandstone reservoir is 36.529 billion cubic metres of natural gas. The reservoir has been assumed to be a depletion drive reservoir; however, the Cole Plot (Figure 6.33) suggests the reservoir experiences a water drive. As such, it is likely that the industry OGIP value has been over-estimated. To check this estimate, equation 5.3 from Chapter 5 (Table 6.14) has been used to estimate a value for the cumulative volume of water influx into the North Morecambe Sherwood Sandstone reservoir, W_e, throughout its productive lifetime up until 2002 (last recorded data).

EQUATION	EQUATION NUMBER
$W_e = \frac{G_p - OGIP(1 - E/E_i)}{E}$	(5.3)

Table 6.14 Equation to estimate the cumulative volume of water influx into a reservoir (W_e). After Dake (1978). See Chapter 5 for definition of symbols.

The estimated value of W_e using equation 5.3 (Table 6.14) for the North Morecambe Sherwood Sandstone reservoir is -0.0675 billion cubic metres. This is further evidence to suggest that the industry estimated value for OGIP is incorrect – if the North Morecambe Sherwood Sandstone reservoir has a water drive as the Cole Plot suggests (Figure 6.33), the estimated value for W_e should be positive. This will be investigated further in section 6.5.1.4.1.

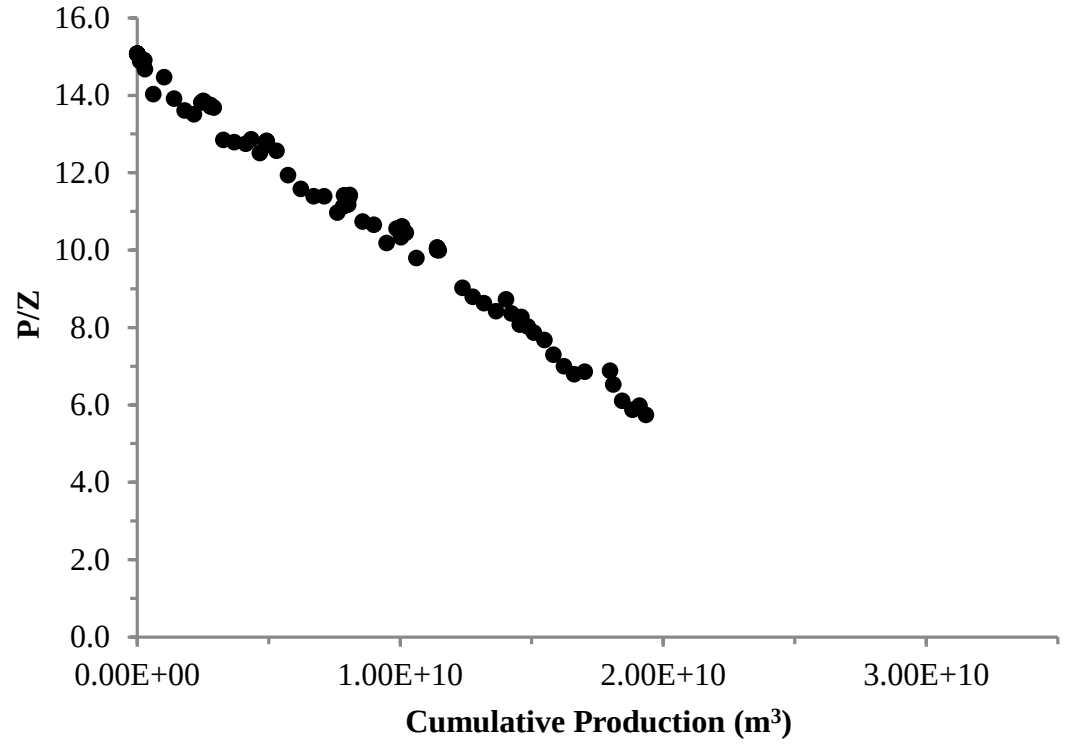

Figure 6.31 North Morecambe Sherwood Sandstone Reservoir material balance plot.

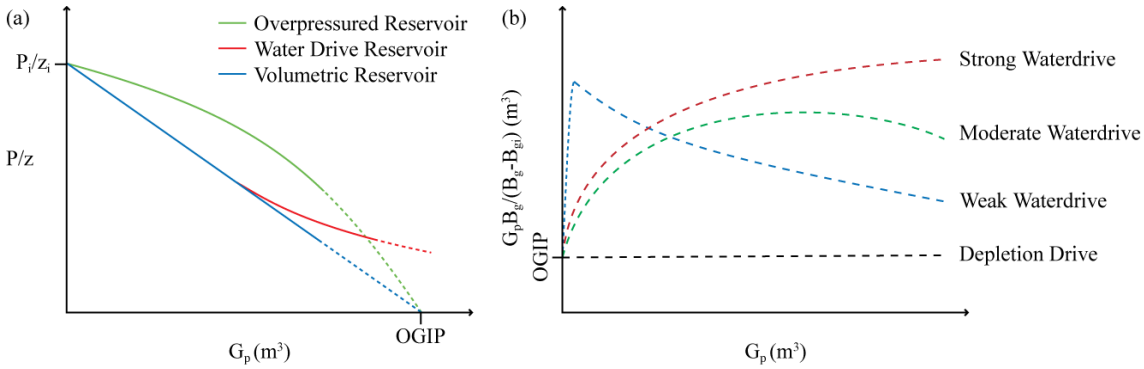

Figure 6.32 Material Balance Methods. (a) The original material balance method of pressure divided by gas compressibility factor against cumulative gas production. The major trends are shown on the graph for an over-pressured reservoir, a water drive reservoir and a volumetric reservoir. Due to the difficulties in solving the original material balance equation within water drive reservoirs, the water drive trend is often difficult to decipher on this graph from a volumetric reservoir trend. Instead a Cole Plot (b) can provide a clear distinction between water drive and volumetric (depletion) drive reservoirs.

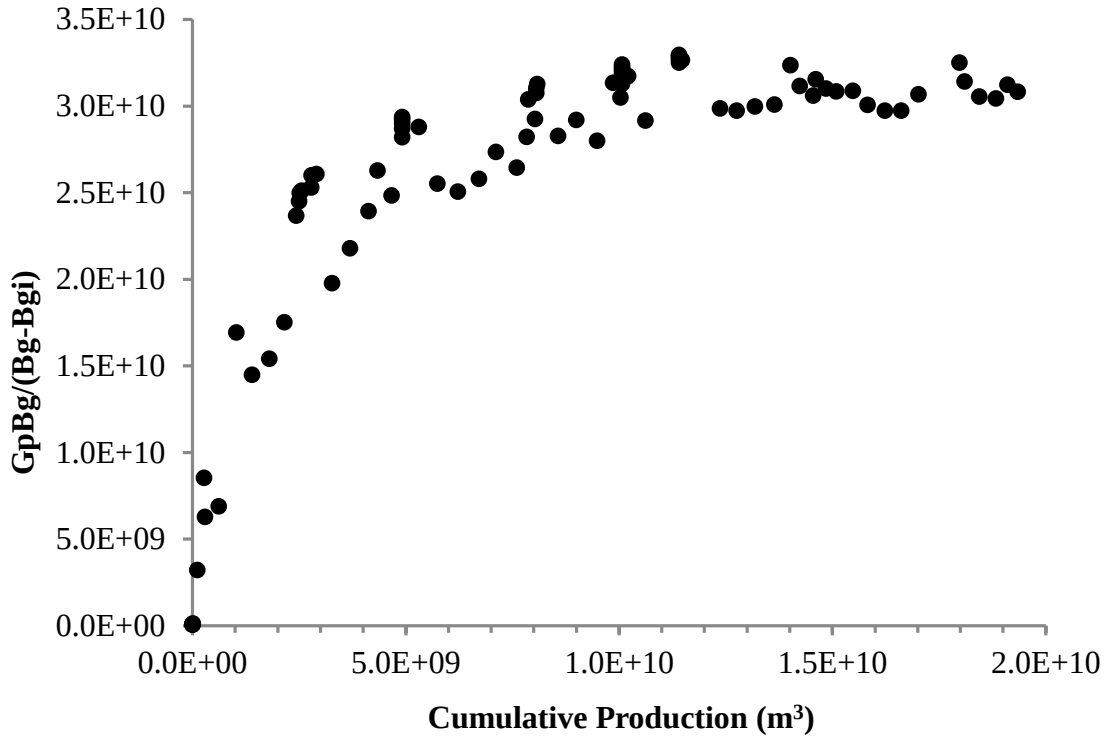

Figure 6.33 North Morecambe Sherwood Sandstone Reservoir Cole Plot.

6.5.1.4. HISTORICAL AQUIFER BEHAVIOUR THROUGHOUT PRODUCTION

6.5.1.4.1. HYDRAULIC DIFFUSIVITY

Due to the North Morecambe Sherwood Sandstone reservoir being a water drive reservoir, it is important to consider hydraulic diffusivity to estimate a lag time for a pressure pulse within the water leg to diffuse over a specified distance. As for the Hewett Upper Bunter Sandstone reservoir (Chapter 5), Monte Carlo simulation was used to estimate hydraulic diffusivity, κ_ϕ, within the reservoir based on the permeability, k, and porosity, ϕ, measured in wells, and the estimated brine viscosity, μ, and bulk compressibility for matrix and fluid, c_{res} and c_{fluid}, respectively. Once again the equations used previously in Chapter 5 were used for estimation here (see Table 6.15). The probability distributions of hydraulic diffusivity computed using Oracle Crystal Ball software are illustrated in Figure 6.34, and the estimated values are displayed in Table 6.16.

HYDRAULIC DIFFUSIVITY EQUATIONS	EQUATION NUMBER
$\kappa_\phi = \frac{k}{\mu \times \phi \times (C_{res} + C_{fluid})}$	(5.3)
$\Delta t = \Delta x^2 / \kappa_\phi$	(5.4)

Table 6.15 Equations previously used in Chapter 5 to estimate hydraulic diffusivity and lag time to diffuse over a specified diffusion distance.

(a) The Entire North Morecambe Sherwood Sandstone Reservoir

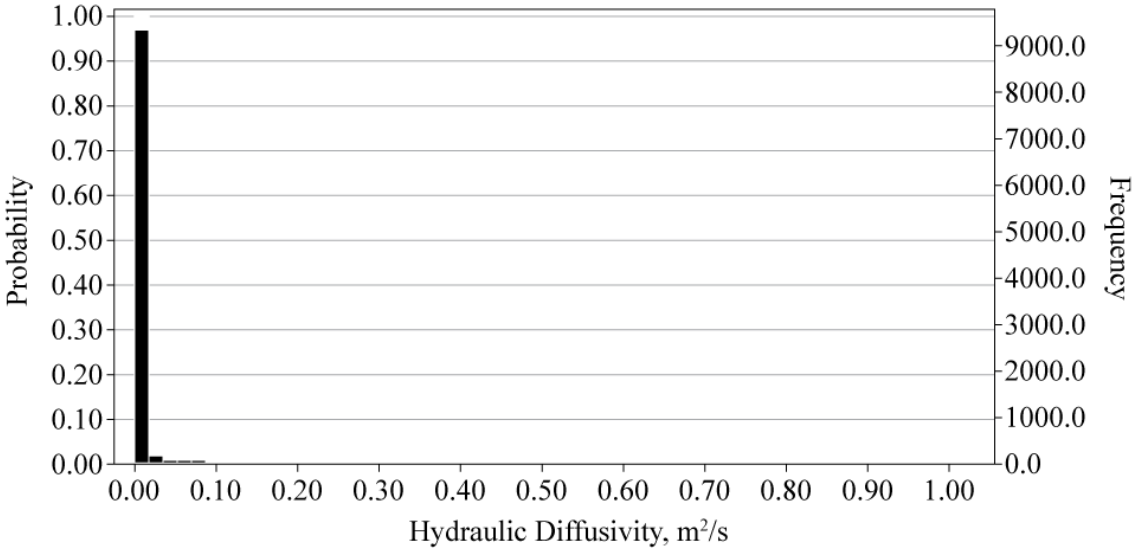

(b) The Illite Free Zone of the North Morecambe Sherwood Sandstone Reservoir

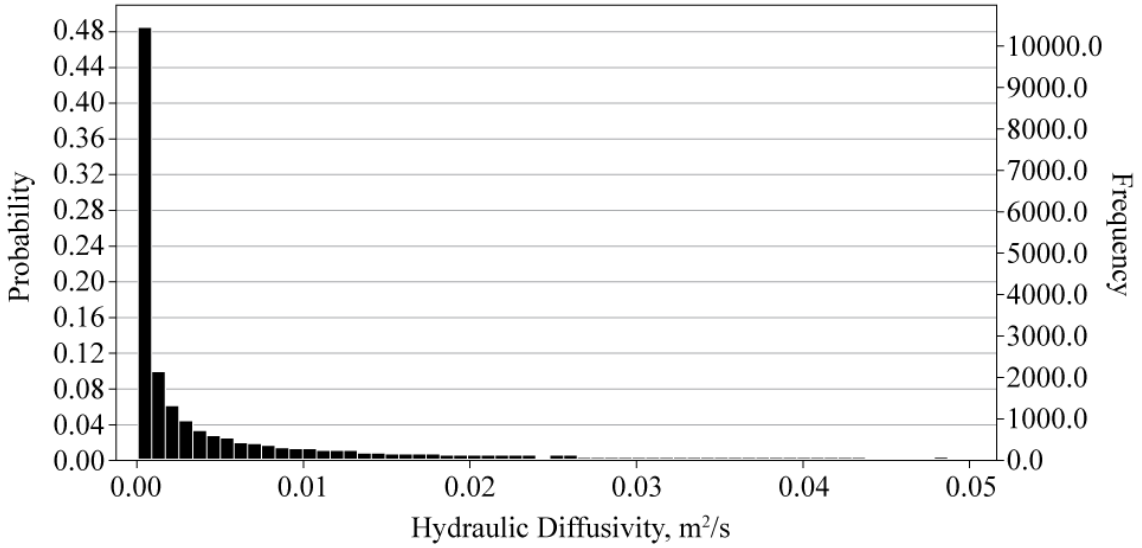

(c) The Illite Affected Zone of the North Morecambe Sherwood Sandstone Reservoir

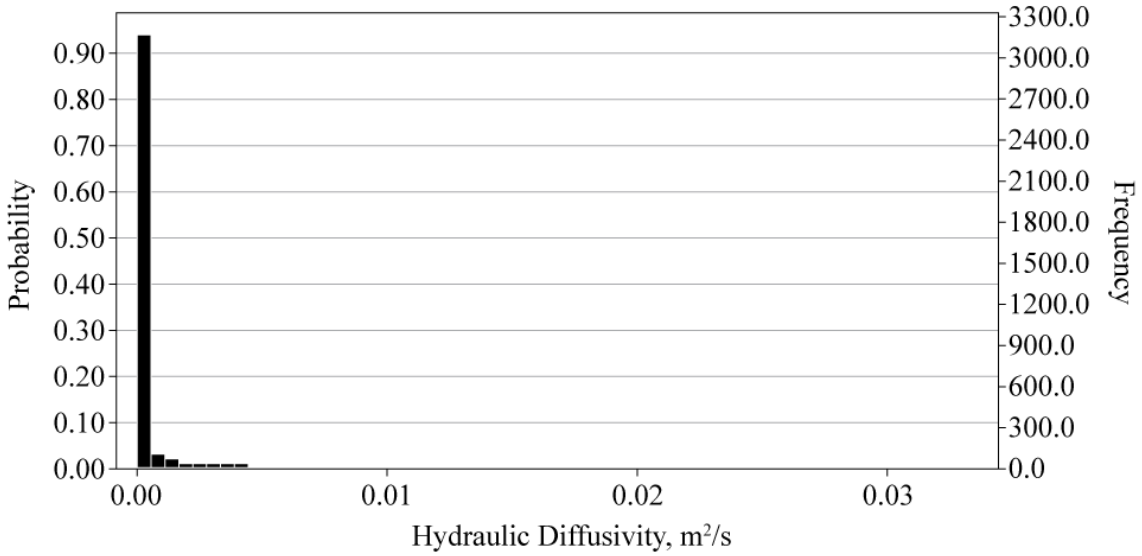

Figure 6.34 North Morecambe Sherwood Sandstone Reservoir forecast charts for hydraulic diffusivity modelled using Oracle Crystal Ball Software. (a) Forecast chart for the entire North Morecambe Sherwood Sandstone reservoir, (b) the illite free zone, and (c) the illite affected zone.

RESERVOIR ZONE	MINIMUM	P10	MEDIAN (P50)	MEAN	P90	MAXIMUM
ENTIRE RESERVOIR	1.13E-10	3.14E-07	1.84E-05	1.23E-02	2.18E-03	3.23E+01
ILLITE FREE ZONE	3.57E-10	4.26E-06	9.28E-04	6.22E-03	1.67E-02	4.62E-01
ILLITE AFFECTED ZONE	1.08E-09	1.77E-07	4.71E-06	6.14E-04	2.64E-04	5.30E-01

Table 6.16 Hydraulic diffusivity estimates (m^2/s) from Monte Carlo simulation in Oracle Crystal Ball software for the North Morecambe Sherwood Sandstone reservoir.

The estimates of hydraulic diffusivity were used to estimate the distance over which aquifer movement has occurred throughout the productive lifetime of eight years within the North Morecambe Sherwood Sandstone reservoir. The mean and median values of hydraulic diffusivity were used to estimate the distance over which aquifer pressures are likely to have been perturbed throughout the productive lifetime, as they were considered to best represent the data. The results are shown in Table 6.17.

6.5.1.4.2. ESTIMATION OF THE CUMULATIVE VOLUME OF WATER INFLUX INTO THE NORTH MORECAMBE SHERWOOD SANDSTONE RESERVOIR

The unsteady state water influx theory of Van Everdingen and Hurst (1949) was used to estimate the cumulative volume of water influx, W_e, from the aquifer, into the North Morecambe Sherwood Sandstone reservoir. Throughout the study the North Morecambe Sherwood Sandstone reservoir was considered to be a bounded aquifer rather than infinite, as the East Irish Sea basin is substantially faulted and, based on the results of Table 6.17, the North Morecambe reservoir is only likely to be in pressure communication with aquifer waters up to a total distance of ca. 2000 m away over the productive lifetime of eight years.

Aquifers can be characterised as either radial or linear. In terms of the North Morecambe Sherwood Sandstone reservoir, the aquifer type was unknown, therefore, both models were assessed throughout the analysis.

For a radial aquifer, equation 5.10, Table 6.18, can be used to estimate the cumulative volume of water influx, W_e, into the North Morecambe Sherwood Sandstone reservoir. It requires calculation of the aquifer constant, U, as defined by equation 5.11, Table 6.18. Estimation of U is dependent on calculation of the encroachment angle, f, using equation 5.12, Table 6.18, which is used for aquifers which subtend angles of less than 360° at the centre of the reservoir-aquifer system. As the North Morecambe Sherwood Sandstone reservoir is bounded by faults to the west, south and east, it is estimated that the angle of water encroachment into the reservoir is 90°, see Figure 6.35. Determination of U also requires the other

necessary parameters, porosity, aquifer height, the compressibility of the rock and fluid and the reservoir radius.

Equation 5.13, Table 6.18, is then used to estimate the aquifer unit function, dimensionless time, t_D, over which water influx occurs, and equation 5.14, Table 6.18, is used to determine the dimensionless radius. The dimensionless cumulative water influx function, $W_D(t_D)$, can then be determined from graphs (Figure 6.36 and Figure 6.37) after Van Everdingen and Hurst (1949), in Dake (1978), using the results of equations 5.13 and 5.14, Table 6.18.

Equation 5.15, Table 6.18, can be used check the W_D value estimated in equation 5.10, Table 6.18: in cases of bounded aquifers, irrespective of the geometry, there is a value of t_D for which the dimensionless water influx reaches a constant maximum value. This value is dependent upon the geometry as defined in equation 5.15, Table 6.18. The final results are displayed in Table 6.19 (a).

For a linear aquifer, equation 5.10, Table 6.18, can again be used to estimate W_e into the North Morecambe Sherwood Sandstone reservoir. It is the same equation as that for the example of a radial aquifer, however, the parameters U and t_D are calculated in a different way, i.e. the radial factors in equations 5.11 and 5.13, Table 6.18, are substituted for linear in equations 5.16 and 5.17, Table 6.18, respectively. Linear aquifer geometry is outlined in Figure 6.38.

The effective length of the aquifer, L, has previously been estimated based on the hydraulic diffusivity calculations (Table 6.17), therefore both equations 5.16 and 5.17, Table 6.18, can be solved. Equation 5.10, Table 6.18, can finally be solved by substituting in the values obtained for U (equation 5.16, Table 6.18). Once again, the dimensionless cumulative water influx function, $W_D(t_D)$, is determined from Figure 6.36 and Figure 6.37. As for the example of a radial aquifer, there is a check for the linear aquifer W_D value estimated in equation 5.10, Table 6.18: for a linear aquifer the maximum value for W_D is 1. The final results are displayed in Table 6.19 (b).

PARAMETER	UNITS	ENTIRE RESERVOIR		ILLITE FREE ZONE		ILLITE AFFECTED ZONE	
		MEAN	MEDIAN	MEAN	MEDIAN	MEAN	MEDIAN
HYDRAULIC DIFFUSIVITY	m^2/s	1.23E-02	1.84E-05	6.22E-03	9.28E-04	6.14E-04	4.71E-06
TIME	years	8.00	8.00	8.00	8.00	8.00	8.00
TIME	secs	2.52E+08	2.52E+08	2.52E+08	2.52E+08	2.52E+08	2.52E+08
DIFFUSION DISTANCE	m^2	3.10E+06	4.63E+03	1.57E+06	2.34E+05	1.55E+05	1.19E+03
AQUIFER LENGTH	m	1760.60	68.07	1253.14	483.89	393.74	34.46

Table 6.17 Estimations of aquifer length in the North Morecambe Sherwood Sandstone reservoir based on hydraulic diffusivity estimates.

RADIAL AQUIFER EQUATIONS	EQUATION NUMBER
$W_e = U\Delta P W_D(t_D)$	5.10
$U = 2\pi f \varphi h (c_w + c_f) r_o^2$	5.11
$f = \frac{(encroachment\ angle)^\circ}{360^\circ}$	5.12
$t_D = \frac{kt}{\varphi\mu(c_w + c_f)r_o^2}$	5.13
$R_{eD} = \frac{r_e}{r_o}$	5.14
$Radial\ W_D(max) = \frac{1}{2}(r_{eD}^2 - 1)$	5.15
LINEAR AQUIFER EQUATIONS	
$W_e = U\Delta P W_D(t_D)$	5.10
$U = wLh\varphi(c_w + c_f)$	5.16
$t_D = \frac{kt}{\varphi\mu(c_w + c_f)L^2}$	5.17

Table 6.18 Radial and linear aquifer equations for the estimation of the cumulative volume of water influx into a reservoir, W_e, previously introduced in Chapter 5. See Chapter 5 for definition of symbols.

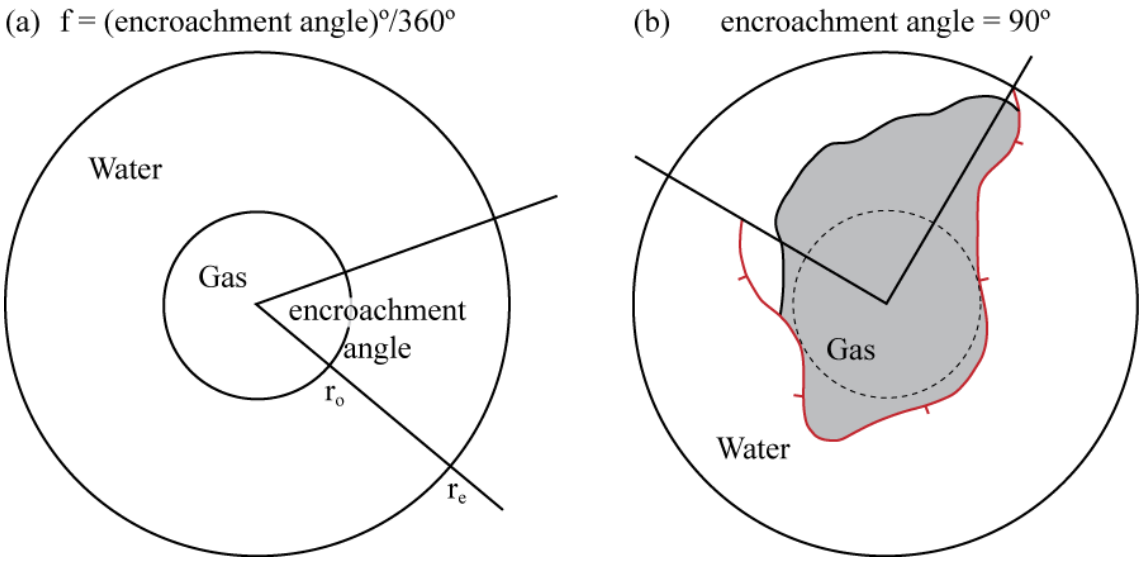

Figure 6.35 Radial aquifer geometry (a) schematic (b) the North Morecambe Sherwood Sandstone reservoir. The North Morecambe Sherwood Sandstone reservoir outline can be observed in (b) with the bounding faults (red) to the west, south and east. The encroachment angle is 90° with water influx from the north.

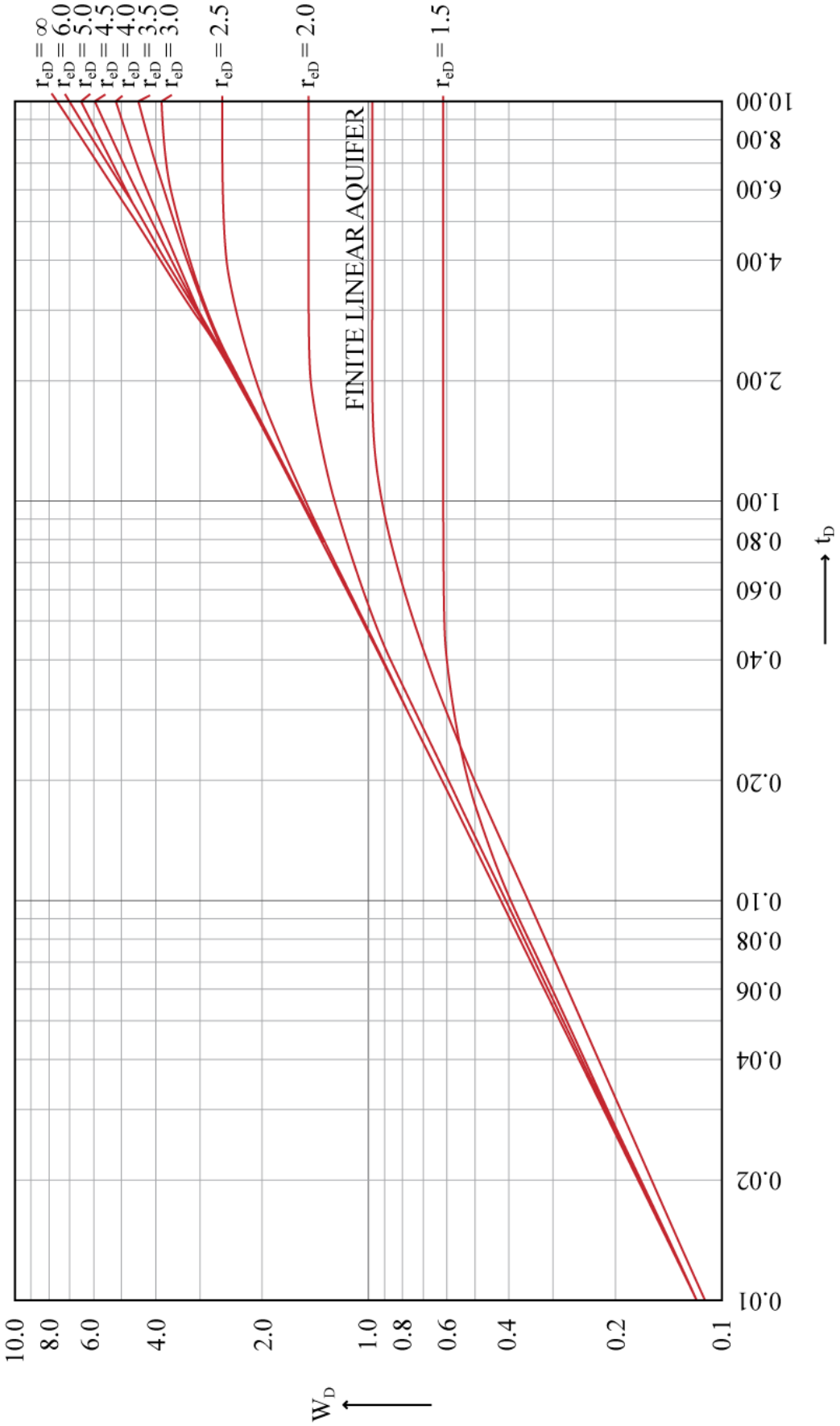

Figure 6.36 Dimensionless water influx for radial and linear flow. After Van Everdingen and Hurst (1949), in Dake (1978).

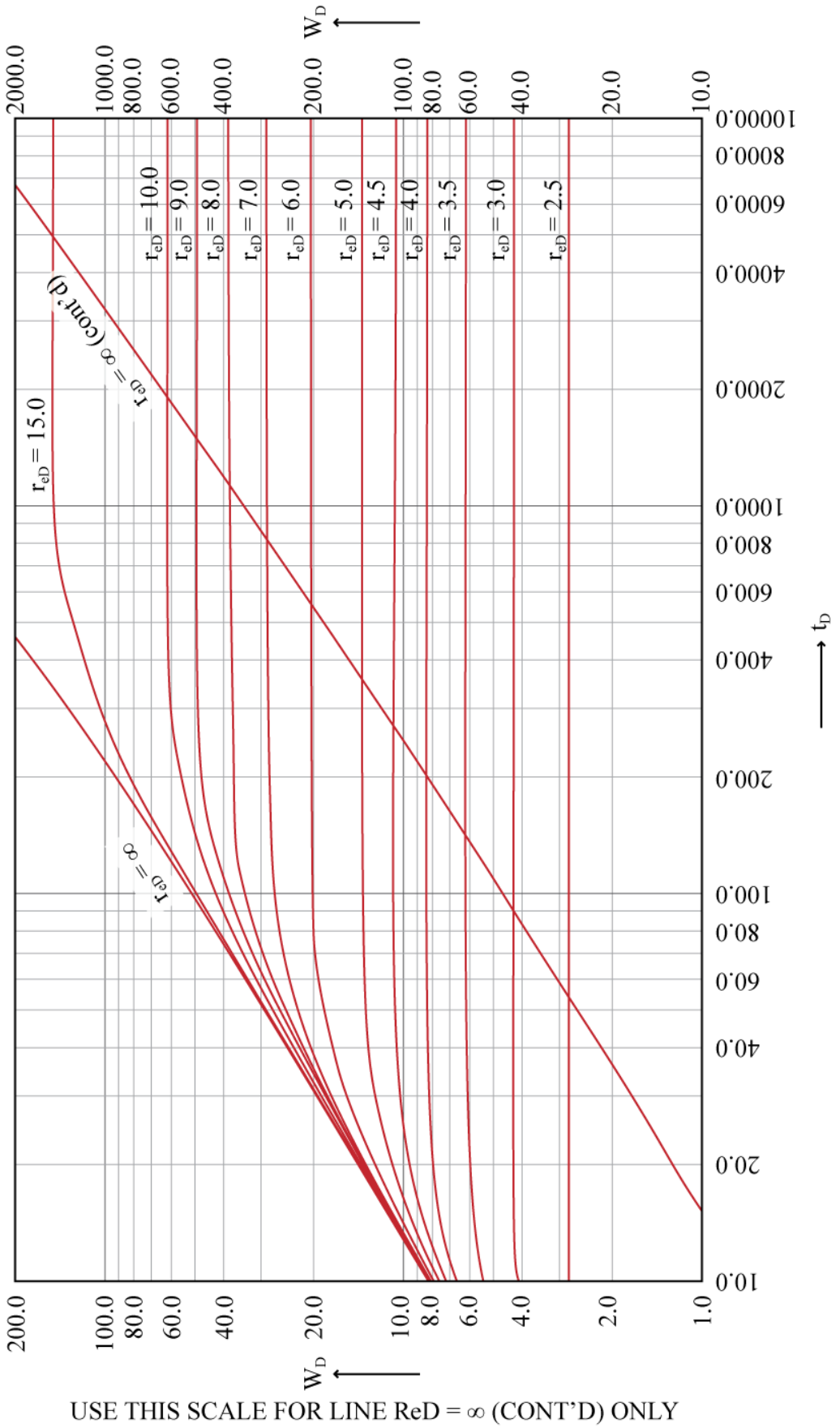

Figure 6.37 Dimensionless water influx for radial and linear flow. After Van Everdingen and Hurst (1949), in Dake (1978).

(a) FINITE RADIAL AQUIFER

PARAMETER	OVERALL RESERVOIR MEAN	ILLITE FREE ZONE MEAN	ILLITE AFFECTED ZONE MEAN
f	0.25	0.25	0.25
t_D	17.10	36.00	4.21
U	2.98	3.41	2.81
R_{eD}	1.64	1.45	1.14
$W_D(t_D)$	0.84	0.55	0.15
W_e (m^3)	1.82E+07	1.39E+07	3.13E+06
Radial W_D (max)	0.840	0.556	0.153

(b) FINITE LINEAR AQUIFER

PARAMETER	OVERALL RESERVOIR MEAN	ILLITE FREE ZONE MEAN	ILLITE AFFECTED ZONE MEAN
t_D	42.10	175.00	207.00
U	2.14	1.74	0.45
$W_D(t_D)$	1.00	1.00	1.00
W_e (m^3)	1.56E+07	1.27E+07	3.29E+06
Linear W_D (max)	1.00	1.00	1.00

Table 6.19 Results of the Van Everdingen and Hurst (1949) unsteady state water influx theory for the North Morecambe Sherwood Sandstone reservoir, as (a) a finite radial aquifer, and (b) a finite linear aquifer.

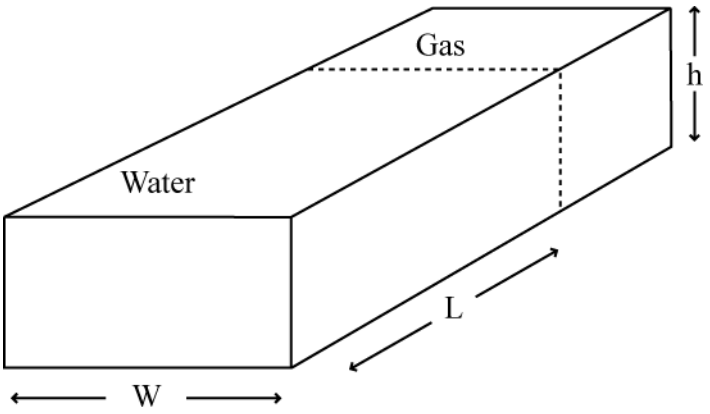

Figure 6.38 Linear aquifer geometry schematic. After Dake (1978).

6.5.1.4.3. ESTIMATING OGIP BASED ON AQUIFER MODELS

We have seen in section 6.5.1.3. that the industry estimated OGIP value of 36.529 billion cubic metres of natural gas for the North Morecambe Sherwood Sandstone reservoir may be incorrect due to the reservoir experiencing a moderate to strong water drive and the corresponding estimated value of W_e (the cumulative volume of water influx into the reservoir) being negative. Using the mean estimates of W_e obtained using the finite radial and finite linear aquifer models (Table 6.19) it is possible to obtain values of OGIP through rearranging equation 5.3 (Table 6.14) to equation 5.18 in Table 6.20.

EQUATION	EQUATION NUMBER
$OGIP = \frac{G_p - W_e E}{1 - E/E_i}$	(5.18)

Table 6.20 Equation to estimate the original gas in place within a water drive reservoir. After Dake (1978). See Chapter 5 for definition of symbols.

Estimates of OGIP were obtained using this method for the mean W_e value of the finite radial aquifer model, the mean finite linear aquifer model, and a "base case" aquifer model whose values represent the average of the two (radial and linear) mean values of W_e. Results are shown in Table 6.21.

PARAMETER	ABBREVIATION	UNITS	VALUE
Cumulative Volume of Gas Produced	G_p	m^3	1.93E+10
Gas Expansion Factor	E	Dimensionless	53.227
Initial Gas Expansion Factor	E_i	Dimensionless	143.000
Finite Radial Aquifer Mean Cumulative Volume of Water Influx	W_e Radial Mean	m^3	1.82E+07
Finite Radial Aquifer Mean Original Gas In Place Estimate	**OGIP Radial Mean**	**m^3**	**2.927E+10**
Finite Linear Aquifer Mean Cumulative Volume of Water Influx	W_e Linear Mean	m^3	1.56E+07
Finite Linear Aquifer Mean Original Gas In Place Estimate	**OGIP Linear Mean**	**m^3**	**2.949E+10**
Base Case Cumulative Volume of Water Influx	W_e Base Case	m^3	1.690E+07
Base Case Original Gas In Place Estimate	**OGIP Base Case**	**m^3**	**2.938E+10**

Table 6.21 Estimates of original gas in place (OGIP) using equation 5.18 (Table 6.20) and based on mean W_e values (cumulative volume of water influx into a reservoir) from aquifer models (section 6.5.1.4.2.).

In comparison with the W_e value estimated using the industry estimates of OGIP of -0.0675 billion cubic metres, all W_e estimates in Table 6.21 are positive values and OGIP estimates are reduced by a maximum of 7.26 billion cubic metres of natural gas. This analysis suggests that the industry estimated OGIP value of 36.529 billion cubic metres is too large. As such, the newly estimated values of OGIP will be input to both theoretical and effective CO_2 storage capacity equations in section 6.5.2.4. as they are considered to be a more accurate representation of the North Morecambe Sherwood Sandstone reservoir.

6.5.2. ESTIMATION OF RESERVOIR FLUID COMPRESSIBILITY AND IMPLICATIONS FOR CO_2 STORAGE CAPACITY ESTIMATION

Estimations of the gas compressibility factor (or Z-factor) of the North Morecambe Sherwood Sandstone reservoir gas composition were made using both RefProp (Lemmon et al., 2013) and the Lawrence Berkeley National Laboratory online calculator, WebGasEOS (Reagan and Oldenburg, 2006) enabling several equations of state to be utilised for analysis.

The calculated results of the Z-factor were input into both methods for calculating theoretical (including Bachu et al. (2007), Holloway et al. (2006) and Tseng et al. (2012)) and effective CO_2 storage capacity (including Tseng et al. (2012)). Once again, through variation of both estimation of Z-factor, the utilisation of several equations of state and the different methods used to calculate CO_2 storage capacity, a range of results were produced.

6.5.2.1. GAS COMPRESSIBILITY FACTOR ESTIMATION

6.5.2.1.1. REFPROP ESTIMATIONS OF GAS COMPRESSIBILITY FACTOR

RefProp (Lemmon et al., 2013) was once again used to investigate Z-factor variability of the gas compositions stated in Table 6.22 at constant temperature, whilst varying pressure and the equation of state used Figure 6.39. The temperature was maintained at the initial reservoir temperature of 33.3 °C (306.483 K) within

the North Morecambe Sherwood Sandstone reservoir as data encompassing temperature change through time was not available. Pressure was varied between the initial reservoir pressure of 12.411 MPa and the final reservoir pressure of 5.184 MPa. Gas compressibility factors were produced for three different equations of state: Peng-Robinson (Peng and Robinson, 1976), GERG-2008 (Kunz and Wagner, 2012), and the AGA8 Model (Starling and Savidge, 1992). Graphs of the results are displayed in Figure 6.39, and the main results to be used in the methods of storage capacity estimation are summarised in Table 6.23.

Figure 6.39 shows the variability of the gas compressibility factor with the particular equation of state used for the gas compositions shown. In general, the GERG-2008 (Kunz and Wagner, 2012) and AGA8 Model (Starling and Savidge, 1992) predict very similar gas compressibilities. At lower pressures the Peng-Robinson equation of state (Peng and Robinson, 1976) predicts a higher degree of gas compressibility for all gas mixes with increasing mole percentages of CO_2. As pressure increases, there is a cross-over and the GERG-2008 (Kunz and Wagner, 2012) and AGA8 Model (Starling and Savidge, 1992) tend to predict the highest gas compressibilities. The cross-over occurs at lower and lower pressures as the mole percentage of CO_2 increases in the overall gas composition.

	MOLE FRACTION					
	Initial	20% CO_2	40% CO_2	60% CO_2	80% CO_2	99% CO_2
NORTH MORECAMBE SHERWOOD SANDSTONE RESERVOIR INITIAL GAS COMPOSITION						
Methane	0.810200	0.648160	0.486120	0.324080	0.162040	0.008102
Ethane	0.061100	0.048880	0.036660	0.024440	0.012220	0.000611
Carbon Dioxide	0.068800	0.255040	0.441280	0.627520	0.813760	0.990688
Nitrogen	0.058900	0.047120	0.035340	0.023560	0.011780	0.000589
Hydrogen	0.000800	0.000640	0.000480	0.000320	0.000160	0.000008
Helium	0.000200	0.000160	0.000120	0.000080	0.000040	0.000002
TOTAL	**1.000000**	**1.000000**	**1.000000**	**1.000000**	**1.000000**	**1.000000**
PURE METHANE						
Methane	1.0000	0.8000	0.6000	0.4000	0.2000	0.0100
Carbon Dioxide	0.0000	0.2000	0.4000	0.6000	0.8000	0.9900
TOTAL	**1.0000**	**1.0000**	**1.0000**	**1.0000**	**1.0000**	**1.0000**
GAS MIX 1 COMPOSITION						
Methane	0.8500	0.6800	0.5100	0.3400	0.1700	0.0085
Ethane	0.0500	0.0400	0.0300	0.0200	0.0100	0.0005
Propane	0.0200	0.0160	0.0120	0.0080	0.0040	0.0002
Nitrogen	0.0800	0.0640	0.0480	0.0320	0.0160	0.0008
Carbon Dioxide	0.0000	0.2000	0.4000	0.6000	0.8000	0.9900
TOTAL	**1.0000**	**1.0000**	**1.0000**	**1.0000**	**1.0000**	**1.0000**
GAS MIX 2 COMPOSITION						
Methane	0.7000	0.5600	0.4200	0.2800	0.1400	0.0070
Ethane	0.2300	0.1840	0.1380	0.0920	0.0460	0.0023
Propane	0.0500	0.0400	0.0300	0.0200	0.0100	0.0005
Nitrogen	0.0200	0.0160	0.0120	0.0080	0.0040	0.0002
Carbon Dioxide	0.0000	0.2000	0.4000	0.6000	0.8000	0.9900
TOTAL	**1.0000**	**1.0000**	**1.0000**	**1.0000**	**1.0000**	**1.0000**
PURE CARBON DIOXIDE						
Carbon Dioxide	1.0000					
TOTAL	**1.0000**					

Table 6.22 Gas mixture compositions used in RefProp (Lemmon et al., 2013) and WebGasEOS (Reagan and Oldenburg, 2006) modelling of fluid properties.

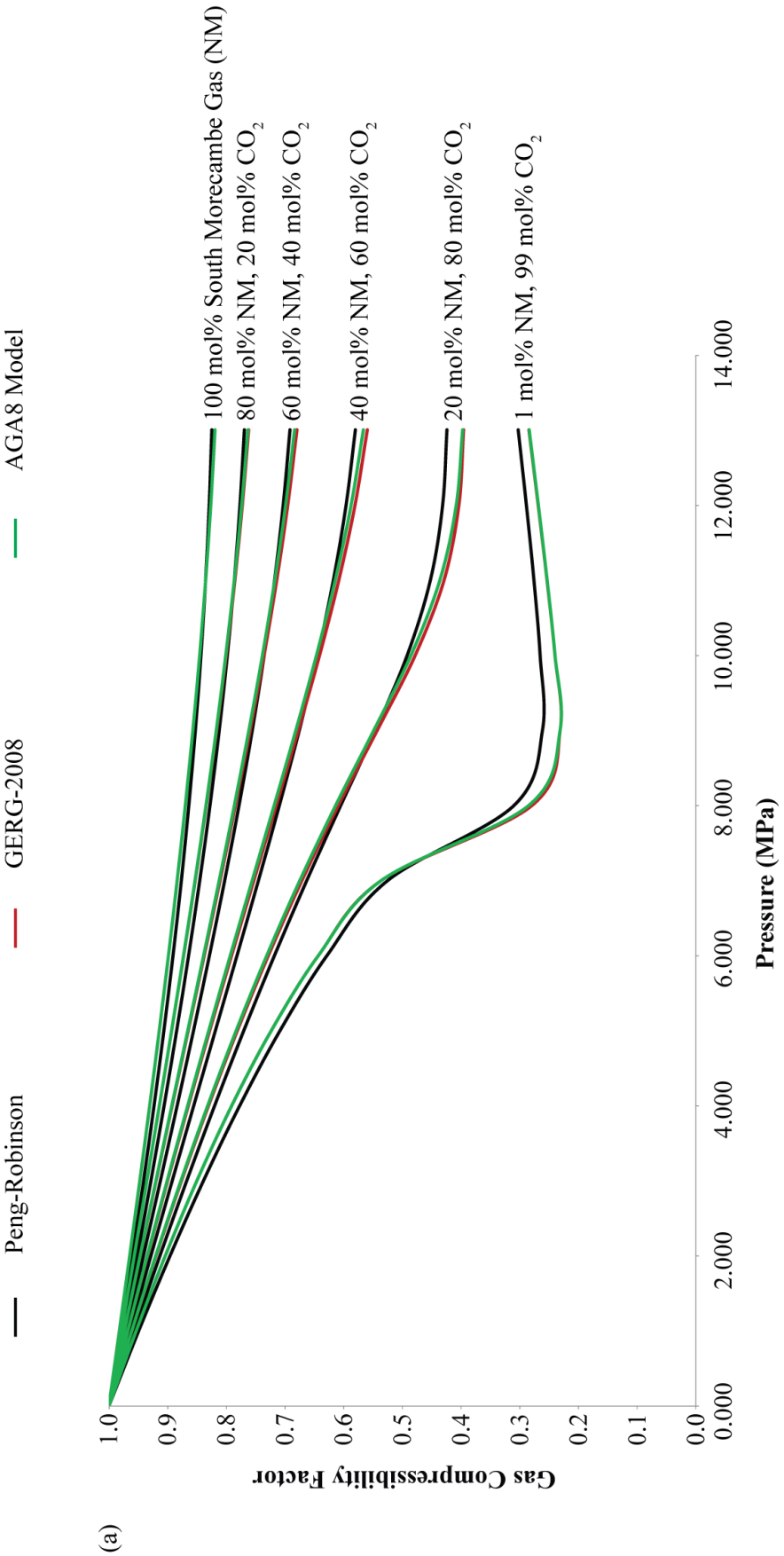
(a)
Gas Compressibility Factor
1.0
0.9
0.8
0.7
0.6
0.5
0.4
0.3
0.2
0.1
0.0
0.000
2.000
4.000
6.000
8.000
10.000
12.000
14.000
Pressure (MPa)
Peng-Robinson
GERG-2008
AGA8 Model
100 mol% South Morecambe Gas (NM)
80 mol% NM, 20 mol% CO2
60 mol% NM, 40 mol% CO2
40 mol% NM, 60 mol% CO2
20 mol% NM, 80 mol% CO2
1 mol% NM, 99 mol% CO2

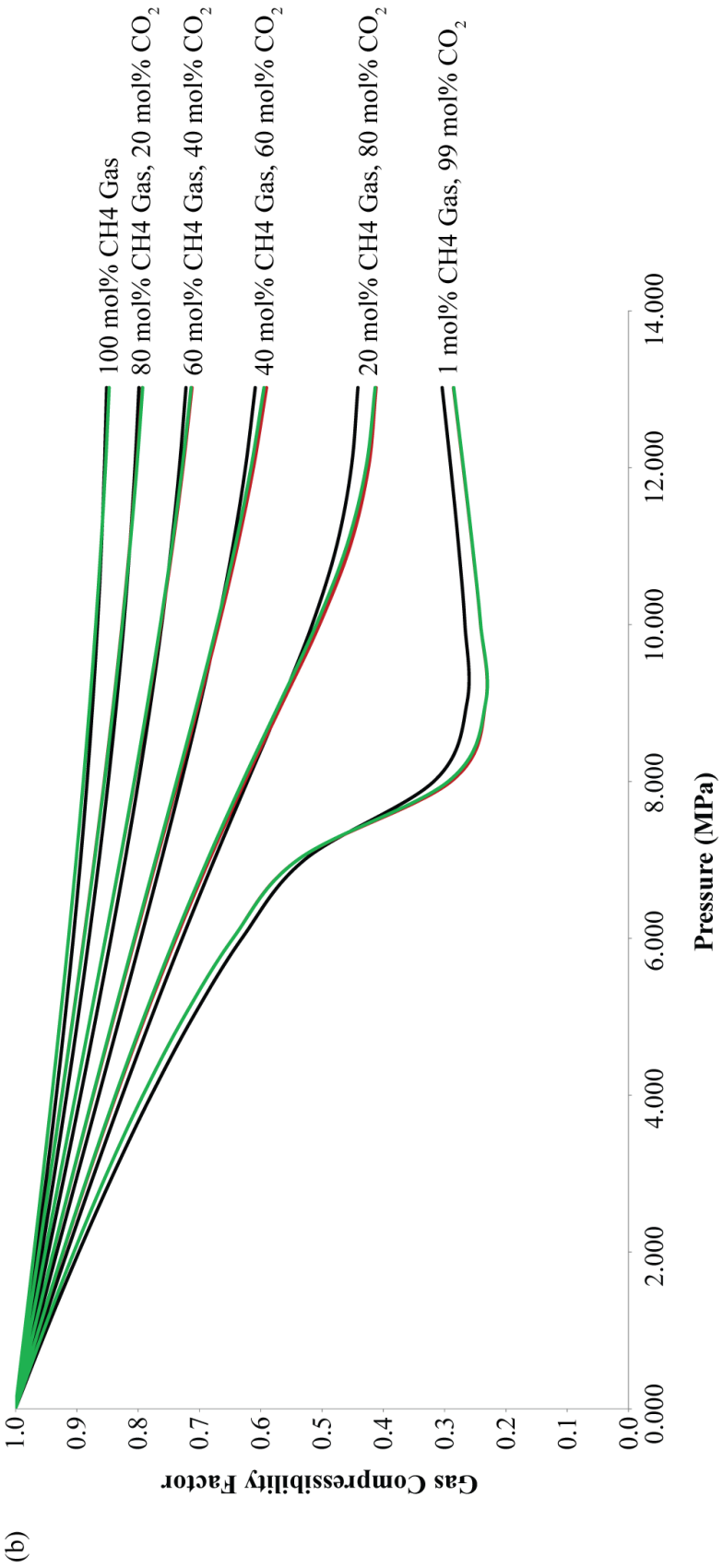
100 mol% CH4 Gas
80 mol% CH4 Gas, 20 mol% CO2
60 mol% CH4 Gas, 40 mol% CO2
40 mol% CH4 Gas, 60 mol% CO2
20 mol% CH4 Gas, 80 mol% CO2
1 mol% CH4 Gas, 99 mol% CO2
Gas Compressibility Factor
Pressure (MPa)
1.0
0.9
0.8
0.7
0.6
0.5
0.4
0.3
0.2
0.1
0.0
0.000
2.000
4.000
6.000
8.000
10.000
12.000
14.000

(b)

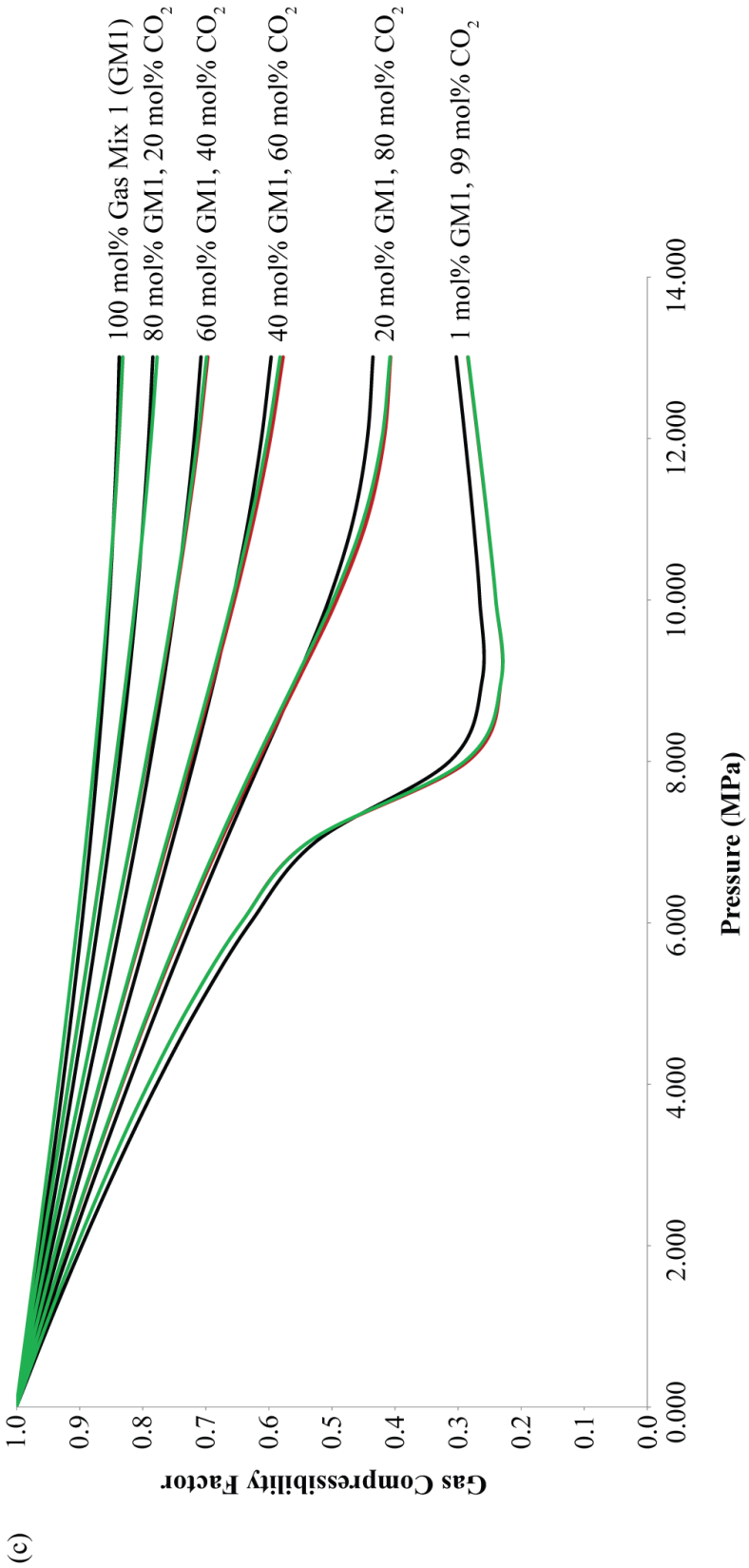
100 mol% Gas Mix 1 (GM1)
80 mol% GM1, 20 mol% CO2
60 mol% GM1, 40 mol% CO2
40 mol% GM1, 60 mol% CO2
20 mol% GM1, 80 mol% CO2
1 mol% GM1, 99 mol% CO2
Gas Compressibility Factor
1.0
0.9
0.8
0.7
0.6
0.5
0.4
0.3
0.2
0.1
0.0
0.000
2.000
4.000
6.000
8.000
10.000
12.000
14.000
Pressure (MPa)

(c)

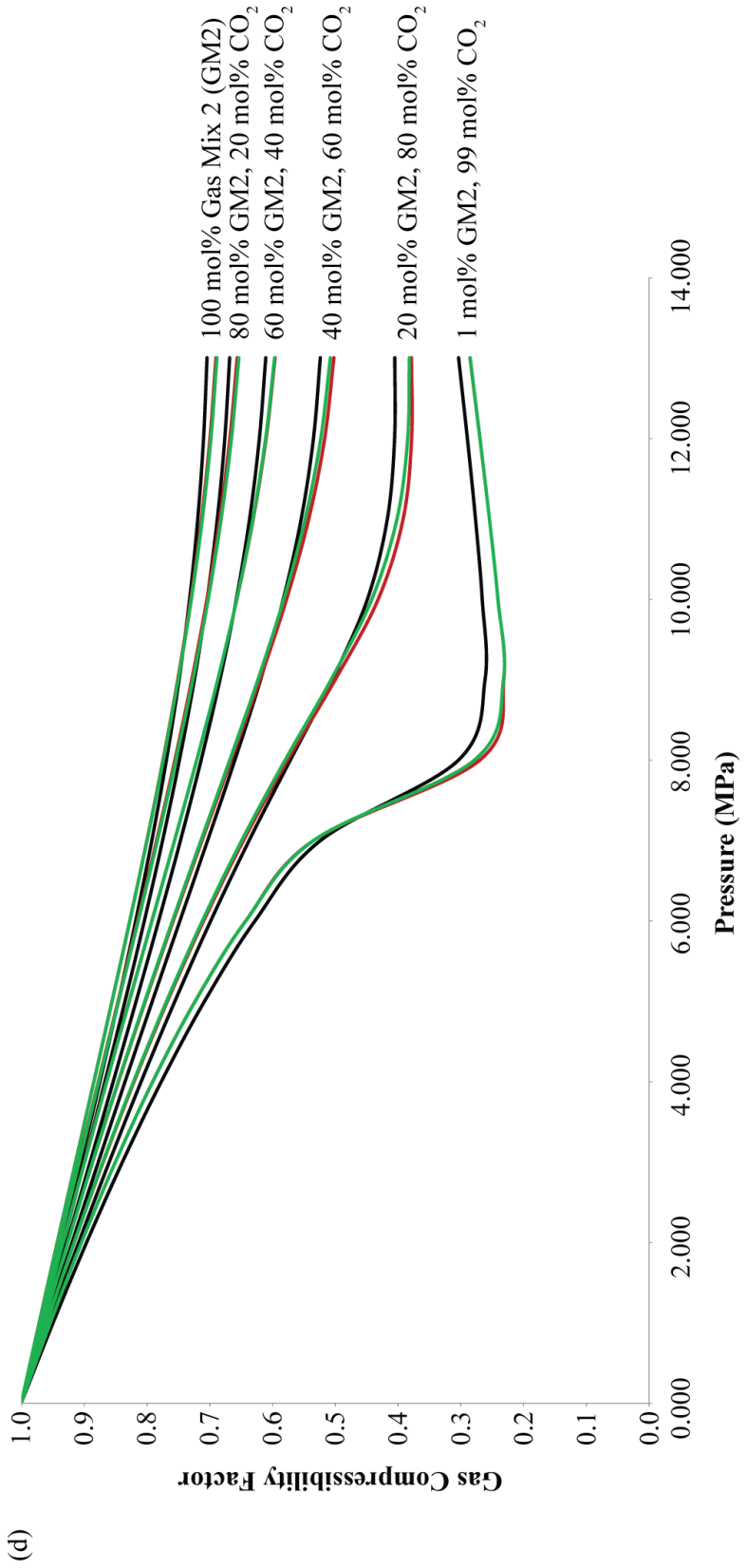
100 mol% Gas Mix 2 (GM2)
80 mol% GM2, 20 mol% CO2
60 mol% GM2, 40 mol% CO2
40 mol% GM2, 60 mol% CO2
20 mol% GM2, 80 mol% CO2
1 mol% GM2, 99 mol% CO2
Gas Compressibility Factor
1.0
0.9
0.8
0.7
0.6
0.5
0.4
0.3
0.2
0.1
0.0
0.000
2.000
4.000
6.000
8.000
10.000
12.000
14.000
Pressure (MPa)

(d)

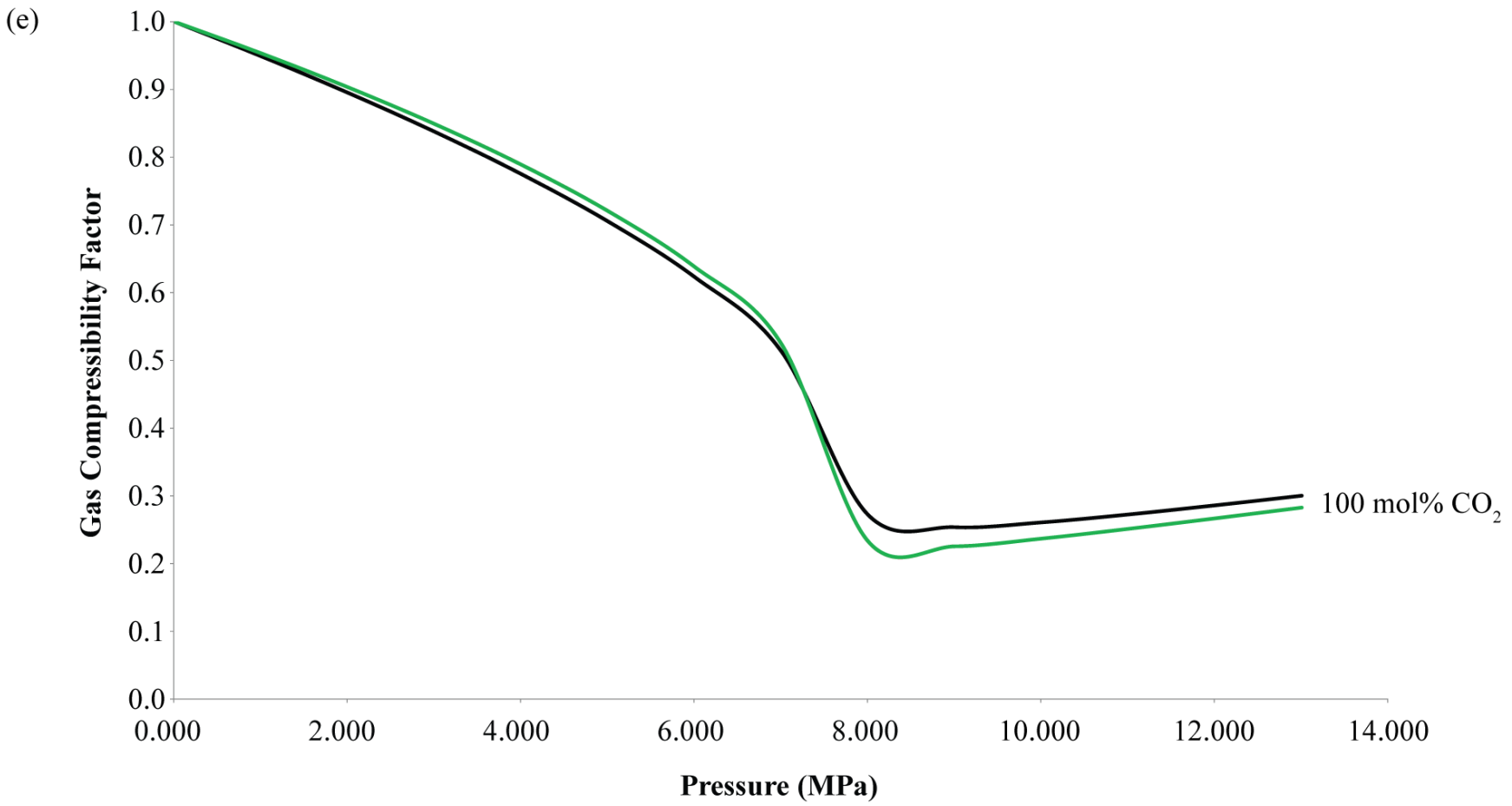

Figure 6.39 North Morecambe Sherwood Sandstone Reservoir Gas Compressibility Factor variation with pressure at constant temperature (33.3 °C) using the Peng-Robinson, GERG-2008 and AGA8 Model Equations of State and different gas compositions, modelled in RefProp (Lemmon et al., 2013). (a) North Morecambe Sherwood Sandstone Reservoir initial gas composition with increasing mol% CO_2; (b) Pure methane with increasing mol% CO_2; (c) Gas mix 1 (as defined in Table 6.22) with increasing mol% CO_2; (d) Gas mix 2 (as defined in Table 6.22) with increasing mol% CO_2; (e) Pure CO_2.

EQUATION OF STATE	PARAMETER	UNITS	NM INITIAL GAS COMPOSITION	PURE METHANE	GAS MIX 1	GAS MIX 2
Peng-Robinson	z_{iCO2}	Dimensionless	0.290	0.290	0.290	0.290
	z_{ihc}	Dimensionless	0.827	0.853	0.839	0.707
	z_{gas}	Dimensionless	0.903	0.916	0.908	0.840
	ρCO_2	kg/m^3	738.65	738.65	738.65	738.65
GERG-2008	z_{iCO2}	Dimensionless	0.272	0.272	0.272	0.272
	z_{ihc}	Dimensionless	0.823	0.850	0.835	0.695
	z_{gas}	Dimensionless	0.911	0.924	0.915	0.850
	ρCO_2	kg/m^3	789.04	789.04	789.04	789.04
AGA8 Model	z_{iCO2}	Dimensionless	0.272	0.272	0.272	0.272
	z_{ihc}	Dimensionless	0.823	0.850	0.835	0.693
	z_{gas}	Dimensionless	0.911	0.924	0.915	0.850
	ρCO_2	kg/m^3	789.06	789.06	789.06	789.06

Table 6.23 Summary of RefProp (Lemmon et al., 2013) estimated isoproperties for various equations of state.

6.5.2.1.2. WEBGASEOS ESTIMATIONS OF GAS COMPRESSIBILITY FACTOR

WebGasEOS (Reagan and Oldenburg, 2006) was again used to estimate the gas compressibility factor of the gas mixtures in Table 6.22 using alternative equations of state including Peng-Robinson (Peng and Robinson, 1976), Peng-Robinson-Stryjek-Vera (Stryjek and Vera, 1986), Redlich-Kwong (Redlich and Kwong, 1949), and Soave-Redlich-Kwong (Soave, 1972). Once again, due to the limited number of species that can be included in the gas mixture analysis, and the lack of integral components to the North Morecambe Sherwood Sandstone reservoir gas composition, it was not possible to simulate results for this mixture. Species lacking in the WebGasEOS tool, but present in the North Morecambe Sherwood Sandstone reservoir gas composition include helium. However, estimations of the gas compressibility factor were predicted for pure methane, gas mix 1, gas mix 2 and pure carbon dioxide fluids, making these results comparable with those of the South Morecambe (this chapter), Hewett Lower Bunter Sandstone reservoir (Chapter 4) and the Hewett Upper Bunter Sandstone reservoir (Chapter 5), and the results of the RefProp analysis of these fluids within the North Morecambe Sherwood Sandstone reservoir (this chapter).

Graphs of the results are shown in Figure 6.40 and a summary of the main isoproperties for input into the storage capacity estimation methodologies are displayed in Table 6.24.

Figure 6.40 shows the variability of the gas compressibility factor with equation of state used as estimated in WebGasEOS (Reagan and Oldenburg, 2006) for the gas compositions shown in Table 6.22, excluding the North Morecambe Sherwood Sandstone reservoir initial gas composition. In general, the Peng-Robinson (Peng and Robinson, 1976) and Peng-Robinson-Stryjek-Vera (Stryjek and Vera, 1986) equations of state predict very similar gas compressibilities. At 100 mole percent natural gas, the Peng-Robinson (Peng and Robinson, 1976) and Peng-Robinson-Stryjek-Vera (Stryjek and Vera, 1986) equations of state predict the highest degree of gas compressibility within the North Morecambe Sherwood Sandstone reservoir, and the Soave-Redlich-Kwong equation of state (Soave, 1972)

predicts the lowest degree of gas compressibility. As increasing mole percentages of CO_2 are incorporated into the gas mixtures (between 20 and 80%), the Redlich-Kwong equation of state (Redlich and Kwong, 1949) predicts the highest degree of gas compressibility in the North Morecambe Sherwood Sandstone reservoir, the Soave-Redlich-Kwong equation of state (Soave, 1972) predicts the lowest gas compressibility factors, and the Peng-Robinson (Peng and Robinson, 1976) and Peng-Robinson-Stryjek-Vera (Stryjek and Vera, 1986) equations of state predict similar gas compressibilities between the two. When there is 99 mole percent CO_2 in the reservoir gas composition, the Peng-Robinson (Peng and Robinson, 1976) and Peng-Robinson-Stryjek-Vera (Stryjek and Vera, 1986) equations of state predict very similar gas compressibilities, and predict the highest degree of gas compressibility in the North Morecambe Sherwood Sandstone reservoir. In comparison, the Redlich-Kwong (Redlich and Kwong, 1949) and Soave-Redlich-Kwong (Soave, 1972) equations of state predict very similar gas compressibilities, and predict the lowest degree of gas compressibility in the North Morecambe Sherwood Sandstone reservoir.

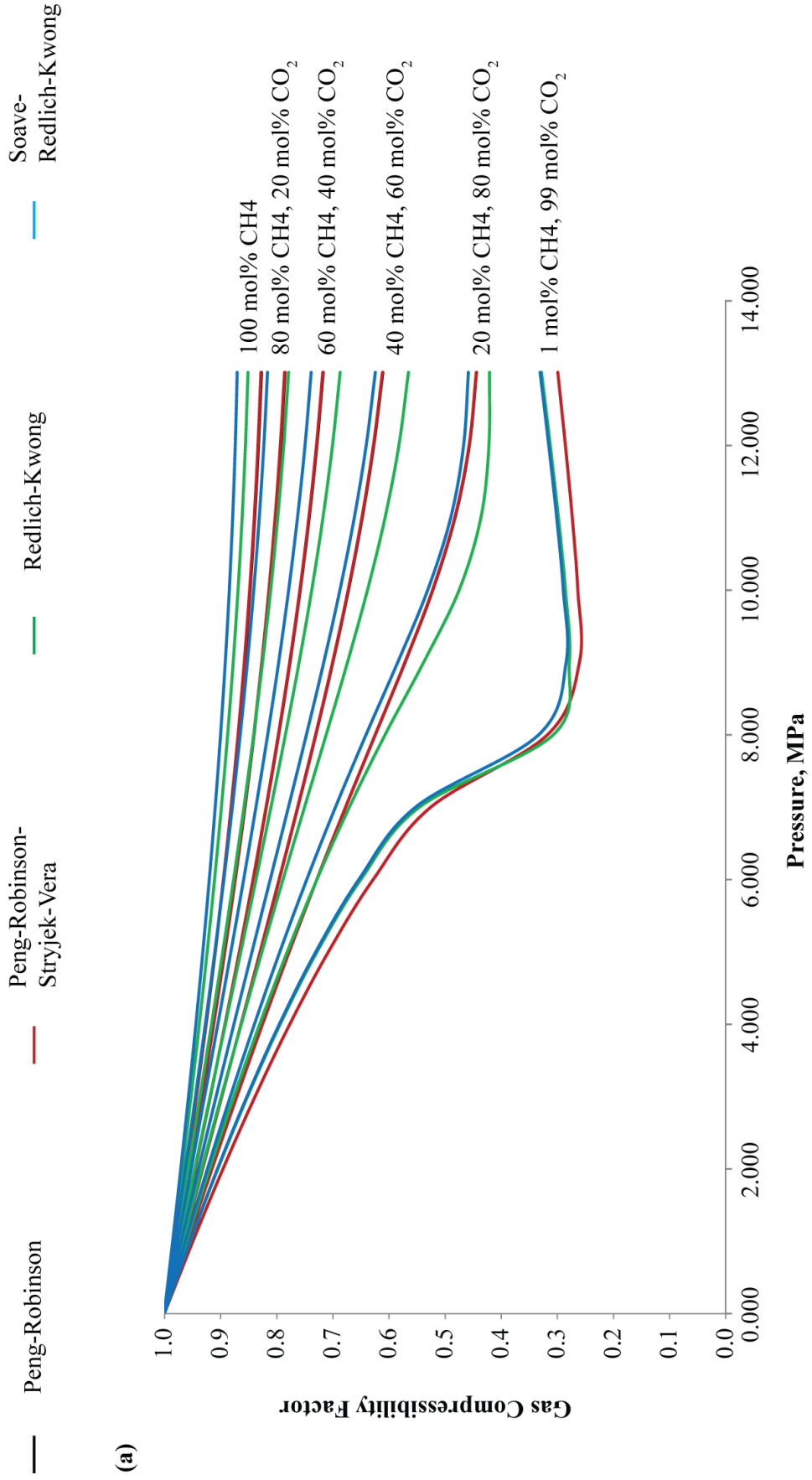
(a)
Peng-Robinson
Peng-Robinson-Stryjek-Vera
Redlich-Kwong
Soave-Redlich-Kwong
100 mol% CH4
80 mol% CH4, 20 mol% CO2
60 mol% CH4, 40 mol% CO2
40 mol% CH4, 60 mol% CO2
20 mol% CH4, 80 mol% CO2
1 mol% CH4, 99 mol% CO2
Gas Compressibility Factor
1.0
0.9
0.8
0.7
0.6
0.5
0.4
0.3
0.2
0.1
0.0
0.000
2.000
4.000
6.000
8.000
10.000
12.000
14.000
Pressure, MPa

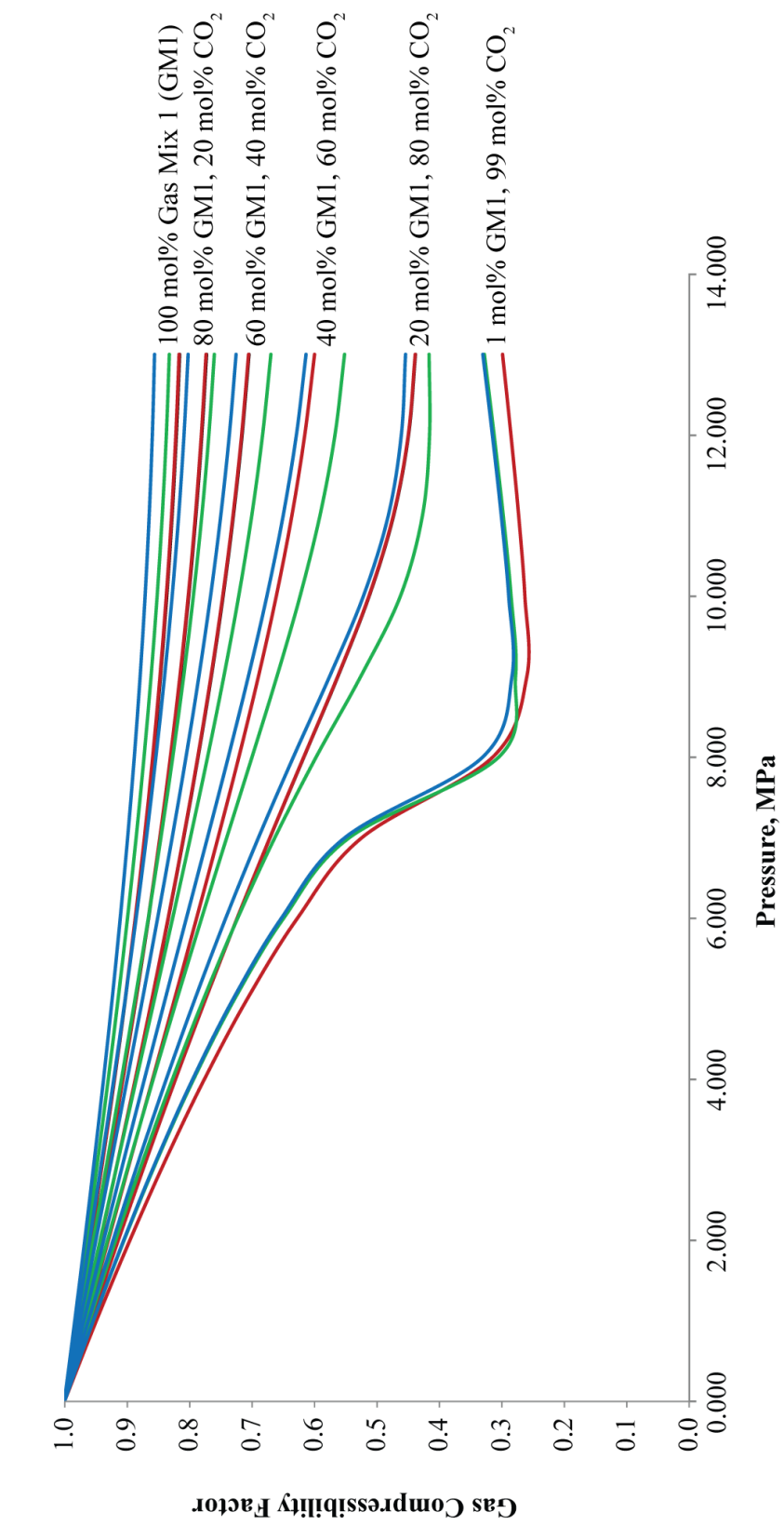
100 mol% Gas Mix 1 (GM1)
80 mol% GM1, 20 mol% CO2
60 mol% GM1, 40 mol% CO2
40 mol% GM1, 60 mol% CO2
20 mol% GM1, 80 mol% CO2
1 mol% GM1, 99 mol% CO2
Gas Compressibility Factor
1.0
0.9
0.8
0.7
0.6
0.5
0.4
0.3
0.2
0.1
0.0
0.000
2.000
4.000
6.000
8.000
10.000
12.000
14.000
Pressure, MPa

(b)

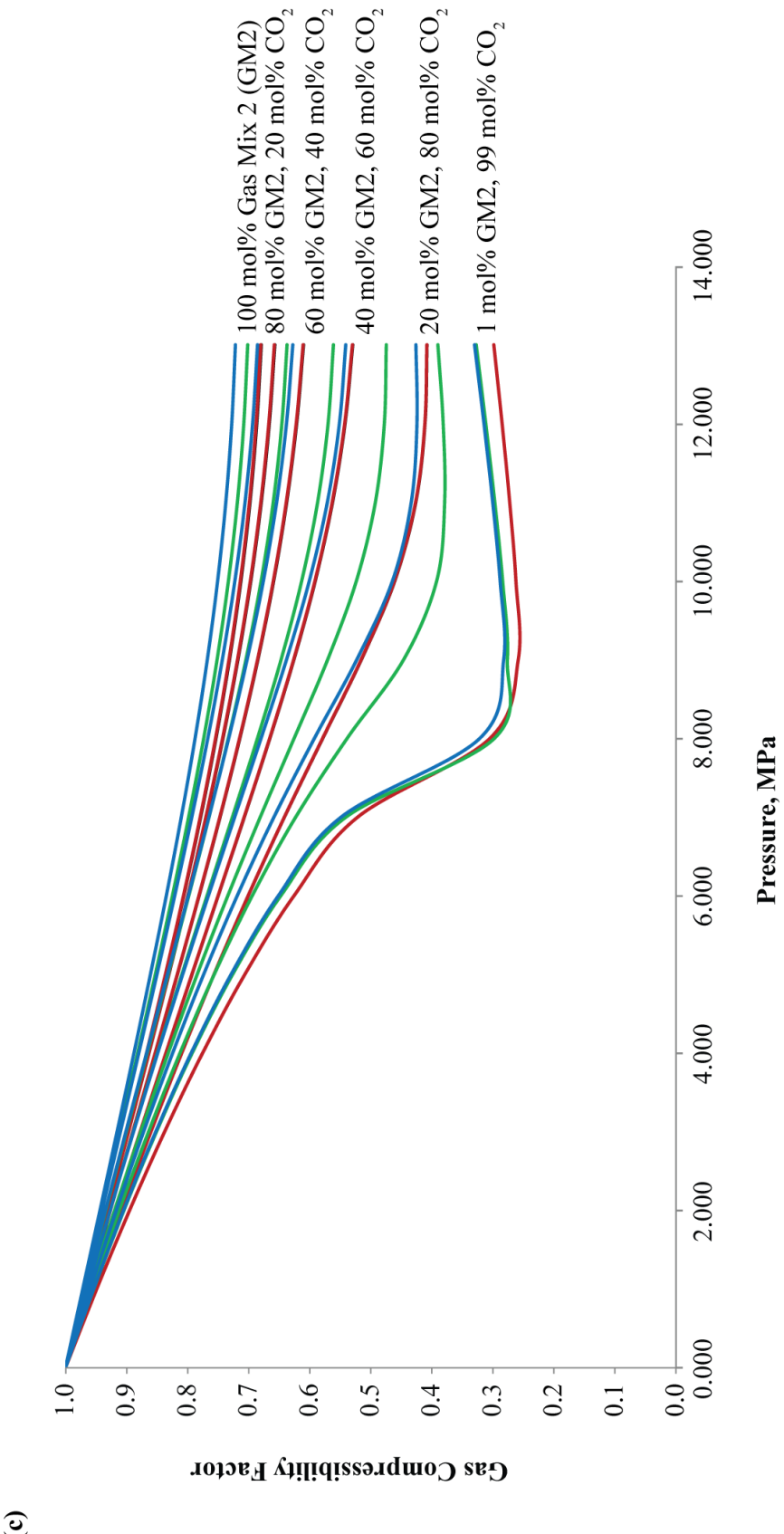
100 mol% Gas Mix 2 (GM2)
80 mol% GM2, 20 mol% CO2
60 mol% GM2, 40 mol% CO2
40 mol% GM2, 60 mol% CO2
20 mol% GM2, 80 mol% CO2
1 mol% GM2, 99 mol% CO2
Gas Compressibility Factor
1.0
0.9
0.8
0.7
0.6
0.5
0.4
0.3
0.2
0.1
0.0
0.000
2.000
4.000
6.000
8.000
10.000
12.000
14.000
Pressure, MPa

(c)

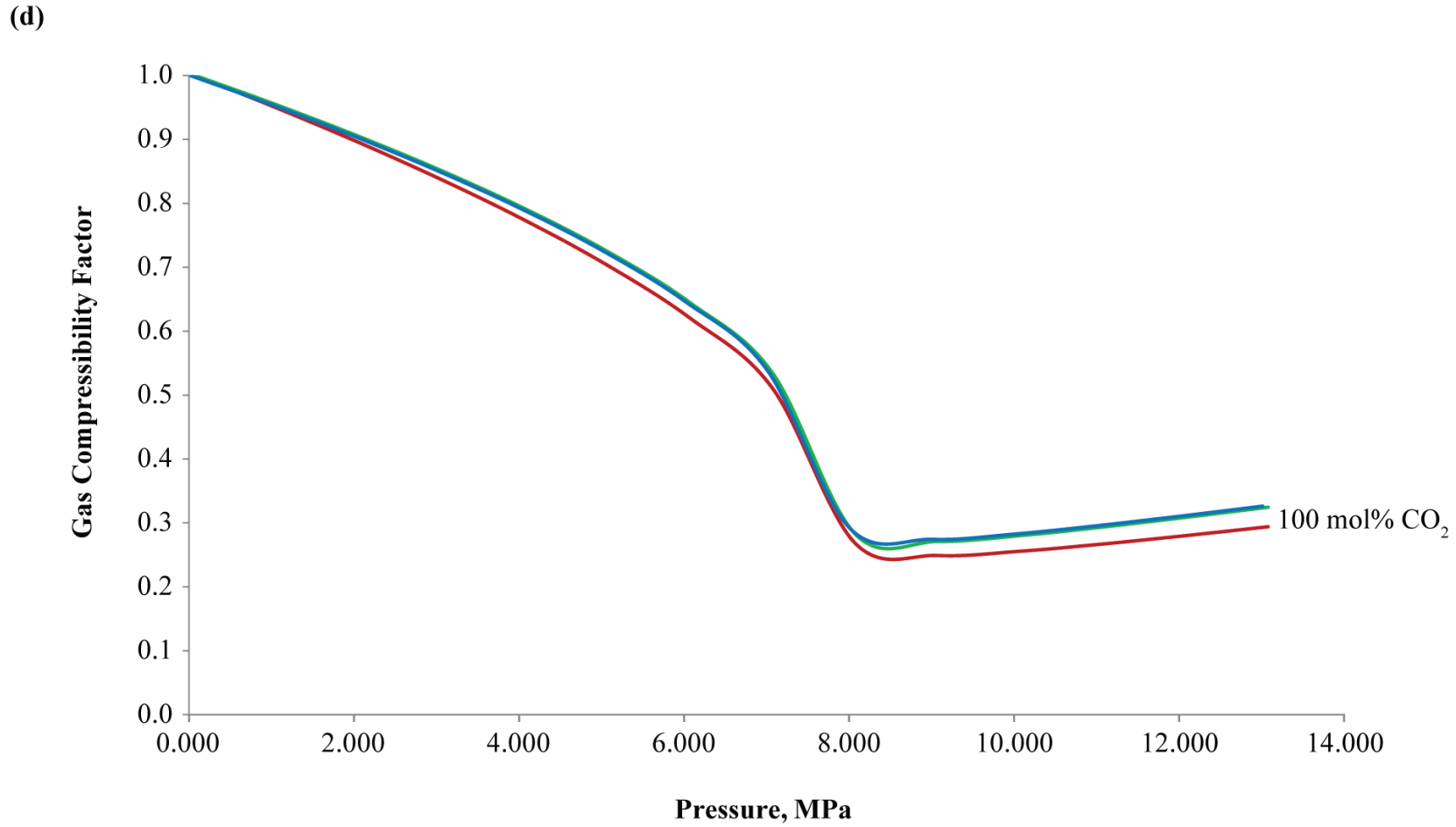

Figure 6.40 North Morecambe Sherwood Sandstone Reservoir Gas Compressibility Factor variation with pressure at constant temperature (33.3 °C) using the Peng-Robinson, Peng-Robinson-Stryjek-Vera, Redlich-Kwong and Soave-Redlich-Kwong Equations of State and different gas compositions, modelled in WebGasEOS (Reagan and Oldenburg, 2006). (a) Pure methane with increasing mol% CO_2; (b) Gas mix 1 (as defined in Table 6.22) with increasing mol% CO_2; (c) Gas mix 2 (as defined in Table 6.22) with increasing mol% CO_2; (d) Pure CO_2.

EQUATION OF STATE	PARAMETER	UNITS	PURE METHANE	GAS MIX 1	GAS MIX 2
Peng-Robinson	z_{iCO2}	Dimensionless	0.285	0.285	0.285
	z_{ihc}	Dimensionless	0.830	0.818	0.683
	z_{gas}	Dimensionless	0.906	0.899	0.830
	ρCO_2	kg/m^3	751.10	751.10	751.10
Peng-Robinson-Stryjek-Vera	z_{iCO2}	Dimensionless	0.285	0.285	0.285
	z_{ihc}	Dimensionless	0.831	0.819	0.684
	z_{gas}	Dimensionless	0.907	0.900	0.831
	ρCO_2	kg/m^3	751.13	751.13	751.13
Redlich-Kwong	z_{iCO2}	Dimensionless	0.315	0.315	0.315
	z_{ihc}	Dimensionless	0.853	0.835	0.705
	z_{gas}	Dimensionless	0.921	0.911	0.847
	ρCO_2	kg/m^3	681.03	681.03	681.03
Soave-Redlich-Kwong	z_{iCO2}	Dimensionless	0.316	0.316	0.316
	z_{ihc}	Dimensionless	0.872	0.858	0.725
	z_{gas}	Dimensionless	0.929	0.921	0.856
	ρCO_2	kg/m^3	677.80	677.80	677.80

Table 6.24 Summary of WebGasEOS Estimated Isoproperties for various Equations of State.

6.5.2.2. GAS FORMATION VOLUME FACTOR ESTIMATION

The gas formation volume factor has been calculated within the North Morecambe Sherwood Sandstone reservoir throughout its productive lifetime using the equations previously defined in Chapter 4 and replicated in this chapter in Table 6.7. The results of the two methods have been plotted in Figure 6.41and can be compared to the industry calculated Z-factor, and resulting estimated gas formation volume factors. The results have been estimated under the initial reservoir temperature condition of 306.483 K, whilst varying pressure.

As can be seen from Figure 6.41, the difference between the results of the two methods and the various equations of state are negligible. This implies that estimates of the gas formation volume factor are very well constrained within the North Morecambe Sherwood Sandstone reservoir, and can be treated with confidence when used within CO_2 storage capacity calculations.

6.5.2.3. ESTIMATION OF CO_2 DENSITY

CO_2 density has been estimated within RefProp (Lemmon et al., 2013) using three equations of state: Peng-Robinson (Peng and Robinson, 1976), GERG-2008 (Kunz and Wagner, 2012), and the AGA8-DC92 Model (Starling and Savidge, 1992). The results were estimated under the initial reservoir temperature conditions of 306.483 K, whilst varying pressure. The results are shown in Figure 6.42.

The results show that CO_2 density increases with pressure. The GERG-2008 (Kunz and Wagner, 2012) and AGA8-DC92 (Starling and Savidge, 1992) equations of state predict very similar CO_2 densities throughout the pressure range shown. The Peng-Robinson equation of state (Peng and Robinson, 1976) predicts very similar CO_2 densities at low pressure, however, above 7.8 MPa, the trend diverges from that of the GERG-2008 (Kunz and Wagner, 2012) and AGA8-DC92 (Starling and Savidge, 1992) equations of state, and predicted CO_2 densities are lower.

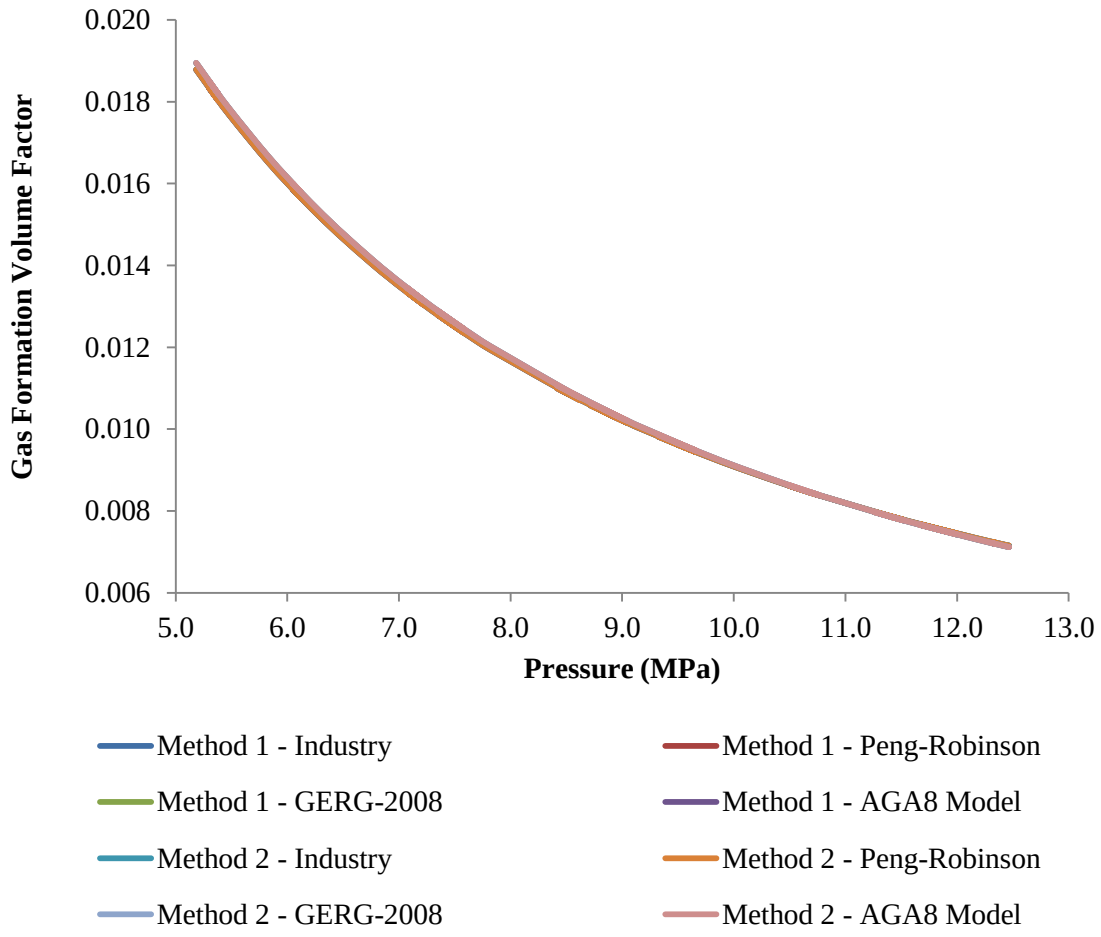

Figure 6.41 Estimation of the gas formation volume factor within the North Morecambe Sherwood Sandstone reservoir using two main methods of calculation and a variety of equations of state, under initial reservoir temperature conditions of 306.483 K. The gas compressibility factor, necessary for calculation of the gas formation volume factor (B_g) was estimated using RefProp (Lemmon et al., 2013). Three equations of state were used: Peng-Robinson (Peng and Robinson, 1976), GERG-2008 (Kunz and Wagner, 2012), and the AGA8-DC92 Model (Starling and Savidge, 1992). These values were compared back to industry calculated values.

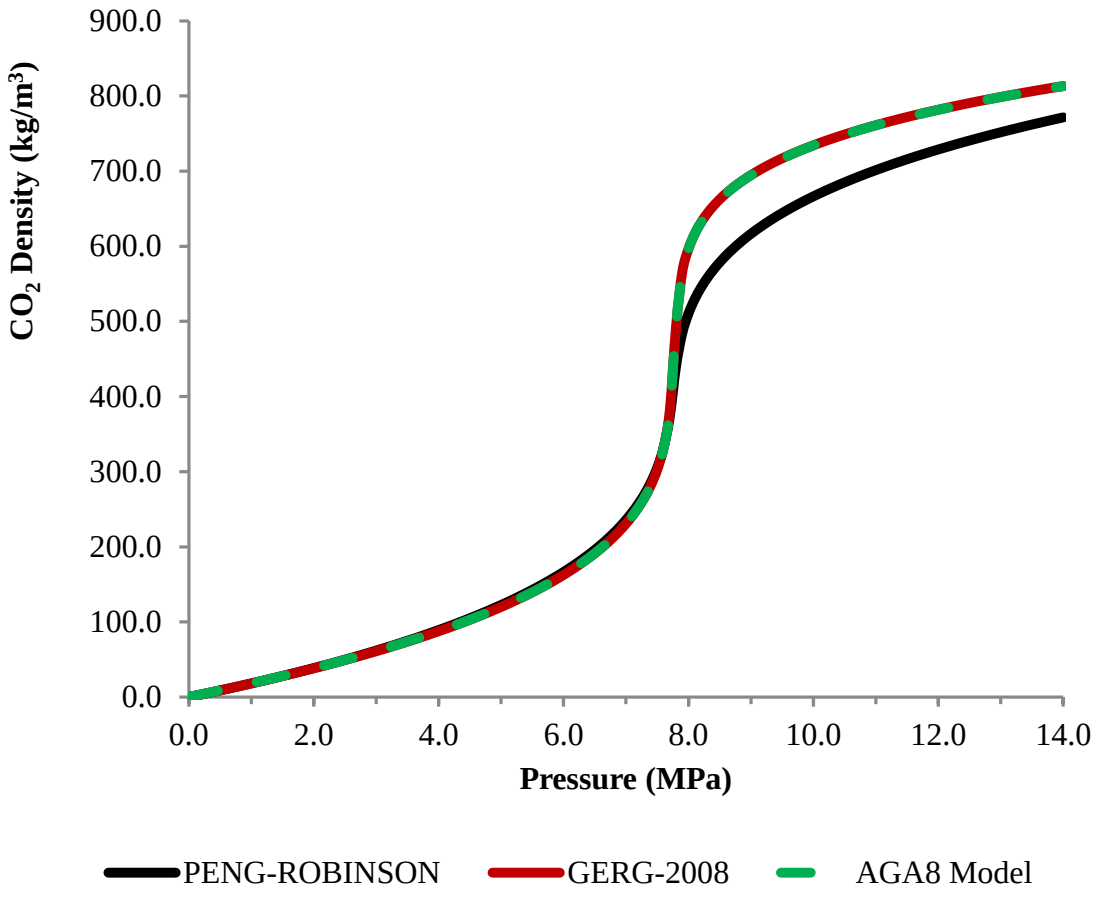

Figure 6.42 Estimations of CO_2 density with pressure within the North Morecambe Sherwood Sandstone reservoir under initial reservoir temperature conditions of 306.483 K. Results have been estimated using RefProp (Lemmon et al., 2013) and various equations of state: Peng-Robinson (Peng and Robinson, 1976), GERG-2008 (Kunz and Wagner, 2012), and the AGA8-DC92 Model (Starling and Savidge, 1992).

6.5.2.4. STORAGE CAPACITY ESTIMATION RESULTS

The estimates of the parameters outlined above, including gas compressibility factor, CO_2 density and gas formation volume factor, for the individual gas compositions were used to calculate both theoretical and effective CO_2 storage capacities of the North Morecambe Sherwood Sandstone reservoir using various published methods.

6.5.2.4.1. THEORETICAL CO_2 STORAGE CAPACITY ESTIMATES

Theoretical CO_2 storage capacity (previously defined in Chapter 1) was estimated for the North Morecambe Sherwood Sandstone reservoir using the methods of Bachu et al. (2007), Holloway et al. (2006), and Tseng et al. (2012).

The North Morecambe Sherwood Sandstone reservoir has produced over 19.342 billion cubic metre of natural gas over its entire productive lifetime, equating to a mass of 16.005 Mt North Morecambe Sherwood Sandstone reservoir gas at standard conditions.

As has been demonstrated previously, the geometric-based approach of Bachu et al. (2007), Table 6.8, equation 1.1, requires the use of parameters that have natural variability within a sandstone reservoir, such as porosity and reservoir height. As such, Monte Carlo simulation has been used once again to reduce the risk of storage capacity estimates produced using this method.

Porosity data was taken from well data made available to Durham University by IHS and assigned a best-fit probability distribution within Oracle Crystal Ball software (Figure 6.27). The best-fit probability distribution for the entire reservoir was a lognormal distribution, for the illite free zone, a logistic distribution and for the illite affected zone, a lognormal distribution. Reservoir height was assigned a uniform distribution due to limited data from wells, i.e. there is an equal chance of obtaining a value for reservoir height between 695.70 and 1178.67 m for the entire reservoir, 553.21 and 967.44 m for the illite free zone and 142.49 and 211.23 m for the illite affected zone. It was not possible to observe the variation of reservoir area as there was no data for this, therefore a standard value of 23997858 m^2

(23.998 km^2) was used for the North Morecambe Sherwood Sandstone reservoir, taken from Cowan and Boycott-Brown (2003).

Monte Carlo simulation then produced the results (probability distributions) illustrated in Figure 6.43 for the entire North Morecambe Sherwood Sandstone reservoir, Figure 6.44 for the illite free zone, and Figure 6.45 for the illite affected zone using the industry estimated OGIP value. Simulated forecast values for the entire North Morecambe Sherwood Sandstone reservoir are shown in Table 6.25 based on (a) the industry estimated OGIP value, (b) the finite radial aquifer model, (c) the finite linear aquifer model, and (d) the base case aquifer model. Simulated forecast values are also shown for the illite free zone in Table 6.26, and the illite affected zone in Table 6.27, based on the industry estimated OGIP values. These results illustrate the vast amount of variability in CO_2 storage capacity estimation. The average range between minimum and maximum storage capacity estimates for the entire North Morecambe Sherwood Sandstone reservoir is 4315.63 Mt CO_2 for the industry estimated OGIP, 5585.03 Mt CO_2 for the finite radial aquifer model, 5360.09 Mt CO_2 for the finite linear aquifer model, 5392.86 Mt CO_2 for the base case aquifer model, 815.62 Mt CO_2 for the illite free zone, and 3022.67Mt CO_2 for the illite affected zone. The mean CO_2 storage capacity values for the industry estimated OGIP value have been plotted alone in Figure 6.46 for the entire North Morecambe Sherwood Sandstone reservoir, Figure 6.47 for the illite free zone, and Figure 6.48 for the illite affected zone. Error bars on the three figures show the minimum, maximum, P10 and P90 values, i.e. the extent of variance.

Theoretical CO_2 storage capacity results by Bachu et al. (2007), Table 6.8, equation 1.2; Holloway et al. (2006), Table 6.8, equation 1.3; and Tseng et al. (2012), Table 6.8, equation 1.4, are based upon the principle that a variable proportion of the pore space occupied by the recoverable reserves will be available for CO_2 storage. The majority of parameters required within the methods are well constrained values which do not show variability. However, as has been demonstrated in section 6.5.1.2., the industry estimated OGIP value may be incorrect and this will affect the storage capacity estimates of Bachu et al. (2007), Table 6.8, equation 1.2, both in terms of the recovery factor, R_f, and the OGIP value, and the storage capacity estimates of Holloway et al. (2006), Table 6.8,

equation 1.3, in terms of the OGIP value. However, the theoretical CO_2 storage capacity method of Tseng et al. (2012), Table 6.8, equation 1.4, is unaffected, consisting only of parameters with well constrained values which do not show variability. As such, the four aquifer models (industry estimates, finite radial, finite linear and base case) have been used once again to provide estimates of OGIP to assess the variability of theoretical CO_2 storage capacity within the North Morecambe Sherwood Sandstone reservoir.

The final results of all the theoretical storage capacity estimation methods are displayed in Figure 6.50. The columns on the bar chart represent the base case aquifer model results and the error bars reflect the results of the finite radial and linear aquifer models. The industry estimated aquifer model results are plotted as circles for comparison.

The mean values of the probability distributions for the entire North Morecambe Sherwood Sandstone reservoir are plotted on Figure 6.50 and stated in Table 6.28 to represent CO_2 storage capacity estimates of the method of Bachu et al. (2007), Table 6.8, equation 1.1. For the alternative methods the final resulting storage capacity estimate is displayed in Figure 6.50 and stated in Table 6.28.

Table 6.28 shows theoretical storage capacity estimates for the North Morecambe Sherwood Sandstone reservoir for different gas compositions: (a) pure methane, (b) gas mix 1 (as defined in Table 6.22), (c) gas mix 2 (as defined in Table 6.22), and (d) the North Morecambe Sherwood Sandstone reservoir initial gas composition. Table 6.28 also states the estimated theoretical storage capacities of the four methods, and for each of the four aquifer models. Capacity estimates vary according to the equation of state used and the tool/software used to model them, i.e. WebGasEOS (Reagan and Oldenburg, 2006) or RefProp (Lemmon et al., 2013). The percentage variation of the storage capacity estimates from the RefProp (Lemmon et al., 2013) estimated Peng-Robinson equation of state (Peng and Robinson, 1976) is also displayed.

The theoretical CO_2 storage capacity estimates of the methods of Bachu et al. (2007), Table 6.8, equation 1.2; Holloway et al. (2006), Table 6.8, equation 1.3; and Tseng et al. (2012), Table 6.8, equation 1.4 are comparable, ranging between 103 and 167 Mt CO_2 for the North Morecambe Sherwood Sandstone reservoir

initial gas composition, based on the finite radial, finite linear and base case aquifer models (see Table 6.28 (d)). In contrast, the results of the method of Bachu et al. (2007), Table 6.8, equation 1.1 give much higher storage capacity estimates, ranging between 1060 and 1150 Mt CO_2 for the North Morecambe Sherwood Sandstone reservoir initial gas composition, based on the finite radial, finite linear and base case aquifer models (Table 6.28 (d)).

Again, the GERG-2008 equation of state (Kunz and Wagner, 2012) always predicts the highest estimate of theoretical CO_2 storage capacity, closely followed by the AGA8-DC92 Model (Starling and Savidge, 1992). When compared to the results of the Peng-Robinson equation of state (Peng and Robinson, 1976) estimated using RefProp (Lemmon et al., 2013), the results predicted using the GERG-2008 equation of state (Kunz and Wagner, 2012) are ~7.0% greater (see Table 6.28). The Soave-Redlich-Kwong equation of state (Soave, 1972) always predicts the lowest estimate of theoretical CO_2 storage capacity. When compared to the results of the Peng-Robinson equation of state (Peng and Robinson, 1976) estimated using RefProp (Lemmon et al., 2013), the results predicted using the Soave-Redlich-Kwong equation of state (Soave, 1972) are ~10.7% lower (see Table 6.28).

RefProp, Peng-Robinson Equation of State

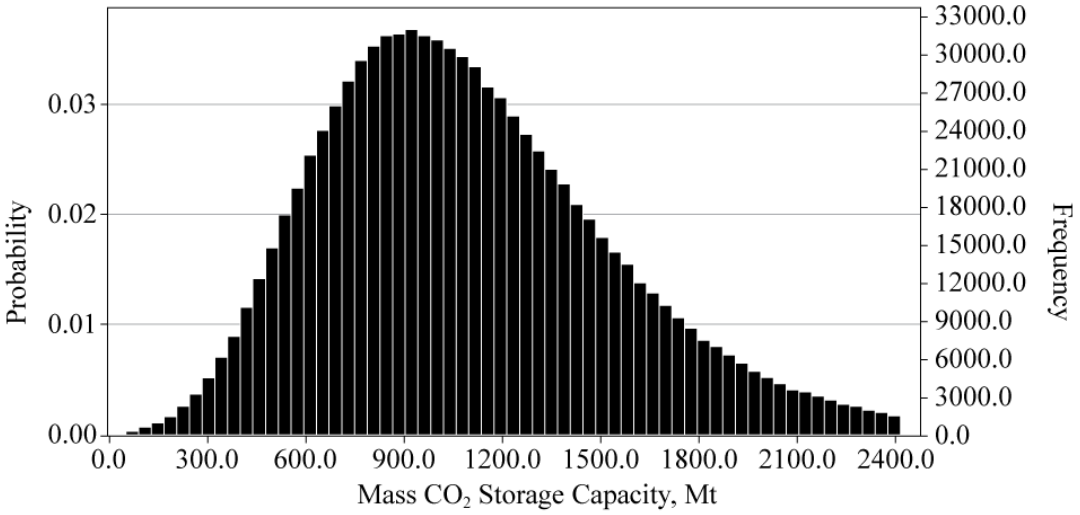

RefProp, GERG-2008 Equation of State

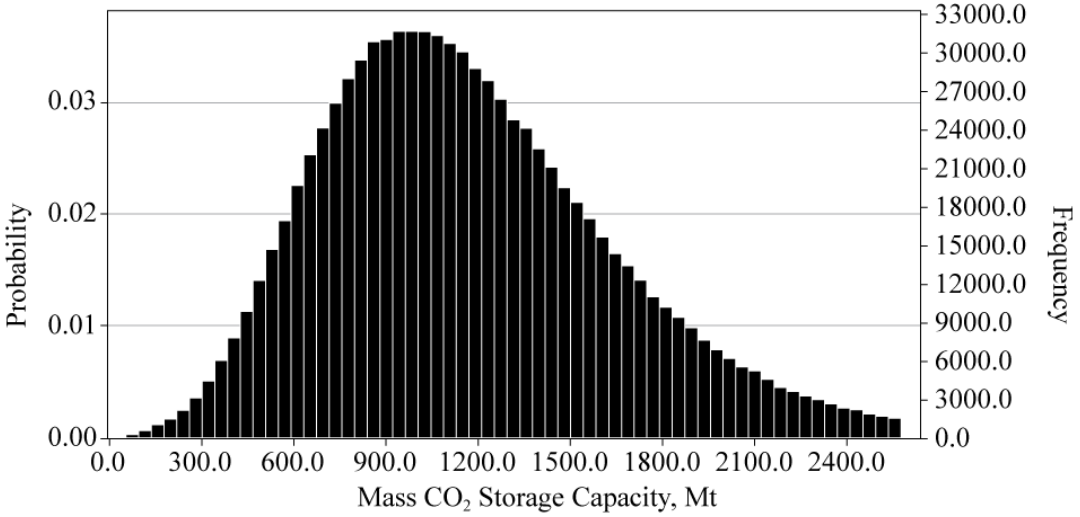

RefProp, AGA8-DC92 Equation of State

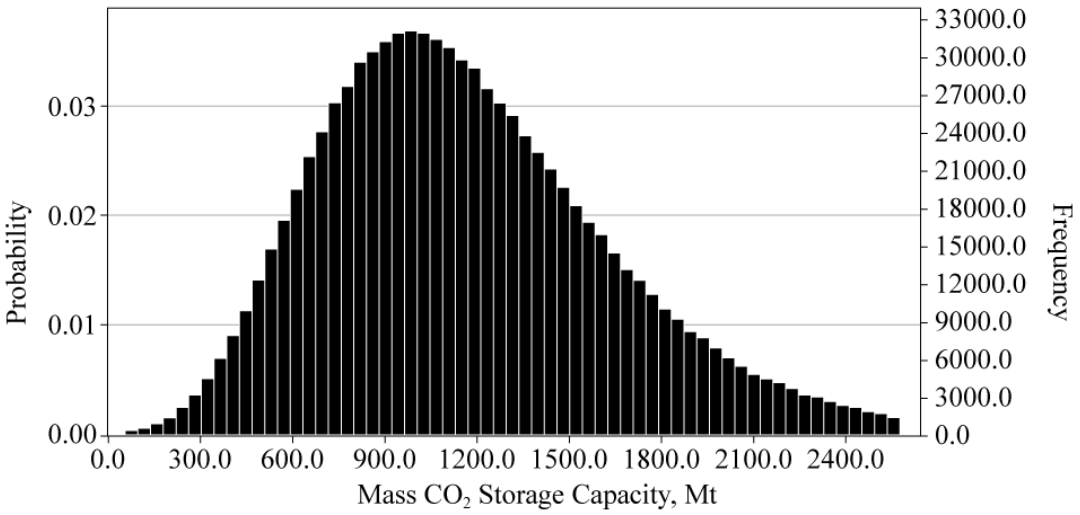

WebGasEOS, Peng-Robinson Equation of State

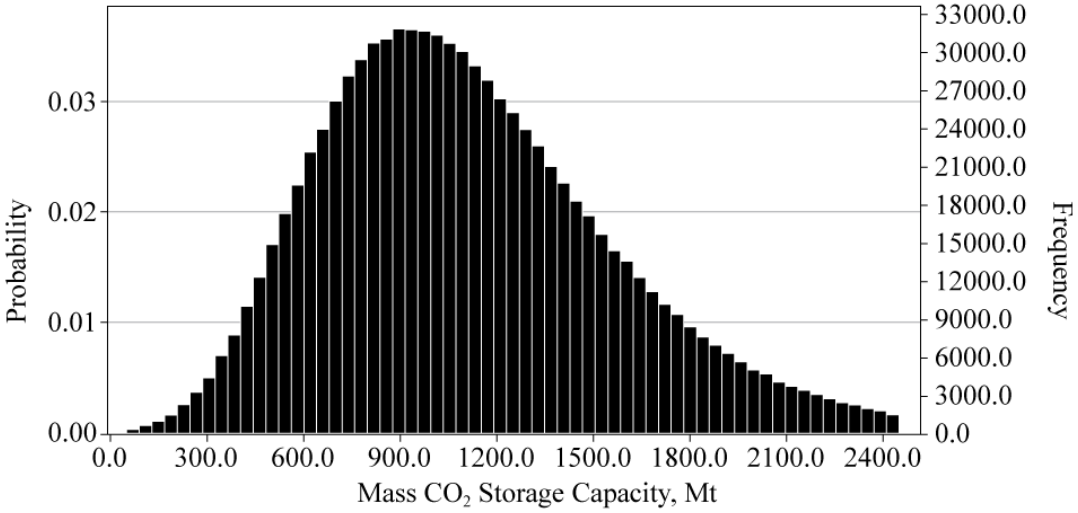

WebGasEOS, Peng-Robinson-Stryjek-Vera Equation of State

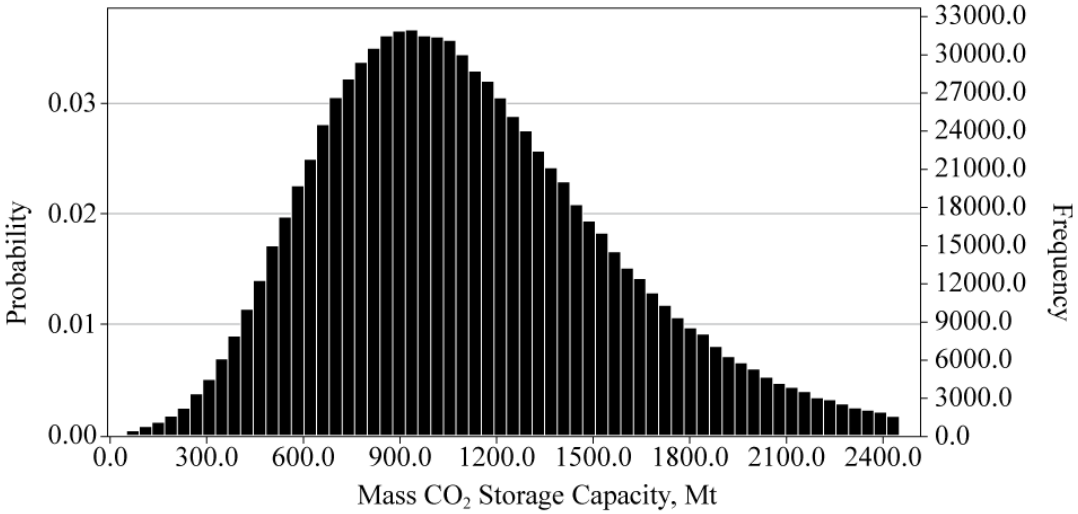

WebGasEOS, Redlich-Kwong Equation of State

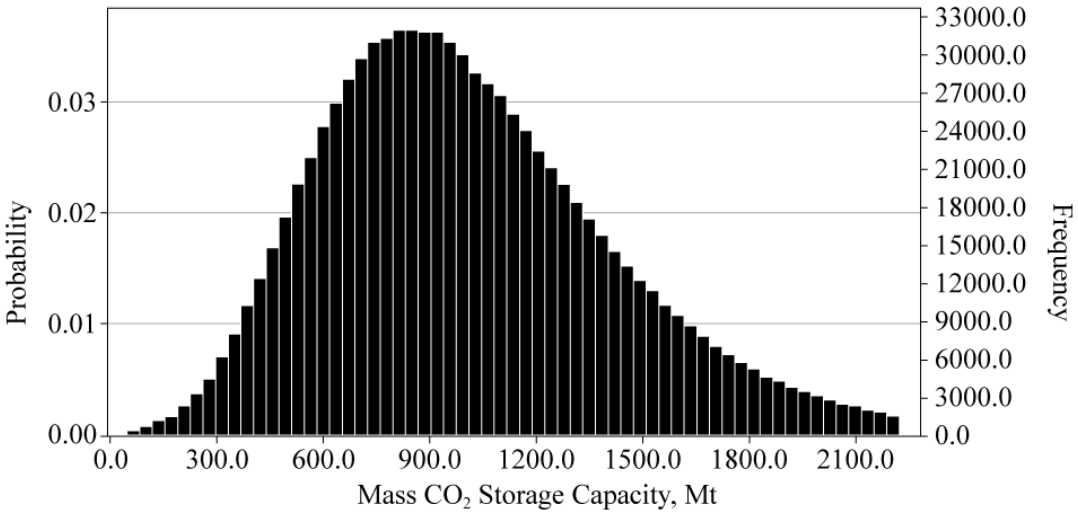

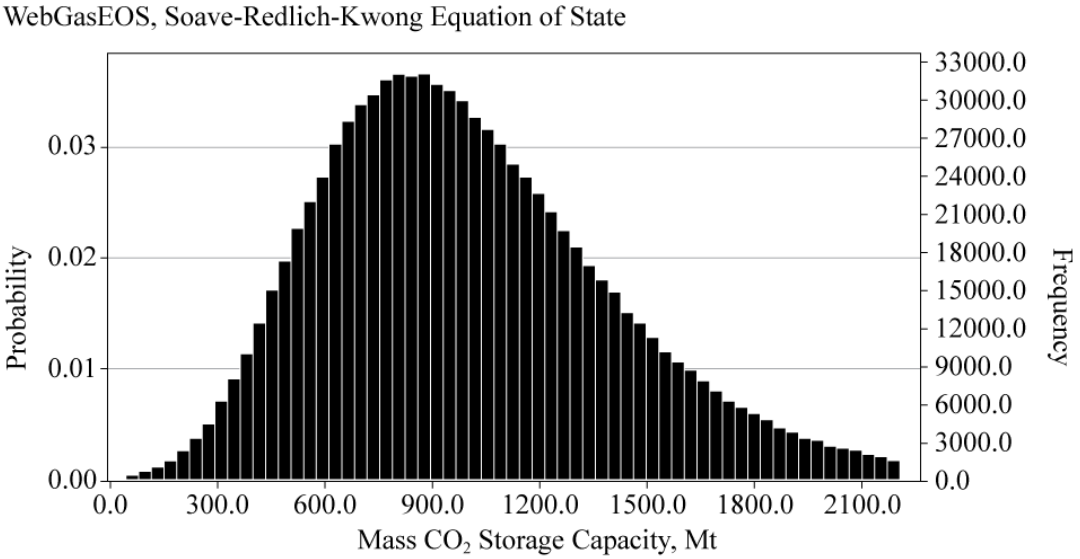

Figure 6.43 Monte Carlo Simulation probability distribution results of mass CO_2 storage capacity within the entire North Morecambe Sherwood Sandstone reservoir using the method of Bachu et al. (2007) Table 6.8, equation 1.1, and varying the equation of state used. The results shown use the industry estimated value of OGIP. Results computed using Oracle Crystal Ball software.

RefProp, Peng-Robinson Equation of State

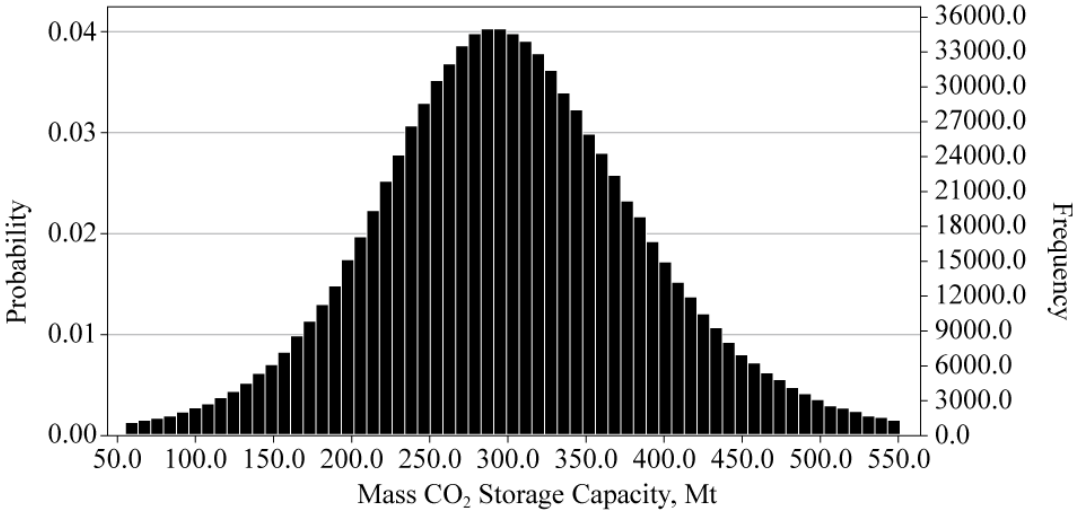

RefProp, GERG-2008 Equation of State

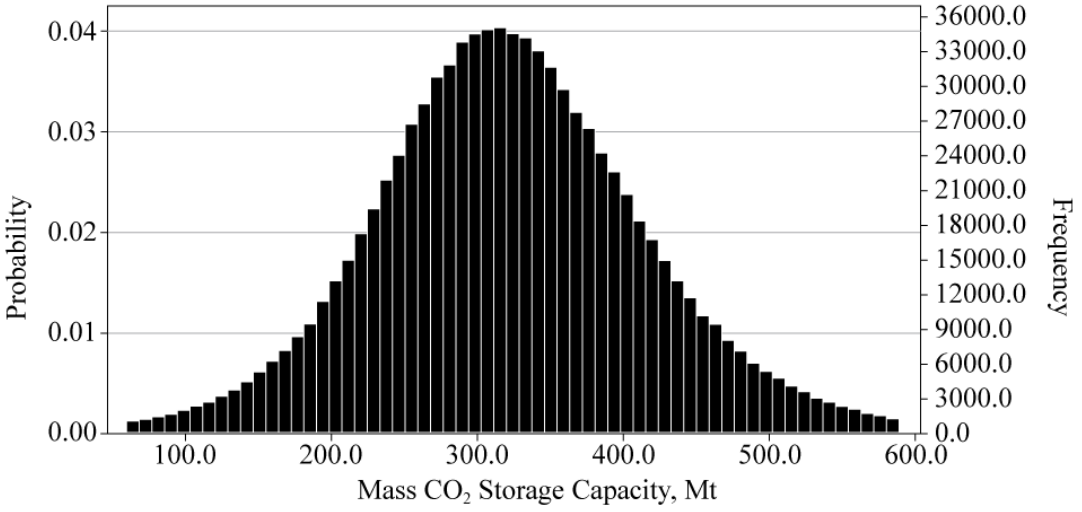

RefProp, AGA8-DC92 Equation of State

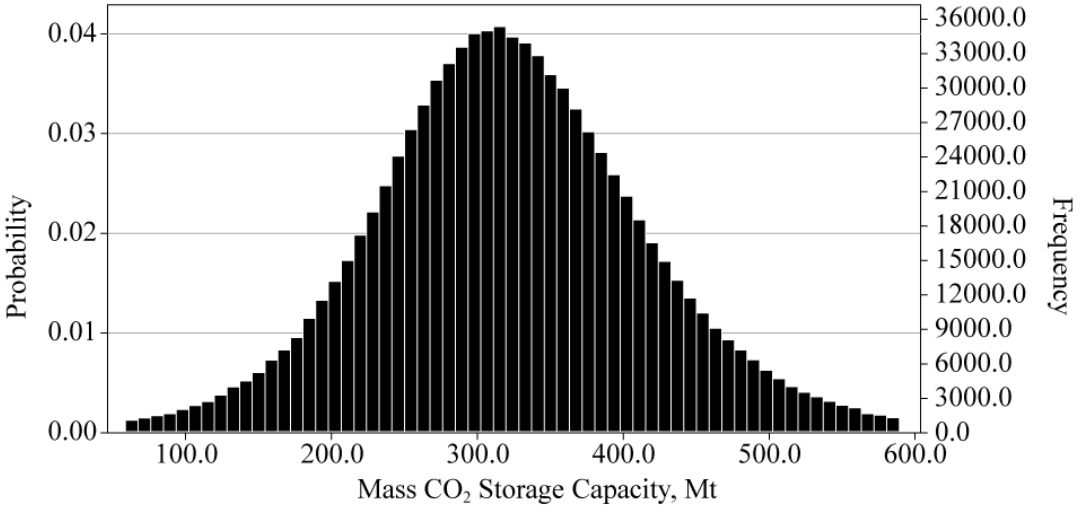

WebGasEOS, Peng-Robinson Equation of State

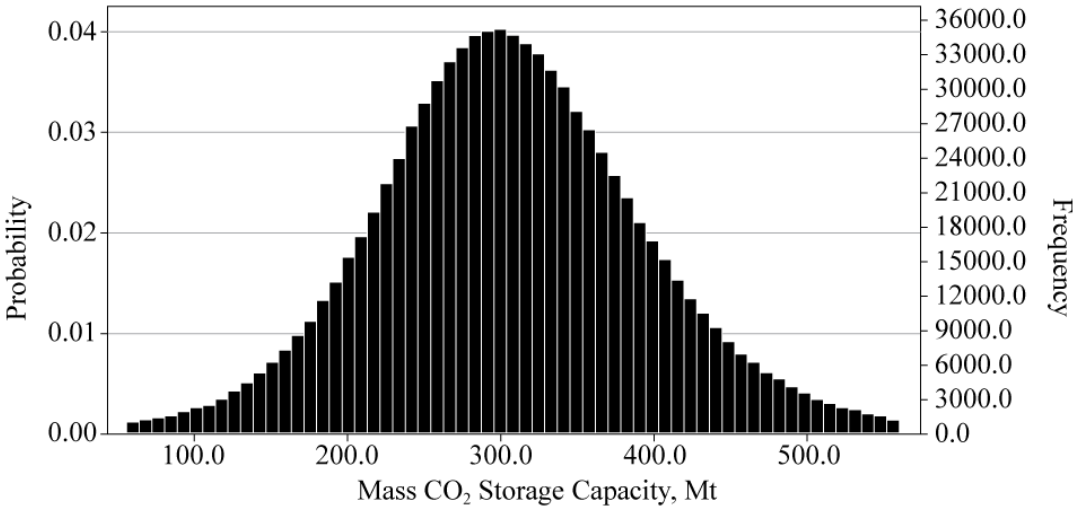

WebGasEOS, Peng-Robinson-Stryjek-Vera Equation of State

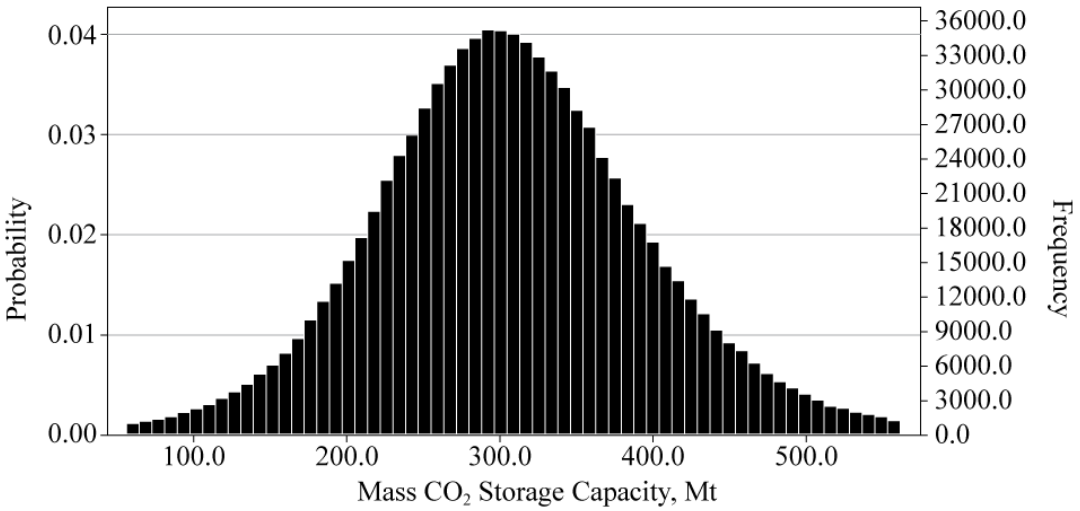

WebGasEOS, Redlich-Kwong Equation of State

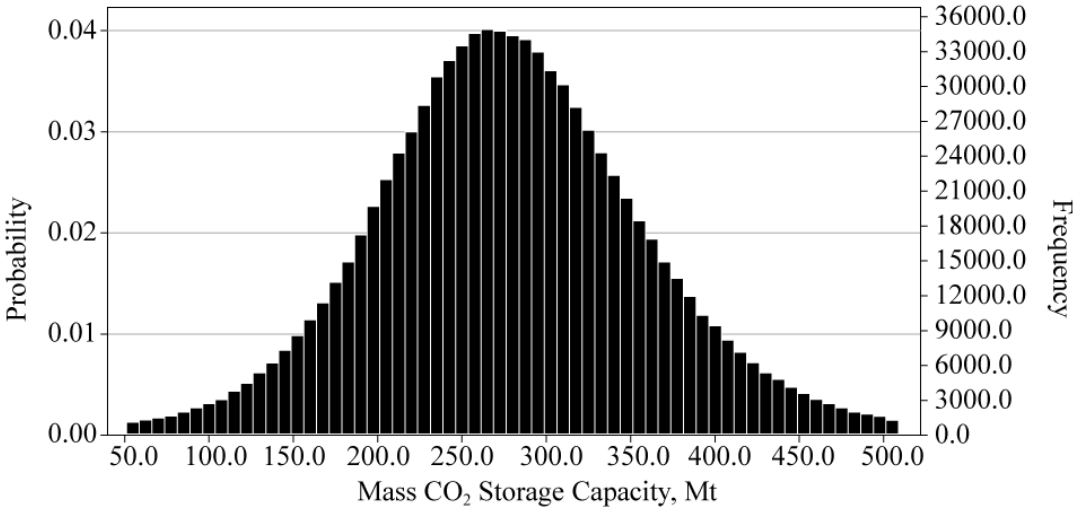

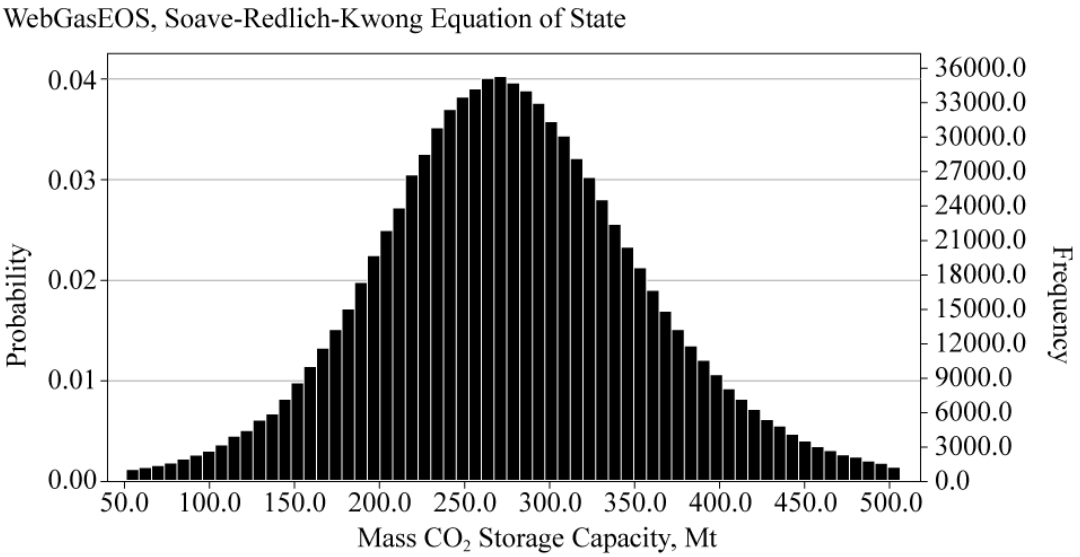

Figure 6.44 Monte Carlo Simulation probability distribution results of mass CO_2 storage capacity within the illite free zone of the North Morecambe Sherwood Sandstone reservoir using the method of Bachu et al. (2007) Table 6.8, equation 1.1, and varying the equation of state used. The results shown use the industry estimated value of OGIP. Results computed using Oracle Crystal Ball software.

RefProp, Peng-Robinson Equation of State

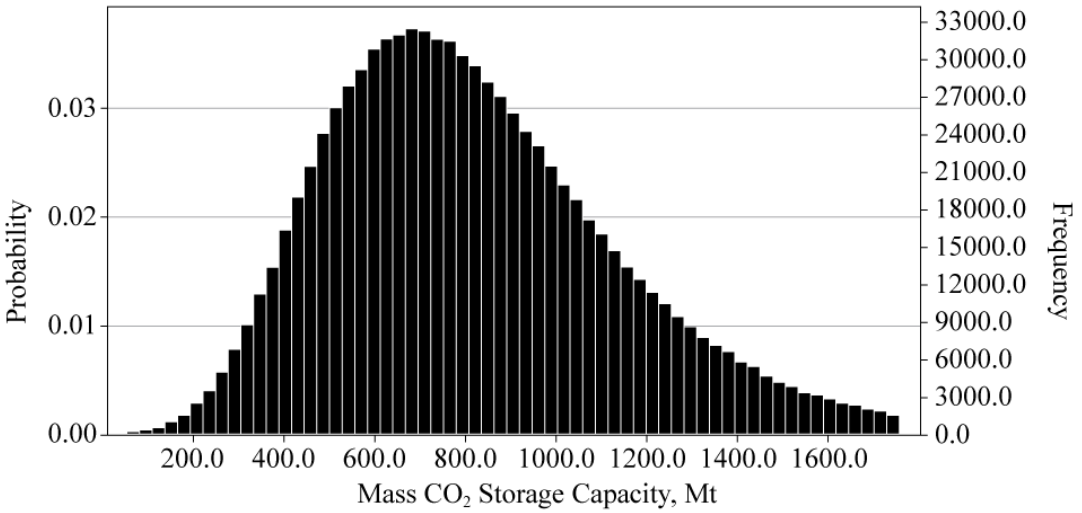

RefProp, GERG-2008 Equation of State

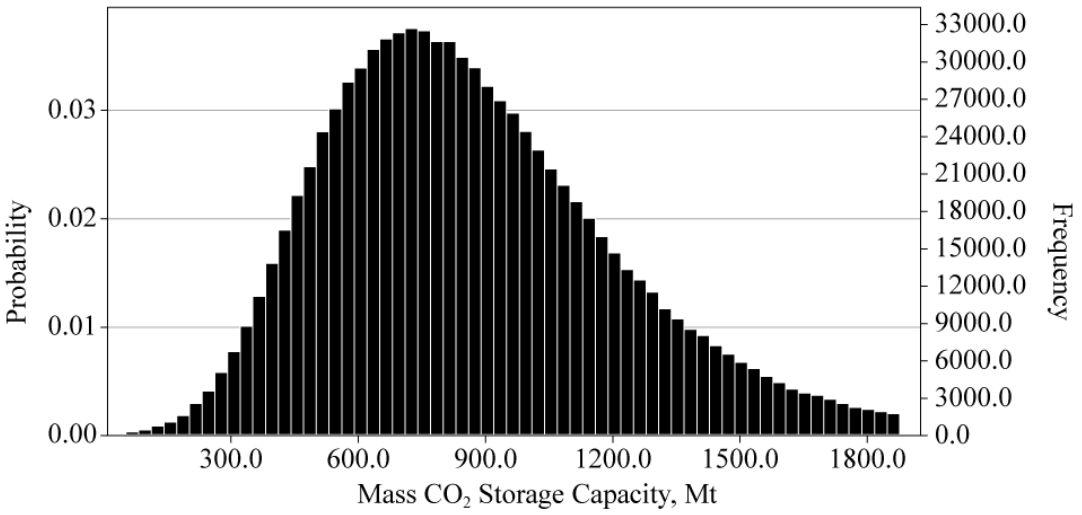

RefProp, AGA8-DC92 Equation of State

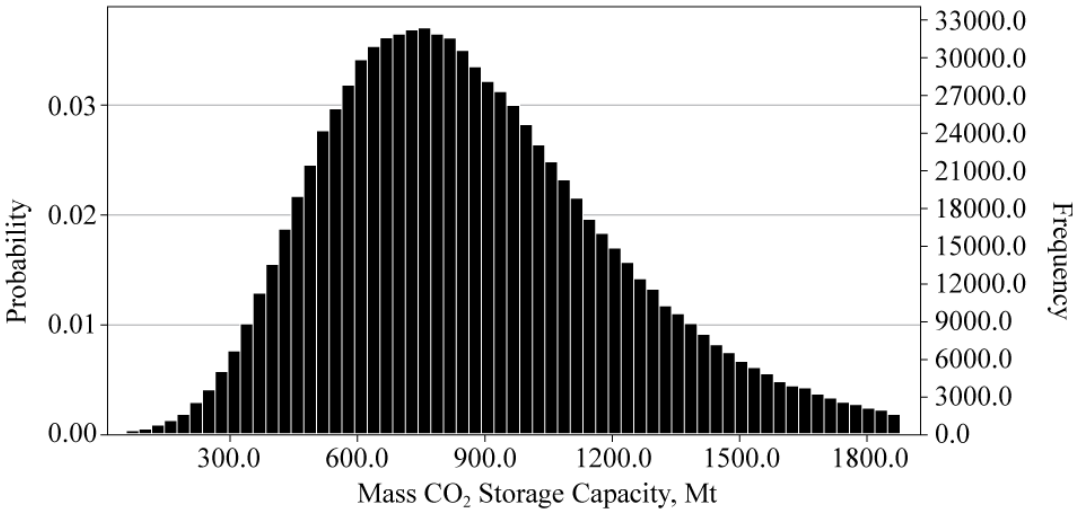

WebGasEOS, Peng-Robinson Equation of State

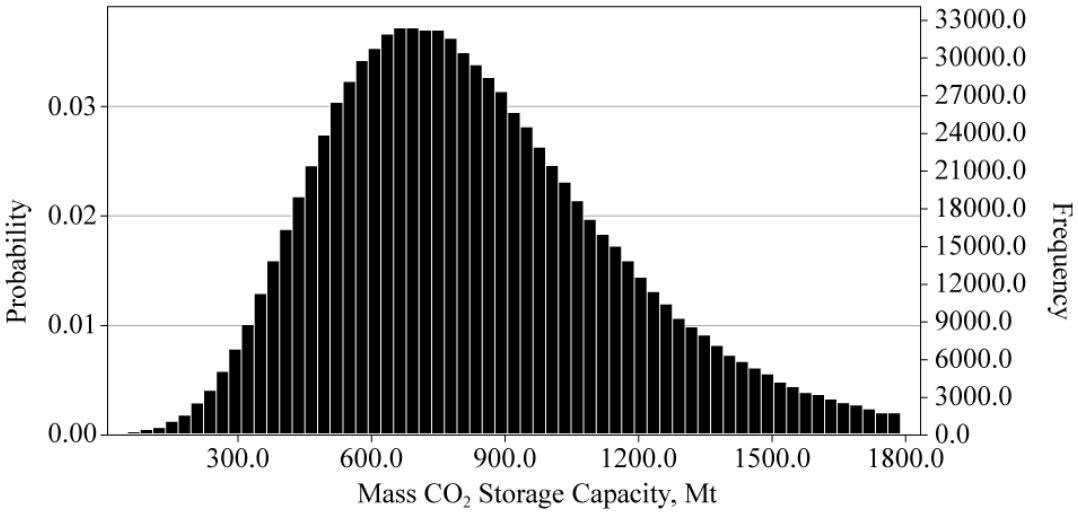

WebGasEOS, Peng-Robinson-Stryjek-Vera Equation of State

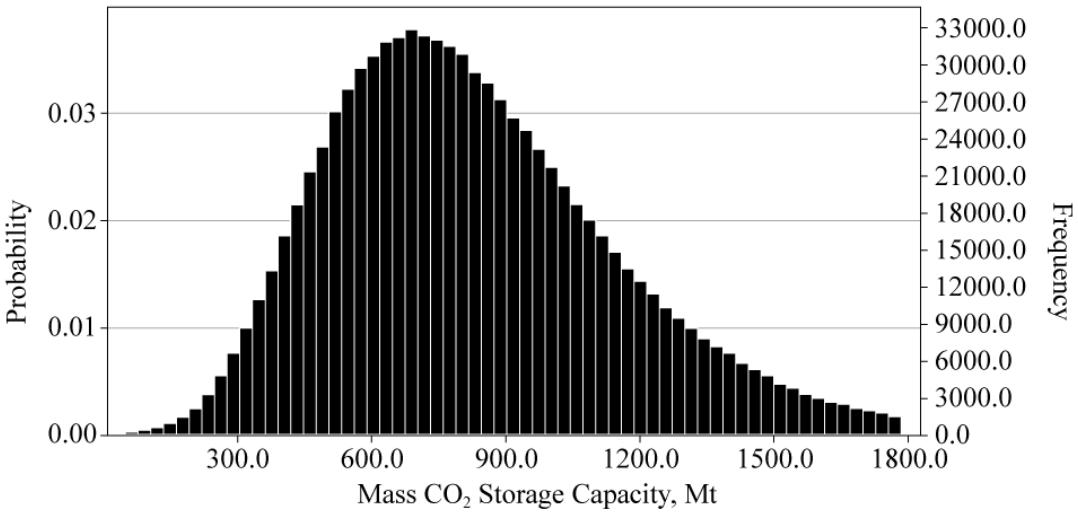

WebGasEOS, Redlich-Kwong Equation of State

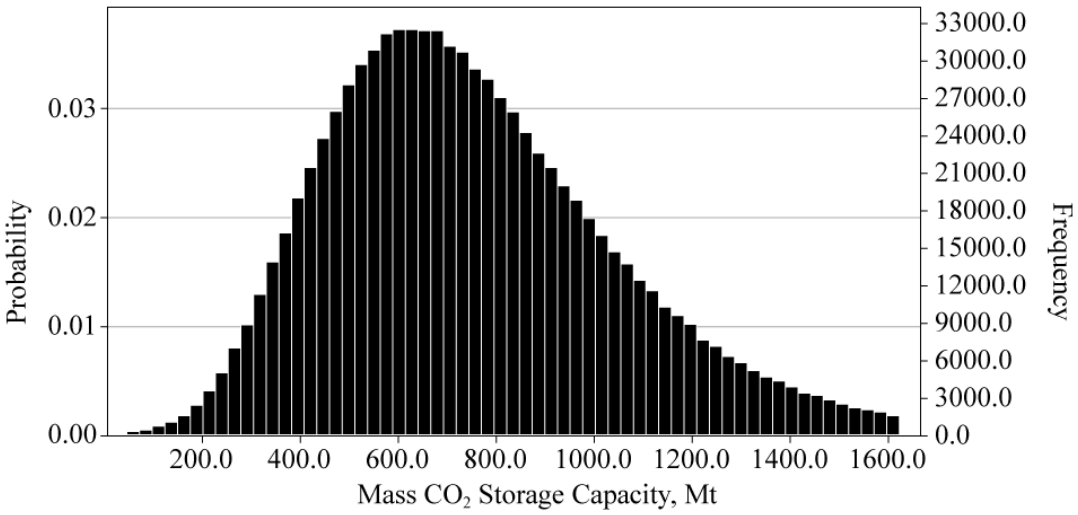

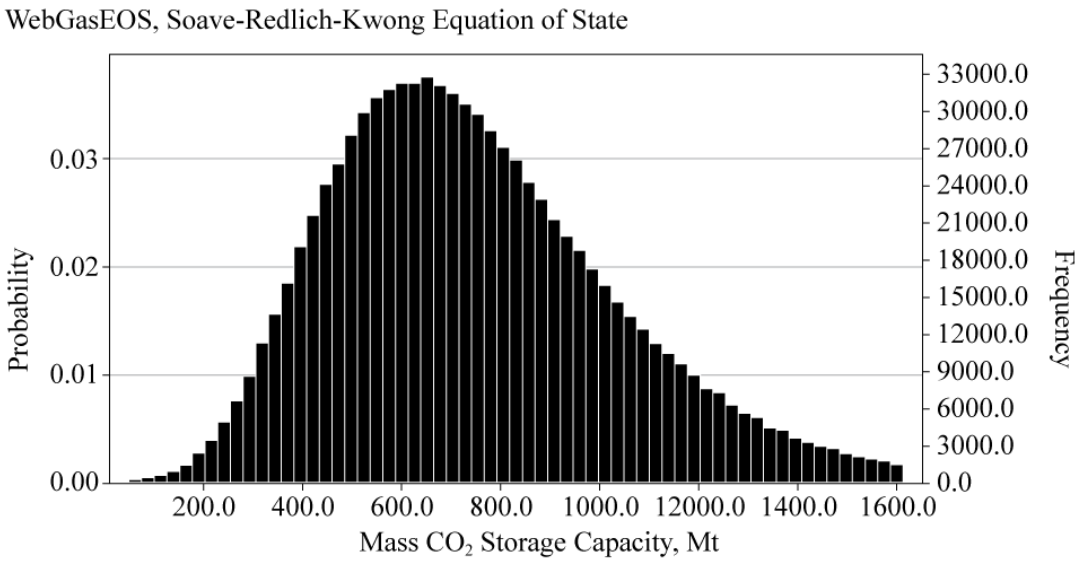

Figure 6.45 Monte Carlo Simulation probability distribution results of mass CO_2 storage capacity within the illite affected zone of the North Morecambe Sherwood Sandstone reservoir using the method of Bachu et al. (2007) Table 6.8, equation 1.1, and varying the equation of state used. The results shown use the industry estimated value of OGIP. Results computed using Oracle Crystal Ball software.

(a) Aquifer Model based on Industry Estimated OGIP Value

MODELLING SOFTWARE	EQUATION OF STATE	MINIMUM	P10	MEDIAN (P50)	MEAN	P90	MAXIMUM
RefProp	Peng-Robinson	51.06	452.88	820.34	869.24	1348.19	4255.80
	GERG-2008	54.53	484.05	876.19	928.33	1439.91	5299.57
	AGA8 Model	54.55	484.35	876.50	928.58	1439.69	4768.35
WebGasEOS	Peng-Robinson	51.95	460.87	834.29	884.10	1371.00	4531.60
	Peng-Robinson-Stryjek-Vera	51.96	460.68	834.25	883.85	1370.41	4477.01
	Redlich-Kwong	47.16	417.70	756.08	801.23	1242.91	3658.83
	Soave-Redlich-Kwong	46.87	415.81	752.43	797.21	1236.20	3576.29

(b) Finite Radial Aquifer Model

MODELLING SOFTWARE	EQUATION OF STATE	MINIMUM	P10	MEDIAN (P50)	MEAN	P90	MAXIMUM
RefProp	Peng-Robinson	51.05	552.44	1011.18	1071.93	1669.01	5187.05
	GERG-2008	54.60	590.28	1080.16	1145.23	1783.50	5974.31
	AGA8 Model	54.54	590.19	1080.01	1145.07	1783.64	5679.99
WebGasEOS	Peng-Robinson	51.95	562.91	1028.35	1090.14	1696.61	5381.16
	Peng-Robinson-Stryjek-Vera	51.90	562.26	1028.37	1090.32	1698.82	7211.00
	Redlich-Kwong	47.07	509.41	931.94	988.11	1538.81	4995.88
	Soave-Redlich-Kwong	46.84	506.76	927.53	983.60	1532.19	5023.80

(c) Finite Linear Aquifer Model

MODELLING SOFTWARE	EQUATION OF STATE	MINIMUM	P10	MEDIAN (P50)	MEAN	P90	MAXIMUM
RefProp	Peng-Robinson	51.11	548.96	1003.92	1064.25	1656.72	5102.01
	GERG-2008	54.55	586.50	1072.18	1137.24	1770.87	5699.08
	AGA8 Model	54.57	586.91	1072.67	1137.00	1770.07	5202.63
WebGasEOS	Peng-Robinson	51.91	557.74	1020.36	1082.13	1685.41	5523.64
	Peng-Robinson-Stryjek-Vera	51.92	558.47	1020.37	1082.13	1684.62	6236.93
	Redlich-Kwong	47.08	506.05	925.60	981.34	1528.12	5047.30
	Soave-Redlich-Kwong	46.89	503.96	921.23	976.64	1520.44	5067.06

(d) Base Case Aquifer Model

MODELLING SOFTWARE	EQUATION OF STATE	MINIMUM	P10	MEDIAN (P50)	MEAN	P90	MAXIMUM
RefProp	Peng-Robinson	51.07	551.23	1007.23	1068.19	1662.91	5931.15
	GERG-2008	54.65	588.40	1076.27	1141.44	1778.04	5598.30
	AGA8 Model	54.57	588.88	1076.88	1141.59	1777.50	5775.44
WebGasEOS	Peng-Robinson	52.20	560.20	1024.19	1086.06	1691.51	5422.07
	Peng-Robinson-Stryjek-Vera	51.96	559.99	1024.80	1086.35	1691.38	5509.83
	Redlich-Kwong	47.09	508.12	928.94	985.17	1533.96	5258.27
	Soave-Redlich-Kwong	46.86	505.26	924.50	980.05	1526.56	4613.37

Table 6.25 Monte Carlo Simulation forecast values for the entire North Morecambe Sherwood Sandstone reservoir for (a) the aquifer model based on the industry estimated OGIP value, (b) the finite radial aquifer model, (c) the finite linear aquifer model, and (d) the base case aquifer model. Results in Mt CO_2.

MODELLING SOFTWARE	EQUATION OF STATE	MINIMUM	P10	MEDIAN (P50)	MEAN	P90	MAXIMUM
RefProp	Peng-Robinson	51.04	163.32	243.47	246.56	333.12	827.89
	GERG-2008	54.53	174.42	260.24	263.51	355.88	905.27
	AGA8 Model	54.54	174.57	260.26	263.55	356.16	934.52
WebGasEOS	Peng-Robinson	51.91	166.12	247.80	250.91	338.96	861.54
	Peng-Robinson-Stryjek-Vera	51.91	166.11	247.79	250.89	338.84	955.16
	Redlich-Kwong	47.07	150.63	224.65	227.52	307.37	835.94
	Soave-Redlich-Kwong	46.84	149.95	223.62	226.41	305.69	746.89

Table 6.26 Monte Carlo Simulation forecast values for the illite free zone of the North Morecambe Sherwood Sandstone reservoir. Results shown are based on the industry estimated value of OGIP. Results in Mt CO_2.

MODELLING SOFTWARE	EQUATION OF STATE	MINIMUM	P10	MEDIAN (P50)	MEAN	P90	MAXIMUM
RefProp	Peng-Robinson	51.82	354.24	613.30	650.26	993.88	2904.14
	GERG-2008	54.94	378.71	655.71	694.92	1061.83	3770.51
	AGA8 Model	54.64	378.86	655.28	694.67	1061.49	3220.36
WebGasEOS	Peng-Robinson	52.27	360.57	624.21	661.48	1010.42	2883.86
	Peng-Robinson-Stryjek-Vera	52.04	360.55	623.87	661.22	1010.24	3354.83
	Redlich-Kwong	47.54	326.77	565.81	599.72	916.51	2835.25
	Soave-Redlich-Kwong	46.99	325.05	562.78	596.57	911.27	2549.99

Table 6.27 Monte Carlo Simulation forecast values for the illite affected zone of the North Morecambe Sherwood Sandstone reservoir. Results shown are based on the industry estimated value of OGIP. Results in Mt CO_2.

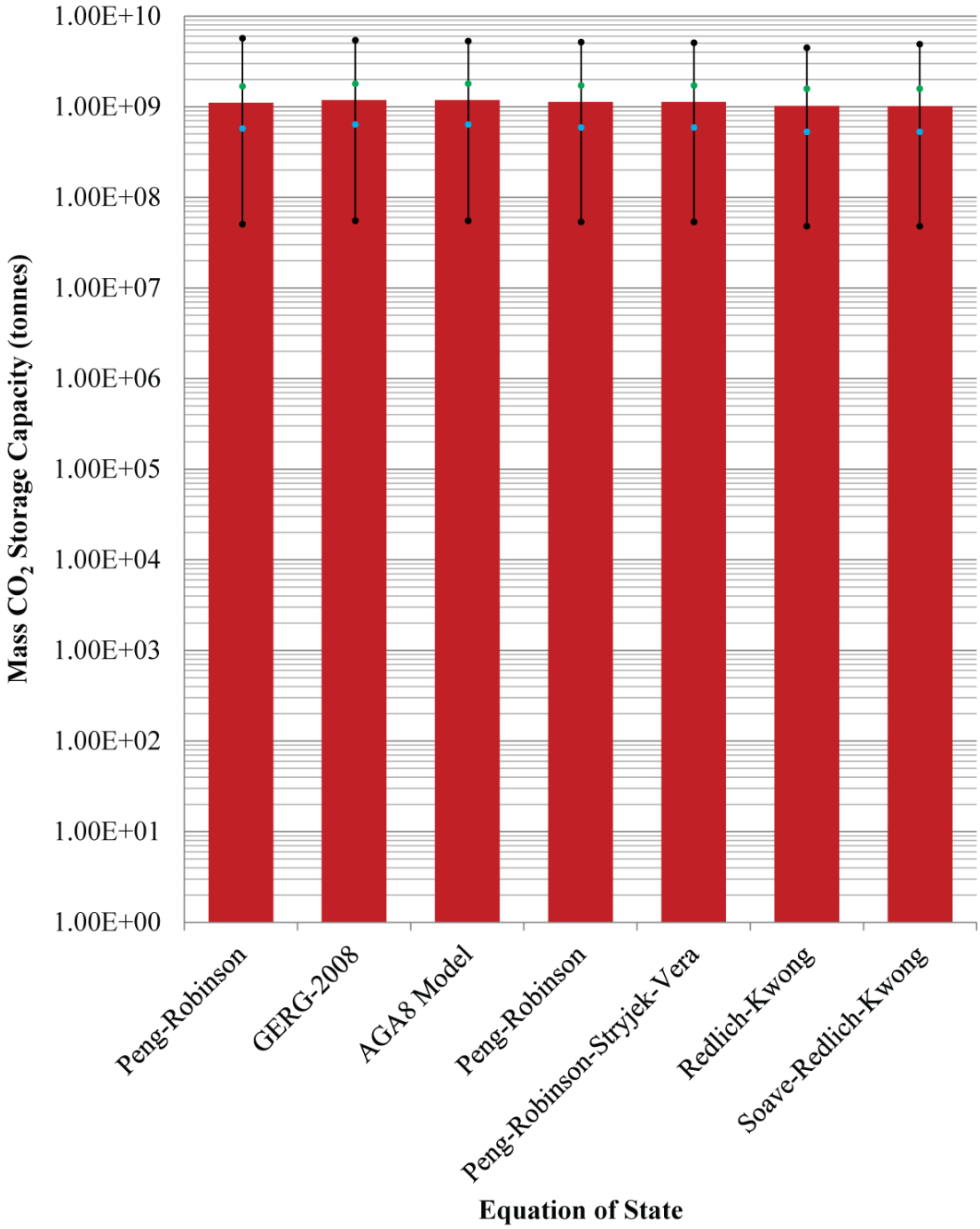

Figure 6.46 Theoretical CO_2 storage capacity of the entire North Morecambe Sherwood Sandstone reservoir estimated using the method of Bachu et al. (2007), Table 6.8, equation 1.1. The results shown use the industry estimate value of OGIP. The red columns plotted are the mean values, and the error bars shown have the minimum and maximum values plotted (black circles), alongside the P10 values (blue circles) and P90 values (green circles), calculated from the probability distribution curves estimated through Monte Carlo Simulation (results displayed previously in Figure 6.43).

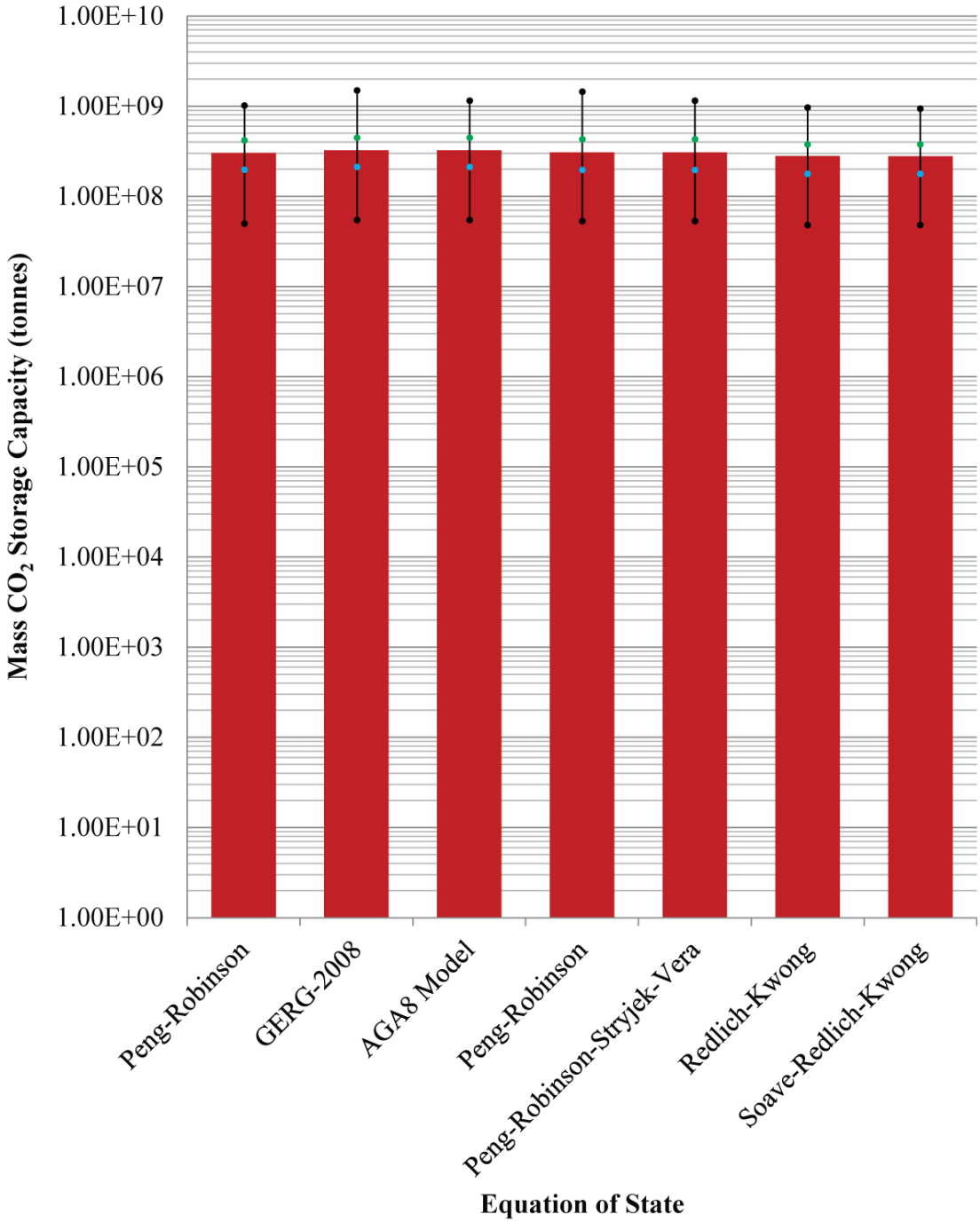

Figure 6.47 Theoretical CO_2 storage capacity of the illite free zone of the North Morecambe Sherwood Sandstone reservoir estimated using the method of Bachu et al. (2007), Table 6.8, equation 1.1. The results shown use the industry estimate value of OGIP. The red columns plotted are the mean values, and the error bars shown have the minimum and maximum values plotted (black circles), alongside the P10 values (blue circles) and P90 values (green circles), calculated from the probability distribution curves estimated through Monte Carlo Simulation (results displayed previously in Figure 6.44).

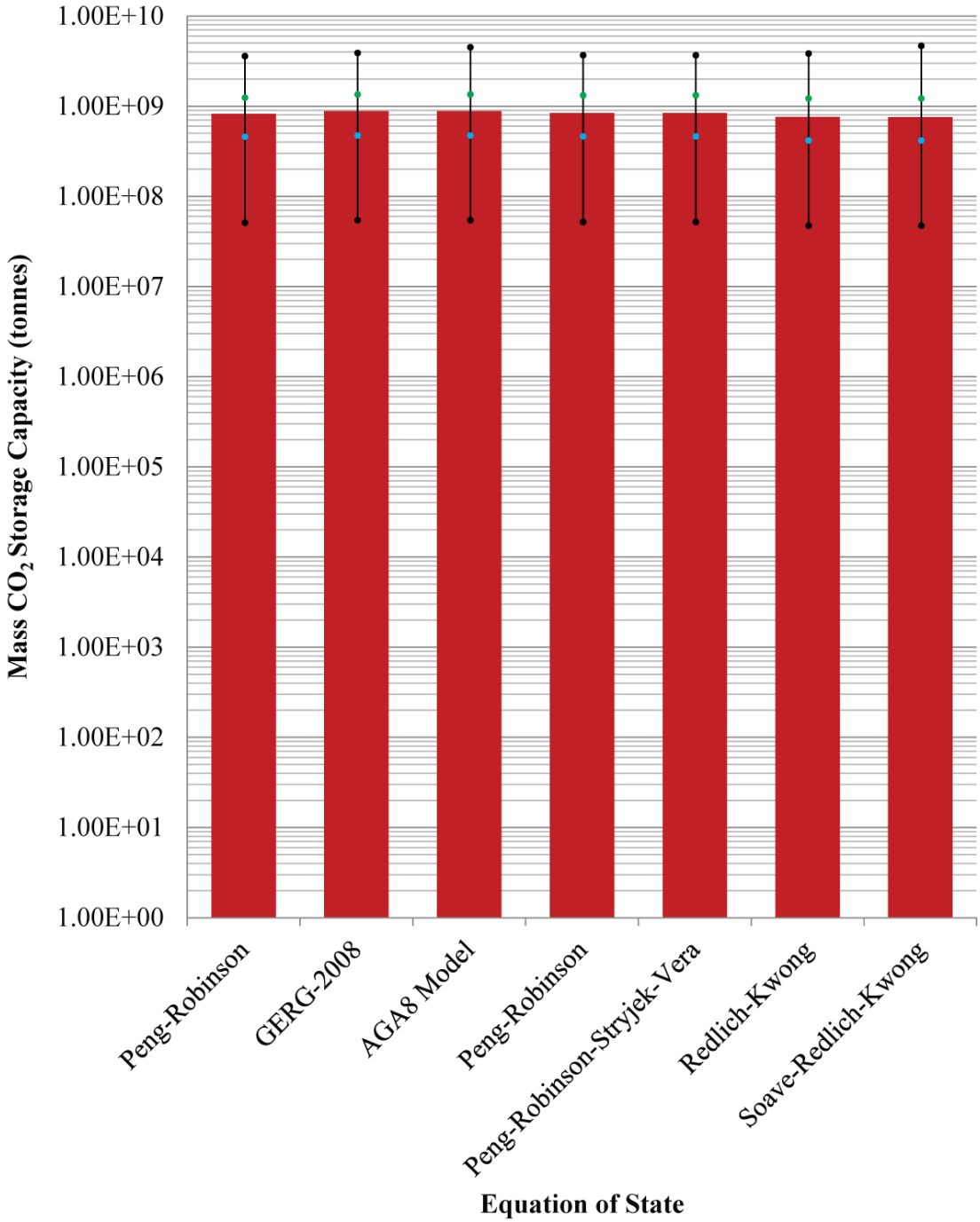

Figure 6.48 Theoretical CO_2 storage capacity of the illite affected zone of the North Morecambe Sherwood Sandstone reservoir estimated using the method of Bachu et al. (2007), Table 6.8, equation 1.1. The results shown use the industry estimate value of OGIP. The red columns plotted are the mean values, and the error bars shown have the minimum and maximum values plotted (black circles), alongside the P10 values (blue circles) and P90 values (green circles), calculated from the probability distribution curves estimated through Monte Carlo Simulation (results displayed previously in Figure 6.45).

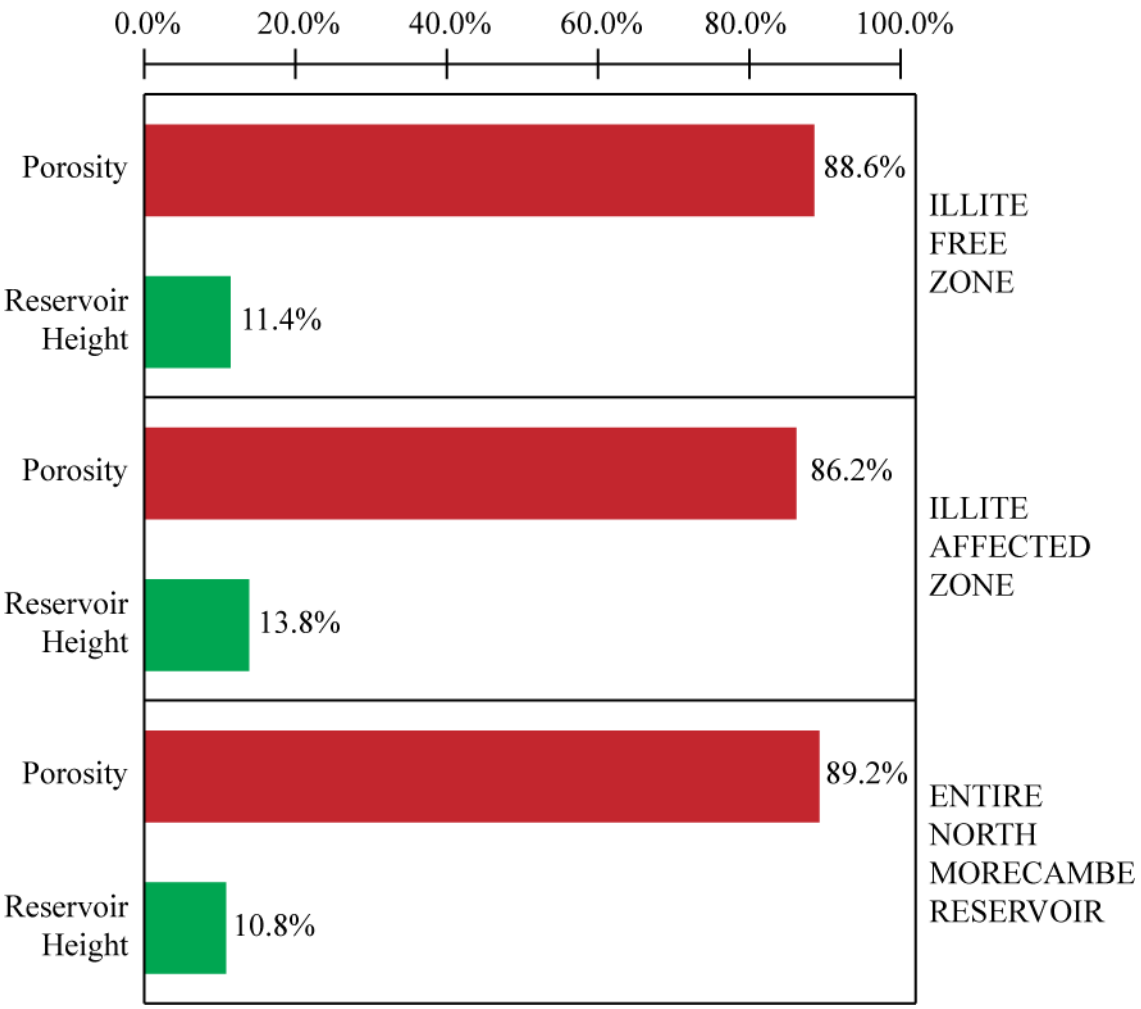

Figure 6.49 Sensitivity analysis run on the method of Bachu et al. (2007) Table 6.8, equation 1.1, throughout Monte Carlo Simulation. The results shown are based on the method using the industry estimated value of OGIP. The results of the final probability distribution of the mass CO_2 storage capacity of the entire North Morecambe Sherwood Sandstone reservoir (Figure 6.43 and Figure 6.46), illite free zone (Figure 6.44 and Figure 6.47) and illite affected zone (Figure 6.45 and Figure 6.48), are most sensitive to porosity, followed by reservoir height.

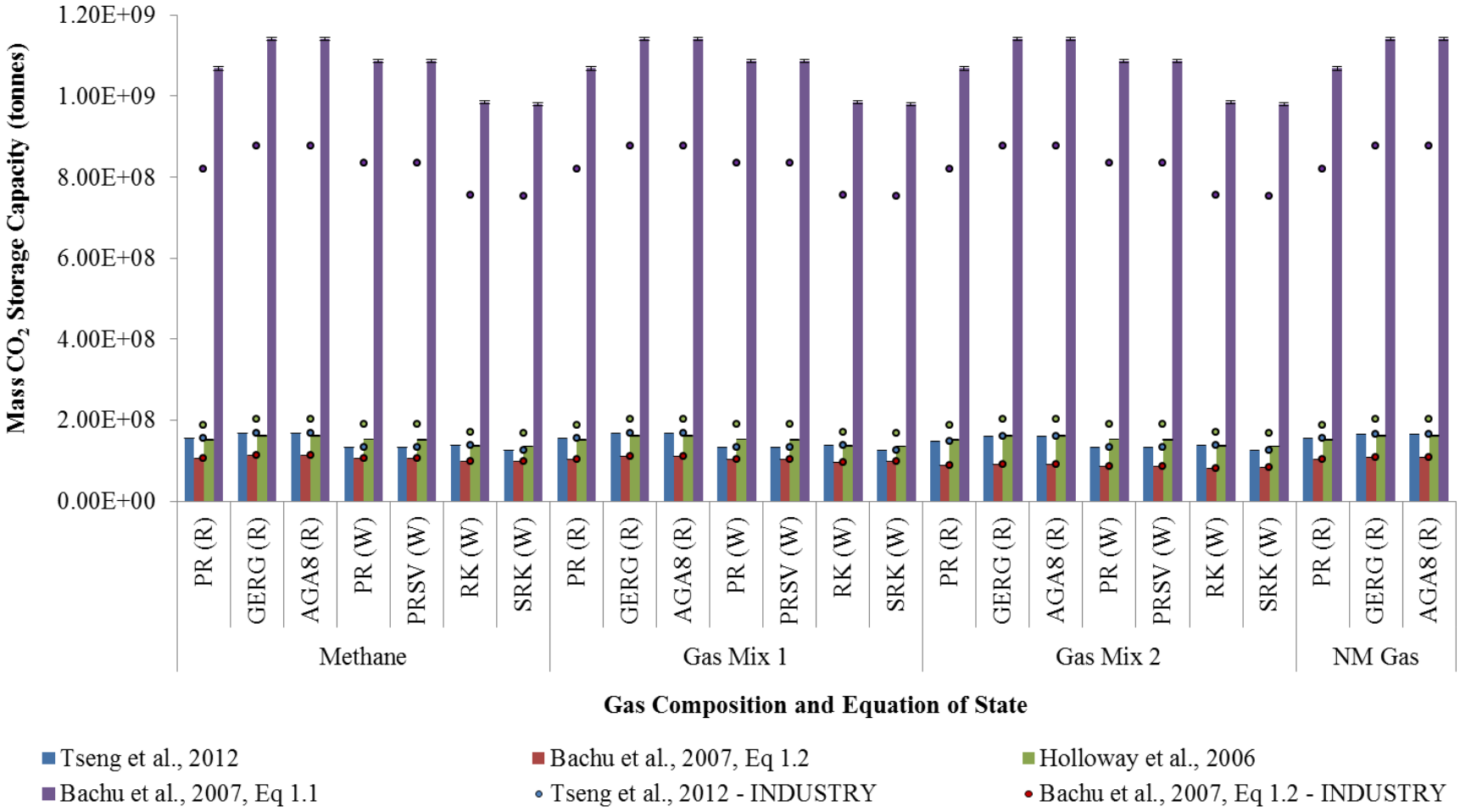

Figure 6.50 Estimated Theoretical CO_2 Storage Capacity of the North Morecambe Sherwood Sandstone reservoir using the methods of Bachu et al. (2007), Holloway et al. (2006) and Tseng et al. (2012). The columns represent the base case aquifer model results and the error bars reflect the results of the finite radial and linear aquifer models. The results using the industry estimated value of OGIP are plotted as circles for comparison.

GAS COMPOSITION	MODELLING TOOL	EQUATION OF STATE	AQUIFER MODEL	Tseng et al., 2012	% of Peng-Robinson (RefProp)	Bachu et al., 2007, Eq 1.2	% of Peng-Robinson (RefProp)	Holloway et al., 2006	% of Peng-Robinson (RefProp)	Bachu et al., 2007, Eq 1.1	% of Peng-Robinson (RefProp)	Average Percentage Variation
METHANE	REFPROP	PR	I	1.56E+08	100.0	1.06E+08	100.0	1.89E+08	100.0	8.20E+08	100.0	100.0
			R	1.56E+08	100.0	1.06E+08	100.0	1.51E+08	100.0	1.07E+09	100.0	100.0
			L	1.56E+08	100.0	1.06E+08	100.0	1.52E+08	100.0	1.06E+09	100.0	100.0
			B	1.56E+08	100.0	1.06E+08	100.0	1.52E+08	100.0	1.07E+09	100.0	100.0
		GERG	I	1.68E+08	107.7	1.13E+08	106.6	2.02E+08	106.9	8.76E+08	106.8	107.0
			R	1.68E+08	107.7	1.13E+08	106.6	1.61E+08	106.6	1.15E+09	107.5	107.1
			L	1.68E+08	107.7	1.13E+08	106.6	1.63E+08	107.2	1.14E+09	107.5	107.3
			B	1.68E+08	107.7	1.13E+08	106.6	1.62E+08	106.8	1.14E+09	106.5	106.9
		AGA8	I	1.68E+08	107.7	1.13E+08	106.6	2.02E+08	106.9	8.77E+08	107.0	107.0
			R	1.68E+08	107.7	1.13E+08	106.6	1.61E+08	106.6	1.15E+09	107.5	107.1
			L	1.68E+08	107.7	1.13E+08	106.6	1.63E+08	107.2	1.14E+09	107.5	107.3
			B	1.68E+08	107.7	1.13E+08	106.6	1.62E+08	106.8	1.14E+09	106.5	106.9
	WEBGASEOS	PR	I	1.34E+08	85.9	1.05E+08	99.1	1.91E+08	101.1	8.34E+08	101.7	96.9
			R	1.34E+08	85.9	1.05E+08	99.1	1.53E+08	101.3	1.09E+09	101.9	97.0
			L	1.34E+08	85.9	1.05E+08	99.1	1.54E+08	101.3	1.08E+09	101.9	97.0
			B	1.34E+08	85.9	1.05E+08	99.1	1.53E+08	100.8	1.09E+09	101.9	96.9
		PRSV	I	1.34E+08	85.9	1.05E+08	99.1	1.89E+08	100.0	8.34E+08	101.7	96.7
			R	1.34E+08	85.9	1.05E+08	99.1	1.52E+08	100.7	1.09E+09	101.9	96.9
			L	1.34E+08	85.9	1.05E+08	99.1	1.53E+08	100.7	1.08E+09	101.9	96.9
			B	1.34E+08	85.9	1.05E+08	99.1	1.52E+08	100.2	1.09E+09	101.9	96.7
		RK	I	1.38E+08	88.5	9.77E+07	92.2	1.70E+08	89.9	7.56E+08	92.2	90.7
			R	1.38E+08	88.5	9.76E+07	92.1	1.37E+08	90.7	9.88E+08	92.3	90.9
			L	1.38E+08	88.5	9.76E+07	92.1	1.38E+08	90.8	9.81E+08	92.5	91.0
			B	1.38E+08	88.5	9.76E+07	92.1	1.37E+08	90.3	9.85E+08	92.1	90.7
		SRK	I	1.26E+08	80.8	9.93E+07	93.7	1.68E+08	88.9	7.52E+08	91.7	88.8
			R	1.26E+08	80.8	9.93E+07	93.7	1.35E+08	89.4	9.84E+08	92.0	89.0
			L	1.26E+08	80.8	9.93E+07	93.7	1.36E+08	89.5	9.77E+08	92.2	89.0
			B	1.26E+08	80.8	9.93E+07	93.7	1.35E+08	89.0	9.80E+08	91.6	88.8

(a) Pure Methane

GAS COMPOSITION	MODELLING TOOL	EQUATION OF STATE	AQUIFER MODEL	Tseng et al., 2012	% of Peng-Robinson (RefProp)	Bachu et al., 2007, Eq 1.2	% of Peng-Robinson (RefProp)	Holloway et al., 2006	% of Peng-Robinson (RefProp)	Bachu et al., 2007, Eq 1.1	% of Peng-Robinson (RefProp)	Average Percentage Variation
GAS MIX 1	REFPROP	PR	I	1.55E+08	100.0	1.04E+08	100.0	1.89E+08	100.0	8.20E+08	100.0	100.0
			R	1.55E+08	100.0	1.04E+08	100.0	1.51E+08	100.0	1.07E+09	100.0	100.0
			L	1.55E+08	100.0	1.04E+08	100.0	1.52E+08	100.0	1.06E+09	100.0	100.0
			B	1.55E+08	100.0	1.04E+08	100.0	1.52E+08	100.0	1.07E+09	100.0	100.0
		GERG	I	1.67E+08	107.7	1.11E+08	106.7	2.02E+08	106.9	8.76E+08	106.8	107.0
			R	1.67E+08	107.7	1.11E+08	106.7	1.61E+08	106.6	1.15E+09	107.5	107.1
			L	1.67E+08	107.7	1.11E+08	106.7	1.63E+08	107.2	1.14E+09	107.5	107.3
			B	1.67E+08	107.7	1.11E+08	106.7	1.62E+08	106.8	1.14E+09	106.5	106.9
		AGA8	I	1.67E+08	107.7	1.11E+08	106.7	2.02E+08	106.9	8.77E+08	107.0	107.1
			R	1.67E+08	107.7	1.11E+08	106.7	1.61E+08	106.6	1.15E+09	107.5	107.1
			L	1.67E+08	107.7	1.11E+08	106.7	1.63E+08	107.2	1.14E+09	107.5	107.3
			B	1.67E+08	107.7	1.11E+08	106.7	1.62E+08	106.8	1.14E+09	106.5	106.9
	WEBGASEOS	PR	I	1.34E+08	86.5	1.03E+08	99.0	1.91E+08	101.1	8.34E+08	101.7	97.1
			R	1.34E+08	86.5	1.03E+08	99.0	1.53E+08	101.3	1.09E+09	101.9	97.2
			L	1.34E+08	86.5	1.03E+08	99.0	1.54E+08	101.3	1.08E+09	101.9	97.2
			B	1.34E+08	86.5	1.03E+08	99.0	1.53E+08	100.8	1.09E+09	101.9	97.0
		PRSV	I	1.34E+08	86.5	1.03E+08	99.0	1.89E+08	100.0	8.34E+08	101.7	96.8
			R	1.34E+08	86.5	1.03E+08	99.0	1.52E+08	100.7	1.09E+09	101.9	97.0
			L	1.34E+08	86.5	1.03E+08	99.0	1.53E+08	100.7	1.08E+09	101.9	97.0
			B	1.34E+08	86.5	1.03E+08	99.0	1.52E+08	100.2	1.09E+09	101.9	96.9
		RK	I	1.38E+08	89.0	9.56E+07	91.9	1.70E+08	89.9	7.56E+08	92.2	90.8
			R	1.38E+08	89.0	9.55E+07	91.8	1.37E+08	90.7	9.88E+08	92.3	91.0
			L	1.38E+08	89.0	9.55E+07	91.8	1.38E+08	90.8	9.81E+08	92.5	91.0
			B	1.38E+08	89.0	9.55E+07	91.8	1.37E+08	90.3	9.85E+08	92.1	90.8
		SRK	I	1.26E+08	81.3	9.77E+07	93.9	1.68E+08	88.9	7.52E+08	91.7	89.0
			R	1.26E+08	81.3	9.76E+07	93.8	1.35E+08	89.4	9.84E+08	92.0	89.1
			L	1.26E+08	81.3	9.76E+07	93.8	1.36E+08	89.5	9.77E+08	92.2	89.2
			B	1.26E+08	81.3	9.76E+07	93.8	1.35E+08	89.0	9.80E+08	91.6	88.9

(b) Gas Mix 1

GAS COMPOSITION	MODELLING TOOL	EQUATION OF STATE	AQUIFER MODEL	Tseng et al., 2012	% of Peng-Robinson (RefProp)	Bachu et al., 2007, Eq 1.2	% of Peng-Robinson (RefProp)	Holloway et al., 2006	% of Peng-Robinson (RefProp)	Bachu et al., 2007, Eq 1.1	% of Peng-Robinson (RefProp)	Average Percentage Variation
GAS MIX 2	REFPROP	PR	I	1.48E+08	100.0	8.78E+07	100.0	1.89E+08	100.0	8.20E+08	100.0	100.0
			R	1.48E+08	100.0	8.77E+07	100.0	1.51E+08	100.0	1.07E+09	100.0	100.0
			L	1.48E+08	100.0	8.77E+07	100.0	1.52E+08	100.0	1.06E+09	100.0	100.0
			B	1.48E+08	100.0	8.77E+07	100.0	1.52E+08	100.0	1.07E+09	100.0	100.0
		GERG	I	1.60E+08	108.1	9.22E+07	105.0	2.02E+08	106.9	8.76E+08	106.8	106.7
			R	1.60E+08	108.1	9.21E+07	105.0	1.61E+08	106.6	1.15E+09	107.5	106.8
			L	1.60E+08	108.1	9.21E+07	105.0	1.63E+08	107.2	1.14E+09	107.5	107.0
			B	1.60E+08	108.1	9.21E+07	105.0	1.62E+08	106.8	1.14E+09	106.5	106.6
		AGA8	I	1.60E+08	108.1	9.19E+07	104.7	2.02E+08	106.9	8.77E+08	107.0	106.7
			R	1.60E+08	108.1	9.19E+07	104.8	1.61E+08	106.6	1.15E+09	107.5	106.7
			L	1.60E+08	108.1	9.19E+07	104.8	1.63E+08	107.2	1.14E+09	107.5	106.9
			B	1.60E+08	108.1	9.19E+07	104.8	1.62E+08	106.8	1.14E+09	106.5	106.6
	WEBGASEOS	PR	I	1.33E+08	89.9	8.63E+07	98.3	1.91E+08	101.1	8.34E+08	101.7	97.7
			R	1.33E+08	89.9	8.62E+07	98.3	1.53E+08	101.3	1.09E+09	101.9	97.8
			L	1.33E+08	89.9	8.62E+07	98.3	1.54E+08	101.3	1.08E+09	101.9	97.8
			B	1.33E+08	89.9	8.62E+07	98.3	1.53E+08	100.8	1.09E+09	101.9	97.7
		PRSV	I	1.33E+08	89.9	8.64E+07	98.4	1.89E+08	100.0	8.34E+08	101.7	97.5
			R	1.33E+08	89.9	8.63E+07	98.4	1.52E+08	100.7	1.09E+09	101.9	97.7
			L	1.33E+08	89.9	8.63E+07	98.4	1.53E+08	100.7	1.08E+09	101.9	97.7
			B	1.33E+08	89.9	8.63E+07	98.4	1.52E+08	100.2	1.09E+09	101.9	97.6
		RK	I	1.37E+08	92.6	8.07E+07	91.9	1.70E+08	89.9	7.56E+08	92.2	91.7
			R	1.37E+08	92.6	8.06E+07	91.9	1.37E+08	90.7	9.88E+08	92.3	91.9
			L	1.37E+08	92.6	8.06E+07	91.9	1.38E+08	90.8	9.81E+08	92.5	92.0
			B	1.37E+08	92.6	8.06E+07	91.9	1.37E+08	90.3	9.85E+08	92.1	91.7
		SRK	I	1.25E+08	84.5	8.26E+07	94.1	1.68E+08	88.9	7.52E+08	91.7	89.8
			R	1.25E+08	84.5	8.25E+07	94.1	1.35E+08	89.4	9.84E+08	92.0	90.0
			L	1.25E+08	84.5	8.25E+07	94.1	1.36E+08	89.5	9.77E+08	92.2	90.0
			B	1.25E+08	84.5	8.25E+07	94.1	1.35E+08	89.0	9.80E+08	91.6	89.8

(c) Gas Mix 2

GAS COMPOSITION	MODELLING TOOL	EQUATION OF STATE	AQUIFER MODEL	Tseng et al., 2012	% of Peng-Robinson (RefProp)	Bachu et al., 2007, Eq 1.2	% of Peng-Robinson (RefProp)	Holloway et al., 2006	% of Peng-Robinson (RefProp)	Bachu et al., 2007, Eq 1.1	% of Peng-Robinson (RefProp)	Average Percentage Variation
NORTH MORECAMBE SHERWOOD SANDSTONE GAS	REFPROP	PR	I	1.55E+08	100.0	1.03E+08	100.0	1.89E+08	100.0	8.20E+08	100.0	100.0
			R	1.55E+08	100.0	1.03E+08	100.0	1.51E+08	100.0	1.07E+09	100.0	100.0
			L	1.55E+08	100.0	1.03E+08	100.0	1.52E+08	100.0	1.06E+09	100.0	100.0
			B	1.55E+08	100.0	1.03E+08	100.0	1.52E+08	100.0	1.07E+09	100.0	100.0
		GERG	I	1.67E+08	107.7	1.09E+08	105.8	2.02E+08	106.9	8.76E+08	106.8	106.8
			R	1.67E+08	107.7	1.09E+08	105.8	1.61E+08	106.6	1.15E+09	107.5	106.9
			L	1.67E+08	107.7	1.09E+08	105.8	1.63E+08	107.2	1.14E+09	107.5	107.1
			B	1.67E+08	107.7	1.09E+08	105.8	1.62E+08	106.8	1.14E+09	106.5	106.7
		AGA8	I	1.67E+08	107.7	1.09E+08	105.8	2.02E+08	106.9	8.77E+08	107.0	106.8
			R	1.67E+08	107.7	1.09E+08	105.8	1.61E+08	106.6	1.15E+09	107.5	106.9
			L	1.67E+08	107.7	1.09E+08	105.8	1.63E+08	107.2	1.14E+09	107.5	107.1
			B	1.67E+08	107.7	1.09E+08	105.8	1.62E+08	106.8	1.14E+09	106.5	106.7

(d) The North Morecambe Sherwood Sandstone Reservoir Initial Gas Composition

Table 6.28 Percentage variation of theoretical CO_2 storage capacity estimation using the methods of Bachu et al. (2007), Holloway et al. (2006), and Tseng et al. (2012) and various equations of state when compared to the results given by the RefProp (Lemmon et al., 2013) estimated Peng-Robinson (Peng and Robinson, 1976) storage capacity estimate for the different gas compositions: (a) pure methane, (b) gas mix 1 (as defined in Table 6.22), (c) gas mix 2 (as defined in Table 6.22), and (d) the North Morecambe Sherwood Sandstone reservoir initial gas composition. PR is the Peng-Robinson equation of state (Peng and Robinson, 1976), PRSV is the Peng-Robinson-Stryjek-Vera equation of state (Stryjek and Vera, 1986), RK is the Redlich-Kwong equation of state (Redlich and Kwong, 1949), and SRK is the Soave-Redlich-Kwong equation of state (Soave, 1972). The storage capacity estimates are shown for the different aquifer models: I is the result calculated using the industry estimated OGIP value, R is the finite radial aquifer model, L is the finite linear radial model and B is the base case aquifer model.

6.5.2.4.2. EFFECTIVE CO_2 STORAGE CAPACITY ESTIMATES

Effective CO_2 storage capacity was estimated using the method of Tseng et al. (2012), Table 6.8, equations 1.6 and 1.7, for a reservoir that experiences a water drive. Results are displayed in Figure 6.51 and Table 6.29. The graph (Figure 6.51) is similar to that for the theoretical CO_2 storage capacity estimation (Figure 6.50) in that the columns on the bar chart represent the base case aquifer model results and the error bars reflect the results of the finite radial and linear aquifer models. The results of the aquifer model based on the industry estimated value of OGIP are also plotted as circles for comparison.

Table 6.29 is similar to Table 6.28 in that it shows the effective CO_2 storage capacity estimates for the North Morecambe Sherwood Sandstone reservoir for different gas compositions: pure methane, gas mix 1 (as defined in Table 6.22), gas mix 2 (as defined in Table 6.22) and the North Morecambe Sherwood Sandstone reservoir initial gas composition. Table 6.29 also states the estimated effective CO_2 storage capacities for each of the four aquifer models. Capacity estimates vary according to the equation of state used and the tool/software used to model them, i.e. WebGasEOS (Reagan and Oldenburg, 2006) or RefProp (Lemmon et al., 2013). The percentage variation of the storage capacity estimates from the RefProp (Lemmon et al., 2013) estimated Peng-Robinson equation of state (Peng and Robinson, 1976) is also displayed.

Due to the limitations of the WebGasEOS online tool (Reagan and Oldenburg, 2006) the North Morecambe Sherwood Sandstone reservoir initial gas composition could only be modelled using RefProp software (Lemmon et al., 2013). The results modelled in RefProp (Lemmon et al., 2013) for the North Morecambe Sherwood Sandstone reservoir show an effective storage capacity ranging between 83.1 and 87.0 Mt CO_2 for the finite radial, finite linear and base case aquifer models. In comparison, the effective storage capacity using the industry estimated OGIP value gives higher estimates between 134.0 and 138.0 Mt CO_2. These results are further discussed in section 6.6.2.

Again, the GERG-2008 equation of state (Kunz and Wagner, 2012), closely followed by the AGA8-DC92 Model (Starling and Savidge, 1992), predict the

highest effective CO_2 storage capacities. The Soave-Redlich-Kwong equation of state (Peng and Robinson, 1976) predicts the lowest effective CO_2 storage capacities.

6.5.2.5. COMPARISON WITH PUBLISHED CO_2 STORAGE CAPACITY ESTIMATES FOR THE NORTH MORECAMBE SHERWOOD SANDSTONE RESERVOIR

Previously published theoretical CO_2 storage capacity estimates for the North Morecambe Sherwood Sandstone reservoir have ranged between 139 and 177 Mt CO_2. All estimations have used the method of Holloway et al., (2006), Table 6.8, equation 1.3. Within this study, theoretical CO_2 storage capacity estimates using the same method of Holloway et al., (2006), Table 6.8, equation 1.3 produced results ranging between 151 and 163 Mt CO_2, based on the finite radial, finite linear and base case aquifer models, and are therefore comparable with the published estimates. However, the results of Holloway et al., (2006), Table 6.8, equation 1.3 are also comparable with estimates of Bachu et al. (2007), Table 6.8, equation 1.2, ranging between 103 and 109 Mt CO_2, and Tseng et al. (2012), Table 6.8, equation 1.4, ranging between 155 and 167 Mt CO_2. Conversely the estimates of Bachu et al. (2007), Table 6.8, equation 1.1, represent the highest storage capacity estimates for the reservoir, ranging between 1060 and 1150 Mt CO_2.

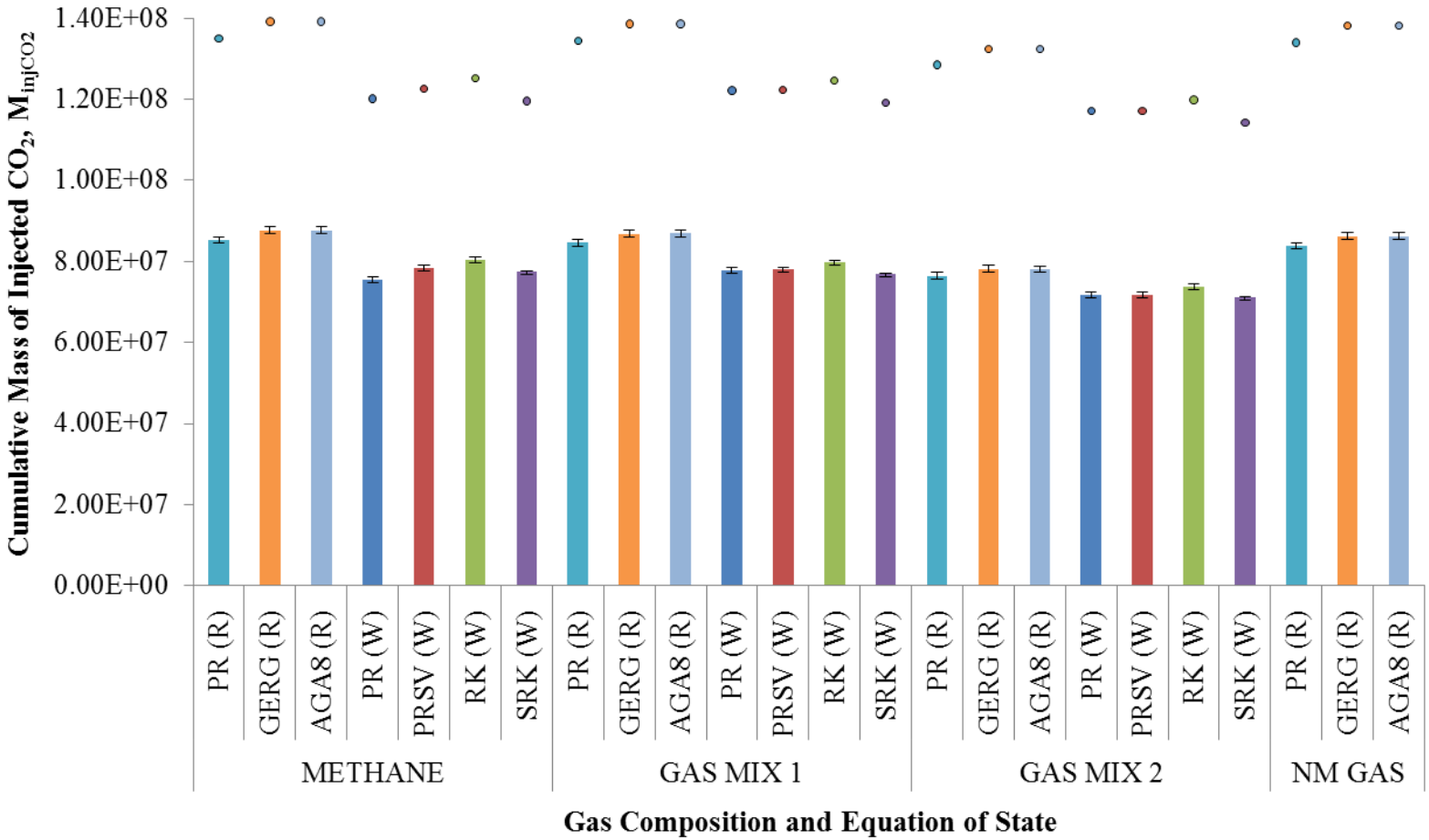

Figure 6.51 Estimated effective CO_2 storage capacity within the entire North Morecambe Sherwood Sandstone reservoir using the method of Tseng et al. (2012) and modelled with both RefProp (Lemmon et al., 2013) and the online tool by the Lawrence Berkeley National Laboratories, WebGasEOS (Reagan and Oldenburg, 2006). The columns represent the base case aquifer model results and the error bars reflect the results of the finite radial and linear aquifer models. The results of the aquifer model based on the industry estimated OGIP value are plotted as circles for comparison.

		REFPROP			WEBGASEOS			
		PR	GERG	AGA8	PR	PRSV	RK	SRK
METHANE	INDUSTRY	1.35E+08	1.39E+08	1.39E+08	1.20E+08	1.23E+08	1.25E+08	1.20E+08
	% of Peng-Robinson (RefProp)	*100.0*	*103.1*	*103.1*	*89.0*	*90.8*	*92.7*	*88.5*
	RADIAL	8.46E+07	8.69E+07	8.69E+07	7.47E+07	7.78E+07	7.98E+07	7.68E+07
	% of Peng-Robinson (RefProp)	*100.0*	*102.8*	*102.8*	*88.3*	*92.0*	*94.3*	*90.8*
	LINEAR	8.61E+07	8.85E+07	8.85E+07	7.61E+07	7.91E+07	8.11E+07	7.76E+07
	% of Peng-Robinson (RefProp)	*100.0*	*102.8*	*102.8*	*88.4*	*91.9*	*94.2*	*90.1*
	BASE CASE	8.53E+07	8.77E+07	8.77E+07	7.54E+07	7.85E+07	8.05E+07	7.75E+07
	% of Peng-Robinson (RefProp)	*100.0*	*102.8*	*102.8*	*88.4*	*91.9*	*94.3*	*90.8*
GAS MIX 1	INDUSTRY	1.35E+08	1.39E+08	1.39E+08	1.22E+08	1.22E+08	1.25E+08	1.19E+08
	% of Peng-Robinson (RefProp)	*100.0*	*103.0*	*103.1*	*90.9*	*90.9*	*92.6*	*88.5*
	RADIAL	8.38E+07	8.61E+07	8.61E+07	7.72E+07	7.73E+07	7.90E+07	7.62E+07
	% of Peng-Robinson (RefProp)	*100.0*	*102.7*	*102.7*	*92.1*	*92.2*	*94.2*	*91.0*
	LINEAR	8.53E+07	8.77E+07	8.77E+07	7.86E+07	7.86E+07	8.04E+07	7.70E+07
	% of Peng-Robinson (RefProp)	*100.0*	*102.7*	*102.7*	*92.0*	*92.1*	*94.2*	*90.2*
	BASE CASE	8.46E+07	8.69E+07	8.69E+07	7.79E+07	7.79E+07	7.97E+07	7.69E+07
	% of Peng-Robinson (RefProp)	*100.0*	*102.7*	*102.7*	*92.1*	*92.2*	*94.2*	*90.9*
GAS MIX 2	INDUSTRY	1.29E+08	1.32E+08	1.32E+08	1.17E+08	1.17E+08	1.20E+08	1.14E+08
	% of Peng-Robinson (RefProp)	*100.0*	*103.1*	*103.0*	*91.1*	*91.2*	*93.3*	*88.9*
	RADIAL	7.57E+07	7.73E+07	7.72E+07	7.10E+07	7.10E+07	7.32E+07	7.05E+07
	% of Peng-Robinson (RefProp)	*100.0*	*102.2*	*102.1*	*93.8*	*93.9*	*96.7*	*93.2*
	LINEAR	7.73E+07	7.90E+07	7.89E+07	7.24E+07	7.24E+07	7.46E+07	7.13E+07
	% of Peng-Robinson (RefProp)	*100.0*	*102.3*	*102.1*	*93.7*	*93.8*	*96.5*	*92.3*
	BASE CASE	7.65E+07	7.82E+07	7.81E+07	7.17E+07	7.17E+07	7.39E+07	7.12E+07
	% of Peng-Robinson (RefProp)	*100.0*	*102.3*	*102.1*	*93.7*	*93.8*	*96.6*	*93.1*
NM GAS	INDUSTRY	1.34E+08	1.38E+08	1.38E+08				
	% of Peng-Robinson (RefProp)	*100.0*	*103.1*	*103.1*				
	RADIAL	8.31E+07	8.54E+07	8.54E+07				
	% of Peng-Robinson (RefProp)	*100.0*	*102.7*	*102.7*				
	LINEAR	8.47E+07	8.70E+07	8.70E+07				
	% of Peng-Robinson (RefProp)	*100.0*	*102.8*	*102.8*				
	BASE CASE	8.39E+07	8.62E+07	8.62E+07				
	% of Peng-Robinson (RefProp)	*100.0*	*102.7*	*102.8*				
	Average Percentage Variation	100.0	102.7	102.7	91.1	92.2	94.5	90.7

Table 6.29 Percentage deviation of effective CO_2 storage capacity estimation within the entire North Morecambe Sherwood Sandstone reservoir using the method of Tseng et al. (2012) and various equations of state when compared to the results given by the RefProp (Lemmon et al., 2013) estimated Peng-Robinson (Peng and Robinson, 1976) storage capacity estimate for the different gas compositions: pure methane, gas mix 1 (as defined in Table 6.22), gas mix 2 (as defined in Table 6.22), and the North Morecambe Sherwood Sandstone reservoir initial gas composition. PR is the Peng-Robinson equation of state (Peng and Robinson, 1976), PRSV is the Peng-Robinson-Stryjek-Vera equation of state (Stryjek and Vera, 1986), RK is the Redlich-Kwong equation of state (Redlich and Kwong, 1949), and SRK is the Soave-Redlich-Kwong equation of state (Soave, 1972). The storage capacity estimates are shown for the different aquifer models: I is the aquifer model based on the industry estimated OGIP value, R is the finite radial aquifer model, L is the finite linear aquifer modal and B is the base case aquifer model.

6.6. DISCUSSION

6.6.1. SUMMARY

The observations over the productive lifetimes of both the South and North Morecambe Sherwood Sandstone reservoirs, and the results of the combined analysis of the various datasets have shown the reservoirs to be reasonable quality storage sites for CO_2. Within both reservoirs, production has been fairly simple and predictable. The South Morecambe reservoir has experienced no water drive throughout production. However, the North Morecambe reservoir has experienced a water drive, although there is no evidence of the water hindering well performance, as was the case in a portion of the productive lifetime of the Hewett Upper Bunter Sandstone reservoir (Chapter 5).

The complexity of the South and North Morecambe Sherwood Sandstone reservoirs lies in the distribution and proportion of illite precipitation within the reservoirs. Cowan (1996) stated that up to 44% of the original gas in place in North Morecambe is trapped (i.e. not producible) within the illite affected zone. This will obviously have a direct effect on the volume of CO_2 that can ultimately be injected stored within the South and North Morecambe reservoirs, especially within South Morecambe where the porosity of the illite affected zone exceeded that of the illite free zone. However, the theoretical and effective CO_2 storage capacity estimation methods of Bachu et al. (2007), Holloway et al. (2006) and Tseng et al. (2012) take into account the recovery factor (i.e. the ratio of the volume of produced hydrocarbons to the original volume in place), therefore, storage capacity estimates within this study should not be affected.

The South Morecambe Sherwood Sandstone reservoir offers the greatest CO_2 storage capacity, with theoretical storage capacity methods of Bachu et al. (2007), Holloway et al. (2006) and Tseng et al. (2012) yielding results in the order of hundreds to thousands of megatons of CO_2 and effective storage capacities of Tseng et al. (2012) constraining the results to hundreds of megatons of CO_2. In comparison, the smaller North Morecambe Sherwood Sandstone reservoir offers theoretical storage capacities in the order of hundreds to thousands of megatons of

CO_2, and effective CO_2 storage capacities in the order of tens of megatons of CO_2 using methods by the same authors.

6.6.2. THE USE OF AQUIFER MODELS FOR THE CORRECT ESTIMATION OF ORIGINAL GAS IN PLACE WITHIN A WATER DRIVE RESERVOIR

Throughout this study, it has been apparent that the original gas in place of 36.529 billion cubic metres of natural gas for the North Morecambe Sherwood Sandstone reservoir was too high. Evidence to suggest this has come from the use of equation 5.3 in Table 6.14 to estimate the cumulative volume of water influx into the reservoir (W_e) over the productive lifetime up until 2002 (the last recorded data for the reservoir). The W_e value obtained using the industry estimated OGIP was negative.

However, it is suggested here that the North Morecambe Sherwood Sandstone reservoir experiences a water drive. Evidence comes from the Cole Plot (Figure 6.33) which shows an overall curved trend indicative of a reservoir that experiences either moderate or strong water drive. It is important to note that the trend observed on Figure 6.33 in no way represents a linear trend which would indicate a depletion drive reservoir.

As such, finite radial and linear aquifer models have again been used to estimate the cumulative volume of water influx (W_e) into the North Morecambe Sherwood Sandstone reservoir. Equation 5.3 (in Table 6.14) was rearranged to equation 5.18 (in Table 6.20) to estimate the original gas in place of the North Morecambe Sherwood Sandstone reservoir based on the estimated W_e values produced from the finite radial, finite linear and base case aquifer models. The OGIP estimates obtained are likely to be more representative of the North Morecambe Sherwood Sandstone reservoir and the W_e values are positive so they represent the cumulative volume of water influx into the reservoir more accurately.

When the estimated OGIP values were input into the theoretical CO_2 storage capacity method of Tseng et al. (2012), Table 6.8, equation 1.4, the results based on all four aquifer models did not vary. This method does not include the OGIP as a

parameter, or any other parameter based on the OGIP estimate, such as the recovery factor, R_f. There method itself is based on well constrained parameters that do not show variability.

The theoretical CO_2 storage capacity method of Bachu et al. (2007), Table 6.8, equation 1.1, requires estimation of the recovery factor, R_f. The recovery factor is equal to the cumulative volume of gas produced divided by the original gas in place, therefore it is dependent on the accurate estimation of the OGIP. As it is likely that the industry estimated OGIP value was over-estimated, a low value for the recovery factor is produced – theoretically, it means a larger of volume of hydrocarbons was estimated to exist in the reservoir than actually are present. As such, the resulting industry estimated theoretical CO_2 storage capacity is lower than those predicted by the finite radial, finite linear and base case aquifer models (see Figure 6.50).

The theoretical CO_2 storage capacity method of Holloway et al. (2006), Table 6.8, equation 1.3, requires estimation of the OGIP. As this was over-estimated using the industry value, the resulting storage capacity estimated using the industry OGIP value is higher than those predicted by the finite radial, finite linear and base case aquifer models (see Figure 6.50).

The theoretical CO_2 storage capacity method of Bachu et al. (2007), Table 6.8, equation 1.2, requires both the recovery factor and OGIP to be estimated. As for the method of Bachu et al. (2007), Table 6.8, equation 1.1, the recovery factor is based on a value for OGIP which has been over-estimated by industry. Therefore a low value for the recovery factor would result in a lower storage capacity estimate. However, the method also requires estimation of the OGIP as a separate necessary parameter. The result is that the storage capacity estimate obtained using the industry estimated OGIP value is, in fact, slightly higher than those estimated using the finite radial, finite linear and base case aquifer models (see Figure 6.50).

The effective CO_2 storage capacity method of Tseng et al. (2012), Table 6.8, equation 1.7, requires estimation of the OGIP and W_e. As the OGIP was previously over-estimated using the industry value, this resulted in a negative value for W_e (see section 6.5.1.3.). Despite this, the resulting industry estimated effective CO_2

storage capacities were much greater than those estimated using the finite radial, finite linear and base case aquifer models (see Figure 6.51).

6.6.3. IMPACT OF EQUATION OF STATE AND METHOD APPLIED ON STORAGE CAPACITY ESTIMATION

Again, six equations of state were used in the investigation of CO_2 storage capacity within the South and North Morecambe Sherwood Sandstone reservoirs. Estimation with RefProp utilised equations of state predicted by the Peng-Robinson (Peng and Robinson, 1976), GERG-2008 (Kunz and Wagner, 2012) and AGA8 Model (Starling and Savidge, 1992). Estimation with WebGasEOS used the Peng-Robinson (Peng and Robinson, 1976) again, Peng-Robinson-Stryjek-Vera (Stryjek and Vera, 1986), Redlich-Kwong (Redlich and Kwong, 1949) and Soave-Redlich-Kwong (Soave, 1972) equations of state.

Within both the South and North Morecambe Sherwood Sandstone reservoir, the variability between the various equations of state in theoretical CO_2 storage capacity estimation are shown in Figure 6.23 and Figure 6.50 respectively for the four gas compositions modelled: pure methane, Gas Mix 1, Gas Mix 2 and the actual initial reservoir gas compositions. Table 6.12 and Table 6.28 show the percentage deviation of the storage capacity estimates away from the RefProp estimated (Lemmon et al., 2013) theoretical CO_2 storage capacity estimates using the Peng-Robinson equation of state (Peng and Robinson, 1976). This equation of state was used for comparison as it can also be modelled within WebGasEOS and therefore results from both programs are comparable.

The theoretical storage capacity estimates for the South Morecambe Sherwood Sandstone initial reservoir composition are comparable using the methods of Tseng et al. (2012), Table 6.8, equation 1.4, and Bachu et al. (2007), Table 6.8, equation 1.2, ranging between 312 and 329 Mt CO_2 depending on the equation of state used. Theoretical storage capacity estimates using the method of Holloway et al. (2006), Table 6.8, equation 1.3, are higher ranging between 764 and 811 Mt CO_2 depending on the equation of state used. However, the highest estimates of theoretical storage capacity within the South Morecambe Sherwood

Sandstone reservoir are achieved using the method of Bachu et al. (2007), Table 6.8, equation 1.1, with mean results for the entire reservoir ranging between 2530 and 2690 Mt CO_2 depending on the equation of state used.

The GERG-2008 equation of state (Kunz and Wagner, 2012), closely followed by the AGA8 Model (Starling and Savidge, 1992) always predicts the highest theoretical CO_2 storage capacities, whereas the Soave-Redlich-Kwong (Soave, 1972) equation of state predicts the lowest storage capacities.

The theoretical CO_2 storage capacity estimates for the North Morecambe Sherwood Sandstone initial reservoir composition are also comparable using the methods of Tseng et al. (2012), Table 6.8, equation 1.4, Holloway et al. (2006), Table 6.8, equation 1.3, and Bachu et al. (2007), Table 6.8, equation 1.2. Estimates range between 103 and 167 Mt CO_2 depending on the equation of state used, and based on the finite radial, finite linear and base case aquifer models. The highest theoretical CO_2 storage capacity estimates are obtained using the method of Bachu et al. (2007), Table 6.8, equation 1.1 with mean results ranging between 1060 and 1150 Mt CO_2 depending on the equation of state used, and based on the finite radial, finite linear and base case aquifer models.

Again, the GERG-2008 equation of state (Kunz and Wagner, 2012), closely followed by the AGA8 Model (Starling and Savidge, 1992) always predicts the highest theoretical CO_2 storage capacities, whereas the Soave-Redlich-Kwong (Soave, 1972) equation of state predicts the lowest storage capacities.

Effective CO_2 storage capacity results for the South Morecambe Sherwood Sandstone reservoir are shown in Figure 6.24 and Table 6.13. The results show an average effective storage capacity within the South Morecambe Sherwood Sandstone reservoir of between 209 and 213 Mt CO_2. The GERG-2008 (Kunz and Wagner, 2012), closely followed by the AGA8 Model (Starling and Savidge, 1992) equations of state, predict the highest effective CO_2 storage capacities, whereas the Redlich-Kwong equation of state (Redlich and Kwong, 1949) predicts the lowest effective storage capacity estimates.

In comparison, the effective CO_2 storage capacity results for the North Morecambe Sherwood Sandstone reservoir are shown in Figure 6.51 and Table 6.29. The results show an effective storage capacity within the North Morecambe

Sherwood Sandstone reservoir of between 83.1 and 87.0 Mt CO_2. The GERG-2008 (Kunz and Wagner, 2012) and AGA8 Model (Starling and Savidge, 1992) equations of state predict the highest storage capacities, and the WebGasEOS (Reagan and Oldenburg, 2006) estimated Peng-Robinson equation of state, the lowest.

As previously discussed in Chapters 4 and 5, it is likely the GERG-2008 (Kunz and Wagner, 2012) and AGA8 Model (Starling and Savidge, 1992) equations of state provide the best representation of storage capacity estimates as they have been specifically developed for the natural gas environment and is more valid, particularly within the region of the vapour-liquid equilibrium.

It is likely that the theoretical and effective CO_2 storage capacity methods of Tseng et al. (2012), Table 6.8, equations 1.4, 1.6 and 1.7, provide the most accurate estimates within both the South and North Morecambe reservoirs, as they require parameters that are generally well constrained and their methods are more complex than the alternative methods within this study.

As it was necessary to assume aquifer models for the North Morecambe Sherwood Sandstone reservoir to accurately estimate the cumulative volume of water influx into the reservoir, W_e, and the OGIP (due to the over-estimation by industry), it is likely that the base case aquifer model (i.e. the mean between the finite radial and finite linear aquifer models) will yield the most accurate values for these parameters. Unfortunately, it was not possible to establish whether the finite radial or finite linear aquifer model was more representative of the North Morecambe Sherwood Sandstone reservoir. As such, it is better to use the base case aquifer model despite there being very little difference between the W_e and OGIP values estimated using the finite radial and finite linear aquifer models.

6.6.4. THE USE OF MONTE CARLO SIMULATION WITHIN CO_2 STORAGE CAPACITY EQUATIONS

This study has again attempted to improve upon previous work (such as that of Bentham (2006), Brook et al. (2003), Holloway et al. (2006) and Kirk (2006)) by attempting to honour all available porosity data within the geometric method of CO_2 storage capacity estimation of Bachu et al. (2007), Chapter 1, equation 1.1.

Porosity data from both the South and North Morecambe Sherwood Sandstone reservoirs were assigned best-fit probability distributions, truncated at 0% porosity (as it is not possible to have a negative value for porosity). Again, Monte Carlo simulation was run thousands of times over which allowed repeated random sampling of the assigned probability distributions to input porosity values into the storage capacity equation. This produced a substantial range of variation in the resulting storage capacity estimates.

Again, it was not possible to assign probability distributions which fit the porosity data with any degree of confidence. When the Anderson-Darling P-value test was applied, which tests for normality, the resulting P-values were both equal to 0.00, i.e. the data do not follow a specified distribution. Therefore, it is not appropriate to conduct Monte Carlo simulation that samples from these distributions to estimate CO_2 storage capacity.

As such, until a better solution can be incorporated into the CO_2 storage capacity method of Bachu et al. (2007), Chapter 1, equation 1.1, which attempts to honour all available porosity data for a reservoir, it is most likely better to use mean porosity values.

6.6.5. LIMITATIONS

Data limitations are apparent within the South Morecambe Sherwood Sandstone pressure dataset. It is apparent from Figure 6.9, showing the cumulative volume of gas production and associated reservoir pressure decline within the South Morecambe reservoir that the pressure readings become sporadic from 1998 onwards. Any pressure measurements taken after 1998 also seem to fluctuate around the expected linear (depletion drive) trend. This has a direct effect on the material balance (P/Z) plot in Figure 6.10, and the Cole Plot for the reservoir in Figure 6.11.

This may be due to issues with “in house” data gathering and/or spreadsheet updating. It is unlikely that the South Morecambe reservoir is entering a new phase where aquifer movement is now being induced into the reservoir following a large volume of gas production, considering the cumulative gas production trend in

Figure 6.9. If a large volume of aquifer water was entering the South Morecambe reservoir, a change in the gas production trend may be expected, however, this is not observed to occur in Figure 6.9. Also, the Cole Plot of the data (Figure 6.11) still shows a marked depletion drive trend.

There was no information provided by Centrica on the cumulative volume of produced water, W_p, from the North Morecambe Sherwood Sandstone reservoir. The parameter, W_p, is not explicitly incorporated within the effective CO_2 storage capacity method of Tseng et al. (2012), Table 6.8, equations 1.6 and 1.7, however, the parameter W_e (the cumulative volume of water influx into the reservoir) is. The parameter W_p is related to W_e through the material balance equation previously stated in Chapter 5 and replicated here in Table 6.30. As such, if W_p is significant enough in volume it should increase the effective CO_2 storage capacity estimate.

MATERIAL BALANCE EQUATION	EQUATION NUMBER
$G(B_{gi}) = (G - G_p)B_g + W_e - W_pB_w$	(5.2)

Table 6.30 The material balance equation previously stated in Chapter 5. See Chapter 5 for definition of symbols. After Archer and Wall (1986).

Due to the lack of information from industry on the volume of W_p, the website of the Department of Energy and Climate Change (DECC, 2013) has been used to estimate the volume of produced water. The resulting volume, even when extrapolated up until present day is approximately three orders of less than that of W_e. Therefore, we can safely ignore the effect of W_p significantly affecting the resulting effective CO_2 storage capacity estimates.

Finally, there is little information on the effect of the presence of illite within both the North and South Morecambe reservoirs during production. Illite precipitation has destroyed permeability within the reservoirs. There is an abundance of permeability data from wells, however, information is lacking laterally between wells, i.e. the lateral distribution is not well defined. Attempts have been made previously to map the lateral distribution on seismic, e.g. Meadows

and Beach (1993a; 1993b), however, this is not necessarily possible as much of the illite affected zone is unresolvable on seismic.

6.7. CONCLUSIONS

The South Morecambe Sherwood Sandstone reservoir is a reasonable quality CO_2 storage site, with simple and predictable behaviour throughout its productive lifetime and no water encroachment hindering well performance. The reservoir has been proven through use of material balance and Cole Plots to be a depletion drive reservoir. It also has a large theoretical and effective storage capacity for CO_2.

The estimated theoretical storage capacity of the South Morecambe Sherwood Sandstone reservoir using the method of Tseng et al. (2012) and the GERG-2008 equation of state (Kunz and Wagner, 2012) was found to be 328 Mt CO_2, and the effective storage capacity was found to be 213 Mt CO_2.

The North Morecambe Sherwood Sandstone reservoir is again of reasonable quality for CO_2 storage. Productive behaviour has been relatively simple and predictable, although there is evidence of a water drive within the reservoir, as observed from Cole Plots of the production data.

The North Morecambe Sherwood Sandstone reservoir offers a smaller theoretical CO_2 storage capacity of 167 Mt CO_2, using the method of Tseng et al. (2012) and the GERG-2008 equation of state (Kunz and Wagner, 2012), and based upon the base case aquifer model. The effective CO_2 storage capacity further constrains this estimate to 86.2 Mt CO_2 using the same method and equation of state, and again based upon the base case aquifer model.

7 Discussion

7.1. KEY RESULTS

The key results from this study are as follows:

1. The material balance approach to theoretical and effective CO_2 storage capacity is considered to be superior to the geometric approach.
2. Theoretical CO_2 storage capacity estimates vary due to (a) the method of storage capacity estimation used, (b) the equations of state used to model relevant parameters, (c) the reservoir drive mechanism (degree of aquifer support), (d) the variability of input parameters, and (e) the overall accuracy of the input parameters.
3. Effective CO_2 storage capacity estimates require the cumulative volume of water influx into a reservoir (W_e) across the productive lifetime of a gas reservoir to be known. This parameter is especially sensitive to the estimated OGIP value, therefore it is paramount this value is accurate to obtain an accurate effective CO_2 storage capacity estimate.
4. Effective capacity coefficients are sensitive to the recovery factor (R_f) and aquifer performance. They can also be used to identify water drive reservoirs that have been incorrectly characterised as depletion drive reservoirs.
5. It is necessary to understand and characterise the dynamic behaviour between two reservoirs in pressure communication throughout their productive lifetimes in order to predict and manage their behaviour throughout CO_2 storage.

These key results are now discussed in more detail throughout the following sections, along with comparisons with and improvements to previous studies.

7.1.1. COMPARISON AND EVALUATION OF GEOMETRIC VERSUS MATERIAL BALANCE APPROACHES TO CO_2 STORAGE CAPACITY ESTIMATION

This study has found that the geometric approach to theoretical CO_2 storage capacity estimation of Bachu et al. (2007), Chapter 1, equation 1.1, has produced results with the widest range of possible outcomes depending on the equation of state used, when compared to the results of the alternative material balance approaches (see Figure 7.1). Much of this variability comes from Monte Carlo simulation of the porosity data. However, when only the mean values are used within the method of Bachu et al. (2007), Chapter 1, equation 1.1, the results produced are still more variable than those of the alternative methods (see the red bars on Figure 7.1).

The geometric method of Bachu et al. (2007), Chapter 1, equation 1.1, uses parameters such as reservoir porosity which are naturally heterogeneous. Conversely, the material balance methods of Bachu et al. (2007), Chapter 1, equation 1.2, Holloway et al. (2006), Chapter 1, equation 1.3, and Tseng et al. (2012), Chapter 1, equation 1.4, use parameters that are well constrained and show little or no variability.

Previous work, such as that of Bentham (2006), Brook et al. (2003), Holloway et al. (2006) and Kirk (2006), has seen the use of mean values for parameters such as reservoir porosity to be input into storage capacity equations. This study has attempted to improve upon these previous studies by honouring all available reservoir porosity data within the geometric theoretical CO_2 storage capacity method of Bachu et al. (2007), Chapter 1, equation 1.1, through use of Monte Carlo simulation. It has been stated within chapters 4, 5 and 6 that the reservoir porosity (and permeability) data have been assigned probability distributions. However, when the Anderson-Darling P-value test was applied, which analyses the goodness-of-fit of a dataset to an assigned probability distribution, the results of all the tests returned a P-value of 0.00, i.e. the data did not follow the specified distribution. Despite this, the assigned probability

distributions were used within the Monte Carlo simulation of the storage capacity equation of Bachu et al. (2007), Chapter 1, equation 1.1. Due to Monte Carlo simulation of the entire probability distribution, a vast range of theoretical CO_2 storage capacity estimates can be observed on Figure 7.1. The lowest estimates reflect the lowest porosities within the data, and vice versa. These are extremes of the data and have a low probability of occurrence. As such, it is more suitable to use mean values of the porosity data within the storage capacity equation. These are visible on Figure 7.1 as red bars.

The Hewett Upper and Lower Bunter Sandstone reservoirs and North and South Morecambe Sherwood Sandstone reservoirs both have a variety of lithofacies distributions. Further work might focus on obtaining the porosity and permeability data from each lithofacies to investigate whether individual probability distributions can be assigned to them. It would be interesting to see if these distributions show a better fit than the one distribution for the entire reservoir as was conducted within this study.

Figure 7.1 (Overleaf). Estimated CO_2 Storage Capacity within Gas Fields by Region. Previously published theoretical CO_2 storage capacities (previously shown in Figure 1.7 of Chapter 1) are displayed as black bars with their source reference written in black on the left hand side of the figure. The theoretical CO_2 storage capacities estimated within this study are displayed as black bars and the source reference of the method used written in red on the left hand side of the figure. The red bars shown on the figure within the black bars marking the theoretical CO_2 storage capacity range of the method of Bachu et al., (2007), are the range of the mean values taken from the probability distributions previously described in Chapters 4, 5, and 6. The green bars illustrate the effective CO_2 storage capacity estimates of Tseng et al., (2012). The storage capacity estimates shown within the water drive gas reservoirs (the Hewett Upper Bunter Sandstone reservoir and the North Morecambe Sherwood Sandstone reservoir) illustrate the results of the base case aquifer model. The individual ranges within the methods of this study show the variability in storage capacity estimates with equation of state used, i.e. Peng-Robinson (Peng and Robinson, 1976), GERG-2008 (Kunz and Wagner, 2012), AGA8 Model (Starling and Savidge, 1992), Peng-Robinson-Stryjek-Vera (Stryjek and Vera, 1986), Redlich-Kwong (Redlich and Kwong, 1949), or Soave-Redlich-Kwong (Soave, 1972).

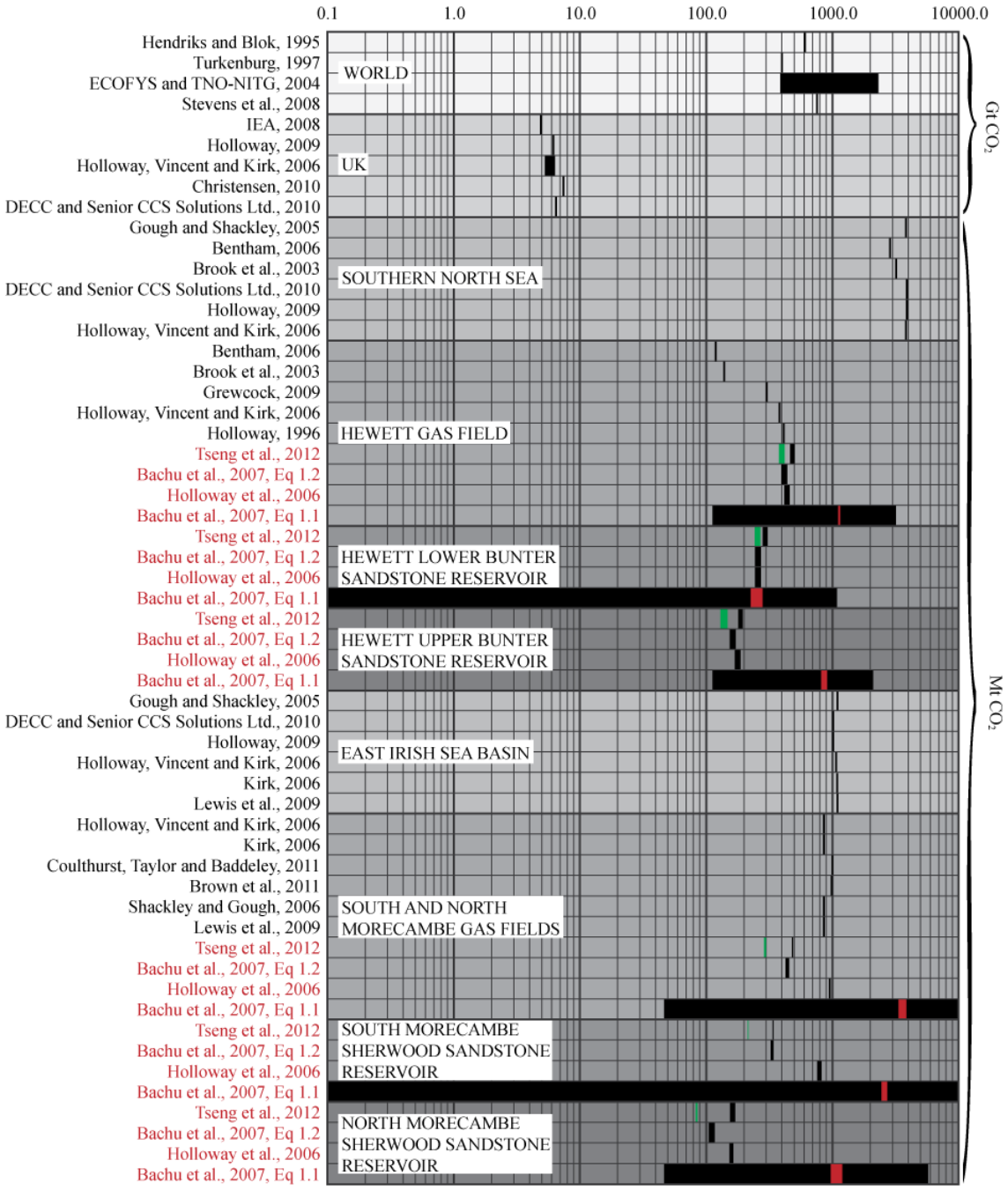
0.1
1.0
10.0
100.0
1000.0
10000.0
Hendriks and Blok, 1995
Turkenburg, 1997
ECOFYS and TNO-NITG, 2004
Stevens et al., 2008
IEA, 2008
Holloway, 2009
Holloway, Vincent and Kirk, 2006
Christensen, 2010
DECC and Senior CCS Solutions Ltd., 2010
Gough and Shackley, 2005
Bentham, 2006
Brook et al., 2003
DECC and Senior CCS Solutions Ltd., 2010
Holloway, 2009
Holloway, Vincent and Kirk, 2006
Bentham, 2006
Brook et al., 2003
Grewcock, 2009
Holloway, Vincent and Kirk, 2006
Holloway, 1996
Tseng et al., 2012
Bachu et al., 2007, Eq 1.2
Holloway et al., 2006
Bachu et al., 2007, Eq 1.1
Tseng et al., 2012
Bachu et al., 2007, Eq 1.2
Holloway et al., 2006
Bachu et al., 2007, Eq 1.1
Tseng et al., 2012
Bachu et al., 2007, Eq 1.2
Holloway et al., 2006
Bachu et al., 2007, Eq 1.1
Gough and Shackley, 2005
DECC and Senior CCS Solutions Ltd., 2010
Holloway, 2009
Holloway, Vincent and Kirk, 2006
Kirk, 2006
Lewis et al., 2009
Holloway, Vincent and Kirk, 2006
Kirk, 2006
Coulthurst, Taylor and Baddeley, 2011
Brown et al., 2011
Shackley and Gough, 2006
Lewis et al., 2009
Tseng et al., 2012
Bachu et al., 2007, Eq 1.2
Holloway et al., 2006
Bachu et al., 2007, Eq 1.1
Tseng et al., 2012
Bachu et al., 2007, Eq 1.2
Holloway et al., 2006
Bachu et al., 2007, Eq 1.1
Tseng et al., 2012
Bachu et al., 2007, Eq 1.2
Holloway et al., 2006
Bachu et al., 2007, Eq 1.1
WORLD
UK
SOUTHERN NORTH SEA
HEWETT GAS FIELD
HEWETT LOWER BUNTER SANDSTONE RESERVOIR
HEWETT UPPER BUNTER SANDSTONE RESERVOIR
EAST IRISH SEA BASIN
SOUTH AND NORTH MORECAMBE GAS FIELDS
SOUTH MORECAMBE SHERWOOD SANDSTONE RESERVOIR
NORTH MORECAMBE SHERWOOD SANDSTONE RESERVOIR
Gt CO2
Mt CO2

7.1.2. THEORETICAL CO_2 STORAGE CAPACITY VARIABILITY

This study has shown that theoretical CO_2 storage capacity estimates vary as a result of several factors: (a) the method of storage capacity estimation used, (b) the equation of state used to model the results, (c) the reservoir drive mechanism (degree of aquifer support), (d) the degree of natural variability of input parameters, and (e) the overall accuracy of the input parameters.

Figure 7.1 shows the variability of CO_2 storage capacity estimates from selected regions, both from the literature and within this study. Within the Hewett Gas Field, i.e. the Hewett Lower and Upper Bunter Sandstone reservoirs, the theoretical CO_2 storage capacity results predicted within this study are generally slightly higher than the published results. The low end of the CO_2 storage capacity range defined using the method of Bachu et al. (2007), Chapter 1, equation 1.1, reflects the published estimate of Bentham (2006), however, the range surpasses the other published estimates, and estimates predicted within this study, with the high end of the range predicting a huge estimate of ~2.2 Gt CO_2 (Figure 7.1). Even the mean results of the method of Bachu et al. (2007), Chapter 1, equation 1.1, predict a range (red bar in Figure 7.1) of storage capacity estimates (dependant on the equation of state used) that are over double the highest estimates using the alternative methods within this study.

Overall, the Hewett Gas Field makes up around 10% of the total theoretical utilisable pore space for CO_2 within the Southern North Sea (Figure 7.1). It has been proposed that injection into the Hewett Lower Bunter Sandstone reservoir will begin at 6600 tonnes/day, equating to a total of 2.409 Mt/year; later in its life the injection rate will increase to 24600 tonnes/day, or 9.6 Mt/year (BakerRDS, 2011b). At the lower injection rate, if applied to both the Hewett Lower and Upper Bunter Sandstone reservoirs, the Hewett Gas Field will have a storage lifetime of between 50 and 208 years; at the higher injection rate the storage lifetime is between 13 and 52 years. Storage lifetime is estimated from both the published estimates and estimates made within this study, excluding those of the method of Bachu et al. (2007), Chapter 1, equation 1.1, which are considered to be erroneously high.

The theoretical CO_2 storage capacity estimates of the South and North Morecambe Sherwood Sandstone reservoirs predicted within this study tend to be lower than those of the published estimates, except those of the method of Bachu et al. (2007), Chapter 1, equation 1.1 (see Figure 7.1). The published estimates have all used the method of Holloway et al. (2006), Chapter 1, equation 1.3. The result predicted within this study using the method of Holloway et al. (2006), Chapter 1, equation 1.3, predicts comparable estimates. Again, the method of Bachu et al. (2007), Chapter 1, equation 1.1, predicts a large range of storage capacity, surpassing both the published storage capacity estimates and those estimated within this study (see Figure 7.1). Also, the mean values occur over a range of storage capacity approximately 2 Gt higher than the highest published estimates (Figure 7.1).

Overall, the South and North Morecambe Sherwood Sandstone reservoirs make up at least 90% of the total theoretical utilisable pore space within the East Irish Sea Basin (Figure 7.1). Proposed injection rates into the South and North Morecambe reservoirs are unknown, however, if injection rates equivalent to those proposed within the Hewett Lower Bunter Sandstone reservoir are used the maximum storage lifetime would be between 178 and 415 years, based on the lower injection rate, and between 45 and 104 years, based on the higher injection rate.

Together, the largest theoretical CO_2 storage capacity estimates from the four reservoirs equate to approximately 1.5 Gt CO_2, excluding the results of the method of Bachu et al. (2007), Chapter 1, equation 1.1. The UK is estimated to have 5-8 Gt of theoretical utilisable pore space for CO_2; therefore the four reservoirs evaluated within this study make up a significant proportion of that pore space (Figure 7.1).

It is apparent from Figure 7.1 that, within this study, the method most susceptible to variability is the geometric storage capacity method of Bachu et al. (2007), Chapter 1, equation 1.1, as it predicts the widest range of estimates. This is a direct result of Monte Carlo simulation. Its very nature is to produce a range of values that can be used to minimise risk when input parameters (such as porosity, reservoir height and reservoir area) show a high degree of natural variability, i.e. the results define the minimum and maximum extremes in the data. Therefore, the

mean values have been included on Figure 7.1, expressed as a range of values (illustrated by the red bars). The range of mean values is a result of the variability of the storage capacity estimates as a result of the equation of state used. The mean ranges of results generally depict storage capacities much higher than those determined using the alternative methods.

The alternative methods of Bachu et al. (2007), Chapter 1, equation 1.2, Holloway et al. (2006), Chapter 1, equation 1.3, and Tseng et al. (2012), Chapter 1, equation 1.4, generally predict comparable theoretical CO_2 storage capacities. The method of Tseng et al. (2012), Chapter 1, equation 1.4, tends to predict slightly higher capacities, and the method of Bachu et al. (2007), Chapter 1, equation 1.2, tends to predict the most conservative theoretical CO_2 storage capacities.

It is also apparent from Figure 7.1 that within this study storage capacity estimates vary depending on reservoir drive mechanism. Depletion drive reservoirs, such as the Hewett Lower Bunter and South Morecambe Sherwood Sandstone reservoirs, show the greatest range in storage capacity estimation using the geometric method of Bachu et al. (2007), Chapter 1, equation 1.1, in comparison to water drive reservoirs, such as the Hewett Upper Bunter and North Morecambe Sherwood Sandstone reservoirs. The sensitivity charts in Chapters 5 and 6 show that the storage capacity results of Bachu et al. (2007), Chapter 1, equation 1.1 are most sensitive to reservoir porosity. The standard deviation of the Hewett Lower Bunter Sandstone reservoir porosity data is 7.52 and for the Hewett Upper Bunter Sandstone reservoir, 6.08. Therefore, the data is more spread within the Hewett Lower Bunter Sandstone reservoir in comparison to the Hewett Upper Bunter Sandstone reservoir. This may account for the wide range of storage capacity estimates we see in depletion drive reservoirs in comparison to water drive reservoirs.

The alternative methods rely on input parameters which can be well constrained, including initial pressures and temperatures within the reservoirs. However, this study has demonstrated that the values of parameters such as the original gas in place (OGIP), which is generally thought to be well constrained, should not necessarily be taken at face value. Both the Hewett Upper Bunter Sandstone reservoir and the North Morecambe Sherwood Sandstone reservoir have

been originally modelled as depletion drive reservoirs. When their individual historical data was represented on a Cole Plot they were proven to have experienced a water drive. As such, the OGIP value, initially based on a depletion drive reservoir model, is an over-estimate, as described in Chapters 5 and 6. Therefore, it is imperative to ascertain whether a proposed storage reservoir experiences a water drive. If the OGIP is over-estimated, it follows that the final storage capacity estimate will also be an over-estimate. This is explored further in section 7.2.

In summary, the theoretical CO_2 storage capacity results show a vast amount of variability. Within the Hewett Gas Field (both Upper and Lower Bunter Sandstone reservoirs) the lowest combined capacity estimate is 108.24 $MtCO_2$ in Bentham (2006). The highest combined capacity estimate is 1175.88 $MtCO_2$ (using mean values), predicted within this study using the geometric method of Bachu et al. (2007), Chapter 1, equation 1.1. This equates to a difference in estimated storage capacity of 1067.64 $MtCO_2$. If the proposed post-demonstration CO_2 injection rate for the Hewett Lower Bunter Sandstone reservoir of 9.6 Mt/year is used (BakerRDS, 2011b), this would lead to a difference in storage lifetime of 111.21 years. Likewise, within the South and North Morecambe Gas Fields, the lowest combined capacity estimate is 438.00 $MtCO_2$, predicted within this study using the material balance method of Bachu et al. (2007), Chapter 1, equation 1.2. The highest combined capacity estimate is 3831.44 $MtCO_2$, predicted within this study using the geometric method of Bachu et al. (2007), Chapter 1, equation 1.1. This equates to a difference in estimated storage capacity of 3393.44 $MtCO_2$. Again, if the same CO_2 injection rate of 9.6 Mt/year is used, this would lead to a difference in storage lifetime of 353.5 years.

This study has illustrated the importance of comparing and evaluating the variability of the results of the different methods of CO_2 storage capacity estimation and their individual input parameters. The difference in estimated CO_2 storage lifetimes can be substantial within a reservoir and this has direct implications for economics – if the estimated storage lifetime of a reservoir is found to be substantially shorter (i.e. tens of years shorter), it may no longer be economically viable to develop for carbon storage.

7.1.3. EFFECTIVE STORAGE CAPACITY VARIABILITY

This study has found that the cumulative volume of water influx into a reservoir, W_e, is particularly sensitive to the estimated value of OGIP, and as such can substantially affect the effective CO_2 storage capacity estimates. It is therefore extremely important that the OGIP value is estimated to a degree of accuracy as it has direct implications for estimates of W_e and both theoretical and effective CO_2 storage capacity – if the OGIP has been over-estimated it follows that storage capacity will be over-estimated, as is demonstrated in Figure 7.2.

Estimation of OGIP is more complex within water drive reservoirs than depletion drive reservoirs. The studies of the Hewett Upper Bunter Sandstone reservoir and the North Morecambe Sherwood Sandstone reservoir have illustrated the difficulties in identifying the reservoir drive mechanism from P/z plots, which has previously been well documented in Agarwal et al. (1965), Bruns et al. (1965), Chierici et al. (1967), Dake (1978), Hagoort (1988), Pletcher (2002) and Vega and Wattenbarger (2000). Both reservoirs show data that fluctuates only slightly about a linear trend, which as a first-pass result may be interpreted as indicative of a depletion drive reservoir. However, when the same data is plotted as a Cole plot, identification of a water drive reservoir is simplified – any deviation from a linear trend whatsoever indicates the presence of a water drive, and the strength of the water drive can be determined from the shape of the curve (Pletcher, 2002). The incorrect characterisation of the reservoir drive mechanism has direct implications for estimation of the OGIP and therefore CO_2 storage capacity. This study has shown that if a water drive reservoir (such as the Hewett Upper Bunter Sandstone reservoir and the North Morecambe Sherwood Sandstone reservoir) is incorrectly characterised as a depletion drive reservoir, the OGIP can be significantly over-estimated resulting in an over-estimation of CO_2 storage capacity.

Figure 7.2 uses the method of Tseng et al. (2012), Chapter 1, equations 1.6 and 1.7. It shows that when the industry estimated OGIP value is kept constant, the resulting effective CO_2 storage capacities are over-estimates in comparison to those where the OGIPs of the finite radial, finite linear and base case models are kept constant. This is because the industry estimated OGIP value is an over-estimate.

Figure 7.2 also shows that when the OGIP values estimated using the finite radial, finite linear and base case aquifer models are kept constant, the resulting storage capacity estimates using the W_e values based on the industry estimate of OGIP, are over-estimates.

This study has improved on previous studies by illustrating the importance of correctly identifying the reservoir drive mechanism and estimating appropriate OGIP values. Previous studies, such as Bentham (2006), have applied a scaling factor to the theoretical CO_2 storage capacity estimates of a group of reservoirs to accommodate the reservoir drive mechanism and reduce the theoretical CO_2 storage capacity estimates to closely resemble an effective CO_2 storage capacity estimate. Within the study of Bentham (2006) the theoretical CO_2 storage capacity estimate of Brook et al. (2003) was reduced to 90% within depletion drive reservoirs, 65% within water drive reservoirs, and 77.5% within both pressure depletion and water drive reservoirs. This method can be applied quickly to a large group of reservoirs, however, it is an inappropriate method to use – CO_2 storage capacity is sensitive to OGIP, which is sensitive to aquifer strength and this method does not accommodate variations in aquifer strength by site.

To analyse this in more detail, the Hewett Gas Field (encompassing both the Upper and Lower Bunter Sandstone reservoirs) had an estimated CO_2 storage capacity of 139.66 Mt CO_2 in the study of Brook et al. (2003). The study of Bentham (2006) assumed both depletion and water drive reservoir mechanisms, and reduced this estimate to 108.24 Mt CO_2. The results of this study have shown that the estimate of Brook et al. (2003) is very conservative in comparison to the other storage capacity estimates from this study and the published literature, and is further reduced within the study of Bentham (2006), (see Figure 7.1). The estimate is almost four times smaller than the combined effective CO_2 storage capacity estimates from the Hewett Upper and Lower Bunter Sandstone reservoirs within this study of 409 Mt CO_2 as estimated using the method of Tseng et al. (2012) and the GERG-2008 equation of state (Kunz and Wagner, 2012).

If the equivalent analysis is conducted on the combined theoretical CO_2 storage capacity estimates for the Hewett Upper and Lower Bunter Sandstone reservoirs, i.e. the reservoir drive mechanism is assumed to be both depletion and

water drive, the storage capacity estimate of 504 $MtCO_2$ is reduced by 77.5% to 390.6 $MtCO_2$. This is still 3.6 times greater than the estimate of Bentham (2006).

The effective CO_2 storage capacity estimate of Tseng et al. (2012) accommodates the reservoir drive mechanism through the inclusion of the parameter W_e (the cumulative volume of aquifer influx into a reservoir). Within depletion drive reservoirs the value of W_e will be zero or negligible. However, within a water drive reservoir this value can be substantial. As such, the combined effective CO_2 storage capacity estimate for the Hewett Upper and Lower Bunter Sandstone reservoirs of 504 $MtCO_2$ will have already factored in a reduction in capacity to accommodate the water drive reservoir (Upper Bunter) along with the depletion drive reservoir estimate (Lower Bunter). The estimate of Bentham (2006) is then 4.7 times smaller than that estimated using the method of Tseng et al. (2012) and the GERG-2008 equation of state (Kunz and Wagner, 2012).

7.1.4. EFFECTIVE CAPACITY COEFFICIENTS

A final way of estimating the variability of effective CO_2 storage capacity estimates is through estimation of the effective capacity coefficient. Effective CO_2 storage capacity constitutes a fraction of the theoretical CO_2 storage capacity. As such, this fraction (the effective capacity coefficient) will range between zero, where no storage is possible, to one, where all theoretically accessible pore volume is occupied by CO_2 (Doughty et al., 2001; Kopp et al., 2009). The effective capacity coefficient can be estimated through use of the following equation:

$$C_e = \frac{Effective\ CO_2\ Storage\ Capacity}{Theoretical\ CO_2\ Storage\ Capacity} \tag{7.1}$$

After Tseng et al. (2012).

Within this study, the theoretical CO_2 storage capacities predicted using the various methods have been input into equation 7.1 against the effective CO_2 storage capacity estimated using the method of Tseng et al. (2012), Chapter 1, equations 1.6 and 1.7. The results are shown in Figure 7.3. For the depletion drive reservoirs

(the Hewett Lower Bunter Sandstone reservoir and the South Morecambe Sherwood Sandstone reservoir) results are shown to vary according to the equation of state and theoretical CO_2 storage capacity method used. For the water drive reservoirs (the Hewett Upper Bunter Sandstone reservoir and the North Morecambe Sherwood Sandstone reservoirs) the results also vary depending on the aquifer model used for storage capacity estimation.

Figure 7.3 (a) shows the effective capacity coefficient results for the Hewett Lower Bunter Sandstone reservoir. The lowest effective capacity coefficient estimates are predicted using the theoretical CO_2 storage capacity method of Tseng et al. (2012), Chapter 1, equation 1.4, with an effective capacity coefficient of 0.81 using the Peng-Robinson equation of state (Peng and Robinson, 1976) estimated within WebGasEOS (Reagan and Oldenburg, 2006). The highest effective capacity coefficients are predicted using the method of Bachu et al. (2007), Chapter 1, equation 1.2, with a coefficient of 0.99 using the Peng-Robinson equation of state (Peng and Robinson, 1976) estimated within WebGasEOS (Reagan and Oldenburg, 2006). The average effective capacity coefficient within the reservoir is 0.93, meaning that the effective CO_2 storage capacity makes use of a significant proportion of the total theoretical pore space. All the theoretical CO_2 storage capacity methods predict similar effective capacity coefficients meaning that the theoretical capacity methods used within this study have all produced good estimates within the Hewett Lower Bunter Sandstone reservoir. Even the mean range of the theoretical CO_2 storage capacity estimates (Figure 7.1) produce comparable theoretical estimates compared to the alternative methods. It is likely that input parameters to the storage capacity equations can be better constrained towards the end of the productive lifetime of a reservoir.

Figure 7.3 (b) shows the effective capacity coefficient results for the South Morecambe Sherwood Sandstone reservoir. The results are much more variable in comparison to those of the Hewett Lower Bunter Sandstone reservoir, despite the South Morecambe Sherwood Sandstone reservoir being a depletion drive reservoir. The lowest effective capacity coefficient estimates are predicted using the theoretical CO_2 storage capacity method of Bachu et al. (2007), Chapter 1, equation 1.1, with an effective capacity coefficient of 0.08 using the GERG-2008 equation of

state (Kunz and Wagner, 2012) estimated within RefProp (Lemmon et al., 2013). The highest effective capacity coefficients are predicted using the method of Bachu et al. (2007), Chapter 1, equation 1.2, with a coefficient of 0.73 using the Redlich-Kwong equation of state (Redlich and Kwong, 1949) estimated using WebGasEOS (Reagan and Oldenburg, 2006). The average effective capacity coefficient within the reservoir is 0.54, excluding the results calculated using the method of Bachu et al. (2007), Chapter 1, equation 1.1, which are considered to be erroneous. The reservoir has a low average effective capacity coefficient in comparison to that of the Hewett Lower Bunter Sandstone reservoir (Figure 7.3 (a)). This is in part due to the South Morecambe Sherwood Sandstone reservoir being only partially depleted; the effective capacity coefficient is expected to increase as production progresses as there will be an increase in available pore space for CO_2.

Figure 7.3 (c) shows the effective capacity coefficient results for the Hewett Upper Bunter Sandstone reservoir. Due to the Hewett Upper Bunter Sandstone reservoir being a water drive reservoir the effective capacity coefficients estimated for each of the aquifer models have been plotted alongside the results using the industry estimates of OGIP and W_e. The effective capacity coefficients calculated using the industry estimated OGIP and W_e values produce erroneous results that predict coefficients >1. This is due to the over-estimated OGIP values and therefore these results can be ignored as they suggest that the effective CO_2 storage capacity is greater than the theoretical CO_2 storage capacity. Using the results of the finite radial, finite linear and base case aquifer models, the lowest effective capacity coefficient estimates are predicted using the theoretical CO_2 storage capacity method of Bachu et al. (2007), Chapter 1, equation 1.1, with an effective capacity coefficient of 0.16 using the finite radial aquifer model and the Peng-Robinson equation of state (Peng and Robinson, 1976) estimated using WebGasEOS (Reagan and Oldenburg, 2006). The highest effective capacity coefficients are predicted using the method of Bachu et al. (2007), Chapter 1, equation 1.2, with a coefficient of 0.91 using the finite linear aquifer model and the Soave-Redlich-Kwong equation of state (Soave, 1972) estimated using WebGasEOS (Reagan and Oldenburg, 2006). The average effective capacity coefficient within the reservoir is 0.81, excluding the results calculated using the

method of Bachu et al. (2007), Chapter 1, equation 1.1, which are considered to be erroneous. The reservoir therefore has a high effective capacity coefficient meaning the effective storage capacity makes up a significant proportion of the total theoretical pore space.

Figure 7.3 (d) shows the effective capacity coefficient results for the North Morecambe Sherwood Sandstone reservoir. Again, due to the reservoir experiencing a water drive, the effective capacity coefficients estimated for each of the aquifer models have been plotted alongside the results using the industry estimates of OGIP and W_e. The effective capacity coefficients calculated using the industry estimated OGIP and W_e values produce erroneously high results; the method of Bachu et al. (2007), Chapter 1, equation 1.2, predicts coefficients > 1. Again, this is due to the over-estimated OGIP values and therefore these results can be ignored. Using the results of the finite radial, finite linear and base case aquifer models, the lowest effective capacity coefficient estimates are predicted using the theoretical CO_2 storage capacity method of Bachu et al. (2007), Chapter 1, equation 1.1, with an effective capacity coefficient of 0.068 using the finite radial aquifer model and the Peng-Robinson equation of state (Peng and Robinson, 1976) estimated using WebGasEOS (Reagan and Oldenburg, 2006). The highest effective capacity coefficients are predicted using the method of Bachu et al. (2007), Chapter 1, equation 1.2, with a coefficient of 0.87 using the finite linear aquifer model and the Redlich-Kwong equation of state (Redlich and Kwong, 1949) estimated using WebGasEOS (Reagan and Oldenburg, 2006). The average effective capacity coefficient within the reservoir is 0.63, excluding the results calculated using the method of Bachu et al. (2007), Chapter 1, equation 1.1, which are considered to be erroneous. The reservoir therefore has a fairly high effective capacity coefficient meaning the effective storage capacity makes up a reasonable proportion of the total theoretical pore space. The estimated effective capacity coefficients are lower within the North Morecambe Sherwood Sandstone reservoir than the Hewett Upper Bunter Sandstone reservoir. This is in part due to the North Morecambe Sherwood Sandstone reservoir being only partially depleted; the effective capacity coefficient is expected to increase as production progresses as there will be an increase in available pore space for CO_2.

It is apparent from the results of Figure 7.3 that effective storage capacity coefficients are sensitive to recovery factor and aquifer performance. The results of the South and North Morecambe Sherwood Sandstone reservoirs have shown that when the recovery factor is low, the effective capacity coefficients are also low. As production progresses there will be an increase in available pore space for injected CO_2, and therefore an increase in the effective capacity coefficient. The effective capacity coefficients are also sensitive to aquifer performance. The results of the Hewett Upper Bunter Sandstone reservoir and the North Morecambe Sherwood Sandstone reservoir show that when a depletion drive model is assumed for these reservoirs (based on the OGIP and W_e estimates from industry) the resulting effective capacity coefficients are erroneously high, and even exceed the top value of 1. This implies that the theoretical storage capacities of the reservoirs are greater than the effective storage capacities and is due to the over-estimated OGIP values. When the OGIP values are corrected using the finite radial, finite linear and base case aquifer models, as used within this study, the final effective capacity coefficients are more representative of the reservoirs evaluated.

(a) The Hewett Upper Bunter Sandstone Reservoir

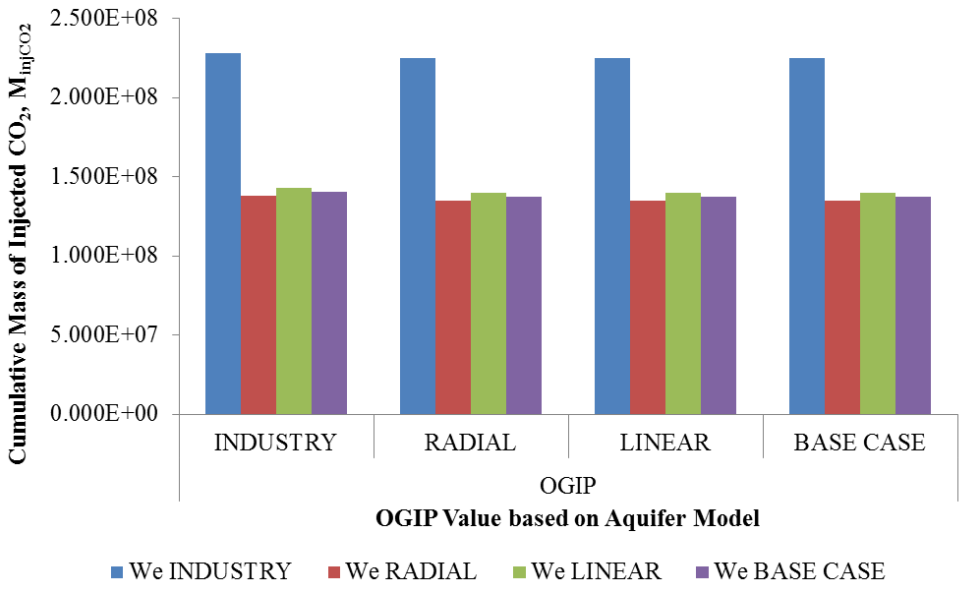

(b) The North Morecambe Sherwood Sandstone Reservoir

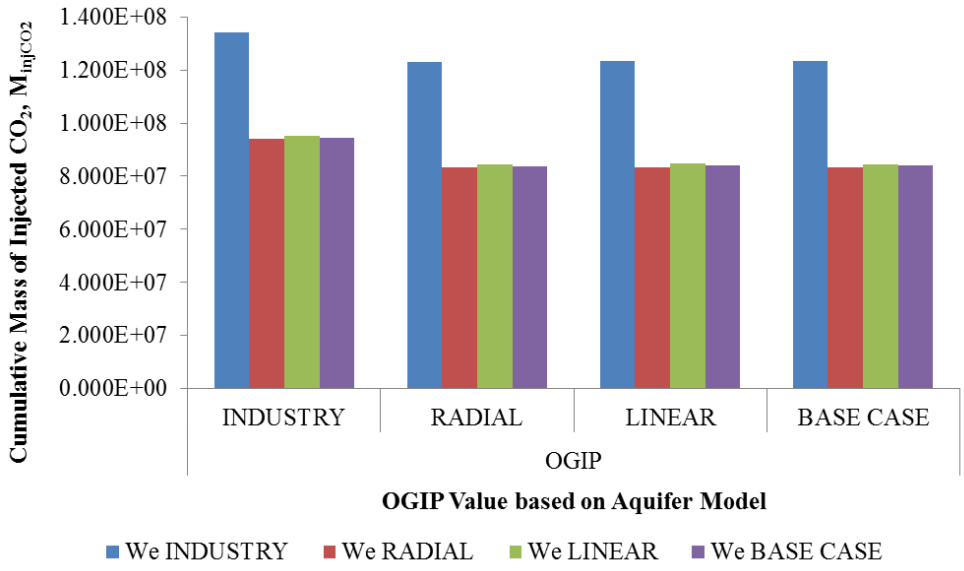

Figure 7.2 The effect of varying W_e on effective CO_2 storage capacity estimation using the method of Tseng et al. (2012), Chapter 1, equations 1.6 and 1.7. Results are modelled using the Peng-Robinson equation of state within RefProp. The OGIP is kept constant as either the industry estimate, the finite radial aquifer model estimate, the finite linear aquifer model estimate, or the base case estimate. The value of W_e is varied in each instance between the estimate from the industry OGIP, the finite radial aquifer model, the finite linear aquifer model, and the base case aquifer model. The predicted effective CO_2 storage capacities are displayed.

(a) Hewett Lower Bunter Sandstone reservoir

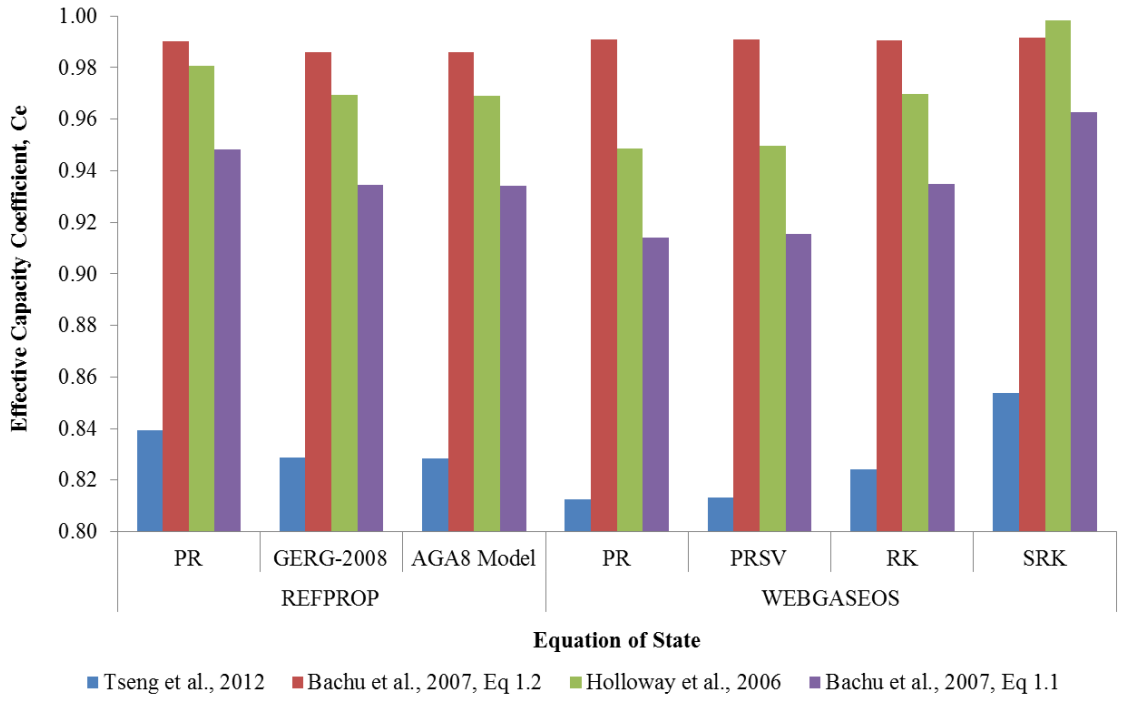

(b) South Morecambe Sherwood Sandstone reservoir

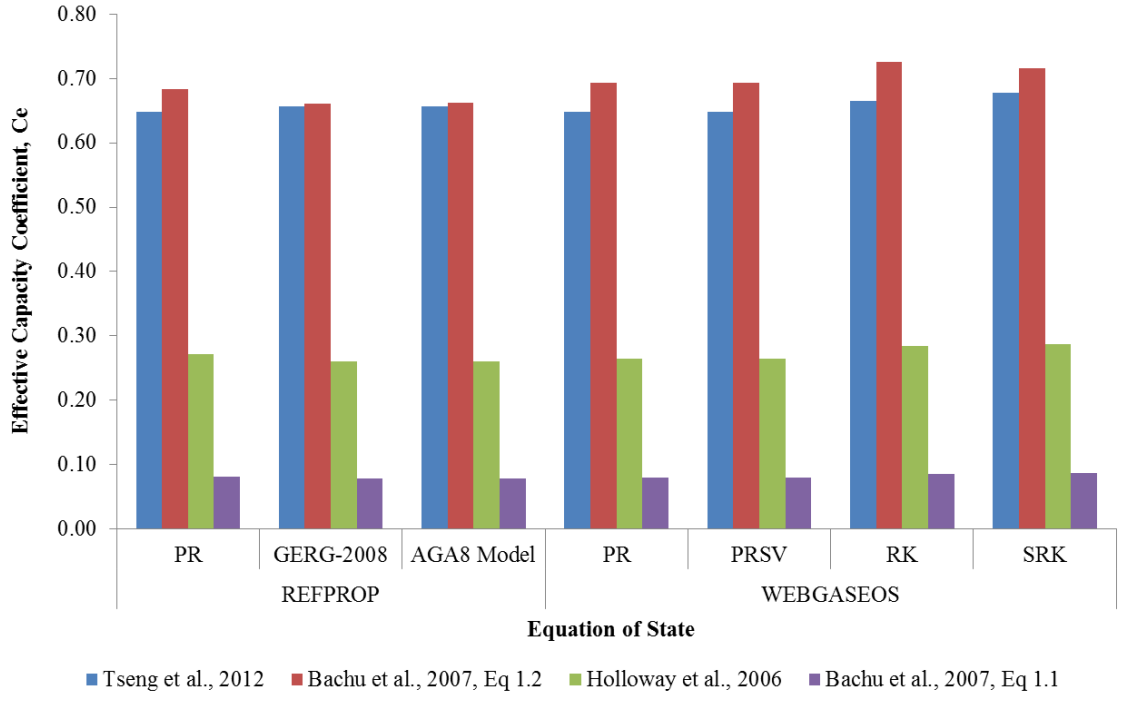

(c) Hewett Upper Bunter Sandstone reservoir

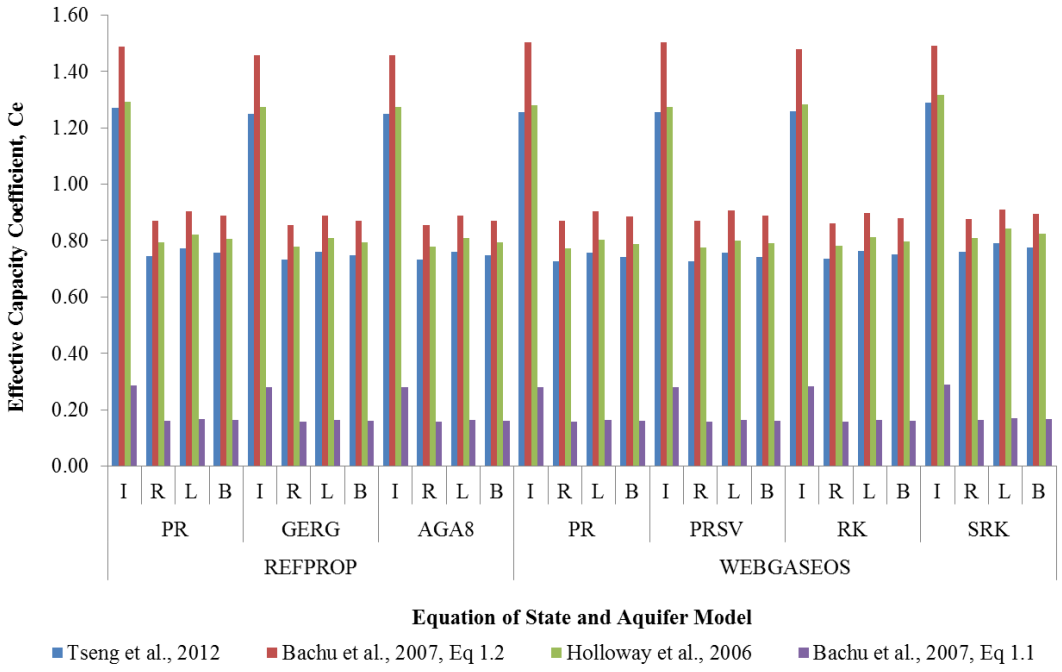

(d) North Morecambe Sherwood Sandstone reservoir

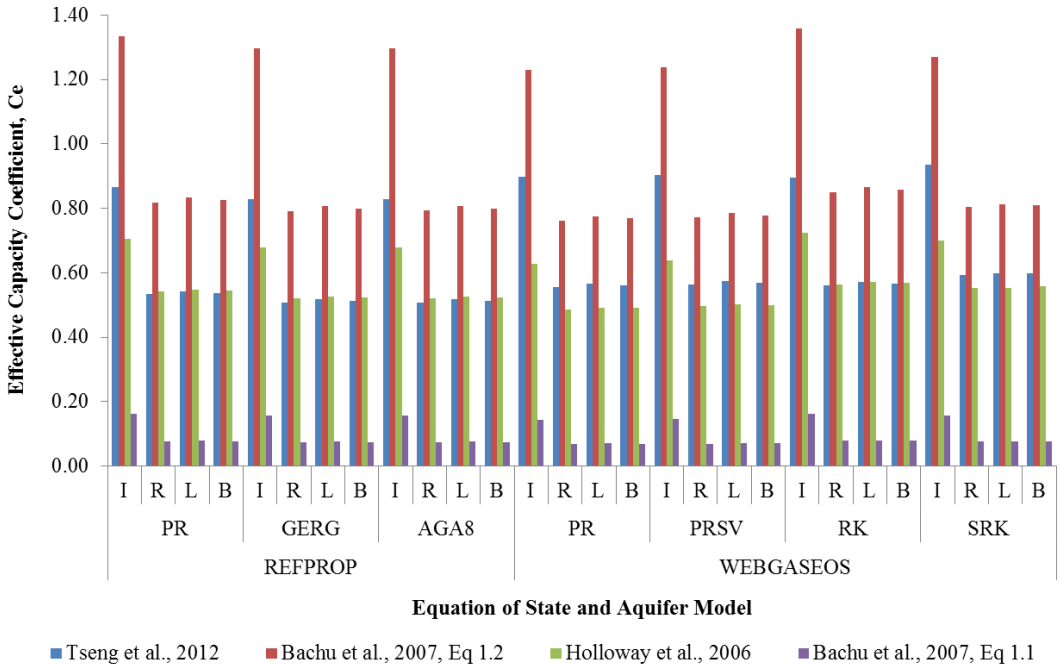

Figure 7.3 The effective capacity coefficients of (a) the Hewett Lower Bunter Sandstone reservoir, (b) the South Morecambe Sherwood Sandstone reservoir, (c) the Hewett Upper Bunter Sandstone reservoir, and (d) the North Morecambe Sherwood Sandstone reservoir, using the method of Tseng et al. (2012), Chapter 7, equations 7.1.

7.1.5. DYNAMIC BEHAVIOUR OF RESERVOIRS IN PRESSURE COMMUNICATION

This study has used the Hewett and Little Dotty Upper Bunter Sandstone reservoirs to demonstrate the importance of understanding the dynamic behaviour of reservoirs in pressure communication throughout production in order to predict future behaviour both during and post-injection of CO_2. To understand the pressure communication and identify pathways, it was necessary to (a) conduct 3-D seismic interpretation of the two reservoirs and fault seal analysis on any integral faults, (b) correctly identify the reservoir drive mechanism using P/z plots and Cole plots, (c) estimate hydraulic head to establish the direction of aquifer flow throughout production, (d) estimate hydraulic diffusivity to estimate a lag time for a pressure pulse within the water leg to diffuse over a specified distance, and (e) use water production data, or where lacking, aquifer modelling, to accurately estimate OGIP. These individual methods have been established previously, however, this is the first study that has linked them together to assess the suitability of a reservoir for CO_2 storage.

Identification of possible pathways for pressure communication rely heavily on the 3-D seismic interpretation and fault seal analysis of the reservoirs. Within this study, it was necessary to identify potential pressure communication pathways around and/or through the North Hewett Fault, which lies between the Hewett and Little Dotty Upper Bunter Sandstone reservoirs. The study found that only the central section of the North Hewett Fault is a structural seal to the hydrocarbon leg within the central eastern flank of the Hewett Upper Bunter sandstone reservoir. The Hewett Upper Bunter reservoir within this region is juxtaposed against down-faulted sealing unit, providing a high sealing potential. This area can be easily picked on seismic, with good well control, and does not rely on clay or shale smear to provide fault seal. However, as the fault continues towards the south east to merge with the western bounding fault of the Dowsing Fault Zone, the Bunter Sandstone seismic pick becomes more uncertain. There is the potential for a localised sand-sand juxtaposed region within the water leg, i.e. has not previously affected the secure containment of hydrocarbons within the Hewett Upper Bunter

Sandstone reservoir. As such, the juxtaposed region will not be critical for the secure storage of CO_2, thus there is no need to consider clay or shale smear to estimate fault seal potential. Due to the limited amount of displacement along the North Hewett Fault at this location, there is likely to be a low probability of fault seal. Previously, the fault will have been a conduit for aquifer movement between the Hewett and Little Dotty Upper Bunter reservoirs in this location, however, hydrocarbon migration is unlikely to have occurred via the same route. In summary, interpreter error will have an effect on the reliability of the final interpretation – the associated uncertainties have previously been described in Bretan (1992b).

The uncertainties associated with shale gouge ratio estimation, and the importance of calibrating results with observations of known sealing faults, have been described previously within Yielding (2012). This study does not rely upon clay or shale smear for the secure containment of hydrocarbons or storage of CO_2 therefore it is not necessary to go into the details here. However, future studies within other reservoirs may rely on clay or shale smear for fault seal, thus an understanding of the uncertainties associated with estimation of the shale gouge ratio will be necessary.

As well as identification of the pathways, it is necessary to understand the pressure regime of the system in order to establish the direction of aquifer flow. This can be achieved through estimation of hydraulic head. Previously, in Chapter 5, the hydraulic head of the Hewett and Little Dotty Upper Bunter Sandstone reservoirs was estimated. The trend throughout the productive lifetime is illustrated in Figure 7.4. It is possible to see that the Little Dotty Upper Bunter Sandstone reservoir retained a higher hydraulic head than the Hewett Upper Bunter Sandstone reservoir throughout the majority of their lifetimes. This implies that fluid flow will be from Little Dotty to Hewett (i.e. from high to lower pressure). However, at the end of production the hydraulic heads in both reservoirs are almost equal (low hydraulic gradient). It is hypothesised that when the Hewett Upper Bunter Sandstone reservoir is re-pressurised with CO_2, the hydraulic head will increase within Hewett, but not in Little Dotty (if it is left plugged and abandoned following production (see Figure 7.4)). Therefore, the direction of aquifer movement will be

reversed (from Hewett to Little Dotty). It is important to note that only water will be displaced from the Hewett Upper Bunter Sandstone reservoir. The final CO_2-water contact of the Hewett Upper Bunter Sandstone reservoir will not exceed the depth of the original gas-water contact due to geological and regulatory restrictions that will be placed on the reservoir. Also, the original gas-water contact within the Hewett Upper Bunter Sandstone reservoir occurred at a depth shallower than that of the area of sand-sand juxtaposition within the southeast section of the North Hewett Fault.

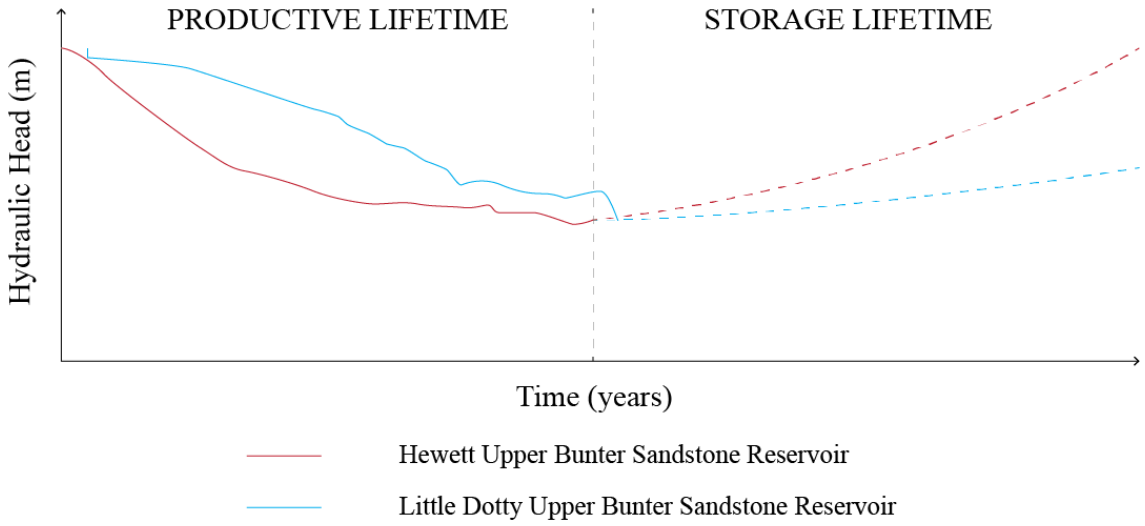

Figure 7.4 Estimates of hydraulic head of the Hewett and Little Dotty Upper Bunter Sandstone reservoirs throughout their productive lifetimes, and predictions of future behaviour if the Hewett Upper Bunter Sandstone reservoir is re-pressurised with CO_2 and the Little Dotty Upper Bunter Sandstone reservoir remains plugged and abandoned.

7.2. LIMITATIONS OF DATA AND FUTURE BEST PRACTICE

The major limitations of this study stem from the type and consistency of data available for analysis. One such limitation was the lack of water production data. Data such as the cumulative volume of produced water, W_p, would have been useful for the accurate estimation of both theoretical and effective CO_2 storage capacity of the reservoirs. This data is not regularly gathered by operators within the oil industry. In many cases, it is not necessary to meter produced water because it is not essential for successful gas production. Nevertheless, greater accuracy in

theoretical and effective CO_2 storage capacity estimation could be achieved within gas reservoirs: W_p is a required parameter to the method of Bachu et al. (2007), Chapter 1, equation 1.1. W_p can also be used to estimate values for W_e using the material balance equation of Archer and Wall (1986), previously stated in Chapter 5, and replicated here in Table 7.1, although there is a great deal of uncertainty associated with this method in terms of the parameters W_p and OGIP. As such, the lack of water production data can have a direct effect on effective CO_2 storage capacity estimation, using the method of Tseng et al. (2012), Chapter 1, equations 1.6 and 1.7, which require values for W_e for estimation. However, values for W_e have been estimated within this study using the alternative method of Van Everdingen and Hurst (1949). As has been demonstrated, this method can be used to achieve reasonably accurate results, although these results could have been evaluated for accuracy if the volume of produced water from the reservoirs was known.

Several limitations are involved with the measurement of reservoir pressure. Firstly, there were no details available on the particular tools used to measure reservoir pressure over the lifetimes (up to ca. 40 years) of the reservoirs evaluated within this study. This study has assumed that the most up-to-date tools were used at the time of measurement; however, this may not be the case. Pressure tool technology has evolved substantially over the last ca. 40 years. The accuracy of early RFT pressure measurement strain gauge tools was within 0.18%. Over the last 20 years, this accuracy has increased by an order of magnitude to 0.025% with the Hewlett Packard quartz gauge tool. Therefore, early reservoir pressure measurements may be a little more unreliable than later ones, although, this small percentage of error will have a negligible impact on storage capacity results.

MATERIAL BALANCE EQUATION	EQUATION NUMBER
$G(B_{gi}) = (G - G_p)B_g + W_e - W_p B_w$	(5.2)

Table 7.1 The material balance equation previously stated in Chapter 5. See Chapter 5 for definition of symbols. After Archer and Wall (1986).

Secondly, no information was available to assess how quickly pressure has been measured within the productive reservoirs. For example, it is not known whether the reservoir was given enough time to re-equilibrate following production, allowing a more accurate reservoir pressure measurement to be obtained. It is not even known if production was continuing from neighbouring wells within the reservoir whilst the pressure was being measured. This could be important for storage capacity estimation; however, it is likely that due to the frequency of pressure measurements throughout the lifetimes of the four reservoirs evaluated here that any erroneous results would be easy to spot from their pressure history graphs.

Thirdly, there have been intervals of shut-in, i.e. a period of no production, within all four reservoirs throughout their productive lifetimes. Within the water drive reservoirs, the Hewett Upper Bunter and the North Morecambe Sherwood Sandstone reservoir, the reservoir pressure has been observed to increase over this time period and has been attributed to the influx of water from underlying aquifers. However, the shut-in periods themselves are not well defined. There is a lack of information on (a) how long the shut-in periods are, (b) the dates of the beginning and end of shut-in, and (c) whether reservoir pressure has been measured at the start, end, during or outside of a shut-in period. This lack of information will not impact storage capacity estimation within a gas reservoir, however, it is useful to be able to understand and characterise reservoir behaviour, particularly aquifer performance within water drive reservoirs.

Another limitation within the production data made available to Durham University was the lack of information on how the gas compressibility factor (Z-factor) had been calculated by industry. The production data used throughout this study often included a table of Z-factor values. However, the method used for estimation was not included. It is unknown as to whether the Z-factor values have been estimated using similar methods as those presented within this study, or whether they have been measured more accurately within a laboratory. Within Chapter 4, the industry estimated Z-factors have been plotted on the material balance plots alongside those estimated using the RefProp estimated Peng-Robinson equation of state for comparison. It was found that there was overall a negligible

difference between the two sets of values, however, the greatest variability was at the beginning of production, and variability decreased as production proceeded.

The storage capacity methods used within this study have their own limitations. One major limitation between them is that some methods such as those of Tseng et al. (2012), Chapter 1, equations 1.4, 1.6 and 1.7, and Bachu et al. (2007), Chapter 1, equation 1.2 enable the input of a particular gas composition via the Z-factor if estimated using software such as those used within this study (RefProp (Lemmon et al., 2013) and WebGasEOS (Reagan and Oldenburg, 2006)). The final storage capacity estimates should theoretically have a greater accuracy than those estimates obtained via methods such as Holloway et al. (2006), Chapter 1, equation 1.3, and Bachu et al. (2007), Chapter 1, equation 1.1, which do not allow the inclusion of a specific gas composition. The method of Tseng et al. (2012), Chapter 1, equations 1.4, 1.6 and 1.7 also consider the residual volume and gas compressibility factor of natural gas within the reservoir as well as that of the injected CO_2, and estimates should therefore have greater accuracy than the alternative methods described within this study.

Initial reservoir temperatures are available for all of the reservoirs evaluated within this study. However, information on the temperature change of the reservoir throughout production is not available, and is a major limitation. Temperature is likely to drop throughout production, although, it is not possible to estimate the total temperature change through indirect methods. Certainly for the North and South Morecambe Sherwood Sandstone reservoirs, this could have a substantial impact on what state the CO_2 can be stored as, and therefore directly impacts CO_2 density and the volume that can be stored (Figure 7.5). If the temperature within the reservoirs drops enough, i.e. below the critical temperature for CO_2 (ca. 31.1 °C or 304.25 K), it may not be possible to store CO_2 as a supercritical fluid. The CO_2 could instead be held as a compressible liquid, as long as the final reservoir exceeds the critical pressure of CO_2 (7.38 MPa), which would substantially reduce the CO_2 density, and hence the volume that can be stored within a reservoir. Methods of storage capacity estimation used within this study only require the initial reservoir temperature to be input, and do not take into account the change in reservoir temperature through time. They presume that the initial conditions of the reservoir

prior to production will be the same with those at the end of injection. Indeed, similar pressures may be met at the end of injection; however, it is unlikely that the temperature will increase back to initial conditions for some time after injection.

Finally, the effective storage capacity method of Tseng et al. (2012), Chapter 1, equations 1.6 and 1.7, further constrains theoretical CO_2 storage capacity estimates through a more detailed analysis of the thermodynamic properties of the residual hydrocarbon and injected CO_2 mixture. Therefore, it does not take into account the integrity of the cap rock. A study by Naylor et al. (2011) suggested that a CO_2 column height up to double that of the original gas column height could theoretically be stored within depleted gas reservoirs. This is due to CO_2 density being substantially higher than natural gas under reservoir conditions, so the buoyancy force on the seal for a fixed column height is much lower (Naylor et al., 2011). However, there are several key concerns with this assumption within the Hewett Upper Bunter Sandstone reservoir. Firstly, there is a lack of laboratory analysis on the cap rock to the Hewett Upper Bunter Sandstone reservoir. Therefore, it must be considered that the minimum capillary entry pressure of the cap rock is that of the buoyancy pressure of the hydrocarbons at initial reservoir conditions to ensure secure storage of CO_2. Secondly, the 3-D structural model revealed an area of sand-sand juxtaposition within the south-east region of the North Hewett Fault, in the vicinity of the branchline with the Dowsing Fault Zone. Prior to, and throughout the productive lifetime of the Hewett Upper Bunter Sandstone reservoir, there has been no evidence of hydrocarbon migration through the juxtaposed region. The initial gas-water-contact (of 920.5 m) within the Hewett Upper Bunter Sandstone reservoir was shallower than the juxtaposed region implying it was located within the water-leg. However, there are concerns that if a CO_2 column height double that of the original gas column height were to be present within the Hewett Upper Bunter Sandstone reservoir, then the juxtaposed region may act as a spill point leading to CO_2 migrating out of the reservoir.

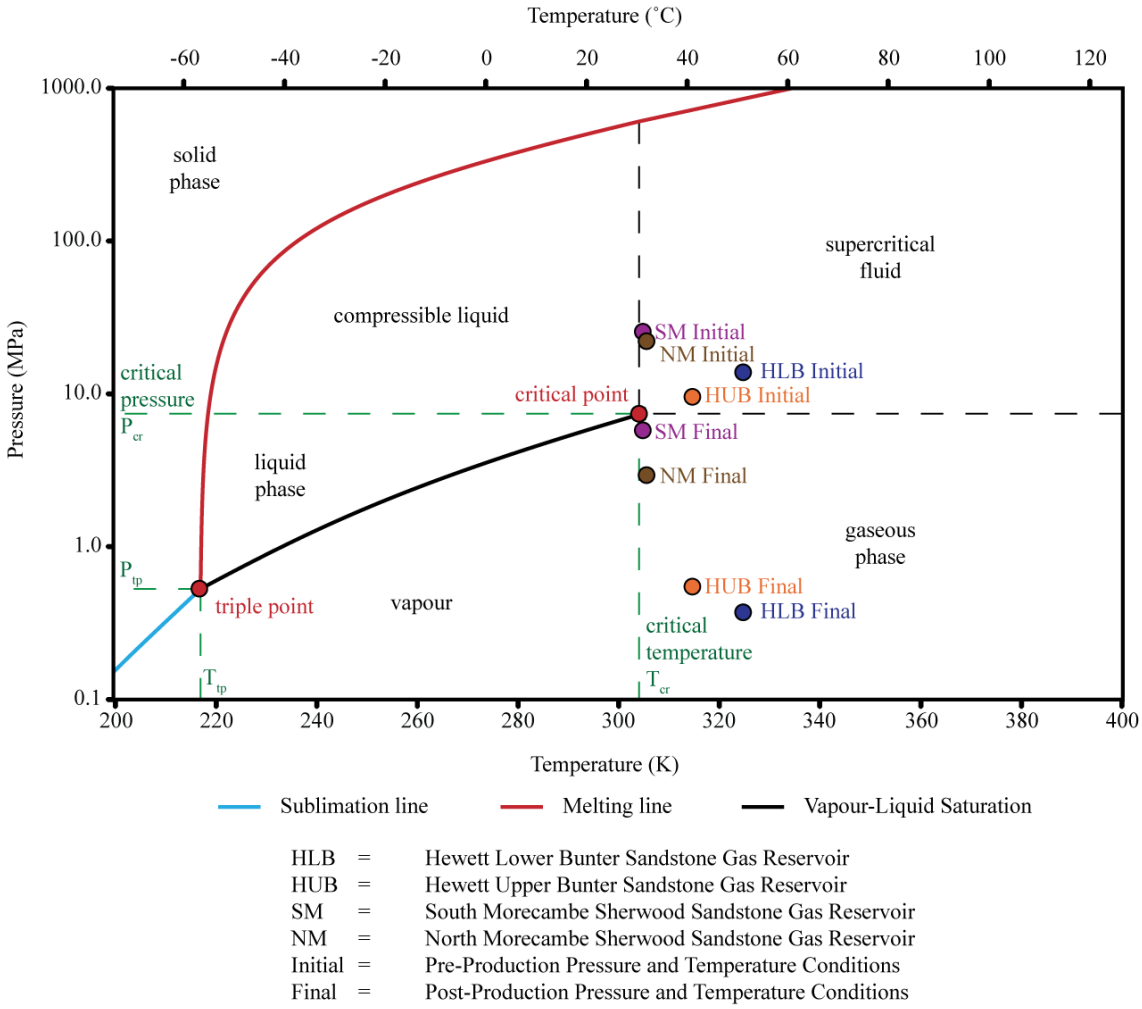

Figure 7.5 Phase diagram for the pure substance, CO_2. The sublimation line, melting line and vapour-liquid saturation line have been estimated using RefProp software (Lemmon et al., 2013) and the Peng-Robinson equation of state (Peng and Robinson, 1976). The phase diagram indicates the phases of CO_2 present at any given temperature and pressure. The critical point is defined by the critical temperature of CO_2 (31.1 °C or 304.25 K) and the critical pressure of CO_2 (7.38 MPa). The triple point occurs where all three phases are in equilibrium together, i.e. the solid-liquid equilibrium (melting line - red), liquid-vapour equilibrium (vapour-liquid saturation line - black) and the solid vapour equilibrium (sublimation line - blue).

In summary, in order to geologically characterise a depleted gas field for CO_2 storage, future operators should:

- Collect water production data throughout the productive lifetime of the field
- Provide more detailed information when measuring reservoir pressure, including information on the particular tool used, whether production is ongoing from the reservoir at the time of measurement or whether the reservoir has been shut-in (and at what stage of shut-in the pressure measurement is taken). Also, the dates of the beginning and end of a shut-in period should be provided
- Provide information on how the Z-factor has been estimated by industry
- Provide detailed information on the gas composition
- Measure reservoir temperature across the lifetime of the reservoir
- Conduct borehole break-out tests so that cap rock integrity can be assessed

7.3. FURTHER RESEARCH

It would be interesting to apply the methods developed within this study to all the reservoirs within the Southern North Sea, East Irish Sea and the remainder of the UK continental shelf on a site specific basis. The conclusions of this study in terms of depletion and water drive reservoirs could be tested further, and comparisons made with storage capacity estimates from the published literature.

Further research related to this study might involve the current aquifer performance nearing the end of production and post-production within the reservoirs that experience a water drive, i.e. the Hewett Upper Bunter Sandstone reservoir and the North Morecambe Sherwood Sandstone reservoir. It is important to gain a greater understanding of aquifer performance so predictions can be made about potential aquifer behaviour throughout CO_2 injection. However, this would require further information from industry such as regular metering of water production.

In terms of developing this study further it would be interesting to conduct reservoir modelling, particularly within the Hewett Upper Bunter Sandstone reservoir and underlying aquifer to model dynamic behaviour. It would also be interesting to run simulations for CO_2 storage, and simulate the migration of a plume of CO_2 within the reservoir.

The StressTester module in TrapTester could be used to estimate the likelihood of fault reactivation with increase in pore pressure from CO_2 injection. If faults were to reactivate with injection, there is a risk of loss of CO_2 from the storage reservoir. StressTester can be used to assess the geomechanics of the faults critical to CO_2 storage and highlight areas more susceptible to becoming critically stressed.

This study did not include an assessment of cap rock integrity in either the Southern North Sea or East Irish Sea basin. This was partly due to a lack of necessary information, such as borehole break-out data. It would be interesting to obtain this data proximal to the storage reservoirs to estimate what pressures the cap rocks over the storage reservoirs are able to withstand and increase the certainty of secure storage of CO_2 within them.

As previously mentioned, porosity and permeability data from the case study reservoirs could be obtained from each lithofacies and assigned probability distributions to investigate whether Monte Carlo simulation would provide more valid CO_2 storage capacity estimates using the geometric method of Bachu et al. (2007), Chapter 1, equation 1.1.

Another study that could be done is to complete structural restoration of the palaeo-water table within the South and North Morecambe Sherwood Sandstone reservoirs within 2D Move software. Illite was precipitated beneath a palaeo-gas-water-contact (Stuart, 1993) during the Triassic when the South and North Morecambe Sherwood Sandstone reservoirs were undergoing early burial (Bushell, 1986). Following rapid burial throughout the Triassic and Jurassic and later tectonism, uplift and erosion throughout the Late Cimmerian Orogeny, the illite affected zone became distributed unevenly throughout the reservoirs (Bushell, 1986). There are difficulties in assessing the distribution of the illite affected zone especially since much of the affected zone cannot be resolved on seismic. It may

be that structural restoration of the interpreted seismic data could provide further information on the distribution of the illite affected zone within both the South and North Morecambe Sherwood Sandstone reservoirs.

8 Conclusions

This study has found that the integrated analysis of reservoir structure, aquifer performance and thermodynamic behaviour is essential for evaluation of the variability of theoretical and effective CO_2 storage capacity estimates.

The storage capacity method of Bachu et al. (2007), Chapter 1, equation 1.1 was found to be the most susceptible to variability. This was attributed to be the direct result of the variability of input parameters to the storage capacity equation, such as the volume of produced water which is related to aquifer strength, i.e. the cumulative volume of aquifer influx, W_e. Variability was also a result of error in the estimation of parameters such as the OGIP – an over-estimate of the OGIP will produce over-estimated storage capacities.

Storage capacity estimation was found to be more precise within depletion drive reservoirs, such as the Hewett Lower Bunter Sandstone reservoir and the South Morecambe Sherwood Sandstone reservoir evaluated within this study. Input parameters can be well and accurately constrained within depletion drive reservoirs. Also, the degree of error associated with the storage capacity estimates decreases as production progresses as input parameters can be constrained with further precision.

In comparison, water drive reservoirs require aquifer modelling to achieve more precise estimates of OGIP and W_e. The Hewett Upper Bunter Sandstone reservoir and the North Morecambe Sherwood Sandstone reservoir evaluated within this study were both considered by industry to be depletion drive reservoirs. However, analysis of Cole Plots has revealed the reservoirs in fact experience water drive. As such, the OGIP values from industry were over-estimates. When corrected using the aquifer models, storage capacity estimates were obtained that seemed more representative of both the reservoirs.

It would be useful to have information on the cumulative volume of water produced, W_p, for the Hewett Upper Bunter and North Morecambe Sherwood Sandstone reservoirs in order to independently check assumptions made within storage capacity estimates, such as the method of Bachu et al. (2007), Chapter 1, equation 1.1. However, the volume of W_p is likely to be small and, as such, will have little effect on storage capacity estimates.

Effective capacity coefficients have been estimated within this study to assess the proportion of pore space available for CO_2 storage. However, the coefficient is again sensitive to OGIP and W_e. If a reservoir, such as the Hewett Upper Bunter Sandstone reservoir and North Morecambe Sherwood Sandstone reservoir, is wrongly characterised as being a depletion drive reservoir, when in fact it experiences a water drive, the resulting OGIP values will be an over-estimate resulting in the subsequent effective CO_2 storage capacity being an over-estimate. When the effective capacity coefficient is estimated, the resulting coefficient is erroneously high, and may even exceed the maximum coefficient value of 1. This occurs when the effective CO_2 storage capacity is greater than the theoretical CO_2 storage capacity estimate.

Overall, precise storage capacity results have been estimated using both the theoretical and effective CO_2 storage capacity methods of Tseng et al. (2012), Chapter 1, equations 1.4, 1.6 and 1.7. The most accurate equation of state was considered to be the GERG-2008 equation of state, which was specifically developed for the natural gas environment and has been shown to represent the thermal and caloric properties of the more accurate experimental data to within their accuracy (Kunz and Wagner, 2012). Its normal range of validity occurs at temperatures between 90 and 450 K and pressures up to 35 MPa (Kunz and Wagner, 2012).

Using the GERG-2008 equation of state (Kunz and Wagner, 2012) and the method of Tseng et al. (2012), Chapter 1, equations 1.4, 1.6 and 1.7, the Hewett Lower Bunter Sandstone reservoir was found to have a theoretical CO_2 storage capacity of 309 Mt CO_2, equating to a storage lifetime of approximately 32 years at the post-demonstration CO_2 injection rate of 9.6 Mt/year (BakerRDS, 2011b), and an effective CO_2 storage capacity of 261 Mt CO_2, equating to a storage lifetime of

approximately 27 years. The South Morecambe Sherwood Sandstone reservoir was found to have a theoretical CO_2 storage capacity of 328 Mt CO_2, equating to a storage lifetime of approximately 34 years, and an effective CO_2 storage capacity estimate of 213 Mt CO_2, equating to a storage lifetime of approximately 22 years.

Theoretical and effective CO_2 storage capacity estimation within the Hewett Upper Bunter Sandstone reservoir and the North Morecambe Sherwood Sandstone reservoir required the use of aquifer models to estimate the volume of W_e and to estimate OGIP values to a greater degree of accuracy than the industry estimated OGIP values. The aquifer model found to best represent the data in both reservoirs was the base case aquifer model – this represented the average W_e and OGIP estimates predicted using the finite radial and finite linear aquifer models, as it was not possible to distinguish which model was more suitable for use within either of the reservoirs.

Using the GERG-2008 equation of state (Kunz and Wagner, 2012), the method of Tseng et al. (2012), Chapter 1, equations 1.4, 1.6 and 1.7, and the W_e values and OGIP estimates predicted using the base case aquifer model, the theoretical CO_2 storage capacity of the Hewett Upper Bunter Sandstone reservoir was found to be 195 Mt CO_2, equating to a storage lifetime of approximately 20 years, and the effective CO_2 storage capacity was found to be 148 Mt CO_2, equating to a storage lifetime of approximately 15 years. Within the North Morecambe Sherwood Sandstone reservoir, theoretical CO_2 storage capacity was estimated to be 167 Mt CO_2, equating to a storage lifetime of approximately 17 years, and the effective CO_2 storage capacity was estimated to be 86.2 Mt CO_2, equating to a storage lifetime of approximately 9 years.

Overall, it was found that depletion drive reservoirs have the potential to be able to store greater volumes of CO_2 than water drive reservoirs – the effect of aquifer influx is to reduce storage capacity. Evidence for this can be seen in the estimation of effective capacity coefficients. Both the Hewett Upper Bunter Sandstone reservoir and the Hewett Lower Bunter Sandstone reservoir have similar recovery factors; however, the average effective capacity coefficient within the Hewett Upper Bunter is 0.81, whereas the average within the Hewett Lower Bunter Sandstone reservoir is 0.93.

This study has illustrated the importance of comparing and evaluating theoretical CO_2 storage capacity estimates. Future best practice should see various methods for CO_2 storage capacity estimation being used to evaluate a prospective reservoir. There was a significant difference in storage capacity estimates between the material balance and geometric approaches towards estimation. When analysing the storage capacity methods individually, the study found that by varying the equation of state used, and considering the variability of other input parameters, the end results did not significantly change. However, one of the most significant outcomes of the study was the effect of the correct identification of reservoir drive mechanism. CO_2 storage capacity can be significantly overestimated if a water drive reservoir has been incorrectly identified as a depletion drive reservoir. Likewise, if water production has never been metered from a reservoir, or data is incomplete, aquifer modelling is necessary to be able to estimate CO_2 storage capacity more precisely. This study has also illustrated how applying a scaling factor to a group of reservoirs to account for the reservoir drive mechanism is inappropriate. Prospective storage sites need to be evaluated individually – a reservoir with a weak water drive is likely to have a greater storage capacity than a reservoir with a strong water drive as less of the pore space will be occupied by water.

Finally, future best practice relies heavily upon operators providing the necessary data for characterisation of the prospective storage site. Water production data that has been collected regularly across the productive lifetime of the reservoir is recommended in preference to estimating water influx using aquifer models. More detail is required in the measurement of reservoir pressure so that any deviations in the pressure dataset from the expected trend can be explained. Information on Z-factor estimation by industry would be preferential. The measurement of reservoir temperature across the lifetime of the reservoir would be useful as it has direct implications for estimating PVT behaviour. It would also be useful to have borehole break-out test data so that cap rock integrity can be assessed which again has direct implications for CO_2 storage capacity.

REFERENCES

Agarwal, R.G., Al-Hussainy, R., Ramey, H.J., Jr., 1965. The Importance of Water Influx in Gas Reservoirs. Journal of Petroleum Technology 17, 1336-1342.

Allan, U.S., 1989. Model for Hydrocarbon Migration and Entrapment within Faulted Structures. AAPG Bulletin 73, 803-811.

Allen, P.A., Allen, J.R., 1990. Basin Analysis, Principles and Applications. Blackwell Scientific, Oxford.

Archer, J.S., Wall, C.G., 1986. Petroleum engineering : principles and practice. Graham & Trotman, London.

Bachu, S., Bonijoly, D., Bradshaw, J., Burruss, R., Holloway, S., Christensen, N.P., Mathiassen, O.M., 2007. CO2 storage capacity estimation: Methodology and gaps. International Journal of Greenhouse Gas Control 1, 430-443.

Bachu, S., Shaw, J.C., 2003. Evaluation of the CO_2 Sequestration Capacity in Alberta's Oil and Gas Reservoirs at Depletion and the Effect of Underlying Aquifers. Journal of Canadian Petroleum Geology 42, 51-61.

Bachu, S., Shaw, J.C., 2005. CO_2 storage in oil and gas reservoirs in western Canada: effect of aquifers, potential for CO_2-flood enhanced oil recovery and practical capacity, in: Rubin, E.S., Keith, D.W., Gilboy, C.F. (Eds.), Proceedings of the Seventh International Conference on Greenhouse Gas Control Technologies. Elsevier, pp. 361-369.

Bachu, S., Shaw, J.C., Pearson, R.M., 2004. Estimation of oil recovery and CO2 Storage Capacity in CO2 EOR incorporating the effect of underlying aquifers, SPE/DOE Symposium on Improved Oil Recovery. Society of Petroleum Engineers, Tulsa, Oklahoma, pp. 1-13.

Bacon, M., Simm, R., Redshaw, T., 2003. 3-D seismic interpretation. Cambridge University Press, Cambridge.

BakerRDS, 2010. Assessment of Natural Integrity, Kingsnorth Carbon Capture and Storage Project, p. 82.

BakerRDS, 2011a. Capacity Assessment - Study Effect of Formation Dehydration/Aquifers, in: E.ON. (Ed.), Kingsnorth Carbon Capture and Storage Project.

BakerRDS, 2011b. Storage Lease Application.

Barnett, J.A.M., Mortimer, J., Rippon, J.H., Walsh, J.J., Watterson, J., 1987. Displacement geometry in the volume containing a single normal fault. AAPG Bulletin 71, 925-937.

Bastin, J.C., Boycott-Brown, T., Sims, A., Woodhouse, R., 2003. The South Morecambe Gas Field, Blocks 110/2a, 110/3a, 110/7a and 110/8a, East Irish Sea. Geological Society, London, Memoirs 20, 107-118.

Bentham, M., 2006. An Assessment of Carbon Sequestration Potential in the UK - Southern North Sea Case Study, Tyndall Centre for Climate Change Research, pp. 1-36.

Benton, M., Cook, E., Turner, P., 2002. Permian and Triassic Red Beds and the Penarth Group of Great Britain. Joint Nature Conservation Committee, Peterborough.

Bouvier, J.D., Kaars-Sijpesteijn, C.H., Kluesner, D.F., Onyejekwe, C.C., van der Pal, R.C., 1989. Three-dimensional seismic interpretation and fault sealing investigations, Nun River Field, Nigeria. AAPG Bulletin 73, 1397-1414.

Boyle, R., 1662. New Experiments Physico-mechanical, Touching the Air: Whereunto is Added a Defence of the Authors Explication of the Experiments Against Obiections of Franciscus Linus and Thomas Hobbes. Hall, H., Oxford.

Bradshaw, J., Bachu, S., Bonijoly, D., Burruss, R., Holloway, S., Christensen, N.P., Mathiassen, O.M., 2007. CO2 storage capacity estimation: Issues and development of standards. International Journal of Greenhouse Gas Control 1, 62-68.

Bretan, P., 1992. Quality Control of Fault Interpretation within SeisWorks/3D or 3DPlus, Newsletter for Landmark/LGC Users. UserNet, pp. 4-5.

Bretan, P., 1992b. Potential Sources of Error and Bias in Fault Interpretation, Technical Newsletter for Landmark Users. UserNet, pp. 6-7.

Brook, M., Shaw, K., Vincent, C., Holloway, S., 2003. Gestco case study 2a-1: Storage Potential of the Bunter Sandstone in the UK sector of the Southern North Sea and the adjacent onshore area of Eastern England. BGS Commissioned Report CR/03/154N, 1-44.

Brown, A.R., 2011. Interpretation of three-dimensional seismic data, 7th ed. ed. American Association of Petroleum Geologists and the Society of Exploration Geophysicists, Tulsa, Oklahoma.

Brown, M., Baddeley, A., Coulthurst, A., Taylor, S., 2011. The East Irish Sea CCS Cluster: A Conceptual Design. Eunomia Research and Consulting, Hydrocarbon Resources Ltd and Peel Energy Ltd, p. 19.

Bruns, J.R., Fetkovich, M.J., Meitzen, V.C., 1965. The Effect of Water Influx on p/z-Cumulative Gas Production Curves. Journal of Petroleum Technology 17, 287-291.

Bushell, T.P., 1986. Reservoir Geology of the Morecambe Field. Geological Society, London, Special Publications 23, 189-208.

Cameron, T.D.J., Crosby, A., Balson, P.S., Jeffery, D.H., Lott, G.K., Bulat, J., Harrison, D.J., 1992. United Kingdom Offshore Regional Report: The Geology of the Southern North Sea. H.M.S.O., London.

Çengel, Y.A., Boles, M.A., 2011. Thermodynamics : an engineering approach, 7th SI ed. ed. McGraw-Hill, Singapore.

Chierici, G.L., Pizzi, G., Ciucci, G.M., 1967. Water Drive Gas Reservoirs: Uncertainty in Reserves from Past History. Journal of Petroleum Technology 19, 237-244.

Childs, C., Nicol, A., Walsh, J.J., Watterson, J., 2003. The growth and propagation of synsedimentary faults. Journal of Structural Geology 25, 633-648.

Clapeyron, E., 1834. Memoire sur la Puissance Motrice de la Chaleur. Journal de l'Ecole Polytechnique 14, 153-191.

Cole, F.W., 1969. Reservoir Engineering Manual. Gulf Publishing Co., Houston.

Colter, V.S., Ebbern, J., 1978. The petrography and reservoir properties of some triassic sandstones of the Northern Irish Sea Basin. Journal of the Geological Society 135, 57-62.

Cooke-Yarborough, P., 1991. The Hewett Field, Blocks 48/28-29-30, 52/4a-5a, UK North Sea, in: Abbots, I.L. (Ed.), United Kingdom Oil and Gas Fields, 25 Years Commemorative Volume, 1 ed. Geological Society, London, pp. 433-442.

Cooke-Yarborough, P., Smith, E., 2003. The Hewett Fields: Blocks 48/28a, 48/29, 48/30, 52/4a, 52/5a, UK North Sea: Hewett, Deborah, Big Dotty, Little Dotty, Della, Dawn and Delilah Fields. Geological Society, London, Memoirs 20, 731-739.

Coulthurst, A., Taylor, S., Baddeley, A., 2011. The East Irish Sea CCS Cluster: A Conceptual Design -Technical Report. Eunomia Research and Consulting, Hydrocarbon Resources Ltd and Peel Energy Ltd, p. 65.

Cowan, G., 1996. The development of the North Morecambe gas field, East Irish Sea Basin, UK. Petroleum Geoscience 2, 43-52.

Cowan, G., Boycott-Brown, T., 2003. The North Morecambe Field, Block 110/2a, East Irish Sea. Geological Society, London, Memoirs 20, 97-105.

CSLF, 2005. A Taskforce for Review and Development of Standards with Regards to Storage Capacity Measurement, pp. 1-20.

Cumming, A.D., Wyndham, C.L., 1975. The geology and development of the Hewett gas field, in: Woodland, A.W. (Ed.), Petroleum and the continental shelf of north-west Europe, 1 ed. John Wiley, pp. 313-325.

Dake, L.P., 1978. Fundamentals of Reservoir Engineering. Elsevier Scientific Publishing Co., Amsterdam.

Dalton, J., 1801. New Theory of the Constitution of Mixed Aeriform Fluids, and Particularly of the Atmosphere. Journal of Natural Philosophy, Chemistry and the Arts 5, 241-244.

Danesh, A., 1998. PVT and phase behaviour of petroleum reservoir fluids. Elsevier.

DECC, 2009. Technical Analysis of Carbon Capture and Storage (CCS) Transportation Infrastructure, pp. 1-67.

DECC, 2011. The Carbon Plan: Delivering our Low Carbon Future, p. 220.

DECC, 2013. Website for the Department of Energy and Climate Change, https://www.gov.uk/government/organisations/department-of-energy-climate-change.

Doughty, C., Pruess, K., Benson, S.M., Hovorka, S.D., Knox, P.R., Green, C.T., 2001. Capacity investigation of brine-bearing sands of the Frio formation for geologic sequestration of CO2.

E.ON, 2009. Capturing Carbon, Tackling Climate Change: A Vision for a CCS Cluster in the South East, pp. 1-12.

Fichter, L.S., Farmer, G.T., Clay, J.S., 1991. Earth Materials and Earth Processes, Third ed. Macmillan Publishing Company.

Frailey, S.M., Finley, R.J., Hickman, T.S., 2006a. CO_2 Sequestration: Storage Capacity Guideline Needed. Oil and Gas Journal 104, 44-49.

Freeman, B., Yielding, G., Badley, M., 1990. Fault correlation during seismic interpretation. First Break 8, 87-95.

Freeman, B., Yielding, G., Needham, D.T., Badley, M.E., 1998. Fault seal prediction: the gouge ratio method. Geological Society, London, Special Publications 127, 19-25.

Gallois, R.W., 2008. The stratigraphy of the Penarth Group (Late Triassic) of the East Devon coast. Geoscience in south-west England - Proceedings of the Ussher Society 11, 287-297.

Gay-Lussac, J.-L., 1802. The Expansion of Gases by Heat. Annales de Chimie 43, 137.

Glennie, K.W., 1990. Introduction to the petroleum geology of the North Sea, 3rd ed. ed. Blackwell, Oxford.

Gluyas, J., Swarbrick, R., 2003. Petroleum Geoscience. Blackwell Publishing

Goudie, A.S., 1985. Duricrusts and Landforms, in: Richards, K.S., Arnett, R.R., Ellis, S. (Eds.), Geomorphology and Soils. George Allen & Unwin, London, pp. 37-57.

Gravetter, F.J., Wallnau, L.B., 1999. Essentials of statistics for the behavioral sciences, 3rd ed. Brooks/Cole Publishing Company.

Grewcock, S., 2009. CO2 Storage - An Oil Industry Perspective. www.oilandgas.co.uk, p. Hewett CO2 Storage Capacity Presentation by Tullow Oil Plc.

Hagoort, J., 1988. Chapter 11: Natural Depletion, in: Hagoort, J. (Ed.), Developments in Petroleum Science. Elsevier Science Publishing Company, New York, pp. 233-261.

Holloway, S., 1996. Final report of the Joule II Project No. CT92-0031, in: Survey, B.G. (Ed.), The Underground Disposal of Carbon Dioxide. British Geological Survey, Keyworth

Nottingham

UK.
Holloway, S., 2005. Underground sequestration of carbon dioxide—a viable greenhouse gas mitigation option. Energy 30, 2318-2333.
Holloway, S., 2009. Storage capacity and containment issues for carbon dioxide capture and geological storage on the UK continental shelf. Proceedings of the Institution of Mechanical Engineers, Part A: Journal of Power and Energy 223, 239-248.
Holloway, S., Vincent, C.J., Kirk, K.L., 2006. Industrial Carbon Dioxide Emissions and Carbon Dioxide Storage Potential in the UK, pp. 1-47.
Howard, A.S., Warrington, G., Ambrose, K., Rees, J.G., 2008. A formational framework for the Mercia Mudstone Group (Triassic) of England and Wales, Keyworth, Nottingham.
Ingebritsen, S.E., Sanford, W.E., 1999. Groundwater in Geologic Processes. Cambridge University Press, Cambridge.
IPCC, 2005. IPCC Special Report: Carbon Dioxide Capture and Storage, in: Metz, B., Davidson, O., de Coninck, H.C., Loos, M., Mayer, L.A. (Eds.). Cambridge University Press, Cambridge, UK, p. 443.
IPCC, 2013. Climate Change 2013: The Physical Science Basis, in: Joussaume, S., Penner, J., Tangang, F. (Eds.), Final Draft Underlying Scientific-Technical Assessment.
Jackson, D.I., Jackson, A.A., Evans, D., Wingfield, R.T.R., Barnes, R.P., Arthur, M.J., 1995. The geology of the Irish Sea, British Geological Survey Series United Kingdom offshore regional report. Balogh Scientific Books.
Jev, B.I., Kaars-Sijpesteijn, C.H., Peters, M.P.A.M., Watts, N.L., Wilkie, J.T., 1993. Akaso Field, Nigeria: Use of Integrated 3-D Seismic, Fault Slicing, Clay Smearing, and RFT Pressure Data on Fault Trapping and Dynamic Leakage. AAPG Bulletin 77, 1389-1404.
Johnson, H., Warrington, G., Stoker, S.J., 1994. 6. Permian and Triassic of the Southern North Sea, in: Knox, R.W.O.B., Cordey, W.G. (Eds.), Lithostratigraphic nomenclature of the UK North Sea. British Geological Survey, Nottingham.
Jolley, S.J., Dijk, H., Lamens, J.H., Fisher, Q.J., Manzocchi, T., Eikmans, H., Huang, Y., 2007. Faulting and fault sealing in production simulation models: Brent Province, northern North Sea. Petroleum Geoscience 13, 321-340.
Kearey, P., Brooks, M., Hill, I., 2002. An introduction to geophysical exploration, 3rd ed. ed. Blackwell Science, Oxford.
Ketter, F.J., 1991. The Esmond, Forbes and Gordon Fields, Blocks 43/8a, 43/13a, 43/15a, 43/20a, UK North Sea. Geological Society, London, Memoirs 14, 425-432.
King, G.R., 1993. Material-Balance Techniques for Coal-Seam and Devonian Shale Gas Reservoirs with Limited Water Influx. SPE Reservoir Engineering 8, 67-72.
Kirk, K.L., 2006. Potential for Storage of Carbon Dioxide in the Rocks Beneath the East Irish Sea, Tyndall Centre Working Papers, Nottingham.
Knipe, R.J., Cowan, G., Balendran, V.S., 1993. The tectonic history of the East Irish Sea Basin with reference to the Morecambe Fields. Geological Society, London, Petroleum Geology Conference series 4, 857-866.
Kopp, A., Probst, P., Class, H., Hurter, S., Helmig, R., 2009. Estimation of CO2 storage capacity coefficients in geologic formations. Energy Procedia 1, 2863-2870.
Kunz, O., Wagner, W., 2012. The GERG-2008 Wide-Range Equation of State for Natural Gases and Other Mixtures: An Expansion of GERG-2004. Journal of Chemical & Engineering Data 57, 3032-3091.
Lehner, F.K., Pilaar, W.F., 1996. On a mechanism of clay smear emplacement in synsedimentary normal faults, in: Norwegian Petroleum Society (Ed.),

Hydrocarbon seals - importance for exploration and production (conference abstracts). Norwegian Petroleum Society, Oslo, p. 4.

Lemmon, E.W., Huber, M.L., McLinden, M.O., 2013. NIST Standard Reference Database 23: Reference Fluid Thermodynamic and Transport Properties-REFPROP, Version 9.1, National Institute of Standards and Technology, Standard Reference Data Program, Gaithersburg.

Lewis, D., Bentham, M., Cleary, T., Vernon, R., O'Neill, N., Kirk, K., Chadwick, A., Hilditch, D., Michael, K., Allinson, G., Neal, P., Ho, M., 2009. Assessment of the potential for geological storage of carbon dioxide in Ireland and Northern Ireland. Energy Procedia 1, 2655-2662.

Lindsay, N.G., Murphy, F.C., Walsh, J.J., Watterson, J., 1993. Outcrop studies of shale smears on fault surfaces. Spec. Publs int. Ass. Sediment 15, 113-123.

Meadows, N.S., Beach, A., 1993a. Structural and climatic controls on facies distribution in a mixed fluvial and aeolian reservoir: the Triassic Sherwood Sandstone in the Irish Sea. Geological Society, London, Special Publications 73, 247-264.

Meadows, N.S., Beach, A., 1993b. Controls on reservoir quality in the Triassic Sherwood Sandstone of the Irish Sea. Geological Society, London, Petroleum Geology Conference series 4, 823-833.

Naylor, M., Wilkinson, M., Haszeldine, R.S., 2011. Calculation of CO2 column heights in depleted gas fields from known pre-production gas column heights. Marine and Petroleum Geology 28, 1083-1093.

Needham, D.T., Yielding, G., Freeman, B., 1996. Analysis of fault geometry and displacement patterns, in: Buchanan, P.G., Nieuwland, D.A. (Eds.), Modern Developments in Structural Interpretation, Validation and Modelling. Geological Society of London, pp. 189-199.

Payne, D.A., 1996. Material-balance calculations in tight-gas reservoirs: The pitfalls of p/z plots and a more accurate technique. SPE Reservoir Engineering 11, 260-267.

Peng, D.-Y., Robinson, D.B., 1976. A New Two-Constant Equation of State. Industrial & Engineering Chemistry Fundamentals 15, 59-64.

Pletcher, J.L., 2002. Improvements to Reservoir Material-Balance Methods. SPE Reservoir Evaluation & Engineering 5, 49-59.

Reagan, M.T., Oldenburg, C.M., 2006. WebGasEOS v1.0 User Guide, Lawrence Berkeley National Laboratory Report LBNL-3188, Lawrence Berkeley National Laboratory, Berkeley CA.

Redlich, O., Kwong, J.N.S., 1949. On the Thermodynamics of Solutions. V. An Equation of State. Fugacities of Gaseous Solutions. Chemical Reviews 44, 233-244.

Shackley, S., McLachlan, C., Gough, C., 2004. The Public Perceptions of Carbon Capture and Storage, Tyndall Centre Working Paper No. 44. Tyndall Centre for Climate Change Research.

Sheriff, R.E., 1995. Exploration seismology / R. E. Sheriff, L. P. Geldart, 2nd ed. ed. Cambridge Univ. Press, Cambridge :.

Shonkwiler, R.W., Mendivil, F., 2009. Explorations in Monte Carlo Methods. Springer.

Soave, G., 1972. Equilibrium constants from a modified Redlich-Kwong equation of state. Chemical Engineering Science 27, 1197-1203.

Standing, M.B., Katz, D.L., 1942. Density of Natural Gases. Transactions of the AIME 146, 140-149.

Starling, K.E., Savidge, J.L., 1992. Compressibility factors of natural gas and other related hydrocarbon gases. American Gas Association, Transmission Measurement Committee Report No. 8, 2nd ed.

Steel, R.J., 1974a. Cornstone (Fossil Caliche): Its Origin, Stratigraphic, and Sedimentological Importance in the New Red Sandstone, Western Scotland. The Journal of Geology 82, 351-369.

Steel, R.J., 1974b. New red Sandstone floodplain and piedmont sedimentation in the Hebridean province, Scotland. Journal of Sedimentary Research 44, 336-357.

Stephens, M.A., 1974. EDF Statistics for Goodness of Fit and Some Comparisons. Journal of the American Statistical Association 69, 730-737.

Stern, N., 2006. Stern review on the economics of climate change. Stern Review on the Economics of Climate Change, UK Treasury.

Stryjek, R., Vera, J.H., 1986. PRSV: An improved peng—Robinson equation of state for pure compounds and mixtures. The Canadian Journal of Chemical Engineering 64, 323-333.

Stuart, I.A., 1993. The geology of the North Morecambe Gas Field, East Irish Sea Basin. Geological Society, London, Petroleum Geology Conference series 4, 883-895.

Stuart, I.A., Cowan, G., 1991. The South Morecambe Field, Blocks 110/2a, 110/3a, 110/8a, UK East Irish Sea. Geological Society, London, Memoirs 14, 527-541.

Tehrani, D.H., 1985. An Analysis of a Volumetric Balance Equation for Calculation of Oil-in-Place and Water Influx. Journal of Petroleum Technology 37, 1664-1670.

Tseng, C.-C., Hsieh, B.-Z., Hu, S.-T., Lin, Z.-S., 2012. Analytical approach for estimating CO2 storage capacity of produced gas reservoirs with or without a water drive. International Journal of Greenhouse Gas Control 9, 254-261.

Tyrrell, S., Haughton, P.D.W., Souders, A.K., Daly, J.S., Shannon, P.M., 2012. Large-scale, linked drainage systems in the NW European Triassic: insights from the Pb isotopic composition of detrital K-feldspar. Journal of the Geological Society 169, 279-295.

UNFCCC, 1998. Kyoto Protocol to the United Nations Framework Convention on Climate Change, United Nations, http://unfccc.int/key_documents/kyoto_protocol/items/6445.php.

UNFCCC, 2013. United Nations Framework Convention on Climate Change, http://unfccc.int/2860.php.

Van Der Meer, B., 2005. Stockage de CO2 dans des réservoirs de gaz naturel. Oil & Gas Science and Technology - Rev. IFP 60, 527-536.

Van Everdingen, A.F., Hurst, W., 1949. The Application of the Laplace Transformation to Flow Problems in Reservoirs. Journal of Petroleum Technology 1, 305-324.

Vega, L., Wattenbarger, R.A., 2000. New Approach for Simultaneous Determination of the OGIP and Aquifer Performance with No Prior Knowledge of Aquifer Properties and Geometry, SPE/CERI Gas Technology Symposium. Society of Petroleum Engineers Inc., Calgary, Alberta, Canada.

Waals, J.D.v.d., 1873. Over de continuiteit van den gas- en vloeistoftoestand. A.W. Sijthoff, Leiden.

Walsh, J.J., Bailey, W.R., Childs, C., Nicol, A., Bonson, C.G., 2003. Formation of segmented normal faults: a 3-D perspective. Journal of Structural Geology 25, 1251-1262.

Walsh, J.J., Watterson, J., 1988. Analysis of the relationship between displacements and dimensions of faults. Journal of Structural Geology 10, 239-247.

Wang, B., Teasdale, T.S., 1987. GASWAT-PC: A microcomputer program for gas material balance with water influx, SPE Petroleum Industry Applications of Microcomputers. Society of Petroleum Engineers, Lake Conroe, Texas, pp. 25-42.

Warrington, G., 1992. Triassic. Geological Society, London, Memoirs 13, 97-106.

Warrington, G., Audley-Charles, M.G., Elliott, R.E., Evans, W.B., Ivimey-Cook, H.C., Kent, P.E., Robinson, P.L., Shotton, F.W., Taylor, F.M., 1980. A correlation of Triassic rocks in the British Isles.

Watterson, J., 1986. Fault dimensions, displacements and growth. PAGEOPH 124, 365-373.

Weber, K.J., Mandl, G., Pilaar, G., Lehner, W.F., Precious, R.G., 1978. The role of faults in hydrocarbon migration and trapping in Nigerian growth fault structures, Offshore Technology conference. Offshore Technology Conference, Texas, pp. 2643-2653.

Wibberley, C.A.J., 2002. Hydraulic Diffusivity of Fault Gouge Zones and Implications for Thermal Pressurisation during Seismic Slip. Earth Planets Space 54, 1153-1171.

Woodcock, N., Strachan, R., 2012. Geological History of Britain and Ireland, 2nd ed. ed. Wiley-Blackwell, Oxford, p. 442.

Woodward, K., Curtis, C.D., 1987. Predictive modelling for the distribution of production-constraining illites - Morecambe Gas Field, Irish Sea, offshore UK, in: Brooks, J., Glennie, K.W. (Eds.), Petroleum geology of North West Europe. Graham and Trotman, London, pp. 205-215.

Yielding, G., 2012. Using probabilistic shale smear modelling to relate SGR predictions of column height to fault-zone heterogeneity. Petroleum Geoscience 18, 33-42.

Yielding, G., Bretan, P., Freeman, B., 2010. Fault seal calibration: a brief review. Geological Society, London, Special Publications 347, 243-255.

Yielding, G., Freeman, B., Needham, D.T., 1997. Quantitative fault seal prediction. Journal Name: AAPG Bulletin; Journal Volume: 81; Journal Issue: 6; Other Information: PBD: Jun 1997, Medium: X; Size: pp. 897-917.

Yielding, G., Lykakis, N., Underhill, J.R., 2011. The role of stratigraphic juxtaposition for seal integrity in proven CO2 fault-bounded traps of the Southern North Sea. Petroleum Geoscience 17, 193-203.

Yilmaz, Ö., Doherty, S.M., 1987. Seismic Data Processing. Society of Exploration Geophysicists, Tulsa, Oklahoma.

A Appendix A: Well-to-Seismic Ties

The following figures (A.1 to A.3) show the well-to-seismic ties within the seismic survey over the Hewett Gas Field and surrounding "D" fields of the Southern North Sea. Figure A.1 shows the location of the well (048/29-04) used to demonstrate the well picks and the intercepting seismic sections. Figure A.2 shows the intercepting seismic sections in more detail with the seismic interpretations that were based on the well picks. Figure A.3 shows the N-S oriented seismic section so that individual interpretations can be seen in more detail.

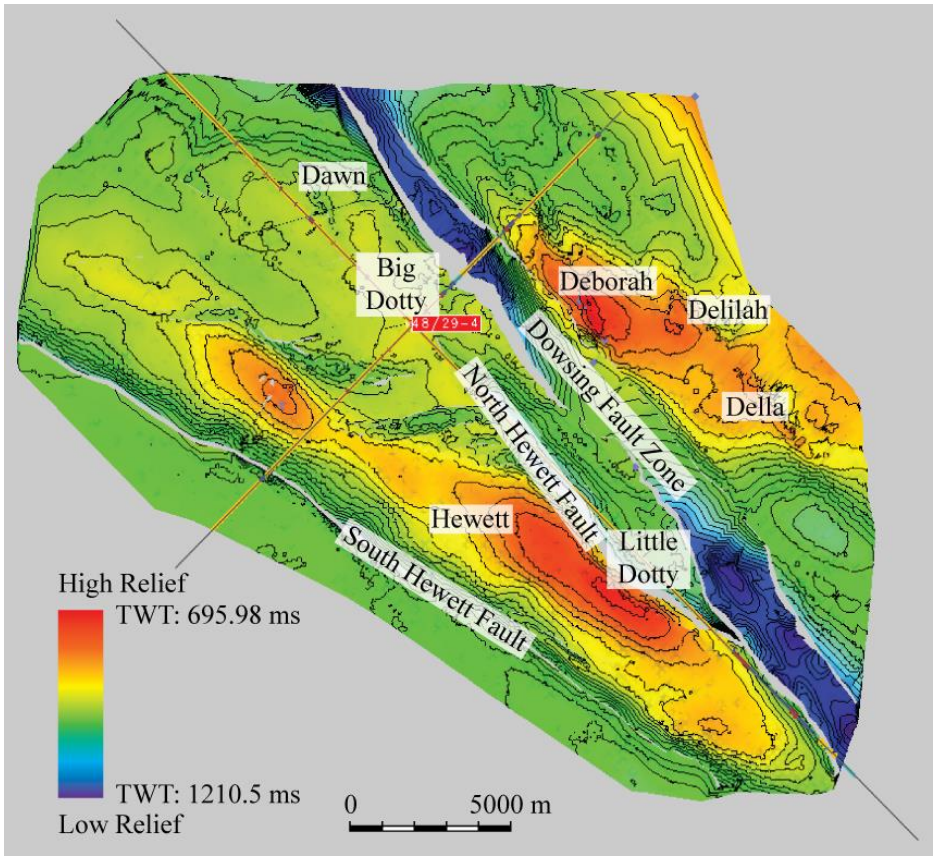

Figure A.1 The Top Bunter Sandstone time structure map with the location of the well, 048/29-04. Two seismic cross sections that intercept the well have been used to demonstrate the well-to-seismic ties within the Hewett Unit seismic survey.

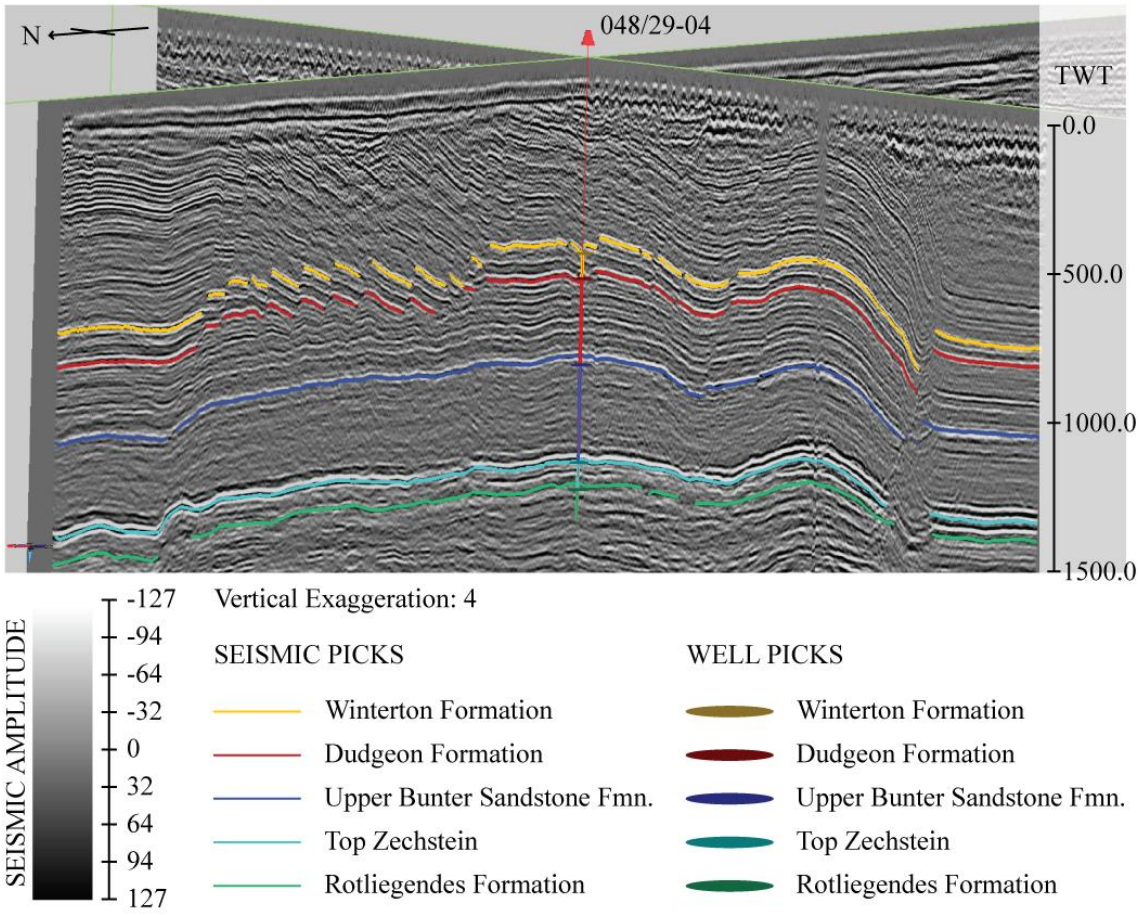

Figure A.2 The two seismic sections that intercept the well, 048/29-04. The figure shows the well picks of the interpreted layers, illustrated as discs on the well trajectory. The seismic shows the interpretations based on the well picks.

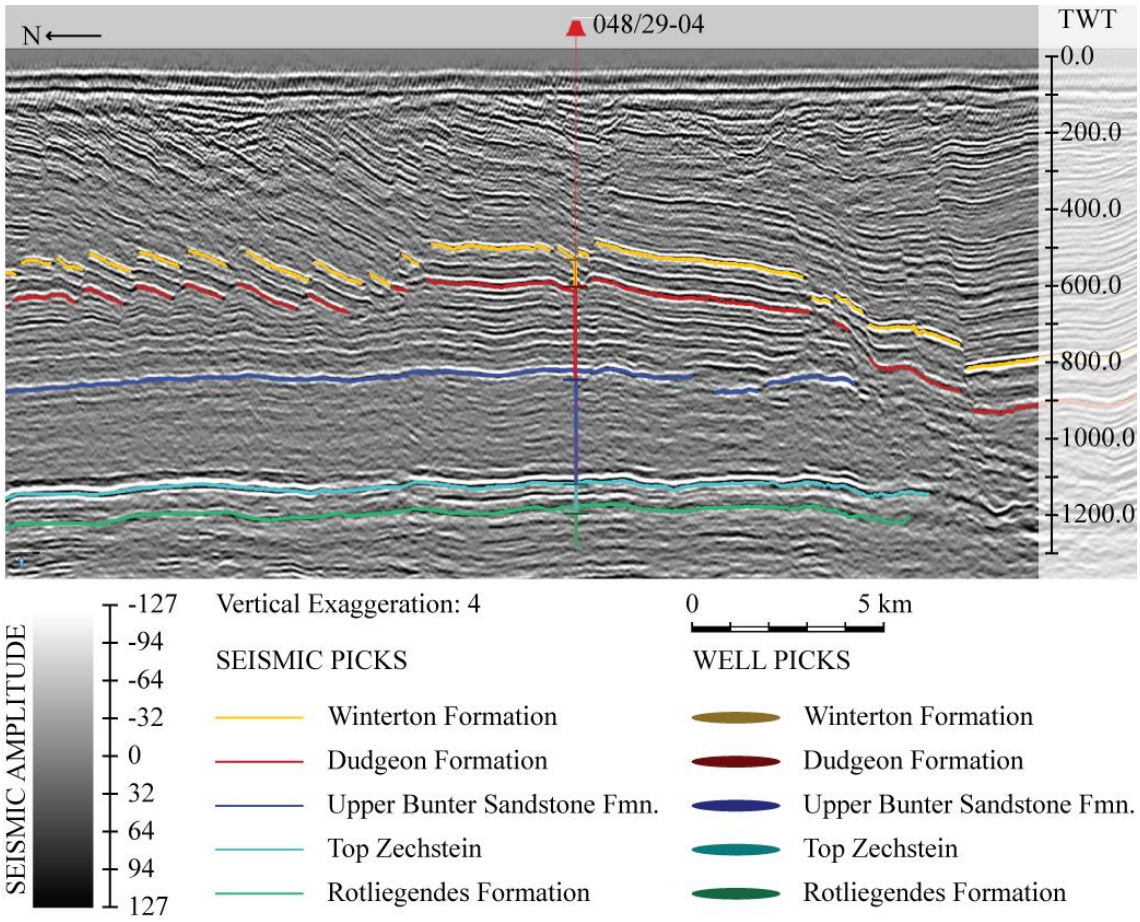

Figure A.3 The N-S oriented seismic section that intercepts well, 048/29-04. The figure shows the well picks of the interpreted layers, illustrated as discs on the well trajectory. The seismic shows the interpretations based on the well picks.

B Appendix B: Time Structure Maps created in Landmark

The following figures show the time structure maps of the seismic interpretations, created in Landmark. Figure B.1 shows the time structure map of the Winterton Formation, Figure B.2 is the Dudgeon Formation, B.3 is the Upper Bunter Sandstone Formation, Figure B.4 is the Top Zechstein, and Figure B.5 is the Rotliegendes Formation.

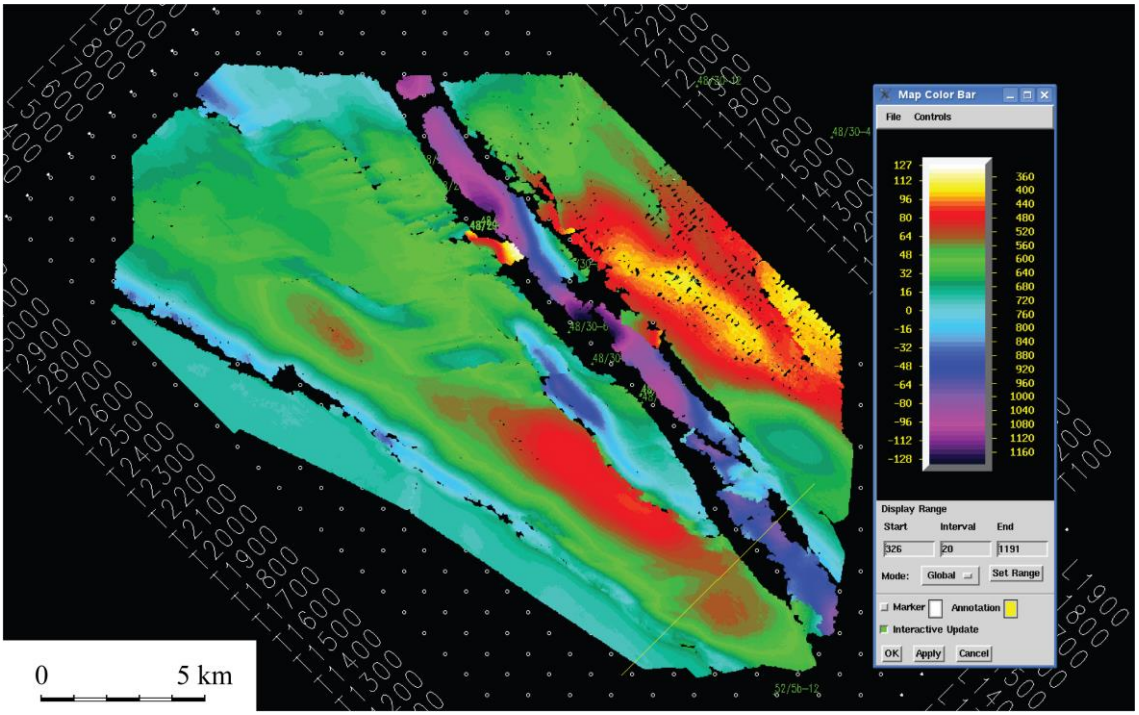

Figure B.1 The time structure map of the Winterton Formation, created in Landmark.

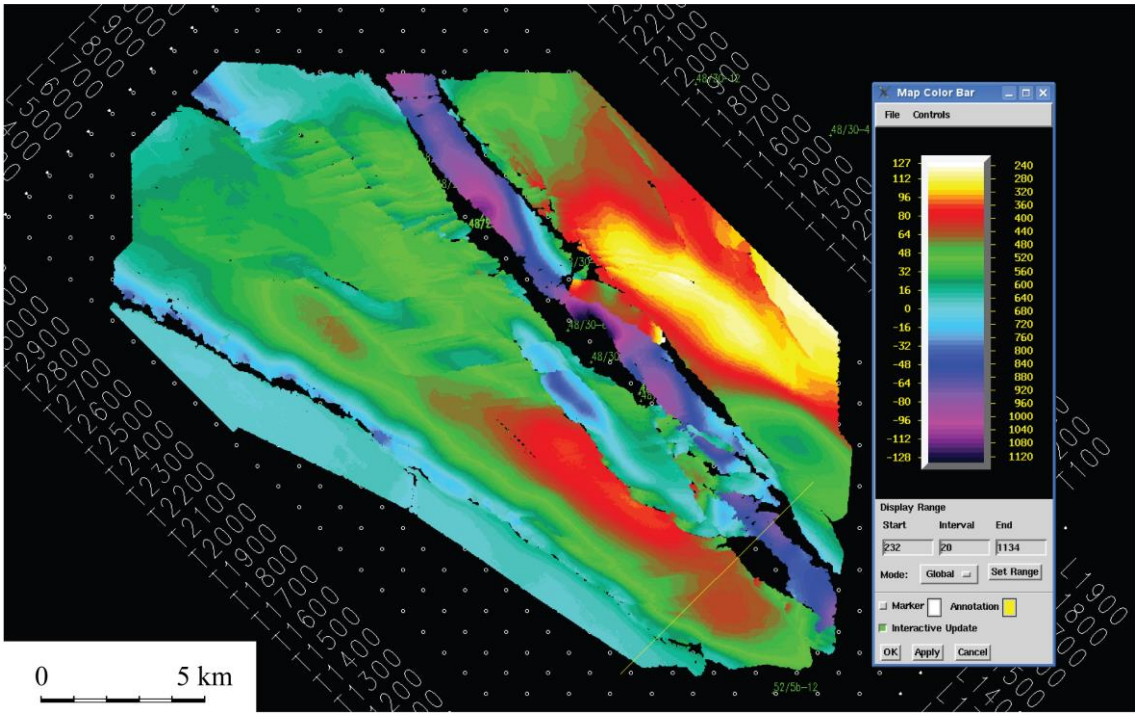

Figure B.2 The time structure map of the Dudgeon Formation, created in Landmark

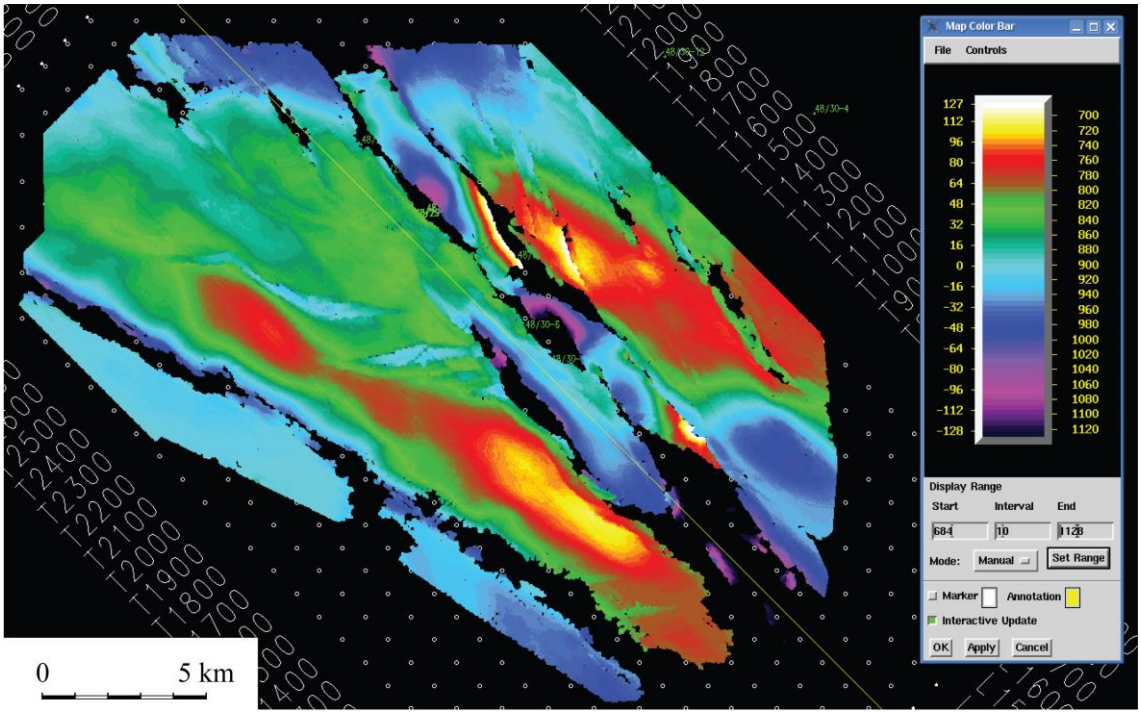

Figure B.3 The time structure map of the Upper Bunter Sandstone Formation, created in Landmark

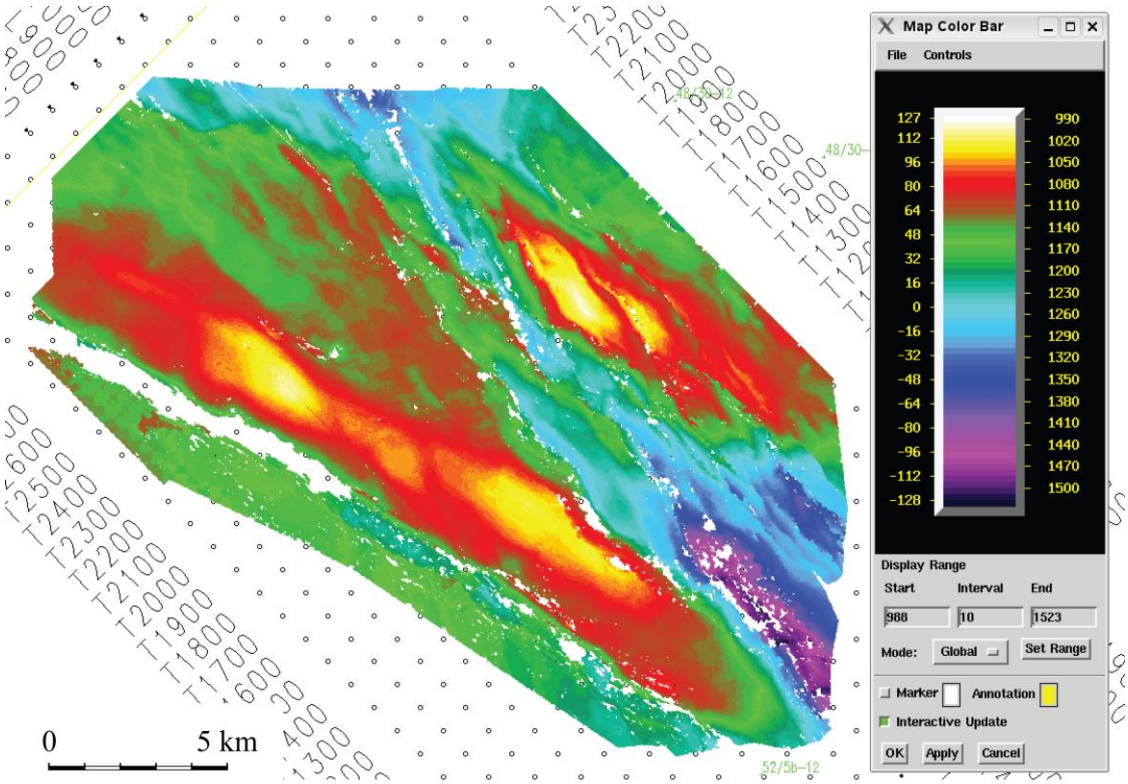

Figure B.4 The time structure map of the Top Zechstein, created in Landmark

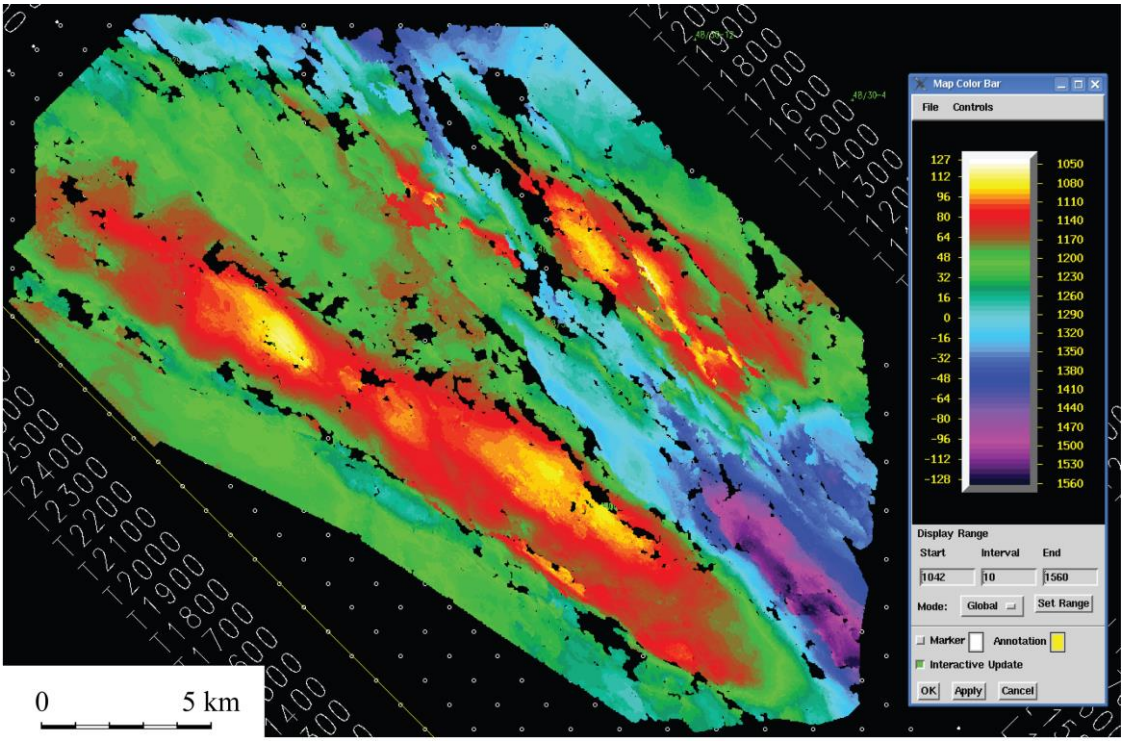

Figure B.5 The time structure map of the Rotliegendes Formation, created in Landmark